Transactions of the ASME

Technical Editor, L. B. FREUND

APPLIED MECHANICS DIVISION

Chairman, CHARLES R. STEELE
Secretary, J. D. ACHENBACH
Associate Editors, S. T. ARIARATNAM
T. BELYTSCHKO
D. B. BOGY
M. M. CARROLL
R. J. CLIFTON
L. B. FREUND
MAURICE HOLT
W. D. IWAN
W. G. KNAUSS
A. S. KOBAYASHI
L. E. MALVERN
R. P. NORDGREN
R. H. PLAUT
R. T. SHIELD
C. T. SUN
J. S. WALKER
G. A. WEMPNER
S. E. WIDNALL

BOARD ON COMMUNICATIONS
Chairman and Vice-President
M. J. RABINS

Members-at-Large
W. BEGELL
W. G. GOTTENBERG
H. C. REEDER
D. KOENIG
M. KUTZ
F. LANDIS
J. W. LOCKE
J. E. ORTLOFF
C. PHILLIPS
K. REID

President, FRANK M. SCOTT
Exec. Dir.
PAUL ALLMENDINGER
Treasurer, ROBERT A. BENNETT

PUBLISHING STAFF
Mng. Dir., Pub., J. J. FREY
Dep. Mng. Dir., Pub.
JOS. SANSONE
Managing Editor,
CORNELIA MONAHAN
Production Editor, SUZANNE MAGIDA
Prod. Asst., MARISOL ANDINO

The Journal of Applied Mechanics (ISSN 0021-8936) is published quarterly for $72 per year by The American Society of Mechanical Engineers, 345 East 47th Street, New York, NY 10017. Second class postage paid at New York, NY and additional mailing offices. POSTMASTER: Send address changes to The Journal of Applied Mechanics, c/o THE AMERICAN SOCIETY OF MECHANICAL ENGINEERS, P.O. Box 3199, Grand Central Station, New York, NY 10163. **CHANGES OF ADDRESS** must be received at Society headquarters seven weeks before they are to be effective. Please send old label and new address.

PRICES: To members, $36.00, annually; to nonmembers, $90.00. Add $6.00 for postage to countries outside the United States and Canada.

INDEXED by the Engineering Index, Inc.

Journal of Applied Mechanics

Published Quarterly by The American Society of Mechanical Engineers

VOLUME 51 • NUMBER 2 • JUNE 1984

TECHNICAL PAPERS

229 The Shear Modulus of Liquid Foam
D. Stamenovic and T. A. Wilson

232 Thin-Shear-Layer Model in Supercritical Hydraulic Flow
H. I. Andersson and T. Ytrehus

239 Hydrodynamical Entrance Length Effects for Duct Flows With Arbitrary Inlet Velocity Profiles
J. P. Du Plessis and D. G. Kröger

244 Bifurication Theory Applied to Oil Whirl in Plain Cylindrical Journal Bearings
C. J. Myers

251 Slow Interactions of Gravity Waves and a Corrugated Sea Bed (84-APM-16)
A. Mitra and M. D. Greenberg

256 The Analysis of Multilayer Elastomeric Bearings (84-APM-19)
J. C. Simo and J. M. Kelly

263 Hydroelastic Instability of Infinite Strips Under Shearing Load on an Elastic Foundation
J. Tani

269 On the Propagation of Bulges and Buckles (84-APM-18)
E. Chater and J. W. Hutchinson

278 On Symmetric Buckling of a Finite Flat-Lying Heavy Sheet (84-APM-13)
C. Y. Wang

283 On the Numerical Implementation of Elastoplastic Models (84-APM-33)
P. J. Yoder and R. G. Whirley

289 The Sliding With Coulomb Friction of a Rigid Indentor Over a Power-Law Inhomogeneous Linearly Viscoelastic Half-Plane
J. R. Walton

294 On the Appearance of the Fractional Derivative in the Behavior of Real Materials (84-APM-23)
P. J. Torvik and R. L. Bagley

299 Applications of Fractional Calculus to the Theory of Viscoelasticity (84-APM-20)
R. C. Koeller

308 The Elastic Inclusion With a Sliding Interface (84-APM-24)
T. Mura and R. Furuhashi

311 The Subsurface Crack Under Conditions of Slip and Stick Caused by a Surface Normal Force (84-APM-17)
F.-K. Chang, M. Comninou, S. Sheppard, and J. R. Barber

317 Subsurface Crack Propagation Due to Surface Traction in Sliding Wear (84-APM-27)
H.-C. Sin and N. P. Suh

324 Contact Between Plates and Unilateral Supports (84-APM-34)
J. P. Dempsey, L. M. Keer, N. B. Patel, and M. L. Glasser

329 The Permanent Deformation of a Cracked Cantilever Struck Transversely at Its Tip
H. J. Petroski

335 On Elastodynamic Diffraction of Waves From a Line-Load by a Crack
A. K. Gautesen

339 Analysis of Tube-Tubesheet Joint Loading Including Thermal Loading (84-APM-15)
A. I. Soler and Xu Hong

345 Investigation of Stress Wave Propagation Through Intersecting Bars (84-APM-22)
K. R. Y. Simha and W. L. Fourney

354 Stability and Vibrations of Geometrically Nonlinear Cylindrically Orthotropic Circular Plates (84-APM-21)
D. Shilkrut

361 Finite Amplitude Vibrations of a Body Supported by Simple Shear Springs (84-APM-28)
M. F. Beatty

367 Endochronic Theory of Cyclic Plasticity With Applications (84-APM-31)
K. C. Valanis and C. F. Lee

375 Three-Dimensional Harmonic Vibrations of a Circular Beam
D. E. Panayotounakos and P. S. Theocaris

383 Influence of Geometric Imperfections and In-Plane Constraints on Nonlinear Vibrations of Simply Supported Cylindrical Panels (84-APM-14)
D. Hui

391 A Method for Reducing the Order of Nonlinear Dynamic Systems (84-APM-32)
S. F. Masri, R. K. Miller, H. Sassi, and T. K. Caughey

399 The Origin of Stability Indeterminacy in a Symmetric Hamiltonian (84-APM-25)
M. R. Hyams and L. A. Month

406 Javelin Dynamics With Measured Lift, Drag, and Pitching Moment
M. Hubbard and H. J. Rust

(Contents continued on Inside Back Cover)

CONTENTS (CONTINUED)

409 **A Parametric Solution to the Elastic Pole-Vaulting Pole Problem**
G. M. Griner

415 **Dynamics of Gyroelastic Continua**
G. M. T. D'Eleuterio and P. C. Hughes

423 **Interactions Between Self and Parametrically Excited Motions in Articulated Tubes** (84-APM-30)
A. K. Bajaj

430 **Another Theorem for Determining the Definiteness of Sign of Functions and Its Applications to the Stability of Permanent Rotations of a Rigid Body** (84-APM-26)
Z.-M. Ge and Y.-J. Wu

BRIEF NOTES

The Equations of Motion of Nonlinear Nonholonomic Variable Mass System With Applications 435
Z.-M. Ge

Transverse Projectile Impacts on Beams 437
R. L. Woodward

On Asymptotic Approximations to Beam Model Shapes 439
E. H. Dowell

Stability of a Rotating Ring Under External Pressure 439
C. Y. Wang

440 Laminar Wall Jet of a Non-Newtonian Fluid Over a Curved Surface
Dr. R. S. R. Gorla

443 Divergence of Cantilever Columns Under Combined Conservative and Follower Loads
A. H. Flax

444 On a Variational Principle for Elastic Displacements and Pressure
E. Reissner

DISCUSSIONS

446-449 Discussion on previously published papers by **T. Yabuta, N. Yoshiza**, and **N. Kojima, D. J. Inman** and **I. Orabi**, and **J. Casey** and **P. M. Naghdi**

BOOK REVIEWS

450 ***Vortex Flows in Nature and Technology*** by **Hans J. Lugt** . . . Reviewed by **H. Aref**

Research Techniques in Nondestructive Testing edited by **R. S. Sharpe** . . . Reviewed by **J. D. Achenbach**

451 ***An Introduction to Macromolecules Second Edition*** by **Leo Mandelkern** . . . Reviewed by **J. H. Weiner**

Probabilistic Methods in the Theory of Structures by **Isaac Elishakoff** . . . Reviewed by **J. T. P. Yao**

452 ***Numerical Solutions of Partial Differential Equations*** edited by **J. Noye** . . . Reviewed by **M. Holt**

Books received by the office of the Technical Editor

ERRATA

453 Erratum on "Compression of Fluid-Filled Spherical Shells by Rigid Indentors," by L. A. Taber and published in the December 1983 Issue

Erratum on "Vibrations of a Free Rectangular Parallelpiped," by J. R. Hutchinson and S. D. Zillmer and published in the March 1983 Issue

---

243, 250, 282	Worldwide Mechanics Meeting List
231, 255, 268, 277, 323	Applied Mechanics Symposium Proceedings
334, 344, 374, 390, 429, 449	Applied Mechanics Symposium Proceedings
238	Change of Address Form
454	Reference Citation Format

The Shear Modulus of Liquid Foam

D. Stamenovic

T. A. Wilson

Department of Aerospace Engineering
and Mechanics,
University of Minnesota,
Minneapolis, Minn. 55455

A strain energy function for liquid foam is formulated by modeling foam as a collection of randomly oriented surfaces with surface tension on the faces. The surfaces are assumed to follow the mean strain. It is assumed that surface forces equilibriate between neighboring elements and hence that the value of surface tension γ is the same on all faces and a function of total surface area. In particular, an expansion of the strain energy function in powers of the strain is used to obtain the value for the shear modulus in the linear elasticity approximation. The predicted value of the shear modulus is $4/15\ \gamma S/V$ where S/V is the surface to volume ratio or $2/5\ \Delta P$, where ΔP is the overpressure of the gas trapped in the foam. In rheometric tests, foam was found to behave as a viscoelastic material. The shear modulus that describes the initial elastic response was found to be about 84 percent of the predicted value.

Introduction

Foam appears to be capable of maintaining its shape if the loading is small. We therefore developed a description of foam as an elastic material. A strain energy function was calculated from a model for the microstructure, and a shear modulus, for small deformations, was obtained from the strain energy. The predicted shear modulus was found to be proportional to surface tension and the surface-to-volume ratio in the undeformed state was found to be independent of the surface tension-surface area properties of the surface-active foaming agent. Surface tension and the surface-to-volume ratio would be difficult to measure. However, the overpressure of the gas trapped in a foam is also proportional to the same parameters and is easily measured. Therefore, the prediction of the model was tested by measuring the ratio of the shear modulus to the overpressure.

The Strain Energy

The air cells of a foam are polyhedra with a variable number of faces. The faces are nearly flat polygons with a variable number of sides. Three faces meet along a line of intersection and four of these lines meet at the corners of adjacent cells. A surface-active agent that lowers surface tension at the air-liquid interface provides the stability of the thin fluid layers that form the cell walls. The mechanical properties of the foam are a result of the surface tension forces on the faces of the cells and the pressure in the gas in the cells.

In the modeling, this microstructure is pictured as a network of randomly oriented surfaces, and the strain energy of the equivalent continuum is obtained by summing the surface energies of the surface elements in the network and the internal energy of the trapped gas. The increment of work done on a surface with surface tension γ during an incremental increase in area ds is $\gamma\ ds$ where γ may depend on surface area. As the foam deforms, the surface elements are assumed to follow the continuum strain field. Equation (1) describes the ratio of deformed to initial area s/s_0 of a surface element with a normal vector that initially lies in a direction described by the polar and azimuthal angles, ϕ and ψ, with respect to the principal axes of the deformation.

$$s/s_0 = [(\alpha_1\alpha_2\cos\ \phi)^2 + (\alpha_2\alpha_3\sin\ \phi\ \cos\ \psi)^2 + (\alpha_3\alpha_1\sin\ \phi\ \sin\ \psi)^2]^{1/2} \tag{1}$$

In this equation, α_1, α_2, and α_3 are the stretch ratios in the principal directions. The ratio of the total surface areas in the deformed and initial states S/S_0 is obtained by integrating equation (1) over all orientations.

$$S/S_0 = (1/2\pi)\int_0^{2\pi}\int_0^{\pi} (s/s_0)\ \sin\ \phi\ d\phi\ d\psi \tag{2}$$

It is assumed that surfactant flows easily between the surfaces of neighboring faces and as a result, surface tension is the same on neighboring faces. It is assumed that the orientations of the faces of each cell form a representative sample and therefore, as the foam deforms and surface area changes, surface tension changes but remains uniform throughout the foam, and its value is determined by the average or overall surface area, not the area of an individual face.

The energy per unit reference volume of foam W is the sum of the surface energy and the internal energy of the trapped gas.

$$W = (S_0/V_0)\int_1^{S/S_0} \gamma\ d(S/S_0) - \int_1^{V/V_0} p\ d(V/V_0) \tag{3}$$

In equation (3), p is the pressure of the trapped gas, S and V

Contributed by the Applied Mechanics Division for publication in the JOURNAL OF APPLIED MECHANICS.

Discussion on this paper should be addressed to the Editorial Department, ASME, United Engineering Center, 345 East 47th Street, New York, N.Y. 10017, and will be accepted until two months after final publication of the paper itself in the JOURNAL OF APPLIED MECHANICS. Manuscript received by ASME Applied Mechanics Division, June, 1983; final revision, October, 1983.

are the surface area, and volume of the foam and subscript zero denotes the reference state. The constitutive equation is obtained from the derivatives of W.

$$T_1 = \frac{1}{\alpha_2 \alpha_3}\left[\frac{S_0}{V_0}\gamma\frac{\partial(S/S_0)}{\partial\alpha_1} - p\frac{\partial(V/V_0)}{\partial\alpha_1}\right] \tag{4}$$

The area ratio is given by equations (1) and (2), and the volume ratio is $\alpha_1\ \alpha_2\ \alpha_3$. The functions $\gamma(S/S_0)$ and $p(V/V_0)$ for the deformation process must be known. The zeroth and first-order terms in an expansion of equation (4) in powers of $(\alpha - 1)$ are given by equation (5)

$$T_1 = [(2\gamma\ S_0/3V_0) - p_0] + \{-V_0(dp/dV)_0 + [-(2/5)\gamma_0 + (4/9)d\gamma/d(S/S_0)|_0][S_0/V_0]\}[\alpha_1 + \alpha_2 + \alpha_3 - 3] + (8/15)(\gamma_0 S_0/V_0)[\alpha_1 - 1] \tag{5}$$

The following values for the derivatives of S/S_0 with respect to α_i, evaluated at $\alpha_i = 1$, were used to obtain equation (5).

$$\partial(S/S_0)/\partial\alpha_i|_0 = 2/3$$

$$\partial^2(S/S_0)/\partial\alpha_i\partial\alpha_j|_0 = \begin{cases} 2/15 & i=j \\ 4/15 & i\neq j \end{cases} \tag{6}$$

In the reference state, the stress must match ambient pressure. Therefore,

$$\Delta p_0 = 2\gamma_0 S_0/3V_0 \tag{7}$$

the overpressure of the trapped gas Δp_0 is called capillary pressure [1]. Equation (7) has been obtained from an energy balance [2], and from a calculation of the force per unit area transmitted across a plane by surface tension on randomly oriented surfaces intersecting the plane [3]. The Lamé coefficients can be obtained from the coefficients of the linear terms in $(\alpha_i - 1)$ in equation (5). They are

$$\lambda = -V_0(dp/dV)_0 + [-(2/5)\gamma_0 + (4/9)d\gamma/d(S/S_0)|_0](S_0/V_0) \tag{8}$$

$$\mu = (4/15)(\gamma_0 S_0/V_0) \tag{9}$$

The shear modulus μ is independent of $d\gamma/d(S/S_0)$ because surface area does not change to order $(\alpha - 1)$ in shear. The bulk modulus is $\lambda + (2/3)\mu = -V_0(dp/dV)_0 + [-(2/9)\gamma_0 + (4/9)d\gamma/d(S/S_0)|_0](S_0/V_0)$. This expression could also be obtained by differentiating the prestress with respect to volume. For typical values of the parameters γ and S_0/V_0, the bulk modulus is dominated by the bulk modulus of the trapped gas.

Resistance to shear is provided entirely by surface tension, and the prediction of a shear modulus for foam given by equation (9) is a new result. A direct experimental test of equation (9) would be difficult because of the difficulty of measuring γ and S_0/V_0. However, capillary pressure is also proportional to the product $\gamma_0\ S_0/V_0$ and is easily measured. Thus, the objective of the experimental work was to test the prediction, $\mu/\Delta p_0 = 0.4$.

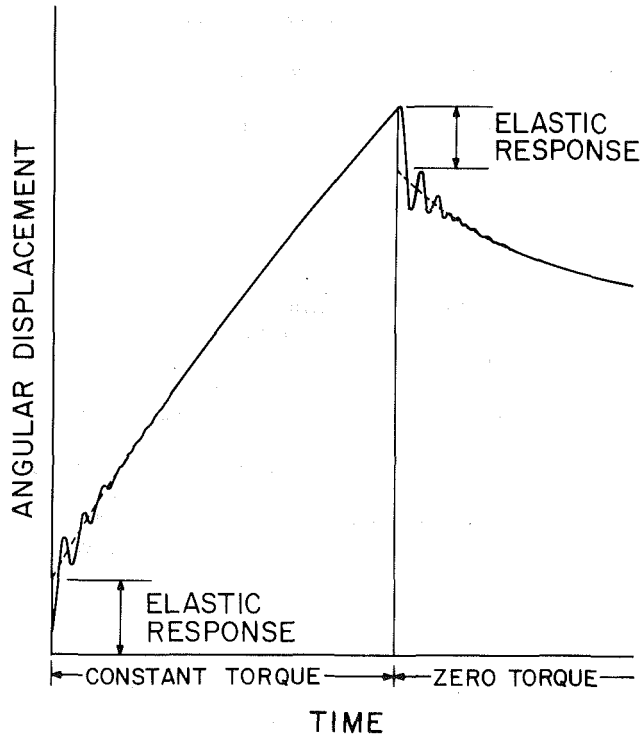

Fig. 1 Angular twist of foam cylinder in response to a constant applied torque

Experimental Testing

A foaming liquid was made of a mixture of pure dry sodium oleate, distilled water, and glycerine, according to the recipe of Courant [4]. Foam was formed by beating the liquid with an electric mixer.

Capillary pressure was measured by the method of Aleinikov [1]. A container was filled with foam and sealed, and the increase in pressure in the container as the foam decayed was measured. Seven samples were tested and Δp_0 was found to be 155 ± 21 N/m^2.

The shear behavior of the foam was measured with a *Deer Rheometer*. The space between the fixed and rotating plates of

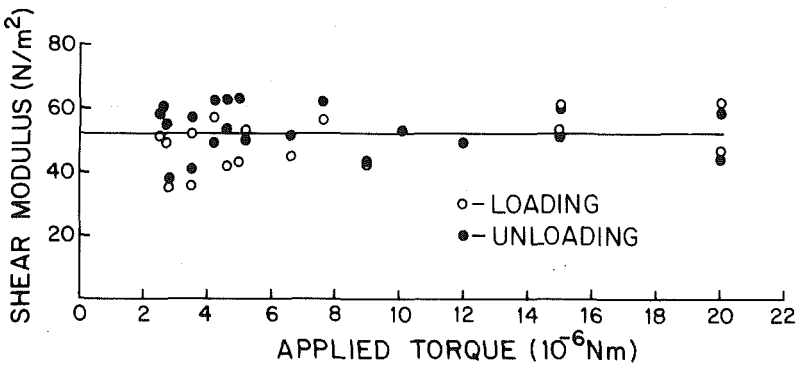

Fig. 2 Shear modulus obtained from loading and unloading curves plotted against applied torque

the rheometer was filled with foam. The sample formed a cylinder with a diameter of 5 cm and a height of 1 cm. A torque M was applied to the upper plate, and its angular deflection $\theta(t)$ was recorded. The torque was released, the response measured, and a different constant torque applied. A representative response curve is shown in Fig. 1. The short-time response to the applied torque was limited by the moment of inertia of the apparatus. After the initial sharp increase in angular deflection and the ensuing damped oscillation, the angular deflection continued to increase, reaching a linear increase with time. The dashed lines shown in Fig. 1 were drawn by extrapolating back through the oscillations by eye, and these dashed lines were used to describe the response of the foam to an applied torque.

For the range of torques that could be covered with the rheometer, the foam samples behaved as a viscoelastic material. Apparently, the geometry of the connection of the cell faces changes under shear, allowing cells to migrate relative to their neighbors at different heights. The initial jump in angular deflection was chosen as the elastic response to be compared with the predictions of the model. As shown in Fig. 2, the shear modulus, calculated from the intitial deflection, the applied torque, and the dimensions of the sample is the same for both loading and unloading and is independent of the magnitude of the applied torque. The value obtained for the shear modulus from these experiments is $51.9 \pm 7.7\ \mathrm{N/m^2}$.

Discussion

The experimentally determined ratio of shear modulus to capillary pressure is 0.33 or 84 percent of the predicted value of 0.4. The value of the shear modulus predicted from the model was expected to be high because of the assumption that the individual surface elements of the foam follow the continuum strain field. The equilibrium configuration of the faces under a shear deformation of the foam, assuming no slipping of the lines of intersection, may be different from the assumed one. The equilibrium configuration is the minimum energy configuration. If the assumed configuration is different from the equilibrium configuration, the strain energy calculated from the assumed configuration must be greater than the strain energy for the equilibrium configuration, and hence, the value of the shear modulus deduced from the model may be high.

This work was undertaken as a first step in developing a model for lung parenchyma, which has a foam-like structure with significant surface energy. The ratio of the shear modulus of parenchyma to transpulmonary gas pressure has been found to be a constant, independent of the initial state of lung inflation [5]. However, the value of the ratio is 0.7, about twice the value for liquid foam, and it will be necessary to include the effects of tissue forces in modeling lung parenchyma.

Acknowledgments

We thank Professor C. Macosko for his help with the rheometry experiments. The work was supported by grant HL 21854 from the USDHHS.

References

1 Bikerman, J. J., *Foams*, Springer-Verlag, New York, 1973.

2 Ross, S., "Bubbles and Foam—New General Law," *Industrial and Engineering Chemistry*, Vol. 61, No. 10, 1969, pp. 48–57.

3 Hoppin, F. G., Jr., and Hildebrandt, J., "Mechanical Properties of the Lung," *Bioengineering Aspects of the Lung*, West, J. B., ed., Marcel Dekker, New York, 1979, pp. 83–162.

4 Courant, R., "Soap Film Experiments With Minimal Surfaces," *The American Mathematical Monthly*, Vol. 47, 1940, pp. 167–174.

5 Hajji, M. A., Wilson, T. A., and Lai-Fook, S. J., "Improved Measurements of Shear Modulus and Pleural Membrane Tension of the Lung," *Journal of Applied Physiology: Respiratory, Environmental and Exercise Physiology*, Vol. 47, 1979, pp. 175–181.

H. I. Andersson
Research Assistent.

T. Ytrehus
Professor.

Institutt for Mekanikk,
Norwegian Institute of Technology,
7034 Trondheim-NTH, Norway

Thin-Shear-Layer Model in Supercritical Hydraulic Flow

A supercritical, free-surface flow on an adverse incline has been modeled as a "thin-shear-layer" with algebraic eddy-viscosity included to account for turbulent shear stresses. The model has been solved numerically by a finite-difference technique for parabolic systems. Turbulent-viscous and adverse gravity effects are found to interact via the free-surface behavior in a way that leads to breakdown of the steady two-dimensional flow. Computed breakdown positions, velocity, and flow depth developments are compared with experimental and semi-empirical hydraulic results.

1 Introduction

In a classical hydraulic situation, liquid flows on a downward slope under the driving action of gravity. If the velocity is supercritical, the flow development including the location of the free surface, is completely independent of conditions prevailing further downstream in the system. In the less classical situation of supercritical flow along an upward slope, a question of fundamental nature then arises: As to what elevation will the supercritical flow proceed for given kinetic energy at the entrance? Simple experiments [1, 2] indicate that this height is of the order of 0.6 of the inlet kinetic energy height at typical supercritical flow conditions. Also, it would be of some interest to study the physical phenomenon that eventually terminates the supercritical upward motion and leads to a breakdown of the flow.

To this end we consider a physical system as sketched in Fig. 1, where liquid is emanating under total head H_t from a horizontal slit at the bottom of a settling tank and enters a wedge-shaped incline of height $L \cdot \sin\alpha < H_t$, L being the length and α being the angle of inclination of the incline. For H_t sufficiently large, the flow remains supercritical all along the incline and therefore shoots over the wedge. By slowly reducing H_t, a critical state is reached at which a breakdown of the flow – apparently in the form of an unsteady hydraulic jump originating at the top of the incline – sets in. The jump immediately rushes down the incline and completely quenches the supercritical motion. This flow behavior was experimentally verified by Madsen [1] and by Andersson et al. [2].

Since the free-surface flow up along the incline is decelerated by gravity, the conditions for a two-dimensional boundary layer separation are present. Actual numerical predictions based on turbulent boundary layer considerations [2] do indeed yield separation points that are sufficiently close to the observed flow breakdown position that the possibility of a separation-induced breakdown cannot be ruled out. In the boundary layer approach, the free stream region was assumed irrotational and laminar. Experimental results [1, 2], however, indicated that at any cross section the free stream zone would contain turbulence generated at sections further upstream. According to these observations, a description of the flow in terms of classical boundary layer theory cannot be justified.

In the present paper, therefore, we resort to a theoretical description of the flow along the adverse incline based on the more general concept of a "thin-shear-layer" (TSL), see e.g., Cebeci and Bradshaw [3]. In this model the viscous and turbulent shear effects are allowed to extend all the way from the solid boundary out to the free surface. The model is based on the boundary layer approximation to the Navier-Stokes equations in primitive variables and with an algebraic two-layer eddy-viscosity formulation for the turbulent shear-stresses incorporated. This description contains several distinct features which are of basic importance to the physical problem considered. The turbulent-viscous and the adverse gravity effects, which are characterized, respectively, by the Reynolds number and the Froude number, are allowed to interact through the free surface behavior. This viscous-gravity coupling is of particular importance for the

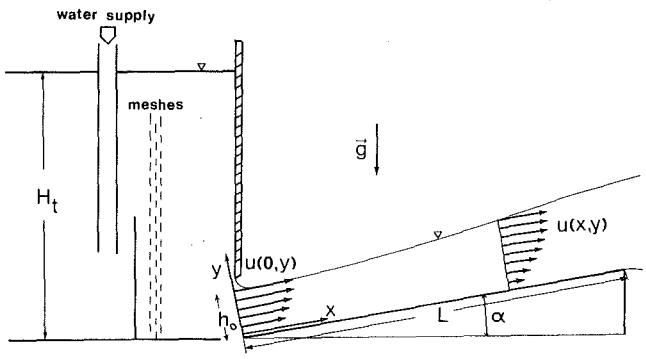

Fig. 1 Sketch of the experimental flume and coordinate system

Contributed by the Applied Mechanics Division for publication in the JOURNAL OF APPLIED MECHANICS.

Discussion on this paper should be addressed to the Editorial Department, ASME, United Engineering Center, 345 East 47th Street, New York, N.Y. 10017, and will be accepted until two months after final publication of the paper itself in the JOURNAL OF APPLIED MECHANICS. Manuscript received by ASME Applied Mechanics Division, March, 1983; final revision, October, 1983.

assessment of the flow breakdown conditions. According to the present model the breakdown occurs when the local Froude number is close to 2, apparently after a dramatic increase in the surface elevation has caused the flow to separate at the bottom.

The actual numerical calculations are based on a finite-difference method with the Box scheme [4, 5] and the Mechul function approach [6] employed in an iterative scheme to determine the elevation of the free surface. The method has been tested on classical laminar film flow [7, 8], and direct comparisons are made with the experiments of Madsen [1] for hydraulic flow on an adverse incline.

2 Theoretical Model

We consider, as illustrated in Fig. 1, the fully turbulent flow along an adverse incline. It is assumed that the free surface is waveless, and that the flow is of the "thin-shear-layer" type. The governing equations for two-dimensional steady flow may thus be written as follows:

$$\frac{\partial u}{\partial x} + \frac{\partial v}{\partial y} = 0 \tag{1}$$

$$u\frac{\partial u}{\partial x} + v\frac{\partial u}{\partial y} = -\frac{1}{\rho}\frac{\partial p}{\partial x} - g\sin\alpha + \frac{1}{\rho}\frac{\partial}{\partial y}\left[\mu\frac{\partial u}{\partial y} - \rho\overline{u'v'}\right] \tag{2}$$

$$0 = -\frac{1}{\rho}\frac{\partial p}{\partial y} - g\cos\alpha \tag{3}$$

Here, equation (1) is the continuity equation, and equations (2) and (3) represent the simplified momentum equations in the x and y-directions, respectively. u and v are the mean velocity components in the streamwise and cross-stream directions, respectively, and $\rho\overline{u'v'}$ is the Reynolds stress due to turbulent fluctuations u' og v'. ρ is the density, μ is the dynamic viscosity of the liquid, and g is the gravitational acceleration.

At the channel bed the usual impermeability and no-slip conditions are applied, i.e.

$$u(x,y) = v(x,y) = 0 \quad \text{at } y = 0 \tag{4}$$

The normal and tangential stress conditions at the free surface can be approximated by:

$$p(x,y) = p_0 \qquad \text{at } y = h(x) \tag{5}$$

$$\frac{\partial u}{\partial y} = 0 \qquad \text{at } y = h(x) \tag{6}$$

where p_0 is the ambient pressure. Further, the conservation of the flow rate per unit channel width gives the additional condition:

$$\int_0^{h(x)} u(x,y)dy = Q \tag{7}$$

Since the system of governing equations (1)–(3) is of parabolic type, an upstream velocity profile $u(0,y)$ must be specified as "initial condition."

To solve the equations (1)–(3) subject to the boundary conditions (4)–(7), it is convenient to relate the Reynolds stress term to the mean velocity distribution by the relation

$$-\rho\overline{u'v'} = \rho\epsilon\frac{\partial u}{\partial y} \tag{8}$$

Here, the eddy-viscosity ϵ can furtermore be related to local mean flow properties. In the present paper we are using a modified version of the algebraic two-layer eddy-viscosity model suggested by Cebeci and Smith [9] and Cebeci [10] for turbulent boundary layers. According to this formulation the turbulent boundary layer is regarded as a composite layer characterized by inner and outer regions:

$$\epsilon_i = \kappa u_\tau y\left[1 - \exp(-y\cdot u_\tau/26\nu)\right]^2 \tag{9}$$

$$\epsilon_0 = \beta u_\tau h \tag{10}$$

where $\nu = \mu/\rho$ is the kinematic viscosity, $u_\tau = (\tau_w/\rho)^{1/2}$ is the friction velocity and $\tau_w = \mu(\partial u/\partial y)_{y=0}$ is the shear stress at the bottom. κ and β are empirical constants, set equal to 0.40 and 0.07, respectively, in accordance with e.g. [3]. The inner eddy-viscosity expression (9) is matched with the outer region expression (10) by the requirement of continuity in ϵ.

Since the present analysis is restricted to free-surface flows of the "thin-shear-layer" type, the flow has a predominant direction and the flow depth $h(x)$ is small compared to a typical length in the streamwise direction. With this assumption, dimensionless variables are introduced, defined by

$$\xi = \frac{x}{h_0} \qquad \eta = \frac{y}{h_0}\sqrt{Re_0} \tag{11}$$

$$\bar{u} = \frac{u}{u_0}, \qquad \bar{v} = \frac{v}{u_0}\sqrt{Re_0}, \qquad \bar{p} = \frac{p - p_0}{\rho u_0^2} \tag{12}$$

where u_0 is the initial mean velocity, h_0 is the initial flow depth, and $Re_0 = Q/\nu$. It is furthermore convenient to introduce a dimensionless stream function $f(\xi,\eta)$ such that

$$\bar{u} = \frac{\partial f}{\partial \eta} \qquad \bar{v} = -\frac{\partial f}{\partial \xi} \tag{13}$$

Then, the momentum equations (2) and (3) and the boundary conditions (4)–(7) transform into

$$(bf'')' = f'\frac{\partial f'}{\partial \xi} - f''\frac{\partial f}{\partial \xi} + F_0^{-2}\cdot\tan\alpha + \frac{\partial \bar{p}}{\partial \xi} \tag{14}$$

$$\bar{p}' = -F_0^{-2}\cdot Re_0^{-1/2} \tag{15}$$

$$f(\xi,0) = f'(\xi,0) = 0 \tag{16}$$

$$f''(\xi,\delta) = 0 \tag{17}$$

$$f(\xi,\delta) = Re_0^{1/2} \tag{18}$$

$$\bar{p}(\xi,\delta) = 0 \tag{19}$$

where the primes denote differentiation with respect to η. The coefficient $b = 1 + \epsilon/\nu$ is obtained from the eddy-viscosity model, equations (9) and (10). F_0 is the initial Froude number defined by

$$F_0 = u_0/(gh_0\cos\alpha)^{1/2}, \tag{20}$$

and $\delta(\xi)$ denotes the value of the cross-stream coordinate η at the free surface.

3 Numerical Formulation and Solution Procedure

It is obvious that the problem defined by equations (14)–(19) is similar to a steady two-dimensional boundary layer problem. The streamwise pressure gradient term $\partial\bar{p}/\partial\xi$ in equation (14) cannot, however, be prescribed as in classical boundary layer theory. The integration of the cross-stream momentum equation (15) subject to the boundary condition (19) reveals that $\partial\bar{p}/\partial\xi$ is related to the unknown flow depth by the equation

$$\frac{\partial \bar{p}}{\partial \xi} = F_0^{-2}Re_0^{-1/2}\frac{d\delta}{d\xi} = F_0^{-2}\frac{dh}{dx} \tag{21}$$

We therefore have a free surface in the problem whose position must be obtained with the solution. In the "rigid lid"

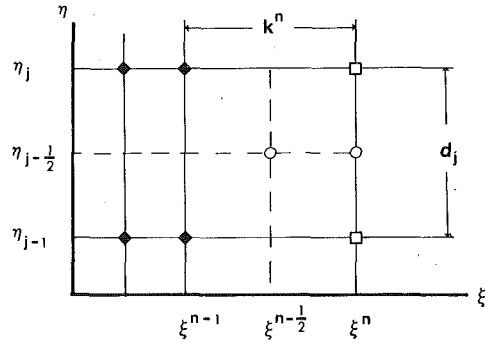

Fig. 2 Net rectangle for the Box method.
♦ known; □ unknown; ○ centering.

approximation recently used by Rastogi and Rodi [11] and Leschziner and Rodi [12], the free surface is replaced by a fictitous plane boundary parallel to the channel bed, i.e., $d\delta/d\xi = 0$, and the pressure is treated as an unknown variable. As a result of this constraint on the flow, a nonzero pressure gradient $\partial\bar{p}/\partial\xi$ is predicted at the surface, and this pressure gradient accounts for, and can be interpreted as, the slope of the surface [12]. Thus, the success of the "rigid lid" approximation indicates that the true surface position $\delta(\xi)$ can be obtained locally by successive iterations until the free surface condition (19) has been satisfied.

According to the Mechul function approach introduced by Cebeci and Keller [6], we treat $\bar{p}(\xi,\eta)$ as an unknown quantity, imposing numerically equation (15) at each ξ-station (see also [5] and [13]). To solve the parabolic system of partial differential equations (14)–(15) subject to the boundary conditions (16)–(19), we use an implicit two-point finite-difference method devised by Keller [4], by marching the solution in the streamwise direction. This method, frequently referred to as the Box scheme, is unconditionally stable and permits arbitrary net spacings. Furthermore, it has second-order accuracy in all variables, and Newton's method—which converges quadratically—is used to solve the nonlinear difference equations.

First, we write the governing partial differential equations in the form of a first-order system, introducing new dependent variables $g(\xi,\eta)$ and $q(\xi,\eta)$:

$$f' = g \tag{22}$$

$$g' = q \tag{23}$$

$$(bq)' = g\frac{\partial g}{\partial \xi} - q\frac{\partial f}{\partial \xi} + F_0^{-2}\cdot\tan\alpha + \frac{\partial \bar{p}}{\partial \xi} \tag{24}$$

$$\bar{p}' = -F_0^{-2}\, Re_0^{-1/2} \tag{25}$$

with the boundary conditions

$$f(\xi,0) = g(\xi,0) = 0 \tag{26}$$

$$q(\xi,\delta) = 0 \tag{27}$$

$$f(\xi,\delta) = \mathrm{Re}_0^{1/2} \tag{28}$$

$$\bar{p}(\xi,\delta) = 0 \tag{29}$$

Next, finite differences are introduced on discrete net points

$$\xi^0 = 0; \quad \xi^n = \xi^{n-1} + k^n \qquad n = 1,2,\ldots N \tag{30}$$

$$\eta_0 = 0; \quad \eta_j = \eta_{j-1} + d_j \qquad j = 1,2,\ldots H \tag{31}$$

using the computational box shown in Fig. 2. Here n and j are sequence numbers, and the values of f, g, q, and $\bar{p}$ at the net point (ξ^n, η_j) are written as f_j^n, g_j^n, q_j^n and $\bar{p}_j^n$. The grid spacing across the flow is varied according to the geometric progression

$$d_j = d_1\cdot(K)^{j-1} \quad j = 1,2,\ldots H \tag{32}$$

with K being the constant ratio between two successive steps, $K = d_j/d_{j-1} = 1.05$. The mesh size next to the free surface is, however, restricted by

$$d_H \le d_1\cdot(K)^{H-1} \tag{33}$$

to satisfy the condition $\eta_H = \delta(\xi^n)$, i.e., the sequence number H denotes a net point at the free surface. In the streamwise direction a constant step length k^n in the range $h_0 - 10h_0$ is used, except close to the entrance where a finer spacing is employed.

Following reference [3], equations (22), (23), and (25) are discretized using centered-difference derivatves for the midpoint $(\xi^n, \eta_{j-1/2})$, whereas in equation (24) the derivatives are centered about the midpoint $(\xi^{n-1/2}, \eta_{j-1/2})$. Thus, values at the corners, only, of the box in Fig. 2 are involved. The difference approximations to the governing equations are then as follows:

$$(f_j^n - f_{j-1}^n)/d_j = \frac{1}{2}(g_j^n + g_{j-1}^n) \tag{34}$$

$$(g_j^n - g_{j-1}^n)/d_j = \frac{1}{2}(q_j^n + q_{j-1}^n) \tag{35}$$

$$(b_j^n q_j^n - b_{j-1}^n q_{j-1}^n)/d_j - \gamma(g^2)_{j-1/2}^n + \gamma(f_q)_{j-1/2}^n$$
$$-\gamma[f_{j-1/2}^{n-1} q_{j-1/2}^n - q_{j-1/2}^{n-1} f_{j-1/2}^n + 2\bar{p}_{j-1/2}^n] = R_{j-1/2}^{n-1} \tag{36}$$

$$(\bar{p}_j^n - \bar{p}_{j-1}^n)/d_j = -F_0^{-2}\, Re_0^{-1/2} \tag{37}$$

where

$$\gamma = \frac{1}{k^n} \tag{38}$$

$$R_{j-1/2}^{n-1} = -(b_j^{n-1}\, q_j^{n-1} - b_{j-1}^{n-1}\, q_{j-1}^{n-1})/d_j + 2F_0^{-2}\cdot\tan\alpha$$
$$+\gamma[-(g^2)_{j-1/2}^{n-1} + (qf)_{j-1/2}^{n-1} - 2\bar{p}_{j-1/2}^{n-1}] \tag{39}$$

and the notation

$$f_{j-1/2} = \frac{1}{2}(f_j + f_{j-1}) \tag{40}$$

is employed for quantities midway between net points. The boundary conditions (26)–(29) yield at $\xi = \xi^n$:

$$f_0^n = g_0^n = 0 \tag{41}$$

$$q_H^n = 0 \tag{42}$$

$$f_H^n = Re_0^{1/2} \tag{43}$$

$$\bar{p}_H^n = 0 \tag{44}$$

Since there is one more boundary condition given by equations (41)–(44) than the number of first-order equations, we use the additional condition (44) to determine the location of the surface. After having made an initial guess $\eta_H^{(0)}$ for the surface coordinate at a streamwise location ξ^n, and having solved the nonlinear system (34)–(37) with boundary conditions (41)–(43), successive iterations of the type

$$\eta_H^{(i+1)} = \eta_H^{(i)} - \Phi\cdot Re_0^{1/2}\cdot F_0^2\bar{p}(\xi^n, \eta_H^{(i)}) \quad i = 0,1,2\ldots \tag{45}$$

are performed, with $\bar{p}(\xi^n, \eta_H^{(i)})$ as obtained with the solution at the ith level of iteration. The sequence is terminated and the numerical solution at the location ξ^n is defined when

$$|\bar{p}(\xi^n, \eta_H^{(i)})| \le \epsilon\bar{p}(\xi^n, 0) \tag{46}$$

where ϵ is taken as 10^{-3}. The parameter Φ in equation (45) is of the order unity, but is adjusted by linear interpolation for every second iteration so as to improve the convergence of the sequence.

The actual solution of the system of $(4H + 4)$ algebraic equatins (34)–(37) and (41)–(43) is, at each ξ-station, arrived

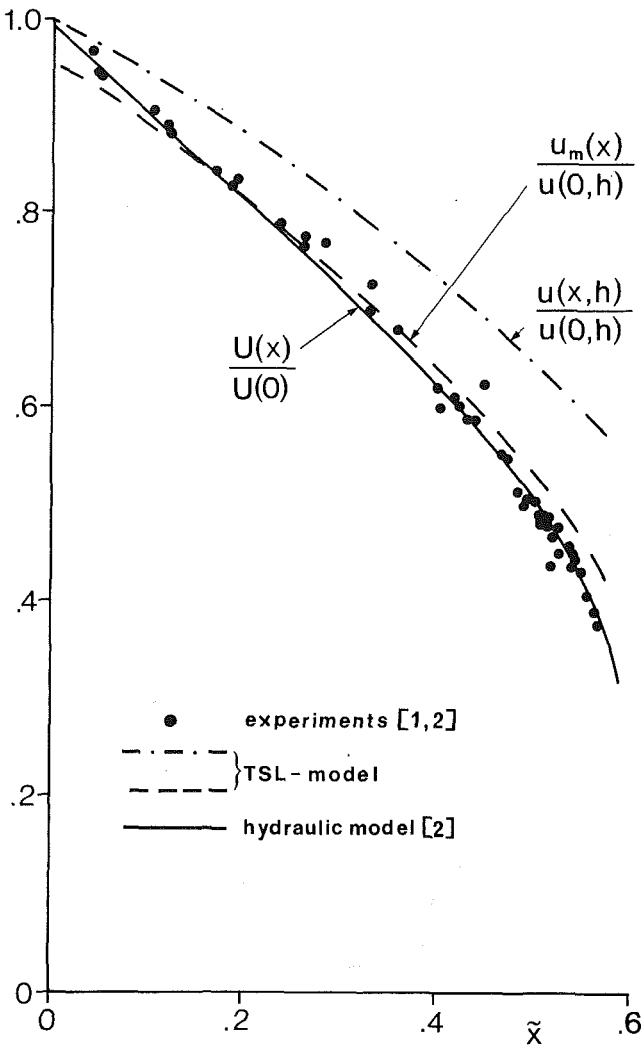

Fig. 3 Velocity variation along the incline. The points denote measured surface velocity $u(x,h)/u(0,h)$ for $6.0 < F_0 < 7.0$. The lines correspond to predictions for $F_0 = 6.13$.

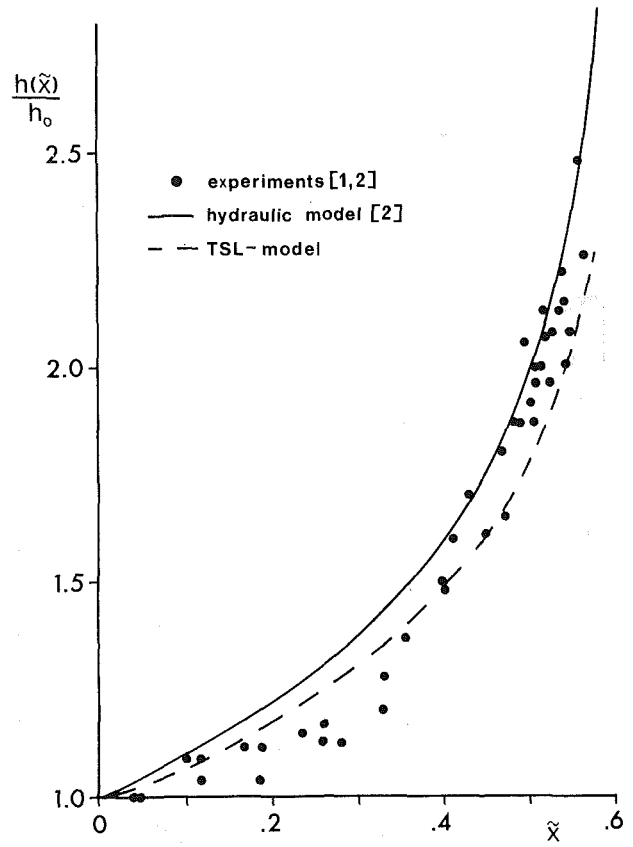

Fig. 4 Flow depth variations along the incline. The points denote measured depths for $6.0 < F_0 < 7.0$. The lines correspond to predictions for $F_0 = 6.13$.

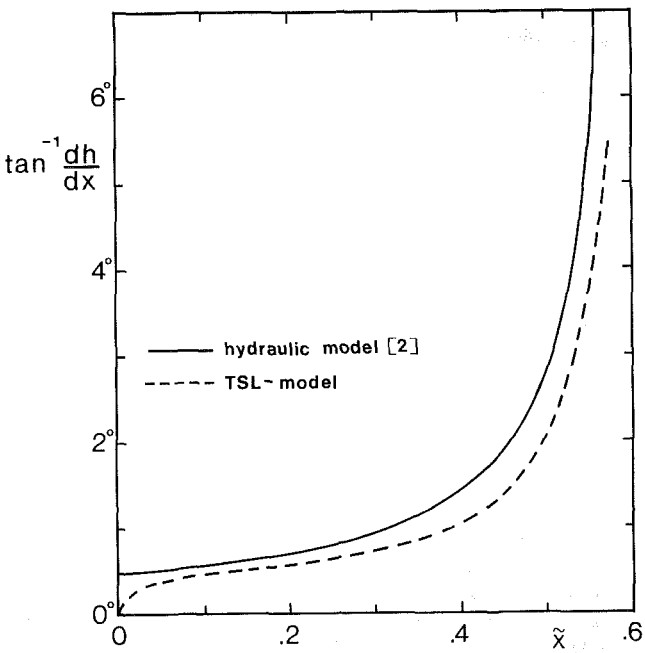

Fig. 5 Physical surface slope (predicted) along the incline

at using Newton's method by considering iterates of the type $(\phi_j^n)^{(i+1)} = (\phi_j^n)^{(i)} + (\delta\phi_j^n)^{(i)}$ for the $(4H + 4)$ unknowns f_j^n, g_j^n, g_j^n, $\tilde{p}_j^n$, $0 \le j \le H$. The resulting linearized system exhibits a block tridiagonal structure, the blocks consisting of 4×4 matrices, and a very efficient block tridiagonal factorization scheme due to Keller [14] is used to compute the solution.

Initial profiles for f, g, and q at $\xi^0 = 0$ are derived from a two-parameter velocity distribution proposed by Pai [15]:

$$u(0,y) = u(0,h_0)\left[1 - a\left(1 - \frac{y}{h_0}\right)^2 - (1-a)\left(1 - \frac{y}{h_0}\right)^{2m}\right] \tag{47}$$

Here we insert values $m = 16$ and $a = 0.05$ to simulate an only slightly developed entrance flow. The initial pressure distribution across the flow is assumed to be linear:

$$p(0,y) = p_0 + \rho g \cos\alpha (h_0 - y) \tag{48}$$

and such that the free surface condition (5) is satisfied.

4 Results and Discussion

Solutions were computed on a UNIVAC 1160 computer for a variety of turbulent supercritical flow conditions, and convergent numerical solutions for a typical grid of 20×100 points were obtained within CPU-times of 30 sec. Grid refinement tests indicated that this mesh-size was sufficient to obtain adequate grid independence. Figures 3–8 show predicted results for a supercritical flow up along a 9.59 deg incline, with initial flow depth $h_0 = 0.023$ m, initial mean velocity $u_0 = 2.89$ m/s, and kinematic viscosity $\nu = 10^{-6}$ m^2/s, from which we obtain $F_0 = 6.13$ and $Re_0 = 6.6 \cdot 10^4$. The results are conveniently presented in terms of the dimensionless streamwise coordinate

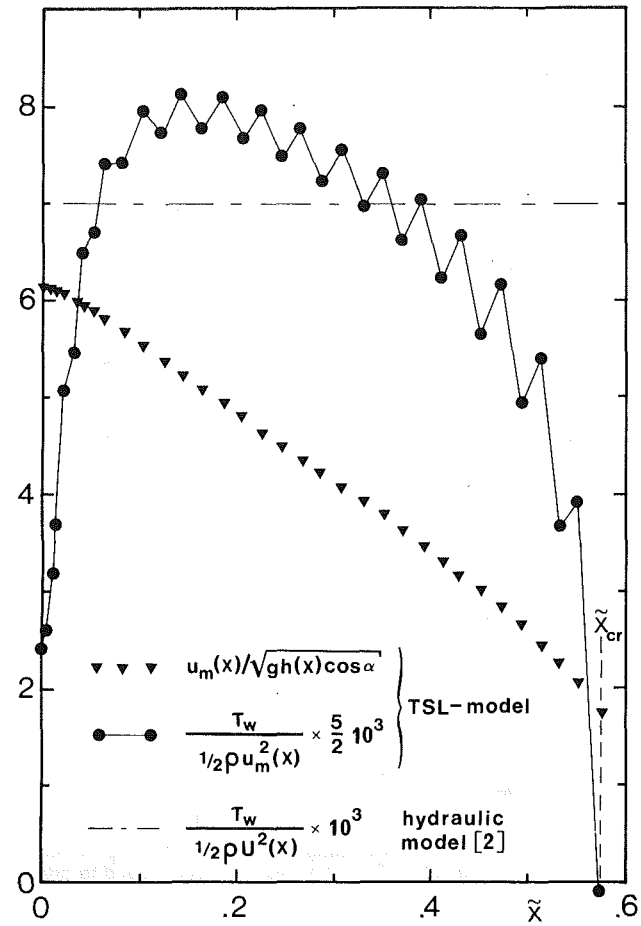

Fig. 6 Predicted variation of local Froude number and wall friction along the incline

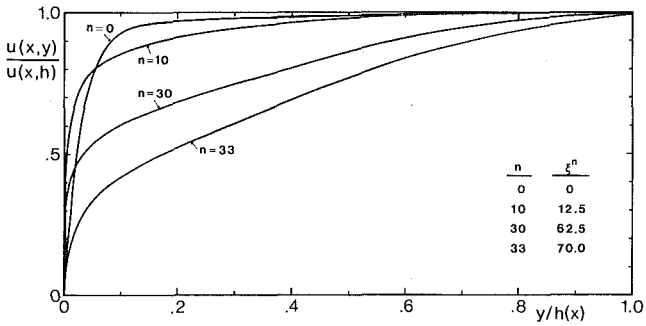

Fig. 7 Predicted velocity profiles

$$\tilde{x} = \frac{x \cdot \sin\alpha}{u(0,h)^2/2g}, \tag{49}$$

which directly yields the ratio of the local potential energy $x \cdot \sin\alpha$ to a typical value for the kinetic energy of the flow at the foot of the incline.

Figure 3 shows the predicted variation of the surface velocity $u(x,h)$ and mean velocity $u_m(x) \equiv Q/h(x)$, both nondimensionalized with respect to the initial surface velocity $u(0,h)$. The solid line represents results obtained with a hydraulic (i.e., one-dimensional) model, as discussed in reference [2]. In that particular formulation the wall friction has been incorporated in the model by a selected value of the friction factor

$$c_f = \frac{\tau_w}{\frac{1}{2}\rho U^2(x)} = 0.007 \tag{50}$$

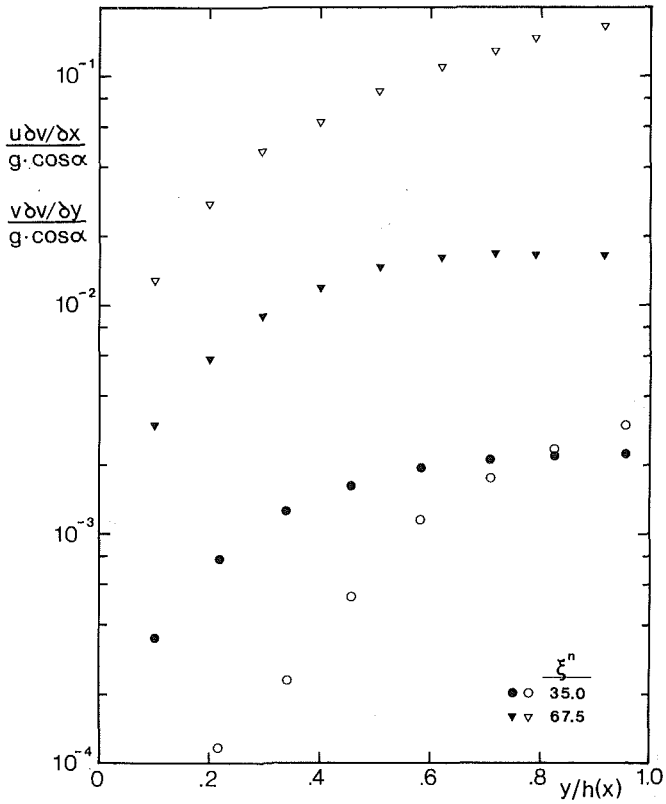

Fig. 8 Cross-stream variation of neglected inertia terms.

$$\nabla \circ \frac{u\partial v/\partial x}{g\cos\alpha} = -F_0^2 Re_0^{-1/2} f' \partial^2 f/\partial\xi^2$$

$$\blacktriangledown \bullet \frac{v\partial v/\partial y}{g\cos\alpha} = F_0^2 Re_0^{-4} \partial f/\partial\xi \cdot \partial f'/\partial\xi$$

where $U(x)$ is the one-dimensional velocity.

The symbols displayed in Fig. 3 denote experimental data for $u(x,h)$. These results were obtained for flows with initial Froude numbers in the range $6.0 < F_0 < 7.0$, and the surface velocity was measured with a pitot tube under stationary flow conditions in a 0.6 m wide experimental flume, as shown in Fig. 1. The results are nondimensionalized with respect to the initial value of the surface velocity, which was obtained from the measured water tank head by assuming the head loss through the sluice gate to be negligible, i.e.,

$$u(0,h) = (2gH_t)^{1/2} \tag{51}$$

Further details concerning the measurements are contained in references [1, 2].

It is observed that the data points in Fig. 3 fall close to the one-dimensional velocity $U(x)$ and the mean velocity $u_m(x)$ obtained by the hydraulic model and the TSL model, respectively. This can probably be ascribed to the application of equation (51), which yields somewhat too large values for the scaling velocity $u(0,h)$.

Experimental data and predicted values for the flow depth $h(x)$ along the incline are displayed in Fig. 4, where the results have been scaled with the initial flow depth h_0. From the results in this figure it appears that the TSL calculations compare more favorably with the experiments at the lower $\tilde{x}$-values, whereas the hydraulic model is more consistent with the measurements at the higher $\tilde{x}$-values.

The governing equation in the hydraulic formulation has a singularity at the local Froude number $F(x) \equiv U(x)/(gh(x)\cos\alpha)^{1/2}$ equal to 1,[2]. Thus, the surface slope dh/dx tends to infinity as $F(x) \to 1$. A similar behavior seems

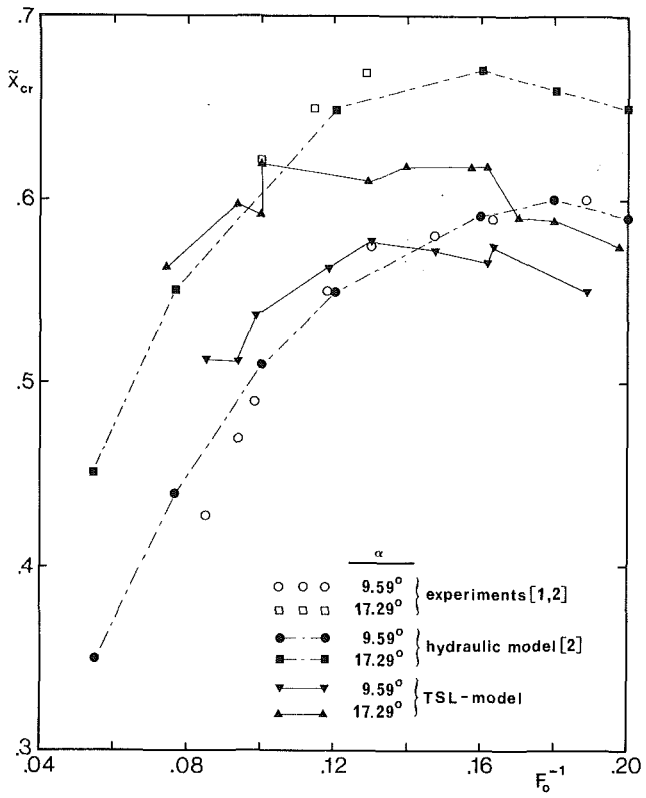

Fig. 9 Breakdown predictions compared with experimental data

to be exhibited also by the TSL model, although at a different critical value of F. Figure 5 shows the increase in the physical surface slope $\tan^{-1}(dh/dx)$ along the incline, and it is observed that the steeper slope is predicted by the hydraulic model. In the TSL formulation, however, the increase in dh/dx is accompanied by a reduction in the bottom shear stress $\tau_w = \mu(\partial u/\partial y)_{y=0}$, Fig. 6, so that the flow adjacent to the channel bed is forced to separate from the bottom. Downstream of this particular streamwise position (denoted by x_{cr}), convergent numerical results could not be obtained. In the TSL formulation this streamwise position therefore defines the breakdown position of the model. The local Froude number is seen to decrease monotonically at an almost constant rate until the critical value $F \lesssim 2$ is approached.

The predicted breakdown typically occurs under slightly supercritical local flow conditions ($F \lesssim 2$, Fig. 6), rather than for critical flow as in the hydraulic model. From these observations it appears that the flow breakdown is caused by an interaction between the free-surface behavior and the bottom shear layer, resulting in a boundary-layer type of separation, although the boundary layer concept itself is strictly not compatible with the present TSL computational model.

It should be noted that the oscillatory nature of the predicted wall friction τ_w in Fig. 6 probably is a result of the actual initial profiles chosen, which obviously yield too low wall shear at $\tilde{x} = 0$. Therefore it is observed that the computed quantity $\tau_w/1/2\rho u_m^2(x)$ first increases sharply up along the incline, then reaches a maximum value and decreases montonically toward zero at the breakdown position. The friction factor $c_f = \tau_w/1/2\rho U^2(x)$ in the hydraulic model [2], which was given the constant value 0.007, equation (50), is seen to be roughly 5/2 times larger than a typical computed value for the corresponding quantity in the TSL model. There is, however, no compelling reason for these two quantities to be equal, in particular since the hydrulic model is a quasi one-dimensional form which is not strictly derived from the partial differential equations for the flow problem like the TSL model is.

Some calculated velocity profiles presented in Fig. 7 give further details on the flow field along the incline. Here, the profile for $n = 0$ is the prescribed initial velocity profile equation (47), and the profile for $n = 33$ represents the predicted velocity distribution at $\tilde{x}_{cr}$. These results show that the flow enters the lower end of the incline as a basically inviscid flow on top of a thin viscous boundary layer. Then, moving downstream, the shear effects appear to be diffused further out from the wall so that the flow becomes a fully viscous-dominated layer, i.e., a thin shear layer.

In deriving the thin-shear-layer version (equations (2) and (3)) from the Navier-Stokes equations, the streamwise diffusion term $\nu\,\partial^2 u/\partial x^2$ was neglected in the x-component, and inertia and viscous terms were neglected altogether in the y-component. To check the validity of these approximations, the neglected terms were evaluated from the computed solution. The ratio of the neglected viscous terms to the gravity term in the corresponding momentum equation was found to be less than 10^{-4} throughout the flow field. The cross-stream variation of the neglected inertia terms are displayed in Fig. 8. The ratio of $u\,\partial v/\partial x$ or $v\,\partial v/\partial y$ to the gravity term $g\cdot\cos\alpha$ is typically of the order 10^{-3} (circles). At the streamwise station next to x_{cr}, however, the contribution from the neglected inertia terms (triangles) is at their largest, but does not—even close to the free surface—exceed 20 percent of the cross-stream gradient given by equation (3). Accordingly, the thin-shear-layer model can be considered a valid approximation to the full Navier-Stokes equations in this type of flow, except, perhaps, in the immediate vicinity of the breakdown position.

A critical flow behavior similar to the one predicted by the theory, was observed also in the experimental flume. If the water tank head H_t was very slowly reduced (with the initial shear layer depth h_0 kept constant), the surface level $h(x)$ would raise. As H_t approached a certain value $H_{t,cr}$, a more pronounced increase in $h(x)$ on the upper part of the incline occured, and for $H_t = H_{t,cr}$ an unsteady hydraulic jump would appear close to the top, rushing upstream and down the plane, thus completely quenching the originally stable flow. Under these conditions the critical position x_{cr} may therefore be approximated by the length L of the inclined channel bed. Using equation (49) and the approximate relation (51) we obtain

$$\tilde{x}_{cr} \approx L\cdot\sin\alpha/H_{t,cr} \tag{52}$$

In Fig. 9 experimental values of $\tilde{x}_{cr}$, defined this way, are compared with predictions from the hydraulic model [2] and with the present TSL calculations for two different angles of inclination. It seems that the hydraulic model yields results that are slightly more consistent with the experiments than does the TSL model, although both models show the same general trend: the existence of a maximum in $\tilde{x}_{cr} = x_{cr}\cdot\sin\alpha/(u^2(0,h)(2g)$ for some value of the initial Froude number in the range $5 \lesssim F_0 \lesssim 8$. The actual maximum value for $\tilde{x}_{cr}$ clearly depends on the angle α, which is to be expected since the viscous effects accumulate along the length x, rather than along the height $x\cdot\sin\alpha$: A large α implies that a high elevation is reached in a short length x, and hence that the viscous losses are reduced. Therefore, the larger α gives the larger $\tilde{x}_{cr}$. The typical figures $0.55 \lesssim \tilde{x}_{cr} \lesssim 0.65$ indicate that the transformation from kinetic to potential energy may proceed at some 55–65 percent efficiency, at most, in this set-up for the range of inclinations considered.

The boundary layer predictions of the breakdown points (separation points) from reference [2] would fall upon curves with negative slope in the $\tilde{x}_{cr}F_o^{-1}$ plane in the whole range of F_0 values, and would, therefore, contradict the general trend in the results in Fig. 9, at least for sufficiently large values of the Froude number F_0.

It should be noted that for the TSL predictions, k^n/ξ_{cr}^n is in the range of 0.04–0.10. Thus, the uncertainty in the $\tilde{x}_{cr}$-results due to the streamwise step-length is typically ± 0.04; i.e., the relative large step-length k^n accounts for the erratic behavior of the predicted $\tilde{x}_{cr}$-values in Fig. 8.

The apparently good agreement between the hydraulic model and the experimental values for $\tilde{x}_{cr}$ is partly due to the fact that the model was particularly calibrated for this quantity; i.e., the friction factor c_f was chosen so as to give the best fit to the experimental values for $\tilde{x}_{cr}$. It may therefore be concluded that the structure of the dissipation is unimportant as far as the free surface is concerned and only the magnitude of the dissipation has any material effect. Thus, if one chooses the magnitude empirically to fit observations one must expect to get good agreement with experiment. Nevertheless, to obtain detailed information of the flow field (e.g., velocity profiles) and to avoid the optimization of any empiricial constant, a two-dimensional formulation of the problem is necessary.

5 Conclusions

The supercritical free-surface flow on an adverse incline has been treated by the "thin-shear-layer model" with algebraic eddy viscosity included to account for turbulent shear stresses. The resulting parabolic system of partial differential equations was solved numericallly by a Keller Box scheme, finite-difference technique.

The computed results are consistent with experimental findings and with semi-empirical hydraulic results as far as velocity, flow depth and breakdown positions are concerned. For quantities like shear stress at the bottom and Froude number at the flow breakdown positions the computed results differ substantially from those in the hydraulic model. In particular, the hydraulic model implies a critical Froude number equal to unity whereas the computed results imply values closely below 2.

The breakdown phenomenon may at least in the computational results be attributed to a separation in the bottom shear layer resulting from a severe steepening of the free surface. This phenomenon is not correctly described in terms of classical boundary layer theory.

The flow breakdown limits the energy recovery to a maximum of 55–65 percent under the conditions considered. These figures could possibly be improved by increasing the slope of the incline.

References

1 Madsen, T., "Hydraulic Flow on an Incline," Diploma Thesis (in Norwegian), Norwegian Institute of Technology, Trondheim, 1981.

2 Andersson, H. I., Madsen, T., and Ytrehus, T., "Hydraulic Flow on Adverse Slopes," Report No. 81:2, Institutt for Mekanikk, Norwegian Institute of Technology, Trondheim, 1981.

3 Cebeci, T., and Bradshaw, P., *Momentum Transfer in Boundary Layers*, McGraw-Hill-Hemisphere, Washington, 1977.

4 Keller, H. B., "A New Difference Scheme for Parabolic Problems," *Numerical Solutions of Partial Differential Equations*, Vol. II, Bramble, J., ed., Academic Press, New York, 1970.

5 Keller, H. B., "Numerical Methods in Boundary Layer Theory," *Annual Review of Fluid Mechanics*, Vol. 10, 1978, pp. 417–433.

6 Cebeci, T., and Keller, H. B., "Laminar Boundary Layers With Assigned Wall Shear," *Proceedings Third International Conference on Numerical Methods in Fluid Dynamics, Lecture Notes in Physics*, Vol. 19, Srpinger-Verlag, Berlin, 1973, pp. 79–85.

7 Andersson, H. I., "Thin-Shear-Layer Models for Two-Dimensional Free-Surface Flows in Sloping Channels," Dr. ing. Thesis, Norwegian Institute of Technology, Trondheim, 1982.

8 Andersson, H. I., "Numerical Solutions of a TSL-Model for Free-Surface Flows," to appear in *Proceedings of Fifth GAMM Conference on Numerical Methods in Fluid Mechanics, Notes on Numerical Fluid Mechanics*, Vieweg Verlag.

9 Cebeci, T., and Smith, A. M. O., "A Finite—Difference Method for Calculating Compressible Laminar and Turbulent Boundary Layers," *Journal of Basic Engineering*, Vol. 92, No. 3, 1970, pp. 523–535.

10 Cebeci, T., "The Behaviour of Turbulent Flow Near a Porous Wall With Pressure Gradient," *AIAA Journal*, Vol. 8, No. 12, 1970, pp. 2152–2156.

11 Rastogi, A. K., and Rodi, W., "Predictions of Heat and Mass Transfer in Open Channels," ASCE *Journal of the Hydraulics Division*, Vol. 104, No.HY3, 1978, pp. 397–420.

12 Leschziner, M. A., and Rodi, W., "Calculation of Strongly Curved Open Channel Flow," ASCE *Journal of the Hydraulics Division*, Vol. 105, No.HY10, 1979, pp. 1297–1314.

13 Cebeci, T., "Calculation of Momentum and Heat Transfer in Internal Flows With Small Regions of Separation," *in: Turbulent Forced Convection in Channels and Bundles*, Vol. I, Kakac, S., and Spalding, D. B., eds., McGraw-Hill-Hemisphere, Washington, 1979.

14 Keller, H. B., "Accurate Difference Methods for Nonlinear Two-Point Boundary Value Problems," *SIAM Journal on Numerical Analysis*, Vol. 11, 1974, pp. 305–320.

15 Pai, S. I., "On Turbulent Flow Between Parallel Plates," ASME JOURNAL OF APPLIED MECHANICS, Vol. 20, 1953, pp. 109–114.

J. P. Du Plessis
Lecturer,
Department of Applied Mathematics.

D. G. Kröger
Professor,
Department of Mechanical Engineering.
Mem. ASME

Faculty of Engineering,
University of Stellenbosch,
7600 Stellenbosch,
South Africa

Hydrodynamical Entrance Length Effects for Duct Flows With Arbitrary Inlet Velocity Profiles

An existing analytical method for predicting the entrance region pressure drop and relating effects in straight ducts of arbitrary cross section is generalized to include the application of arbitrary inlet velocity profiles. The only requirement for the use of the derived theoretical results is the availability of integrable (analytically or numerically) expressions for the inlet and the fully developed velocity profiles for the cross-sectional geometry under consideration. The derived results are applied to the case of the transition of fully developed laminar tube flow to fully developed circular-sectorial flow. The latter may be induced by the introduction of a flow divider into the tube. The numerical results are tabulated and also presented graphically.

Introduction

The hydrodynamical development of laminar incompressible flow in the entrance region of a straight duct leads to an overall change in the axial pressure drop over the entrance length. Whenever flow in a duct of length comparable to that of the entrance length is studied, this total pressure defect induced by the flow development, has to be taken into consideration. Lundgren et al. [1] presented an analysis in this respect on duct flows where the duct may be of arbitrary cross section. In their derivation of pressure drop results, the following assumptions were made according to the laminar entrance region flow of an incompressible fluid in a straight duct:

(*i*) the Navier-Stokes equation is satisfied by the flow field;
(*ii*) mass conservation is applicable through the continuity equation;
(*iii*) all physical properties of the fluid are constant;
(*iv*) pressure variations in any cross-sectional plane are neglected;
(*v*) the longitudinal shear component $\partial^2 u/\partial x^2$ is negligible relative to the transverse shear components $\partial^2 u/\partial y^2 + \partial^2 u/\partial z^2$,
(*vi*) the momentum equation may be linearized; and
(*vii*) incremental pressure drop numbers derived, respectively, through the concepts of momentum and mechanical energy are identical despite the introduction of the said linearization.

The analysis of Lundgren et al. [1] reveals the following result for the incremental pressure drop number for flow development from a uniform inlet profile in a duct of cross-sectional area A:

$$\bar{K}(\infty) = \frac{2}{A}\iint_A [(u_\infty/u_m)^3 - (u_\infty/u_m)^2]dA \tag{1}$$

with the incremental pressure drop number $\bar{K}(x)$ defined by:

$$\bar{K}(x) = 4x^+ Re(f_{app} - f) \tag{2}$$

and ∞ referring to the fully developed region.

The expression (1) arrived at by Lundgren et al. [1] for the incremental pressure drop number is a function of only the geometry of the cross-sectional area of the duct and the fully developed axial velocity u_∞/u_m. The inlet velocity profile, being uniform, is implicitly present as unity, namely

$$u_0/u_m = 1 \tag{3}$$

In this paper a generalization to equation (1) is discussed, allowing explicitly for the inlet velocity profile. The analytical procedure of Lundgren et al. [1] is closely followed, the only alteration being the explicit incorporation of an arbitrary inlet velocity profile. The end result may clearly not be cast in such a simple form as equation (1), but the usefulness is greatly extended. The newly derived expression should reduce to equation (1) in the special case of a uniform inlet profile.

Analysis

The analysis presented at length by Lundgren et al. [1] may be carried through with the inclusion of any particular inlet velocity profile. Integration and the subsequent linearization of the axial component of the Navier-Stokes equation leads to the following expression for the incremental pressure drop number:

$$\bar{K}_m(\infty) = \frac{2}{Au_m^2}\iint_A [u_\infty^2 - u_0^2 + \epsilon u_\infty (u_\infty - u_0)]dA \tag{4}$$

Contributed by the Applied Mechanics Division for publication in the JOURNAL OF APPLIED MECHANICS.
Discussion on this paper should be addressed to the Editorial Department, ASME, United Engineering Center, 345 East 47th Street, New York, N.Y. 10017, and will be accepted until two months after final publication of the paper itself in the JOURNAL OF APPLIED MECHANICS. Manuscript received by ASME Applied Mechanics Division, February, 1983; final revision, August, 1983.

The velocity weighting factor ϵ was introduced by Lundgren et al. [1] and $\bar{K}_m(\infty)$ is thus known from the inlet and the outlet velocity profiles except for the constant ϵ.

Following Lundgren et al., the equation for mechanical energy may subsequently be integrated to provide the following expression for the pressure drop number:

$$\bar{K}_e(\infty) = \frac{1}{A}\iint_A \left[(u_\infty/u_m)^3 - (u_0/u_m)^3 + \epsilon\frac{u_\infty^2 - 2u_\infty u_0 + u_0^2}{u_m^2}\right]dA \tag{5}$$

The assumption that the incremental pressure drop numbers $\bar{K}_m(\infty)$ and $\bar{K}_e(\infty)$, respectively, derived from the momentum and the mechanical energy equations, are identical, implies that the expressions given in equations (4) and (5) are equal to one another in value. Hence follows

$$\epsilon = \frac{\iint_A \left[(u_\infty/u_m)^3 - (u_0/u_m)^3 - \frac{2(u_\infty^2 - u_0^2)}{u_m^2}\right]dA}{\iint_A [(u_\infty/u_m)^2 - (u_0/u_m)^2]dA} \tag{6}$$

The constant ϵ may thus be obtained directly by either analytical or numerical integration for any set of inlet and fully developed velocity profiles. The fully developed profile is of course determined uniquely by the cross-sectional shape of the duct. Also of importance is the fact that only the prescribed inlet and fully developed profiles are needed to fix the value of ϵ. The next step is to calculate, with the known value of ϵ, either $\bar{K}_m(\infty)$ from equation (4) or $\bar{K}_e(\infty)$ from equation (5), each of which produces the same value for $\bar{K}(\infty)$. Thus follows

$$\bar{K}(\infty) = 2/A\iint_A \left[(u_\infty/u_m)^2 - (u_0/u_m)^2 + \frac{\epsilon u_\infty(u_\infty - u_0)}{u_m^2}\right]dA \tag{7}$$

and

$$\bar{K}(\infty) = 1/A\iint_A \left[(u_\infty/u_m)^3 - (u_0/u_m)^3 + \frac{\epsilon(u_\infty - u_0)^2}{u_m^2}\right]dA \tag{8}$$

In the special case of a uniform inlet profile substitution of ϵ from (6) in (7) yields equation (1).

An indication of the hydrodynamic entrance length is provided by the following result derived by McComas [3] for the case of uniform inlet flow:

$$L_{hy}^+ = \frac{(u_{\max}/u_m)^2 - 1 - \bar{K}(\infty)}{4fRe} \tag{9}$$

It was, however, pointed out by Shah and London [4] that this expression provides values of the entrance lengths that are too low. Nevertheless, if the derivation of McComas is generalized to cover the cases of nonuniform inlet profiles, the following expression for arbitrary inlet velocity profiles is arrived at:

$$L_{hy}^+ = \frac{(u_{\max}/u_m)^2 - (\tilde{u}_0/u_m)^2 - \bar{K}(\infty)}{4fRe} \tag{10}$$

A complication of this expression is the presence of the velocity $\tilde{u}_0$, denoting the value of the velocity at the inlet along the streamline which leads to the maximum velocity in the fully developed region. Since the inlet position of this streamline is generally unknown, the velocity $\tilde{u}_0$ cannot be calculated. Unless some means can be found to determine the latter, equation (10) is of no practical value.

The momentum flux correction factor for laminar flow in a straight duct is defined by

$$k_d(x) = 1/A\iint_A (u/u_m)^2 dA \tag{11}$$

and the kinetic energy correction factor by

$$k_e(x) = 1/A\iint_A (u/u_m)^3 dA \tag{12}$$

The values of these two correction factors also follow directly from integration of the velocity profiles at the specific axial position in question. It should be noted that only for the special case of a uniform inlet velocity profile does the following result hold:

$$\bar{K}(\infty) = 2[k_e(\infty) - k_d(\infty)] \tag{13}$$

The analytical results presented in this section will now be applied to the case of developing flow in a straight duct of circular-sectorial cross section where the inlet profile may be uniform or parabolic.

Flow in a Duct of Circular-Sectorial Cross Section

In the case of fully developed flow in a duct of circular-sectorial cross section the Navier-Stokes equation leads to the following expression for the axial velocity component (Eckert and Irvine [5]):

$$u_\infty = -\frac{ca^2}{4}\xi_\phi(r,\theta) \quad \text{for} \quad 0 < 2\phi \le 2\pi \tag{14}$$

with

$$c = \frac{1}{\mu}\frac{d\bar{p}}{dx}$$

and

$$\xi_\phi(r,\theta) = (r/a)^2\left(\frac{\cos 2\theta}{\cos 2\phi} - 1\right) + \frac{16(2\phi)^2}{\pi^3}\sum_{n=1,3,..}^{\infty}(-1)^{\frac{n+1}{2}}(r/a)^{\frac{n\pi}{2\phi}}\frac{\cos\frac{n\pi\theta}{2\phi}}{n\left(n+\frac{4\phi}{\pi}\right)\left(n-\frac{4\phi}{\pi}\right)} \tag{15}$$

The mean axial velocity u_m is given by:

$$u_m = -\frac{ca^2}{4}\psi_\phi(r,\theta) \tag{16}$$

with $\psi_\phi(r,\theta)$ in the following form after Shah and London [4]:

$$\psi_\phi(r,\theta) = \frac{\tan 2\phi}{4\phi} - 1/2 - 64/\pi^2(2\phi/\pi)^3\sum_{n=1,3,..}^{\infty}\frac{1}{n^2\left(n+\frac{4\phi}{\pi}\right)\left(n-\frac{4\phi}{\pi}\right)} \tag{17}$$

The fully developed velocity profile may henceforth be obtained from equations (14)–(16), namely by

$$u_\infty/u_m = \xi_\phi/\psi_\phi \tag{18}$$

The momentum and the energy correction factors follow from the application of this result to equations (11) and (12), respectively. Numerical values in this respect, obtained by the present authors by means of numerical integration, are presented in Table 1. A uniform grid system of 100 × 100 nodes was used in the computations to provide an accuracy of

Table 1 Numerical results for various quantities relating to entrance region effects in cases of circular-sectorial flow

2ϕ	$\bar{K}(\infty)$	ϵ	$\bar{K}^p(\infty)$	ϵ^p	$k_d(\infty)$	$k_e(\infty)$	L_{hy}^+
5	2.645	1.370	3.616	1.918	1.558	2.880	0.0704
10	2.411	1.296	3.059	1.811	1.525	2.731	0.0586
15	2.238	1.243	2.644	1.733	1.499	2.618	0.0519
20	2.105	1.203	2.325	1.674	1.478	2.530	0.0475
25	2.001	1.174	2.073	1.630	1.460	2.461	0.0444
30	1.918	1.150	1.871	1.596	1.446	2.405	0.0420
35	1.850	1.132	1.706	1.570	1.434	2.359	0.0401
40	1.795	1.117	1.568	1.549	1.424	2.322	0.0386
45	1.749	1.105	1.452	1.534	1.415	2.290	0.0374
50	1.711	1.096	1.353	1.521	1.408	2.264	0.0364
55	1.678	1.087	1.267	1.512	1.402	2.241	0.0355
60	1.651	1.080	1.193	1.504	1.397	2.222	0.0347
65	1.627	1.075	1.127	1.498	1.392	2.206	0.0340
70	1.607	1.069	1.069	1.493	1.388	2.191	0.0335
75	1.589	1.065	1.018	1.488	1.385	2.179	0.0329
80	1.574	1.061	0.971	1.485	1.382	2.168	0.0325
85	1.560	1.058	0.930	1.482	1.379	2.159	0.0321
90	1.548	1.055	0.892	1.480	1.377	2.151	0.0317
95	1.538	1.052	0.857	1.476	1.375	2.144	0.0313
100	1.529	1.050	0.825	1.473	1.373	2.137	0.0310
105	1.521	1.048	0.796	1.470	1.371	2.132	0.0307
110	1.513	1.046	0.770	1.468	1.370	2.127	0.0305
115	1.507	1.044	0.745	1.465	1.369	2.122	0.0302
120	1.501	1.043	0.722	1.463	1.367	2.118	0.0300
125	1.496	1.041	0.700	1.460	1.366	2.114	0.0298
130	1.491	1.040	0.681	1.458	1.365	2.111	0.0296
135	1.487	1.039	0.662	1.455	1.365	2.108	0.0295
140	1.483	1.038	0.645	1.453	1.364	2.106	0.0293
145	1.480	1.037	0.628	1.450	1.363	2.103	0.0291
150	1.477	1.036	0.613	1.448	1.363	2.101	0.0290
155	1.474	1.035	0.598	1.445	1.362	2.099	0.0289
160	1.471	1.035	0.585	1.443	1.362	2.097	0.0288
165	1.469	1.034	0.572	1.441	1.361	2.096	0.0286
170	1.467	1.033	0.560	1.439	1.361	2.094	0.0285
175	1.465	1.033	0.549	1.437	1.360	2.093	0.0284
180	1.463	1.032	0.538	1.435	1.360	2.092	0.0283
210	1.455	1.030	0.483	1.426	1.358	2.086	0.0278
240	1.449	1.028	0.442	1.420	1.357	2.082	0.0275
270	1.446	1.027	0.410	1.418	1.356	2.079	0.0272
300	1.442	1.026	0.383	1.417	1.356	2.077	0.0270
330	1.440	1.026	0.361	1.419	1.355	2.075	0.0268
360	1.437	1.025	0.343	1.422	1.355	2.073	0.0267

∓ 0.01 percent. The hydrodynamical entrance length expression (9) by McComas [3] is a function of the maximum velocity value. Since flow in a wedge-shaped duct is symmetrical about the $\theta = 0$ plane, the position $(\hat{r}, \hat{\theta})$ of maximum velocity was computed by application of the well-known secant method to a search along the $\theta = 0$ coordinate line, for the position where

$$\frac{\partial \xi}{\partial r} = \frac{1}{a}\chi(r,0) = 0 \tag{19}$$

with

$$\chi(r,\theta) = 2\left(\frac{r}{a}\right)\left(\frac{\cos 2\theta}{\cos 2\phi} - 1\right)$$

$$+ \frac{16(2\phi)^2}{\pi^3} \sum_{n=1,3,..}^{\infty} (-1)^{\frac{n+1}{2}} \left(\frac{r}{a}\right)^{\frac{n\pi}{2\phi}-1} \frac{\cos\frac{n\pi\theta}{2\phi}}{n^2 - \left(\frac{4\phi}{\pi}\right)^2} \tag{20}$$

Table 2 consists of a listing of some computed values for results in accordance with the present section. Values of L_{hy}^+ according to equation (9) are presented in Table 1.

The series solutions presented in equations (15), (17), and (20) are not defined for apex angles $\pi/2$ and $3\pi/2$ so that special attention is needed to provide numerical values at these removable singularities. The dimensionless quantity fRe may be evaluated for fully developed flow in circular-sectorial ducts from (Shah and London [4]):

$$fRe = \frac{8}{\psi_\phi}\left(\frac{\phi}{1+\phi}\right)^2 \tag{21}$$

Discussion Regarding Sectorial Flow

In the particular case of a semicircular cross section a series solution is available according to the paper of Weigand [6]. The present results were tested against such a solution [2] and, although the numerical results were identical, the convergence rate of the infinite series was found to be much slower in the latter case. The nonsquared velocity terms present in equations (7) and (8) also necessitate the introduction of a large number of grid nodes, as was mentioned earlier. On the contrary, equation (1) contains only higher powers of the velocity values and these are accurately computed by far fewer nodes than in the first case.

The present results for $\bar{K}(\infty)$ are similar to those of Sparrow and Haji-Sheikh (published by Shah and London [4]) for $2\phi = 180$ deg, but a discrepancy of up to 5.6 percent is present in the case of smaller values of the apex angle.

In Fig. 2 the numerical results of the present study for fRe, $\bar{K}(\infty)$, $\bar{K}^p(\infty)$, and L_{hy}^+ are represented graphically. $\bar{K}^p(\infty)$

Table 2 Numerical values of fRe and the radial position and magnitude of the maximum velocity for fully developed circular-sectorial flow

2ϕ	fRe	$\hat{r}$	u_{max}/u_m	2ϕ	fRe	$\hat{r}$	u_{max}/u_m
5	12.262	0.918	2.664	185	15.802	0.476	2.060
10	12.504	0.870	2.518	190	15.836	0.471	2.060
15	12.728	0.834	2.425	195	15.868	0.467	2.059
20	12.936	0.803	2.356	200	15.899	0.463	2.058
25	13.130	0.778	2.309	205	15.929	0.459	2.058
30	13.310	0.755	2.270	210	15.957	0.455	2.057
35	13.478	0.735	2.239	215	15.985	0.451	2.056
40	13.635	0.717	2.214	220	16.011	0.447	2.056
45	13.782	0.700	2.193	225	16.037	0.444	2.055
50	13.920	0.685	2.176	230	16.061	0.440	2.055
55	14.049	0.671	2.162	235	16.085	0.437	2.054
60	14.171	0.658	2.149	240	16.108	0.433	2.054
65	14.286	0.646	2.138	245	16.130	0.430	2.054
70	14.394	0.634	2.129	250	16.151	0.427	2.053
75	14.495	0.623	2.121	255	16.171	0.423	2.053
80	14.592	0.613	2.114	260	16.191	0.420	2.053
85	14.683	0.604	2.108	265	16.210	0.417	2.052
90	14.766	0.595	2.102	270	16.228	0.414	2.052
95	14.850	0.586	2.098	275	16.246	0.411	2.052
100	14.928	0.577	2.093	280	16.263	0.408	2.052
105	15.001	0.569	2.089	285	16.279	0.406	2.051
110	15.071	0.562	2.086	290	16.295	0.403	2.051
115	15.137	0.554	2.083	295	16.310	0.400	2.051
120	15.200	0.547	2.080	300	16.325	0.398	2.050
125	15.260	0.541	2.078	305	16.340	0.395	2.050
130	15.318	0.534	2.075	310	16.353	0.393	2.050
135	15.372	0.528	2.073	315	16.367	0.390	2.050
140	15.424	0.522	2.072	320	16.380	0.388	2.050
145	15.474	0.516	2.070	325	16.392	0.385	2.049
150	15.522	0.510	2.068	330	16.405	0.383	2.049
155	15.527	0.505	2.067	335	16.416	0.380	2.049
160	15.611	0.500	2.066	340	16.428	0.378	2.049
165	15.652	0.495	2.064	345	16.439	0.376	2.049
170	15.692	0.490	2.063	350	16.449	0.374	2.048
175	15.730	0.485	2.062	355	16.460	0.372	2.048
180	15.767	0.480	2.061	360	16.470	0.370	2.048

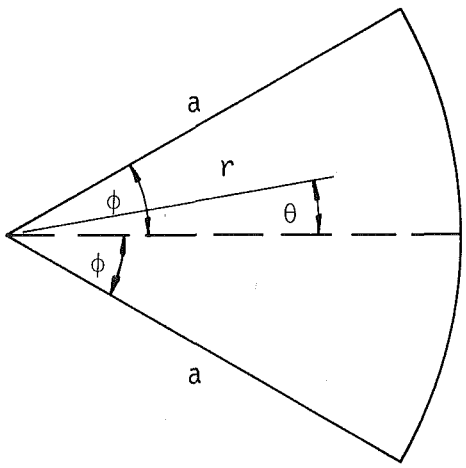

Fig. 1 Notation for the problem under consideration

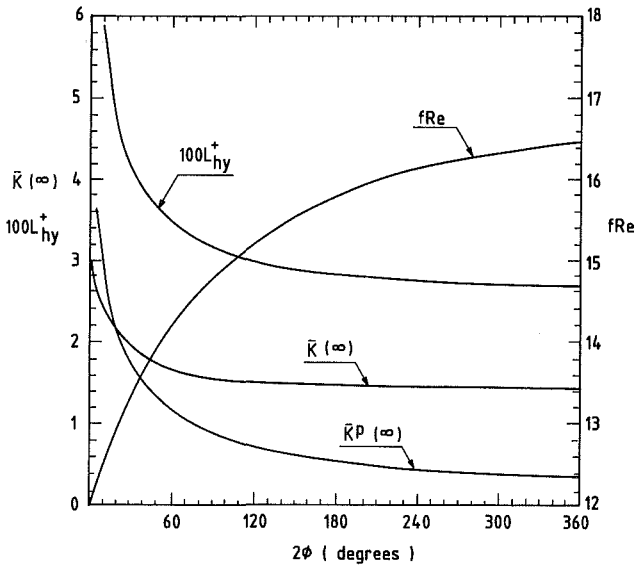

Fig. 2 Circular sector ducts: fRe, $\bar{K}(\infty)$, $\bar{K}^p(\infty)$ and L_{hy}^+ as from the values of Tables 1 and 2

denotes the pressure drop number in the special case of a parabolic inlet profile and is calculated from equation (7) or (8). Most interesting is the apex angle $(2\phi)_{cr} = 27.9$ deg $\simeq$ ½ radian for which the incremental pressure drop numbers for the uniform and the parabolic inlet profiles are of the same magnitude, namely 1.95. In the case of ϕ-values less than ϕ_{cr}, $\bar{K}(\infty) < \bar{K}^p(\infty)$ and vice versa. Numerical values for the pressure drop numbers for flow development from uniform and parabolic inlet profiles are included in Table 1. According to these results the values of the differences in the squared velocity terms are, in all uniform inlet cases, more than twice the values of the corresponding pressure drop numbers. The hydrodynamical entrance length thus decreases with increase in ϕ in a way similar to the decrease in the overall value of the velocity terms.

Conclusion

The results obtained in this paper form a useful

generalization to the work of Ludgren et al. [1]. It allows the introduction of arbitrary inlet velocity profiles in the study of hydrodynamical entrance-length pressure drops. The special case of sectorial flow, for which numerical results are presented with the flow development taking place from a nonuniform inlet profile, serves as an example of the field of application of the analysis. Also pointed out is the still unresolved problem of calculating the value of the velocity $\tilde{u}_0$. Once this is accomplished for any specific geometry the corresponding hydrodynamical entrance length may be calculated from equation (10).

References

1 Lundgren, T. S., Sparrow, E. M., and Starr, J. B., "Pressure Drop due to the Entrance Region in Ducts of Arbitrary Cross Section," ASME *Journal of Basic Engineering*, Vol. 86, 1964, pp. 620–626.

2 Du Plessis, J. P., "Laminar Flow and Heat Transfer in a Smooth Tube With a Twisted-Tape Insert," Ph.D. thesis, University of Stellenbosch, Stellenbosch, South Africa, 1982.

3 McComas, S. T., "Hydrodynamic Entrance Lengths for Ducts of Arbitrary Cross Section," ASME *Journal of Basic Engineering*, Vol. 89, 1967, pp. 847–850.

4 Shah, R. K., and London, A. L., "Laminar Flow Forced Convection in Ducts," *Advances in Heat Transfer*, Supplement 1, Thomas, F. I., and Hartnett, J. P., eds., Academic Press, London, 1978.

5 Eckert, E. R. G., and Irvine, T. F., "Flow in Corners of Passages With Non-Circular Cross Sections," ASME *Journal of Basic Engineering*, Vol. 89, 1967, pp. 847–850.

6 Weigand, A., "The Problem of Torsion in Prismatic Members of Circular Segmental Cross Section," NACA Tech. Memo. No. 1182, Translation of: "Das Torsionsproblem für Stäbe von Kreisabschnittförmigem Querschnitt," Luftfahrt-Forschung, Band 20, Lfg. 12, Feb. 8, 1944, pp. 333–340.

Bifurcation Theory Applied to Oil Whirl in Plain Cylindrical Journal Bearings

C. J. Myers
Department of Applied Mathematical Studies,
University of Leeds,
Leeds LS2 9JT, England

An analysis of the self-excited oscillations of a rotor supported in fluid film journal bearings is presented. It is shown that Hopf bifurcation theory may be used to investigate small-amplitude periodic solutions of the nonlinear equations of motion for rotor speeds close to the speed at which the steady-state equilibrium position becomes unstable. A numerical investigation supports the findings of the analytic work.

Introduction

Under certain operating conditions the hydrodynamic forces generated in fluid film journal bearings are capable of sustaining a self-excited oscillation in which energy is transferred from rotation of the rotor into a whirling motion. This flutter-type instability is normally referred to as oil whirl. If the amplitude of oscillation becomes too large it may significantly affect machine performance, or endanger its safe operation. There is therefore a need to understand the nature of oil whirl and to identify the important parameters.

Conventional analysis of the problem by linearizing the hydrodynamic forces about the equilibrium position [1-3] indicates that the journal becomes unstable above a particular rotor speed (the threshold speed). Apart from the pioneer work of Lund and Saibel [4], who developed the method of averaging, investigation of nonlinear effects has been confined mainly to numerical integration [5-7]. Such investigations are not entirely satisfactory, either because the authors fail to account for rupture of the oil film in the bearing, or because a complete parametric study was not undertaken.

This paper uses Hopf bifurcation theory to investigate the existence of small-amplitude periodic solutions of equations which describe the motion of a rotor supported in fluid film bearings. It is shown that the existence of stable limit cycles for rotor speeds in excess of the threshold speed is confined to a specific region of parameter space and outside this region unstable limit cycles exist below the threshold speed. Numerical integration supports the analytic results and shows how the limit cycle develops as the rotor speed is increased. The combined approach establishes the onset of oil whirl as a bifurcation phenomenon and identifies several features not previously observed.

Contributed by the Applied Mechanics Division for publication in the JOURNAL OF APPLIED MECHANICS.

Discussion on this paper should be addressed to the Editorial Department, ASME, United Engineering Center, 345 East 47th Street, New York, N.Y. 10017, and will be accepted until two months after final publication of the paper itself in the JOURNAL OF APPLIED MECHANICS. Manuscript received by ASME Applied Mechanics Division, August, 1981; final revision, August, 1983.

Hopf Bifurcation Theory

Hopf bifurcation theory is concerned with the bifurcation of periodic orbits from equilibrium points of a system of O.D.E. as a parameter crosses a critical value. Consider the differential equation:

$$\frac{d\mathbf{x}}{dt} = \mathbf{F}(\mathbf{x}, \nu) \tag{1}$$

which is a real n-dimensional, autonomous, first-order system of O.D.E. ($n \geq 2$) and ν is a real parameter. Assume that:

(*i*) $\mathbf{x} = \mathbf{a}^{\nu}$ is an equilibrium point of equation (1);

(*ii*) the Jacobean matrix $\mathbf{F}_{\mathbf{x}}(\mathbf{a}^0, 0)$ has exactly two nonzero, purely imaginary eigenvalues $\pm i\Omega_0 (\Omega_0 > 0)$ and $(n - 2)$ eigenvalues with nonzero real parts;

(*iii*) $\mathbf{F}$ is differentiable in a neighborhood of $(\mathbf{x}, \nu) = (\mathbf{a}^0, 0)$;

(*iv*) $(d\alpha/d\nu) \neq 0$, where $\alpha(\nu) + i\Omega(\nu)$ denotes that eigenvalue of $\mathbf{F}_{\mathbf{x}}(\mathbf{a}^{\nu}, \nu)$ that is a continuous extension of $+ i\Omega_0$.

Under these conditions Hopf [8] proved that a nonconstant periodic orbit bifurcates from $(\mathbf{x}, \nu) = (\mathbf{a}^0, 0)$. Hopf also supplied a uniqueness theorem and information regarding stability. A major difficulty with the theory lies in its application to concrete examples, particularly in determining the direction of bifurcation (i.e., for $\nu < 0$, or $\nu > 0$) and the stability of the periodic orbit. Several authors have subsequently sought to simplify Hopf's original approach in this respect [9-12]. These methods require a transformation of the equations by introducing new variables, which for equations with $n \geq 3$ and several nonlinear terms become very complicated. Poore (13) has removed many of these difficulties by deriving algebraic criteria that are sufficient to determine the direction of bifurcation and the stability of the periodic orbit.

To simplify Poore's work assume that the derivative $(d\alpha/d\nu)_{\nu=0} > 0$ and the remaining $(n - 2)$ eigenvalues of $\mathbf{F}_{\mathbf{x}}(\mathbf{a}^0, 0)$ have negative real parts. Excluding the special case

in which bifurcation occurs only for $\nu \equiv 0$, one of two possibilities may occur:

(*i*) a stable periodic orbit bifurcates from $(\mathbf{x}, \nu) = (\mathbf{a}^0, 0)$ for $\nu > 0$ (supercritical bifurcation), or

(*ii*) an unstable orbit bifurcates from $(\mathbf{x}, \nu) = (\mathbf{a}^0, 0)$ for $\nu < 0$ (subcritical bifurcation).

Note that only one-sided bifurcation can occur.

The direction of bifurcation is determined through the sign of a certain quantity; $\delta'(0)$, using Poore's notation. If $\delta'(0) > 0$ supercritical bifurcation takes place, whereas if $\delta'(0) < 0$ subcritical bifurcation occurs. Poore (13) has established algebraic formulas that enable the sign of $\delta'(0)$ to be determined. The formulas derived by Poore do not require $\mathbf{F}(\mathbf{x}, \nu)$ to be in any special form nor is it necessary to transform the equations to new variables, which, in applications to concrete examples is a considerable advantage.

Application of Bifurcation Theory to Oil Whirl

The purpose of this section is to:

(*i*) Establish the existence of a Hopf bifurcation to equations that govern oil whirl in a simple rotor system, and hence prove the existence of small-amplitude periodic solutions to these equations.

(*ii*) Determine the direction of bifurcation and the stability of the orbit by using Poore's formulas.

The model is of a rigid, symmetric rotor mounted in two identical, plain cylindrical journal bearings. The investigation is confined to cylindrical whirling in which the two ends of the rotor remain in phase so that it is sufficient to consider only one bearing, which then supports a load equal to half the weight of the rotor. Let the rotor mass be $2M$ and the journal center have displacements X and Y (Fig. 1) then the equations of motion of the journal are:

$$\frac{Md^2X}{dt^2} = F_x(X, Y, \dot{X}, \dot{Y}, \sigma); \frac{Md^2y}{dt^2} = F_y(X, Y, \dot{X}, \dot{Y}, \sigma),$$

$$\sigma = LR^3\omega\mu/Fc^2 \tag{2}$$

The force components F_x, F_y consist of the hydrodynamic forces generated in the bearing, together with the applied load F (Fig. 1) and in general they are nonlinear in the four arguments X, Y, $\dot{X}$, $\dot{Y}$. The Sommerfeld number σ is defined in the foregoing, where L is the bearing length in the axial direction, R the bearing radius, ω the angular rotor speed, c the radial clearance, and μ the lubricant viscosity.

Equations (2) may be nondimensionalized by writing:

$$x = X/c \quad y = Y/c \quad \gamma = \omega t \quad \bar{\omega} = (Mc/F)^{1/2}\omega \quad f_x = F_x/\sigma F \quad f_y = F_y/\sigma F \tag{3}$$

which yields

$$x'' = \frac{\sigma}{\bar{\omega}^2} f_x(x, y, x', y', \sigma) \qquad y'' = \frac{\sigma}{\bar{\omega}^2} f_y(x, y, x', y', \sigma) \tag{4}$$

The hydrodynamic forces are calculated by integrating the hydrodynamic oil film pressure, p, generated in the bearing, which is obtained by solving the lubrication equation—the Reynolds equation [14]. In this investigation an analytic solution is obtained by using the "long bearing approximation" (see Appendix). In solving the Reynolds equation it is common to use polar coordinates which are the eccentricity ratio ϵ (defined as the eccentricity of the journal center A normalized with respect to the radial clearance c), and the attitude angle ϕ (the angle between the load direction and the load connecting the centers of the bearing and the journal). The hydrodynamic forces are calculated as a radial force, F_r and a tangential force, F_t. Referring to Fig. 1:

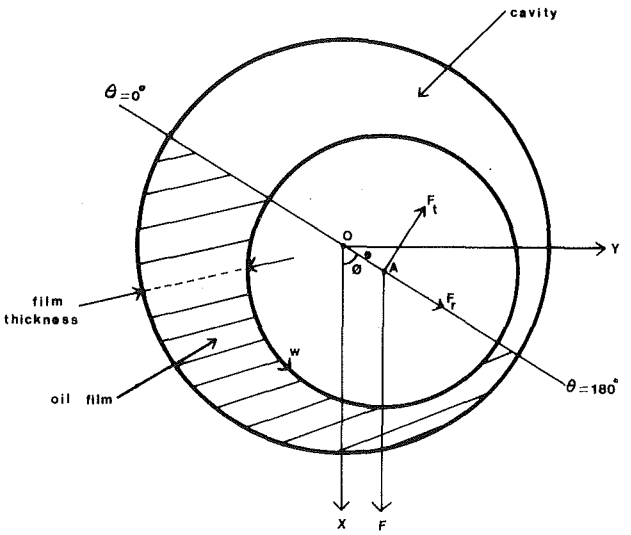

Fig. 1 Diagram of a journal bearing

$$f_x = 1/\sigma + f_r\cos\phi - f_t\sin\phi \quad f_y = f_r\sin\phi + f_t\cos\phi \quad : f_r = F_r/\sigma F \quad f_t = F_t/\sigma F \tag{5}$$

In this investigation the forces F_r, F_t include the effect of film rupture by assuming that the film extends only over the converging film section of the bearing (see Appendix).

With the origin of the $X-Y$ coordinate system located at the bearing center 0 the relationship between the polar and Cartesian coordinate is:

$$x = \epsilon\cos\phi \qquad y = \epsilon\sin\phi \tag{6}$$

This transformation, together with equation (5), defines f_x and f_y as functions of x, y, x', y'. It also follows that since f_r, f_t are differentiable functions of $\epsilon, \epsilon', \phi, \phi'$ then f_x, f_y are differentiable functions of x, y, x', y'.

To apply the Hopf bifurcation theorem, it is necessary to convert equations (4) to a first-order system of O.D.E. Writing:

$$x_1 = x \quad x_2 = x' \quad x_3 = y \quad x_4 = y' \tag{7}$$

equations (4) become:

$$x_1' = x_2$$

$$x_2' = \frac{\sigma}{\bar{\omega}^2} f_x(x_1, x_2, x_3, x_4, \sigma)$$

$$x_3' = x_4$$

$$x_4' = \frac{\sigma}{\bar{\omega}^2} f_y(x_2, x_2, x_3, x_4, \sigma)$$

or

$$\frac{\mathbf{d}}{d\gamma}\mathbf{x} = \mathbf{F}(\mathbf{x}, \bar{\omega}, \sigma) \tag{8}$$

The system of equations (8) is now in a suitable form for the application of the Hopf bifurcation theorem, with $\bar{\omega}$, the normalized rotor speed taking on the role of the parameter ν in the general theory.

Equilibrium Solutions. Denoting steady-state conditions by the subscript s, it can be shown that:

$$\mathbf{F}(\mathbf{x}_s, \bar{\omega}, \sigma) = 0 \Rightarrow \sigma(\epsilon_s) = (f_{rs}^2 + f_{ts}^2)^{-1/2} = \frac{(2+\epsilon_s^2)(1-\epsilon_s^2)}{6\epsilon_s\{\pi^2(1-\epsilon_s^2) + 4\epsilon_s^2\}^{1/2}} \tag{9}$$

and

$$\tan\phi_s = \frac{f_{ts}}{(-f_{rs})} = \pi(1-\epsilon_s^2)^{1/2}/2\epsilon_s \tag{10}$$

Equation (9) establishes the relationship between the Sommerfeld number and the steady-state value of the eccentricity ratio; equation (10) describes the locus of the journal center under steady-state conditions (Fig. 2).

Stability of the Equilibrium Position may be examined by calculating the Jacobean matrix of **F** with respect to **x**:

$$\mathbf{A}(\bar{\omega}) = (\nabla_{\mathbf{x}}\mathbf{F}(\mathbf{x},\bar{\omega}))_{\mathbf{x}=\mathbf{x}_s} = \begin{bmatrix} 0 & 1 & 0 & 0 \\ -K_{xx}/\bar{\omega}^2 - B_{xx}/\bar{\omega}^2 & -K_{xy}/\bar{\omega}^2 - B_{xy}/\bar{\omega}^2 \\ 0 & 0 & 0 & 1 \\ -K_{yx}/\bar{\omega}^2 - B_{yx}/\bar{\omega}^2 & -K_{yy}/\bar{\omega}^2 - B_{yy}/\bar{\omega}^2 \end{bmatrix} \tag{11}$$

where

$$K_{xy} = -\sigma(\partial f_x/\partial x_3)_s \ , \ B_{xy} = -\sigma(\partial f_x/\partial x_4)_s \quad \text{etc.} \tag{12}$$

The eight force derivatives, denoted in the foregoing, are referred to as velocity and displacement coefficients and, in nondimensional form, are functions of ϵ_s (see Appendix).

The eigenvalues of the matrix $A(\bar{\omega})$ satisfy the characteristic equation:

$$\lambda^4 + \frac{1}{\bar{\omega}^2}(B_{xx}+B_{yy})\lambda^3 + \frac{1}{\bar{\omega}^2}\{(K_{xx}+K_{yy}) + \frac{1}{\bar{\omega}^2}(B_{xx}B_{yy}-B_{xy}B_{yz})\}\lambda^2 + \frac{1}{\bar{\omega}^4}\{B_{xx}K_{yy}+B_{yy}K_{xx}-B_{xy}K_{yx}-B_{yx}K_{xy}\}\lambda + \frac{1}{\bar{\omega}^4}\{K_{xx}K_{yy}-K_{xy}K_{yx}\} = 0 \tag{13}$$

The roots of this equation are examined by using Routh's criterion (15) which leads to the condition:

$$\bar{\omega} < \bar{\omega}_0 \quad \text{for stability} \tag{14}$$

$\bar{\omega}_0$, the normalized threshold speed, is a function of ϵ_s only.

As the threshold speed is exceeded, a single pair of eigenvalues cross into the right half plane and the journal becomes unstable. The stability borderline $(\bar{\omega}_0/\epsilon_s)$ is shown in Fig. 3 (the other curves are explained later). For $\epsilon_s > 0.8$ the journal is always stable $(\bar{\omega}_0 = \infty)$, while for $\epsilon_s < 0.8$ there is a bifurcation point in parameter space at $(\epsilon_s, \bar{\omega}_0)$. The nondimensional whirl frequency $(\bar{\Omega}_0 = \Omega_0/\omega)$ is easily calculated from equation (13) and is given in Table 1. Since $\bar{\Omega}_0 \neq 0$ for $\epsilon_s < 0.8$ the eigenvalues that cross the imaginary axes at $(\epsilon_s, \bar{\omega}_0)$ do not pass through the origin.

The derivative $(d\bar{\alpha}/d\bar{\omega})_{\bar{\omega}=\bar{\omega}_0}$ is also required ($\bar{\alpha}(\omega) + i\bar{\Omega}(\omega)$ denotes the eigenvalue of A that is a continuous extension of $+i\bar{\Omega}_0$). In this calculation it is necessary to consider

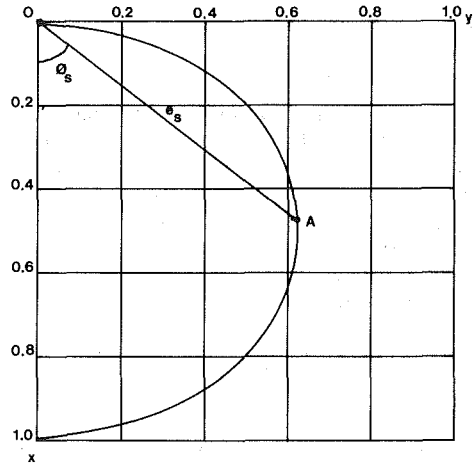

Fig. 2 Theoretical steady-state locus of the journal center

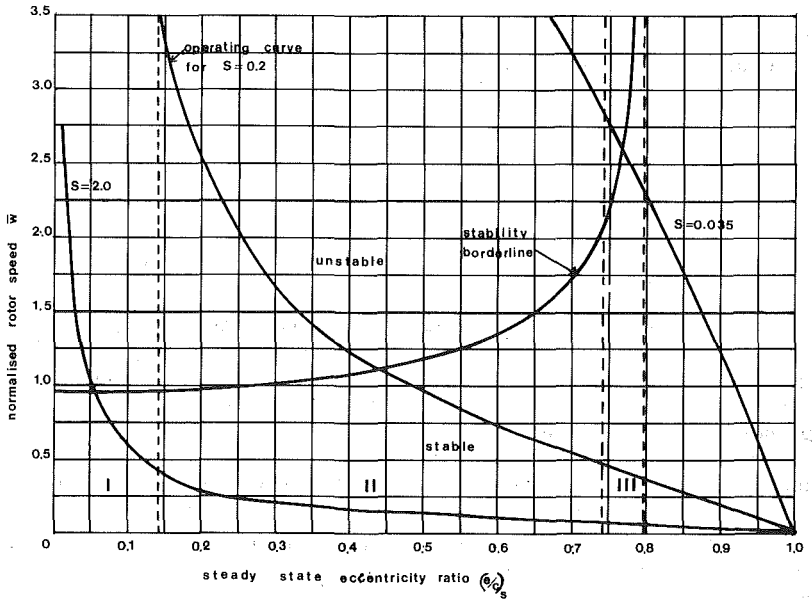

Fig. 3 Stability chart

Table 1 Results of bifurcation theory

ϵ_s	σ	$\bar{\omega}_0$	$S_0 = \sigma/\omega_0$	$(d\bar{\alpha}/d\bar{\omega})_0$	$\bar{\Omega}_0$	$\delta'(0)$
0.01	10.61	0.94	11.26	0.04	1.15	<0
0.05	2.12	0.95	2.24	0.19	1.15	<0
0.10	1.06	0.95	1.11	0.35	1.14	<0
0.14	0.76	0.96	0.79	0.45	1.13	<0
0.15	0.70	0.96	0.73	0.47	1.13	>0
0.20	0.53	0.98	0.54	0.54	1.11	>0
0.30	0.35	1.03	0.34	0.55	1.07	>0
0.40	0.25	1.10	0.23	0.46	1.02	>0
0.50	0.19	1.21	0.16	0.35	0.96	>0
0.60	0.15	1.37	0.11	0.23	0.88	>0
0.70	0.11	1.73	0.07	0.10	0.72	>0
0.74	0.10	2.13	0.05	0.05	0.60	>0
0.75	0.10	2.31	0.04	0.04	0.55	<0
0.76	0.09	2.57	0.04	0.03	0.50	<0
0.77	0.09	2.98	0.03	0.02	0.43	<0
0.78	0.09	3.77	0.02	0.01	0.35	<0
0.79	0.08	6.43	0.01	0.0	0.20	<0

the relationship between the parameters ω, σ, and ϵ_s. A change in the rotor speed ω alters the Sommerfeld number and hence the corresponding equilibrium position. A system parameter S is therefore introduced, independent of the rotor speed, and constant for any rotor system (assuming constant lubricant viscosity):

$$\text{Define} \qquad \sigma = S\bar{\omega} \Rightarrow S = LR^3\mu/(FMc)^{1/2}c^2 \tag{15}$$

A series of operating curves for different values of S is shown in Fig. 3 where each curve illustrates the relationship between the rotor speed and the corresponding equilibrium position. The derivative $(d\bar{\alpha}/d\bar{\omega})_{\bar{\omega}=\bar{\omega}_0}$ is calculated from equation (13) for constant S and tabulated in Table 1 (note $(d\bar{\alpha}/d\bar{\omega})_{\bar{\omega}=\bar{\omega}_0} > 0$).

To summarize, it has been shown that the system of equations (8) possess the following properties:

(*i*) $\mathbf{F}(\mathbf{x},\bar{\omega})$ is differentiable in a neighborhood of $(\mathbf{x},\bar{\omega}) = (\mathbf{x}_s,\bar{\omega}_0)$;
(*ii*) a locus of equilibrium points determined by the Sommerfeld number;
(*iii*) the matrix $\mathbf{A}^{\bar{\omega}_0}$ has a single pair of complex conjugate purely imaginary eigenvalues $\pm i\bar{\Omega}_0(\bar{\Omega}_0 > 0)$ for each $\epsilon_s < 0.8$. The remaining two eigenvalues have negative real parts;
(*iv*) $(d\bar{\alpha}/d\bar{\omega})_{\bar{\omega}=\bar{\omega}_0} > 0$ for each $\epsilon_s < 0.8$.

Therefore, the conditions of the Hopf bifurcation theorem are satisfied and the existence of small-amplitude periodic solutions of the system at speeds close to the threshold speed has been *proved*. It remains to determine the direction of bifurcation and the stability of the periodic orbit. This information is deduced by calculating the sign of the quantity $\delta'(0)$ which may be determined from the algebraic formulas derived by Poore [13]. Use of the formula requires the calculation of the following:

(*i*) the left and right eigenvectors for the eigenvalue $+i\bar{\Omega}_0$ of $\mathbf{A}^{\bar{\omega}_0}$.
(*ii*) the elements of the matrices $\mathbf{F}_{xx}$ and $\mathbf{F}_{xxx}$.
(*iii*) the inverse of the matrices $\mathbf{A}^{\bar{\omega}_0}$ and $(\mathbf{A}^{\bar{\omega}_0} - 2i\bar{\Omega}_0\mathbf{I})$.

Although the application of the formula is long and tedious it is relatively straightforward.

Results

The calculated values of $\delta'(0)$ are given in Table 1. The results indicate that there are three separate regions of parameter space (Fig. 3).

Regions *I*($0 < \epsilon_s \leq 0.14$) and *III*($0.74 < \epsilon_s < 0.8$). In these regions $\delta'(0) < 0$ and therefore subcritical bifurcation occurs (i.e., for $\bar{\omega} < \bar{\omega}_0$). From the remarks made earlier it follows that the bifurcated periodic orbit is unstable. From the uniqueness theorem proved by Hopf [8] no small-amplitude orbits can exist for $\bar{\omega} > \bar{\omega}_0$ (but there may be large-amplitude orbits).

Region *II*($0.14 < \epsilon_s \leq 0.74$). The largest of the three regions: $\delta'(0) > 0$ and therefore supercritical bifurcation occurs (i.e., for $\bar{\omega} > \bar{\omega}_0$). The bifurcated periodic orbit is stable.

Numerical Investigation

A numerical investigation was carried out to verify the results of the theory and to investigate how the whirl orbits develop at speeds well away from the threshold speed. The equations of motion (8) were integrated on a digital computer using a variable-order Adam's method [16]. The results are summarized here by selecting three different values of the system parameter S = 0.035, 0.2, and 2.0. These particular values were chosen because they each cross the stability borderline in a separate region of parameter space (Fig. 3). For each value of S the equations were integrated for a range of values of the rotor speed and initial conditions. Particular emphasis was placed on the effect of the initial conditions on the final motion of the journal (if at all). Results are shown in graphic form obtained by using a Calcomp plotter (Figs. 4, 5). Each plot represents the motion of the journal center (the circle at $\epsilon = 1$ is known as the clearance circle and represents the orbit of the journal center when the journal surface makes contact with the bearing side).

Figure 4 illustrates the behavior of a rotor with a system parameter of 0.035. Well below its threshold speed the journal is stable and spirals into the equilibrium position (Figs. 4(*i*), 4(*ii*). However, at a rotor speed of 2.5 ($< \bar{\omega}_0$) there are two different solutions depending on the initial conditions (Figs. 4(*iii*), 4(*iv*)). Close to its equilibrium position the journal is stable (Fig. 4(*iii*)), but if started a long way from its equilibrium position the final motion is a large-amplitude limit cycle (Fig. 4(*iv*)). This is evidence for the existence of a stable limit cycle surrounding the unstable one established by bifurcation theory. The same features are observed at a rotor speed of 2.6, which is still just below the threshold speed (Figs. 4(*v*), 4(*vi*))—the limit cycle is slightly larger. Above the threshold speed the journal is unstable for all initial conditions and approaches the bearing side (Figs. 4(*vii*), 4(*viii*)).

The behavior of a rotor with a system parameter equal to 0.2 is shown in Fig. 5. For rotor speeds below the threshold speed only the equilibrium solution was found (Figs. 5(*i*), 5(*ii*)). However, immediately above the threshold speed a stable small-amplitude whirl orbit appears, independent of the initial conditions (Figs. 5(*iii*), 5(*iv*)). This is the stable periodic orbit established by bifurcation theory. The amplitude of the orbit increases steadily as the rotor speed is

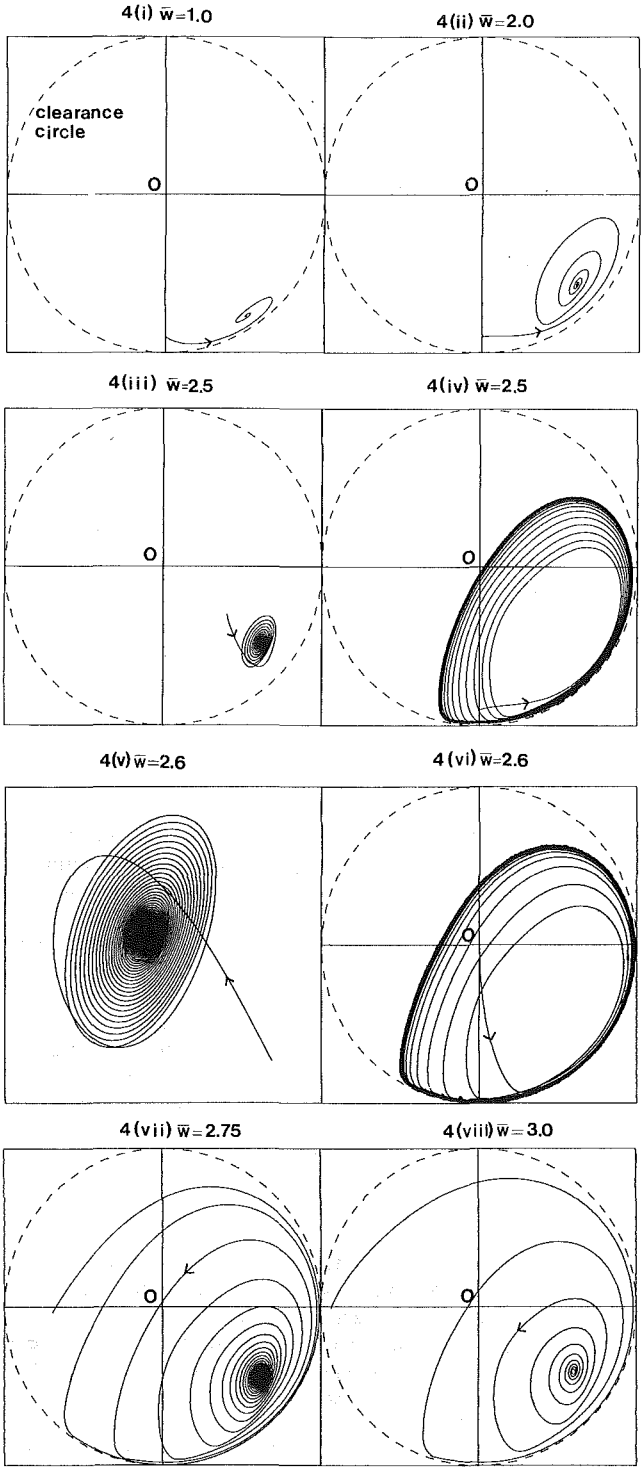

Fig. 4 Whirl orbits for a rotor with a system parameter = 0.035

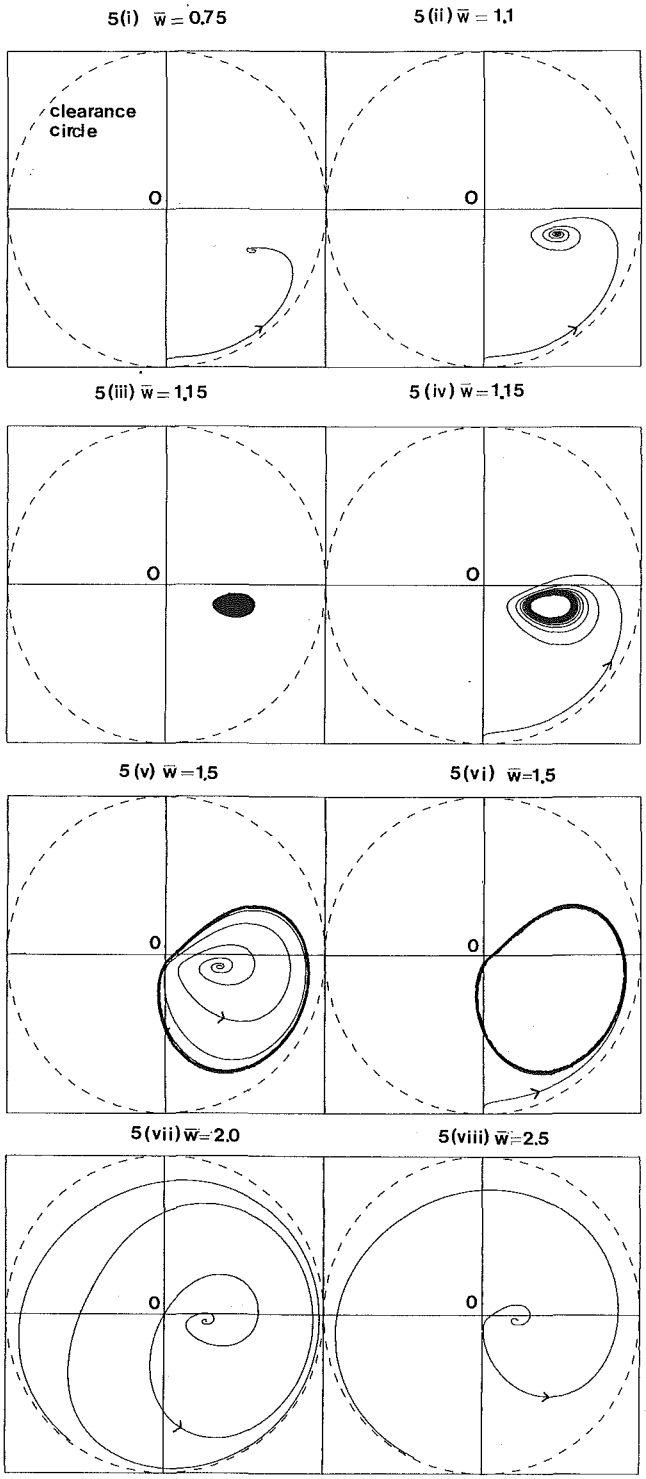

Fig. 5 Whirl orbits for a rotor with a system parameter = 0.2

increased, but the orbit remains independent of the initial conditions (Figs. 5(*v*), 5(*vi*)), before becoming completely unstable at a speed of 2.0 (Figs. 5(*vii*), 5(*viii*)).

The behavior of a rotor with a system parameter equal to 2.0 is similar to the system with $S = 0.035$ below the threshold speed with a stable limit cycle surrounding the unstable one. Two solutions are still possible above the threshold speed—a stable limit cycle or complete instability depending on the initial conditions. A detailed numerical investigation suggests that the bifurcation behavior of the system is as shown in Fig. 6(*iii*); behavior of the systems for $S = 0.035$ and 0.2 are as shown in Figs. 6(*i*), 6(*ii*) respectively.

Discussion of the Model

It is appropriate finally to comment briefly on the model that has been used in this paper—a long bearing operating with a half film. The model is a simple one and was chosen because it provides simple analytic expressions for the hydrodynamic forces (see Appendix). The model allows for cavitation, but the author is aware that the boundary conditions employed represent a crude description of both oil film rupture and film reformation [17]. Use of a more accurate model in this respect would be extremely complicated (the difficulty being in determining the direction of bifur-

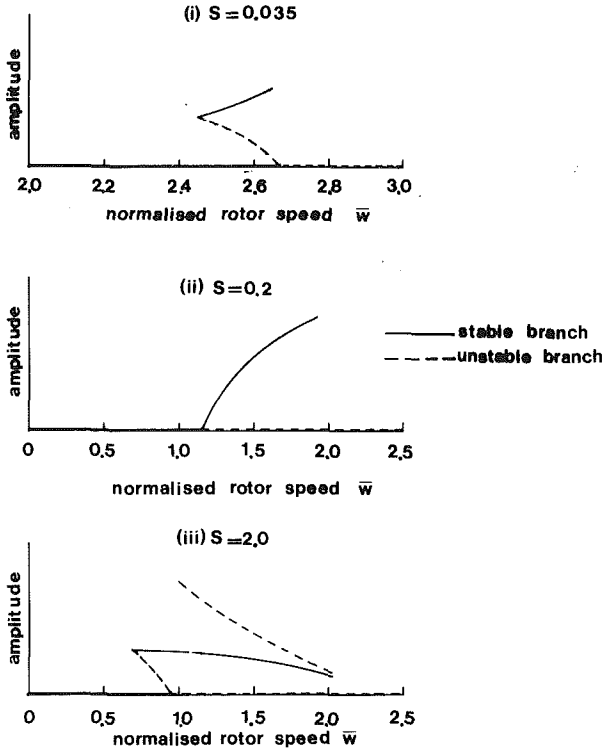

Fig. 6 Bifurcation diagrams for different rotor systems

cation). It should be stressed that a more accurate model does not alter the bifurcation character of the problem, but merely the value of the threshold speed and whirl frequency for a particular ϵ_s. It would be extremely interesting to know if a different model also has regions of parameter space in which the bifurcation is of different character.

Conclusion

The onset of oil whirl in a simple rotor system supported in fluid film journal bearings is a bifurcation phenomenon which may be examined using Hopf bifurcation theory. The existence of small-amplitude periodic solutions of the equations of motion that govern oil whirl has been established for rotor speeds close to the threshold speed. For the particular case studied (i.e., a long bearing with a half film) the bifurcation may be subcritical, or subcritical depending on the value of ϵ_s.

A numerical investigation supports the findings of the analytic work and a combination of the two methods provides a comprehensive examination of the features of the equations that govern oil whirl. When supercritical bifurcation occurs there is a gradual transition from stability to instability; a stable, small-amplitude whirl orbit appears as soon as the rotor speed exceeds its threshold value. The amplitude of the orbit increases gradually as the speed is increased and the journal does not become unstable until well above its threshold speed. When subcritical bifurcation occurs the behavior of the rotor is more complicated and, in general, dependent on the initial conditions. Stable orbits may exist both above and below the threshold speed; there is no gradual transition from stability to instability.

Since the features described in this paper are due to the nonlinearity of the equations the limitations of a purely linearized approach are exposed. This is not to say that nonlinear effects should always be included in bearing calculations, but there should certainly be a greater awareness of the role that the nonlinear terms may play.

Acknowledgments

The author wishes to thank Mr. D. Knapp, Dr. M. D. Savage, and Dr. C. M. Taylor for their supervision and helpful comments without which this work would not have been possible. Thanks are also due to the Science Research Council for their financial support.

References

1 Hori, Y., "A Theory of Oil Whip," ASME JOURNAL OF APPLIED MECHANICS, Vol. 81, 1959, pp. 189–198.

2 Holmes, R., "The Vibration of a Rigid Shaft on Short Sleeve Bearings," Journal of Mechanical Engineering Science, Vol. 2, 1960, pp. 337–341.

3 Lundholm, G., "The Axial Groove Journal Bearing Considering Cavitation and Dynamic Stability," *Acta Polytechnica*, Scandinavica, Mechanical Engineering Series No. 58, Stockholm, 1971.

4 Lund, J. W., and Saibel, E., "Oil-whip Whirl Orbits of a Rotor in Sleeve Bearings," ASME *Journal of Engineering for Industry*, Vol. 89, 1967, pp. 813–823.

5 Reddi, M. M., and Trumpler, P. R., "Stability of the High-speed Journal Bearing Under Steady Load," ASME *Journal of Engineering for Industry*, Vol. 84, 1962, pp. 351–358.

6 Mitchell, J. R., Holmes, R., and Byrne, J., "Oil Whirl of a Rigid Rotor in 360° Journal Bearings: Further Characteristics," *Proceedings of the Institution of Mechanical Engineers*, Vol. 180, 1965–1966, pp. 593–610.

7 Huggins, N. J., "Nonlinear Modes of Vibration of a Rigid Rotor in Short Journal Bearings," *Proceedings of the Second Lubrication and Wear Conference*, Institute of Mechanical Engineers, Paper 18, 1964, pp. 238–245.

8 Hopf, E., "Abzweigung einer Periodischen Lösung von einer Stationören Losung einer Differential—Systems," *Ber. Vesh. Sochs Akad Wins. Leipzig. Math. Nat. kl.*, Vol. 95, 1942, pp. 3–22.

9 Friedrichs, K. O., *Advanced Ordinary Differential Equations*, Gordon and Breach, New York, 1965.

10 Joseph, D. D., and Sattinger, D. H., "Bifurcating Time Periodic Solutions and Their Stability," *Archives for Rational Mechanics and Analysis*, Vol. 45, 1972, pp. 79–109.

11 Marsden, J. E., and McCracken, M., *The Hopf Birfurcation and its Applications*, Springer, New York, 1976.

12 Hsü, I. D., and Kazarinoff, N. D., "An Applicable Hopf Bifurcation Formula and Instability of Small Periodic Solutions of the Field-Noyes Model," *Journal of Mathematical Analysis and its Applications*, Vol. 55, 1976, pp. 61–90.

13 Poore, A. B., "On the Theory and Application of the Hopf-Friedrichs Bifurcation Theory," *Archive for Rational Mechanics and Analysis*, Vol. 60, 1976, pp. 371–392.

14 Pinkus, O., and Sternlicht, B., *Theory of Hydrodynamic Lubrication*, McGraw-Hill, New York, 1961.

15 Hartog, D., *Mechanical Vibrations*, McGraw-Hill, New York, 1947.

16 Hall, G., and Watt, J. M., *Modern Numerical Methods for Ordinary Differential Equations*, Clarendon Press, Oxford, 1976.

17 Dowson, D., and Taylor, C. M., "Cavitation in Bearings," *Ann. Rev. Fluid Mech.*, Vol. 11, 1979, pp. 35–66.

APPENDIX

Neglecting flow in the axial direction the Reynolds equation for a journal bearing is [14]:

$$\frac{d}{d\theta}\left\{(1+\epsilon\cos\theta)^3\,\frac{dp}{d\theta}\right\}=6\mu\left(\frac{R}{c}\right)^2\left\{(2\dot{\phi}-\omega)\,\epsilon\sin\theta+2\dot{\epsilon}\cos\theta\right\}$$

and is referred to as the "long bearing approximation."

The equation may be integrated, together with appropriate boundary conditions to obtain the hydrodynamic pressure generated in the bearing. Here it is assumed that the oil film occupies only the converging half of the bearing (Fig. 1) and a cavity exists in the diverging region [1], which yields boundary conditions.

$p(0)=p(\pi)=0;\quad p\equiv 0 \quad$ for $\quad \pi<\theta<2\pi$ (zero pressure corresponds to atmospheric pressure)

The hydrodynamic forces are then calculated by integrating the pressure distribution in two perpendicular directions (Fig. 1):

$$F_r = LR\int_0^{\pi} p(\theta)\ \cos\theta d\theta \quad F_t = LR\int_0^{\pi} p(\theta)\ \sin\theta d\theta$$

$$=> -\frac{F_r}{F} = 6\sigma\left\{\frac{2\epsilon^2(1-2\dot{\phi})}{(2+\epsilon^2)(1-\epsilon^2)} + \frac{[\pi^2(2+\epsilon^2)-16]\dot{\epsilon}}{\pi(2+\epsilon^2)(1-\epsilon^2)^{3/2}}\right\},$$

$$\frac{F_t}{F} = 6\sigma\left\{\frac{\pi\epsilon(1-2\dot{\phi})}{(2+\epsilon^2)(1-\epsilon^2)^{1/2}} + \frac{4\epsilon\dot{\epsilon}}{(2+\epsilon^2)(1-\epsilon^2)}\right\}$$

The eight velocity and displacement coefficients are calculated by differentiating equations (5) with respect to $x,y,\dot{x},\dot{y}$ and using equations (6)

$$B_{xx} = \frac{2\{2\epsilon[\pi^2(2+\epsilon_s^2)-16]+\pi^2(1-\epsilon_s^2)[\pi^2(1+\epsilon_s^2)+8\epsilon_s^2]\}}{\pi\epsilon_s(1-\epsilon_s^2)^{1/2}\{\pi^2(1-\epsilon_s^2)+4\epsilon_s^2\}^{3/2}}$$

$$B_{xy} = B_{yx} = \frac{2\epsilon_s B_{yy}}{\pi(1-\epsilon_s^2)^{1/2}} = \frac{2(\pi^2-8)(2+\epsilon_s^2)}{\{\pi^2(1-\epsilon_s^2)+4\epsilon_s^2\}^{3/2}}$$

$$K_{xx} = \frac{2\epsilon_s K_{xy}}{\pi(1-\epsilon_s^2)^{1/2}} = \frac{2\{8\epsilon_s^2(2+\epsilon_s^4)+\pi^2(1-\epsilon_s^2)(2-\epsilon_s^2+2\epsilon_s^4)\}}{(2+\epsilon_s^2)(1-\epsilon_s^2)\{\pi^2(1-\epsilon_s^2)+4\epsilon_s^2\}3/2}$$

$$K_{yx} = \frac{\pi\{4\epsilon_s^4-\pi^2(1-\epsilon_s^2)^2\}}{\epsilon_s(1-\epsilon_s^2)^{1/2}\{\pi^2(1-\epsilon_s^2)+4\epsilon_s^2\}3/2}$$

$$K_{yy} = \frac{2\{4\epsilon_s^2+\pi^2(2-\epsilon_s^2)\}}{\{\pi^2(1-\epsilon_s^2)+4\epsilon_s^2\}3/2}$$

Slow Interactions of Gravity Waves and a Corrugated Sea Bed

A. Mitra
Department of Environmental Resources Engineering, Humboldt State University, Arcata, Calif. 95521

M. D. Greenberg
Department of Mechanical and Aerospace Engineering, University of Delaware, Newark, Del. 19711

The effect of a corrugated sea bed on the linear theory of gravity water waves is considered. By straining the time variable, a perturbation solution is found in ϵ (the ratio of corrugation amplitude to mean water depth), through first order, for a wave system that is arbitrarily oriented with respect to the corrugations. That solution breaks down when the wave number k normal to the corrugation is a half-integer multiple of the wave number 2ω of the corrugations, i.e., when $k = \omega, 2\omega, \ldots$. Of these singularities, the first ($k = \omega$) appears at the first order. To obtain a uniformly valid zeroth-order solution we include a zeroth-order reflected wave system, and obtain an alternation between incident and reflected waves on a time scale of order $0(\epsilon^{-1})$. As representative of the other singular wave numbers, we consider $k = 3\omega$, which singularity appears at the third order, and obtain a uniformly valid solution through second order (for the shallow water limit). Nonlinear effects are considered to the extent of noting that the zeroth-order linear and nonlinear results are identical, even for the first singular wave number $k = \omega$.

Introduction

The mutual interaction of sea bed topography and gravity water waves is of considerable interest to coastal engineers, especially insofar as certain topographies are capable of protecting the beach by the reflection of wave energy. Of fundamental interest is the case of a sinusoidally corrugated sea bed wherein the corrugations are doubly infinite (in the horizontal direction normal to the corrugations), or where there is present only a finite "patch" of corrugations. These two subcases have been studied analytically, most recently, by Davies [1-3], and companion experimental results have been reported by Heathershaw [4]. An extensive literature review is provided in [1].

In connection with the problem of a zeroth-order wave traveling normal to a doubly infinite corrugation, Davies obtains, at the next order, two corrections: one wave whose wave number is the sum of the wave numbers of the zeroth-order wave and the corrugation, and which is always onward transmitted, and one whose wave number is the difference of those wave numbers and which is reflected if the wave number of the zeroth-order wave is less than that of the corrugation. Furthermore, Davies notes that the amplitude of the reflected wave tends to infinity as the wave number of the zeroth-order wave approaches half the wave number of the corrugation, so that his perturbation solution is not uniformly valid. He also notes that the second-order solution is singular for *all* wave numbers. In the present paper, we examine the singularities, and obtain uniformly valid solutions by a straining of the time variable.

Of course, resonant interactions have been discussed in the literature in a number of settings. For instance, Rhines and Bretherton [5] encountered such resonance in their study of Rossby waves in an ocean with a sinusoidal bed, Rhines [6] explored the main features of wave propagation in a periodic medium by applying Floquet theory to the relevant Hill's equation, and Mitra and Greenberg [7] encountered an infinite sequence of resonances in their study of Kelvin-Helmholtz instability of a free surface in the presence of a corrugated sea bed.

Formulation

We consider the linearized theory of gravity water waves in the presence of a corrugated sea bed. Assuming the flow to be irrotational and incompressible, we have $\mathbf{q} = \nabla\phi$, where $\mathbf{q}$ is the fluid velocity field, $\nabla = \hat{\mathbf{i}}\,\partial/\partial x + \hat{\mathbf{j}}\,\partial/\partial y + \hat{\mathbf{k}}\,\partial/\partial z$, $\phi(\mathbf{x},t)$ is the velocity potential, t is the time, and where x,y,z are the right-handed cartesian coordinates depicted in Fig. 1. It is known [8] that ϕ is governed by the boundary value problem

$$\nabla^2\phi = 0, \quad -h(x) < z < 0, \quad x^2 + y^2 < \infty, \tag{1a}$$

$$\phi_{tt} + g\phi_z = 0, \quad z = 0, \quad x^2 + y^2 < \infty, \tag{1b}$$

$$\phi_z = -h'(x)\phi_x, \quad z = -h(x), \quad x^2 + y^2 < \infty, \tag{1c}$$

where g is the gravitational acceleration,

$$h(x) = d(1 + \epsilon\cos 2\omega x), \quad 0 < \epsilon << 1, \quad \omega > 0 \tag{2}$$

is the undisturbed water depth (Fig. 1), and subscripts denote partial derivatives.

To find bounded wave motions, we use the assumed smallness of ϵ and seek a strained time variable solution

Contributed by the Applied Mechanics Division for presentation at the 1984 PVP Conference and Exhibition, Joint with Applied Mechanics Division and Materials Division, San Antonio, Texas, June 17-21, 1984 of THE AMERICAN SOCIETY OF MECHANICAL ENGINEERS.

Discussion on this paper would be addressed to the Editorial Department, ASME, United Engineering Center, 345 East 4th Street, New York, N.Y. 10017, and will be accepted until two months after final publication of the paper itself in the JOURNAL OF APPLIED MECHANICS. Manuscript received by ASME Applied Mechanics Division, September, 1982; final revision, June, 1983. Paper No. 84-APM-16.

Copies will be available until February, 1985.

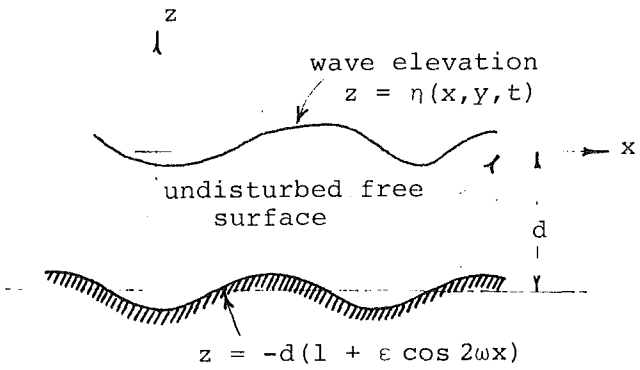

Fig. 1 Flow geometry

$$\phi(\mathbf{x},t)=\phi_0(\mathbf{x},\tau)+\epsilon\phi_1(\mathbf{x},\tau)+\ \ldots, \tag{3a}$$

$$\tau=(1+\alpha_1\epsilon+\alpha_2\epsilon^2+\ \ldots)t. \tag{3b}$$

Putting (3) into (1) we have, through $0(\epsilon^2)$, the problem sequence

$$0(1):\quad \nabla^2\phi_0=0,\quad -d<z<0 \tag{4a}$$

$$\phi_{0\tau\tau}+g\phi_{0z}=0,\quad z=0 \tag{4b}$$

$$\phi_{0z}=0,\quad z=-d \tag{4c}$$

$$0(\epsilon):\quad \nabla^2\phi_1=0,\quad -d<z<0 \tag{5a}$$

$$\phi_{1\tau\tau}+g\phi_{1z}=-2\alpha_1\phi_{0\tau\tau},\quad z=0 \tag{5b}$$

$$\phi_{1z}=2\omega d\sin 2\omega x\,\phi_{0x}+d\cos 2\omega x\,\phi_{0zz},\quad z=-d \tag{5c}$$

$$0(\epsilon^2):\quad \nabla^2\phi_2=0,\quad -d<z<0 \tag{6a}$$

$$\phi_{2\tau\tau}+g\phi_{2z}=-2\alpha_1\phi_{1\tau\tau}-(\alpha_1{}^2+2\alpha_2)\phi_{0\tau\tau},\quad z=0 \tag{6b}$$

$$\phi_{2z}=2\omega d\sin 2\omega x\,\phi_{1x}+d\cos 2\omega x\phi_{1zz}$$
$$-\omega d^2\sin 4\omega x\,\phi_{0xz}-\frac{1}{4}d^2(1+\cos 4\omega x)\phi_{0zzz},\quad z=-d \tag{6c}$$

we can see that (8) includes traveling waves ($A=0$ or $B=0$), standing waves ($A=\pm B$), and combinations.

Before turning to the $0(\epsilon)$ and $0(\epsilon^2)$ systems, we note, for reference, that

$$\nabla^2\phi=0,\quad -d<z<0 \tag{11a}$$

$$\phi_{\tau\tau}+g\phi_z=e^{i(Rx+Sy+T\tau)},\quad z=0 \tag{11b}$$

$$\phi_z=0,\quad z=-d \tag{11c}$$

admits the solution

$$\phi=\frac{\cosh L(z+d)}{gL\sinh Ld-T^2\cosh Ld}e^{i(Rx+Sy+T\tau)}, \tag{12}$$

and that

$$\nabla^2\phi=0,\quad -d<z<0 \tag{13a}$$

$$\phi_{\tau\tau}+g\phi_z=0,\quad z=0 \tag{13b}$$

$$\phi_z=e^{i(Rx+Sy+T\tau)},\quad z=-d \tag{13c}$$

admits the solution

$$\phi=\left[\frac{(T^2\sinh Ld-gL\cosh Ld)\cosh L(z+d)}{L(gL\sinh Ld-T^2\cosh Ld)}+\frac{\sinh L(z+d)}{L}\right]e^{i(Rx+Sy+T\tau)}, \tag{14}$$

provided that the denominators are nonzero; in each case, $L=\sqrt{(R^2+S^2)}$. If we *do* have $gL\sinh LD-T^2\cosh Ld=0$ then we will say that $\exp i(Rx+Sy+T\tau)$ is a *secular term*. By virtue of (9), we see that $\exp i(\pm kx\pm ly\pm\sigma\tau)$ will be secular for any combination of signs. Put another way, $\exp i(\pm kx\pm ly\pm\sigma\tau)$ will be secular because it is a solution of the *homogeneous* system (4).

Now turning to the $0(\epsilon)$ system (5), we see that the $\phi_{0\tau\tau}$ term, in (5*b*), is secular, so we must set

$$\alpha_1=0. \tag{15}$$

Using (14), we have, as the solution of (5),

$$\phi_1=\frac{Ad}{2}(K^2+2\omega k)\left[\frac{(\sigma^2\sinh K^+d-gK^+\cosh K^+d)\cosh K^+(z+d)}{K^+(gK^+\sinh K^+d-\sigma^2\cosh K^+d)}+\frac{\sinh K^+(z+d)}{K^+}\right]e^{i[(k+2\omega)x+ly-\sigma\tau]}$$
$$+\frac{Ad}{2}(K^2-2\omega k)\left[\frac{(\sigma^2\sinh K^-d-gK^-\cosh K^-d)\cosh K^-(z+d)}{K^-(gK^-\sinh K^-d-\sigma^2\cosh K^-d)}+\frac{\sinh K^-(z+d)}{K^-}\right]e^{i[(k-2\omega)x+ly-\sigma\tau]}+[B]+CC, \tag{16}$$

over $x^2+y^2<\infty$.

Solution for Nonsingular Case

Looking for wavelike solutions, we choose ϕ_0 of the form

$$\phi_0=a(z)e^{i(\mathbf{k}\cdot\mathbf{x}-\sigma\tau)}+b(z)e^{i(\mathbf{k}\cdot\mathbf{x}+\sigma\tau)}+CC, \tag{7}$$

where $\mathbf{k}\cdot\mathbf{x}=kx+ly$, and where *CC* stands for the complex conjugate of the preceding terms on the right-hand side. It will suffice to consider $k>0$. In the event that $l=0$, the wave crests are parallel to the corrugations. Putting (7) into (4), we find that

$$\phi_0=\cosh K(z+d)[Ae^{i(\mathbf{k}\cdot\mathbf{x}-\sigma\tau)}+Be^{i(\mathbf{k}\cdot\mathbf{x}+\sigma\tau)}]+CC$$
$$\equiv A\cosh K(z+d)e^{i(\mathbf{k}\cdot\mathbf{x}-\sigma\tau)}+[B]+CC, \tag{8}$$

where A and B are arbitrary constants, $K=\sqrt{(k^2+l^2)}$, and

$$\sigma^2=gK\tanh Kd. \tag{9}$$

We use the shorthand notation $[B]$ to denote the term(s) obtained from the preceding A term(s) under the substitutions $A\to B$, $\tau\to-\tau$. Since the free surface elevation η is given [8] by

$$\eta(x,y,t)=-\frac{1}{g}\phi_t(x,y,0,t), \tag{10}$$

where $K^\pm=\sqrt{[(k\pm2\omega)^2+l^2]}$.

Finally, we consider the $0(\epsilon^2)$ system (6) in order to compute α_2. To accomplish that we need to focus on the secular terms in (6*b*) and (6*c*). Specifically, we express those equations as

$$\phi_{2\tau\tau}+g\phi_{2z}=2\alpha_2A\sigma^2\cosh Kd\,e^{i(kx+ly-\sigma\tau)}+[B]+CC,\quad z=0 \tag{17a}$$

$$\phi_{2z}=AQe^{i(kx+ly-\sigma\tau)}+[B]+CC+NST,\quad z=-d \tag{17b}$$

where

$$Q=\frac{d^2}{4}\left[(k^2+2\omega k+l^2)^2\frac{\sigma^2\sinh K^+d-gK^+\cosh K^+d}{K^+(gK^+\sinh K^+d-\sigma^2\cosh K^+d)}+(k^2-2\omega k+l^2)^2\frac{\sigma^2\sinh K^-d-gK^-\cosh K^-d}{K^-(gK^-\sinh K^-d-\sigma^2\cosh K^-d)}\right], \tag{18}$$

and where *NST* stands for *nonsecular terms*. If we insist on eliminating each of the secular terms we find that $A=B=0$, which is unacceptable. In fact, we only need the secular terms to bear a certain relationship to one another. If we seek a response to the $\exp i(kx+ly-\sigma\tau)$, $\exp i(kx+ly+\sigma\tau)$ secular terms in the form

$$\phi_2=[D\cosh K(z+d)+E\sinh K(z+d)]e^{i(kx+ly-\sigma\tau)}$$
$$+[F\cosh K(z+d)+G\sinh K(z+d)]e^{i(kx+ly+\sigma\tau)}, \tag{19}$$

then (17a) yields

$$E=2\alpha_2 A\sigma^2\frac{\cosh^2 Kd}{gK}, \tag{20a}$$

$$G=2\alpha_2 B\sigma^2\frac{\cosh^2 Kd}{gK}, \tag{20b}$$

and (17b) yields

$$E=A\frac{Q}{K}, \tag{21a}$$

$$G=B\frac{Q}{K}. \tag{21b}$$

And, comparing (20) and (21), we see that

$$\alpha_2=\frac{gQ}{2\sigma^2\cosh^2 Kd}=\frac{Q}{K\sinh 2Kd}, \tag{22}$$

while A and B remain arbitrary.

We may now obtain η, through first-order terms, from (10), as

$$\eta=-\frac{1}{g}\phi_{0\tau}\Big|_{z=0}-\frac{\epsilon}{g}\phi_{1\tau}\Big|_{z=0}+0(\epsilon^2)$$

$$=i\sigma dA\Big\{\frac{\cosh Kd}{gd}e^{i(kx+ly-\sigma\tau)}$$

$$+\frac{\epsilon}{2}\Big(\frac{k(k+2\omega)+l^2}{(\sigma^2-gK^+\tanh K^+d)\cosh K^+d}e^{i[(k+2\omega)x+ly-\sigma\tau]}$$

$$+\frac{k(k-2\omega)+l^2}{(\sigma^2-gK^-\tanh K^-d)\cosh K^-d}e^{i[(k-2\omega)x+ly-\sigma\tau]}$$

$$+0(\epsilon^2)\Big\}+[B]+CC. \tag{23}$$

The phase speed of the exp $i[(k-2N\omega)x+ly-\sigma\tau]$ harmonic ($N=0,\pm1$) is $\sigma[1+\alpha_2\epsilon^2+0(\epsilon^3)]/\sqrt{(k-2N\omega)^2+l^2}$.

Since *long waves* (i.e., the *shallow wave theory* [8]) are of special interest, let us indicate the long wave limit of (23). In that case $Kd<<1$, $K^+d<<1$, and $K^-d<<1$, so that

$$\eta=\frac{i\sigma A}{g}\{e^{i(kx+ly-\sigma\tau)}$$

$$-\frac{\epsilon}{8\omega}\Big[\frac{k(k+2\omega)+l^2}{k+\omega}e^{i[(k+2\omega)x+ly-\sigma\tau]}$$

$$-\frac{k(k-2\omega)+l^2}{k-\omega}e^{i[(k-2\omega)x+ly-\sigma\tau]}\Big]$$

$$+0(\epsilon^2)\}+[B]+CC, \tag{24}$$

where

$$\sigma=\sqrt{gd}\,K \tag{25}$$

and

$$\tau=\Big\{1+\frac{\epsilon^2}{32\omega K^2}\Big[\frac{[k(k-2\omega)+l^2]^2}{k-\omega}$$

$$-\frac{[k(k+2\omega)+l^2]^2}{k+\omega}\Big]+0(\epsilon^3)\Big\}t. \tag{26}$$

We note, as a partial check on the algebra, that we have obtained these same results, (24)–(26), by applying straining directly to the well-known linear shallow water equation

$$\nabla\cdot[gh(x)\nabla\eta]=\eta_{tt}. \tag{27}$$

Singularities

We see from (16) and (23) that the perturbation series breaks down when $\sigma^2\approx gK^+\tanh K^+d$ or $\sigma^2\approx gK^-\tanh K^-d$. Recalling (9), it follows that such breakdown occurs when

$$k\approx\omega. \tag{28}$$

If the perturbation procedure were carried further, we would find breakdowns not only at $k\approx\omega$, but at $k\approx 2\omega$, 3ω, . . . , as well, i.e., *when the x-wise wave number of the disturbance is a half-integer multiple of the wave number* (2ω) *of the corrugation*. Of these singular wave numbers, we will see that most practical interest attaches to the first, $k\approx\omega$.

It is interesting that the singularity at $k\approx\omega$ can be "detuned," i.e., reduced to any desired degree, by choosing $|l|$ sufficiently close to ω. For instance, consider the exp $i[(k-2\omega)x+ly-\sigma\tau]$ term in (16), the coefficient of which is infinite when $k=\omega$ since then $gK^-\sinh K^-d-\sigma^2\cosh K^-d=0$ in the denominator. This term is the response to the

$$\frac{Ad}{2}(K^2-2\omega k)e^{i[(k-2\omega)x+ly-\sigma\tau]} \tag{29}$$

term on the right-hand side of (5c), which term can be eliminated by adjusting l so that $|l|=\omega$, since then $K^2-2\omega k=k^2+l^2-2\omega k=\omega^2+l^2-2\omega^2=0$. In short, the wave number $k\approx\omega$ is *non*singular if $|l|$ is sufficiently close to ω, i.e., if the first-order wave crests are sufficiently close to an angle of 45 deg relative to the crests of the corrugations. This curious situation is mentioned by Rhines [6] in connection with the shallow water theory. However, we note here that setting $|l|=\omega$ does not truly eliminate the $k=\omega$ singularity; it merely suppresses it so that it does not appear until the next order perturbation.

The Singular Case $k=\omega$

In this section we consider the case $k\approx\omega$ (with $|l|\neq\omega$). More specifically, we consider the "worst" case, the equality $k=\omega$.

To motivate the form to assume for ϕ_0 it is helpful to look back at the form of ϕ_0 and ϕ_1 in the expansion $\phi\sim\phi_0+\epsilon\phi_1$ for the *non*singular case. In fact it will suffice to look at (24), and to observe the structure as k increases from zero toward ω. If we regard the exp $i(kx+ly-\sigma\tau)$ term as an incident wave, then we see that the exp $i[(k+2\omega)x+ly-\sigma\tau]$ correction is a transmitted wave, and that the exp $i[(k-2\omega)x+ly-\sigma\tau]$ correction is a reflected wave (since $k-2\omega<0$ in the present discussion). Furthermore, the reflection coefficient tends to infinity as $k\to\omega$. Of course the perturbation solution breaks down as $k\to\omega$, but in a crude sense the large $0(\epsilon)$ reflection suggests that we need to include a reflection term in the 0(1) part of η when k is close to ω, i.e., a reflection with respect to the corrugation. Thus, let us choose ϕ_0 in the form

$$\phi_0=\cosh K(z+d)[Ae^{i(\omega x+ly-\sigma\tau)}+Be^{i(-\omega x+ly-\sigma\tau)}]+CC, \tag{30}$$

where $K=\sqrt{(\omega^2+l^2)}$ and $\sigma=\sqrt{(gK\tanh Kd)}$. (By comparison, the direction cosine pairs in (8) are all the same, namely k,l.) Then (5b) and (5c) become

$$\phi_{1\tau\tau}+g\phi_{1z}=2\alpha_1\sigma^2\cosh Kd\,[Ae^{i(\omega x+ly-\sigma\tau)}$$

$$+Be^{i(-\omega x+ly-\sigma\tau)}]+CC,\quad z=0 \tag{31a}$$

$$\phi_{1z}=\frac{l^2-\omega^2}{2}d[Ae^{i(-\omega x+ly-\sigma\tau)}$$

$$+Be^{i(\omega x+ly-\sigma\tau)}]+CC+NST,\quad z=-d, \tag{31b}$$

respectively.

Using the same strategy as in our calculation of α_2 in the nonsingular case, we seek the response to the exp $i(\omega x+ly-\sigma\tau)$, exp $i(-\omega x+ly-\sigma\tau)$ secular terms in (31) in the form

$$\phi_1=[D\cosh K(z+d)+E\sinh K(z+d)]e^{i(\omega x+ly-\sigma\tau)}$$

$$+[F\cosh K(z+d)+G\sinh K(z+d)]e^{i(-\omega x+ly-\sigma\tau)}. \tag{32}$$

With this choice, a short calculation yields the two solutions

$$\alpha_1 = \frac{d(\omega^2 - l^2)}{2K \sinh 2Kd}, \quad B = -A, \tag{33a}$$

and

$$\alpha_1 = -\frac{d(\omega^2 - l^2)}{2K \sinh 2Kd}, \quad B = A. \tag{33b}$$

Thus, with the benefit of superposition,

$$\phi_0 = \cosh K(z+d)[A_1 e^{i[\omega x + ly - \sigma(1+\alpha\epsilon)t]} - A_1 e^{i[-\omega x + ly - \sigma(1+\alpha\epsilon)t]} + A_2 e^{i[\omega x + ly - \sigma(1-\alpha\epsilon)t]} + A_2 e^{i[-\omega x + ly - \sigma(1-\alpha\epsilon)t]}] + CC, \tag{34}$$

where $\alpha = d(\omega^2 - l^2)/(2K \sinh 2Kd)$.

To express (34) in a more suggestive form we introduce two changes in notation. First, we set $A_1 = (a_1/4) \exp(i\psi_1)$, $A_2 = (a_2/4) \exp(i\psi_2)$, and, second, we introduce a "fast time" t' and a "slow time" t'' as

$$\sigma t' = \sigma t - \frac{\psi_1 + \psi_2}{2}, \tag{35a}$$

$$\sigma t'' = \alpha\epsilon\sigma t - \frac{\psi_1 - \psi_2}{2}, \tag{35b}$$

in which case (34) becomes

$$\phi_0 = \cosh K(z+d)\{\cos \sigma t''[-a_1 \sin \omega x \sin(ly - \sigma t') + a_2 \cos \omega x \cos(ly - \sigma t')] + \sin \sigma t''[a_1 \sin \omega x \cos(ly - \sigma t') - a_2 \cos \omega x \sin(ly - \sigma t')]\}. \tag{36}$$

Correspondingly,

$$\eta \sim -\frac{1}{g}\phi_{0t}\Big|_{z=0} \sim -\frac{1}{g}\phi_{0t'}\Big|_{z=0} = \cos \sigma t''[c_1 \sin \omega x \cos(ly - \sigma t') + c_2 \cos \omega x \sin(ly - \sigma t')] + \sin \sigma t''[c_1 \sin \omega x \sin(ly - \sigma t') + c_2 \cos \omega x \cos(ly - \sigma t')] \tag{37}$$

where we have absorbed a factor of $-(\sigma/g) \cosh Kd$ into the arbitrary constants a_1, a_2, and called the results c_1, c_2; (37) includes traveling waves, standing waves, and combinations, depending on c_1, c_2. Especially interesting are the cases where $c_2 = \pm c_1$. For instance, if $c_2 = c_1 \equiv c$, then

$$\eta \approx c[\cos \sigma t'' \sin(\omega x + ly - \sigma t') + \sin \sigma t'' \cos(-\omega x + ly - \sigma t')]. \tag{38}$$

The solution given by (38) is characterized by a slow reflection process, i.e., an alternation between the $\sin(\omega x + ly - \sigma t')$ and $\cos(-\omega x + ly - \sigma t')$ wave systems, with a period of alternation

$$\text{Period} = \frac{2\pi}{\alpha\sigma\epsilon} = 0(\epsilon^{-1}). \tag{39}$$

This slow energy transfer has already been noted in the literature for the long wave limit, e.g., in Rhines [6], though Rhines procedes instead by applying Floquet theory to the separated form of (27). Observe from (33) that $\alpha \to 0$ as $d \to \infty$, so that the period is very long for deep water. Hence the reflection process may be of limited practical interest in the intermediate and deep water limit.

For the long wave limit one can extend the foregoing results from $k = \omega$ to $k \approx \omega$. Let $k = (1 + \beta\epsilon)\omega$, where β is an arbitrary 0(1) constant. Then (27) becomes

$$gd\left\{\left[\left(1 + \epsilon \cos\frac{2k}{1+\beta\epsilon}x\right)\eta_x\right]_x + \left(1 + \epsilon \cos\frac{2k}{1+\beta\epsilon}x\right)\eta_{yy}\right\} = \eta_{tt}. \tag{40}$$

With $x/(1+\beta\epsilon) = \bar{x}$, $y/(1+\beta\epsilon) = \bar{y}$, and $t/(1+\beta\epsilon) = \bar{t}$, equation (40) becomes

$$dg\{[(1 + \epsilon \cos 2k\bar{x})\eta_{\bar{x}}]_{\bar{x}} + (1 + \epsilon \cos 2k\bar{x})\eta_{\bar{y}\bar{y}}\} = \eta_{\bar{t}\bar{t}}, \tag{41}$$

which is of the same form as before, when we had $k = \omega$. Thus, the long wave version of (38),

$$\eta \sim c[\cos\sqrt{gd(\omega^2 + l^2)}t'' \sin(\omega x + ly - \sqrt{gd(\omega^2 + l^2)}t') + \sin\sqrt{gd(\omega^2 + l^2)}t'' \cos(-\omega x + ly - \sqrt{gd(\omega^2 + l^2)}t')] \tag{42}$$

still holds subject to the replacements $\omega \to (1 + \beta\epsilon)\omega$, $x \to x/(1+\beta\epsilon)$, $y \to y/(1+\beta\epsilon)$, $t \to t/(1+\beta\epsilon)$.

The Singular Case $k = 3\omega$

For $k \approx \omega, 3\omega, 5\omega, \ldots$, the singularities appear first at the perturbations of order 1, 3, 5, . . . , respectively. For $k \approx 2\omega, 4\omega, \ldots$, however, their appearance is somewhat delayed; e.g., for $k \approx 2\omega$ they do not appear until the perturbation of order 6. Thus after $k \approx \omega$, the next to appear is $k \approx 3\omega$. Hence, in this section we mention $k = 3\omega$, as representative of the "higher order" singularities. If, for the sake of algebraic simplicity, we limit our attention to the long wave limit (shallow water theory), with $l = 0$, we obtain

$$\eta \sim \eta_0 = [\cos \sigma t''(c_1 \cos 3\omega x \cos \sigma t' + c_2 \sin 3\omega x \sin \sigma t') - \sin \sigma t''(c_1 \cos 3\omega x \sin \sigma t' + c_2 \sin 3\omega x \cos \sigma t')], \tag{43}$$

where

$$\sigma t' = \sigma\left(1 - \frac{207}{1152}\epsilon^2\right)t - \frac{\psi_1 + \psi_2}{2}, \tag{44a}$$

$$\sigma t'' = \frac{3}{1024}\sigma\epsilon^3 t - \frac{\psi_1 - \psi_2}{2}. \tag{44b}$$

As before, the cases $c_2 = \pm c_1$ reveal a slow reflection process, although in this case the period of the reflection process is

$$\text{Period} = \frac{2048\pi}{9\omega\sqrt{gd}\epsilon^3} = 0(\epsilon^{-3}) \tag{45}$$

which is perhaps too long to be of interest in most applications. For instance, if we adopt, as representative (Langhorne [9]), the values $\omega = \pi/10$ meters^{-1}, $d = 10$ meters, and $\epsilon = 0.05$, then the period (45) is around 21 days! And the period is even longer than $0(\epsilon^3)$ for the other singular wave numbers $k = 2\omega, 4\omega, 5\omega, 6\omega, \ldots$. Only for the smallest singular wave number, $k = \omega$, does the period seem to be short enough to be of practical interest. For example, for the case selected above the reflection period (as given by [9] with $\alpha = 1/4$ and $\sigma = \omega\sqrt{gd}$ in the long wave limit) is only around 2.7 minutes.

Nonlinear Effects

In this section we take a limited look at the effects of nonlinearity. The full nonlinear boundary value problem is (see [8])

$$\nabla^2\phi = 0, \quad -h(x) < z < \eta(x,y,t) \tag{48a}$$

$$\eta_t - \phi_z + \eta_x\phi_x + \eta_y\phi_y = 0, \quad z = \eta(x,y,t) \tag{48b}$$

$$g\eta + \phi_t + \frac{1}{2}(\phi_x{}^2 + \phi_y{}^2 + \phi_z{}^2) = 0, \quad z = \eta(x,y,t) \tag{48c}$$

$$\phi_z = -h'(x)\phi_x, \quad z = -h(x) \tag{48d}$$

over $x^2 + y^2 < \infty$.

It is found that the secularity condition is unaffected by the nonlinear terms, so that the zeroth-order solutions (for ϕ_0, η_0, α_1) are the same as predicted by the linear theory presented in the foregoing sections – at least for $k \neq 2\omega, 3\omega, 4\omega, \ldots$, since in those cases we must go beyond $0(\epsilon)$ in order to finalize the first-order solution.

Conclusions

We first examined the effect of a corrugated sea bed on the linear theory of gravity waves. Considering a linear combination of zeroth-order waves moving in the directions $\pm(k\hat{\mathbf{i}}+l\hat{\mathbf{j}})$, we obtained solutions for ϕ and η which are uniformly valid (in space and time) through $0(\epsilon)$, with the help of a straining of the time variable (not included in [1]), provided that $k \neq \omega, 2\omega, \ldots$. The amplitudes of the $+(k\hat{\mathbf{i}}+l\hat{\mathbf{j}})$ directed wave and the $-(k\hat{\mathbf{i}}+l\hat{\mathbf{j}})$ directed wave were found to be independent so that one can form traveling waves, standing waves, or combinations. Each of these zeroth-order waves admits two first-order corrections, as seen in (23). Consider, for example, the $+(k\hat{\mathbf{i}}+l\hat{\mathbf{j}})$ directed zeroth-order wave. It admits one first-order $[(k+2\omega)\ \hat{\mathbf{i}} + l\hat{\mathbf{j}}]$ wave, whose crests are more closely aligned with the corrugations, and one first-order $[(k-2\omega)\ \hat{\mathbf{i}} + l\hat{\mathbf{j}}]$ wave, whose crests are less closely aligned with the corrugations. Thus, we will refer to the latter wave as "reflected." The amplitude of this first-order reflected wave tends to infinity as $k \to \omega$, and this fact led us to include a reflected zeroth-order wave in the singular case $k = \omega$. A uniformly valid zeroth-order solution was thus obtained for $k = \omega$. This solution exhibits the possibility of direction reversal on a time scale of order ϵ^{-1}, as has been reported in the literature for a variety of physical settings (e.g. [6]).

It was also noted that the $k = \omega$ singularity could be suppressed until the next order perturbation by setting $|l| = \omega$ (in which case the zeroth-order wave crests are at an angle of 45 deg to the corrugations).

As in the $k = \omega$ case, the higher singularities ($k = 2\omega, 3\omega, \ldots$) require the inclusion of reflected zeroth-order waves, and one again obtains the slow reversal phenomenon, although on a much longer time scale than for $k = \omega$.

Finally, nonlinear effects were considered to the extent of noting that the linear and nonlinear zeroth-order solutions are identical – provided that $k \neq 2\omega, 3\omega, \ldots$, with no information obtained for the cases $k \approx 2\omega, 3\omega, \ldots$.

Acknowledgment

The authors are grateful to Professor Robert A. Dalrymple (University of Delaware) for reading an early version of this paper and for pointing out the Davies and Heathershaw references.

References

1 Davies, A. G., "Some Interactions Between Surface Water Waves and Ripples and Dunes on the Seabed," Institute of Oceanographic Sciences, England, Report No. 108, 1980.

2 Davies, A. G., "On the Interaction Between Surface Waves and Undulations of the Seabed," *J. Marine Research*, in press.

3 Davies, A. G., "The Reflection of Wave Energy by Undulations on the Seabed," *J. Dynamics of Atmospheres and Oceans*, in press.

4 Heathershaw, A. D., "Seabed-Wave Resonance and Sand Bar Growth," manuscript.

5 Rhines, P. B., and Bretherton, F., "Topographic Rossby Waves in a Rough-Bottomed Ocean," *J. Fluid Mechanics*, Vol. 61, No. 3, 1973, pp. 583–607.

6 Rhines, P. B., "Wave Propagation in a Periodic Medium With Application to the Ocean," *Rev. Geophysics and Space Physics*, Vol. 8, No. 2, 1970, pp. 303–319.

7 Mitra, A., and Greenberg, M. D., "Effect of a Wavy Bottom on Kelvin-Helmholtz Instability," *J. Hydronautics*, Vol. 8, No. 2, 1974, pp. 53–57.

8 Stoker, J. J., *Water Waves*, Interscience, New York, 1957.

9 Langhorn, D. N., "Offshore Engineering and Navigational Problems: the Relevance of Sandwave Research," in conjunction with the Institute of Oceanographic Sciences, London, 1978, 21 pp.

The Analysis of Multilayer Elastomeric Bearings

J. C. Simo
Post Doctoral Fellow.

J. M. Kelly
Mem. ASME

Division of Structural Engineering
and Structural Mechanics,
Department of Civil Engineering,
University of California,
Berkeley, Calif. 94720

When a multilayer elastomeric bearing is sheared by end loads, the top and bottom surfaces of a typical plate are subjected to a shear stress distribution which causes bending of the plate. A new approach to the analysis of these bearings is presented which systematically takes into account the flexibility and subsequent warping of the plates. First, the displacement field of the bearing and the shear stress distribution are derived, within the framework of classical linear elasticity, from compatibility conditions between rubber pad and steel plate. Next, use of a second-order approximation to the nonlinear equilibrium equations leads to a new expression for the critical load of the bearing which depends on the bending stiffness of the plate. Under the assumption of perfectly rigid plates, this expression is in agreement with previous formulations. For flexible plates, however, the proposed expression shows that previous formulations lead to an overestimate of the buckling load which might become important for extremely thin plates and low values of the shear modulus of the rubber.

Introduction

A multilayer elastomeric bearing is a type of composite column consisting of alternate layers of thin rubber sheets bonded to metal plates. Due to the extremely high value of the *bulk modulus* relative to the *shear modulus* in natural rubber, such an arrangement prevents the lateral expansion of the rubber layers and, therefore, results in a column capable of withstanding high compressive loads with only a small axial deflection while, at the same time, preserving the low shear resistance of rubber to shearing [1-2].

The high compressive stiffness and low shear stiffness make these barings useful as vibrations mounts, shock absorbers, or bridge pads, and recently in earthquake engineering as base isolation devices for the protection of buildings against strong ground motions [3]. When used as seismic isolation mounts for buildings, the multilayer elastomeric bearing carry the vertical load of the building with small deformation while producing a very low fundamental frequency in the horizontal direction. This requires a very low horizontal stiffness; typically the vertical and horizontal stiffness differ by a factor of 300-400. The horizontal stiffness can be varied by selecting the total height of elastomer and the vertical stiffness can be increased by using many thin layers separated by steel plates. The thickness of the plates plays no role in these design considerations and the steel plates are generally taken to be rigid. However, low fundamental frequency in horizontal motion leads to a beariong, which although short (Fig. 1 and Fig. 3), is prone to buckling under vertical load due to the very low values of its shear stiffness [1]. The stability analysis used at present assumes the steel plates to be rigid and there is no way to assess the influence of the plate flexibility in the buckling load. The plates may be made thick enough, by rule of thumb or by experiment, to ensure that their deformation is in fact negligible. But this will add to the total height of the bearing and thus affect the buckling load. Space requirements also limit the height of the bearing. Thus it is important to have a theory for the stability of elastomeric bearings which includes the flexibility of the reinforcing plates.

In the past, the stability analysis of elastomeric bearings has been based on the approximate linearized theory of buckling developed by Haringx [4], in which the effective compression bending and shear stiffness of the composite column are determined from the apparent compressive bending and shear stiffness of a single column unit [1, 2]. Expressions for these elastic constants can be found in the literature [5-7]. As shown in [8], Haringx's treatment may be derived as a second-order approximation to the nonlinear equilibrium equations of finite elasticity under the "plane sections remain plane" assumption. For laminated bearings, this kinematic assumption amounts to considering the plates to be perfectly rigid so that the axial warping is completely restrained. An extension of Haringx's formulation to the case of plates of an arbitrary shape, not necessarily flat although perfectly rigid, has been reported in [9].

The systematic neglect of the flexibility of the plate is, therefore, the central assumption in previous analyses of the stability of multilayer elastomeric bearings. In many applications this assumption is quite unrealistic. Figure 1 shows an elastomeric bearing for a base isolation system, under test

Contributed by the Applied Mechanics Division for presentation at the 1984 PVP Conference and Exhibition, Joint with Applied Mechanics Division and Materials Division, San Antonio, Texas, June 17-21, 1984 of THE AMERICAN SOCIETY OF MECHANICAL ENGINEERS.

Discussion on this paper should be addressed to the Editorial Department, ASME, United Engineering Center, 345 East 47th Street, New York, N.Y. 10017, and will be accepted until two months after final publication of the paper itself in the JOURNAL OF APPLIED MECHANICS. Manuscript received by ASME Applied Mechanics Division, September, 1982; final revision, July, 1983. Paper No. 84-APM-19.

Copies will be available until February, 1985.

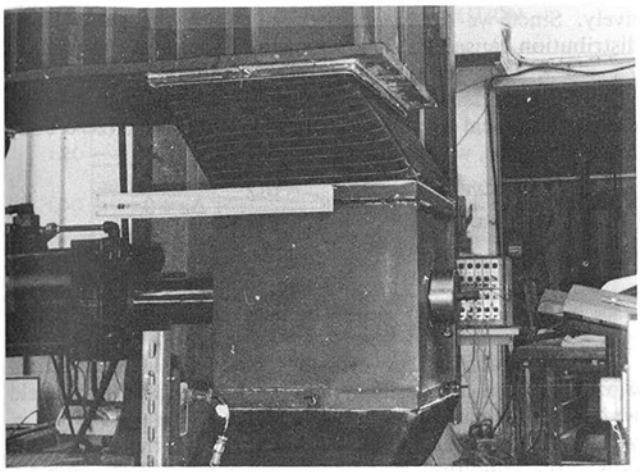

Fig. 1 Multilayer elastomeric bearing used in seismic base-isolation systems under experimental test at the Earthquake Simulator Laboratory of the Earthquake Engineering Research Center (E.E.R.C.) of the University of California, Berkeley

at the E.E.R.C of the University of California, Berkeley. The severe warping experienced by the plates is apparent and a physical explanation for this effect is illustrated in Fig. 2. Due to the shearing of the column, the top and bottom surfaces of any plate are subjected to a shear stress distribution that causes bending of the thin plate. In this paper, a theory that consistently includes the effect of the finite stiffness of the plate will be developed. Our formulation can be outlined as follows.

(*i*) The distribution of shearing stress acting on a typical plate is first obtained by enforcing compatibility of displacements and shear stress between metal plate and rubber layer. The dependence of the lateral deflection of the bearing only on the axial coordinate is the key assumption made beyond those of the linear theory of elasticity. Such an assumption amounts to neglecting the in-plane extension of the plate.

(*ii*) Integration of the strain-displacement relations leads to an expression of the displacement field which includes a warping function depending on stiffness of the plate and proportional to the amount of shear. Thus, the "plane sections remain plane" assumption no longer holds in the present approach. In the context of the linear theory, the resulting field equations correspond to a Timoshenko type of beam theory in which the explicit expression of the shear coefficient depends on the stiffness of the plate. The limiting cases in which the stiffness of the plate tends to either zero or infinity are also examined.

(*iii*) The stability of the bearing is examined by considering second-order equilibrium equations discussed in [10]. For completeness, a brief justification of these equilibrium equations is given in the Appendix. The resulting second-order theory leads to an expression for the buckling load that depends on the stiffness of the plate through the shear coefficient. This expression yields values of the buckling load always lower than those predicted by Haringx's formulation. In the limit, as the plate becomes infinitely stiff, both predictions coincide.

Basic Assumptions

A composite beam in the form of a typical multilayer elastomeric bearing is illustrated in Fig. 3. The x_1-axis, normal to the steel plates, is the axial axis of the bearing. In the analysis of the composite system consisting of the rubber layers and steel plates, we assume that the lateral displacement of the composite system u_2 depends solely on the axial

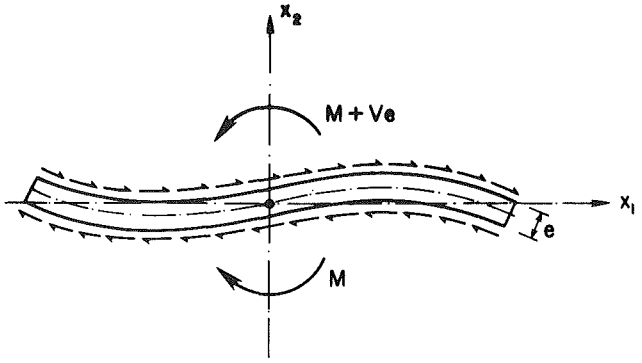

Fig. 2 Physical motivation for the warping of the plate

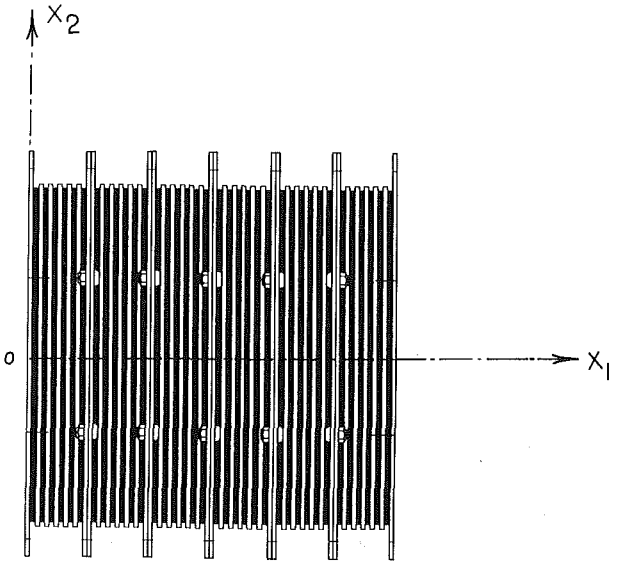

Fig. 3 A typical multilayer elastomeric bearing

coordinate x_1. For closely spaced plates, this assumption amounts to neglecting the in-plane extension of the plates and the bulging effect of the elastomer. In addition, we assume a state of plane strain (or stress) so that the plates are subjected to *cylindrical bending* and further reference to the x_3 coordinate may be omitted. The displacement field of the composite system then takes the form

$$u_1 = u(x_1, x_2), \quad u_2 = v(x_1) \tag{1}$$

Denoting by a superposed "prime" differentiation with respect to the indicated variable, the components of the infinitesimal strain tensor ϵ are given by

$$\epsilon_{11} = \frac{\partial u}{\partial x_1}, \quad \epsilon_{12} = \frac{1}{2}\left[v'(x_1) + \frac{\partial u}{\partial x_2}\right], \quad \epsilon_{22} = \epsilon_{33} = 0 \tag{2}$$

Let G denote the shear modulus of the rubber. We assume the metal plates to be thin enough so that the shearing stress is determined exclusively by the deformation of the rubber. Hence, from (2) the constitutive equation for the shear stress is

$$\sigma_{12} = 2G\,\epsilon_{12} = G\left[v'(x_1) + \frac{\partial u}{\partial x_2}\right] \tag{3}$$

By differentiating both sides of equation (3) with respect to x_2 it follows that

$$\frac{\partial^2 u}{\partial x_2^2} = \frac{1}{G}\frac{\partial \sigma_{12}}{\partial x_2} \tag{4}$$

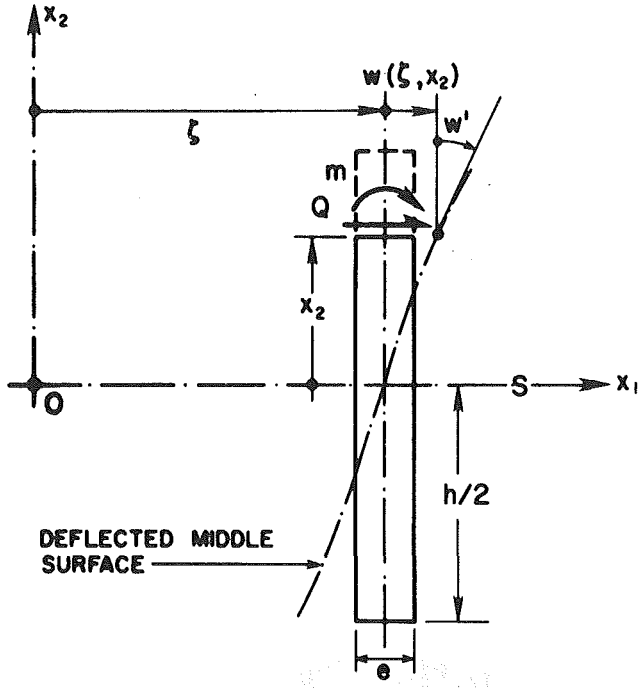

Fig. 4 Geometry of a typical plate

It will be shown herein that the form of the axial displacement $u(x_1,x_2)$ follows from the compatibility between the rubber pad and metal plate.

Analysis of the Plates

A typical plate of thickness e, normal to the x_1-axis and located at $x_1=\zeta$, is shown in Fig. 4. It is assumed that the thickness e is small enough so the usual Kirchhoff's assumption is applicable. Our objective is to obtain the *shear stress* distribution on the top and bottom surfaces of the plate due to *shearing* of the column.

Equilibrium equation for the Shear Stress. If $w(\zeta,x_2)$ designates the deflection of the middle surface $x_1=\zeta$ of the plate, the slope of the deflected surface is $w'(\zeta,x_2) = dw(\zeta,x_2)/dx_2$, and the displacement field is then given by

$$u_1(x_1,x_2)=w(\zeta,x_2),$$

$$u_2(x_1,x_2)=-[x_1-\zeta]\frac{dw(\zeta,x_2)}{dx_2} \tag{5}$$

where $x_1\epsilon(\zeta-e/2,\zeta+e/2)$ and $x_2\epsilon(-h/2,h/2)$. The components of the infinitesimal strain tensor ϵ are

$$\epsilon_{22}=-[x_1-\zeta]\frac{d^2w(\zeta,x_2)}{dx_2^2},\quad \epsilon_{12}=0,\quad \epsilon_{33}=0 \tag{6}$$

The bending m and shear force Q acting on a section of the plate a distance x_2 from the axial axis x_1 of the bearing are defined as

$$m=-\int_{\zeta-e/2}^{\zeta+e/2}[x_1-\zeta]\sigma_{22}dx_1,\quad Q=\int_{\zeta-e/2}^{\zeta+e/2}\sigma_{12}dx_1 \tag{7}$$

In terms of the Young modulus E_p and the Poisson's ratio υ_p of the plate, the *bending stiffness* of the plate is given by $D_p=E_pe^3/12(1-\nu_p^2)$, and from (6) and (7) the constitutive equation for the bending moment m takes the form

$$m=D_p\frac{d^2w(\zeta,x_2)}{dx_2^2} \tag{8}$$

Let τ^-, σ^- and τ^+, σ^+ be the *tangential* and *normal* stresses acting on the surfaces $x_1=\zeta-e/2$ and $x_1=\zeta+e/2$, respectively. Since we are concerned only with the shear stress distribution caused by shearing of the column, we must have $\tau^-=\tau^+$. Thus, setting $\tau\equiv\tau^-=\tau^+$, and defining $\Delta\sigma\equiv\sigma^+-\sigma^-$, by standard integration through the thickness e of the plate of the local equilibrium equations $\sigma_{\alpha\beta,\beta}=0$ (*zero* body force assumed), we obtain

$$\frac{dm}{dx_2}+Q-e\tau=0,\quad \frac{dQ}{dx_2}+\Delta\sigma=0 \tag{9}$$

from which it follows

$$\frac{d^2m}{dx_2^2}-e\frac{d\tau}{dx_2}=\Delta\sigma \tag{10}$$

By *compatibility* between the axial displacement field $u(x_1,x_2)$ of the composite system, and the displacement field $w(\zeta,x_2)$ of the plate we must have $w(\zeta,x_2)=u(\zeta-e/2,x_2)=u(\zeta+e/2,x_2)$. Thus, since the shear stress field σ_{12} must satisfy the condition $\tau=\sigma_{12}(\zeta-e/2,x_2)=\sigma_{12}(\zeta+e/2,x_2)$, equations (4) may be written as

$$\frac{d^2w(\zeta,x_2)}{dx_2^2}=\frac{1}{G}\frac{d\tau}{dx_2} \tag{11}$$

Making use of (11), constitutive equation (8), and the equilibrium equation $(9)_1$, the bending moment m and the shear force Q may be expressed in terms of the shearing stress τ as

$$m=\frac{D_p}{G}\frac{d\tau}{dx_2},\quad Q=-\frac{D_p}{G}\frac{d^2\tau}{dx_2^2}+e\tau \tag{12}$$

and by substitution into equation (10) we arrive at

$$L\,\tau\equiv\frac{d^3\tau}{dx_2^3}-\left[\frac{Ge}{D_p}\right]\frac{d\tau}{dx_2}=\left[\frac{Ge}{D_p}\right]\frac{\Delta\sigma}{e},\quad x_2\epsilon\left(-\frac{h}{2},\frac{h}{2}\right) \tag{13}$$

which is the differential equation of equilibrium for the shearing stress $\tau\equiv\sigma_{12}(\zeta-e/2,x_2)\equiv\sigma_{12}(\zeta+e/2,x_2)$.

Boundary Conditions. The distribution of shear stresses on the plate must be such that the resultant moment and shear force at the ends $x_2=\pm h/2$ of the plate vanish. Furthermore, the symmetry of the problem demands the shear stress σ_{12} to be an even function of x_2 in the interval $(-h/2,h/2)$. Thus, making use of (12) we have the boundary conditions

$$\tau(+x_2)=\tau(-x_2),\quad \frac{d\tau}{dx_2}\Big|_{x_2=\pm\frac{h}{2}}=0,$$

$$\left[\frac{d^2\tau}{dx_2^2}-\lambda^2\tau\right]\Big|_{x_2=\pm\frac{h}{2}}=0 \tag{14}$$

where the parameter $\lambda^2\equiv Ge/D_p$ has been introduced for convenience.

It is noted, however, that the *completely homogeneous* problem $L\,\tau_H=0$ with boundary conditions (14) admits the *nontrivial* solution $\tau_H=constant$. Thus, by Fredholm alternative theorem [13], the problem posed by equation (13) with boundary conditions (14) is undetermined up to an arbitrary constant. In addition, for this problem to have a solution, the forcing function $f(x_2)=\lambda^2\Delta\sigma/e$ must be orthogonal to the solutions of the completely homogeneous problem and, therefore, meet the condition

$$\int_{-h/2}^{h/2}\Delta\sigma\,dx_2=0 \tag{15}$$

which shows that the resultant of the normal stresses acting on the plate *must be a moment* say ΔM. A unique solution for the problem posed by equation (13) with boundary conditions (14) is obtained by requiring that

$$\int_{-h/2}^{h/2}\tau dx_2=V \tag{16}$$

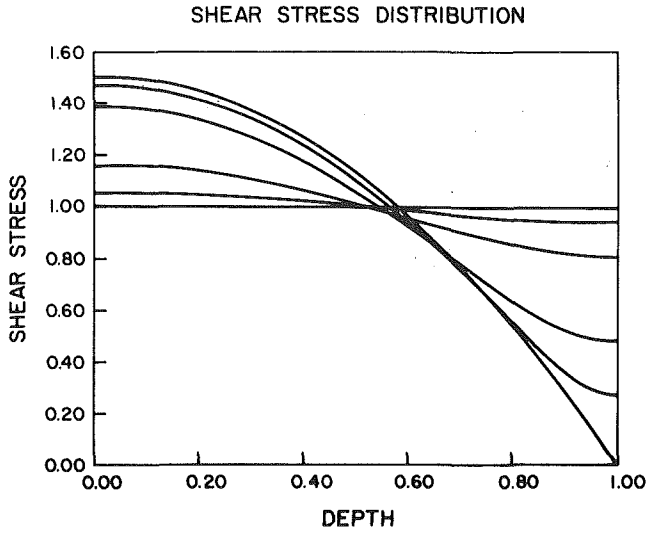

Fig. 5 Shear stress distribution

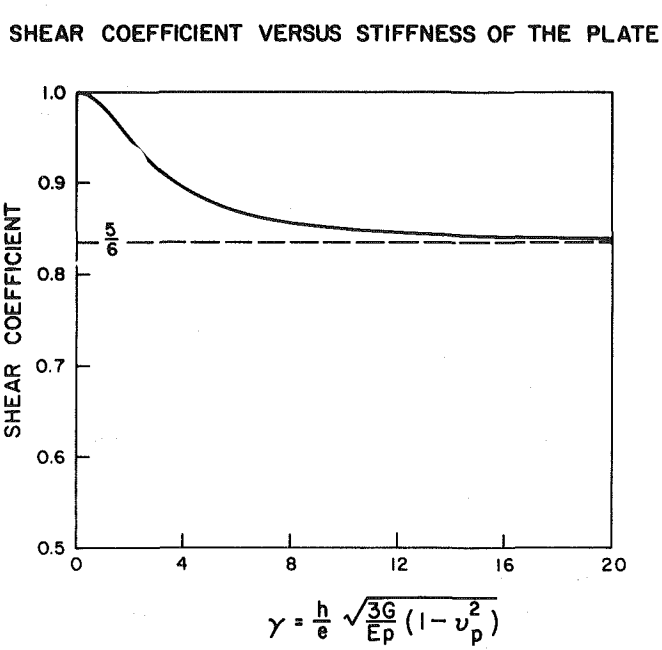

Fig. 6 Variation of the shear coefficient K with the stiffness of the plate

where $V \equiv V(\zeta - e/2) = V(\zeta + e/2)$ is the resultant shear force acting on both sides $x_1 = \zeta - e/2$ and $x_1 = \zeta + e/2$ of the plate. By multiplying equation (13) by x_2, integration by parts and enforcement of conditions (14) it is found that the resultant moment ΔM is related to the shear force V through the overall equilibrium condition

$$\Delta M \equiv -\int_{-h/2}^{h/2} \Delta\sigma\, x_2\, dx_2 = -Ve \tag{17}$$

Shear Stress Distribution. The explicit solution of the boundary value problem posed by equation (13) with boundary conditions (14) and condition (16) requires an explicit expression for the resultant normal stresses $\Delta\sigma$ acting on the plate. In view of conditions (15) and (17) we may assume that $\Delta\sigma$ is distributed linearly over the plate and, therefore, given by

$$\Delta\sigma = -\frac{\Delta M}{I} x_2 = \frac{Ve}{I} x_2 \tag{18}$$

where $I = 1/12\ h^3$. The solution of the boundary value problem is then easily found to be

$$\tau = \frac{V}{h}\left[\frac{3}{2}\left(1 - \frac{4x_2^2}{h^2}\right) - \frac{3}{\gamma^2}\left(1 - \frac{\gamma}{\mathrm{Sinh}(\gamma)}\,\mathrm{Cosh}\left(\frac{2\gamma x_2}{h}\right)\right)\right] \tag{19}$$

where

$$\gamma \equiv \sqrt{\frac{3G}{E_p}(1-\nu_p^2)}.$$

The shear stress τ given by equation (19) is plotted for various values of the parameter γ in Fig. 5. We note that as the plate becomes more flexible; i.e; $E_p \to 0$ or $e \to 0$, the parameter $\gamma \to \infty$ and the shear stress τ tends ot the parabolic distribution $\tau \to 3V/2h\ [1 - 4x_2^2/h^2]$. On the other hand, as the plate becomes stiffer, $\gamma \to 0$ and the shear stress $\tau \to V/h$; i.e., a uniform distribution over the plate.

The Composite System

Kinematics. Once the distribution of the shear stress τ is known, the expression for the axial displacement $u_1 = u(x_1, x_2)$ follows by integrating (3) and substitution of the expression for τ given by (19). The result is

$$u_1 = \bar{u}(x_1) - x_2\nu'(x_1) + \frac{V(x_1)}{Gh}\left[\frac{3}{2}x_2 - \frac{2}{h^2}x_2^3 - \frac{3}{\gamma^2}\left[x_2 - \frac{h}{2\mathrm{Sinh}(\gamma)}\,\mathrm{Sinh}\left(\frac{2\gamma x_2}{h}\right)\right]\right) \tag{20}$$

where the function $\bar{u}(x_1)$ represents the axial displacement of the x_1-axis.

To express the displacement field fully in terms of kinematic variables we introduce, as in [11], the *average* rotation $\bar{\psi}(x_1)$ of a cross section defined by

$$\bar{\psi}(x_1) = -\frac{1}{I}\int_{-h/2}^{h/2} x_2 u_1(x_1, x_2)\, dx_2 \tag{21}$$

where $I = h^3/12$ is the moment of inertia of the cross section. The substitution of (20) into (21) shows that the angle $\bar{\psi}(x_1)$ is related to the resultant shear force $V(x_1)$ by

$$\bar{\psi}(x_1) = \nu'(x_1) - \frac{V(x_1)}{G\Omega\kappa} \tag{22}$$

where the constant κ has the expression

$$\kappa = \frac{5/6}{1 - \frac{5}{2\gamma^2}\left[1 - 3\left(\frac{1}{\gamma\mathrm{Tanh}(\gamma)} - \frac{1}{\gamma^2}\right)\right]} \tag{23}$$

Equation (22) relates, through $G\Omega\kappa$, the resultant shear force $V(x_1)$ acting on a cross section of the composite system to the angle $\bar{\beta}(x_1) \equiv \nu'(x_1) - \bar{\psi}(x_1)$, the difference between the slope of the deformed neutral axis and the average angle of rotation of the cross section. Hence, the angle $\bar{\beta}(x_1)$ gives a measure of the average distortion of a cross section due to shear, and the constant $\Omega\kappa$ represents an "effective" shear area. The parameter κ, plotted in Fig. 6 γ, has then an analogous significance to that of the shear coefficient in Timoshenko beam theory [11]. In fact, in the limit as $\gamma \to \infty$ and the plate becomes infinitely flexible, it follows from (23) that $\kappa \to 5/6$ which is in agreement with the expression for the shear coefficient of a rectangular section when $\nu = 0$, [11].

The displacement field of the composite system then takes the following final form

$$u_1 = \bar{u}(x_1) - x_2\bar{\psi}(x_1) - \phi(x_2)\kappa\bar{\beta}(x_1), \quad u_2 = \nu(x_1) \tag{24}$$

where the shear coefficient κ is given by (23), and in addition

$$\phi(x_2) = \left[\frac{1}{\kappa} - \frac{3}{2} + \frac{3}{\gamma^2}\right]x_2 + \frac{2}{h^2}x_2^3 - \frac{3h}{2\gamma^2 \mathrm{Sinh}(\gamma)} \mathrm{Sinh}\left(\frac{2\gamma x_2}{h}\right)$$

$$\gamma = \frac{h}{e}\sqrt{\frac{3G}{E_p}(1-\nu_p^2)} \tag{25}$$

$$\bar{\beta}(x_1) = \nu'(x_1) - \bar{\psi}(x_1)$$

The dependence of the warping function $\phi(x_2)$ given by equation $(25)_1$ on the stiffness of the plate, through the parameter γ defined by $(25)_2$, is noted.

Constitutive Equations. For the *bending moment* $M(x_1)$ defined by

$$M(x_1) = -\int_{-h/2}^{h/2} \sigma_{11} x_2 dx_2, \tag{26}$$

the constitutive assumption is expressed by *the linear* relationship:

$$M(x_1) = K_B \bar{\psi}'(x_1) \tag{27}$$

where K_B is the so-called *apparent bending stiffness* of the system [6, 7]. Equation (27) is consistent with (26), the definition (21) of $\bar{\psi}(x_1)$, and the linear relationship $\sigma_{11} = E_A \epsilon_{11}$, where the elastic constant of the composite system E_A is $E_A = K_B/I$. The constitutive equation for the shear force follows immediately from equation (22), namely

$$V(x_1) = G\Omega\kappa[\nu'(x_1) - \bar{\psi}(x_1)] \tag{28}$$

where the shear coefficient κ is given by (23). The shear modulus G should be replaced by $G\, e_R/e_T$ where e_T is the total height of a single column unit and e_R the height of the rubber pad and one plate [1].

Equilibrium Equations, Linear Theory. The equilibrium equations in terms of the resultant shear force and bending moment, follow by integration of the equilibrium equations of linear elasticity over the cross section of the bearing in the standard manner. The well-known result is

$$M'(x_1) + V(x_1) = 0, \quad V'(x_1) + q(x_1) = 0 \tag{29}$$

being $q(x_1)$ the applied transversal load.

The set of equations governing the linear response of the composite system consists of the constitutive equations (27) and (28) together with the equilibrium equations (29). Formally, they correspond to a Timoshenko type of beam theory. However, the displacement field given by (24), obtained by enforcing compatibility of stress and displacements between the steel plate and rubber pad, includes a warping of the cross section that depends on the stiffness of the plate. The expression for the effective shear coefficient given by (23) is then consistently derived from this displacement pattern.

Limiting Cases. Two limiting cases of the theory are possible.

(*a*) *The Stiffness of the Plate* $D_p \to \infty$. From equations (19), (23), and (25) it follows that the asymptotic expansions as $\gamma \to 0$ for the shear stress τ, the shear coefficient κ and the warping function $\phi(x_2)$ are

$$\tau = \frac{V(x_1)}{\Omega} + O(\gamma^2), \quad \phi(x_2) = 0 + O(\gamma^2), \quad \kappa = 1 - \frac{2}{105}\gamma^2 + O(\gamma^4) \tag{30}$$

Since $\phi(x_2) \to 0$ uniformly in $(-h/2, h/2)$, in the limit as the plates become infinitely stiff we recover the classical Bernoulli kinematic assumption. Furtheremore, since the shear coefficient takes the value $\kappa = 1$ in the limit as $\gamma \to 0$, our derivation provides a rational justification for the usual choice of $G\Omega$ as the effective shear stiffness of columns with extremely stiff plates [1]. This is the only case considered in previous formulations where the flexibility of the plate is neglected.

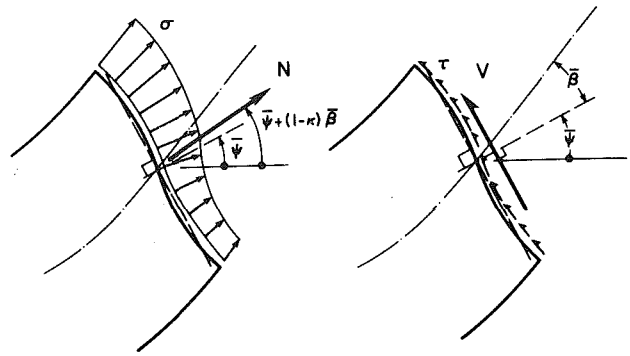

Fig. 7 Resultant *N* of normal stresses and resultant *V* of tangential stresses

(*b*) *The Stiffness of the Plate* $D_p \to 0$. This limiting situation corresponds to a homogeneous beam with elastic constants G and $E = E_A$. Again, from equations (19), (23), and (25) we find that in the limit as $\gamma \to \infty$ the distribution of shear stresses, the shear coefficient κ and the warping function $\phi(x_2)$ reduce to

$$\tau = \frac{5}{4}\left[1 - \frac{4x_2^2}{h^2}\right]\bar{\beta}(x_1), \quad \phi(x_2) = \frac{2}{h^2}x_2^3 - \frac{3}{10}x_2, \quad \kappa = \frac{5}{6} \tag{31}$$

The constitutive equations (27) and (28) together with the equilibrium equations (29) show that in the limit as the thickness of the plate or its stiffness tend to zero, we recover the classical Timoshenko beam theory with shear coefficient $\kappa = 5/6$. Notice however, that the usual "plane sections remain plane" deformation pattern no longer holds in the present approach due to the presence of the warping function $\phi(x_2)$, given by $(31)_2$, in the kinematics (24).[1] It is the warping of the cross section that leads to the expression for the shear coefficient [10].

The Nonlinear Theory

In this section we consider the stability of the bearing when subjected to end loads. To obtain an estimate of the buckling load, it suffices to consider a second-order theory.[2] First, we consider a second-order approximation to the nonlinear equilibrium equations. We may think of this approximation as derived by establishing the equilibrium in a (deformed) configuration obtained by an update of the reference (undeformed) configuration with the infinitesimal displacement field. Next, we further simplify the formulation by introducing the customary assumption of negligible extension in the axial direction, leading to a linearized eigenvalue problem for the critical load.

Second-Order Equilibrium Equations. For a straight beam of length L and cross section Ω, which is acted on by end loads and zero body force, a second-order approximation to the nonlinear equilibrium equations in terms of stress resultants takes the form

[1] Instead of the angle $\bar{\psi}(x_1)$ defined by (21), one could choose $\psi_0 = \partial u_1/\partial x_2|_{x_2=0}$ as in [12]. Although $\psi_0 \neq \bar{\psi}$, they are uniquely related by $5\bar{\psi} = 4\psi_0 + \nu'$, and thus either choice leads to an equivalent (Timoshenko) beam theory. The difference becomes relevant when specifying boundary conditions.

[2] Second-order theories are systematically obtained by "successive approximations" (Signorini's expansion. See e.g. [15] Sect. 63–67).

$$
\begin{aligned}
N - \bar{\psi} V &= -P \\
V + [\kappa\bar{\psi} + (1-\kappa)\nu']N &= -H \\
M' + \nu' P &= [1+\bar{u}']H
\end{aligned} \tag{32}
$$

where κ is the shear coefficient as given in [10, 11], and P and H the axial (compressive) and vertical loads applied at the left end, respectively. A superposed "prime" denotes differentiation with respect to the axial coordinate X_1 in the reference (*undeformed*) configuration. A detailed derivation of equations (32) for the gernal case of an arbitrary cross section Ω is found in [10]. A justification of these second-order equilibrium equations is given in the Appendix, and a geometric explanation of the result is contained in Fig. 7. Due to the warping of the cross section Ω, the resultant of normal stresses N no longer remains normal to the average plane of bending defined by the angle $\bar{\psi}$ but is shifted an extra angle $(1-\kappa)\ [\nu' - \bar{\psi}]$. On the other hand, the resultant of shear stresses V is always parallel to the average plane of bending. We note that if $\kappa \equiv 1$, then "plane sections remain plane" and equations (32) reduce to a form which may be derived by elementary procedures.

The nonlinear equilibrium equations for an elastomeric bearing are then obtained simply by inserting in (32) the expression (23) for the shear coefficient that depends on the stiffness D_p of the plates.

The Eigenvalue Problem for the Critical Load. A linearized eigenvalue problem for the critical load P can be obtained by assuming that the column is "almost" inextensible in the axial direction. Explicitly

$$
\|\bar{u}'\| = \max_{0\le x\le L} |\bar{u}'| = \textit{higher order} \quad \text{so that} \quad 1+\bar{u}' \approx 1 \tag{33}
$$

Such an assumption is particularly accurate in the stability analysis of a multilayer elastomeric bearing due to the extremely high values of its compressive stiffness [1-7]. If the plates are regarded as *perfectly rigid*, then $\kappa = 1$ and equations (32) together with (33) reduce to the set of equilibrium equations considered in [9].

Due to assumption (33) the constitutive equation (30) for the shear force remains unchanged (see [10] for the details) and equations (32) together with (27) and (30) lead to the problem

$$
\begin{aligned}
\left[1 - \frac{(1-\kappa)P}{G\Omega\kappa}\right]\nu'(X_1) + \frac{H}{G\Omega\kappa} &= \left[1+\frac{P}{G\Omega}\right]\bar{\psi}(X_1) \\
K_B\bar{\psi}''(X_1) + P\nu'(X_1) &= H, \quad X_1 \in (0,L)
\end{aligned} \tag{34}
$$

From (34) it follows that both the average rotation $\bar{\psi}(X_1)$ and the lateral deflection $\nu(X_1)$ are governed by

$$
L\ \bar{\psi}(X_1) = 0, \quad L\ \nu(X_1) = 0, \quad X_1 \in (0,L) \tag{35a}
$$

where L is the linear operator defined by

$$
L \equiv \frac{K_B\left[1 - \dfrac{(1-\kappa)P}{G\Omega\kappa}\right]}{1 + \dfrac{P}{G\Omega}} \frac{d^4}{dX_1^4} + P\frac{d^2}{dX_1^2} \tag{35b}
$$

When proper boundary conditions are appended, one is led to a linear self-adjoint eigen-value problem for the compressive critical load P_{crit}. The result may be related to the Euler's critical load of the column P_E as

$$
P_{crit} = \frac{2P_E}{1 + \dfrac{(1-\kappa)P_E}{G\Omega\kappa} + \left[\left(1 + \dfrac{(1-\kappa)P_E}{G\Omega\kappa}\right)^2 + \dfrac{4P_E}{G\Omega}\right]^{1/2}} \tag{36}
$$

This critical load should be compared with that due to Haringx which neglects the flexibility of the plate and is given by

$$
P_{crit}^H = \frac{2P_E}{1 + \left[1 + \dfrac{4P_E}{G\Omega}\right]^{1/2}} \tag{37}
$$

Clearly, $P_{crit} < P_{crit}^H$ except in the limit when $\kappa \to 1$, the plates are perfectly rigid, and both expressions coincide. In addition, the completely different asymptotic behavior exhibited by expressions (36) nad (37) for extremely low values of the shear stiffness $G\Omega$ should be noted. While the asymptotic expansion of (36) exhibits a linear behavior; i.e.,

$$
P_{crit} \to \frac{(1-\kappa)P_E}{G\Omega\kappa} \quad \text{as} \quad \frac{G\Omega}{K_B} \to 0 \tag{38}
$$

the asymptotic expansion of expression (37) gives

$$
P_{crit}^H \to \sqrt{\frac{G\Omega}{P_E}}P_E \quad \text{as} \quad \frac{G\Omega}{K_B} \to 0 \tag{39}
$$

For extremely low values of the shear stiffness $G\Omega$, Haringx's expression could severely overestimate the buckling load of the column. Differences of the order of 10 percent in the experimental measurement of buckling loads of columns with flexible plates have been reported in the literature [9].

Conclusions

A theory for multilayer elastomeric bearings which consistently includes the effect of the finite flexibility of the plates has been presented. Explicit expressions for the shear stress distribution and the axial displacement of the bearing have been developed.

Within the framework of a second-order approximation to the nonlinear equilibrium equations of finite elasticity, the formulation presented leads to an expression for the critical load of column that depends on the stiffness of the plate in a simple manner. This expression yields values of the critical load always lower than those predicted by Haringx's expression for the buckling load which systematically neglects the flexibility of the plates, and reduces to the latter in the limiting situation of perfectly rigid plates.

The simplicity of the proposed expression for the buckling load makes its use attractive in design to allow the thickness of the reinforcing plates to be selected in a rational way.

References

1 Gent, A. N., "Elastic Stability of Rubber Compression Springs," *J. Mech. Engng. Sc.*, Vol. 6, No. 4, 1964, pp. 318-326.

2 Beatty, M. F., "Elastic Stability of Rubber in Compression," in *Finite Elasticity*, Riolin, R. S., ed., *ASME, AMD*, Vol. 27, pp. 125-150.

3 Derham, C. J., and Thomas, A. G., "The Design of Seismic Isolation Bearings," *Control of Seismic Response of Piping Systems and Other Structures by Base Isolation*, Kelly, J. M., ed., Report No. UCB/EERC-81/01, 1981.

4 Haringx, J. A., "On Highly Compressive Helical Springs and Rubber Rods and Their Applications to Free Mountings," Parts I, II, III. *Philips Res. Reports*, 1948-1949.

5 Roccard, Y., "Note sur le Calcul des Proprietes Elastiques des Supports en Caoutchouc Adherent," *J. Phys. Radium*, Vol. 8, 1937, pp. 111-122.

6 Gent, A. N., and Lindley, P. B., "The Compression of Bonded Rubber Blocks," *Proc. Instn. Mech. Engrs.*, Vol. 173, No. 3, 1959, pp. 111-122.

7 Gent, A. N., and Meinecke, E. A., "Compression, Bending and Shear of Bonded Rubber Blocks," *Polymer Engineering and Science*, Vol. 10, No. 1, 1970, pp. 48-53.

8 Simo, J. C., and Kelly, J. M., "Two-Dimensional Finite Elasticity Analysis of the Stability of Multilayer Elastomeric Bearings," Report No. UCB/SESM-81/06, Dept. Civil Eng., University of California, Berkeley, 1981.

9 Schapery, R. A., and Skala, D. L., "Elastic Stability of Elastomeric Columns," *Int. J. Solids Structures*, Vol. 12, 1976, pp. 401-417.

10 Simo, J. C., "A Consistent Formulation of Nonlinear Theories of Elastic Beams and Plates," Report No. UCB/SESM-82/06, Dept. Civil. Eng., University of California, Berkeley, 1982.

11 Cowper, G. R., "The Shear Coefficient in Timoshenko's Beam Theory," ASME JOURNAL OF APPLIED MECHANICS, Vol. 33, 1966.

12 Levison, M., "A New Theory for Rectangular Beams," *Journal of Sound and Vibration*, Vol. 74, 1981, pp. 81-87.

13 Stakgold, I., *Green Function and Boundary Value Problems*, Wiley, New York, 1979.
14 Gurtin, M., *Topics in Finite Elasticity*, Society for Industrial and Applied Mathematics, Philadelphia, 1981.
15 Truesdell C., and Noll; W., "The Non-Linear Field Theories of Mechanics," in *Handbuch der Physik*, Flugge, S., ed., Vol. III/3, Springer-Verlag, Berlin 1965.

APPENDIX

We consider the simplified two-dimensional case in which the (undeformed) cross section is $\Omega = (-h/2, h/2)$. For a deformation $\mathbf{x} = \chi(\mathbf{X})$ of the beam $B = (0, L) \times \Omega$, the local nonlinear equilibrium equations may be written as [14]

$$\text{DIV } \mathbf{P} + \rho_{ref} B = \mathbf{O}, \quad \mathbf{P}\mathbf{F}^T = \mathbf{F}\mathbf{P}^T \tag{A.1}$$

where $\mathbf{P}$ is the first *Piola–Kirchoff* (two-point) stress tensor, $\mathbf{F}$ the deformation gradient, $\mathbf{B}$ the body force per unit volume, and ρ_{ref} the density in the reference configuration. The *stress vector* acting on a *deformed* cross section, measured per unit of *reference* (*undeformed*) area Ω, is given by

$$\mathbf{T} = \mathbf{P} \cdot \hat{\mathbf{N}} \equiv P_{11} \hat{\mathbf{E}}_1 + P_{21} \hat{\mathbf{E}}_2 \tag{A.2}$$

where $\{\hat{\mathbf{E}}_1, \hat{\mathbf{E}}_2\}$ is a *fixed* cartesian frame such that $\hat{\mathbf{N}} \equiv \hat{\mathbf{E}}_1$ is the unit normal to the reference (*undeformed*) cross section Ω. Assuming *zero* body force, integration of equations (A.1) over Ω and use of Green's formula yields

$$\frac{d}{dX_1} \int_\Omega \begin{Bmatrix} P_{11} \\ P_{21} \end{Bmatrix} d\Omega + \begin{Bmatrix} q(X_1) \\ 0 \end{Bmatrix} = \mathbf{O} \tag{A.3}$$

where $q(X_1)\hat{\mathbf{E}}_2$ is the applied (vertical) force, and Ω is simply the open interval $(-h/2, h/2)$. Let $\{\hat{\mathbf{l}}, \hat{\mathbf{n}}\}$ be the "moving" frame composed by unit vector fields *normal* and *tangential* to the *deformed* cross section. This frame is related to the *fixed* frame $\{\hat{\mathbf{E}}_1, \hat{\mathbf{E}}_2\}$ according to

$$\begin{Bmatrix} \hat{\mathbf{n}} \\ \hat{\mathbf{l}} \end{Bmatrix} = \mathbf{\Lambda} \begin{Bmatrix} \hat{\mathbf{E}}_1 \\ \hat{\mathbf{E}}_2 \end{Bmatrix}, \qquad \mathbf{\Lambda} \equiv \frac{1}{\sqrt{C_{22}}} \begin{bmatrix} F_{22} & -F_{12} \\ F_{12} & F_{22} \end{bmatrix} \tag{A.4}$$

where $\mathbf{C} = \mathbf{F}^T\mathbf{F}$. In terms of the stress fields (σ, τ) *normal* and *tangential* to the deformed cross section, the stress vector $\mathbf{T}$ in (A.2) may be expressed as $\mathbf{T} = \sigma\,\hat{\mathbf{n}} + \tau\hat{\mathbf{l}}$, and equation (A.3) takes the form

$$\frac{d}{dX_1} \int_\Omega \mathbf{\Lambda}^T \begin{Bmatrix} \sigma \\ \tau \end{Bmatrix} d\Omega + \begin{Bmatrix} q(X_1) \\ 0 \end{Bmatrix} = \mathbf{O} \tag{A.5}$$

We note that in the *linear* theory, $\mathbf{\Lambda} \equiv 1$ in (A.5), and $(\sigma, \tau) \equiv (\sigma_{11}, \sigma_{12})$, with σ_{ij} being the components of the *infinitesimal* stress tensor. If attention is restricted to a *second-order approximation* to (A.5), then only the *linear part* $\bar{\mathbf{\Lambda}}$ of $\mathbf{\Lambda}$ enters in (A.5). For the linear kinematics given by (24) and (31), which is exact for Saint-Venant's problem with Poisson ratio $\nu = 0$ [10], use of $(A.4)_2$ leads to the following expression for $\bar{\mathbf{\Lambda}}$

$$\bar{\mathbf{\Lambda}} = 1 + \begin{bmatrix} 0 & \psi \\ -\psi & 0 \end{bmatrix} + \kappa\phi'(X_2) \begin{bmatrix} 0 & \beta \\ -\beta & 0 \end{bmatrix} \tag{A.6}$$

where a superposed "prime" denotes differentiation with respect to X_2, and $\phi(X_2)$ is the *warping* function given by $(31)_3$. Substitution of (A.6) into (A.5) yields $(q(X_1) \equiv 0)$

$$\frac{d}{dX_1} \left(\int_\Omega \begin{Bmatrix} \sigma \\ \tau \end{Bmatrix} d\Omega + \bar{\psi} \int_\Omega \begin{Bmatrix} -\tau \\ \sigma \end{Bmatrix} d\Omega + \kappa\bar{\beta} \int_\Omega \begin{Bmatrix} -\tau \\ \sigma \end{Bmatrix} d\Omega \right) = \mathbf{O} \tag{A.7}$$

To within second order, the resultant N of normal stress and the resultant V of tangential stresses, acting on the deformed cross section, are given by [10]

$$N = \int_\Omega \sigma d\Omega, \quad V = \int_\Omega \tau d\Omega, \tag{A.8}$$

We note that within the second-order approximation, the last term in (A.7) can be estimated by replacing (σ, τ) by its linear part $(\sigma_{11}, \sigma_{12})$. Since the following identities hold

$$\bar{\beta} \int_\Omega \phi' \sigma_{12} d\Omega = \kappa\bar{\beta}^2 \int_{-h/2}^{h/2} \phi'(1 - \phi') dX_2 \equiv 0,$$

$$\bar{\beta} \int_\Omega \phi' \sigma_{11} d\Omega \equiv (1 - \kappa)\bar{\beta} \int_\Omega \sigma_{11} d\Omega \approx (1 - \kappa)\bar{\beta} N \tag{A.9}$$

equation (A.7) reduces to

$$\frac{d}{dX_1}(N - \bar{\psi}V) = 0, \quad \frac{d}{dX_1}(V + [\bar{\psi} + (1 - \kappa)\bar{\beta}]N) = 0 \tag{A.10}$$

By integration we obtain $(32)_{1,2}$. The moment equilibrium equation $(32)_3$ can also be derived from (A.1), or directly checked by elementary procedures.

Hydroelastic Instability of Infinite Strips Under Shearing Load on an Elastic Foundation

J. Tani
Associate Professor,
Institute of High Speed Mechanics,
Tohoku University,
Sendai, Japan
Mem. ASME

The paper examines the hydroelastic instability of an infinitely long plate subjected to shearing load with two different boundary conditions, one side of which is exposed to an incompressible inviscid flow, and the other side supported on an elastic foundation. The analysis is based on the small deflection plate theory and the classical linearized potential flow theory. The Galerkin method and Fourier transforms are used. It is found that the effects of the shearing load and the elastic foundation on the divergence velocity can be illustrated by a single curve for both clamped and simply supported cases.

Introduction

The hydroelastic instability of flat panels has been studied extensively by many investigators [1-23]. For example, Dugundji, Dowell, and Perkin [1] examined theoretically and experimentally the aeroelastic instability of an infinite panel on an elastic foundation in a subsonic flow. They reported weak divergence followed by traveling wave flutter. Thereafter, Dowell [2] and Weaver and Unny [5] indicated that the instability of the infinite panel in subsonic or water flow becomes one of static divergence. Ellen [6] discussed that the post-divergence flutter would not occur if the three-dimensional finite panel were considered. On the other hand, less attention has been paid to the effect of shearing load on the hydroelastic instability, owing to mathematical difficulty, except for recent author's study [24]. However, this problem is of great technical importance, since the panels between stiffeners used in ships and ocean structures are sometimes subjected to shearing load.

The purpose of this paper is to examine the hydroelastic instability of an infinitely long plate with finite width, when its upper surface is exposed to an incompressible inviscid fluid flowing in the longish direction of the plate, its lower surface is supported on a continuous elastic foundation, and both its edges are subjected to shearing load. On the basis of the small deflection plate theory and the classical linearized potential flow theory, the problem is solved for both simply supported and clamped cases by means of the Galerkin method and Fourier transforms. The divergence and flutter velocities are determined for various values of the shearing load and the spring stiffness of the elastic foundation. It is found that the divergence velocity is lower than the flutter one, irrespective of the shearing load, the elastic foundation, and the boundary condition. Hence the effects of the shearing load, the elastic foundation, and the boundary condition on the divergence velocity is clarified in detail.

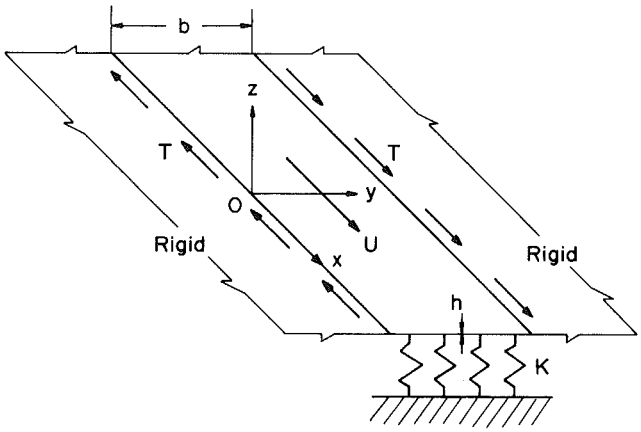

Fig. 1 Geometry of a strip and coordinate system

Basic Equations and Boundary Conditions

Consider an infinitely long plate with thickness h and finite width b subjected to shearing load T per unit length along both edges, one side of which is exposed to an incompressible inviscid fluid flowing with uniform velocity U in the longish direction, and the other side supported on a continuous linear elastic foundation with spring stiffness K. Taking the coordinate system as shown in Fig. 1 and denoting by W, P, and ρ_m the deflection of the plate, the perturbation pressure of fluid on the plate, and the mass density of the plate, respectively, the equation governing the motion of plate is, from the small deflection theory,

$$\rho_m h W_{,tt} + D\nabla_2^4 W - 2TW_{,xy} + KW + P = 0 \qquad (1)$$

where

Contributed by the Applied Mechanics Division for publication in the JOURNAL OF APPLIED MECHANICS.
Discussion on this paper should be addressed to the Editorial Department, ASME, United Engineering Center, 345 East 47th Street, New York, N.Y. 10017, and will be accepted until two months after final publication of the paper itself in the JOURNAL OF APPLIED MECHANICS. Manuscript received by ASME Applied Mechanics Division, January, 1983; final revision, August, 1983.

$$D=\frac{Eh^3}{12(1-\nu^2)},\ \nabla_2^4=\left(\frac{\partial^2}{\partial x^2}+\frac{\partial^2}{\partial y^2}\right)^2$$

In these equations, D, E, ν, and t are the flexural rigidity, Young's modulus, Poisson's ratio, and time, respectively, while subscripts following a comma stand for differentiation.

For the boundary conditions at $y=0$ and b, the following two cases will be considered:

$$(s)\ W=W_{,yy}=0,\quad (c)\ W=W_{,y}=0 \tag{2}$$

The perturbation pressure on the plate is given by the linearized Bernoulli equation

$$P=-\rho_f(\Phi_{,t}+U\Phi_{,x})_{z=0} \tag{3}$$

where ρ_f is the density of fluid and Φ is a perturbation velocity potential due to the deformed plate. For inviscid, incompressible, irrotational fluid, Φ is determined by solving Laplace's equation

$$\nabla_3^2\Phi=0 \tag{4}$$

with conditions

$$\Phi_{,z|z=0}=W_{,t}+UW_{,x}\ \text{ for } 0\leqq y\leqq b$$
$$=0\qquad \text{elsewhere} \tag{5}$$

and $\Phi=0$ at $z\to\infty$,

where

$$\nabla_3^2=\frac{\partial^2}{\partial x^2}+\frac{\partial^2}{\partial y^2}+\frac{\partial^2}{\partial z^2}$$

Here, the following nondimensional notations are introduced for convenience:

$$\xi=\frac{\pi x}{a},\quad \eta=\frac{\pi y}{b},\quad \zeta=\frac{\pi z}{b},\quad \alpha=\frac{b}{a}$$

$$k=\frac{b^2K}{\pi^4D},\quad \lambda=\frac{b^2T}{\pi^2D},\quad \Omega_0=\left(\frac{\pi}{b}\right)^2\sqrt{\frac{D}{\rho_m h}}$$

$$\tau=\Omega_0 t,\quad \phi=\frac{\pi\Phi}{bh\Omega_0},\quad w=\frac{W}{h},\quad p=\frac{P}{\rho_m h^2\Omega_0{}^2} \tag{6}$$

$$\mu=\frac{\rho_f b}{\rho_m h},\quad \omega=\frac{\Omega}{\Omega_0},\quad \bar{V}^2=\mu V^2=\frac{\rho_f b^3U^2}{\pi^2D}$$

where a is a half wavelength of the deformed plate, while α, k, λ, V, and μ are the factors of a wavelength, a spring factor, a load, a velocity, and a mass ratio, respectively. With these notations, equations (1–5) can be rewritten as follows:

$$L(w)\equiv w_{,\tau\tau}+\bar{\nabla}_2^4w-2\alpha\lambda w_{,\xi\eta}+kw+p=0 \tag{7}$$

$$(s)\ w=w_{,\eta\eta}=0,\quad (c)\ w=w_{,\eta}=0\ \text{ at }\ \eta=0,\pi \tag{8}$$

$$p=-(\mu/\pi)(\phi_{,\tau}+\alpha V\phi_{,\xi})_{\zeta=0} \tag{9}$$

$$\bar{\nabla}_3^2\phi=0 \tag{10}$$

$$\phi_{,\zeta|\zeta=0}=w_{,\tau}+\alpha Vw_{,\xi}\ \text{ for } 0\leqq\eta\leqq\pi$$
$$=0\qquad \text{elsewhere} \tag{11}$$

where $\phi=0$ at $\zeta\to\infty$ and

$$\bar{\nabla}_2^2=\alpha^2\frac{\partial^2}{\partial\xi^2}+\frac{\partial^2}{\partial\eta^2},\quad \bar{\nabla}_3^2=\alpha^2\frac{\partial^2}{\partial\xi^2}+\frac{\partial^2}{\partial\eta^2}+\frac{\partial^2}{\partial\zeta^2}$$

To determine the stability behavior of the plate, we must first solve the boundary-value problem posed by equations (10) and (11), substitute this solution into equation (9), and then solve the resulting equation (7) under the boundary conditions (8).

Method of Solution

Considering equations (8), one puts the deflection w as

$$w=e^{i\omega\tau}\sum_n g_m(a_m\cos\xi+b_m\sin\xi),\quad (m=1,2,3,\ldots)$$

$$(s)\ g_m=\sin m\eta,\ (c)\ g_m=\cos(m-1)\eta-\cos(m+1)\eta \tag{12}$$

where a_m and b_m are unknown parameters. Corresponding to equation (12), the perturbation velocity potential ϕ will be in the following form:

$$\phi=e^{i\omega\tau}[\phi_1(\eta,\zeta)\cos\xi+\phi_2(\eta,\zeta)\sin\xi] \tag{13}$$

Substitution of equation (13) into equation (10) yields

$$\phi_{j,\eta\eta}+\phi_{j,\zeta\zeta}-\alpha^2\phi_j=0,\quad (j=1,2) \tag{14}$$

The general solution of equations (14) satisfying the vanishing condition at $\zeta\to\infty$ is of the form

$$\phi_j=\int_0^\infty e^{-\epsilon\zeta}[A_j(q)\cos q\eta+B_j(q)\sin q\eta]dq,\quad (j=1,2) \tag{15}$$

where $\epsilon^2=\alpha^2+q^2$, and $A_j(q)$ and $B_j(q)$ are arbitrary functions of q. These arbitrary functions are determined by using equations (11) and (12), and Fourier integral theory. Thus

$$\phi_j=\sum_m\left[i\omega\begin{pmatrix}a_m\\b_m\end{pmatrix}+\alpha V\begin{pmatrix}b_m\\-a_m\end{pmatrix}\right]\psi_m(\eta,\zeta)$$
$$(j=1,2;\quad m=1,2,3,\ldots) \tag{16}$$

$$\psi_m(\eta,\zeta)$$
$$=\frac{1}{\pi}\int_0^\infty\frac{me^{-\epsilon\zeta}}{\epsilon(q^2-m^2)}[\cos q\eta-(-1)^m\cos(\pi-\eta)q]dq:\ (s)$$
$$=\frac{4}{\pi}\int_0^\infty\frac{mqe^{-\epsilon\zeta}[\sin q\eta-(-1)^m\sin(\pi-\eta)q]}{\epsilon[q^2-(m-1)^2][q^2-(m+1)^2]}dq:\ (c) \tag{17}$$

The perturbation pressure on the plate may now be determined by substitution of equation (16) into equation (9). So far one has obtained expressions for w and p in terms of a_m and b_m, satisfying exactly the boundary conditions. For the determination of a_m and b_m, one applies Galerkin's method to equation (7), which yields the following conditions:

$$\int_{-\pi}^{\pi}\int_0^\pi L(w)g_n\begin{pmatrix}\cos\xi\\\sin\xi\end{pmatrix}d\eta d\xi=0,\quad (n=1,2,3,\ldots) \tag{18}$$

After performing the aforementioned integration and rearrangement, one finally obtains the following equations:

$$\sum_m\left[(R_{nm}-\omega^2M_{nm}-\bar{V}^2A_{nm})\begin{pmatrix}a_m\\b_m\end{pmatrix}+(\lambda Q_{nm}-i\omega\bar{V}B_{nm})\begin{pmatrix}b_m\\-a_m\end{pmatrix}\right]=0,$$
$$(m,n=1,2,3,\ldots) \tag{19}$$

In these equations, for the simply supported case,

$$R_{nm}=\pi^2[(\alpha^2+\eta^2)^2+k]\delta_{n,m}/2$$
$$M_{nm}=\pi^2\delta_{n,m}/2+\mu nmK_{nm}/\pi$$

$$A_{nm}=\alpha^2nmK_{nm}/\pi,\quad B_{nm}=-2\alpha\sqrt{\mu}nmK_{nm}/\pi \tag{20}$$

$$Q_{nm}=\frac{2\pi\alpha nm[(-1)^{n+m}-1]}{n^2-m^2},$$

$$K_{nm}=\int_0^\infty\frac{1+(-1)^{n+m}-[(-1)^n+(-1)^m]\cos\pi q}{\epsilon(q^2-n^2)(q^2-m^2)}dq$$

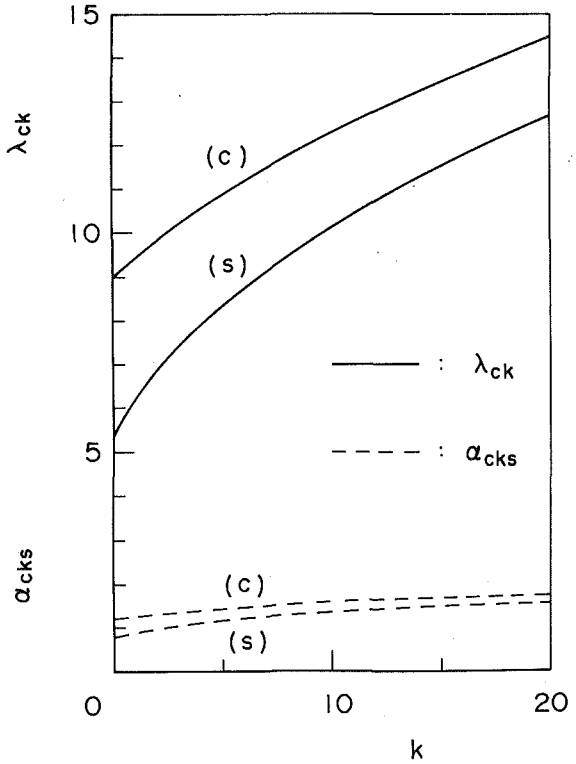

Fig. 2 Relations between the buckling load λ_{ck}, the corresponding wavelength α_{cks}, and the spring factors k of the simply supported strip (s) and the clamped one (c)

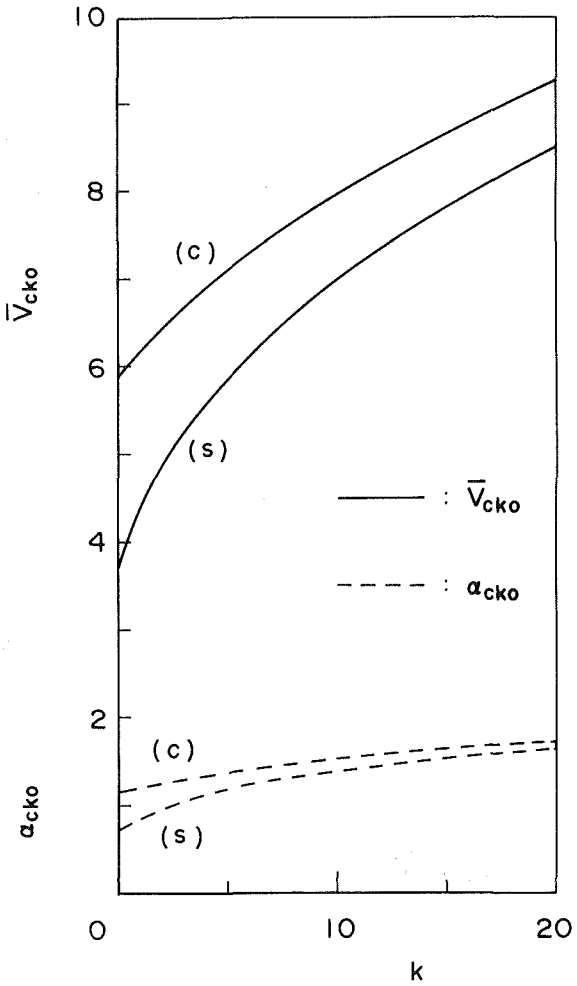

Fig. 3 Relations between the divergence velocity $\bar{V}_{cko}$, the corresponding wavelength α_{cko}, and the spring factors k of the strip without shearing load

and for the clamped case,

$$R_{nm} = \pi^2[D_{m-1}(\delta_{m+n,2}+\delta_{n,m}-\delta_{m-n,2}) - D_{m+1}(\delta_{n-m,2}-\delta_{n,m})]$$

$$M_{nm} = \pi^2(\delta_{m+n,2}+2\delta_{m,n}-\delta_{|m-n|,2})/2+16\mu nmK_{nm}/\pi$$

$$A_{nm} = 16\alpha^2 nmK_{nm}/\pi, \quad B_{nm} = -32\alpha\sqrt{\mu}nmK_{nm}/\pi \qquad (21)$$

$$Q_{nm} = \frac{32\pi\alpha nm(m^2+n^2-2)[(-1)^{n+m}-1]}{(n^2-m^2)[(n-m)^2-4][(n+m)^2-4]},$$

$$D_m = (\alpha^2+m^2)^2+k$$

$$K_{nm} = \int_0^\infty \frac{q^2\{1+(-1)^{n+m}+[(-1)^n+(-1)^m]\cos\pi q\}}{\epsilon[q^2-(n-1)^2][q^2-(n+1)^2][q^2-(m-1)^2][q^2-(m+1)^2]}\,dq$$

where $\delta_{n,m}$ is the Kronecker delta and the integrals can be evaluated numerically.

For a nontrivial solution to equation (19), the determinant of the coefficients must vanish, which results in the characteristic equation

$$\Delta(k,\alpha,\lambda,\mu,\bar{V},\omega)=0 \qquad (22)$$

Under the specified boundary conditions, the determinant Δ will be a function of k, α, λ, μ, $\bar{V}$, and ω. Hence, for given values of k, α, λ, μ, and $\bar{V}$, one can determine the value of the complex frequency, $\omega=\omega_R+i\omega_I$. For $\omega_R\neq 0$ and $\omega_I<0$, the motion of the plate is unstable (so-called flutter instability). For $\omega_R=0$ and $\omega_I<0$, the plate is statically unstable (so-called divergence instability). Continuously changing the values of the wavelength α, one can determine the minimum value of $\bar{V}$ and the corresponding value of α for which flutter or divergence occurs. These give the critical velocity V_c and wavelength α_c. Through the detailed numerical calculation, the divergence velocity was found to be lower than the flutter one, independent of the shearing load, the elastic foundation and the boundary condition. Further, while the divergence mode was the form of standing waves, the flutter mode was one of traveling waves. It is expected that the stability boundary of the present problem also is one corresponding to static divergence as the results obtained by Dowell [2], and Weaver and Unny [5]. In the near future, author intends to report the flutter instability of panels in a compressible fluid with the effect of structural damping taken into consideration. Hence, the following numerical results are shown with particular focus on the divergence instability. The buckling load of the plate under shearing load can be determined by setting $\mu=\bar{V}=\omega=0$ into equation (22).

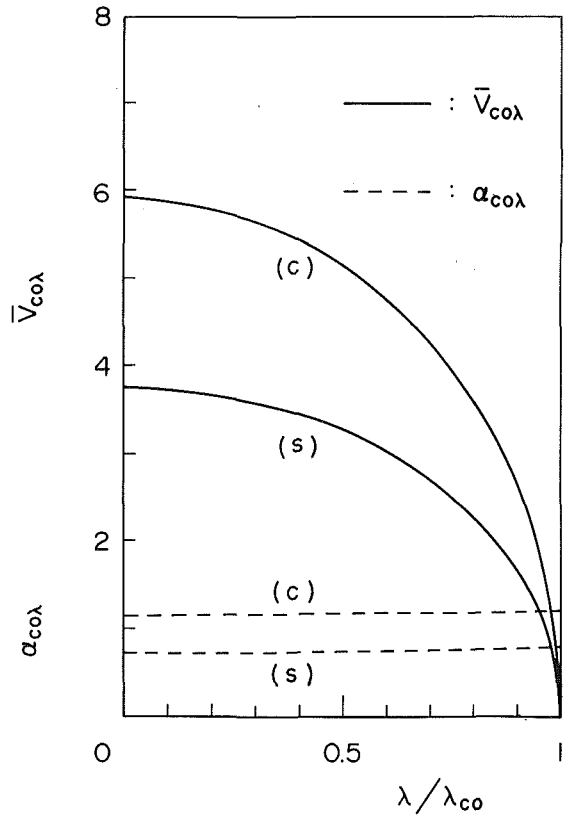

Fig. 4 Relations between the divergence velocity $\bar{V}_{co\lambda}$, the corresponding wavelength $\alpha_{co\lambda}$, and the shearing load factor λ of the strip without the elastic foundation

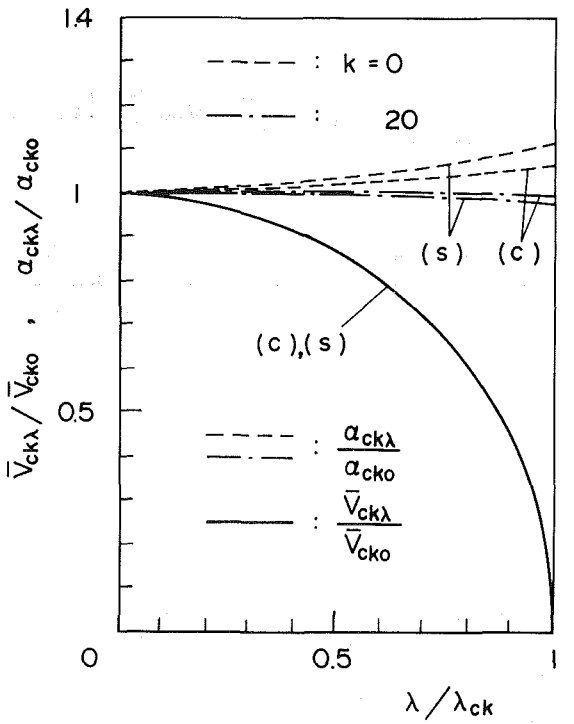

Fig. 5 Relations between the divergence velocity $\bar{V}_{ck\lambda}$, the corresponding wavelength $\alpha_{ck\lambda}$, and the shearing load factor λ of the strip on the elastic foundation k

Numerical Results and Discussions

On the basis of the preceding analyses, numerical calculations are carried out for various values of the shearing load and the spring stiffness of the elastic foundation. Well-converged solutions are obtained by taking four terms for each unknown parameters a_m and b_m in the simply supported case, and 10 terms in the clamped one.

First, we consider the buckling problem of infinite strips under shearing load on the elastic foundation. The buckling load factor λ_{ck} and the corresponding wavelength factor α_{cks} are determined for various values of the spring factor k and illustrated in Fig. 2. In this case, exact solutions can be obtained easily by putting $w_{,\tau\tau}=p=0$ in equation (7) and integrating this equation directly. The difference between the present approximate and exact solutions was 0.2 percent at the most. Excellent agreement was obtained. It can be seen from Fig. 2 that the buckling load increases considerably and the corresponding wavelength factors increase slightly with the spring stiffness of the foundation and the restriction on the edge rotation of the plate.

Next, the effect of the elastic foundation on the diveregence velocity of the plate without shearing load ($\lambda=0$) is examined with the results shown in Fig. 3. It can be seen from this figure that the divergence velocity $\bar{V}_{cko}$ increases considerably and the corresponding wavelength factor α_{cko} increases slightly with the spring stiffness k of the foundation and the restriction on the edge rotation of the plate. The present results $\bar{V}_{coo}$ and α_{coo} for the simply supported plate without the elastic foundation ($k=0$) agree precisely with those obtained by Dowell [2]. While the flutter velocity and the corresponding wavelength were determined for the simply supported plate without the elastic foundation and the shearing load, and confirmed to agree well with those obtained by Dowell [2], and Weaver and Unny [5], these result will not be presented here.

Furthermore, the effect of the shearing load on the divergence velocity of the plate without the elastic foundation ($k=0$) is examined with the results shown in Fig. 4. In this figure, λ_{co} is the buckling shearing load of the plate without the elastic foundation for each case (*c*) and (*s*). It can be seen from Fig. 4 that the shearing load reduces the divergence velocity $\bar{V}_{co\lambda}$ and slightly increases the divergence wavelength factor $\alpha_{co\lambda}$. This tendency is somewhat different from the result for the plate with finite length and infinite width exposed to an incompressible inviscid fluid flowing in the direction of the finite length. That is, a shearing load smaller than one-half of the buckling load does not affect the divergence instability in the latter case [24].

Finally, the arithmetic effects of the elastic foundation and the shearing load on the divergence velocity $\bar{V}_{ck\lambda}$ and the corresponding wavelength factor $\sigma_{ck\lambda}$ are examined with the results shown in Fig. 5. In this figure, λ_{ck} is the buckling shearing load for each case, and $\bar{V}_{cko}$ and α_{cko} are the divergence velocity and the corresponding wavelength factors of the plate without shearing load ($\lambda=0$) for each case. The following observation can be made from this normalized figure. The relation between the divergence velocity and the shearing load for the simply supported plate almost agrees with that for the clamped one, irrespective of the spring stiffness of the elastic foundation. The relation between the divergence wavelength and the shearing load slightly changes as the shearing load increases and the spring stiffness varies.

The effects of the shearing load, the elastic foundation, and the boundary condition on the divergence mode are examined also. Typical results for the plate without the elastic foundation ($k=0$) are shown in Figs. 6 and 7, with the contour lines with the maximum amplitude of the deflection w taken as unity. Since the effect of the elastic foundation on the general feature of the divergence mode is very small, its results are omitted. It can be seen that, with the application of the shearing load, the nodal lines are changed obliquely in the loading direction and this divergence mode almost agrees with the buckling one. The divergence wavelength α slightly

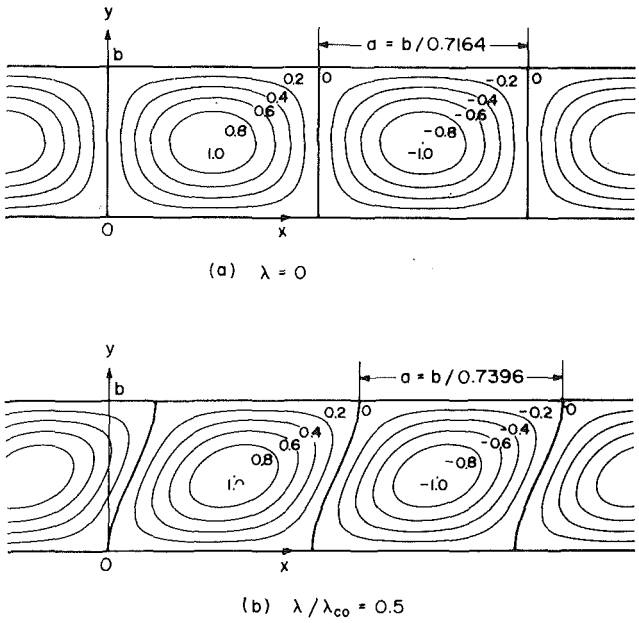

Fig. 6 Divergence modes of the simply supported strip (s)

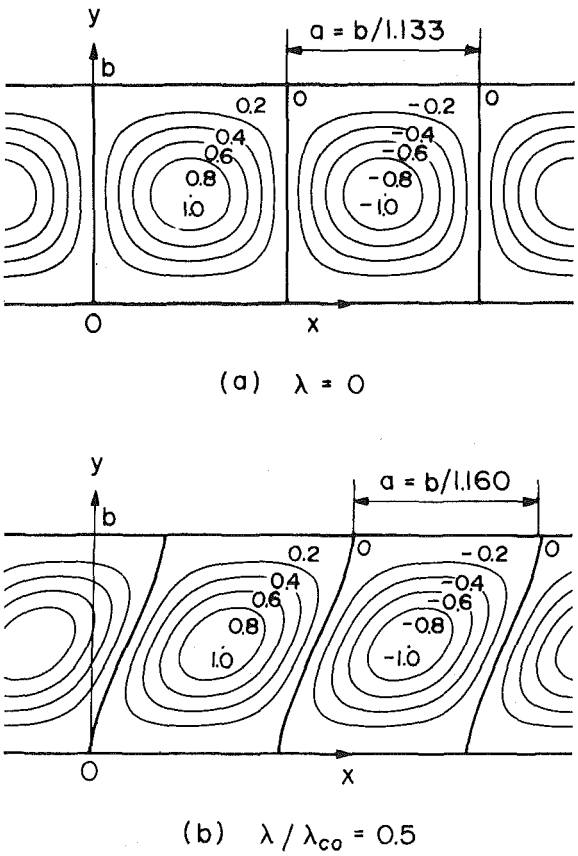

Fig. 7 Divergence modes of the clamped strip (c)

decreases with the shearing load. The difference in the boundary condition changes the divergence wavelength and the contour lines near both the edges of the plate.

Conclusion

The influences of the shearing load and the elastic foundation on the hydroelastic instability of infinite strips are examined on the basis of the small deflection plate theory and the classical linearized potential flow theory. The main results obtained here may be summarized as follows.

(1) The divergence velocity and the corresponding wavelength factors of the strip without shearing load increase with the spring stiffness of the elastic foundation.

(2) Increase in the shearing load reduces the divergence velocity and slightly increases the divergence wavelength factor of the strip without the elastic foundation.

(3) The divergence velocity, the buckling load, and the corresponding wavelength factors increase due to the restriction of the edge rotation of the strip.

(4) When the divergence velocity and the corresponding wavelength of the strip under shearing load on the elastic foundation are normalized by those of the strip without shearing load, and the shearing load by the buckling load for each case, the relation between the shearing load and the divergence velocity of the strip on the elastic foundation is shown in a single curve, irrespective of the boundary condition of the strip.

(5) The divergence mode of the strip under shearing load almost agrees with the buckling mode.

Acknowledgments

The author would like to thank Emeritus Prof. N. Yamaki, Tohoku University, for valuable discussion. This work was supported financially by Prof. H. Abe, Tohoku University. The helpful and important comments of two referees and Prof. S. T. Ariaratnam are gratefully acknowledged.

References

1 Dugundji, J., Dowell, E., and Perkin, B., "Subsonic Flutter of Panels on Continuous Elastic Foundations," *AIAA Journal*, Vol. 1, No. 5, 1963, pp. 1146–1154.

2 Dowell, E. H., "Flutter of Infinitely Long Plates and Shells Part I: Plate," *AIAA Journal*, Vol. 4, No. 8, 1966, pp. 1370–1377.

3 Weaver, D. S., and Unny, T. E., "The Hydroelastic Stability of Flat Plate," ASME JOURNAL OF APPLIED MECHANICS, Vol. 37, No. 3, 1970, pp. 823–827.

4 Gislason, T., Jr., "Experimental Investigation of Panel Divergence at Subsonic Speeds," *AIAA Journal*, Vol. 9, No. 11, 1971, pp. 2252–2258.

5 Weaver, D. S., and Unny, T. E., "The Influence of a Free Surface on the Hydroelastic Stability of a Flat Panel," ASME JOURNAL OF APPLIED MECHANICS, Vol. 39, No. 1, 1972, pp. 53–58.

6 Ellen, C. H., "The Stability of Simply Supported Rectangular Surfaces in Uniform Subsonic Flow," ASME JOURNAL OF APPLIED MECHANICS, Vol. 40, No. 1, 1973, pp. 68–72.

7 Kornecki, A., "Influence of Subsonic Potential Flow on the Buckling of Thin Panels under Edge Compression," *AIAA Journal*, Vol. 13, No. 1, 1975, pp. 106–107.

8 Kornecki, A., Dowell, E. H., and O'Brien, J., "The Aeroelastic Instability of Two-Dimensional Panels in Uniform Incompressible Flow," *Journal of Sound and Vibration*, Vol. 47, No. 2, 1976, pp. 163–178.

9 Ellen, C. H., "The Stability of an Isolated Rectangular Surface Embedded in Uniform Subsonic Flow," ASME JOURNAL OF APPLIED MECHANICS, Vol. 44, No. 2, 1977, pp. 201–206.

10 Kim, Y. T., and Scarton, H. A., "Flow-Induced Bending of Rectangular Plates," ASME JOURNAL OF APPLIED MECHANICS, Vol. 44, No. 2, 1977, pp. 207–212.

11 Matsuzaki, Y., and Fung, Y.-C., "Stability Analysis of Straight and Buckled Two-Dimensional Channels Conveying an Incompressible Flow," ASME JOURNAL OF APPLIED MECHANICS, Vol. 44, No. 4, 1977, pp. 548–552.

12 Tani J., "Hydroelastic Instability of Infinitely Long Magnetoelastic Plates," *Bulletin of the Japan Society of Mechanical Engineers*, Vol. 20, No. 143, 1977, pp. 528–533.

13 Tani J., "Influence of a Uniform Magnetic Field of the Hydroelastic Instability of a Ferromagnetic Plate," *Journal of Sound and Vibration*, Vol. 51, No. 4, 1977, pp. 475–482.

14 Ellen, C. H., "The Non-Linear Stability of Panels in Incompressible Flow," *Journal of Sound and Vibration*, Vol. 54, No. 1, 1977, pp. 117–121.

15 Holmes, P. J., "Bifurcations to Divergence and Flutter in Flow-Induced Oscillations: A Finite Dimensional Analysis," *Journal of Sound and Vibration*, Vol. 53, No. 4, 1977, pp. 471–503.

16 Matsuzaki, Y., and Fung, Y.-C., "Nonlinear Stability Analysis of a Two-Dimensional Model of an Elastic Tube Conveying a Compressible Flow," ASME JOURNAL OF APPLIED MECHANICS, Vol. 46, No. 1, 1979, pp. 31–36.

17 Shahrokh, K., and Ellen, C. H., "The Stability of Partially Rigid Two-Dimensional Surfaces in Uniform Incompressible Flow," *Journal of Sound and Vibration*, Vol. 65, No. 3, 1979, pp. 339–351.

18 Grotberg, J. B., and Davis, S. H., "Fluid-Dynamic Flapping of Collapsible Cannel: Sound Generation and Flow Limitation," *Journal of Biomechanics*, Vol. 13, No. 3, 1980, pp. 219–230.

19 Matsuzaki, Y., and Ueda, T., "Reexamination of Unsteady Fluid Dynamics Forces on a Two-Dimensional Finite Plate at Small Mach Numbers," ASME JOURNAL OF APPLIED MECHANICS, Vol. 47, No. 4, 1980, pp. 720–724.

20 Matsuzaki, Y., "Reexamination of Stability of a Two-Dimensional Finite Panel Exposed to an Incompressible Flow," ASME JOURNAL OF APPLIED MECHANICS, Vol. 48, No. 3, 1981, pp. 472–478.

21 Cook, P. L., and Holmes, M., "Waves and Dispersion Relations for Hydroelastic Systems," *SIAM Journal of Applied Mathematics*, Vol. 41, No. 2, 1981, pp. 271–287.

22 Busch-Vishniac, I. J., "Fluid Loading of Plates Under Tension," *Journal of Acoustical Society of America*, Vol. 71, No. 2, 1982, pp. 498–500.

23 Garrad, A. D., and Carpenter, P. W., "On the Aerodynamics Forces Involved in Aeroelastic Instability of Two-Dimensional Panels in Uniform Incompressible Flow," *Journal of Sound and Vibration*, Vol. 80, No. 3, 1982, pp. 437–439.

24 Tani, J., "Hydroelastic Instability of Orthotropic Panels With Infinite Width Under Shearing Load," to be published in *Journal of Sound and Vibration*.

On the Propagation of Bulges and Buckles[1]

E. Chater

J. W. Hutchinson
Mem. ASME

Division of Applied Sciences,
Harvard University,
Cambridge, Mass. 02138

Two examples illustrate the propagation of instability modes under quasi-static, steady-state conditions. The first is the inflation of a long cylindrical party balloon in which a bulge propagates down the length of the balloon. The second is the collapse of a long pipe under external pressure as a result of buckle propagation. In each example, there is a substantial barrier to the initiation of the instability mode. Once initiated, however, the mode will not arrest if the pressure is in excess of the quasi-static, steady-state propagation pressure. It is this critical pressure that is determined in this paper for each of the two examples.

1 Introduction

While not a problem of great technological importance, the inflation of a common cylindrical party balloon provides a good illustration of the phenomenon of the propagation of an instability. If one were to record the pressure in the balloon as a function of its volume during the inflation process, one would obtain a record such as that shown in Fig. 1. A bulge first starts to form when the peak pressure is attained. It forms and localizes at some section with an initial weakness or at one of the ends of the balloon due to local nonuniformity. With continued inflation, the pressure falls to a constant level as the bulge slowly propagates along the balloon. During the steady-state portion of the inflation process the radii of the bulged and unbulged sections do not change, as depicted in Fig. 1. The transition front between these two sections simply propagates, or translates, into the unbulged section. This is a quasi-static process in that air mass (essentially volume), and not pressure, is prescribed to increase at a slow rate. A photograph of a partially inflated cylindrical balloon in the steady-state phase of the inflation process is shown in Fig. 2. Our analysis will focus on the critical pressure p^* associated with quasi-static, steady-state bulge propagation and on the states on either side of the transition.

The balloon problem is analogous in several respects to the second problem we will consider, which is the collapse of a long cylindrical shell, or pipe, due to the propagation of a buckle along its length. This problem is of some importance in connection with the collapse of undersea pipelines. We address the problem of the external pressure p^* required to propagate a buckle down the pipe under steady, quasi-static conditions. This critical pressure is especially significant since at any pressure below p^*, buckles cannot propagate, while at any prescribed pressure above p^*, the buckle once initiated will run dynamically, collapsing the entire length of pipe.

2 Steady-State Bulge Propagation Along a Cylindrical Balloon

To gain a qualitative understanding of the origin of the initial bulging process and the subsequent quasi-static bulge propagation along a cylindrical party balloon, one need only consider the relation of pressure to change of volume for a cylindrical section of the balloon. Consider purely cylindrical membrane deformations of a section such that at any pressure p the shape is always cylindrical with current radius R and thickness t. The circumferential stress is $\sigma_2 = pR/t$ and the axial stress is $\sigma_1 = pR/(2t)$. The qualitative form of the curve of pressure as a function of volume for a cylindrical section of balloon that has unit volume in the undeformed state is shown in Fig. 3. The volume change results from axial as well as circumferential stretch. It will be assumed that the balloon is inflated under isothermal conditions, and that the pressure-volume relation in Fig. 3 for purely cylindrical deformations corresponds to isothermal deformation of the balloon rubber. A curve calculated using a constitutive law for an actual rubber will be displayed later.

The initial bulging is a consequence of the local peak in the curve of pressure against volume for purely cylindrical deformations. The qualitative argument for initial bulge formation parallels that of Considére for necking of metal bars in tension. One section, which is slightly weaker than the rest of the balloon, attains the peak first and then bulges under falling pressure while the remainder of the balloon "unloads" without bulging. The bulge has localized in the manner described in general terms by Tvergaard and Needleman [1]. However, unlike tensile necking in common metals and many other problems involving localized instability modes, the bulge starts to spread as inflation is continued. Spreading, or propagation, is associated with the upturn in the curve of pressure versus volume for the cylindrical section. The increasing resistance of a bulged section to

Contributed by the Applied Mechanics Division for presentation at the 1984 PVP Conference and Exhibition, Joint with Applied Mechanics Division and Materisls Division, San Antonio, Texas, June 17-21, 1984 of THE AMERICAN SOCIETY OF MECHANICAL ENGINEERS.

Discussion on this paper should be addressed to the Editorial Department, ASME, United Engineering Center, 345 East 47th Street, New York, N.Y. 10017 and will be accepted until two months after final publication of the paper itself in the JOURNAL OF APPLIED MECHANICS. Manuscript received by ASME Applied Mechanics Division, June, 1983. Paper No. 84-APM-18.

Copies will be available until February, 1985.

[1] Dedicated to the memory of B. O. Almroth.

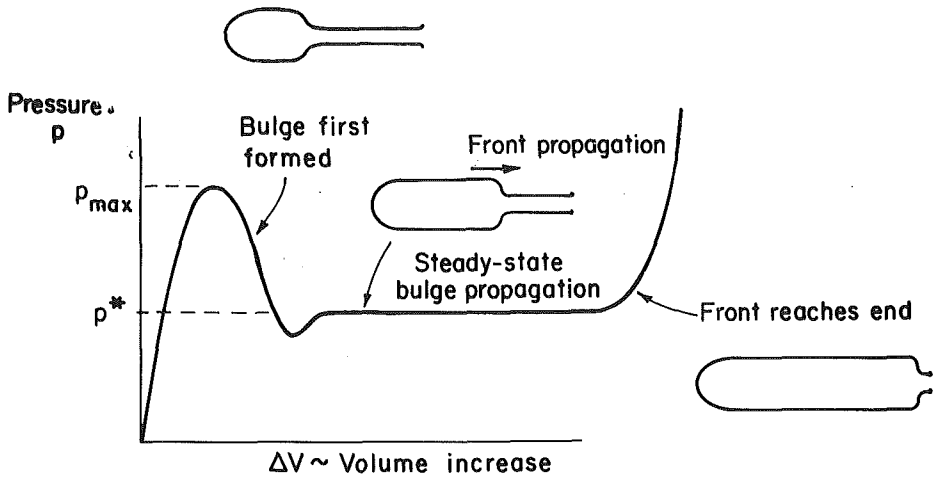

Fig. 1 Inflation of a cylindrical party balloon

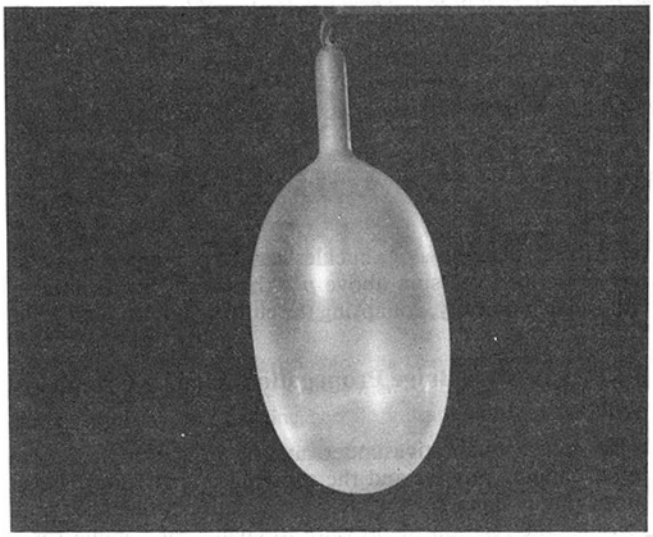

Fig. 2 Common party balloon showing transition between bulged and unbulged sections

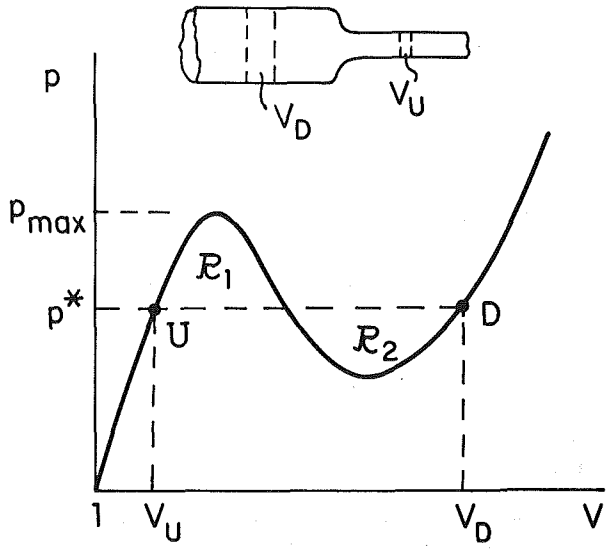

Fig. 3 *p(V)* for purely cylindrical deformation of a cylindrical segment of unit initial volume. Quasi-static, steady-state propagation condition requires $\mathcal{R}_1 = \mathcal{R}_2$.

further volume expansion terminates the localization process and forces the bulge to propagate laterally into the neighboring section.

Condition for Steady-State Propagation. As discussed in the Introduction and as depicted in Fig. 1, the inflation process soon reaches a steady state in which the pressure is constant and the radii of the bulged and unbulged sections do not change. The transition front between these two sections attains a fixed shape which simply translates along the balloon engulfing the unbulged section. We will be concerned with steady-state inflation under a sufficiently slow rate of air injection such that inertial effects are negligible. This is quasi-static bulge propagation in which the advance of the transition front is controlled by the rate of air injection. Depending on the properties of the balloon material and on its length, the initial bulging process may occur dynamically, under a prescribed mass of air, with the bulging section growing at the expense of the remainder of the balloon.

The equation determining the quasi-static propagation pressure p^* under steady-state conditions follows immediately from the energy balance requirement that the work done by p^* must equal the change of strain energy stored in the balloon in any advance of the transition front.

Let V_U and V_D denote the volumes of cylindrical sections, each with unit undeformed volume, associated with states U and D far ahead of and far behind, respectively, the transition. Because the shape of the transition is fixed, the change in volume of the balloon when the transition front shifts forward to engulf a new section that has unit undeformed volume is precisely $V_D - V_U$, and the work done by the pressure is $p^*(V_D - V_U)$. This work of the pressure is equal to the work, ΔW, done on a section of unit undeformed volume as it passes from state U to state D through the transition, i.e.,

$$p^*(V_D - V_U) = \Delta W \tag{1}$$

Now, for a rubberlike material for which a strain energy function is assumed to exist (under the assumed isothermal conditions), ΔW is independent of the details of the deformation history in the transition and depends only on the end states D and U. In particular, we may calculate ΔW using purely cylindrical deformations to connect states D and U. Doing so, we note that

$$\Delta W = \int_{V_U}^{V_D} p(V)\, dV \tag{2}$$

where $p(V)$ denotes the relation of pressure to volume for purely cylindrical deformations of a section of unit undeformed volume, such as that depicted in Fig. 3. Thus, from (1) and (2), the equation for the pressure p^* for quasi-static, steady-state bulge propagation is

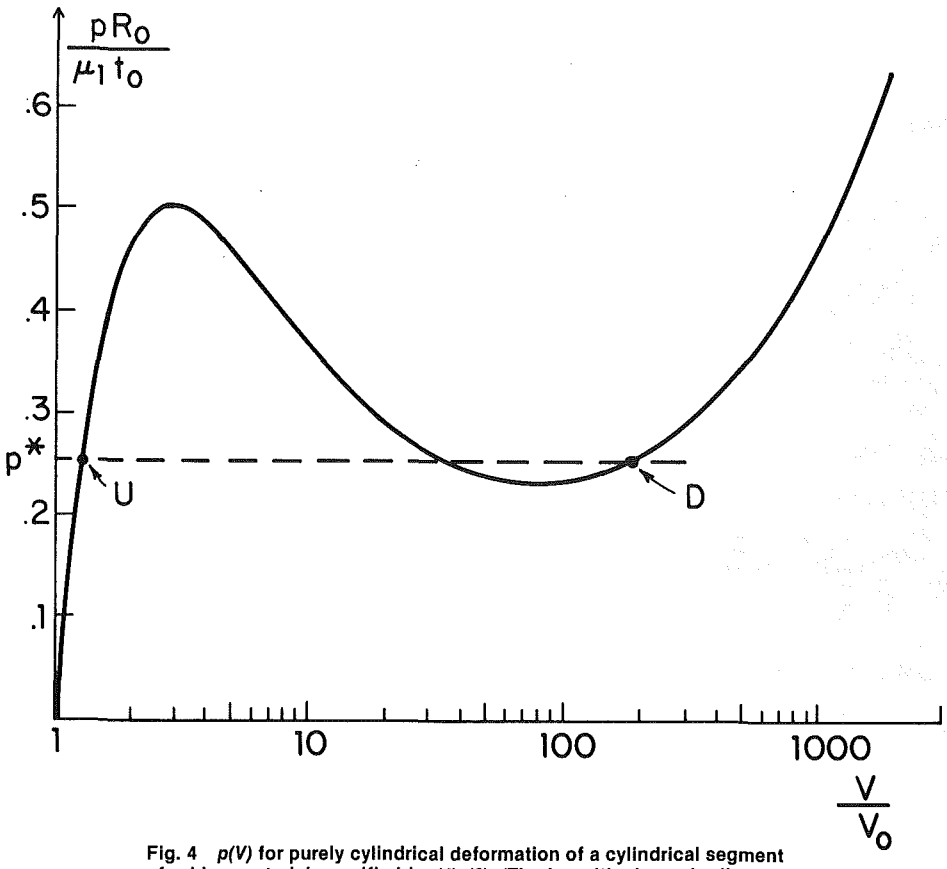

Fig. 4 *p(V)* **for purely cylindrical deformation of a cylindrical segment of rubber material specified by (4)-(6). (The logarithmic scale distorts the areas of the two lobes.)**

$$p^*(V_D - V_U) = \int_{V_U}^{V_D} p(V)\,dV \tag{3}$$

Equation (3) has the simple graphical solution indicated in Fig. 3. By (3), the equality of the rectangular area $p^*(V_D - V_U)$ with the area under the curve $p(V)$ between V_U and V_D is equivalent to the condition that the areas of the two lobes, $\mathfrak{R}_1$ and $\mathfrak{R}_2$, be equal. In the literature of phase transitions, this graphical solution involving conjugate thermodynamical variables is known as Maxwell's condition for two coexisting phases [2]. For the balloon, equation (3) is the condition that a transition between bulged and unbulged sections exist whether the transition is stationary or whether it is propagating quasi-statically under inflation or deflation.

The quasi-static propagation pressure p^* is less than the local peak pressure $p_{\max}$ a cylindrical segment can support by about a factor of two, which will be shown in the following example. In other words, it takes a substantially larger pressure to initiate a bulge than to propagate it, as depicted in Fig. 1, and as experienced by anyone familiar with blowing up party balloons. The relevance of the Maxwell construction to other instability propagation problems has been noted in [3, 4]. Characteristic of the general class of phenomena is a substantial barrier to the initiation of the instability mode. Once initiated, the mode encounters less resistance and spreads at reduced load.

Predictions for a Specific Rubber Material. Ogden [5] proposed a strain energy density function for incompressible, isotropic rubberlike materials in the form

$$\Phi = \sum_{i=1}^{3} \mu_i I(\alpha_i) \tag{4}$$

where

$$I(\alpha) = \alpha^{-1}(\lambda_1^\alpha + \lambda_2^\alpha + \lambda_3^\alpha - 3) \tag{5}$$

and where the λ_i are the three stretches. To fit Treloar's isothermal data for rubber, Ogden proposed

$$\alpha_1 = 1.3, \quad \alpha_2 = 5.0, \quad \alpha_3 = -2.0$$
$$\text{with} \tag{6}$$
$$\mu_2 = 2.01 \times 10^{-3}\mu_1 \quad \text{and} \quad \mu_3 = -1.59 \times 10^{-2}\mu_1$$

where μ_1 is a ground state modulus which will not have to be specified here. The curve of nondimensional p as a function of V for purely cylindrical deformations of a cylindrical segment of this material is shown in Fig. 4. Here R_0, t_0, and V_0 denote the values of the radius, thickness, and volume of the undeformed cylindrical segment. The local peak pressure is

$$p_{\max} = 0.504\mu_1 t_0/R_0 \tag{7}$$

The Maxwell condition (3) for p^* and states U and D gives

$$p^* = 0.255\mu_1 t_0/R_0 \tag{8}$$

and

$$\begin{aligned} &\lambda_1^U = 1.006, \quad \lambda_2^U = 1.125, \quad V_U = 1.273V_0 \\ &\lambda_1^D = 4.484, \quad \lambda_2^D = 6.507, \quad V_D = 189.8V_0 \end{aligned} \tag{9}$$

where the one-direction is parallel to the cylindrical axis of the balloon and the two-direction is along its circumference. (Note that a logarithmic scale is used for the abscissa in Fig. 4 so that the two lobes formed by the Maxwell line do not have equal areas in that plot.) The steady-state inflation pressure is almost exactly one half $p_{\max}$. The measured volume expansion of the balloon of Fig. 2 in state D is about $V_D \cong 130V_0$, which is somewhat less than the prediction (9) for a balloon of Treloar's rubber characterized by (4).

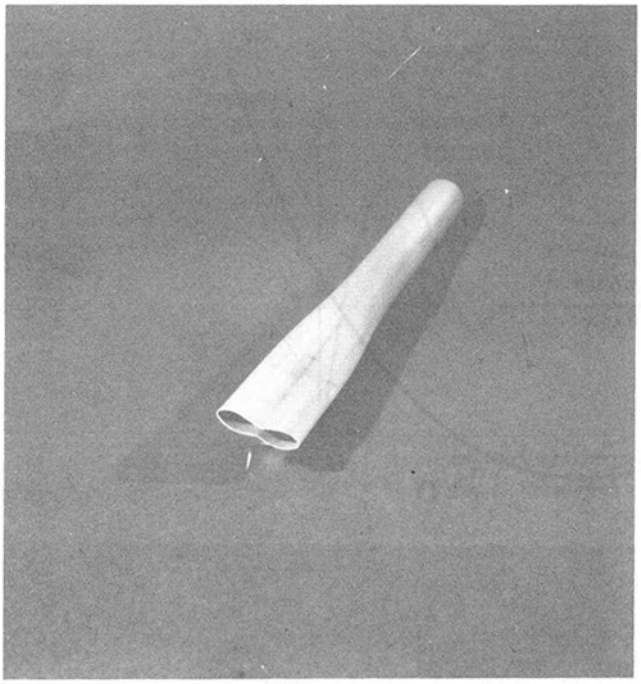

Fig. 5 Section of one of Kyriakides' specimens showing the transition between the buckled and unbuckled regions of the pipe.

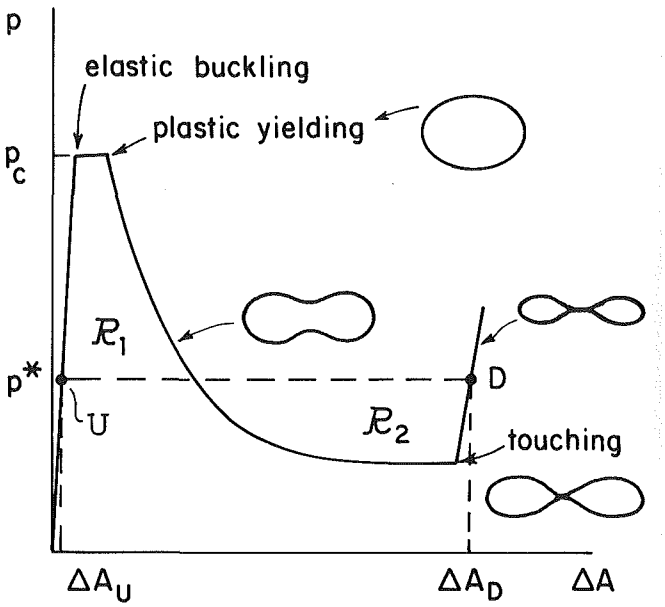

Fig. 6 Buckling and post-buckling behavior of a ring undergoing plane strain deformation. Quasi-static propagation pressure p^* is given by the condition $\mathcal{R}_1 = \mathcal{R}_2$ for a pipe of material characterized by deformation theory.

3 Buckle Propagation Along a Pipe Subject to External Pressure

We now direct attention to the problem for the smallest pressure at which a buckle, once initiated, will propagate the entire length of a cylindrical shell or pipe. Palmer and Martin [6] have given one of the early accounts of this phenomenon as related to the collapse of undersea pipelines, and Mesloh, Johns, and Sorenson [7] conducted the first systematic experimental study of the problem using both small and full-scale specimens. Kyriakides [8] and Kyriakides and Babcock [9, 10] have carried out the most extensive theoretical and experimental study of a number of aspects of buckle propagation and arrest on externally pressurized pipes. The approach we discuss in the following makes close contact with the work of Kyriakides and Babcock and, in particular, we will compare our theoretical predictions for the smallest propagation pressure to some of their experimental results.

A photograph of one of Kyriakides' test specimens is shown in Fig. 5. The section of pipe shown was cut from a much longer pipe. It displays the three regions of interest: the collapsed region, the unbuckled region, and the transition. In conducting the test, a substantial dent was introduced near one end of the long pipe. The pipe was then subjected to external pressure in an apparatus consisting of an external shell surrounding the pipe. Air or water was pumped at a given rate into the cavity between the pipe and the outer shell. Under quasi-static propagation of interest here, the buckle spreads at a rate that is controlled by the (slow) rate of injection of the pressurizing medium. After a brief transient, the propagating buckle settles down to a steady-state condition in which the transition moves down the pipe under constant pressure p^* leaving a plastically collapsed pipe behind it.

Buckling and Post-Buckling Behavior of a Ring Under Plane Strain Deformations. The classical elastic buckling pressure of an infinitely long cylndrical shell of radius R and thickness t due to plane strain ring buckling is

$$p_c = \frac{E}{4(1-\nu^2)}\left(\frac{t}{R}\right)^3 \tag{10}$$

where E is Young's modulus and ν is Poisson's ratio. The associated hoop stress in the shell at buckling is $\sigma_c = -p_c R/t$ and the axial stress is $\sigma_c/2$. The pipes that have been tested have ratios of radius to thickness in the range from about 15–50, roughly corresponding to the range of interest for undersea pipelines. In this range, the materials of the test specimens, and of the pipelines themselves, have sufficiently high-yield stresses such that any perfect pipe would begin to buckle elastically. That is, the stress state $(\sigma_c, \sigma_c/2)$ falls within the initial yield surface of the pipe material. In the present study, we will also confine attention to the range of parameters such that the classical buckling stress of the perfect pipe is within the elastic limit.

Kyriakides and Babcock [8–10] and Kyriakides and Arikan [11] have emphasized the relevance of the post-buckling behavior of a circular ring to the understanding of the buckle propagation problem, and the ring behavior is central to our approach as well. A schematic curve of pressure, p, as a function of reduction in cross-sectional area, ΔA, is shown in Fig. 6 for a perfect, infinitely long cylindrical shell undergoing ring buckling. This is a plane-strain ring mode in that the deformation is independent of the axial coordinate and the axial component of strain associated with bending is zero.

Buckling starts when the pressure attains p_c, as already described. Ovalization proceeds under a very slight rise in pressure until plastic yielding starts at the regions of highest curvature change. Once yielding starts, the pressure carrying capacity falls precipitously. As ovalization progresses, most of the deformation becomes confined to four "hinges" at the quarter points of the ring and the pressure falls more slowly. Then, when the area reduction has reached about 75 percent of the original cross-sectional area, touching of two opposite quarter points occurs, as depicted in Fig. 6. Touching braces the ring and immediately results in a substantial stiffening so that the pressure again increases very rapidly with relatively little additional area reduction [11].

Touching and the attendant rise in pressure is crucial to the work balance relation, and therefore some further

background to its occurrence is now given. In the original tests of Kyriakides and Babcock the importance of touching, per se, was not obvious and no effort was made to ascertain whether or not it occurred in the limit of quasi-static propagation. In the unloaded state the opposite walls of the collapsed section are definitely not in contact, but no conclusion can be drawn from this observation since elastic spring back always occurs. We are grateful to Kyriakides for conducting further tests on two additional specimens under quasi-static test conditions. In these tests he determined unambiguously that touching does occur in the collapsed section of the pipe behind the transition (private communication).

Deformation Theory Analysis of Quasi-Static, Steady-State Buckle Propagation. A second crucial aspect in our approach is the idealized material model we adopt. We characterize the material by the deformation theory of plasticity, which is a small-strain, nonlinearly elastic constitutive relation. In the steady-state buckle propagation problem elastic unloading is not an important feature. Almost every material point in the pipe experiences a monotonic plastic loading history as the transition fronts sweeps by it. In the quasi-static propagation limit, the transition between the collapsed and uncollapsed sections of the pipe is very gradually occurring over about 10 pipe diameters [8]. To a rough approximation, any short cylindrical segment of the pipe experiences a deformation history similar to the ring deformation depicted in Fig. 6. In addition to circumferential bending associated with the ring deformation, some axial bending along with in-plane straining must occur in the transition. In other words, although the stress history of any material point may involve monotonic loading, it is not a strictly proportional stressing history. By invoking deformation theory, we will be neglecting any path-dependent effects associated with the nonproportional stressing that occurs in the transition.

Now consider the work balance for steady-state propagation under quasi-static conditions at pressure p^*. By making the same simple arguments used in the balloon problem, one arrives at the work balance relation

$$p^*(\Delta A_D - \Delta A_U) = \Delta W \tag{11}$$

Here, ΔA_D and ΔA_U denote area reductions associated with segments far behind and far ahead of the transition, and ΔW is the stress work absorbed by each ring segment of unit length as it is engulfed by the transition deforming it from state U to state D. For a pipe of deformation theory material, states D and U are plane-strain ring solutions. Furthermore, because of the path independence of deformation theory, ΔW may be determined using the ring solution even though each ring segment departs from the plane-strain ring behavior in the transition. The stress work difference, ΔW, is just the work done on the plane strain ring in deforming it from state U to state D, i.e.,

$$\Delta W = \int_{\Delta A_U}^{\Delta A_D} p(\Delta A)\, d\Delta A \tag{12}$$

where $p(\Delta A)$ denotes the relation of pressure to area reduction for the ring under plane strain deformations. Thus, the equation for p^* is

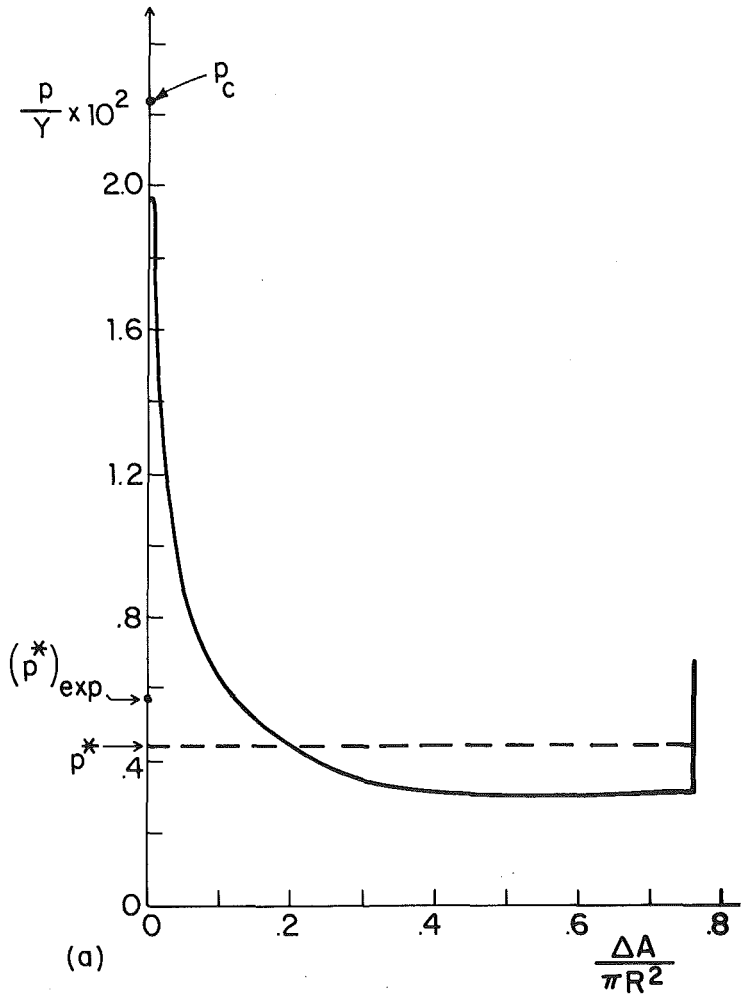

Fig. 7(a) $R/t = 14.3$

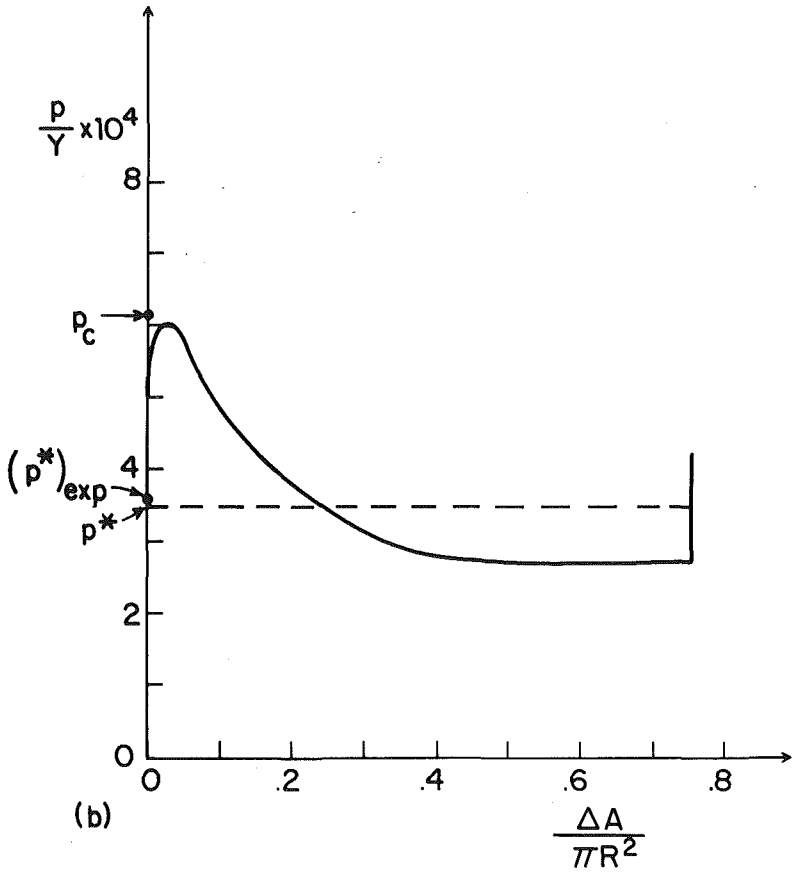

Fig. 7(*b*) $R/t = 47.4$

Fig. 7 Curves of $p(\Delta A)$ for cylindrical segments of two pipes in the test series. In each case, $Y/E = 0.0042$ and $n = 30$.

$$p^*(\Delta A_D - \Delta A_U) = \int_{\Delta A_U}^{\Delta A_D} p(\Delta A)\, d\Delta A \tag{13}$$

with the same graphical interpretation as in the balloon problem, as indicated in Fig. 6.

Comparison With Some Experiments. We have carried out accurate calculations of p^* for some pipes of AL-6061-T6 for which Kyriakides [8] reported quasi-static buckle propagation pressures. The yield stresses of the pipes in the test series ranged from $Y = 280$ to 370 MPa. We selected eight pipes for which the uniaxial stress-strain curves were available with Y being in the range from 286 to 296 MPa. The uniaxial curves given in [8] were closely approximated by the formula

$$\epsilon = \frac{\sigma}{E} + \left(0.005 - \frac{Y}{E}\right)\left(\frac{\sigma}{Y}\right)^n \tag{14}$$

where $E = 6.9 \times 10^4$ MPa, with $Y/E = 0.0042$ and $n = 30$ or with $Y/E = 0.0043$ and $n = 28$.

The pipes varied in radius to thickness from 14.3–47.4 and, as already mentioned, a perfect version of each would begin buckling in the elastic range. Some of the details of the calculation of the relation $p(\Delta A)$ for the plane-strain ring problem are described in the Appendix. Two examples are shown in Fig. 7 for the pipes in the series with the largest and smallest values of R/t. The elastic contraction of the ring prior to buckling is so small that almost no reduction of area shows up in Fig. 7 before the peak is attained. To facilitate the numerical calculation of $p(\Delta A)$, a very small initial imperfection was introduced in the form of an initial ovalization of the ring amounting to an additional radius difference of 0.005 times the ring thickness. For this reason, the peak value

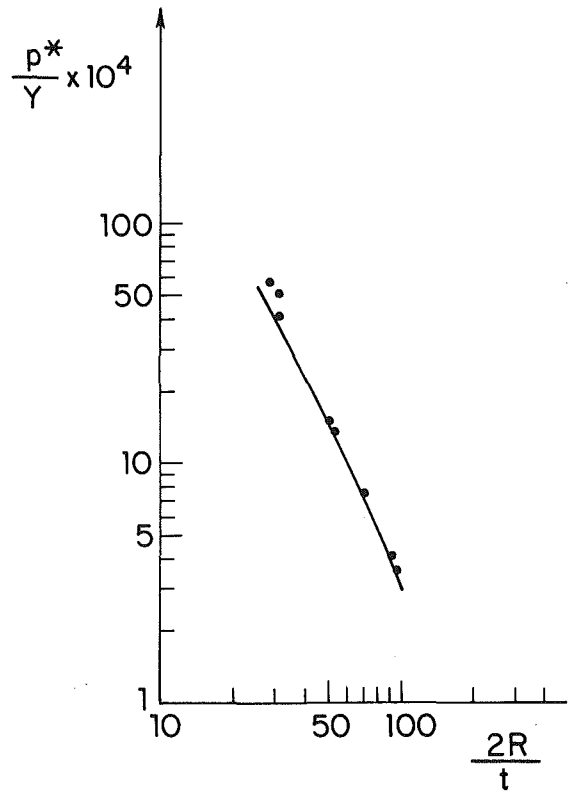

Fig. 8 Comparison of theoretical prediction for p^* (solid line) with experimental results of [8] (solid points)

Table 1

R(mm)	t(mm)	R/t	(experimental) p^*(MPa)	(theoretical) p^*(MPa)	Y(MPa)
12.7	0.889	14.3	1.68	1.29[a]	290
19.1	1.245	15.3	1.55	1.15[b]	297
14.3	0.914	15.6	1.23	1.11[b]	297
12.7	0.509	25.0	0.441	0.431[a]	290
19.1	0.737	25.9	0.395	0.394[a]	290
17.5	0.508	34.4	0.227	0.207[b]	297
25.4	0.559	45.5	0.121	0.110[b]	293
34.9	0.737	47.4	0.103	0.101[a]	286

[a] Calculated with $Y/E = 0.0042$ and $n = 30$
[b] Calculated with $Y/E = 0.0043$ and $n = 28$

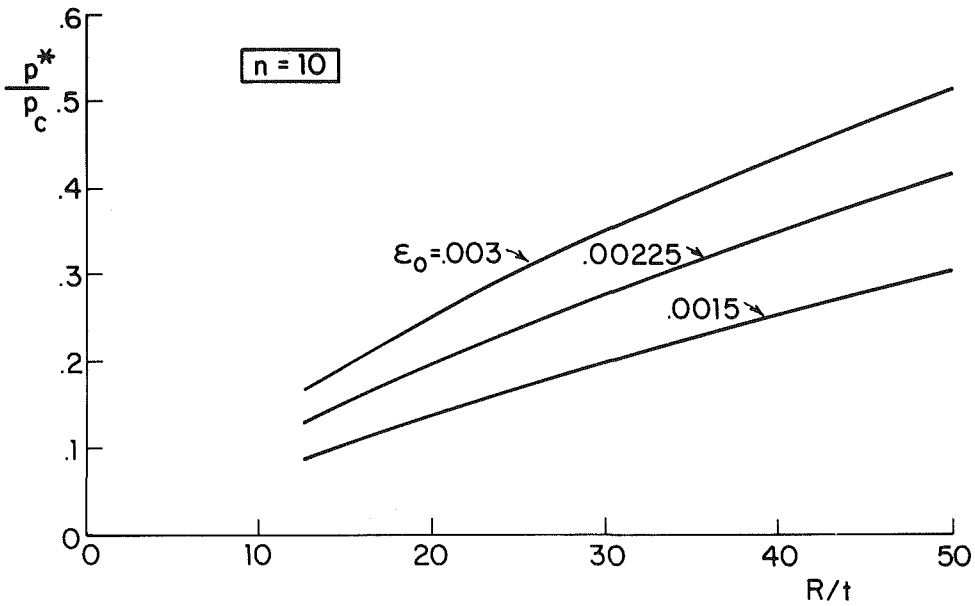

Fig. 9 p^*/p_c for various initial yield strains ϵ_0 for $n = 10$.

of p does not quite attain p_c. The error in p^* associated with the introduction of the imperfection is very small, as can readily be estimated.

Touching occurs at $\Delta A \cong 0.75\pi R^2$. We did not compute $p(\Delta A)$ beyond touching. For simplicity, we took the relation to have a vertical slope once touching occurred. This neglects a small contribution to the area of the lobe below the Maxwell line. The theoretical prediction for p^* determined from (13) is shown in each of the plots of Fig. 7 along with the experimental value.

The comparison between theory and experimental data for the eight pipes is graphed in Fig. 8. The theoretical curve in this figure was determined using $Y/E = 0.0042$ and $n = 30$, but essentially identical results are obtained using $Y/E = 0.0043$ and $n = 28$. Numerical data for the eight shells are given in Table 1. Except for the two pipes with the smallest values of R/t, the theoretical prediction for p^* underestimated the experimental propagation pressure by no more than 10 percent, and for three of the pipes the prediction is within 2 percent. The theoretical predictions for the two pipes with the smallest values of R/t underestimate the experimental propagation pressures by about 25 percent.

The results of a limited parameter study are presented in Figs. 9 and 10 in the form of curves of p^*/p_c versus R/t for various values of ϵ_0 and n. The uniaxial stress-strain curve in each case was the Ramberg-Osgood relation

$$\epsilon/\epsilon_0 = \sigma/\sigma_0 + (3/7)(\sigma/\sigma_0)^n \tag{15}$$

where $\epsilon_0 = \sigma_0/E$. The predictions for p^* are more sensitive than one might first suppose to the parameters characterizing the uniaxial stress-strain curve. For this reason, we have not attempted to make further comparisons with additional experimental results in [8] since detailed uniaxial material data were not available for the other test specimens. In this connection, it is almost certainly the uniaxial data associated with the circumferential direction that is relevant when the pipe material displays appreciable anisotropy.

It can be noted in Figs. 9 and 10 that the pipes with the smallest values of R/t have the smallest ratios of p^* to p_c. Buckle propagation pressures as low as 1/10 to 1/4 of the classical ring buckling pressure (10) are seen for pipes with R/t values in the range from 15–20. Such low buckle propagation pressures are surprising in light of the fact that the long cylindrical shell under external pressure is not normally regarded as very imperfection-sensitive even when plastic yielding occurs in the post-buckling response. It does take a substantial dent or blow to initiate a buckle that will then propagate. A pipe meeting normal tolerances should have no difficulty supporting pressures that are several times p^* as long as they are below p_c. However, if substantial dents or blows are possible, the pressure must be below p^* if it is to be certain that collapse of a full length of pipe will not occur. The spreading of a buckle due to an initial imperfection is studied in more detail for a model problem in [3].

Limitations of the Method. There is no question that deformation theory gives an oversimplified description of the pipe material for the buckle propagation problem. That the deformation theory predictions for p^* do so well, particularly for the pipes with the larger values of R/t, is probably a consequence of the gradual transition so that the departure from plane-strain ring behavior is not too marked. In every

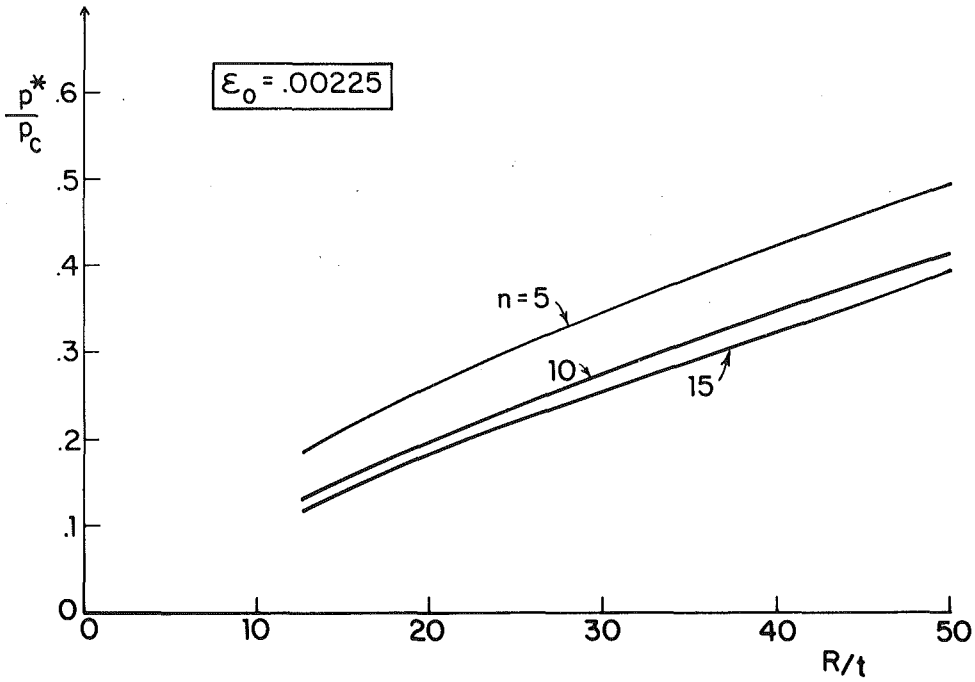

Fig. 10 p^*/p_c for various strain hardening exponents n for $\epsilon_0 = 0.00225$.

case, the deformation theory prediction for p^* underestimated the experimental result. This is not surprising since deformation theory is expected to underestimate the work absorbed, ΔW, by each ring segment as it is engulfed by the transition.

The simple analysis presented here provides the propagation pressure p^* and the states far ahead and behind the transition but no information about the transition itself. In the case of the balloon, we have formulated and solved the axisymmetric membrane problem for the full problem, including the transition, and this solution will be reported elsewhere, along with some results related to the energy associated with the transition. The corresponding problem for the pipe is much harder even when deformation theory is invoked.

We have made some attempts to base the calculation of p^* on an incremental theory of plasticity, but only with limited success at this stage. When deformation theory is abandoned and material path dependence is accounted for, the behavior in the transition must be analyzed. The appropriate shell problem is incomparably more difficult than the ring problem on which the deformation theory analysis is based. Nevertheless, at some level of approximation, it will probably be necessary to incorporate the effect of the material path dependence to improve on the present method for estimating p^*. Furthermore, if it is desired to predict the relation between the steady-state velocity of propagation at pressures above p^*, it will almost certainly be necessary to improve on the material model. As reported in [8], the transition is sharper in the dynamic problem than it is in the quasi-static one, and this makes it more likely that path-dependent effects are important in the transition.

Acknowledgment

C. D. Babcock, A. C. Palmer, and S. Kyriakides each helped to inform us about the buckle propagation problem. We are particularly indebted to S. Kyriakides for conducting the additional tests determining whether or not the opposite walls of the collapsed pipe come into contact under quasi-static propagation conditions. The work of E. C. was supported in part by the Natural Sciences and Engineering Research Council of Canada and by the National Science Foundation under Grant MEA-82-13925. The work of J. W. H. was supported in part by the National Science Foundation under Grant MEA-82-13925 and by the Division of Applied Sciences, Harvard University.

References

1 Tvergaard, V., and Needleman, A., "On the Localization of Buckling Patterns," ASME JOURNAL OF APPLIED MECHANICS, Vol. 47, 1980, pp. 613-619.

2 James, R. D., "Co-Existent Phases in the One-Dimensional Static Theory of Elastic Bars," *Archive for Rational Mechanics and Analysis*, Vol. 72, 1979, pp. 99-140.

3 Chater, E., Hutchinson, J. W., and Neale, K. W., "Buckle Propagation on a Beam on a Nonlinear Elastic Foundation," to appear in a *Proceedings of the IUTAM Symposium on Collapse*, University College, London, Aug. 1982.

4 Hutchinson, J. W., and Neale, K. W., "Neck Propagation," to be published in *Journal of Mechanics and Physics of Solids*.

5 Ogden, R. W., "Elastic Deformations of Rubberlike Solids," in *Mechanics of Solids, The Rodney Hill 60th Anniversary Volume*, Hopkins, H. G., and Sewell, M. J., eds., Pergamon Press, 1982, pp. 499-538.

6 Palmer, A. C., and Martin, J. H., "Buckle Propagation in Submarine Pipelines," *Nature*, Vol. 254, 1975, pp. 46-48.

7 Mesloh, R., Johns, T. G., and Sorenson, J. E., "The Propagating Buckle," *Proceedings BOSS 76*, Vol. 1, 1976, pp. 787-797.

8 Kyriakides, S., "The Propagating Buckle and its Arrest," Ph.D. Thesis, California Institute of Technology, Pasadena, Calif., 1980.

9 Kyriakides, S., and Babcock, C. D., "Experimental Determination of the Propagation Pressure of Circular Pipes," ASME *Journal of Pressure Vessel Technology*, Vol. 103, 1981, pp. 328-336.

10 Kyriakides, S., and Babcock, C. D., "Large Deflection Collapse Analysis of an Inelastic Inextensional Ring under External Pressure," *International Journal of Solids and Structures*, Vol. 17, 1981, pp. 981-993.

11 Kyriakides, S., and Arikan, E., "Post-Buckling Behavior of Inelastic Inextensional Rings Under External Pressure," ASME JOURNAL OF APPLIED MECHANICS, Vol. 50, 1983, pp. 537-543.

APPENDIX

Numerical Scheme for Ring Analysis

The method used to generate the relation $p(\Delta A)$ shown in Fig. 7 is similar in many respects to the method employed in [10]. In the present study, for convenience, we did not enforce inextensionality, although the extensionality is not expected to have much effect on p^*. Furthermore, we constrained the ring

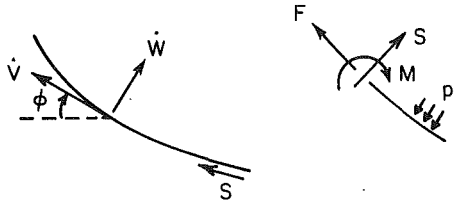

Fig. 11 Sign conventions for the ring analysis

deformations to be plane strain with zero axial component of strain, consistent with the fact that the ring segment is part of a long cylindrical shell.

The equilibrium equations for a ring in the deformed state are

$$\begin{aligned} dM/ds + S &= 0 \\ dS/ds - \kappa F &= p \\ dF/ds + \kappa S &= 0 \end{aligned} \tag{16}$$

where M, S, and F are the moment, resultant transverse shear stress, and resultant stretching stress with the sign conventions shown in Fig. 11. The curvature in the current state is $\kappa(s)$ and the distance along the ring midsurface is s. With $\dot{w}$ and $\dot{v}$ as the displacement increments normal and tangent, respectively, to the current middle surface, the increments of rotation, strain and curvature are

$$\begin{aligned} \dot{\phi} &= d\dot{w}/ds - \kappa\dot{v} \\ \dot{\epsilon} &= d\dot{v}/ds + \kappa\dot{w} \\ \dot{\kappa} &= d\dot{\phi}/ds \end{aligned} \tag{17}$$

With s_{ij} as the stress deviator, $\sigma_e = (3s_{ij}s_{ij}/2)^{1/2}$ as the effective stress, and $E_s(\sigma_e)$ as the secant modulus of the uniaxial stress-strain curve, the deformation theory relation for multiaxial stress states is

$$\epsilon_{ij} = \frac{1+\nu}{E}s_{ij} + \frac{1-2\nu}{E}\sigma_{pp}\delta_{ij} + \frac{3}{2}\left(\frac{1}{E_s} - \frac{1}{E}\right)s_{ij} \tag{18}$$

Let ϵ_{22} be the hoop strain and ϵ_{11} be the axial component of strain, with σ_{33} as the stress component in the direction normal to the middle surface. Under the conditions that $\sigma_{33}=0$ and $\epsilon_{11}=0$, one can derive an incremental expression from (18) relating $\dot{\epsilon} \equiv \dot{\epsilon}_{22}$ to $\dot{\sigma} \equiv \dot{\sigma}_{22}$ in the form $\dot{\sigma} = \bar{E}_t\dot{\epsilon}$, where $\bar{E}_t$ is the plane-strain tangential modulus which depends on the stress at the particular point in the ring. The incremental form of the constitutive relation for the ring is

$$\begin{aligned} \dot{F} &= L_1\dot{\epsilon} + L_2\dot{\kappa} \\ \dot{M} &= L_2\dot{\epsilon} + L_3\dot{\kappa} \end{aligned} \tag{19}$$

Here,

$$L_i = \int_{-t/2}^{t/2} \bar{E}_t z^{i-1} dz$$

with z as the coordinate measured from the ring middle surface.

After writing the equilibrium equations (16) in incremental form, we obtained four first-order differential equations with $\dot{S}$, $\dot{\phi}$, $\dot{\epsilon}$, and $\dot{\kappa}$ as dependent variables. This is a convenient choice of variables since $\dot{S}$ and $\dot{\phi}$ vanish at the quarter symmetry points. At each stage of the deformation history, the system of four first-order equations was integrated numerically. Then, the displacement increments were obtained by integrating the first two equations of (17) subject to $\dot{v}=0$ at quarter symmetry points. The increment in area reduction is $-\int\dot{w}ds$. An accurate evaluation of the integral on the right-hand side of (13) was obtained by fitting the discretized results for $p(\Delta A)$ using cubic splines.

On Symmetric Buckling of a Finite Flat-Lying Heavy Sheet

C. Y. Wang
Professor,
Department of Mathematics and Mechanical Engineering,
Michigan State University,
East Lansing, Mich. 48824
Mem. ASME

An elastic sheet with non-negligible density and finite length lies horizontally on the ground. The ends are clamped and subjected to compressive forces. Depending on the force, the sheet may be regarded as "long" or "short" with different characteristics. The critical buckling load, redefined as the force below which the sheet will always return to the horizontal state under any finite disturbance, is higher than the Euler buckling load of a weightless sheet. When deflections are small and finite the sheet is stable for given end displacement, but is unstable for given force. Approximate analytic solutions compare well with the results of exact numerical integration.

Introduction

Figure 1 shows an originally horizontal elastic sheet of non-negligible density. The sheet is buckled by bringing the clamped ends closer together. This problem is important in the handling of thin materials such as paper, textiles, sheet metal, and plastics. It is also important in the vertical buckling of railroad tracks [1]. Theoretically, the buckling of such a flat-lying heavy sheet raises both analytical and conceptual difficulties, some of which will be addressed in this paper.

Early works on the stability of an infinite flat-lying sheet may be traced back to the 1930s [2]. Using linear beam theory, Martinet [3] found the relationship

$$F' = 20.18\, EI/l'^2 \tag{1}$$

Here F' is the axial compressive force (per unit length), EI is the flexural rigidity (E = Young's modulus/(1 − (Poisson ratio)^2), I = (thickness)^3/12), and l' is the half length of the lifted section. The same relationship was later rederived by Nusayr and Paslay [4].

The nonlinear post-buckling state was first attempted by Kerr [5] who modeled the continuous sheet by two rigid connected segments. Exact numerical solution of the continuous sheet was obtained by Wang [6]. Among other results, Wang showed that the horizontal force-displacement curve of the infinite sheet has negative slope, i.e., less force is required to maintain a larger displacement. Thus given a constant compressive force the initially horizontal sheet may not buckle at all, but when adequately perturbed the sheet will catastrophically collapse completely. This result is opposite to the Euler beam where the force-displacement curve has positive slope, with stable post-buckling equilibrium states.

Suppose we consider a flat-lying heavy sheet of finite length. As length decreases, the results of reference [6] should gradually approach the Euler beam, since stiffness becomes increasingly important. How this transition occurs is the aim of this paper.

Formulation

We will consider symmetric buckling shown in Fig. 1. A cartesian coordinate system (x', y') is attached at the midpoint. Let s' be the arc length from the origin and θ be the local angle of inclination. The sheet has a total length of $2L$. A local moment balance gives

$$F'ds' \sin\theta + m + dm = \rho s' ds' \cos\theta + m \tag{2}$$

Here m is the local moment and ρ is the weight per arc length. If the sheet is thin enough, the local moment is proportional to the local curvature:

$$m = EI\frac{d\theta}{ds'} \tag{3}$$

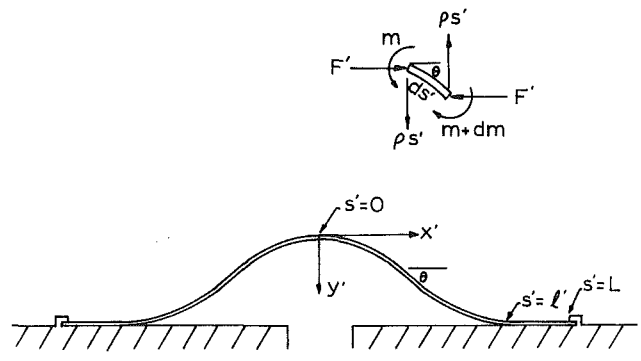

Fig. 1 The coordinate system

Contributed by the Applied Mechanics Division for presentation at the 1984 PVP Conference and Exhibition, Joint with Applied Mechanics Division and Materials Division, San Antonio, Texas, June 17-21, 1984 of THE AMERICAN SOCIETY OF MECHANICAL ENGINEERS.

Discussion on this paper should be addressed to the Editorial Department, ASME, United Engineering Center, 345 East 47th Street, New York, N.Y. 10017, and will be accepted until two months after final publication of the paper itself in the JOURNAL OF APPLIED MECHANICS. Manuscript received by ASME Applied Mechanics Division, April, 1983; final revision, July, 1983. Paper No. 84-APM-13.

Copies will be available until February, 1985.

We nondimensionalize all lengths by L, the force by EI/L^2, and drop primes. Equations (2) and (3) yield

$$\frac{d^2\theta}{ds^2} = Bs\cos\theta - F\sin\theta \tag{4}$$

where $B \equiv \rho L^3/EI$ is a nondimensional parameter representing the relative importance of density to flexural rigidity.

Now define the *long* sheet as one that, after buckling, has nonzero segments in contact with the ground ($s' = \pm l'$ to $s' = \pm L$ in Fig. 1). In this case the buckled region is independent of the length L and the sheet may be regarded as of infinite length, a case studied in reference [6]. We define the *short* sheet as one that has only the end points ($s' = \pm L$) in contact with the ground. We expect, as the two end points are brought closer together, the character of the sheet changes from that of the long sheet to the short sheet.

Due to symmetry, we consider only positive s. The boundary condition at zero is

$$\theta(0) = 0 \tag{5}$$

In addition, for the long sheet

$$\theta(l) = \frac{d\theta}{ds}(l) = 0 \tag{6}$$

and for the short sheet

$$\theta(1) = 0 \tag{7}$$

After $\theta(s)$ is obtained, the configuration of the lifted section can be determined by

$$\frac{dx}{ds} = \cos\theta, \quad \frac{dy}{ds} = \sin\theta \tag{8}$$

$$x(0) = y(0) = 0 \tag{9}$$

The Long Sheet

For small B and small θ equation (4) becomes

$$\frac{d^2\theta}{ds^2} = Bs - F\theta \tag{10}$$

Using the boundary conditions equations (5) and (6), we obtain

$$\theta = \frac{B}{F}\left(s - \frac{l\sin\sqrt{F}\,s}{\sin\sqrt{F}\,l}\right) \tag{11}$$

and the condition

$$\tan\sqrt{F}\,l = \sqrt{F}\,l \tag{12}$$

The smallest root is

$$\sqrt{F}\,l = 4.4934095 \tag{13}$$

Thus the long sheet ($l < 1$) is defined by

$$F > 20.19073 \tag{14}$$

otherwise the sheet is considered a short sheet.

For large B and/or large deflections, direct numerical integration of equation (4) is necessary. Let

$$(s,x,y) = B^{-1/3}(r,u,v) \tag{15}$$

Equations (4), (5), (8), and (9) become

$$\frac{d^2\theta}{dr^2} = r\cos\theta - H\sin\theta, \quad \theta(0) = 0 \tag{16}$$

$$\frac{du}{dr} = \cos\theta, \quad \frac{dv}{dr} = \sin\theta, \quad u(0) = v(0) = 0 \tag{17}$$

where $H \equiv FB^{-2/3}$. For given H we guess $d\theta/dr(0)$ and integrate equations (16) and (17) by the fifth order Runge-Kutta-Fehlberg algorithm until θ is zero again, say at $r = r^*$. The value of $d\theta/dr(0)$ is adjusted until $d\theta/dr(r^*) = 0$. Then for any $B > (r^*)^3$

$$l = r^*B^{-1/3}, \quad F = HB^{2/3}, \quad \frac{d\theta}{ds}(0) = \frac{d\theta}{dr}(0)B^{1/3} \tag{18}$$

$$\delta = [r^* - u(r^*)]B^{-1/3}, \quad b = v(r^*)B^{-1/3} \tag{19}$$

Here δ is the lateral displacement of one end and b is the maximum height. Figure 2 shows the results. These curves are consistent with reference [6] which uses different normalized parameters.

The Stability and Perturbation Analysis of the Short Sheet

When the length is short, we expect flexural rigidity to be a dominant factor. For stability, we assume small θ and even smaller B. Let

$$B = \epsilon^3 << 1 \tag{20}$$

$$\theta = \epsilon\theta_0 + \epsilon^3\theta_1 + \ldots \tag{21}$$

$$F = F_0 + \epsilon^2 F_1 + \ldots \tag{22}$$

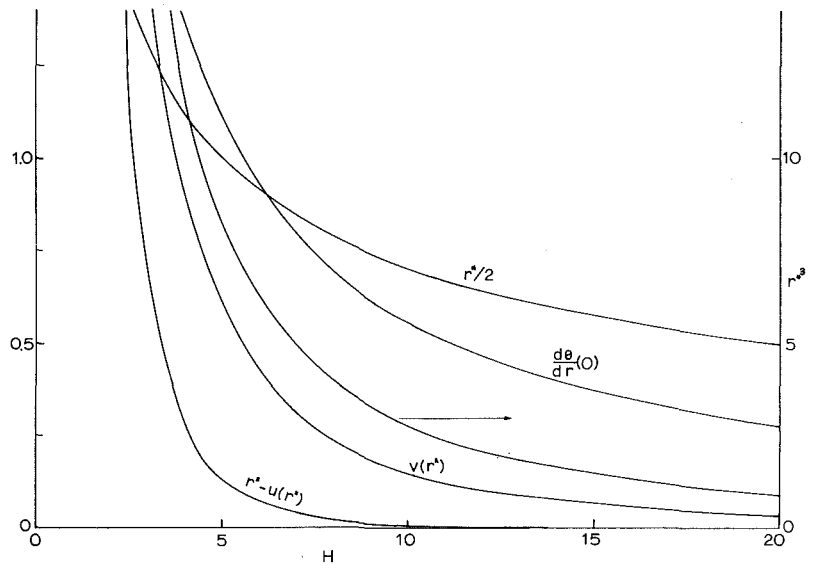

Fig. 2 Characteristics of the long lying sheet

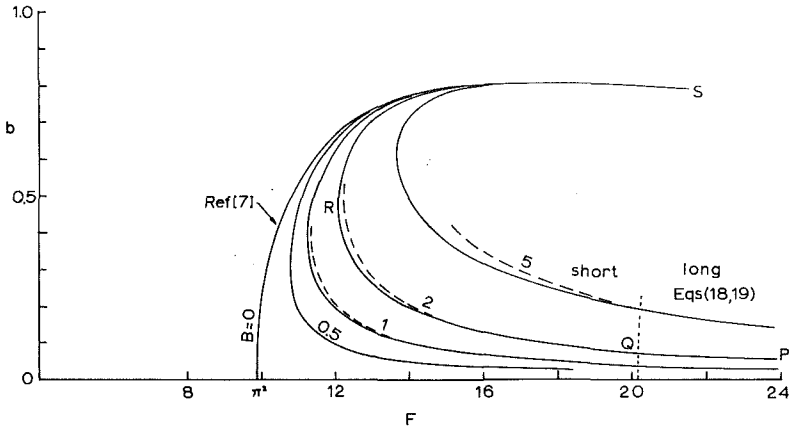

Fig. 3 Maximum height b versus compressive force F. Dotted line indicates the boundary of short and long lying sheets. Dashed lines are approximations, equations (34) and (38).

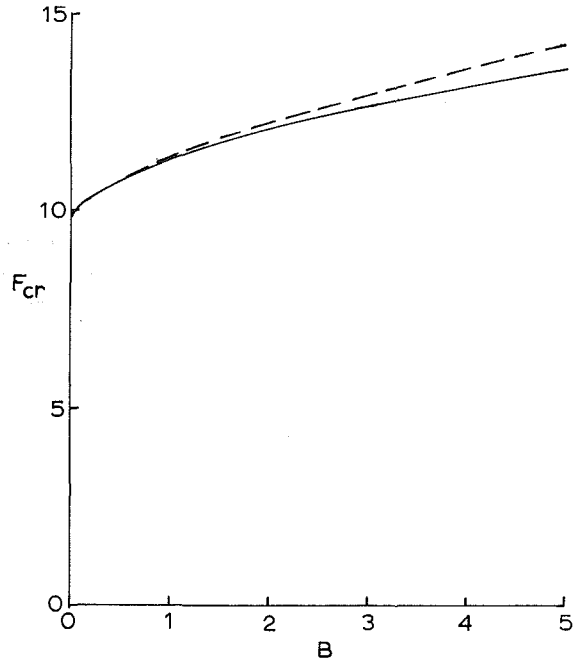

Fig. 4 The critical buckling load. Dashed line is equation (29).

Equation (4) becomes

$$\frac{d^2\theta_0}{ds^2} + F_0\theta_0 = 0 \tag{23}$$

$$\frac{d^2\theta_1}{ds^2} + F_0\theta_1 = s + \frac{F_0\theta_0^3}{6} - F_1\theta_0 \tag{24}$$

The boundary conditions equations (5) and (7) give

$$\theta_0(0) = \theta_0(1) = 0, \quad \theta_1(0) = \theta_1(1) = 0 \tag{25}$$

The zeroth-order solution is

$$\theta_0 = C \sin \pi s, \quad F_0 = \pi^2 \tag{26}$$

where C is an arbitrary constant and F_0 is the Euler buckling load. The solution to the first-order equation, satisfying the boundary conditions, is

$$\theta_1 = C_1 \sin \pi s + \frac{C^3}{192} \sin 3\pi s + \frac{s}{\pi^2}(1 + \cos \pi s) \tag{27}$$

and

$$F_1 = \frac{\pi^2 C^2}{8} + \frac{2}{\pi C} \tag{28}$$

The constant C_1 may be set equal to zero without loss of generality since it can be absorbed into the zeroth-order solutions as follows. Let $C = C' - \epsilon^2 C_1$ in equations (21) and (22) and we find equations (26)–(28) are invariant if $C' = C$ and $C_1 = 0$. If we vary C_1 directly the effect will be felt inthe $0(\epsilon^4)$ term of F.

For the critical buckling load (as defined later), we seek the minimum of equation (28). Set $dF_1/dC = 0$ to obtain $C = 2/\pi$. Then

$$F_{cr} = (F_0 + \epsilon^2 F_1 + \ldots)_{\min} = \pi^2 + \frac{3}{2} B^{2/3} + 0(B^{4/3}) \tag{29}$$

The buckled configuration can be obtained from equations (8) and (9) and the perturbation

$$x = x_0 + \epsilon^2 x_1 + \ldots \quad y = \epsilon y_0 + \ldots \tag{30}$$

We find

$$\frac{dx_0}{ds} = 1, \quad \frac{dy_0}{ds} = \theta_0, \quad \frac{dx_1}{ds} = -\frac{\theta_0^2}{2} \tag{31}$$

The solution is

$$x_0 = s, \quad y_0 = \frac{C}{\pi}(1 - \cos \pi s), \quad x_1 = \frac{C^2}{4}\left(\frac{1}{2\pi} \sin 2\pi s - s\right) \tag{32}$$

The lateral displacement of one end is

$$\delta = 1 - x(1) = \frac{C^2}{4} B^{2/3} + 0(B^{4/3}) \tag{33}$$

The maximum vertical displacement is

$$b = y(1) = \frac{2C}{\pi} B^{1/3} + 0(B) \tag{34}$$

The normalized moment is

$$\frac{d\theta}{ds} = C\pi \cos \pi s B^{1/3} + \left(\frac{\pi C^3}{64} \cos 3\pi s + \frac{1}{\pi^2} + \frac{1}{\pi^2} \cos \pi s - \frac{s}{\pi} \sin \pi s\right) B + O(B^{5/3}) \tag{35}$$

Thus

$$\frac{d\theta}{ds}(0) = C\pi B^{1/3} + \left(\frac{\pi C^3}{64} + \frac{2}{\pi^2}\right) B + 0(B^{5/3}) \tag{36}$$

$$\frac{d\theta}{ds}(1) = -C\pi B^{1/3} - \frac{\pi C^3}{64} B + 0(B^{5/3}) \tag{37}$$

The amplitude C is related to force F by

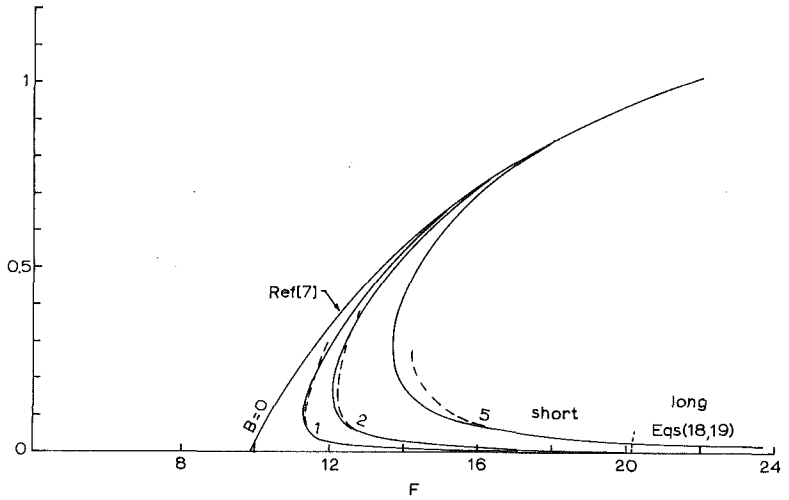

Fig. 5 Lateral displacement δ as a function of F. Dashed lines are approximations, equations (33) and (38).

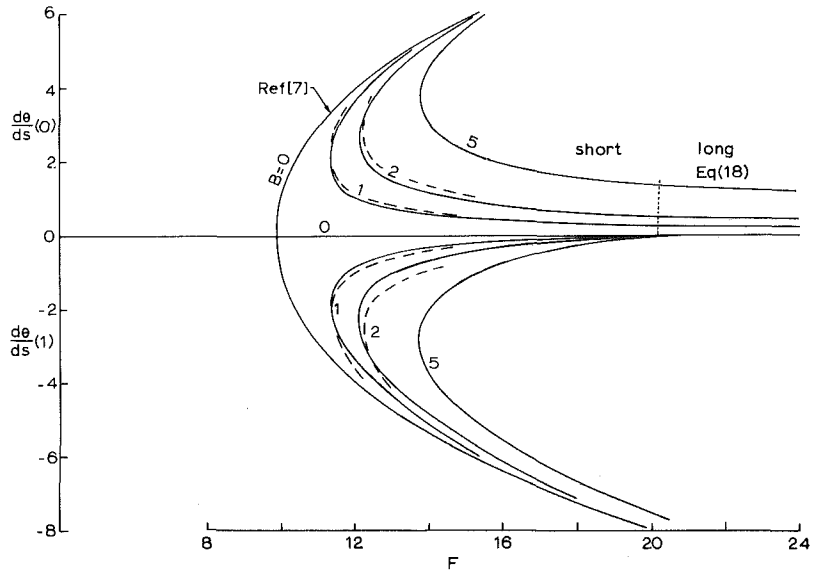

Fig. 6 The normalized moments at $s = 0$ and $s = 1$. Dashed lines are approximations, equations (36)-(38).

$$F=\pi^2+\left(\frac{\pi^2C^2}{8}+\frac{2}{\pi C}\right)B^{2/3}+0(B^{4/3}) \tag{38}$$

Post-Buckling Characteristics of the Short Sheet

Numerical integration is used for large deflections. The method is simialr to that of the long sheet, except shooting is not necessary. Pick any $d\theta/dr(0)$ and integrate equations (16) and (17) till $\theta(r^*) = 0$, then

$$B=(r^*)^3, \quad F=H(r^*)^2, \quad \delta=1-[u(r^*)/r^*] \tag{39}$$

$$b=v(r^*)/r^*, \quad \frac{d\theta}{ds}(0)=r^*\frac{d\theta}{dr}(0), \quad \frac{d\theta}{ds}(1)$$

$$=r^*\frac{d\theta}{dr}(r^*) \tag{40}$$

Figure 3 shows the maximum height b as a function of the horizontal force F for various constant B. The curve $B = 0$ is obtained from the Euler beam data in reference [7] or from more accurate data in reference [8]. Bifurcation occurs at $F = \pi^2$ which is the critical buckling load. For $B \neq 0$ no such bifurcation exists. Let us study the curve $B = 2$. The segment to the right of the dotted line, PQ, represents the long sheet defined previously. The segment QR is the part of the short sheet that has negative slope. The segment RS has positive slope and tends to the $B = 0$ curve, indicating increased effect of flexural rigidity. As discussed before, force-displacement curves with negative slope are unstable to given force, but are stable to given displacement. Suppose a compressive force of $F = 14$ is applied. The sheet may not buckle at all. But when perturbed, say $b > 0.2$, the sheet will collapse, passing through the state at R and settle on the stable point at $F = 14$, $b = 0.76$.

Now we will redefine the critical buckling force as the force below which the sheet will always return to the trivial state, under any disturbance, finite or infinitesimal. This stability definition was inferred by Zajac [9] and Kerr [5] on related problems and differs slightly from the classical infinitesimal stability advocated in reference [7]. Under this new definition, the critical buckling force for $B = 2$ is at R, $F_{cr} = 12.1$. Notice that the perturbation needed ($b = 0.47$) is quite large at this critical buckling force.

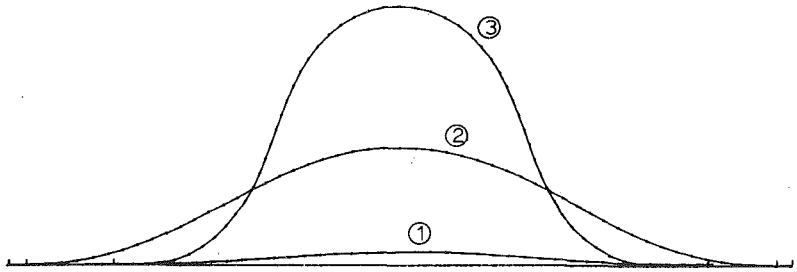

Fig. 7 Sheet configurations for $B = 2$. ①: $F = 31.75$; ②: $F = 12.7$; and ③: $F = 12.7$.

If we eliminate C from equations (34) and (38) we obtain the small B approximations shown as dashed lines in Fig. 3. It seems the validity of our perturbation series can be extended to $B = 0(1)$ provided b remains small. The critical buckling load F_{cr} as a function of B is shown in Fig. 4. Our approximate formula, equation (29) is slightly higher than the exact numerical result.

Figure 5 depicts the end displacement δ as a function of F. The transition from the long sheet to the Euler beam is clearly shown. Figure 6 shows that the moment at $s = 0$, which is also the maximum moment, has similar behavior. The moment at the end $s = 1$ becomes zero for the long sheet ($F > 20.19073$).

Figure 7 shows the computed configurations for a sheet of given length ($B = 2$). Curve ① at $F = 31.75$, $\delta = 0.00084$ belongs to the long sheet category. Curves ② and ③ at $F = 12.7$, $\delta = 0.046$, and $\delta = 0.275$ have short sheet characteristics. Curves ① and ② are unstable to given constant F but are stable to given displacement δ. For example, at fixed $F = 12.7$ curve ② would readily snap into curve ③ which is stable.

Discussion

The behavior of the flat-lying sheet with density ($B \neq 0$) is quite different from the Euler beam which has zero density ($B = 0$). The Euler beam has a conventional pitch fork bifurcation, with the trivial branch unstable to infinitesimal disturbances. The heavy sheet has only one branch (e.g., *PQRS* in Fig. 3) which does not intersect the trivial axis (zero is not a solution to equation (4)). For given F the heavy sheet is stable to infinitesimal disturbances but may be unstable to finite disturbances. Therefore we have extended the definition of the critical buckling load to include these situations.

Our results compare well with those of Kerr [5], who modeled the heavy sheet by two rigid, elastically connected bars. The perturbation to the short sheet was attempted by Vielsack [10], who assumed a center region dominated by rigidity and a boundary region near to ends where density is important. This assumption is incorrect because rigidity effects are proportional to local curvature and the boundary region shows as large a curvature as the central region at critical buckling (Figs. 6 and 7). Consequently his result for F does not agree with our equation (38), which is the correct perturbation solution.

References

1 Kerr, A. D., "The Stress and Stability Analyses of Railroad Tracks," ASME Journal of Applied Mechanics, Vol. 41, 1974, pp. 841–848.

2 Kerr, A. D., "Étude Relative à la Stabilité de la Voie Ferrée dans le Plan Vertical," *Rail Int.*, Vol. 15, 1974, pp. 169–183.

3 Martinet, M. A., "Flambement des Voies sans Joints sur Ballast et Rail de Grande Longueur," *Revue Génèrale des Chemins de Fer*, 1936, pp. 212–230.

4 Nusayr, A. M., and Paslay, P. R., "Buckling of an Infinite Sheet With One Sided Constraint," ASME Journal of Applied Mechancis, Vol. 39, 1972, pp. 302–303.

5 Kerr, A. D., "A Model Study for Vertical Track Buckling," *High Speed Gound Transportation J.*, Vol. 7, 1973, pp. 351–368.

6 Wang, C. Y., "The Ridging of Heavy Elastica," *Zeit. Angew, Math. Mech.*, Vol. 61, 1981, pp. 125–126.

7 Timoshenko, S. P., and Gere, J. M., *Theory of Elastic Stability*, McGraw-Hill, New York, 1961.

8 Wang, C. Y., and Watson, L. T., "On the Large Deformation of *C*-Shaped Springs, *Int. J. Mech. Sci.*, Vol. 22, 1980, pp. 395–400.

9 Zajac, E. E., "The Deflection and Buckling of a Beam-Column With a One-Sided Constraint," *Zeit. Angew. Math. Phys.*, Vol. 12, 1961, pp. 536–546.

10 Vielsack, P., "Einseitiges Knicken eines Schweren Stabes," *Zeit. Angew. Math. Mech.*, Vol. 61, 1981, pp. 55–58.

P. J. Yoder
School of Mechanical Engineering,
Georgia Institute of Technology,
Atlanta, Ga. 30332
Associate Mem. ASME

R. G. Whirley
Department of Applied Mechanics 104-44,
California Institute of Technology,
Pasadena, Calif. 91125
Student Mem. ASME

On the Numerical Implementation of Elastoplastic Models

A closed-form solution is given for the way stresses evolve during an elastoplastic time step under conditions of purely kinematic hardening or softening. When isotropic effects are included, the analysis becomes more difficult, so a perturbation solution is developed. These solutions are then compared with various algorithms commonly used in finite element programs in order to assess the trade-offs between accuracy and computational efficiency.

Introduction

With the advent of the modern computer, it is now possible to study a broad range of practical problems involving plasticity which do not lend themselves to analytical solution. This development has kindled a renewed interest in the problem of modeling nonlinear materials. A number of researchers have devised ways to narrow the gulf between the bilinear stress-strain diagrams of conventional plasticity and the gradually rounded curves characteristic of most real materials [1–7]. The tendency has been toward more complicated mathematical models with vastly enlarged fields of material parameters.

In the midst of this rush toward complexity, Krieg and Krieg [8] voice a word of caution. They note that even the simplest of the traditional models, the case of perfect plasticity with a von Mises yield criterion, is usually implemented with considerable error in structural analysis programs. To be sure, all of the approximate schemes they test converge upon the exact stress-strain law in the limiting case of small strain increments, but given the localized slippage inherent in plasticity theory, it is manifestly difficult to keep the strain increments uniformly small throughout the domain. Thus, in the region where slipping is most likely to occur, the strain increments are apt to be largest and the accuracy worst.

One way to resolve this difficulty is to base the stress-strain calculations for each time step directly on the analytical solution that Krieg and Krieg use as a benchmark for their study. This approach has not achieved widespread acceptance, though, nor is it advocated even by Krieg and Krieg. They describe the exact solution as computationally slow and intimate that (unlike the approximate schemes they survey) it cannot readily be extended to the important cases of strain hardening and strain softening [8, 9]. Now, the first of these concerns seems legitimate, but the second turns out to be unfounded, because the exact solution does indeed generalize to accommodate hardening and softening. Krieg and Krieg overlook this possibility, evidently because they approach the issue from the standpoint of traditional stress-space plasticity, which treats perfect plasticity as a special, singular case. Within the framework of strain-space plasticity, however, a single formulation is able to prescribe the types of constitutive behavior associated with any of the traditional hardening/softening laws [5, 6]. Thus, when one carries over to strain space the line of argument leading to the Krieg and Krieg solution, the result is a new solution which applies equally well to the cases of kinematic strain hardening, perfect plasticity, and kinematic strain softening. The inclusion of isotropic effects in the hardening law makes a full analytical solution impossible, but even here the analysis points the way to a new class of highly accurate algorithms.

In the first section of this paper, accordingly, there is a review of the strain-space formulation of plasticity and of its relationship to the more traditional stress-space version. Then comes an exposition of the exact solution, to be followed in turn by brief descriptions of four approximate schemes current in the literature. The paper closes by offering an assessment of the trade-offs between computational speed and accuracy for the various methods.

Strain-Space Plasticity

The basic idea of framing plasticity theory with reference to strain space rather than stress space has received considerable attention over the years [1, 5, 6, 11–15]. To clarify the difference between the two approaches, consider the one-dimensional case of a bilinear spring. By analogy to traditional plasticity, one might describe the response by treating stress as the independent variable, computing the strain that would have arisen elastically from this stress, and then adding on the plastic strain ϵ^P, as indicated in Fig. 1(*a*). On the other hand, it is just as reasonable to take strain as the independent variable, as suggested in Fig. 1(*b*), and obtain the corresponding stress by subtracting from the elastic stress the amount σ^R by which stress has been relaxed due to plastic effects.

Contributed by the Applied Mechanics Division for presentation at the 1984 PVP Conference and Exhibition, Joint with Applied Mechanics Division and Materials Division, San Antonio, Texas, June 17–21, 1984 of THE AMERICAN SOCIETY OF MECHANICAL ENGINEERS.

Discussion on this paper should be addressed to the Editorial Department, ASME, United Engineering Center, 345 East 47th Street, New York, N.Y. 10017, and will be accepted until two months after final publication of the paper itself in the JOURNAL OF APPLIED MECHANICS. Manuscript received by ASME Applied Mechanics Division, June, 1983; final revision, October, 1983. Paper No. 84-APM-33.

Copies will be available until February, 1985.

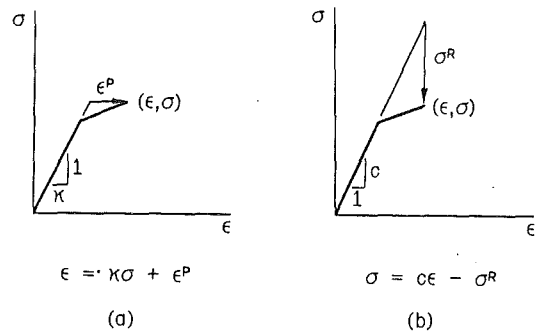

Fig. 1 Traditional versus strain-space plasticity

In the fully three-dimensional case, the traditional stress-space description of plasticity begins by setting

$$\epsilon = \kappa\sigma + \epsilon^P, \tag{1}$$

where κ denotes the Hookean compliance tensor. Changes in the plastic strain ϵ^P are governed by a yield function, which may be specified to be of the von Mises type,

$$\hat{\Phi}(\sigma,\epsilon^P,\Lambda) = |\sigma' - \gamma\epsilon^P|^2 - \rho^2(\Lambda), \tag{2}[1]$$

where

$$\Lambda = \int_0^t \frac{2}{3}|\dot{\epsilon}^P|\,dt.$$

The yield surface, along which $\hat{\Phi}$ vanishes, turns out in this case to be a hypersphere in deviatoric stress space whose initial radius $\rho(0)$ equals the uniaxial yield stress of the virgin material. The functional dependence of ρ upon Λ allows for quite general isotropic hardening/softening, while the parameter γ introduces a kind of kinematic hardening/softening which leads to bilinear stress-strain diagrams when only one yield surface is used.

Invoking the consistency condition in conjunction with the normality rule leads to a set of expressions governing the growth of plastic strain. The three distinct cases of strain hardening, perfect plasticity, and strain softening have to be dealt with separately. They correspond, respectively, to cases where $[\gamma + (2/3)(d\rho/d\Lambda)]$ is positive, zero, and negative. For the strain-hardening case, one arrives ultimately at the constitutive law [Γ+]:

$|\sigma' - \gamma\epsilon^P| \le \rho(\Lambda)$ always. (α)

When $|\sigma' - \gamma\epsilon^P| = \rho(\Lambda)$ (β)

and $(\sigma' - \gamma\epsilon^P)\cdot\dot{\sigma}' > 0$, ($\gamma$)

$$\dot{\epsilon} = \kappa\dot{\sigma} + \frac{(\sigma' - \gamma\epsilon^P)\cdot\dot{\sigma}'}{\left(\gamma + \frac{2}{3}\frac{d\rho}{d\Lambda}\right)\rho^2}(\sigma' - \gamma\epsilon^P). \quad (\delta) \qquad [\Gamma+]$$

Otherwise $\dot{\epsilon} = \kappa\dot{\sigma}$. ($\epsilon$)

Similar rules apply for the cases of perfect plasticity and strain softening, denoted [Γ0] and [Γ−] in reference [5]. It is important to point out that these three constitutive laws all differ from one another, particularly with regard to loading criteria.

Like the one-dimensional example considered at the beginning of this section, the three-dimensional theory of plasticity outlined in the foregoing possesses an analog in strain space. The starting point for strain-space plasticity is to set

$$\sigma = \mathbf{c}\epsilon - \sigma^R, \tag{3}$$

where $\mathbf{c}$ denotes the Hookean stiffness tensor. The stress relaxation tensor σ^R remains constant so long as the current strain lies within the so-called relaxation surface, which is the locus of strains satisfying the equation

$$0 = \hat{F}(\epsilon,\sigma^R,L) = |\epsilon' - \mathbf{c}\sigma^R|^2 - r^2(L), \tag{4}$$

where

$$L = \int_0^t \frac{2}{3}|\dot{\sigma}^R|\,dt.$$

The relaxation function $\hat{F}$ is obviously patterned after the von Mises yield function; the parameters c and L allow for analogs to kinematic and isotropic hardening/softening. A work principle dictates that the rate of stress relaxation $\dot{\sigma}^R$ extend outward from the relaxation surface [5, 6]. This fact, together with the requirement that the relaxation surface follow ϵ' during a period of stress relaxation, leads to the constitutive law [C]:

$|\epsilon' - c\sigma^R| \le r(L)$ always. (a)

When $|\epsilon' - c\sigma^R| = r(L)$ (b)

and $(\epsilon' - c\sigma^R)\cdot\dot{\epsilon}' > 0$, ($c$)

$$\dot{\sigma} = \mathbf{c}\dot{\epsilon} - \frac{(\epsilon' - c\sigma^R)\cdot\dot{\epsilon}'}{\left(c + \frac{2}{3}\frac{dr}{dL}\right)r^2}(\epsilon' - c\sigma^R). \quad (d) \qquad [C]$$

Otherwise, $\dot{\sigma} = \mathbf{c}\dot{\epsilon}$ (e)

This single set of relations covers the three cases of strain hardening, perfect plasticity, and strain softening. Indeed, if one sets

$$c = \frac{1}{2G}\left(\frac{1}{2G}\gamma + 1\right) \quad \text{and} \quad r(x) \equiv \frac{1}{2G}\rho\left(\frac{1}{2G}x\right) \tag{5}$$

where G is the elastic shear modulus, it is possible to make

$$\sigma^R = 2G\epsilon^P \tag{6}$$

$$2Gr = \rho, \tag{7}$$

and

$$2G(\epsilon' - c\sigma^R) = \sigma' - \gamma\epsilon^P \tag{8}$$

throughout the deformation. Continuing in this vein, one ultimately establishes that the stress and strain-space formulations produce equivalent constitutive behavior [5, 6]. That is, [C] is equivalent to [Γ+] for cases of strain hardening, to [Γ0] for perfect plasticity, and to [Γ−] for strain softening. Recently, Casey and Naghdi [16, 17] have expressed misgivings about this claim, but their remarks suggest that the disagreement is primarily a matter of semantics [17].

The Exact Solution

Having sketched out the formalism of strain-space plasticity, it is appropriate now to consider the problem set forth by Krieg and Krieg [8]. Suppose that over the course of a time step $[t_i, t_f]$ a particle's strain changes from ϵ_i to ϵ_f. Given that the initial stress is σ_i, the objective is to determine the final stress state σ_f. The elastic part of σ_f is of course easily found, so the real challenge is to solve for the final value of stress relaxation, σ_f^R.

Now σ^R remains constant when the strain state lies inside the relaxation surface, so the first step toward a solution is to find the point where the strain trajectory cuts through the surface. Call this contact strain ϵ_c and the corresponding time t_c. Finding ϵ_c and t_c is straightforward since the strain rate $\dot{\epsilon}$ is assumed to be constant. As noted by Krieg and Krieg, this is a reasonable simplification since most structural analysis

[1] Here and throughout this paper, $\mathbf{a}'$ denotes the deviatoric part of $\mathbf{a}$, $\mathbf{a}\cdot\mathbf{b}$ is used as a shorthand for $3/2\sum_{i=1}^{3}\sum_{j=1}^{3} a_{ij}b_{ij}$, and $|\mathbf{a}| = \sqrt{\mathbf{a}\cdot\mathbf{a}}$.

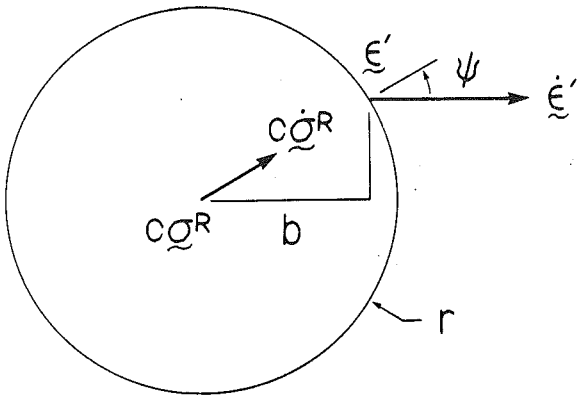

Fig. 2 Geometric interpretation of the angle ψ

programs avoid computing higher derivatives of strain in order to keep storage requirements and computational complexity down to manageable levels.

The assumption of a constant strain rate also leads to the identity,

$$\dot{\epsilon}' - \frac{d}{dt}\left[\frac{(\epsilon' - c\sigma^R)\cdot\dot{\epsilon}'}{|\dot{\epsilon}'|^2}\right]\dot{\epsilon}' = c\,\frac{\dot{\sigma}^R\cdot\dot{\epsilon}'}{|\dot{\epsilon}'|^2}\,\dot{\epsilon}'. \tag{9}$$

For every ϵ along the trajectory between ϵ_c and ϵ_f, equation (4) holds, so it is possible to define an angle ψ through the relation

$$(\epsilon' - c\sigma^R)\cdot\dot{\epsilon}' = r(L)\,|\dot{\epsilon}'|\cos\psi \tag{10}$$

To visualize the significance of equations (9) and (10), consider a special case where the shear strains all vanish. Then, as depicted in Fig. 2, ψ becomes the angle between the current normal to the relaxation surface and the strain trajectory. The center of the surface, $c\sigma^R$, is moving, and the right-hand side of (9) represents the component of its "velocity" in the direction of the strain trajectory. The left-hand side of (9) breaks down this component into the rate that segment b is shrinking plus the speed of ϵ'. Although this visualization holds only for a special case, the analysis is in no way affected by the presence or absence of shear strains.

Invoking (3) in conjunction with equation (*d*) of the constitutive law [C] and then substituting from (10), one finds that

$$\dot{\sigma}^R = \frac{|\dot{\epsilon}'|\cos\psi}{c + \frac{2}{3}\frac{dr}{dL}}\,\frac{(\epsilon' - c\sigma^R)}{r(L)}. \tag{11}$$

This result, in conjunction with (4) leads to

$$\dot{r} = \eta\,|\dot{\epsilon}'|\cos\psi, \tag{12}$$

where

$$\eta = \frac{\frac{2}{3}\frac{dr}{dL}}{c + \frac{2}{3}\frac{dr}{dL}}. \tag{13}$$

To obtain the differential equation governing the evolution of $\psi(t)$, take the inner product of each term in (9) with respect to $\dot{\epsilon}'$, recalling that this strain rate is a constant, and substitute in from (10). Then, invoking (11), (12), and (13) and simplifying, one arrives at

$$\dot{\psi} = -\frac{|\dot{\epsilon}'|}{r(L)}\sin\psi. \tag{14}$$

The form of (14) is somewhat awkward for cases where r is time-dependent. However, if one solves (14) for r, takes the time derivative, and substitutes in from (12), it is found that

$$\ddot{\psi} = (1+\eta)\cot\psi\,(\dot{\psi})^2.$$

This form admits a first integral; choosing the constant of integration in conformity with (14), one obtains

$$\dot{\psi} = -\frac{|\dot{\epsilon}'|}{r_c(\sin\psi_c)^{\eta}}(\sin\psi)^{1+\eta} \tag{15}$$

where r_c and ψ_c are the radius and angle evaluated at the contact point.

Equation (15) can be integrated analytically for the two limiting values of η, zero, and one. Denoting these solutions by $\psi_{00}(t)$ and $\psi_{10}(t)$, respectively, one finds that the final value of ψ,

$$\psi_f = \psi_{00}(t_f) = 2\tan^{-1}\left[\exp\left\{-\frac{|\dot{\epsilon}'|}{r_c}(t_f - t_c)\right\}\tan\left(\frac{\psi_c}{2}\right)\right] \tag{16a}$$

when $\eta = 0$;

$$\psi_f = \psi_{10}(t_f) = \cot^{-1}\left[\frac{|\dot{\epsilon}'|}{r_c\sin\psi_c}(t_f - t_c) + \cot\psi_c\right] \tag{16b}$$

when $\eta = 1$.

In view of (5) and (13), the expression in (16*a*) applies to cases of perfect plasticity and purely kinematic hardening or softening. The cases covered by (16*b*), on the other hand, are somewhat more difficult to characterize in terms of the traditional hardening laws. Strictly speaking, (16*b*) is applicable only to a rather obscure mixture of kinematic softening ($\gamma = -2G$) and isotropic hardening. For other values of γ, the constitutive behavior becomes more and more nearly elastic as η approaches one, and (16*b*) applies in a limiting sense in this circumstance. For the special case of purely isotropic hardening, incidentally, the parameter η equals the ratio of the plastic to the elastic shear stiffness.

For more general combinations of isotropic and kinematic effects, two options present themselves. One is to integrate equation (15) numerically, as was done in preparing Figs. 4 and 5. This approach affords great accuracy, but in practice the computations are prohibitively slow. An alternative is to expand $\psi(t)$ about $\eta = 0$ and/or 1 and make use of the corresponding perturbation solutions. The details of this procedure are outlined in the Appendix.

However one finds ψ_f, the final value of the radius r_f can be obtained by equating the right-hand sides of (14) and (15) at time $t = t_f$:

$$r_f = r_c\left(\frac{\sin\psi_c}{\sin\psi_f}\right)^{\eta}. \tag{17}$$

All that remains is to find the final values of stress and stress relaxation. A careful examination of (3) and equation (*d*) from constitutive law [*C*] reveals that as long as r is smooth, all time derivatives of σ^R evaluated at time $t = t_c$ exist and are linear combinations of $(\epsilon_c' - c\sigma_c^R)$ and $\dot{\epsilon}'$. Therefore

$$\epsilon_f' - c\sigma_f^R = \alpha[(\epsilon_c' - c\sigma_c^R) + \beta\dot{\epsilon}']. \tag{18}$$

The constants α and β are evaluated by invoking (4) and (10) at time $t = t_f$. Thus,

$$\alpha = \frac{r_f\sin\psi_f}{r_c\sin\psi_c}, \qquad \beta = \frac{(r_f/\alpha)\cos\psi_f - r_c\cos\psi_c}{|\dot{\epsilon}'|}. \tag{19}$$

Now that σ_f^R is known from (18), the final value of stress is given by (3). This concludes the presentation of the exact solution.

It may be useful, however, to indicate briefly how to recast this exact solution in the language of stress-space plasticity. The first step in a stress-space implementation is to multiply

the deviatoric strain increment by $2G$ and add it to the old deviatoric stress to get a trial stress state σ_t'. If the trial stress lies within the yield surface, the final deviatoric stress is simply the trial stress. Otherwise, one solves for the contact point, finding σ_c' and t_c. The contact value of ψ, in view of (10), (7), and (8), is given by

$$(\sigma_c' - \gamma\epsilon_c^P) \cdot \dot{\epsilon}' = \rho_c |\dot{\epsilon}'| \cos\psi_c. \tag{20}$$

The next step is to find r_c and η, invoking (7), (13), and (5), and then solve (15) by some appropriate means to get ψ_f. The parameters α and β can then be evaluated through recourse to (19), and the increment in plastic strain is found from

$$\frac{\sigma_t' - \sigma_c'}{2G} - 2Gc(\epsilon_f^P - \epsilon_c^P) = \frac{\alpha - 1}{2G}(\sigma_c' - \gamma\epsilon_c^P) + \alpha\beta\dot{\epsilon}' \tag{21}$$

This last equation is obtained by substituting (6) and (7) into (18) and noting that $\sigma_t' - \sigma_c' = 2G(\epsilon_f' - \epsilon_c')$. Finally, the updated stress is given by

$$\sigma_f = \sigma_c + \mathbf{c}\dot{\epsilon}(t - t_c) - 2G(\epsilon_f^P - \epsilon_c^P) \tag{22}$$

There is no real obstacle to coding either version of the exact solution. The strain-space version seems preferable when the deformations are taken as infinitesimal, for in this case the elastoplastic stiffness can be calculated without having to find the stresses. This can save on both computation and storage costs. Also, strain-space plasticity generalizes conveniently to accommodate multilinear constitutive behavior [6]. All one need do is place loading surfaces in strain space, invoke the solution for each of them, and sum their respective contributions to the stress relaxation. The stress-space version, on the other hand, may be more convenient when finite deformations are in view. This is true because most of the schemes advanced thus far for implementing finite deformations plasticity are formulated in terms of the stress-space theory [9, 18, 19]. Ultimately, the choice is a matter of personal taste.

The Approximate Algorithms

Four approximate algorithms for implementing plasticity will now be outlined. The first is based on the strain-space formulation of plasticity; the other three are carried out in stress-space. Each can handle cases of strain hardening as well as of perfect plasticity. This may seem surprising for the stress-space schemes, but it is possible because the three constitutive laws [Γ+], [Γ0], and [Γ−] all lead to a single expression for the elastoplastic stiffness under conditions of loading.

The ***assumed trajectory method*** was introduced recently, in references [5, 20]. A contact point is sought, just as for the exact solution, and, assuming the relaxation surface has been active over the time step, the surface is updated in one of two ways. If the strain increment protrudes less than one radius from the surface, then the new center is placed along a line running from the old center toward the midpoint of the protruding section. If, on the other hand, the strain increment extends more than one radius beyond the surface, the trajectory is approximated by a line extending from the old center to a point half a radius back from the tip of the strain increment. Either way, the location of the new center is given in terms of a single parameter, which is evaluated by invoking the consistency condition (4) at the end of the time step. Then r_f, σ_f^R, and σ_f are found through recourse to (4) and (3).

The ***tangent stiffness-radial return*** method has, in one form or another, been a traditional favorite for use in structural analysis programs [8–10, 21]. Again, a test is done to determine whether or not the loading surface has been active. If so, the elastoplastic stiffness is evaluated at the contact point and used to obtain a revised estimate for the plastic portion of the stress increment. Substituting this into equation (δ) of [Γ+] and using the contact values of σ and ϵ^P throughout the time step, one finds in view of (1) the corresponding increment of plastic strain. This leads directly to an updated position and radius for the yield surface. The final stress is then moved radially (i.e., toward or away from $\gamma\epsilon^P$, as the case may be) so that it lies exactly on the yield surface.

The ***secant stiffness-radial return*** method, introduced by Rice and Tracey [22], is very similar to the tangent stiffness-radial return method [8, 9]. The only difference is that the elastoplastic stiffness and the formula for $\dot{\epsilon}^P$ from [Γ+] are evaluated not at the contact stress but rather at a point midway between the contact stress and the trial stress.

The ***radial return*** method is the oldest and simplest of the stress-space algorithms—and also the most consistently accurate [8–10, 23] for cases of perfect plasticity. After finding the trial stress, one assumes a plastic strain increment parallel to the full deviatoric strain increment, with the factor of proportionality based on the special case of a purely radial loading. This approximation leads immediately to an update in the position and radius of the yield surface. The trial stress is then moved either toward or away from the new center so as to satisfy the consistency condition.

Error Analysis

The new analytical solution provides a useful benchmark against which to evaluate the performance of the approximate algorithms. Tests of this sort have already been carried out for the special case of perfect plasticity [5, 8, 9, 20], but cases involving strain hardening have received rather less attention [10]. It remains to be seen, therefore, how strongly the trends reported for perfect plasticity are influenced by the introduction of hardening. Also lacking is a systematic assessment of how well the algorithms estimate changes in the radius of the loading surface. These considerations motivate a new round of tests for cases of purely kinematic and isotropic hardening. For each case the mechanical response is taken to be bilinear under conditions of proportional loading, with the ratio of elastic to elastoplastic shear stiffness equal to 10. In accordance with the ground rules of Krieg and Krieg, an initial state is chosen, which lies directly on the loading surface, and although principal directions are held constant, a variety of strain increments is considered. Since the final value of strain ϵ_f is a known quantity, the elastoplastic state at the close of the time step will be fully specified as soon as σ_f^R is determined, in view of (3) and (4). It follows that for any of the four algorithms, the overall accuracy is completely characterized by the errors arising in the magnitude and orientation of the radial vector $(\epsilon_f' - c\sigma_f^R)$:

$$\delta = 100 \text{ percent} - \frac{|\epsilon_f' - c\sigma_f^R|_{\text{approx}}}{|\epsilon_f' - c\sigma_f^R|_{\text{exact}}} \tag{23}$$

$$\theta = \cos^{-1}\frac{(\epsilon_f' - c\sigma_f^R)_{\text{exact}} \cdot (\epsilon_f' - c\sigma_f^R)_{\text{approx}}}{|\epsilon_f' - c\sigma_f^R|_{\text{exact}}\,|\epsilon_f' - c\sigma_f^R|_{\text{approx}}} \tag{24}$$

These parameters can be related to the stress-space theory through recourse to equation (8). Consistent with the notation of Krieg and Krieg, θ is chosen to be negative whenever the final radial vector, $(\epsilon_f' - c\sigma_f^R)$, ends up lying more nearly parallel than it should to the initial one, $(\epsilon_c' - c\sigma_c^R)$.

Figure 3 gives the test results for the case of kinematic hardening. Since the radius of the loading surface remains constant under conditions of kinematic hardening, the parameter δ will always be zero and need not be plotted. The contours of θ for the four methods look qualitatively similar to the results given elsewhere [20, 8] for the case of perfect plasticity, except that in general the errors shown here are smaller by some 20 percent. An attempt was made while preparing the contour plots to keep track of how much

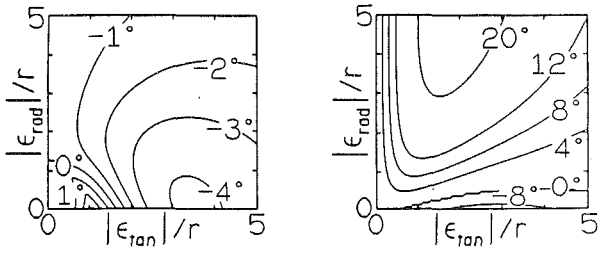

Fig. 3 The angular error θ for the case of kinematic hardening

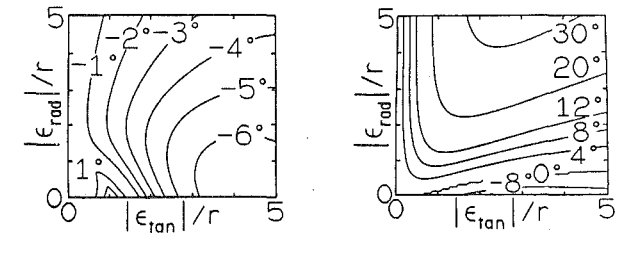

Fig. 4 The annular error θ for the case of isotropic hardening

computing time each algorithm consumed. In round figures, the assumed trajectory, tangent stiffness, secant stiffness, and radial return methods used respectively 80, 75, 80, and 60 percent of the time required by the exact solution. These figures, viewed in light of the contour plots, suggest that radial return is the optimal choice when moderate amounts of error can be tolerated, and that for more accurate work the exact solution itself should be used. Although subincrementation has in the past been advocated as a means of achieving accuracy [8, 10], this option no longer seems worthy of consideration.

The test results for isotropic hardening are given in Figs. 4 and 5. The angle errors, plotted in Fig. 4, are scarcely distinguishable from those associated with kinematic hardening. Far more noteworthy are the plots of radius error contained in Fig. 5. The tangent stiffness method leads to radius errors of up to 30 percent, an order of magnitude higher than those occurring with any other method. A similar finding was reported by Shreyer, Kulak, and Kramer [10], although they did not investigate the assumed trajectory and secant stiffness methods. Evidently, when the yield surface radius is variable, the tangent stiffness method should be avoided. Among the other methods, radial return is probably the best choice when moderate amounts of error can be tolerated. For more accurate work the exact solution again seems preferable to schemes based on subincrementation, although a closed-form solution for ψ_f is no longer available. The error in ψ_f—and thus the parameter θ—can be kept below a quarter of a degree by using the cubic interpolation formula derived in the Appendix. This compares favorably to the errors reported in [10] for subincrementation, and is only marginally more time consuming than the exact algorithm used for the kinematic case.

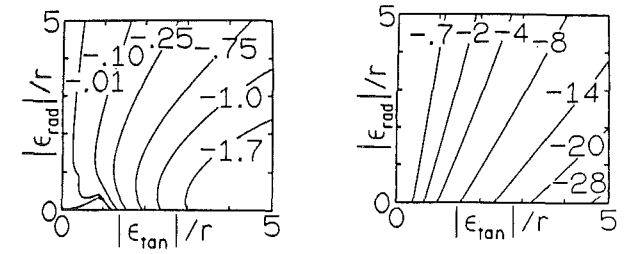

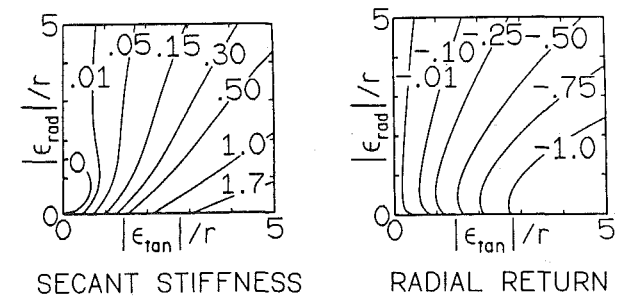

Fig. 5 The radius error δ for the case of isotropic hardening

Conclusions

In accordance with the conclusions of Krieg and Krieg, the radial return method continues to stand out among the approximate algorithms on account of its conceptual simplicity, computational speed, and accuracy. However, it does lead to radius errors on the order of 1 percent and angular errors of some 10 deg.

When greater accuracy than this is required, computations should be based directly on the exact solution, either in its closed-form version, which is appropriate for perfect plasticity and kinematic hardening, or else in one of the asymptotic representations given in the Appendix. These options take from 50 to 100 percent more computation time than radial return but are virtually error-free. Accordingly, they promise to be more efficient computationally than methods that rely on subincrementation. The exact solution can be applied to stress as well as to strain-space loading surfaces, and thus can be generalized in any of the standard ways to accommodate finite deformations. It also extends readily to the case of multilinear response curves. It should prove useful in a broad range of computational applications.

References

1 Drucker, D. C., "Stress-Strain Relations in the Plastic Range: A Survey of Theory and Experiment," Office of Naval Research Contract N7 onr-358, Brown University, Dec., 1950.

2 Iwan, W. D., "On a Class of Models for the Yielding Behavior of Continuous and Composite Systems," ASME JOURNAL OF APPLIED MECHANICS, Vol. 34, 1967, pp. 612-617.

3 Mroz, Z., "On the Description of Anisotropic Workhardening," *Journal of the Mechanics and Physics of Solids*, Vol. 15, May, 1967, pp. 163-175.

4 Prevost, J. H., "Mathematical Modeling of Monotonic and Cyclic Undrained Clay Behavior," *International Journal for Numerical and Analytical Methods in Geomechanics*, Vol. 1, No. 2, Apr.-June, 1977, pp. 195-216.

5 Yoder, P. J., "A Strain-Space Plasticity Theory and Numerical Implementation," EERL 80-07, California Institute of Technology, Pasadena, Calif., Aug., 1980.

6 Yoder, P. J., and Iwan, W. D., "On the Formulation of Strain-Space Plasticity With Multiple Loading Surfaces," ASME JOURNAL OF APPLIED MECHANICS, Vol. 48, 1981, pp. 773-778.

7 Dafalias, Y. F., and Popov, E. P., "Plastic Internal Variables Formalism in Cyclic Plasticity," ASME JOURNAL OF APPLIED MECHANICS, Vol. 43, 1976, pp. 645-651.

8 Krieg, R. D., and Krieg, D. B., "Accuracies of Numerical Solution Methods for the Elastic-Perfectly Plastic Model," ASME *Journal of Pressure Vessel Technology*, Vol. 99, 1977, pp. 510-515.

9 Krieg, R. D., and Key, S. W., "Implementation of a Time Independent Plasticity Theory into Structural Computer Programs," Sandia Laboratories, Albuquerque, N.M., 1976.

10 Schreyer, H. L., Kulak, R. F., and Kramer, J. M., "Accurate Numerical Solutions for Elastic-Plastic Models," ASME *Journal of Pressure Vessel Technology*, Vol. 101, 1979, pp. 226-234.

11 Lenskii, V. S., "Analysis of Plastic Behaviour of Metals Under Complex Loading," *Plasticity: Proceedings of the Second Symposium on Naval Structural Mechanics*, Lee, E. H., and Symonds, P. S., eds., Pergamon Press, New York, 1960, pp. 259-278.

12 Palmer, A. C., and Pearce, J. A., "Plasticity Theory Without Yield Surfaces," *Proceedings of the Symposium on the Role of Plasticity in Soil Mechanics*, Cambridge, 1973, pp. 188-200.

13 Naghdi, P. M., and Trapp, J. A., "The Significance of Formulating Plasticity Theory with Reference to Loading Surfaces in Strain Space," *International Journal of Engineering Science*, Vol. 13, No. 9/10, Sept./Oct., 1975, pp. 785-797.

14 Naghdi, P. M., "Some Constitutive Restrictions in Plasticity," *Constitutive Equations in Viscoplasticity: Computational and Engineering Aspects*, AMD, ASME, Vol. 20, 1976, pp. 79-93.

15 Casey, J., and Naghdi, P. M., "On the Characterization of Strain-Hardening in Plasticity," ASME JOURNAL OF APPLIED MECHANICS, Vol. 48, 1981, pp. 285-296.

16 Casey, J., and Naghdi, P. M., "On the Nonequivalence of the Stress Space and Strain Space Formulations of Plasticity Theory," ASME JOURNAL OF APPLIED MECHANICS, Vol. 50, 1983, pp. 350-354.

17 Discussion of [6] and Authors' Closure ASME JOURNAL OF APPLIED MECHANICS, Vol. 49, 1982, pp. 460-462.

18 McMeeking, R. M., and Rice, J. R., "Finite-Element Formulations for Problems of Large Elastic-Plastic Deformation," *International Journal of Solids and Structures*, Vol. 11, No. 5, 1975, pp. 601-616.

19 Nagtegaal, J. C., "Some Recent Developments in Combined Geometric and Nonlinear Finite Element Analysis," *Recent Advances in Nonlinear Computational Mechanics*, Hinton, E., Owen, D. R. J., and Taylor, C., eds., Pineridge Press, Swansea, U.K., 1982, pp. 87-117.

20 Iwan, W. D., and Yoder, P. J., "Computational Aspects of Strain-Space Plasticity," *ASCE Journal of Engineering Mechanics*, Vol. 109, No. 1, Feb., 1983, pp. 231-243.

21 Marcal, P. V., "A Stiffness Method for Elastic-Plastic Problems," *International Journal of Mechanical Sciences*, Vol. 7, 1965, pp. 229-238.

22 Rice, J. R., and Tracey, D. M., "Computational Fracture Mechanics," *Numerical and Computer Methods in Structural Mechanics*, Fenves, S. J., Perrone, N., Robinson, A. R., and Schnobich, W. C., eds., Academic Press, New York, 1973, pp. 585-623.

23 Wilkins, M. L., "Calculation of Elastic-Plastic Flow," *Methods of Computational Physis*, Vol. 3, Alder, B., Fernback, S., and Rotenbeerg, M., eds., Academic Press, New York, 1964.

24 Gradshteyn, I. S., and Ryzhik, I. M., *Table of Integrals, Series, and Products*, Academic Press, New York, 1965.

APPENDIX

As noted previously, the angle $\psi(t)$ satisfying equation (15) admits a closed-form representation only when η equals either zero or one. To deal with intermediate values of η, one approach is to seek perturbation solutions valid for η near these limiting values. Toward this end let the dependent variable

$$\psi(t) = \psi_{00}(t) + \eta\,\psi_{01}(t) + 0(\eta^2) \tag{A.1a}$$

$$\psi(t) = \psi_{10}(t) + (\eta-1)\psi_{11}(t) + 0((\eta-1)^2). \tag{A.1b}$$

and introduce Taylor series expansions about η equal to zero and one for the factor $(\sin\psi/\sin\psi_c)^\eta$. Substituting the expansions about $\eta=0$ into (15) and collecting like powers in η, one finds that

$$\dot{\psi}_{00} = -\gamma \sin\psi_{00} \tag{A.2a}$$

$$\dot{\psi}_{01} = -\gamma\left[(\cos\psi_{00})\psi_{01} + \left(\ln\frac{\sin\psi_{00}}{\sin\psi_c}\right)\sin\psi_{00}\right], \tag{A.3a}$$

where

$$\gamma = |\dot{\epsilon}'|/r_c. \tag{A.4}$$

Similarly, the expansions about $\eta = 1$ lead to

$$\dot{\psi}_{10} = -\gamma\frac{\sin^2\psi_{10}}{\sin\psi_c} \tag{A.2b}$$

$$\dot{\psi}_{11} = -\gamma\left[2\frac{\sin\psi_{10}\cos\psi_{10}}{\sin\psi_c}\psi_{11} + \frac{\sin^2\psi_{10}}{\sin\psi_c}\ln\left(\frac{\sin\psi_{10}}{\sin\psi_c}\right)\right]. \tag{A.3b}$$

The appropriate initial conditions are

$$\psi_{00}(t_c) = \psi_{10}(t_c) = \psi_c \tag{A.5}$$

$$\psi_{01}(t_c) = \psi_{11}(t_c) = 0. \tag{A.6}$$

Solutions to the zeroth-order problems are given in equation (16). Finding the first-order solutions turns out to be straightforward, albeit tedius.

$$\psi_{01}(t) = \operatorname{sech}[\gamma(t-t_c-\tau)]\left[\gamma(t-t_c)\ln\sin\psi_c + \int_{-\gamma\tau}^{\gamma(t-t_c-\tau)} \ln\cosh\times dx\right], \tag{A.7a}$$

where $\tau = \dfrac{1}{\gamma}\ln\tan\left(\dfrac{1}{2}\psi_c\right)$;

$$\psi_{11}(t) = \frac{1}{\left[\dfrac{\gamma}{\sin\psi_c}(t-t_c)+\cot\psi_c\right]^2+1}\left[\frac{\gamma}{\sin\psi_c}(t-t_c)\{\ln\sin\psi_c-1\}+\frac{1}{2}\left\{\frac{\gamma}{\sin\psi_c}(t-t_c)+\cot\psi_c\right\}\ln\left\{\left[\frac{\psi}{\sin\psi_c}(t-t_c)+\cot\psi_c\right]^2+1\right\}+\cot\psi_c\ln\sin\psi_c+\tan^{-1}\left\{\frac{\gamma}{\sin\psi_c}(t-t_c)+\cot\psi_c\right\}-\frac{\pi}{2}+\psi_c\right]. \tag{A.7b}$$

The integral in (A.7a) does not admit a closed-form representation, although a power series expansion for it can be found in section 2.479.7 of [24]. A more practical approach is to integrate numerically.

If η lies within 0.05 of either zero or one, it seems best to use just one of the perturbation solutions, which ever is more appropriate. For intermediate values of η, on the other hand, the authors recommend an interpolation, cubic in η, which matches both of the perturbation solutions:

$$\psi^* = (2\psi_{00}+\psi_{01}-2\psi_{10}+\psi_{11})\eta^3 + (-3\psi_{00}-2\psi_{01}+3\psi_{10}-\psi_{11})\eta^2 + \psi_{01}\eta+\psi_{00}. \tag{A.8}$$

The Sliding With Coulomb Friction of a Rigid Indentor Over a Power-Law Inhomogeneous Linearly Viscoelastic Half-Plane[1]

J. R. Walton
Department of Mathematics
Texas A&M University
College Station, Texas 77843

In a previous paper, the title problem was solved for a homogeneous power-law linearly viscoelastic half-plane. Such material has a constant Poisson's ratio and a shear modulus with a power-law dependence on time. In this paper, the shear modulus is assumed also to have a power-law dependence on depth from the half-plane boundary. As in the earlier paper, only a quasi-static analysis is presented, that is, the enertial terms in the equations of motion are not retained and the indentor is assumed to slide with constant speed. The resulting boundary value problem is reduced to a generalized Abel integral equation. A simple closed-form solution is obtained from which all relevant physical parameters are easily computed.

1 Introduction

In a previous paper [3] a quasi-static analysis was presented for the problem of a rigid asperity sliding with Coulomb friction over the surface of a homogeneous and isotropic power-law linearly viscoelastic half-plane. The power-law model may be characterized by a linear constitutive law with a constant Poisson's ratio, ν, and a shear modulus, μ, of the form

$$\mu(t) = \mu_c (t/t_c)^{-\alpha} \tag{1}$$

where t denotes time, t_c is a characteristic relaxation time, and μ_c is a characteristic modulus. In [3], a simple closed-form solution for the normal stress under the moving indentor was obtained by reduction of the boundary value problem to a generalized Abel integral equation. The Abel equation was then solved by transformation to an equivalent Riemann-Hilbert boundary value problem.

Of prime importance in viscoelastic punch problems is the prediction of the horizontal force, f_h, impeding the motion of the indentor. In general, it is non zero even for frictionless contact and symmetric asperity shapes. This is due to the asymmetrical distribution of material under the indentor. The friction coefficient, c_f, is then defined to be the ratio of f_h to the total vertical load, λ, on the contact set, C, due to the weight of the punch. That is,

$$f_h = \int_C \sigma_{yy}(x) u_{y,x}(x) dx \tag{2}$$

$$\lambda = \int_C \sigma_{yy}(x)\, dx \tag{3}$$

$$c_f = f_h/\lambda \tag{4}$$

where $\sigma_{yy}(x)$ is the normal stress on the half-plane surface and $u_{y,x}(x)$ is the x-partial derivative of the normal surface displacement u_y. In [3], simple expressions were derived for the foregoing three parameters, f_h, λ, and c_f, fo three canonical punch shapes: parabolic (as an approximation to a cylinder), wedge, and flat.

An additional parameter of interest for physical simulations of moving asperity problems is the depth of penetration of the punch into the medium. The depth of penetration, d, is defined here to be the distance between the leading contact point on the punch and the tangent line passing through the apex. This choice of definition of the depth of penetration is motivated by the fact that it is both easily controlled in physical experiments (such as drag box simulations of pipe-soil interactions) and easily calculated for the mathematical model employed here.

The assumption of a simple power-law behavior in time for the shear modulus introduces certain unphysical features into the model, principally through the short and long-time asymptotic behavior of the modulus. For example, in [3] it was shown that for frictionless sliding and $1/2 < \alpha < 1$, the stress under the indentor possesses a singularity at the leading contact point, even for a smooth parabolic punch. Moreover, the material does not wrap around the apex of the punch, but rather, contact occurs only on the leading face of the indentor.

However, as pointed out in [3] and several references in its accompanying bibliography, these physically unrealistic

[1]This work was supported in part by a contract with the American Gas Association and by a contract with the Office of Naval Research, ONR Contract No. N00014-75-C-0325.

Contributed by the Applied Mechanics Division for publication in the JOURNAL OF APPLIED MECHANICS.

Discussion on this paper should be addressed to the Editorial Department, ASME, United Engineering Center, 345 East 47th Street, New York, N.Y. 10017 and will be accepted until two months after final publication of the paper itself in the JOURNAL OF APPLIED MECHANICS. Manuscript received by ASME Applied Mechanics Division, July, 1983; final revision, October, 1983.

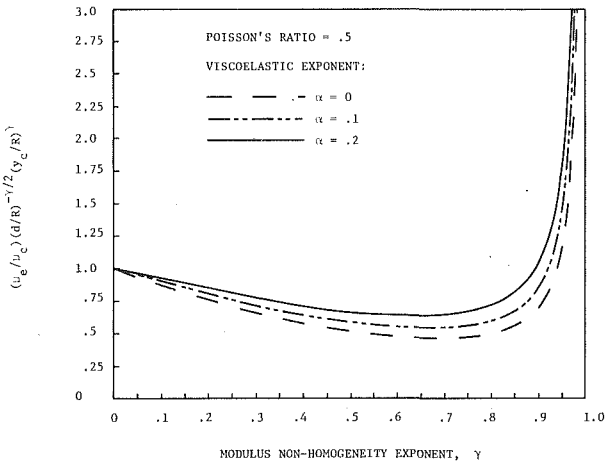

Fig. 1 An illustration of the result (39)

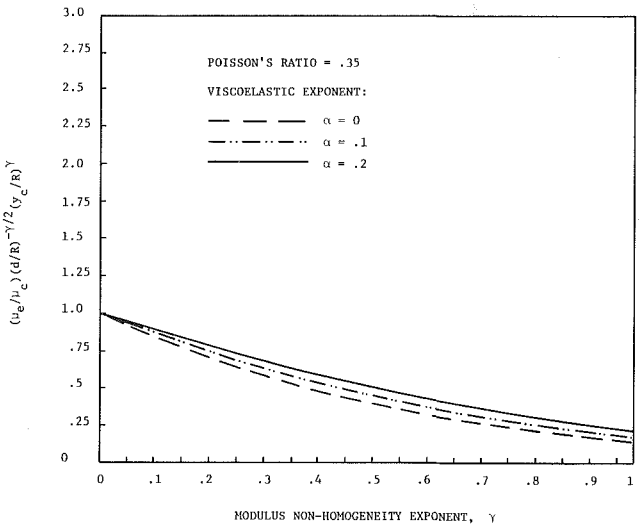

Fig. 2 An illustration of the result (39)

consequences of the pure power-law model do not render it unacceptable for engineering predictions. While the model is apparently suspect for predicting the details of the stress and displacement fields, it does very well in the prediction of f_h and c_f, better, for example, than the standard linear solid or even exponential models with a fairly large number of relaxation times. This is because the power-law model fits real viscoelastic data (e.g., for rubber and many polymeric materials) in simple relaxation tests over large time intervals better than does the standard linear solid. To do as well with more general exponential models, it is often necessary to incorporate a large number of relaxation times. Moreover, for such exponential models the boundary value problems corresponding to punch problems are much more complicated to solve than for the power-law model.

In this paper, the quasi-static punch problem is reconsidered, except that the viscoelastic shear modulus is also assumed to have a power-law depth dependence. Specifically, the shear modulus $\mu(t,y)$ has the form

$$\mu(t,y)=\mu_c(t/t_c)^{-\alpha}(y/y_c)^{\gamma} \tag{5}$$

where y_c is a characteristic depth from the half-plane surface and $0\le\gamma\le 1$. Again it may at first appear that a model with a simple power-law depth dependence is physically unreasonable and therefore uninteresting, except perhaps for purely mathematical reasons. However, there are real materials (e.g., sea bottom mud) whose mechanical behavior obeys such a power-law model over very broad ranges of time and depth. Use of the power-law model therefore provides for these materials important qualitative and quantative information on the dependence of f_h and c_f on the material viscoelasticity and inhomogeneity.

For example, the physical problem that motivated this study is that of a pipeline (rigid indentor) moving over the ocean floor (viscoelastic half-space). Experimental evidence [2] suggests that for the purpose of predicting the forces on the pipe, the mechanical behavior of the mud on the ocean bottom can be described effectively by the power-law model (5). It should be remarked that for the pipeline-mud interaction, the Coulomb friction assumption does not appear to be applicable. It is incorporated in the analysis presented here because of its possible applicability to other physical scenarios and for its theoretical and mathematical interest.

Another physical situation for which the power-law model (5) may provide useful insight is when the frictional interaction between the punch and the material half-space produces a significant thermal gradient which in turn produces a depth-dependent softening of the material. Such might occur for a rubber tire sliding rapidly over pavement or a metal-polymeric material interaction in which friction produces a local temperature rise above the glass transition temperature.

In the next section, the transformation of the governing boundary value problem to a generalized Abel integral equation is presented. The solution of the Abel equation is derived in Section 3 and certain physically important parameters are computed for a parabolic punch. Only a parabolic indentor profile is considered since with it the salient features of the model are easily illustrated. Moreover, the parabolic punch is a shape applicable to the pipeline-mud problem that motivated this investigation. The paper concludes with a section in which the results of numerical experiments are presented in order to illustrate the magnitude of the effect on force predictions of the material inhomogenity assumption.

2 Derivation of Integral Equation

The problem to be studied is that of determining the plane-strain quasi-static stress and displacement fields in a linearly viscoelastic half-plane that are produced by a punch sliding with Coulomb friction on the half-plane surface. The punch is assumed to be sliding to the left with constant speed v and be such that the contact set is a single interval. The specific boundary value problem to be solved is then

$$\sigma_{ij,j}=0 \quad -\infty<x_1<\infty,\ x_2>0$$

$$\sigma_{ij}=2\mu^* d\epsilon_{ij}+\delta_{ij}\frac{2\nu}{1-2\nu}\mu^* d\epsilon_{kk}$$

$$\delta_{12}(x_1,0)=-k\sigma_{22}(x_1,0),\quad -\infty<x_1<\infty$$

$$\sigma_{22}(x_1,0)=0,\ x_1<a-vt \text{ or } x_1>b-vt \tag{7}$$

$$u_{2,1}(x_1,0)=-f'(x_1+vt),\ a-vt<x_1<b-vt, \tag{8}$$

where σ_{ij}, ϵ_{ij}, and u_i are the viscoelastic stress, strain, and displacement fields, $g_{,i}$ denotes partial differentiation; $f'(\cdot)$ is the derivative of the punch profile $f(\cdot)$; ν is Poisson's ratio (assumed to be constant); μ is the shear modulus; k is a constant; δ_{ij} is the Kroneker delta, and $f^*d\epsilon$ denotes the Riemann-Stieltjes convolution

$$f^*d\epsilon=\int_{-\infty}^{\infty} f(t-s)d\epsilon(s).$$

The construction of the solution of the preceding equations is facilitated by adoption of the Galilean variable $x=x_1+vt$ and the change of variables, $y_1=y$, $\sigma_{11}=\sigma_{xx}$, $\sigma_{12}=\sigma_{xy}$, $u_1=u_x$, etc. For the shear modulus we take the power-law model (5). A Fourier transform in x may now be applied to

reduce the boundary value problem to an integral equation over the contact interval (a,b).

A key step in the Fourier transform method is the construction of the so called viscoelastic transfer function, i.e., the function $T(p)$ for which

$$\hat{\sigma}_{yy},(p,0) = T(p)\hat{u}_y(p,0) \tag{9}$$

where $\hat{f}(p,y)$ denotes the Fourier transform

$$\hat{f}(p,y) = \int_{-\infty}^{\infty} f(x,y)e^{-ixp}dx.$$

Rather than directly perform the calculations for the inhomogeneous half-plane analogous to those presented in [1] for the homogeneous case, we appeal to the viscoelastic correspondence principle. Use can then be made of the known integral boundary relation between elastic stresses and displacements for a power-law depth-dependent shear modulus. Specifically, it is shown in Gladwell [1] (pp. 301-311) that

$$u_y^e(x,y) = \int_{-\infty}^{\infty} [g_{12}sgn(x-t)\sigma_{xy}^e(t,0) - g_{22}\sigma_{yy}^e(t,0)]\,|x-t|^{-\gamma}dt \tag{10}$$

where u_y^e, σ_{xy}^e, and σ_{yy}^e are the elastic displacement and stresses. The constants g_{12} and g_{22} are given by

$$\begin{aligned} g_{12} &= (1-\nu)I\cos(\pi q/2)/[\pi\mu_c^e\gamma] \\ g_{22} &= (1-\nu)Iq\sin(\pi q/2)/[\pi\mu_c^e\gamma(1-\gamma)] \\ q &= [(1+\gamma)(1-\gamma\nu/(1-\nu))]^{1/2} \\ I &= 2^{\gamma}(\gamma+2)B((\gamma+q+3)/2,\ (\gamma-q+3)/2). \end{aligned}$$

The elastic shear modulus adopted by Gladwell has the form

$$\mu^e(y) = \mu_c^e y^{-\gamma}.$$

The viscoelastic transfer function may now be derived by Fourier transformation of (10) and substitution of the transformed viscoelastic shear modulus for μ_c^e. (Recall that x is the Galilean variable $x_1 + vt$. Thus $\mu(t,x_2)$ is a function of x and y, and $\hat{\mu}$ denotes its Fourier transform with respect to x.) In this way it can be shown that

$$T(p) = \frac{-q(1-\nu)I\sin(q\pi/2)y_c^{\gamma}(ip)^{-\alpha}|p|^{\gamma-1}(1-i\delta\,\mathrm{sgn}(p))}{\mu_c(vt_c)^{\alpha}\Gamma(1-\alpha)\Gamma(2+\gamma)\cos(\gamma\pi/2)}, \tag{11}$$

where sgn(•) is the signum function and

$$\delta = (k/q)(1+\gamma)\cot(q\pi/2)\cot(\gamma\pi/2).$$

We remark that the Coulomb boundary condition (6) has been incorporated into the transfer function (11).

Substitution of (11) into (9) followed by Fourier inversion and the application of the boundary conditions (7) and (8) produces the desired integral equation for the unknown normal stress, $\sigma_{yy}(x,0)$, under the known punch, $f(x)$. Only a parabolic punch profile will be considered here. Therefore, for $f'(x)$ we take

$$f'(x) = -x/R$$

where R is a constant (cylinder radius). Moreover, it is convenient to consider separately the two cases: $0 \le \alpha < \gamma < 1$ and $0 \le \gamma < \alpha < 1$.

Case I. $0 \le \alpha < \gamma < 1$. Define the constant K_0 by

$$K_0 = \frac{\Gamma(1-\alpha)\Gamma(2+\gamma)\cos(\gamma\pi/2)}{q(1-\nu)I\sin(q\pi/2)}. \tag{12}$$

Then, after multiplication by (ip), (9) becomes

$$-K_0\mu_c(vt_c)^{\alpha}y_c^{-\gamma}\hat{u}_{y,x} = (ip)^{-\alpha}|p|^{\gamma-1}(1-\delta i\,\mathrm{sgn}(p))\hat{\sigma}_{yy,x}. \tag{13}$$

An easy calculation shows that

$$\begin{aligned} &(1/2)\int_{-\infty}^{\infty} e^{ixp}\hat{\sigma}_{yy,x}(ip)^{-\alpha}|p|^{\gamma-1}dp \\ &= \Gamma(\gamma-\alpha)\Big[\cos(\gamma\pi/2)\int_x^{\infty}\sigma_{yy,x}(t)(t-x)^{\alpha-\gamma}dt \\ &\quad + \cos((\gamma-2\alpha)\pi/2)\int_{-\infty}^{x}\sigma_{yy,x}(t)(x-t)^{\alpha-\gamma}dt\Big] \end{aligned} \tag{14}$$

and

$$\begin{aligned} &(1/2)\int_{-\infty}^{\infty} e^{ixp}\sigma_{yy,x}(i\,\mathrm{sgn}(p))(ip)^{-\alpha}|p|^{\gamma-1}dp \\ &= \Gamma(\gamma-\alpha)\Big[\sin(\gamma\pi/2)\int_x^{\infty}\sigma_{yy,x}(t)(t-x)^{\alpha-\gamma}dt \\ &\quad - \sin((\gamma-2\alpha)\pi/2)\int_{-\infty}^{x}\sigma_{yy,x}(t)(x-t)^{\alpha-1}dt\Big]. \end{aligned} \tag{15}$$

Fourier inversion of (13) together with (7), (14), and (15) produces the generalized Able integral equation

$$\begin{aligned} &-K_0\mu_c(vt_c)^{\alpha}y_c^{-\gamma}(\pi/\Gamma(\gamma-\alpha))u_{y,x}(x) \\ &= [\cos(\gamma\pi/2) - \delta\sin(\gamma\pi/2)]\int_x^b\sigma_{yy,x}(t)(t-x)^{\alpha-\gamma}dt \\ &\quad + [\cos((\gamma-2\alpha)\pi/2) + \delta\sin((\gamma-2\alpha)\pi/2)] \\ &\quad \int_a^x\sigma_{yy,x}(t)(x-t)^{\alpha-\gamma}dt. \end{aligned} \tag{16}$$

Introducing the parameters K_1, ω, α' and β' given by

$$\begin{aligned} K_1 &= K_0\cos(\omega\pi/2)/\cos(\beta'\pi/2) \\ \delta &= \tan(\omega\pi/2) \\ \alpha' &= 1+\alpha-\gamma \\ \beta' &= \gamma+\omega, \end{aligned} \tag{17}$$

equation (16) becomes

$$\begin{aligned} &-K_1\mu_c(vt_c)^{\alpha}y_c^{-\gamma}(\pi/\Gamma(1-\alpha'))u_{y,x} \\ &= \int_x^b\sigma_{yy,x}(t)(t-x)^{\alpha'}dt \\ &\quad - \frac{\cos((\beta'+2\alpha')\pi/2)}{\cos(\beta'\pi/2)}\int_a^x\sigma_{yy,x}(t)(x-t)^{\alpha'-1}dt. \end{aligned} \tag{18}$$

Equation (18) is the desired generalized Abel equation for Case I. It should be noted that equation (18) is functionally identical to equation (8) of [3] for a homogeneous power-law viscoelastic half plane.

Case II. $0 \le \gamma < \alpha < 1$. For Case II, line (13) is replaced by

$$-K_0\mu_c(vt_c)^{\alpha}y_c^{-\gamma}\hat{u}_{y,x} = (ip)^{1-\alpha}|p|^{\gamma-1}(1-\delta i\,\mathrm{sgn}(p))\hat{\sigma}_{yy}. \tag{19}$$

Fourier inversion of (19) produces

$$\begin{aligned} &-K_0\mu_c(vt_c)^{\alpha}y_c^{-\gamma}(\pi/\Gamma(1+\gamma-\alpha))u_{y,x}(x) \\ &= [\cos(\gamma\pi/2) - \delta\sin(\gamma\pi/2)]\int_x^b\sigma_{yy}(t)(t-x)^{\alpha-\gamma-1}dt \\ &\quad - [\cos((\gamma-2\alpha)(\pi/2) + \delta\sin((\gamma-2\alpha)\pi/2] \\ &\quad \int_a^x\sigma_{yy}(t)(x-t)^{\alpha-\gamma-1}dt. \end{aligned} \tag{20}$$

New defining α'' and β'' by

$$\alpha'' = \alpha - \gamma$$
$$\beta'' = \gamma + \omega$$

we obtain the desired generalized Abel integral equation for Case II,

$$-K_1 \mu_c (vt_c)^{\alpha} y_c^{-\gamma} (\pi/\Gamma(1-\alpha'')) u_{y,x}(x) = \int_x^b \sigma_{yy}(t)(t-x)^{\alpha''-1} dt$$
$$- \frac{\cos((\beta''+2\alpha'')\pi/2)}{\cos(\beta''\pi/2)} \int_a^x \sigma_{yy}(x)(x-t)^{\alpha''-1} dt. \quad (22)$$

In the next section, the solutions to (18) and (22) are presented.

3 Solution of Generalized Abel Equation

Since $f'(x) = -x/R$, we may utilize in the solution of (18) and (22) much of the analysis developed in [3] for a parabolic indentor sliding over a homogeneous half plane. First consider (22). From the solution given on p. 313 of [3] (after correction of the obvious misprints) we obtain

$$\sigma_{yy}(x) = -(K_1/R)\mu_c (vt_c)^{\alpha} y_c^{-\gamma} [1 + (\tan^{-1}(\beta''\pi/2))^2]^{-1/2}$$
$$\left[(1/\Gamma(1-\alpha'')) \int_x^b (b-t)^{(\beta''-1)/2} (t-a)^{(1-\beta''-2\alpha'')/2} dt \right.$$
$$- \frac{\Gamma((\beta''+1)/2)(1-2\alpha''-\beta'')(b-a)^{1-\alpha''}}{2\Gamma(2-\alpha'')\Gamma((1+\beta''+2\alpha'')/2)} \int_x^b (b-t)^{(\beta''+2\alpha''-1)/2}$$
$$\left. (t-a)^{-(\beta''+1)/2} (t-x)^{-\alpha''} dt \right]. \quad (23)$$

The form of the solution given by (23) can be simplified. First observe that

$$\int_x^b (b-t)^{(\beta''+2\alpha''-1)/2} (t-a)^{-(\beta''+1)/2} (t-x)^{-\alpha''} dt$$
$$= (b-a)^{-(\beta''+1)/2} \sum_{n=0}^{\infty} \frac{((\beta''+1)/2)n}{n!}$$
$$(b-a)^{-n} \int_x^b (t-x)^{-\alpha''} (b-t)^{(\beta''+2\alpha''-1)/2+n} dt$$
$$= (b-a)^{-(\beta''+1)/2} \sum_{n=0}^{\infty} \frac{((\beta''+1)/2)n}{n!} (b-a)^{-n}$$
$$\times (b-x)^{n+(\beta''+1)/2} B(1-\alpha'', n+(\beta''+2\alpha''+1)/2)$$

where $(\gamma)_n$ denotes the Pochhammer symbol, $(\gamma)_n = \Gamma(\gamma+n)/\Gamma(\gamma)$, and $B(\cdot,\cdot)$ is the beta function. Differentiation of (24) results in

$$\frac{d}{dx} \int_x^b (b-t)^{(\beta''+2\alpha''-1)/2} (t-a)^{-(\beta''+1)/2} (t-x)^{-\alpha''} dt$$
$$= - \frac{\Gamma(1-\alpha'')\Gamma((\beta''+2\alpha''+1)/2)}{\Gamma((\beta''+1)/2)}$$
$$\times (b-a)^{\alpha''} 2(b-x)^{(\beta''-1)/2} (x-a)^{(-\beta''+2\alpha''+1)/2}. \quad (25)$$

Differentiating (23) and applying (25) and (21) yields

$$\sigma_{yy,x}(x) = (K_2/R)\mu_c (vt_c)^{\alpha} y_c^{-\gamma} (b-x)^{(\gamma+\omega+1)/2} (x-a)^{-(2\alpha-\gamma+\omega+1)/2}$$
$$\cdot (x + (b-a)(\omega+\alpha)/(1+\gamma-\alpha)) \quad (26)$$

where K_2 is given by

$$K_2 = K_1 [1 + (\tan^{-1}((\gamma+\omega)\pi/2))^2]^{-1/2} / \Gamma(1+\gamma-\alpha). \quad (27)$$

Moreover, from the analysis in [3] it follows that the contact interval endpoints, a and b, are given by

$$a = -\frac{(b-a)}{2}(1+\gamma+\omega)/(1+\gamma-\alpha)$$
$$b = \frac{(b-a)}{2}(1+\gamma-2\alpha-\omega)/(1+\gamma-\alpha). \quad (28)$$

Combining (26) and (28) we obtain

$$\sigma_{yy,x}(x) = (K_2/R)\mu_c (vt_c)^{\alpha} y_c^{-\gamma} (b-x)^{(\gamma+\omega-1)/2} (x-a)^{-(2\alpha-\gamma+\omega+1)/2} (x+a+b). \quad (29)$$

From (29) it now follows by a simple integration that

$$\sigma_{yy}(x) = -(K_3/R)\mu_c (vt_c)^{\alpha} y_c^{-\gamma} (b-x)^{(\gamma+\omega+1)/2} (x-a)^{(1+\gamma-\omega-2\alpha)/2} \quad (30)$$

where $K_3 = K_2/(1+\gamma-\alpha)$. Line (30) is the desired solution for Case II.

For Case I, it is equation (18) that must be solved. Although equation (18) is a generalized Abel equation of the same functional form as (22), it is apparent that the solution given on p. 313 of [3] that was applied to (22) cannot be used for (18). The reason for this is that (18) relates $\sigma_{yy,x}$ rather than σ_{yy} to $u_{y,x}$. If the solution on p. 313 in [3] were employed on (18), then (23) with α'' replaced by α' and σ_{yy} replaced by $\sigma_{yy,x}$ would be the solution to (18). But such a solution is physically and mathematically unacceptable. For example, the right side of (23) is a continuous function at $x=b$ for all permissible values of α, γ, and ω, whereas, it is clear that for certain values of α, γ, and ω, $\sigma_{yy,x}$ is singular as $x \to b$.

The solution to (18) may be constructed by appealing to the general solution method described in [3]. Specifically, we apply formula (21) on p. 306 of [3]. It may then be shown that $\sigma_{yy,x}$ for Case I is given by (29) in the foregoing, that is, the solution for Case I is the same as for Case II. Consequently, σ_{yy} for Case I is also given by (30) and the contract interval endpoints, a and b, by (28). The calculations required to construct the solution of equation (18) are lengthy but straight forward. Therefore, they will be omitted.

We remark that setting $\gamma = 0$ in (30) yields a simpler form for the solution in the case of a homogeneous half space than was presented in [3]. Moreover, when $\alpha = 0$, line (30) is the solution for a power-law inhomogeneous linearly elastic material. An attractive feature of the power-law inhomogeneous linear viscoelastic model is that it admits a solution to this import canonical punch problem that has the same simple functional form as the solution to the corresponding problem for homogeneous linearly elastic material. Consequently, it is a relatively simple matter to determine both qualitatively and quatitatively the effect of adding material viscoelasticity and inhomogeneity to a basic linear elastic model.

We remark further than from (28)–(30) it follows easily that $\sigma_{yy}(x)$ is continuous at $x=b$ for all admissible values of α, γ, and ω. However, at $x=a$, $\sigma_{yy}(x)$ is continuous if and only if $\alpha + (\omega-\gamma)/2 < 1/2$. For $\alpha + (\omega-\gamma)/2 = 1/2$, σ_{yy} has a jump discontinuity at $x=a$ and for $\alpha + (\omega-\gamma)/2 > 1/2$ it has a singularity of order $(1+\gamma-\omega-2\alpha)/2$ at $x=a$. Moreover, if $\alpha + (\omega-\gamma)/2 \geq 1/2$, $\sigma_{yy}(x)$ is monotone on (a,b), whereas, if $\alpha + (\omega-\gamma)/2 < 1/2$, it has a unique maximum at

$$\bar{x} = -(b-a)(\alpha+\omega)/(1+\gamma-\alpha)$$
$$= (b+a).$$

Finally, we note that for $\alpha + (\omega-\gamma)/2 < 1/2$, the material wraps around the punch, whereas, for $\alpha + (\omega-\gamma)/2 \geq 1/2$ the contact set is entirely on the leading face of the punch. These observations are generalizations to inhomogeneous material

of similar observations made in [3] for homogeneous power-law material.

This section concludes with the calculation of the four physical parameters f_h, λ, and c_f and d. Due to the simple nature of $\sigma_{yy}(x)$ for a parabolic indentor, their calculation is routine. Consequently none of the details of the calculations are included here. It can easily be verified by substitution of (30) into (3) that

$$\lambda = -K_3(\mu_c/R)(vt_c)^{\alpha} y_c^{-\gamma} B((3+\gamma-\omega-2\alpha)/2, (3+\gamma+\omega)/2)(b-a)^{2+\gamma-\alpha}. \tag{31}$$

Similarly, from (2) we obtain

$$f_h = \frac{(2+\gamma-\alpha)(\alpha+\omega)}{(3+\gamma-\alpha)(1+\gamma-\alpha)} \lambda(b-a)/R, \tag{32}$$

and combining (4), (31), and (32) yields

$$c_f = \frac{(2+\gamma-\alpha)(\alpha+\omega)}{(3+\gamma-\alpha)(1+\gamma-\alpha)} (b-a)/R. \tag{33}$$

Finally, from (28) and the fact that the depth of penetration, d, is given by $d = a^2/(2R)$, we see that d is given by

$$d = (1/2R)((b-a)/2)^2(1+\gamma+\omega)^2/(1+\gamma-\alpha)^2. \tag{34}$$

4 Numerical Examples

The principal focus of the numerical study of the theoretical results was the following problem: Find an "effective depth," y_1, such that the force on the indentor predicted by the inhomogeneous material model equals the force predicted by a homogeneous model with shear modulus equal to the inhomogeneous modulus evaluated at $y = y_1$. Hence, the value of the modulus of the mud at depth $y = y_1$ can be thought of as an "effective modulus" for predicting the horizontal force on the indentor.

This question is answered quite easily. For the sake of simplicity it will be assumed that there is no Coulomb frictional force, i.e., $\omega = 0$. Moreover, d/R will be regarded as an input parameter since, for example, it is easily controlled in dragbox experiments of a pipe sliding over mud. From (31), (32), and (34) it is easily seen that, assuming an inhomogeneous model,

$$f_h = K_4(\alpha,\gamma)^{R\mu_c} (vt_c/R)^{\alpha} (y_c/R)^{-\gamma} ((b-a)/R)^{3+\gamma-\alpha}, \tag{35}$$

with

$$(b-a)/R = 2(2d/R)^{1/2}(1+\gamma-\alpha)/(1+\gamma) \tag{36}$$

and

$$K_4(\alpha,\gamma) \equiv -K_3(\alpha,\gamma)B((3+\gamma-2\alpha)/2,\ (3+\gamma)/2). \tag{37}$$

For a homogeneous material model with modulus given by the inhomogeneous model evaluated at an effective depth, y_1, i.e., for which

$$\mu(t) = \mu_c(y_1/y_c)^{\gamma}(t/t_c)^{-\alpha} \equiv \mu_e(t/t_c)^{-\alpha},$$

the predicted force is given by (35)-(37) with $\gamma = 0$ and μ_e substituted for μ_c. Hence

$$f_h = K_4(\alpha,0)R\mu_e(vt_c/R)^{\alpha}((b-a)/R)^{3-\alpha} \tag{38}$$

with

$$(b-a)/R = 2(2d/R)^{1/2}(1-\alpha).$$

Equating f_h in both (35) and (38), it is seen that

$$(y_1/y_c)^{\gamma} = \mu_e/\mu_c = \frac{K_4(\alpha,\gamma)}{K_4(\alpha,0)} (y_c/R)^{-\gamma} \times \left[\frac{1+\gamma-\alpha}{1+\gamma}\right]^{3+\gamma-\alpha} (1-\alpha)^{\alpha-3/2\gamma}(2d/R)^{\gamma/2}. \tag{39}$$

To illustrate the result (39), the value of $(\mu_e/\mu_c)(d/R)^{-\gamma/2}(y_c/R)^{\gamma}$ was computed for several values of α, γ, and ν and is displayed in the following graphs. It should be noted that $\gamma = 1$ and $\nu = 1/2$ is a singular limit in that (μ_e/μ_c) becomes unbounded as γ and ν tend to 1 and 1/2, respectively.

References

1 Gladwell, G. M. L., *Contact Problems in the Classical Theory of Elasticity*, Sijthoff and Noordhoff, Germantown, Md., 1980.

2 Schapery, R. A., private communication.

3 Walton, J. R., Nachman, A., and Schapery, R. A., "The Sliding of a Rigid Indentor Over a Power-Law Viscoelastic Half Space," *Quart J. Mech. Appl. Math.*, Vol. 31, No. 3, 1978, pp. 295-321.

On the Appearance of the Fractional Derivative in the Behavior of Real Materials

P. J. Torvik
Professor and Head,
Department of Aeronautics
and Astronautics,
Air Force Institute of Technology,
WPAFB, Ohio 45433
Mem. ASME

R. L. Bagley[1]
Associate Professor,
Department of Engineering Mechanics,
USAF Academy,
Colorado Springs, Col.

Generalized constitutive relationships for viscoelastic materials are suggested in which the customary time derivatives of integer order are replaced by derivatives of fractional order. To this point, the justification for such models has resided in the fact that they are effective in describing the behavior of real materials. In this work, the fractional derivative is shown to arise naturally in the description of certain motions of a Newtonian fluid. We claim this provides some justification for the use of ad hoc relationships which include the fractional derivative. An application of such a constitutive relationship to the prediction of the transient response of a frequency-dependent material is included.

Introduction

A number of authors have implicitly or explicitly used the fractional calculus as an empirical method of describing the properties of viscoelastic materials. Nutting's [1] modeling of stress relaxation phenomenon by fractional powers of time, rather than by decaying exponentials, is equivalent, as is Gemant's observation that the stiffness and damping of viscoelastic materials are proportional to fractional powers of frequency [2]. He suggested, in fact, that time differentials of fractional order might model such behavior [3]. Scott-Blair noted that fractional-order time derivatives [4] would simultaneously model stress relaxation and frequency dependence.

The viscoelastic behavior of geological strata and of metals and glasses have been modeled by Caputo [5, 6] and by Caputo and Minardi [7] through the use of constitutive relationships employing the fractional calculus. Recent work has shown that constitutive equations containing fractional derivatives are effective in describing the frequency-dependent behavior of viscoelastic polymers [8] and that the fractional calculus leads to well-posed problems for the motion of structures containing elastic and viscoelastic components [9], even when incorporated into a finite-element approach [10]. A particular virtue of constitutive relations containing fractional derivatives is that they lead to a casual response at zero time [9], thereby having a distinct advantage over convolution methods employing a structural damping model in that they may be safely employed to predict transient response.

Our recent work has emphasized the fractional calculus approach to modeling materials usually considered viscoelastic. Both three-parameter models, of the form,

$$\sigma(t) = G_0\epsilon(t) + G_1 D^\alpha[\epsilon(t)], \tag{1}$$

and five-parameter models, of the form,

$$\sigma(t) + bD^\beta[\sigma(t)] = G_0\epsilon(t) + G_1 D^\alpha[\epsilon(t)] \tag{2}$$

have been explored. Here, $\sigma(t)$ and $\epsilon(t)$ are the stress and strain histories, and b, G_0, G_1, α, and β are parameters of the model to be determined by least-squares fits to experimental data. Four-parameter models reduced from the five-parameter model by setting $\alpha = \beta$ are especially attractive. Models for 30 materials have been established [11].

Fractional differentiation is an operator that generalizes the order of differentiation to fractional values. It is the inverse of the operation of fractional integration attributed to Riemann and Liouville. The fractional derivative of order α is defined [12] as

$$D^\alpha[x(t)] \equiv \frac{1}{\Gamma(1-\alpha)} \frac{d}{dt} \int_0^t \frac{x(\tau)}{(t-\tau)^\alpha} d\tau \quad 0<\alpha<1. \tag{3}$$

The fractional derivative model, equation (2), portrays the mechanical properties of materials in the rubbery region, through the transition region, and into the glassy region. For a typical material, this spans six or more decades of frequency.

In view of the surprising success that has been obtained with an empirical model containing so few parameters, one is inclined to ask if there might not be a theoretical basis behind the model. Such a basis has been found, and is reported elsewhere [13]. Nonetheless, fractional derivatives are a somewhat unusual means of describing the behavior of real materials and we believe it of interest to demonstrate that the

[1] Formerly, Graduate Student, Air Force Institute of Technology.

Contributed by the Applied Mechanics Division for presentation at the 1984 PVP Conference and Exhibition, Joint with Applied Mechanics Division and Materials Division, San Antonio, Texas, June 17–21, 1984 of THE AMERICAN SOCIETY OF MECHANICAL ENGINEERS.

Discussion on this paper should be addressed to the Editorial Department, ASME, United Engineering Center, 345 East 47th Street, New York, N.Y. 10017, and will be accepted until two months after final publication of the paper itself in the JOURNAL OF APPLIED MECHANICS. Manuscript received by ASME Applied Mechanics Division, July, 1982. Paper No. 84-APM-23.

Copies will be available until February, 1985.

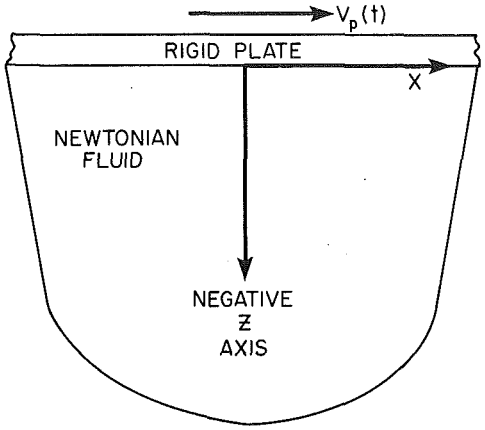

Fig. 1 Semi-infinite fluid sheared by rigid plate

response of a system containing familiar natural elements can be expressed in terms of fractional derivatives.

A Fractional Derivative Relationship for a Homogeneous Newtonian Fluid

We have found that a fractional derivative relationship can be identified in the solution to a classic problem in the motion of viscous fluids. In Stoke's Second Problem, one seeks the behavior of a half-space of Newtonian, viscous fluid undergoing the motion induced by the prescribed uniform sinusoidal motion of a plate on the surface. We will consider such a fluid half-space, initially at rest, and permit the plate at the boundary to commence a general transverse motion, as in Fig. 1. We will show that the resulting shear stress at any point in the fluid can be expressed directly in terms of a fractional order time derivative of the fluid velocity profile.

The equation of motion,

$$\rho \frac{\partial v}{\partial t} = \mu \frac{\partial^2 v}{\partial z^2}, \tag{4}$$

is the diffusion equation, where ρ is the fluid density, μ is the viscosity, and v is the profile of the transverse fluid velocity; a function of time, t, and the distance, z, from the "wetted" plate.

By taking the Laplace transform, we obtain an ordinary differential equation

$$\rho[s\bar{v}(s,z) - v(0,x)] = \mu \frac{d^2\bar{v}(s,z)}{dz^2}, \tag{5}$$

where

$$\bar{v}(s,z) = \int_0^\infty e^{-st} v(t,z)\, dt = \mathcal{L}[v(t,z)] \tag{6}$$

and $v(0,z)$ is the initial velocity profile in the fluid. If we take the initial velocity of the fluid to be zero and apply the boundary conditions, that the velocity of the fluid at the "wetted" plate must match the velocity of the plate, $v_p(t)$, and that the velocity of the fluid in the half-space must be bounded, we have:

$$\bar{v}(s,z) = \bar{v}_p(s) e^{\left(\frac{\rho s}{\mu}\right)^{1/2} z} \tag{7}$$

where $\bar{v}_p(s)$ is the transform of the prescribed velocity of the plate.

Having obtained the transform of the velocity profile in the fluid, $\bar{\sigma}(s,z)$, by writing the transformed shear stress relationship for the Newtonian fluid,

$$\sigma(t,z) = \mu \frac{\partial v(t,z)}{\partial z} \tag{8}$$

$$\bar{\sigma}(s,z) = \mu \frac{\partial \bar{v}(s,z)}{dz} \tag{9}$$

The resulting expression for the transform of the stress in terms of the transform of the velocity, equation (7), is

$$\bar{\sigma}(s,z) = \sqrt{\mu\rho}\sqrt{s}\, \bar{v}(s,z) \tag{10}$$

We can bring this transform back into the time domain by observing it to be the product of two transforms.

$$\bar{\sigma}(s,z) = \sqrt{\mu\rho}\, \frac{1}{\sqrt{s}}\, s\bar{v}(s,z) \tag{11}$$

$$\bar{\sigma}(s,z) = \sqrt{\mu\rho}\, \mathcal{L}\left[\frac{1}{\Gamma(1/2)t^{1/2}}\right] \cdot \mathcal{L}\left[\frac{\partial v}{\partial t}\right] \tag{12}$$

Thus, the stress is the convolution of two functions of time, or

$$\sigma(t,z) = \frac{\sqrt{\mu\rho}}{\Gamma(1/2)} \int_0^t \frac{\frac{\partial}{\partial \tau} v(\tau,z)}{(t-\tau)^{1/2}}\, d\tau \tag{13}$$

Since the initial velocity profile, $v(0,z)$, was taken to be zero, equation (13) can be shown to be equivalent to

$$\sigma(t,z) = \sqrt{\mu\rho}\, \frac{1}{\Gamma(1/2)} \frac{\partial}{\partial t} \int_0^t \frac{v(\tau,z)}{(t-\tau)^{1/2}}\, d\tau \tag{14}$$

The expression in the brackets is precisely in the form of a derivative of fractional order with respect to time, as defined in equation (3). The order of the differentiation is 1/2, and the partial derivative is indicated because the convolution integral is a function of t and z. In operator format, equation (14) becomes

$$\sigma(t,z) = \sqrt{\mu\rho} D_{(t)}^{1/2}[v(t,z)] \tag{15}$$

The subscript, t, in parentheses, is used to denote that the fractional differentiation is with respect to time. The form of this solution is similar to that found by Donaldson [14] in presenting general solutions to the diffusion equation by using fractional calculus.

Although equation (15) appears to be an unusual relationship between stress and velocity, it should be recalled that it was obtained by requiring the satisfaction of the customary stress-velocity relationship for a Newtonian fluid. Equation (15) is not the constitutive relationship for the Newtonian fluid. The constitutive relationship is equation (8). Equation (15), however, does describe the relationship between stress and velocity everywhere in the fluid for this particular geometry (semi-infinite fluid domain) and loading (prescribed velocity at the boundary). The importance of this, in the present context, is that a fractional derivative has been shown to describe the behavior of a real, physical system, without resorting to empiricism.

Motion of an Immersed Plate

Consider now the rigid plate of mass m immersed in a Newtonian fluid of infinite extent and connected by a massless spring of stiffness K to a fixed point. The system is depicted in Fig. 2. We assume that the small motions of the spring do not disturb the fluid, and that the area of the plate, A, is sufficiently large as to produce in the fluid adjacent to the plate the velocity field and stresses developed in the preceding section, see equations (7) and (15).

Summing forces on the plate, we find the differential equation describing the displacement, X, of the plate to be

$$m\ddot{X} = F_x = -K X - 2A\, \sigma(t,0) \tag{16}$$

Substituting the stress from equation (15), and using $V_p(t,0) = \dot{X}(t)$, we arrive at the somewhat surprising result

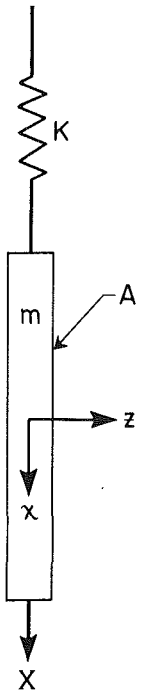

Fig. 2 The immersed plate

$$m\frac{d^2X}{dt^2}+2A\sqrt{\mu\,\rho}D^{3/2}_{(t)}X+K\,X=0 \tag{17}$$

where

$$D^{3/2}X\equiv D^{1/2}\frac{dX}{dt}=\frac{d}{dt}D^{1/2}X \tag{18}$$

Thus, the fractional derivative is found to appear in the differential equation which describes the motion of a simple, physical system consisting of familiar mechanical and fluid components. Moreover, its presence may be anticipated in any system characterized by localized motion in a viscous fluid. Such is the case for oscillations of a polymeric material. We believe this accounts for the success of a fractional derivative in modeling these materials.

Application to Transient Response of an Elastomer

A three-parameter model, equation (1), was developed to fit experimental data for 3-M 467[2] adhesive at 75°F. Data [15] obtained under steady sinusoidal oscillation were used. Parameters were found to be

α = 0.56

G_0 = 1.0 lb/in.^{2}

G_1 = 7.3 lb-sec$^{0.56}$/in.^{2}

The data and the model are compared in Fig. 3. A transient experiment was designed as the most effective means of testing the ability of the model to predict behavior over a wide range of frequencies. Pads of 3-M 467 material were used as a viscoelastic spring in the one degree-of-freedom system shown in Fig. 4. Details of the experiment are given elsewhere [9].

The specific objective was to compare measured and predicted values of the acceleration transfer function, i.e., the ratio of the transforms of the acceleration-time history to the force-time history. The oscillator mass was tapped with an impedance head. The output (the force-time history) and the

[2] 3-M 467 is a product of the Minnesota Mining and Manufacturing Company, St. Paul, Minnesota.

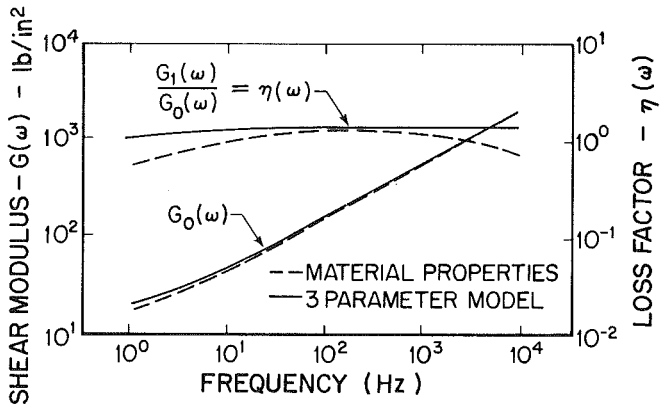

Fig. 3 Material properties of 3M-467 and predictions of three-parameter model

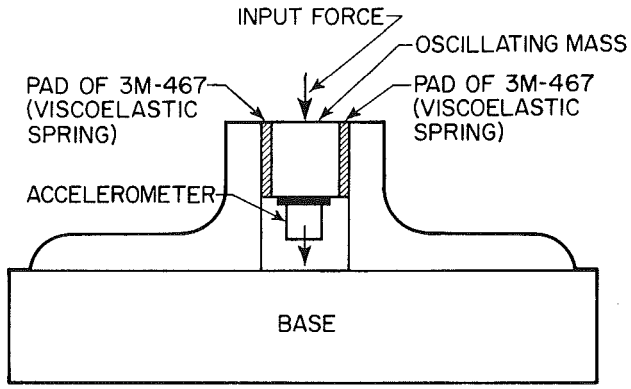

Fig. 4 Single degree-of-freedom system with viscoelastic spring

output of the accelerometer were each sampled at 2×10^4 measurements per sec. All frequencies above 8Khz level were filtered. Both transforms were computed by using fast Fourier transforms.

A transfer function was predicted for the system by assuming a state of pure shear in each pad,

$$\epsilon(t)=x(t)/\delta \tag{19}$$

Where $x(t)$ is the displacement of the oscillator, and δ is the pad thickness.

The restoring force on the oscillator is then

$$f_p(t)=\frac{2A}{\delta}\,(G_0+G_1D^{\alpha}_{(t)})x(t) \tag{20}$$

Here A is the area of each shear pad and the stress-strain relationship is taken to be the three-parameter model.

The equation relating the applied force and the acceleration is then

$$f(t)=m\,\ddot{x}(t)+f_p(t) \tag{21}$$

Taking the Fourier transform of the equations of motion, equations (20) and (21), enables an acceleration transfer function to be determined. The result is:

$$\frac{(i\omega)^2X(\omega)}{F(\omega)}=\left\{m+\frac{2A}{\delta}\,\frac{[G_0+G_1(i\omega)^{\alpha}]}{(i\omega)^2}\right\}^{-1} \tag{22}$$

Experiments with five different combinations of mass and pad area were conducted. The transfer function for each case was obtained by averaging six runs. Values of system parameters for two cases are given in Table 1. The results of each experiment were then compared with the prediction, equation (22). In all cases, both amplitude and phase were found to be in satisfactory agreement. Results for Case 1 (Figs. 5 and 6) and Case 5 (Figs. 7 and 8) are typical of those obtained. Further comparisons are to be found in [9].

Table 1 System parameters for oscillators

Case	Mass (including accelerometer)	Pad thickness (δ)	Pad areas (s)
1	18.8×10^{-3} slug	2.2×10^{-2} in.	1.55 in.^{2}
5	3.48×10^{-3} slug	2.0×10^{-2} in.	0.555 in.^{2}

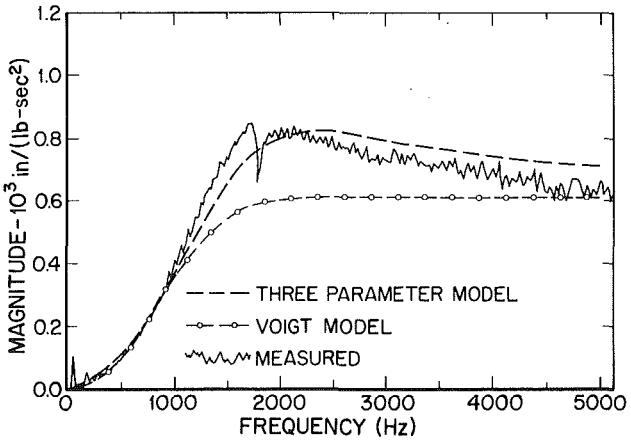

Fig. 5 The magnitude of the transfer function for Case 1

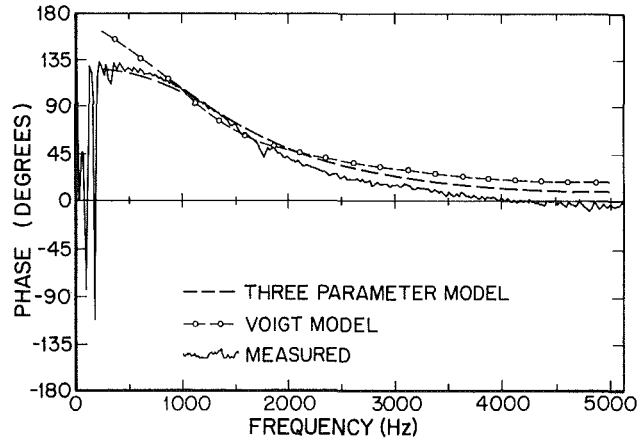

Fig. 6 The phase of the transfer function for Case 1

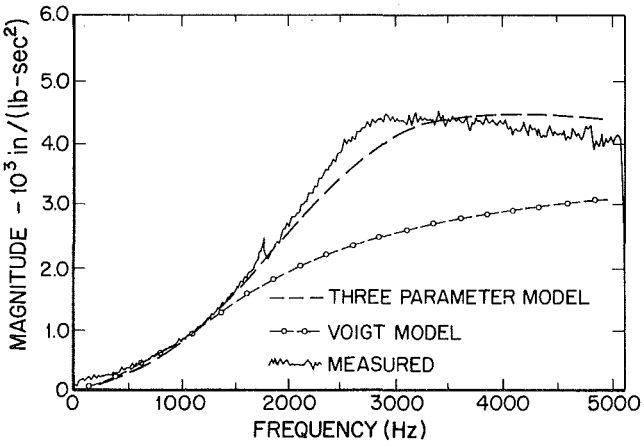

Fig. 7 The magnitude of the transfer function for Case 5

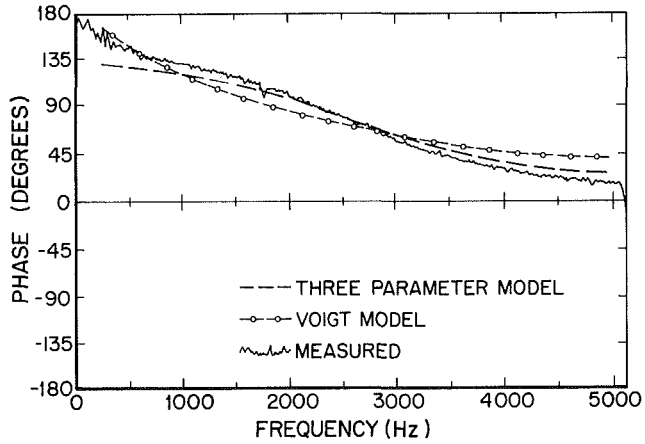

Fig. 8 The phase of the transfer function for Case 5

For purposes of comparison, the 3M-467 adhesive was also modeled as a Voigt solid. Parameters chosen to match the sinusoidal data at 1 Khz led to a constitutive relationship:

$$\sigma(t) = G_0\,\epsilon(t) + G_1\,\dot{\epsilon}(t) \tag{23}$$

$$G_0 = 630 \text{ lb/in.}^2 \tag{24}$$

$$G_1 = 0.113 \text{ lb-sec/in.}^2 \tag{25}$$

Predictions of the acceleration transfer function for this constitutive relationship may be obtained from equation (22) with $\alpha = 1$. Some results are given on Figs. 5–8, and additional comparisons in [9]. In all cases, the predictions of the Voigt model deviate significantly at frequencies much above the frequency (1 Khz) used for parameter determination. The mid-frequency prediction would be improved by choosing model parameters at a higher frequency, but the improvement would be at the expense of agreement at the lower frequency. The superior ability of the three-parameter model with a fractional derivative to predict quantitatively the transfer function over a range of frequencies and a variety of systems is evident. There is, however, a qualitative distinction between the predictions of the Voigt model and those of the three-parameter model which may be even more significant. The transfer function for the Voigt model is a monotonically increasing function for any possible choice of model parameters. The data, on the other hand, clearly show the presence of a maximum, as do the predictions of the three-parameter model. Thus, the advantage of the improved description of the frequency-dependent modulus afforded by the three-parameter model is evident even for the relatively narrow range of frequencies occurring in this realistic simulation of the transient response of a damped structure.

Summary and Discussion

Fractional derivatives have been used to describe the behavior of viscoelastic materials, but their use has been viewed as a somewhat artificial means of generating constitutive equations. We have shown here that the fractional derivative arises naturally if a familiar system, the rigid plate bounded by a Newtonian fluid, is viewed in a certain way. Stresses at any point in the interior of the fluid in motion were found to be proportional to a fractional derivative of the local velocity.

A consequence of this is the somewhat surprising results that the in-plane oscillations of a rigid plate immersed in a Newtonian fluid do *not* generate a retarding force proportional to the velocity. Rather, the retarding force is found to be proportional to a fractional derivative of order 3/2 of the displacement. This occurs because the depth of fluid participating in the motion is not the same for all motion, as it is

in a fully developed steady flow. The phenomena may be best understood by considering such a plate to be in simple harmonic motion. At a high frequency, only a thin boundary layer is excited; thus the average shear stress *in the Newtonian fluid* is high. At a lower frequency, the same amplitude of plate motion allows a greater depth of fluid to participate in the motion. Consequently, the shear stress in the Newtonian fluid is less. Since the excitation of the fluid is a process of diffusion, rather than wave propagation, and the diffusion time is governed by the period of the oscillation, the penetration distances (and therefore the average shear stress) depend on the square root of the frequency. Such a dependence in the frequency domain is associated with a temporal dependence of the "one-half" derivative. Thus, fractional derivatives are shown to occur naturally in systems containing Newtonian fluids.

Data for the elastomer 3M-467 was found to be well described by a three-parameter model, with stress being proportional to strain and to the "0.56" time derivative of strain. The model, obtained from data for sinusoidal motion, was used to predict response of a single degree-of-freedom oscillator to an impulse. A comparison of the predicted and observed acceleration transfer functions showed good agreement, and the fractional derivative model was observed to be both qualitatively and quantitatively superior for this prediction to a Voigt model of the same material.

The fractional derivative appears naturally in the behavior of real materials. Thus, there is some basis for suspecting that the utility of constitutive relationships involving fractional derivatives for describing the behavior of real materials may not be just a happy coincidence.

Acknowledgment

The authors are indebted to Dr. John R. Shea, formerly of the faculty of the Air Force Institute of Technology and now a member of the staff of the Institute for Defense Analysis for helpful discussions on the Stokes' problem, and to the staff of the Materials Laboratory, Air Force Wright Aernautical Laboratories for assistance in the experiments herein described. Some of this work is taken from a dissertation by the junior author submitted to the Air Force Institute of Technology in partial fulfillment of the requirements for the Doctor of Philosophy.

References

1 Nutting, P. G., "A New Generalized Law of Deformation," *Journal of the Franklin Institute*, Vol. 191, pp. 679-685.

2 Gemant, A., "A Method of Analyzing Experimental Results Obtained from Elasto-Viscous Bodies," *Physics*, Vol. 7, 1936, pp. 311-317.

3 Gemant, A., "On Fractional Differentials," *Philosophical Magazine*, Vol. 25, 1938, pp. 540-549.

4 Graham, A., "The Phenomenological Method in Rheology," *Research*, London, 1953, pp. 92-96.

5 Caputo, M., *Elasticita e Dissipazione*, Zanichelli, Bologna, 1969.

6 Caputo, M., "Vibrations of an Infinite Plate With a Frequency Independent Q," *J. Acoust. Soc. Am.*, Vol. 60, 1976, pp. 632-637.

7 Caputo, M., and Minardi, F., *Pure Appl. Geophys.*, Vol. 91, 1971, pp. 134-137.

8 Bagley, R. L., and Torvik, P. J., "A Generalized Derivative Model for an Elastomer Damper," *Shock and Vibration Bulletin*, No. 49, Part 2, Sept. 1979.

9 Bagley, R. L., *Applications of Generalized Derivatives to Viscoelasticity*, Ph.D. dissertation, Air Force Institute of Technology, 1979; also published as AFML-TR-79-4103, Nov. 1979.

10 Bagley, R. L., and Torvik, P. J., "Fractional Calculus—A Different Approach to the Finite Element Analysis of Viscoelastically Damped Structures," *AIAA Journal*, Vol. 21, No. 5, 1983, pp. 741-748.

11 Bagley, R., L., "Fractional Derivative Models for a Family of Corning Glasses," Technical Report to be published by the Air Force Wright Aeronautical Laboratories.

12 Ross, B., "A Brief History and Exposition of the Fundamental Theory of Fractional Calculus," *Lecture Notes in Mathematics*, Vol. 457, Springer, Verlag, New York, 1975, pp. 1-36.

13 Bagley, R. L., and Torvik, P. J., "A Theoretical Basis for the Application of Fractional Calculus to Viscoelasticity," *Journal of Rheology*, Vol. 27, No. 3, 1983, pp. 201-210.

14 Donaldson, J. A., "A Family of Integral Representatives for the Solutions of the Diffusion Equation," *Lecture Notes in Mathematics*, Vol. 457, Spring-Verlag, New York, 1975, pp. 147-150.

15 Jones, D. I. G., Personal Communication.

Applications of Fractional Calculus to the Theory of Viscoelasticity

R. C. Koeller
Department of Mechanical Engineering,
University of Colorado,
Denver, Colo. 80202

The connection between the fractional calculus and the theory of Abel's integral equation is shown for materials with memory. Expressions for creep and relaxation functions, in terms of the Mittag-Leffler function that depends on the fractional derivative parameter β, are obtained. These creep and relaxation functions allow for significant creep or relaxation to occur over many decade intervals when the memory parameter, β, is in the range of 0.05–0.35. It is shown that the fractional calculus constitutive equation allows for a continuous transition from the solid state to the fluid state when the memory parameter varies from zero to one.

1 Introduction

Volterra [1, 2] was an early contributor to the study of materials with memory and was a major contributor to the theory of integral equations that is associated with viscoelasticity. The association and exploitation of integral equations with viscoelasticity have been given by Rabotnov [3]. Gurtin and Sternberg [4] use the concept of Stieltjes Convolution in their review article on the linear theory of viscoelasticity. The treatment of viscoelasticity as a model made up of springs and dashpots is discussed in most books on viscoelasticity [5–8].

The concept of using fractional calculus in the formulation of constitutive equations for materials with memory has been proposed many times during the last 60 years. A review of the early contributors of the application of fractional calculus to viscoelasticity has been given in a recent paper by Bagley and Torvik [9]. In this paper they show that fractional calculus models of viscoelastic materials are in harmony with the molecular theories describing the behavior of viscoelastic materials. A general fractional calculus polynomial operator constitutive equation was introduced by Bagley [10] and Bagley and Torvik [11]. They applied this fractional polynomial operator equation to study damped structures and showed that the motion of the structure can be determined using a small number of empirical parameters. Roger [12] extends Bagley and Torvik's theory to include temperature effects by means of the temperature shift function. He then uses Bode diagrams to find values of the parameters of the complex modulus which is a ratio of polynomials of fractional order in reduced frequency.

In this paper I will show the connection of fractional calculus to the theory of linear viscoelasticity as well as generalize some of the concepts of Rabotnov's theory [3]. It will be shown that Rabotnov's theory of Hereditary Solid Mechanics is equivalent to requiring that the stress in the dashpot be proportional to the fractional derivative of the strain in the dashpot. That is, the dashpot in the Kelvin-Voigt and Maxwell models will be replaced by a fractional calculus element, which I call the spring-pot. The spring-pot has the property that its constitutive equation has continuity from the ideal solid state to the ideal fluid state. These fractional calculus models which are presented have corresponding fractional calculus polynomial operator forms and hence can be related to the general constitutive equation of Bagley and Torvik [10, 11]. The method of integral equations used in this paper leads to results that are expressed in terms of the Mittag-Leffler function and has some advantages over the method that uses Laplace transforms. The constitutive equations obtained are within the modern theory of materials with memory. Some of the applications for the use of these fractional calculus models includes structural damping, soil mechanics, material processing, polymer science, and the determination of properties of biological materials.

2 Mathematical Preliminaries

In general the notation of Rabotnov [3] will be used. Consider first some of the important results of the theory of Volterra's integral equation of the second kind with parameter lambda. Volterra's integral equation of the second kind with parameter λ is given by [13–15].

$$u(t) = v(t) + \lambda \int_0^t K(t,\tau)u(\tau)\,d\tau, \tag{2.1}$$

where $u(t)$ is the unknown function, $v(t)$ is the known function, and $K(t,\tau)$ is the known kernal. With the introduction of the Volterra operator K^*, this integral equation may be simply written as

Contributed by the Applied Mechanics Division for presentation at the 1984 PVP Conference and Exhibition, Joint with Applied Mechanics Division and Materials Division, San Antonio, Texas, June 17–21, 1984 of THE AMERICAN SOCIETY OF MECHANICAL ENGINEERS.

Discussion on this paper should be addressed to the Editorial Department, ASME, United Engineering Center, 345 East 47th Street, New York, N.Y. 10017, and will be accepted until two months after final publication of the paper itself in the JOURNAL OF APPLIED MECHANICS. Manuscript received by ASME Applied Mechanics Division, March, 1983; final revision, September, 1983. Paper No. 84-APM-20.

Copies will be available until February, 1985.

$$v=(1-\lambda K^*)u, \tag{2.2}$$

where a Volterra operator K^* is a mapping of functions into functions defined as

$$K^*u=\int_0^t K(t,\tau)u(\tau)d\tau. \tag{2.3}$$

The function $K(t,\tau)$ is called the kernal of the Volterra operator K^*. In both (2.1) and (2.3) the lower limit of integration has been taken to be 0: however, any real number may be taken as the lower limit in the theory of Volterra's integral equation of the second kind. It is easy to show that the set of all Volterra operators form a linear vector space and that multiplication of members of this space is given by

$$M^*=K^*L^*, \tag{2.4}$$

where the kernal $M(t,\tau)$ of M^* is related to the kernals $K(t,\tau)$ of K^* and $L(t,\tau)$ of L^* by

$$M(t,\tau)=\int_\tau^t K(t,s)L(s,\tau)ds. \tag{2.5}$$

The solution to Volterra's integral equation of the second kind may be obtained by the method of successive substitution and it is given by

$$u=[1+\lambda\Gamma^*(\lambda)]v, \tag{2.6}$$

where

$$\Gamma^*(\lambda)=K^*+\lambda K^{*2}+\lambda^2K^{*3}+\ \ldots\ \lambda^{n-1}K^{*n}+\ \ldots\ . \tag{2.7}$$

The Volterra operator $\Gamma^*(\lambda)$ depends on the parameter λ and is sometimes called the resolvent operator of the Volterra operator K^*. The kernal of $\Gamma^*(\lambda)$ will be denoted by $\Gamma(\lambda;t,\tau)$ and it may be written out with the aid of (2.3), (2.4), (2.5) and (2.7). The main results from the theory of Volterra's integral equation, which will be used in the subsequent analysis, are now recorded. If $\Gamma^*(\lambda)$ is the resolvent operator of the Volterra operator K^*, then

$$\begin{gathered}(1-\lambda K^*)^{-1}=1+\lambda\Gamma^*(\lambda),\\ \Gamma^*(\lambda)=K^*(1-\lambda K^*)^{-1},\\ [1-\lambda\Gamma^*(\mu)]^{-1}=1+\lambda\Gamma^*(\lambda+\mu),\\ \Gamma^*(\lambda)\Gamma^*(\mu)=\frac{1}{\lambda-\mu}[\Gamma^*(\lambda)-\Gamma^*(\mu)].\end{gathered} \tag{2.8}$$

In what follows let α be a negative number between -1 and 0 and let $\beta=1+\alpha$, so that β is a positive number between 0 and 1. When the kernal $K(t,\tau)$ of the Volterra operator K^* is a singular kernal of the form

$$K(t,\tau)=G(t,\tau)(t-\tau)^\alpha;\quad -1\le\alpha\le 0, \tag{2.9}$$

then the corresponding integral equation (2.1) is said to be a generalized Abel integral equation [15]. In particular, when the function $G(t,\tau)$ is equal to the reciprocal of the Gamma function evaluated at $1+\alpha$, the kernal $K(t,\tau)$ is called the Abel kernal and the corresponding Volterra operator is called the Abel operator. Following Rabotnov [3], denote the Abel operator by I_α^* and its kernal by

$$I_\alpha(t)=\frac{t^\alpha h(t)}{\Gamma(1+\alpha)};\quad -1\le\alpha\le 0, \tag{2.10}$$

where $\Gamma(x)$ is the Gamma function and $h(t)$ is the Heaviside unit step function. The resolvent of the Abel operator I_α^* will be denoted by $\mathcal{E}_\alpha^*(\lambda)$ and its kernal by $\mathcal{E}_\alpha(\lambda;t)$. The kernal of $\mathcal{E}_\alpha^*(\lambda)$ is called the fractional exponential function and it is given by

$$\mathcal{E}_\alpha(\lambda;t)=t^\alpha\sum_{n=0}^\infty\frac{\lambda^n t^{n(1+\alpha)}}{\Gamma[(1+n)(1+\alpha)]}. \tag{2.11}$$

The Abel operator's kernal is a difference kernal so that the theory of viscoelasticity based on the Abel operator will be a nonaging theory. The Abel operator I_α^* and its resolvent $\mathcal{E}_\alpha^*(\lambda)$ satisfy the general equations (2.8), that is

$$\begin{gathered}(1-\lambda I_\alpha^*)^{-1}=1+\lambda\mathcal{E}_\alpha^*(\lambda),\\ \mathcal{E}_\alpha^*(\lambda)=I_\alpha^*(1-\lambda I_\alpha^*)^{-1},\\ [1-\lambda\mathcal{E}_\alpha^*(\mu)]^{-1}=1+\lambda\mathcal{E}_\alpha^*(\lambda+\mu),\\ \mathcal{E}_\alpha^*(\lambda)\mathcal{E}_\alpha^*(\mu)=\frac{1}{\lambda-\mu}[\mathcal{E}_\alpha^*(\lambda)-\mathcal{E}_\alpha^*(\mu)].\end{gathered} \tag{2.12}$$

Additional relationships which will be used in the subsequent development are

$$\begin{gathered}I_{\alpha_1}^*I_{\alpha_2}^*f(t)=I_{1+\alpha_1+\alpha_2}^*f(t),\\ D^nI_\alpha^*f(t)=I_\alpha^*D^nf(t),\end{gathered} \tag{2.13}$$

and

$$\mathcal{E}_\alpha^*(\lambda)h(t)=\frac{1}{\lambda}[E_\beta(\lambda t^\beta)-1]h(t), \tag{2.14}$$

where $D=d/dt$, n is an integer, $f(t)$ is an arbitrary member of the Heaviside class of functions, and $E_\beta(x)$ is the Mittag-Leffler function [16-18]. The Mittag-Leffler function is defined by

$$E_\beta(x)=1+\sum_{n=1}^\infty\frac{x^n}{\Gamma(1+\beta n)}, \tag{2.15}$$

and its asymptotic expansion [18, 19], is

$$E_\beta(x)\sim-\sum_{n=1}^\infty\frac{x^{-n}}{\Gamma(1-\beta n)}. \tag{2.16}$$

In particular, when $\alpha=0$ or $\beta=1$, the Mittag-Leffler function is $\exp(x)$. Also for $\alpha=0$ the Abel operator is just integration and when $\alpha=1$ it is the identity operator, that is

$$I_0^*f(t)=\int_0^t f(\tau)d\tau,\quad I_{-1}^*f(t)=f(t). \tag{2.17}$$

To relate the fractional calculus to the theory of Abel's integral equation, a summary of some of the important results of the fractional calculus [20-23] will be given. Integration of fractional order β is denoted by the operator $D^{-\beta}$ and is taken to be

$$D^{-\beta}f(t)=\int_0^t\frac{(t-\tau)^{\beta-1}}{\Gamma(\beta)}f(\tau)d\tau. \tag{2.18}$$

A set of Riemann-Liouville fractional integrals are given in Volume 2 of the *Tables of Integral Transforms* [24]. Since $\beta=1+\alpha$, the fractional integral (2.18) is related to the Abel operator I_α^*(2.10) by

$$D^{-\beta}f(t)=I_\alpha^*f(t). \tag{2.19}$$

Fractional differentiation for $\beta\epsilon[0.1]$ may be defined by [23,24]

$$D^\beta f(t)=DD^{\beta-1}f(t). \tag{2.20}$$

Since $\beta-1$ is negative it follows from (2.18) that

$$D^{\beta-1}f(t)=\int_0^t\frac{(t-\tau)^{-\beta}}{\Gamma(1-\beta)}f(\tau)d\tau, \tag{2.21}$$

so that fractional differentiation as defined by (2.20) is related to the Abel operator by

$$D^\beta f(t)=DI_{-\beta}^*f(t) \tag{2.22}$$

From (2.19) one finds

$$D^\beta I_\alpha^*f(t)=f(t), \tag{2.23}$$

and hence $D^\beta I_\alpha^*=I_\alpha^*D^\beta=1$, if $f(0)=0$. This completes the mathematical introduction to this paper.

I conclude this section with a summary of the constitutive equations of the linear theory of viscoelasticity. Let σ_{ij} be the cartesian components of the stress tensor and ϵ_{ij} be the cartesian components of the infinitesimal strain tensor, then by

the Riesz representation of linear functionals [4], the constitutive equation for a nonaging linear viscoelastic material is

$$\sigma_{ij}(t) = (G_{ijkl} * d\epsilon_{kl})(t) = \int_{-\infty}^{t} G_{ijkl}(t-\tau) d\epsilon_{kl}(\tau), \tag{2.24}$$

where $*$ denotes the Stieltjes convolution and $G_{ijkl}(t)$ are the cartesian components of the relaxation modulus tensor. The inverse relation of (2.24) is

$$\epsilon_{ij}(t) = (J_{ijkl} * d\sigma_{kl})(t) = \int_{-\infty}^{t} J_{ijkl}(t-\tau) d\sigma_{kl}(\tau), \tag{2.25}$$

where $J_{ijkl}(t)$ are the cartesian components of the creep compliance tensor. When σ_{ij} and ϵ_{ij} are members of the Heaviside Class, then (2.24) and (2.25) may be written as

$$\sigma_{ij}(t) = G_{ijkl}(0^+)\epsilon_{kl}(t) + \int_{0^+}^{t} \epsilon_{kl}(t-\tau) \frac{dG}{dt} ijkl(\tau) d\tau, \tag{2.26}$$

and

$$\epsilon_{ij}(t) = J_{ijkl}(0^+)\sigma_{kl} + \int_{0^+}^{t} \sigma_{kl}(t-\tau) \frac{dJ}{dt} ijkl(\tau) d\tau, \tag{2.27}$$

respecively. Equations (2.26) and (2.27) may be put into the form of a system of Volterra's integral equations if one introduces the following notation

$$\frac{dG}{dt} ijkl(t) = \lambda \Gamma_{ijpq}(t) G_{pqkl}(0^+), \tag{2.28}$$

and

$$\frac{dJ}{dt} ijkl(t) = -\lambda J_{ijpq}(0^+) K_{pqkl}(t), \tag{2.29}$$

where $K_{ijkl}(t)$ are the cartesian components of the difference kernal of the integral equation and $\Gamma_{ijkl}(t)$ are the cartesian components of the resolvent kernal. Substitution of (2.29) and (2.28) into (2.27) and (2.26), respectively, and rearranging terms one finds

$$G_{ijkl}(0^+)\epsilon_{kl} = (\delta_{ik}\delta_{jl} - \lambda K^*_{ijkl})\sigma_{kl}, \tag{2.30}$$

and

$$\sigma_{ij} = (\delta_{ip}\delta_{jq} + \lambda \Gamma^*_{ijpq}) G_{pqkl}(0^+)\epsilon_{kl}. \tag{2.31}$$

The creep function and relaxation function are related to these kernals by

$$J_{ijkl}(t) = J_{ijpq}(0^+)\left[\delta_{pk}\delta_{ql} - \lambda \int_0^t K_{pqkl}(\tau) d\tau\right], \tag{2.32}$$

and

$$G_{ijkl}(t) = \left[\delta_{ip}\delta_{jq} + \lambda \int_0^t \Gamma_{ijpq}(\tau) d\tau\right] G_{pqkl}(0^+). \tag{2.33}$$

With the introduction of the tensors $\mathbf{v} = G_{ijkl}(0^+)\epsilon_{kl}\mathbf{e}_i \otimes \mathbf{e}_j$, $\mathbf{u} = \sigma_{ij}\mathbf{e}_i \otimes \mathbf{e}_j$, $\mathbf{K} = K_{ijkl}\mathbf{e}_i \otimes \mathbf{e}_j \otimes \mathbf{e}_k \otimes \mathbf{e}_l$ and $\mathbf{\Gamma} = \Gamma_{ijkl}\mathbf{e}_i \otimes \mathbf{e}_j \otimes \mathbf{e}_k \otimes \mathbf{e}_l$ one obtains the tensor equivalent forms of (2.2) and (2.6). Equations (2.2)–(2.8) remain valid in their tensor equivalent forms. When one restricts attention to the isotropic theory of viscoelasticity then one may express the constitutive equations in terms of two scalar equations.

In what follows I simply write the constitutive equations as

$$\sigma = G * de \quad \text{and} \quad e = J * d\sigma, \tag{2.34}$$

or equivalently in terms of the corresponding Volterra operators as

$$\sigma = G^* \dot{e} \quad \text{and} \quad e = J^* \dot{\sigma}, \tag{2.35}$$

where the correct interpretation of σ and e needs to be made. For example, in the theory of isotropic viscoelasticity the constitutive equations are [4]

$$s_{ij} = G_1 * de_{ij}, \quad \sigma_{kk} = G_2 * d\epsilon_{kk}, \tag{2.36}$$

where s_{ij} are the deviatoric components of the stress tensor and e_{ij} are the deviatoric components of the infintesimal strain tensor.

The application of models made up of springs and dashpots are useful in so far as they give a physical insight to the response of viscoelastic materials due to an input of stress or strain. It must be remembered that the phenomenological foundation of viscoelasticity is based on the theory of materials with memory. For the nonlinear theory it is based on the Volterra-Frechet representation theorem of nonlinear functionals, which in particular for the linear case, is the Riesz representation theorem. These representation theorems do not give explicit mathematical forms for the creep and relaxation functions. The use of springs and dashpots will be generalized to include fractional derivatives and fractional integrals. The fractional derivative element, called a spring-pot, does not have a mechanical interpretation at present, but it is useful to delineate forms for the creep and relaxation functions. It is in this spirit that I generalize the concept of models to include elements that involve fractional derivatives and fractional integrals. The creep and relaxation functions obtained are generalizations of those obtained from the Kelvin-Voigt and Maxwell models and they reduce to these classical results when the parameter β, called the memory parameter, is chosen to be unity. Since differintegral operators of noninteger order are linear functionals which possess the properties of translation-invariance, nonretroactivity, and continuity it is clear that differintegral operators are admissible in the phenomenological theory of hereditary stress-strain laws.

3 Creep and Relaxation Functions for the Fractional Calculus Element

A fractional calculus element is defined as an element whose stress is proportional to the fractional derivative of the strain. Let F be the coefficient of viscosity for a dashpot element and E be the modulus of elasticity for the spring element. A fractional calculus element whose constitutive law satisfies

$$\sigma(t) = F\eta^{\alpha} D^{1+\alpha} e(t), \quad -1 \le \alpha \le 0$$

or equivalently

$$\sigma(t) = E\eta^{\beta} D^{\beta} e(t), \quad 0 \le \beta \le 1 \tag{3.1}$$

is said to be a spring-pot. In the foregoing, $\eta = F/E$ is a characteristic time which will be called the relaxation time or creep time depending on the specific model under consideration. Equation (3.1) contains the two limit cases of a spring and a dashpot, since

$$\lim_{\alpha \to -1} F\eta^{\alpha} D^{1+\alpha} e(t) = F\eta^{-1} D^0 e(t) = Ee(t)$$

and

$$\lim_{\alpha \to 0} F\eta^{\alpha} D^{1+\alpha} e(t) = F\eta^0 De(t) = F\dot{e}(t). \tag{3.2}$$

Thus the element defined by (3.1) has the characteristics of both a spring and dashpot, hence the name spring-pot. When $\beta = 0$ the material has perfect memory and when $\beta = 1$ the material has no memory. For value of β between 0 and 1 the material exhibits memory so that β may be considered to be a nondimensional memory parameter. To find the relaxation modulus for a spring-pot element set $e(t) = h(t)$. The output stress is the relaxation modulus $G(t)$ and it is obtained as follows:

$$G(t)=F\eta^{\beta-1}D^{\beta}h(t)=F\eta^{\beta-1}I^{*}_{-\beta}Dh(t)$$

$$=F\eta^{\beta-1}I^{*}_{-\beta}\delta(t)=F\eta^{\beta-1}\int_0^t\frac{(t-\tau)^{-\beta}}{\Gamma(1-\beta)}h(t-\tau)\delta(\tau)d\tau$$

$$=F\eta^{\beta-1}\frac{t^{-\beta}}{\Gamma(1-\beta)}h(t)=EI_{-\beta}(t/\eta), \tag{3.3}$$

where $\delta(t)$ is the Dirac delta function and use has been made of (2.22), (2.13*b*), (2.10), and the properties of the Abel operator. From (2.17*b*) it follows that $1/t^{\beta}\Gamma(1-\beta)$ has the weak limit $\delta(t)$ as β tends to one. A proof that the Riesz distribution has as its weak limit the Dirac's delta function is given by Güttinger [25, p. 527]. Since $\beta=1+\alpha$, the relaxation modulus of the spring-pot element reduces to that of the dashpot element when $\alpha\to 0$ and to the spring element when $\alpha\to -1$, that is

$$\lim_{\alpha\to 0}G(t)=F\delta(t) \quad \text{and} \quad \lim_{\alpha\to -1}G(t)=Eh(t). \tag{3.4}$$

The strain-stress constitutive relationship for a spring-pot may be obtained from (3.1) and (2.23), so that

$$e(t)=\frac{1}{F\eta^{\alpha}}I^{*}_{\alpha}\sigma(t). \tag{3.5}$$

When $\sigma(t)=h(t)$ the output strain is the creep compliance that is denoted by $J(t)$, thus

$$J(t)=\frac{1}{F\eta^{\alpha}}I^{*}_{\alpha}h(t)=\frac{1}{F\eta^{\alpha}}\int_0^t\frac{(t-\tau)^{\alpha}}{\Gamma(1+\alpha)}h(t-\tau)h(\tau)d\tau$$

$$=\frac{1}{E\eta^{1+\alpha}}\frac{t^{1+\alpha}}{\Gamma(1+\alpha)}h(t)=\frac{1}{E\Gamma(1+\beta)}\left(\frac{t}{\eta}\right)^{\beta}h(t). \tag{3.6}$$

If the notation of the Abel kernal is extended to positive values of the parameter α, then one may write

$$J(t)=\frac{1}{E}I_{\beta}\left(\frac{t}{\eta}\right). \tag{3.7}$$

The two special limit values of the dashpot and spring elements are, respectively,

$$\lim_{\alpha\to 0}J(t)=\frac{t}{F}h(t) \quad \text{and} \quad \lim_{\alpha\to -1}J(t)=\frac{1}{E}h(t). \tag{3.8}$$

The creep compliance of a spring-pot for various values of the memory parameter β is shown in Fig. 1, while the relaxation modulus is plotted in Fig. 2. From these figures it is clear that a wide variety of responses can be obtained when the spring-pot element is combined with either a spring element and/or viscous element.

The fractional calculus representation (3.1) may be put into a Volterra operator form by using (2.22), (2.13*b*), and the definition of η. This results in the following equality

$$\sigma(t)=F\eta^{\beta-1}D^{\beta}e(t)=E\eta^{\beta}I^{*}_{\beta}\dot{e}(t). \tag{3.9}$$

Gerasimov [26] has applied constitutive equations of the Volterra type to the study of internal friction in materials. Bland [6] states that the fractional calculus constitutive equation was suggested by G. W. Scott Blair [27-31]. Scott Blair's format was not put into a form that would clearly indicate the two limiting cases of a spring-pot. The fractional calculus model was motivated by Nutting's [32, 33] observation that the creep rate may be expressed as a simple power law. Gross [34] took the creep compliance as a constant plus a simple power law and then obtained, by the use of the Laplace transform, the corresponding relaxation modulus which he expressed in terms of the Mittag-Leffler function. Slonimsky [35] and Smit and de Vries [36] introduce a model which is an intermediate body between Hooke's elastic body and a Newtonian viscous liquid. They then extend their fractional calculus model, which is a spring-pot, to incorporate a Kelvin-Voigt type body. Stiassnie [37] recently looked into constitutive equations in the format as suggested by Scott Blair. These fractional calculus equations are also described in Bland [6, p. 54]. If one considers a chain of N parallel spring-pots with corresponding $\eta_i=F_i/E_i$ and β_i; $i=1,2,\cdots N$, with the property that the strain of all elements is the same, then

$$\sigma(t)=\sum_{i=1}^{N}\eta_i^{\beta_i-1}F_iD^{\beta_i}e(t). \tag{3.10}$$

In the limit (3.10) becomes

$$\sigma(t)=\int_0^1 E(\beta)[\eta(\beta)]^{\beta}D^{\beta}e(t)d\beta. \tag{3.11}$$

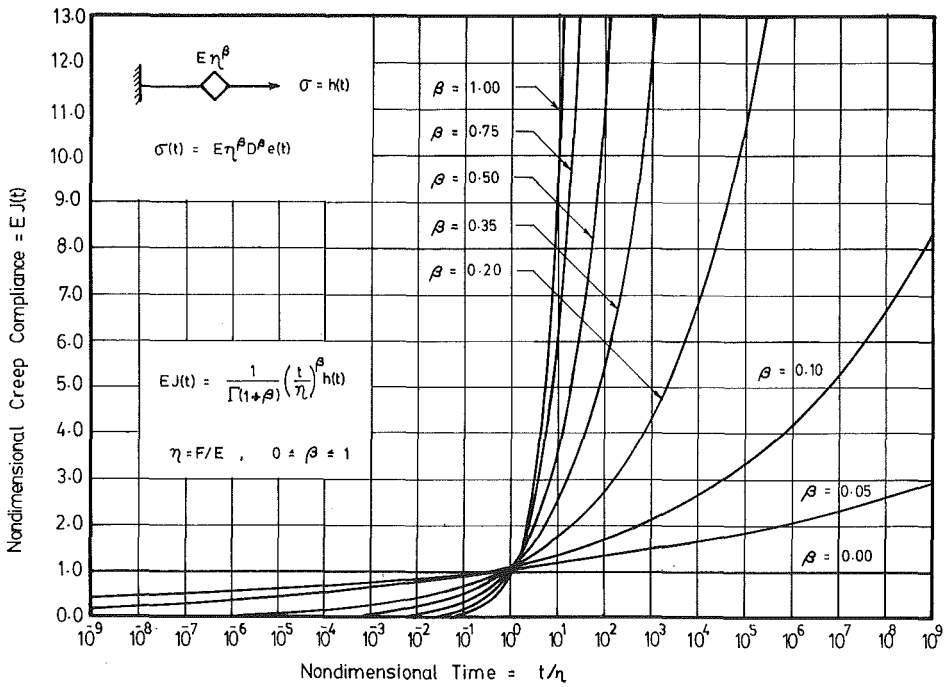

Fig. 1 Creep compliance for a spring-pot

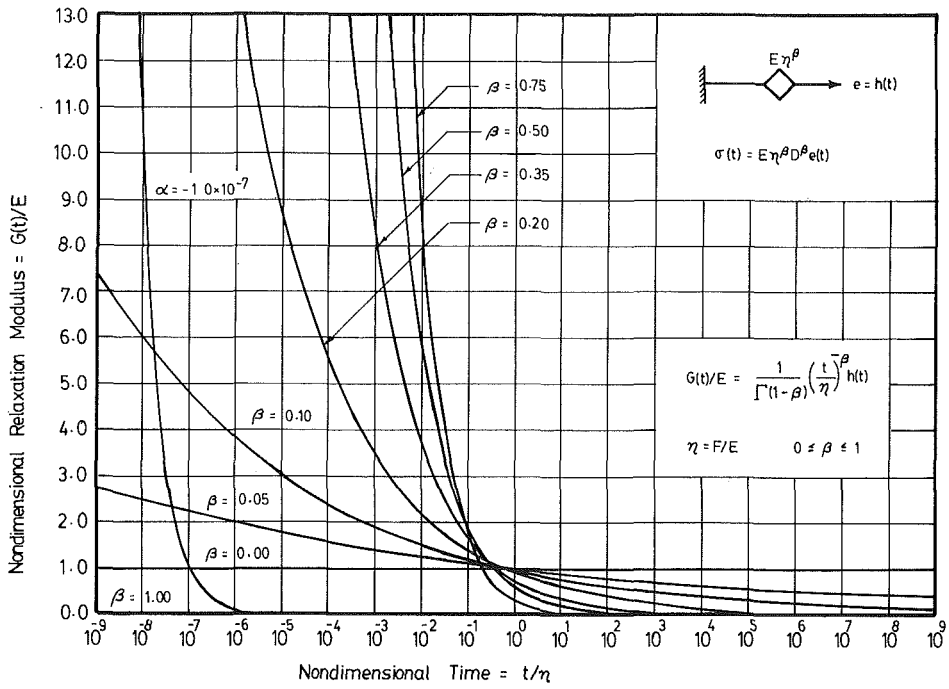

Fig. 2 Relaxation modulus for a spring-pot

Equation (3.11) is a special case of a more general input-output model proposed in [38]. Wainwright's model for the input $x(t)$ and the output $y(t)$ is

$$y(t)=\int_{-\infty}^{\infty} G(\beta)D^{\beta}x(t)\,d\beta, \tag{3.12}$$

where $G(\beta)$ may be continuous or may involve generalized functions. Caputo [39, 40] and Caputo and Mainardi [41] used operators with weighting functions similar to (3.11) or (3.12).

In what follows the viscous element in the Kelvin-Voigt model, as well as the Maxwell model, will be replaced by the spring-pot. Results are then compared to previous proposed fractional calculus models, as well as Rabotnov's theory of Hereditary Solid Mechanics.

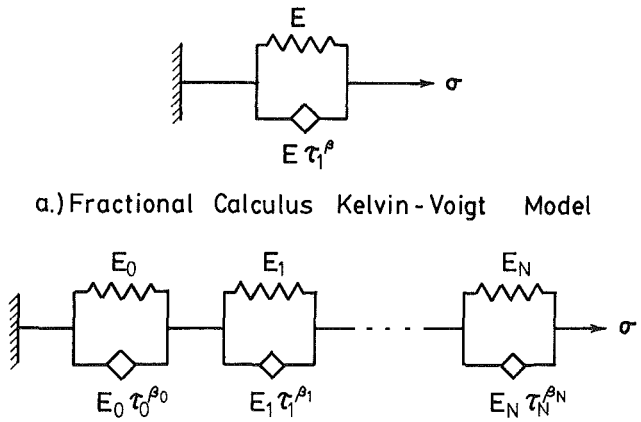

Fig. 3 Fractional calculus Kelvin-Voigt solid models

4 Fractional Calculus Kelvin-Voigt Solid Models

In the study of viscoelasticity the spring and dashpot parallel model, known as the Kelvin-Voigt model, is often used as a first approximation for the study of viscoelastic solids. If the dashpot is replaced by a spring-pot, then the Kelvin-Voigt model will be a fractional calculus model. This model will be called the Kelvin-Voigt fractional calculus solid model. Figure 3(*a*) shows this model where the spring-pot element is displayed like a diamond as suggested by Bagley and Torvik [42]. Since the Kelvin-Voigt model is a characteristic creep model, let $\tau_1 = F/E$ be the corresponding creep time when $\alpha=0$. The stress is the same on both elements so that one obtains

$$\sigma(t)=Ee(t)+{\tau_1}^{\alpha}FD^{1+\alpha}e(t)$$

$$={E\tau_1}^{1+\alpha}\left(D^{1+\alpha}+\frac{1}{{\tau_1}^{1+\alpha}}\right)e(t). \tag{4.1}$$

One obtains the inverse relationship of (4.1) by using (2.23) and the second of (2.12). Thus

$$I_{\alpha}^{*}\sigma(t)={E\tau_1}^{1+\alpha}\left(1+\frac{1}{{\tau_1}^{1+\alpha}}I_{\alpha}^{*}\right)e(t),$$

so that

$$e(t)=\frac{1}{E{\tau_1}^{\beta}}I_{\alpha}^{*}\left[1+\frac{1}{{\tau_1}^{\beta}}I_{\alpha}^{*}\right]^{-1}\sigma(t),$$

or

$$e(t)=\frac{1}{E{\tau_1}^{\beta}}\mathcal{E}_{\alpha}^{*}\left(-\frac{1}{{\tau_1}^{\beta}}\right)\sigma(t), \tag{4.2}$$

where the result of Abel's integral equation (2.12*b*) has been used. To find the creep compliance set $\sigma=h(t)$ in (4.2) and use (2.14) to obtain

$$J(t)=\frac{1}{E}\left\{1-E_{\beta}\left[-\left(\frac{t}{\tau_1}\right)^{\beta}\right]\right\}h(t). \tag{4.3}$$

When $\alpha=0$ or $\beta=1$, equation (4.3) reduces to the well-known creep compliance of a Kelvin-Voigt model, namely

$$J(t)\Big|_{\beta=1}=\frac{1}{E}(1-e^{-t/\tau_1})h(t). \tag{4.4}$$

From (4.1) and (3.3) the relaxation modulus is obtained when one sets $e(t)=h(t)$ and $\sigma(t)=G(t)$. The relaxation modulus for a Kelvin-Voigt fractional calculus model is

$$G(t)=E\left[h(t)+I_{-\beta}\left(\frac{t}{\tau_1}\right)\right], \tag{4.5}$$

and this reduces to the classical results when the spring-pot becomes a dashpot, that is

$$G(t)\Big|_{\beta=1}=E[h(t)+\tau_1\delta(t)]. \tag{4.6}$$

It should be noted that the fractional calculus constitutive equation (4.1) for the Kelvin-Voigt model may be put into the form as given by Rabotnov [3, p. 93] if one uses (2.22) and (2.13*b*), that is

$$\sigma(t)=Ee(t)+E\tau_1{}^{\beta}I^{*}_{-\beta}\dot{e}(t). \tag{4.7}$$

Consider now the general case of a Kelvin-Voigt chain model, where the dashpots are replaced by spring-pots, as shown in Fig. 3(*b*). Special cases may be obtained from this generalized Kelvin-Voigt fractional calculus model by proper selection of coefficients. Since Kelvin-Voigt models are characteristic creep type models, let $\tau_n=F_n/E_n$ be the characteristic creep time of the nth chain, where F_n is the viscosity of the nth spring-pot as α tends to 0 and E_n is the modulus of elasticity of the nth spring-pot as α tends to -1. E_n is also the elastic modulus of the spring in the nth chain and $F_n\tau_n{}^{\alpha_n}=E_n\tau_n{}^{\beta_n}$ is the portionality coefficient of the nth spring pot. For this model the stress is the same in each of the chains, while the total strain is the sum of the strains of the chains. The strain in the nth chain is obtained by a similar procedure as that for a single Kelvin-Voigt fractional calculus model. With $e_n(t)$ as the strain in the nth chain and with corresponding change in the notation of (4.2) one finds that

$$e_n(t)=\frac{1}{E_n\tau_n{}^{\beta_n}}\mathcal{E}^{*}_{\alpha_n}\left(-\frac{1}{\tau_n{}^{\beta_n}}\right)\sigma(t). \tag{4.8}$$

Thus the total strain, which is the sum of the strains of the chains is

$$e(t)=\sum_{n=0}^{N}e_n(t)=\sum_{n=0}^{N}\frac{1}{E_n\tau_n{}^{\beta_n}}\mathcal{E}^{*}_{\alpha}\left(-\frac{1}{\tau_n{}^{\beta_n}}\right)\sigma(t). \tag{4.9}$$

where $N+1$ is the total number of chains in the model. Equation (4.9) represents the strain-stress constitutive equation for the generalized Kelvin-Voigt fractional calculus model. The creep compliance for this model is

$$J(t)=\sum_{n=0}^{N}\frac{1}{E_n}\left\{1-E_{\beta_n}\left[-\left(\frac{t}{\tau_n}\right)^{\beta_n}\right]\right\}h(t), \tag{4.10}$$

where $E_{\beta_n}(x)$ is the Mittag-Leffler function and when $\beta_n=1$ for $n=0, 1, \ldots N$ the classical results are recovered.

In order to have an initial strain due to a suddenly applied stress set the first creep time equal to zero, so that (4.9) becomes

$$e(t)=\left[\frac{1}{E_0}+\sum_{n=1}^{N}\frac{1}{E_n\tau_n{}^{\beta_n}}\mathcal{E}^{*}_{\alpha_n}\left(-\frac{1}{\tau_n{}^{\beta_n}}\right)\right]\sigma(t). \tag{4.11}$$

Under special cases the inverse of this constitutive equation may be obtained by the Laplace transforms method, or by use of the multiplication formula (2.12*d*). Also (4.11) may be expressed as a fractional polynomial operator acting on stress which is equal to another fractional polynomial operator acting on strain. For the case when $N=1$, the inverse is easily obtained with the aid of (2.12*c*) and it is given by

$$\sigma(t)=E_0\left[1-\frac{E_0}{E_1\tau_1{}^{\beta}}\mathcal{E}^{*}_{\alpha}\left(-\frac{1}{t_1{}^{\beta}}\right)\right]e(t), \tag{4.12}$$

where $\beta=\beta_1=F_1/E_1$ and t_1 is the relaxation time given by

$$t_1=\frac{\tau_1}{\sqrt[\beta]{1+E_0/E_1}}. \tag{4.13}$$

Hence the creep compliance and the relaxation modulus for a three-element fractional calculus solid model are

$$J(t)=\frac{1}{E_0}\left\{1+\frac{E_0}{E_1}\left\{1-E_{\beta}\left[-\left(\frac{t}{\tau_1}\right)^{\beta}\right]\right\}\right\}h(t), \tag{4.14}$$

and

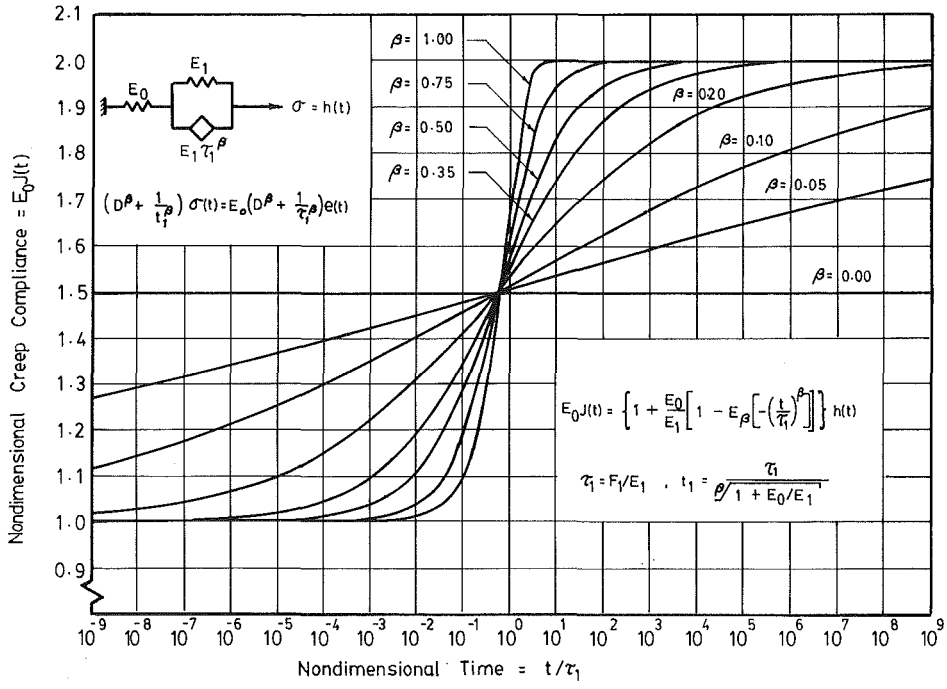

Fig. 4 Creep compliance for a three-element fractional calculus solid model

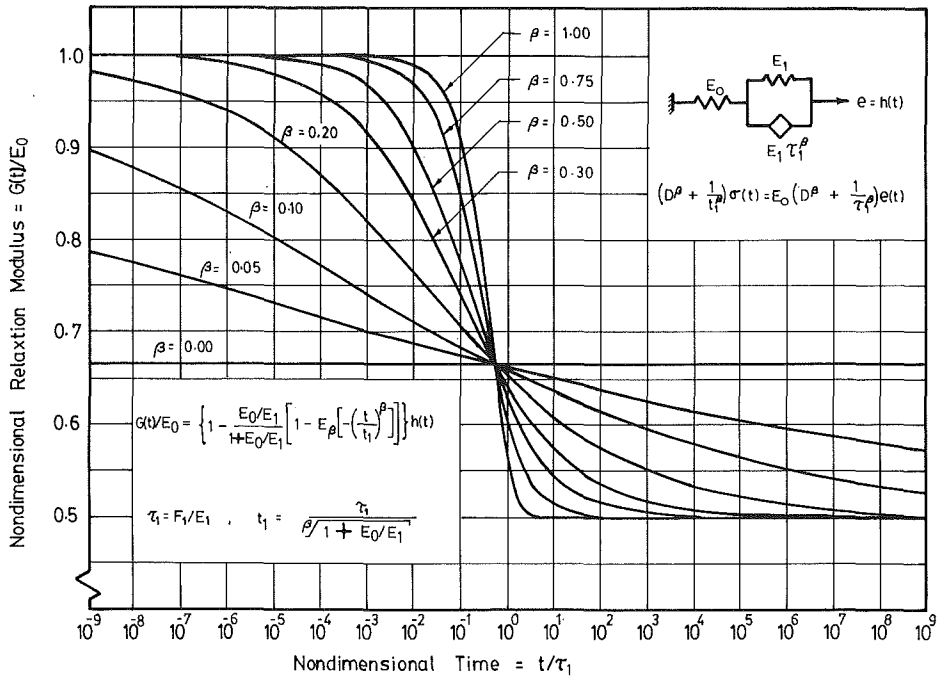

Fig. 5 Relaxation modulus for a three-element fractional calculus solid model

$$G(t)=E_0\left\{1-\frac{E_0/E_1}{1+E_0/E_1}\left\{1-E_\beta\left[-\left(\frac{t}{t_1}\right)^\beta\right]\right\}\right\}h(t), \quad (4.15)$$

respectively. Equation (4.14) is equivalent to Rabotnov's natural approximation to the creep kernel by a fractional exponential function [3, p. 87, and 79]. The fractional differential equation associated with the three-element fractional calculus solid model may be obtained from (4.12), (2.12), (2.23), and (4.13). This results in the following fractional differential equation

$$\left(D^\beta+\frac{1}{t_1^\beta}\right)\sigma(t)=E_0\left(D^\beta+\frac{1}{{\tau_1}^\beta}\right)e(t), \quad (4.16)$$

for the three-element model. The creep and relaxation functions have been obtained by the Laplace transform method in Caputo and Mainardi [41] for a fractional differential equation in the form of (4.16).

Equations (4.14) and (4.15) are plotted nondimensionally on semilogarithmic paper for various values of β and for the case $E_0/E_1=1$. However, due to the form of (4.14) and (4.15) these graphs may be scaled for various other values of E_0/E_1. Since the exponential function of negative arguments varies significantly only over two decade intervals, it follows that for modeling creep or relaxation data the classical three parameter solid, that is the curve $\beta=1$ of Fig. 4 or 5, will not account for viscoelastic behavior that occurs over four decade intervals. Other techniques, such as [43] may be used: however, it should be remembered that relaxation and creep times have physical meaning [44] and thus should be chosen with care. It is seen from Figs. 4 and 5 that a three-element fractional calculus solid model allows for significant creep or relaxation to occur over many decade intervals when β is in the range of 0.05–0.35. If the creep time τ_1 is equal to 1 sec, then these curves represent the time interval from 1 nanosecond to 32 years. At present, the creep time defined by the fractional calculus approach does not have physical meaning and only when $\beta=1$ does it have the usual meaning. Initial reduction of oil shale data indicates that a three element fractional calculus solid model gives very good agreement with the experimental data.

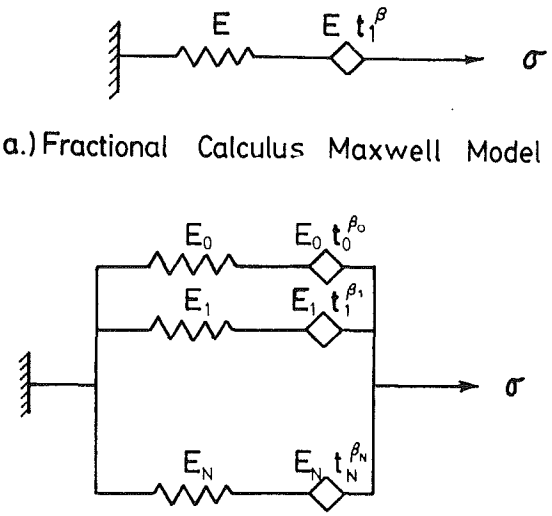

Fig. 6 Fractional calculus Maxwell fluid models

5 Fractional Calculus Maxwell Fluid Models

Rabotnov limits his discussion to viscoelastic solids, but it is straightforward to extend the concepts to viscoelastic fluids. First I will obtain the creep and relaxation functions for a Maxwell model when the dashpot is replaced by a spring-pot and then I will discuss the generalization of this model. Figure 6(*a*) shows the fractional calculus Maxwell model where the spring-pot element is displayed like a diamond. It is clear that this model allows for an instantaneous response and a continuous flow. Since this model is a characteristic relaxation model let $t_1=F/E$, where F and E are the coefficients of the spring-pot for its limiting values of α. Now for this model the total strain is the sum of the strain in the spring and spring-pot. From (3.5) the strain in the spring-pot is $(1/Et_1{}^\beta)I_\alpha^*\sigma(t)$,

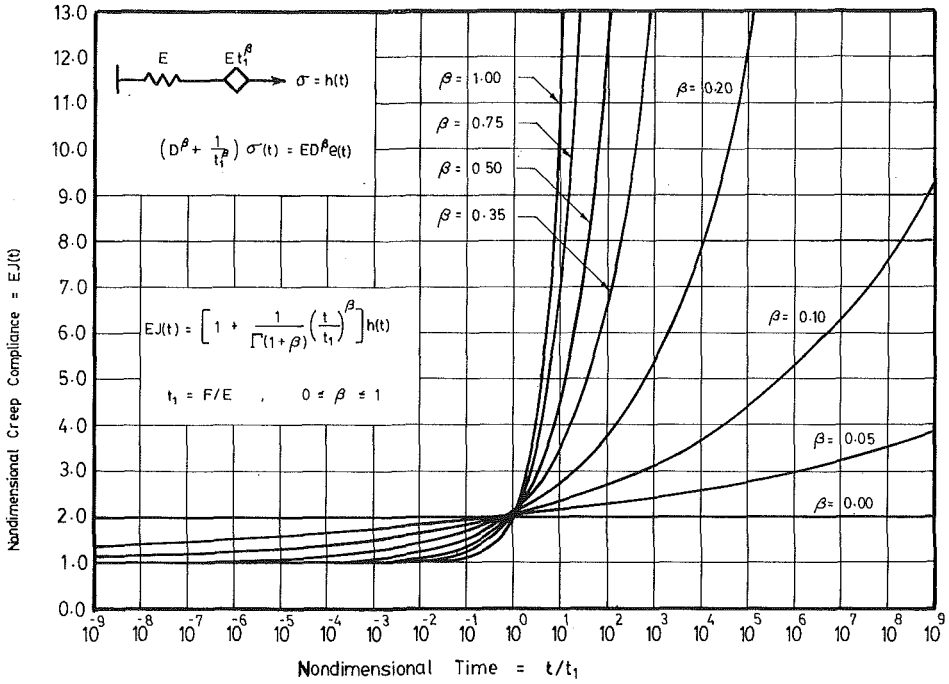

Fig. 7 Creep compliance for a fractional calculus Maxwell fluid model

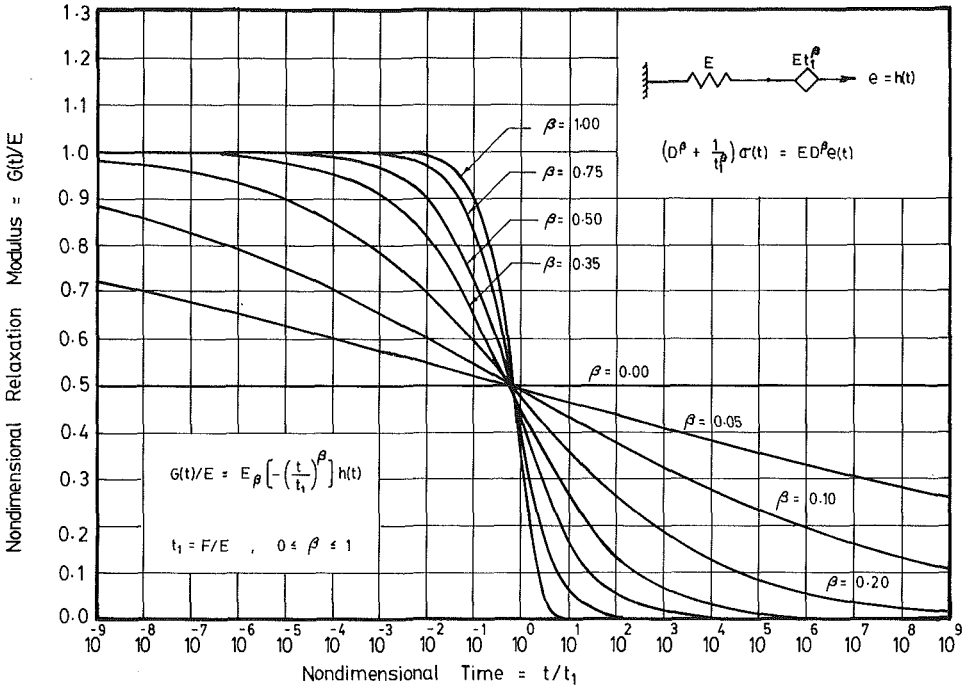

Fig. 8 Relaxation modulus for a fractional calculus Maxwell fluid model

while the strain in the spring is $\sigma(t)/E$. Thus the total strain for the fractional calculus Maxwell fluid model is

$$e(t) = \frac{1}{E}\left(1 + \frac{1}{t_1{}^{\beta}} I_{\alpha}^{*}\right)\sigma(t). \tag{5.1}$$

The inverse relationship of (5.1) is obtained from (2.12*a*) with $\lambda = -1/t_1{}^{\beta}$ and it is given by

$$\sigma(t) = E\left[1 - \frac{1}{t_1^{\beta}} \mathcal{E}_{\alpha}^{*}\left(-\frac{1}{t_1^{\beta}}\right)\right] e(t). \tag{5.2}$$

From (5.1) one obtains the creep compliance and from (5.2) the relaxation modulus is obtained. With the aid of (2.10) one finds for the creep compliance the formula

$$J(t) = \frac{1}{E}\left[1 + \frac{1}{\Gamma(1+\beta)}\left(\frac{t}{t_1}\right)^{\beta}\right] h(t), \tag{5.3}$$

and from (2.14) the relaxation modulus is

$$G(t) = E E_{\beta}\left[-\left(\frac{t}{t_1}\right)^{\beta}\right] h(t), \tag{5.4}$$

where $\beta = 1 + \alpha$.

Figure 7 shows the creep compliance for a fractional calculus Maxwell fluid model. It is clear that for this model the creep compliance is the sum of the creep compliance of the spring and spring-pot and hence this figure is the same as Fig. 1 except that the nondimensional creep functions differ by

one. Since $J(t)$ and $G(t)$ are Stieltjes inverses the relaxation function does not tend to infinity as time tends to zero. Figure 8 shows the relaxation modulus for the model under consideration. Its nondimensional relaxation modulus is just the Mittag-Leffler function evaluated at the value $-x^{\beta}$. The results just obtained are equivalent to the results obtained by Gross [34] since he assumed a creep function in a format similar to (5.3).

Figure 6(*b*) shows a fractional calculus Maxwell chain model where the spring-pot elements are displayed like diamonds. The strain in each of the fractional calculus Maxwell elements is the same, while the stress is the sum of the stresses of the Maxwell elements. Hence, it follows that

$$\sigma(t) = \sum_{n=0}^{N} E_n \left[1 - \frac{1}{t_n^{\beta_n}} \mathcal{E}^*_{\alpha_n}\left[-\left(\frac{1}{t_n^{\beta_n}}\right)\right] e(t), \right. \tag{5.5}$$

and that the relaxation modulus is

$$G(t) = \sum_{n=0}^{N} E_n E_{\beta_n}\left[-\left(\frac{t}{t_n}\right)^{\beta_n}\right] h(t). \tag{5.6}$$

Under special cases the inverse relation may be obtained in a manner similar to the classical theory of the Maxwell chain model. It is clear that many more creep and relaxation functions may be obtained for other fractional calculus models. In particular the fractional calculus model consisting of a fractional calculus Maxwell element in series with a fractional calculus Kelvin-Voigt element should be an excellent model to describe primary and secondary creep of materials.

6 Conclusions

Rabotnov's theory of Hereditary Solid Mechanics has been generalized and its relationship to the fractional calculus has been shown. Creep and relaxation functions for various fractional calculus models have been obtained and these functions are very useful in the reduction of creep and relaxation data. The fractional calculus basic element, which is the spring-pot, allows for the continuous transition from the fluid state to the solid state. The spring-pot is combined with springs and its relationship with the fractional polynomial operators is discussed.

Acknowledgments

I would like to thank the students in my graduate class at University of Colorado at Denver for their inquisitiveness and their interest in the understanding of Rabotnov's book. I would also like to express my appreciation to Major Ronald L. Bagley and Professor Peter J. Torvik for their encouragement.

References

1 Volterra, V., "Sulle Equazioni Integro-Differenziali della Theoria dell'Elasticità," *Atti Reale Accad. naz. Lincei. Rend. Cl. sci. fis., mat. e natur.*, Vol. 18, 1909, pp. 295–300.

2 Volterra, V., *Lecons sur les Fonctions de Lignes*," Gauthier-Villard, Paris, 1913.

3 Rabotnov Yu, N., *Elements of Hereditary Solid Mechanics*," Mir Publishers, Moscow, 1980.

4 Gurtin, M. E., and Sternberg, E., "On the Linear Theory of Viscoelasticity," *Arch. Ration. Mech. and Anal.*, Vol. 11, 1962, pp. 291–356.

5 Flügge, W., *Viscoelasticity*, 2nd ed., Springer-Verlag, New York, Heidelberg, Berlin, 1975.

6 Bland, D. R., *The Theory of Linear Viscoelasticity*, Pergamon Press, Oxford, 1960.

7 Ferry, J. D., *Viscoelastic Properties of Polymers*, Wiley, New York, 1980, 3rd ed.

8 Christensen, R. M., *Theory of Viscoelasticity, An Introduction*, Academic Press, New York, 1971.

9 Bagley, R. L., and Torvik, P. J., "A Theoretical Basis for the Application of Fractional Calculus to Viscoelasticity," *J. of Rheology*, Vol. 27, No. 3, 1983, pp. 201–210.

10 Bagley, R. L., "Application of Generalized Derivatives to Viscoelasticity," Ph.D. dissertation, Air Force Institute of Technology, also published as Air Force Materials Laboratory, TR-79-4103, Nov., 1979.

11 Bagley, R. L., and Torvik, P. J., "Fractional Calculus—A Different Approach to the Analysis of Viscoelastically Damped Structures," *AIAA Journal*, Vol. 21, No. 5, May 1983, pp. 741–748.

12 Roger, L., "Operators and Fractional Derivatives for Viscoelastic Constitutive Equations," *J. of Rheology*, to appear.

13 Lovitt, W. V., *Linear Integral Equations*, Dover, New York, 1950.

14 Tricomi, F. G., *Integral Equation*, Interscience Publishers, New York, London, 1957.

15 Yosida, K., *Lectures on Differential and Integral Equations*, Interscience, New York, 1960.

16 Bieberbach, L., *Lehrbuch Der Funktionentheorie, Band II*, Chelsea, 1945.

17 Lindelof, E., *Calcul Des Residus*, Chelsea, 1947.

18 Erdelyi, Magnus, Oberheltinger, and Tricomi, *Higher Transcendental Functions*, Vol. 3, McGraw-Hill, 1954, pp. 206–209.

19 Annin, B. D., "Asymptotic Expansion of an Exponential Function of Fractional Order," *Prikl. Matem i Mekh.*, Vol. 25, 1961, pp. 796–798.

20 Oldham, K. B., and Spanier, J., *The Fractional Calculus*, Academic Press, 1974.

21 Ross, B., "A Brief History and Exposition of the Fundamental Theory of Fractional Calculus," *Lecture Notes in Mathematics*, Vol. 457, Springer-Verlag, 1975, pp. 1–36.

22 Wainwright, W. L., "An Application of Fractional Calculus to a Mathematical Modeling Problem," *CUMER-76-9*, Department of Mechanical Engineering, College of Engineering, Boulder, Colo., 1976.

23 Liverman, T. P. G., *Generalized Functions and Direct Operational Methods*, Vol. 1, Prentice-Hall, Englewood Cliffs, N.J., 1964.

24 Erdelyi, Magnus, Oberheltinger, and Tricomi, *Tables of Integral Transforms*, Vol. 2, McGraw-Hill, 1954, pp. 181–214.

25 Güttinger, W., *Generalized Functions and Dispersion Relations in Physics*, Vol. 14, 1966, pp. 483–602.

26 Gerasimov, A. N., "Generalization of Linear Laws of Deformation and its Application to Problems of Internal Friction," *Prikl. Matem i Mekh.*, Vol. 12, 1948, pp. 251–260.

27 Scott Blair, G. W., "The Role of Psychophysics in Rheology," *J. Colloid Sci.*, Vol. 2, 1947, pp. 21–32.

28 Scott Blair, G. W., *Measurements of Mind and Matter*, Philosophical Library Inc., New York, 1956.

29 Scott Blair, G. W., "Some Aspects of the Search for Invariants," *British J. Philos Sci.*, Vol. 1, 1950, pp. 230–244.

30 Scott Blair, G. W., and Caffyn, J. E., "An Application of the Theory of Quasi-Properties to the Treatment of Anomalous Stress-Strain Relations," *Philos. Mag.*, Vol. 40, 1949, pp. 80–94.

31 Scott Blair, G. W., Psychorheology: "Links Between the Past and the Present," *J. Texture Stud.*, Vol. 5, 1974, pp. 3–12.

32 Nutting, P. G., "A Study of Elastic Viscous Deformation," *Proc. Amer. Soc. Test. Mater.*, Vol. 21, 1921, pp. 1162–1171.

33 Nutting, P. G., "A New General Law of Deformation," *J. of the Franklin Institute*, Vol. 191, May 1921, pp. 679–685.

34 Gross, B., "On Creep and Relaxation," *J. of Appl. Phys.*, Vol. 18, 1947, pp. 212–221.

35 Slonimsky, G. L., "Laws of Mechanical Relaxation Processes in Polymers," *J. of Polymer Sci.*, Part C, No. 16, 1967, pp. 1667–1672.

36 Smit, W., and de Vries, H., "Rheological Models Containing Fractional Derivatives," *Rheol. Acta*, Vol. 6, 1970, pp. 525–534.

37 Stiassnie, M., "On the Application of Fractional Calculus for the Formulation of Viscoelastic Models," *Appl. Math. Modelling*, Vol. 3, 1979, pp. 300–302.

38 Wainwright, W. L., A Functional Relation, *Lecture Notes in Mathematics*, Vol. 457, Springer-Verlag, 1975, pp. 298–305.

39 Caputo, M., "Linear Models of Dissipation whose Q is Almost Frequency Independent-II," *Geophys. J. R. Astr. Soc.*, Vol. 13, 1967, pp. 529–539.

40 Caputo, M., *Elasticita e Dissipazione*, Zanichelit, Bolognia, Italy, 1969.

41 Caputo, M., and Mairardi, F., "A New Dissipation Model Based on Memory Mechanism," *Pure and Applied Geophysics*, Vol. 91, 1971, pp. 134–147.

42 Bagley, R. L., and Torvik, P. J., "A Generalized Derivative Model for an Elastomer Damper," *Shock Vibr. Bull.*, No. 49, Part 2, Sept. 1979, pp. 135–143.

43 Gottenberg, W. G., and Christensen, R. M., "Prediction of the Transient Response of a Linear Viscoelastic Solid," ASME JOURNAL OF APPLIED MECHANICS, Vol. 33, 1966, pp. 449–450.

44 Koeller, R. C., and Raj, R., "Diffusing Relaxation of Stress Concentration at Second Phase Particles," *Acta Metallurgica*, Vol. 26, 1978, pp. 1551–1558.

T. Mura
Mem. ASME

R. Furuhashi[1]

Department of Civil Engineering
and Materials Research Center,
Northwestern University,
Evanston, Ill. 60201

The Elastic Inclusion With a Sliding Interface

It is found that when an ellipsoidal inclusion undergoes a shear eigenstrain and the inclusion is free to slip along the interface, the stress field vanishes everywhere in the inclusion and the matrix. It is assumed in the analysis that the inclusion interface cannot sustain any shear traction. There exists a shear deformation that transforms an ellipsoid into the identical ellipsoid without changing its orientation (ellipsoid invariant transformation). This is not true, however, for a spheroidal inclusion. The amount of slip and the associated stress field are calculated for a spherical inclusion for a given uniform eigenstrain ϵ_{ij}^*.

1 Introduction

An inclusion is defined as a subdomain Ω in domain, D, where eigenstrain (stress-free transformation strain, misfit strain, nonelastic strain) ϵ_{ij}^* is given in Ω and is zero in $D-\Omega$. The elastic moduli in Ω (inclusion) and $D-\Omega$ (matrix) are assumed to be the same.

Most of the inclusion problems solved by Goodier [1], Edward [2], Eshelby [3], Willis [4], Kinoshita and Mura [5], Yang and Chou [6], among others, assume the continuity of displacement at the interface of inclusion (perfect bonding).

This condition of perfect bonding is sometimes inadequate in describing mechanical behavior of inclusions. Inclusions in high-strength steel, for instance, are easily debonded by a few cyclic loadings. Grain boundary sliding in polycrystals and granular media can be observed even at room temperature.

When sliding is allowed along the inclusion interface, the well-known solution of Eshelby [3] must be substantially modified. To the authors' knowledge, no conclusive research has been reported about this sliding inclusion.

In this paper we report a striking result of a sliding ellipsoidal inclusion under a shearing eigenstrain and a result for a sliding spherical inclusion under more general eigenstrains. The conditions for continuity of the normal traction and the normal displacement at the interface are imposed in analysis and the shear stress along the interface is required to vanish.

2 Statement of the Problem

Consider an isotropic and infinitely extended elastic body, containing a uniform (constant) eigenstrain ϵ_{ij}^* in an ellipsoidal subdomain Ω bounded by

$$x_1^2/a_1^2 + x_2^2/a_2^2 + x_3^2/a_3^2 = 1. \tag{1}$$

We investigate a solution of the elastic field when sliding takes place along the inclusion interface. The equations of equilibrium for the stress tensor are

$$\sigma_{ij,j} = 0 \quad \text{in } D. \tag{2}$$

Hooke's law is

$$\sigma_{ij} = C_{ijkl}(u_{k,l} - \epsilon_{kl}^*), \tag{3}$$

where $\epsilon_{kl}^* = 0$ in matrix $D-\Omega$. The condition for continuity of the traction on the inclusion interface S is

$$[\sigma_{ij}]n_j = 0 \quad \text{on } S, \tag{4}$$

where $[\sigma_{ij}] = \sigma_{ij}(\text{out}) - \sigma_{ij}(\text{in})$ and n_i is the outward unit normal on S. The continuity condition for the normal displacement on S is

$$[u_i]n_i = 0 \quad \text{on } S. \tag{5}$$

The condition for vanishing shear stress on S is

$$\sigma_{ij}n_j - \sigma_{jk}n_j n_k n_i = 0 \quad \text{on } S, \tag{6}$$

$$\sigma_{ij}n_j = \alpha n_i \quad \text{on } S, \tag{6a}$$

where α is a variable scalar.

The slip on S is expressed by a vector b_i,

$$b_i = -[u_i] \quad \text{on } S. \tag{7}$$

The solution for the system of equations (2)–(6) tends to zero at infinity.

3 Uniqueness of Solution

Uniqueness of the solution for (2)–(6) is shown. Suppose that two solutions u_i^1, u_i^2, for displacements and σ_{ij}^1, σ_{ij}^2 for the corresponding stresses exist. Then, we have, for $\Delta u_i = u_i^1 - u_i^2$, $\Delta\sigma_{ij} = \sigma_{ij}^1 - \sigma_{ij}^2$,

$$\Delta\sigma_{ij,j} = 0, \tag{2}'$$

$$\Delta\sigma_{ij} = C_{ijkl}\Delta u_{k,l}, \tag{3}'$$

[1] Present address: Faculty of Engineering, Meiji University, Tokyo, Japan.

Contributed by the Applied Mechanics Division for presentation at the 1984 PVP Conference and Exhibition, Joint with Applied Mechanics Division and Materials Division, San Antonio, Texas, June 17–21, 1984 of THE AMERICAN SOCIETY OF MECHANICAL ENGINEERS.

Discussion on this paper should be addressed to the Editorial Department, ASME, United Engineering Center, 345 East 47th Street, New York, N.Y. 10017, and will be accepted until two months after final publication of the paper itself in THE JOURNAL OF APPLIED MECHANICS. Manuscript received by ASME Applied Mechanics Division, May, 1983; final revision, September, 1983. Paper No. 84-APM-24.

Copies will be available until February, 1985.

$$[\Delta\sigma_{ij}]n_j = 0 \qquad \text{on } S, \tag{4}'$$

$$[\Delta u_i]n_i = 0 \qquad \text{on } S, \tag{5}'$$

$$\Delta\sigma_{ij}n_j = \Delta\alpha n_i \quad \text{on } S \tag{6a}'$$

and $\Delta u_i = 0$ at infinity. Consider positive-definite volume integrals,

$$I \equiv \int_\Omega \Delta\sigma_{ij}\Delta u_{i,j}dD + \int_{D-\Omega} \Delta\sigma_{ij}\Delta u_{i,j}dD. \tag{8}$$

When I is transformed by Gauss' theorem to surface integrals, we have

$$I = \int_{\partial\Omega} \Delta\sigma_{ij}\Delta u_i n_j dS + \int_{\partial(D-\Omega)} \Delta\sigma_{ij}\Delta u_i n_j dS \tag{9}$$

where $\partial\Omega$ and $\partial(D-\Omega)$ are the boundary of Ω and the inner boundary of $D-\Omega$, both of which are equal to S, and n_i is the respective outward unit normal. From (4)', I is written as

$$I = -\int_{\partial\Omega} \Delta\sigma_{ij}n_j[\Delta u_i]dS. \tag{10}$$

Finally, conditions (6a)' and (5)' lead to

$$I = -\int_S \Delta\alpha n_i[\Delta u_i]dS = 0. \tag{11}$$

Since (8) is positive-definite for $\Delta\sigma_{ij}$, we conclude that $\sigma_{ij}^1 = \sigma_{ij}^2$.

4 Somigliana's Dislocations

The shear stress on the inclusion interface in Eshelby's inclusion is relaxed by interface sliding (Somigliana's dislocation). Therefore, the solution for (2)–(6) is the sum of Eshelby's solution and Volterra's solution obtained by Somigliana's dislocations distributed on S, where the dislocation density is b_i given by (7).

Eshelby's solution (perfect bonding) is ($d\mathbf{x}' = dx_1'dx_2'dx_3'$)

$$u_i^E(\mathbf{x}) = -\frac{\partial}{\partial x_k}\int_\Omega G_{ij}(\mathbf{x}-\mathbf{x}')C_{jklm}\epsilon_{lm}^*(\mathbf{x}')d\mathbf{x}' \tag{12}$$

and Volterra' solution (sliding) (Mura 1982, p. 39) is

$$u_i^V(\mathbf{x}) = \frac{\partial}{\partial x_k}\int_S G_{ij}(\mathbf{x}-\mathbf{x}')C_{jklm}b_l(\mathbf{x}')n_m dS, \tag{13}$$

where $G_{ij}(\mathbf{x}-\mathbf{x}')$ is the Green's function of elasticity. The solution is the sum,

$$u_i = u_i^E + u_i^V. \tag{14}$$

where b_l on S is properly chosen, u_i can satisfy conditions (2)–(6). Following Asaro [7], the function b_i in (13) is extended to inside Ω. Then, Gauss' theorem leads to

$$u_i^V(\mathbf{x}) = \frac{\partial}{\partial x_k}\int_\Omega G_{ij}(\mathbf{x}-\mathbf{x}')C_{jklm}b_{l,m}(\mathbf{x}')d\mathbf{x}' + b_i(\mathbf{x}), \tag{15}$$

where the property of the Green's function,

$$C_{lmjk}G_{ij,km}(\mathbf{x}-\mathbf{x}') = -\delta_{li}\delta(\mathbf{x}-\mathbf{x}') \tag{16}$$

is used. $\delta(\mathbf{x}-\mathbf{x}')$ is the Dirac delta function, and δ_{li} is Kronecker's delta. The stress corresponding to u_i^V is obtained from

$$\sigma_{ij}^V = C_{ijkl}u_{k,l}^V. \tag{17}$$

The stress in Ω corresponding to u_i^E is

$$\sigma_{ij}^E = C_{ijkl}(u_{k,l}^E - \epsilon_{kl}^*). \tag{18}$$

The solution for stresses is obtained as the sum, $\sigma_{ij} = \sigma_{ij}^E + \sigma_{ij}^V$. These stresses (17) and (18) are written from (12) and (15) as

$$\sigma_{ij}^V(\mathbf{x}) = -C_{ijkl}\left\{\int_\omega C_{pqmn}\epsilon_{mn}^{**}(\mathbf{x}')G_{kp,ql}(\mathbf{x}-\mathbf{x}')d\mathbf{x}' + \epsilon_{kl}^{**}(\mathbf{x})\right\}, \tag{19}$$

$$\sigma_{ij}^E(\mathbf{x}) = -C_{ijkl}\left\{\int_\omega C_{pqmn}\epsilon_{mn}^{*}(\mathbf{x}')G_{kp,ql}(\mathbf{x}-\mathbf{x}')d\mathbf{x}' + \epsilon_{kl}^{*}(\mathbf{x})\right\}, \tag{20}$$

where

$$\epsilon_{ij}^{**} = -(1/2)(b_{i,j} + b_{j,i}). \tag{21}$$

When b_i, which is originally defined on S, is extended into Ω, the impotent components (Furuhashi and Mura 1979) are excluded. These impotent components vanish on S and take arbitrary values in Ω but do not contribute any stress field.

The stresses expressed by (19) and (20) satisfy the conditions (2) and (4). It is also known that u_i^E is continuous through S so that $[u_i^E] = 0$. Therefore, u_i expressed by (14) satisfies condition $-[u_i] = b_i$. We have to choose b_i such that

$$b_i n_i = 0 \quad \text{on } S \tag{22}$$

and $\sigma_{ij} = \sigma_{ij}^V + \sigma_{ij}^E$ satisfies condition (6) or (6a).

5 Special Cases

Shearing Eigenstrains. Observing (19)–(21), we realize that if

$$\epsilon_{ij}^* + \epsilon_{ij}^{**} = 0, \tag{23}$$

$\sigma_{ij} = \sigma_{ij}^E + \sigma_{ij}^V = 0$. Therefore, condition (6) is satisfied.

For an arbitrary but uniform ϵ_{ij}^*, (23) leads to

$$b_i = \epsilon_{ij}^* x_j - \omega_{ij}x_j, \tag{24}$$

where ω_{ij} is a rotation and $\omega_{ij} = -\omega_{ji}$. Unfortunately, condition (22) is not generally satisfied by (24). Expression (24) does satisfy (22), however, under a special configuration when uniform shear eigenstrains ($\epsilon_{ij}^* = 0$ for $i = j$) are distributed in an ellipsoidal domain with no degeneracy ($a_1 \neq a_2 \neq a_3$).

When (24) is substituted into (22), we have

$$\begin{aligned}&\{\epsilon_{12}^*(1/a_1^2 + 1/a_2^2) - \omega_{12}(1/a_1^2 - 1/a_2^2)\}x_1x_2 \\ &\qquad + \{\epsilon_{31}^*(1/a_3^2 + 1/a_1^2) \\ &-\omega_{31}(1/a_3^2 - 1/a_1^2)\}x_3x_1 + \{\epsilon_{23}^*(1/a_2^2 + 1/a_3^2) \\ &\qquad -\omega_{23}(1/a_2^2 - 1/a_3^2)\}x_2x_3 = 0\end{aligned} \tag{25}$$

For an arbitrarily given ϵ_{ij}^* there exists a set of solutions for ω_{ij}, where $a_1 \neq a_2 \neq a_3$,

$$\begin{aligned}\omega_{12} &= \epsilon_{12}^*(1/a_1^2 + 1/a_2^2)/(1/a_1^2 - 1/a_2^2) \\ \omega_{31} &= \epsilon_{31}^*(1/a_3^2 + 1/a_1^2)/(1/a_3^2 - 1/a_1^2) \\ \omega_{23} &= \epsilon_{23}^*(1/a_2^2 + 1/a_3^2)/(1/a_2^2 - 1/a_3^2)\end{aligned} \tag{26}$$

When (26) is substituted in (24), we have

$$\begin{aligned}b_1 &= 2x_2a_1^2\epsilon_{12}^*/(a_1^2 - a_2^2) - 2x_3a_1^2\epsilon_{13}^*/(a_3^2 - a_1^2), \\ b_2 &= 2x_3a_2^2\epsilon_{23}^*/(a_2^2 - a_3^2) - 2x_1a_2^2\epsilon_{12}^*/(a_1^2 - a_2^2), \\ b_3 &= 2x_1a_3^2\epsilon_{13}^*/(a_3^2 - a_1^2) - 2x_2a_3^2\epsilon_{23}^*/(a_2^2 - a_3^2).\end{aligned} \tag{27}$$

Therefore, it is concluded that for uniform shear eigenstrains a sliding ellipsoidal inclusion causes no stress field.

This means that the misfit caused by ϵ_{ij}^* in Eshelby's inclusion is completely relaxed by the interface sliding given by (27). The displacement is obtained from (14) with (12), (15), and (24) and it is $u_i = b_i$. It means equivalently that the shear deformation given by (27) transforms the ellipsoid (1) into the identical ellipsoid. Suppose that point (x_1, x_2, x_3) is trans

formed into point (x_1', x_2', x_3') by the displacement given by (27). Solving x_i in terms of x_i' from

$$x_i' = x_i + b_i \tag{28}$$

by using (27) and substituting into (1), we have

$$(x_1')^2/a_1^2 + (x_2')^2/a_2^2 + (x_3')^2/a_3^2 = 1 \tag{29}$$

when higher order terms than ϵ_{ij}^* are neglected (linear elasticity). This rather striking fact is reconsidered for the two-dimensional case, where $\epsilon_{i3}^* = 0$ and $b_3 = 0$. When (28) is solved for x_i, we have

$$\begin{aligned} x_1 &= x_1' - x_2' 2a_1^2 \epsilon_{12}^*/(a_1^2 - a_2^2) \\ x_2 &= x_1' 2a_2^2 \epsilon_{12}^*/(a_1^2 - a_2^2) + x_2' \end{aligned} \tag{30}$$

Substituting (30) into $x_1^2/a_1^2 + x_2^2/a_2^2 = 1$ leads to

$$(x_1'^2/a_1^2 + x_2'^2/a_2^2)/(1 + \Delta^2) = 1, \tag{31}$$

where

$$\Delta^2 = 4a_1^2 a_2^2 (\epsilon_{12}^*)^2/(a_1^2 - a_2^2)^2. \tag{32}$$

The ellipse $x_1^2/a_1^2 + x_2^2/a_2^2 = 1$ expands uniformly by shear deformation without changing the shape unless Δ^2 is neglected. Otherwise the concept in linear elasticity that no shear deformation causes a volume change of material does not hold. However, the magnitude of ϵ_{12}^* has a limitation so that the linear elasticity may hold. The limitation is given by the inequality

$$4a_1^2 a_2^2 (\epsilon_{12}^*)^2/(a_1^2 - a_2^2)^2 << 1 \tag{33}$$

The solution (27) is an exact solution in the framework of linear elasticity which requires ϵ_{12}^* to be subjected to the restriction given by (33). ϵ_{12}^* under this restriction depends on (a_1/a_2). For a sphere, for instance, ϵ_{ij}^* must be infinitely small (namely zero).

Under (27) the ellipsoid (1) restores the shape and orientation by rotation (26) after displacements of material points. This is not, however, the case of a sphere that is always deformed to an ellipsoid by shear. The restoration of the sphere shape is impossible by rotation. In these cases of degeneracy of ellipsoids (spheroidal and sphere), nonvanishing stress fields are left in the material after slight relaxation by the interface sliding.

Spherical Inclusions. Ghahremani [8] obtained the solution for an isotropic elastic medium, containing a sliding spherical inhomogeneity, subjected to uniform tension at infinity. Since we are interested in the anomaly of a spherical inclusion, as mentioned in the last section, the following problem is investigated.

Consider a uniform otherwise general eigenstrain $\epsilon^*{}_{ij}$ in the domain bounded by S,

$$x_i x_i = a^2, \tag{34}$$

where a is the radius of the sphere. The sphere can slide and the shear stress at the interface vanishes. Since $n_i = x_i/a$ on S, equation (6) becomes

$$\sigma_{ij} x_j a^2 - \sigma_{jk} x_j x_k x_i = 0. \tag{35}$$

The interface shear stress found in Eshelby's inclusion is relaxed by sliding b_i along the interface. Then, b_i will be proportional to the shear stress in Eshleby's inclusion. Therefore, it is natural to assume that b_i has the same form as the shear,

$$b_i = B_{ij} x_j a^2 - B_{jk} x_j x_k x_i \tag{36}$$

where B_{ij} are symmetric unknown constants. It is easily seen that condition (22) is satisfied. After tedious calculation for (19) we have found that condition (6) is satisifed when

$$B_{ij} = \frac{14(7 - 5\nu)}{3(25 - 2\nu)a^2} \epsilon_{ij}^* \tag{37}$$

where ν is Poisson's ratio. Eshelby's solution σ_{ij}^E in Ω given by

$$\sigma_{ij}^E = -2\mu \frac{7 - 5\nu}{15(1 - \nu)} \epsilon_{ij}^* - 2\mu \frac{5\nu + 1}{15(1 - \nu)} \delta_{ij} \epsilon_{kk}^*, \tag{38}$$

where μ is the shear modulus. σ_{ij}^V in Ω is a polynomial of the second degree of coordinates, where (19) is evaluated by using (21) and (36) with the result of Asaro and Barnett [7] or Mura and Kinoshita [5]. The final expression for σ_{ij}^V is so long to write down that it is omitted here.

For more general cases where the inclusion is ellipsoidal and eigenstrains are of nonshear type, a competely different approach by the use of Boussinesq methods is convenient. Some results along this line will be reported in a separate paper.

Acknowledgments

This research was supported by the U.S. Army grant No. DAAG29-81-k-0090. We also thank Professors J. Dundurs and D. M. Barnett for their useful discussion of the manuscript.

References

1 Goodier, J. N., "On the Integration of the Thermoplastic Equations," *Philosophical Magazine*, Vol. 23, 1937, pp. 1017-1032.

2 Edward, R. H., "Stress Concentrations Around Spheroidal Inclusions and Cavities," ASME JOURNAL OF APPLIED MECHANICS, Vol. 18, 1951, pp. 19-30.

3 Eshelby, J. D., "The Determination of the Elastic Field of an Ellipsoidal Inclusion and Related Problems," *Proceedings of the Royal Society*, Series A, Vol. 241, 1957, pp. 376-396.

4 Willis, J. R., "Anisotropic Elastic Inclusion Problems," *Quarterly Journal of Mechanics and Applied Mathematics*, Vol. 17, 1964, pp. 157-174.

5 Kinoshita, N., and Mura, T., "Elastic Fields of Inclusions in Anisotropic Media," *Phys. Stat. Sol. (a)*, Vo. 5, 1971, pp. 759-768.

6 Yang, H. C., and Chou, Y. T., "Antiplane Strain Problems of an Elliptic Inclusion in an Anisotropic Medium," ASME JOURNAL OF APPLIED MECHANICS, Vol. 44, 1977, pp. 437-441.

7 Asaro, R. J., "Somigliana Dislocations and Internal Stresses; With Application to Second Phase Hardening," *International Journal of Engineering Science*, Vol. 13, 1975, pp. 271-286.

8 Ghahremani, F., "Effect of Grain Boundary Sliding on Anelasticity of Polycrystals," *International Journal of Solids and Structures*, Vol. 16, 1980, pp. 825-845.

The Subsurface Crack Under Conditions of Slip and Stick Caused by a Surface Normal Force

F.-K. Chang
Maria Comninou
Mem. ASME
Sheri Sheppard
Student Mem. ASME
J. R. Barber

Department of Mechanical Engineering
and Applied Mechanics,
University of Michigan,
Ann Arbor, Mich. 48109

A solution is given for the elastic stress field in a half plane containing a plane crack parallel to the surface and subjected to a uniform normal pressure and a concentrated normal load. Frictional slip according to Coulomb's law is permitted between the crack faces. As the load is increased, a slip zone originates and grows either from a crack tip or from an intermediate point. Various arrangements of slip and stick zones can occur depending on the magnitude of the load and its location relative to the crack. At very high loads, the crack faces start to separate, but this case is not treated in the present paper.

Introduction

The phenomenon of surface slip due to static and moving surface loads has been studied in a series of publications [1–5], which considered the problem of an elastic layer pressed on an elastic substrate. This geometry approximates the contact problem for cylinders with shrink fitted tires. In particular, the results of [5] can be compared with experimental data obtained by Anscombe and Johnson [6] on the rolling of two steel cylinders, one of which is fitted with a steel tire.

A related problem of interest concerns the propagation of a crack parallel to the surface of a solid due to a series of moving loads. Railway wheels, rails, and other surfaces loaded in rolling contact are prone to "spalling failure" in which a subsurface crack propagates parallel to the surface until eventually a thin plate of material is detached, Hundy [7]. The propagation process depends on the stress intensity factors at the crack tips and these will be in turn influenced by frictional contact between the crack faces during the loading cycle as a moving load passes overhead.

In this paper we consider the static situation as a preliminary study to the inherently transient problem of the moving load. When the load is sufficiently high, we find that slip occurs between the crack faces in either one or two zones whose location depends on the position of the load and the extent of the crack. If the slip zones extend to one or both of the crack tips, singular shear tractions are developed ahead of the tip giving a mode *II* stress intensity factor. Otherwise, the stress field near the tips remains bounded and the frictional contact between the faces inhibits crack propagation. Unfortunately, there are as yet no experimental data with which these results can be compared.

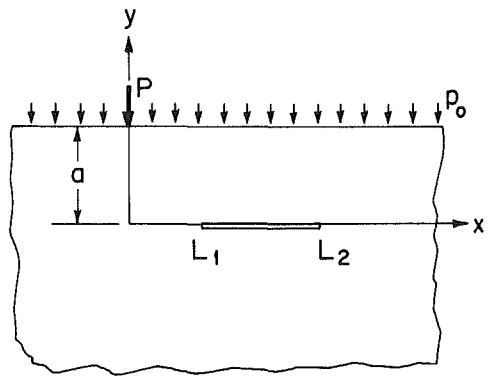

Fig. 1 Geometry of the problem

Formulation

Consider the geometry of Fig. 1. A crack of length $L_2 - L_1$ is located at depth a parallel to the surface of an elastic half plane. A compressive force P and a uniform pressure p_0 are applied on the surface of the half plane. In this analysis, the coordinate system is defined so that the force P acts at the point (0, a), while the location and extent of the crack are considered variable, i.e., the parameters L_1, L_2 may take any (including negative) values. The force is allowed to increase monotonically in magnitude. The faces of the crack can transmit frictional forces and Coulomb's law of friction is assumed.

As long as the crack faces remain in conditions of stick, the

Contributed by the Applied Mechanics Division for presentation at the 1984, PVP Conference and Exhibition, Joint with Applied Mechanics Division and Materials Division, San Antonio, Texas, June 17-21, 1984 of THE AMERICAN SOCIETY OF MECHANICAL ENGINEERS.

Discussion on this paper should be addressed to the Editorial Department, ASME, United Engineering Center, 345 East 47th, Street New York, N.Y. 10017, and will be accepted until two months after final publication of the paper itself in the JOURNAL OF APPLIED MECHANICS. Manuscript received by ASME Applied Mechanics Division, April, 1983; final revision August, 1983. Paper No. 84-APM-17.

Copies will be available until February, 1985.

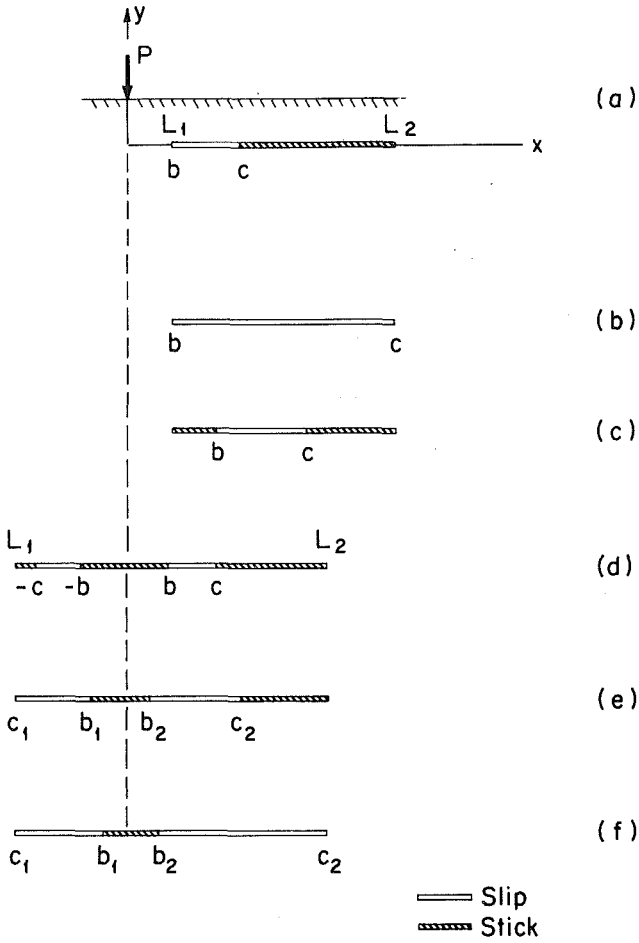

Fig. 2 Arrangements of slip zones (mirror images not shown)

Flamant solution [8] is valid and the tractions on the plane of the crack are

$$\sigma_{xy}(x,0) = \frac{2P}{\pi}\frac{a^2 x}{(a^2+x^2)^2} \tag{1}$$

$$\sigma_{yy}(x,0) = -p_0 - \frac{2P}{\pi}\frac{a^3}{(a^2+x^2)^2} \tag{2}$$

The limiting case of a crack extending from $-\infty$ to $+\infty$ is the problem of the layer pressed on a substrate treated in [1]. In this case, slip starts at the two symmetric locations x^* and $-x^*$ where

$$\left|\frac{x^*}{a}\right| = \frac{1}{3}[(3+4f^2)^{1/2}+2f] \tag{3}$$

when the load P reaches the critical value P^* given by

$$\frac{P^*}{p_0 a} = \frac{8\pi f\,[f(3+4f^2)^{1/2}+3+2f^2]^2}{27[(3+4f^2)^{1/2}-f]} \tag{4}$$

where f is the coefficient of friction. As the force is increased, the two symmetric slip zones expand in both directions. The ends of the slip zones furthest from the load expand faster than the near ends. The extent and location of the slip zones versus the dimenionless load parameter $P/p_0 a$ is given in Fig. 6 of [1] for various coefficients of friction. This problem can be used for guidance in the various slip configurations associated with localized slip of the finite extent crack.

Depending on the location of the point $|x^*|$ in relation to the finite crack we may distinguish the following cases:

I. $-x^* < x^* < L_1$

II. $-x^* < L_1 < x^* < L_2$

III. $L_1 < -x^* < x^* < L_2$

There are three more cases symmetric to the foregoing, which correspond to mirror image slip configurations and are not considered separately.

Case *I*. As the load is increased from P^*, slip starts for some value $P > P^*$ at L_1 leading to the arrangement of Fig. 2(*a*), where slip occurs in the interval $b < x < c$, where $b = L_1$. As the load is increased further, the slip zone is expected to expand until it reaches the end point L_2. The entire crack is then under condition of slip, Fig. 2(*b*).

Case *II*. A slip zone detached from the crack tips appears first in the vicinity of x^*, Fig. 2(*c*). As the load increases, the slip zone spreads and it eventually reaches the left or right tip depending on the relative location of x^*. The arrangement of Fig. 2(*a*) or its mirror image results. It is also possible to arrive at configuration Fig. 2(*e*) if $L_1 < 0$.

Case *III*. When both points $|x^*|$ are inside the crack extent and $L_1 < 0$, two detached slip zones appear, symmetric about the origin, as shown in Fig. 2(*d*). As long as slip does not reach the crack tips, their location is immaterial and the situation is identical to that described in [1]. For a finite crack, slip will eventually reach one of the crack tips first, depending on the location of the points $|x^*|$. We then have the arrangement of Fig. 2(*e*) or its mirror image. As the load is further increased, slip penetrates the other crack tip, too, Fig. 2(*f*).

The analysis follows closely that of [1–3] and only the main steps will be presented here for easy reference. The tractions on $y = 0$ can be expressed as a sum of two terms. The first term is due to the surface load (Flamant solution and uniform compression) and the second is a corrective solution, the purpose of which is to account for the slip zone(s). The corrective solution is obtained as a distribution of edge dislocations of the glide type with density $B(x)$. The possibility of separation (which would require a distribution of climb edge dislocations) is not included in the present formulation. Accordingly, the normal $N(x)$ and shear $S(x)$ tractions become

$$N(x) = -p_0 - \frac{2P}{\pi}\frac{a^3}{(a^2+x^2)^2} + \frac{2\mu}{\pi(\kappa+1)}\int_\Gamma B(\xi)\,K_n(x,\xi)\,d\xi \tag{5}$$

$$S(x) = \frac{2P}{\pi}\frac{a^2 x}{(a^2+x^2)^2} + \frac{2\mu}{\pi(\kappa+1)}\int_\Gamma B(\xi)\,K_s(x,\xi)\,d\xi \tag{6}$$

where

$$K_n(x,\xi) = \frac{8a^3}{R^4}\left(-3+16\frac{a^2}{R^2}\right) \tag{7}$$

$$K_s(x,\xi) = \frac{1}{x-\xi} + \frac{x-\xi}{R^2}\left(-1+\frac{12a^2}{R^2}-\frac{64a^4}{R^4}\right) \tag{8}$$

$$R^2 = 4a^2 + (x-\xi)^2 \tag{9}$$

μ is the shear modulus and $\kappa = 3-4\nu$ for plane strain, ν being the Poisson's ratio. The range of integration Γ is the union of the slip zones (interval (b, c) or (b_2, c_2) and (c_1, b_1)).

Guided by the Flamant solution, we anticipate positive slip for $x > 0$ and negative slip for $x < 0$. We can then express Coulomb's law in the slip zones(s) as

$$S(x) = -f\,\mathrm{sgn}\,x\,N(x) \quad \text{in } \Gamma \tag{10}$$

$$N(x) \le 0 \quad \text{in } \Gamma \tag{11}$$

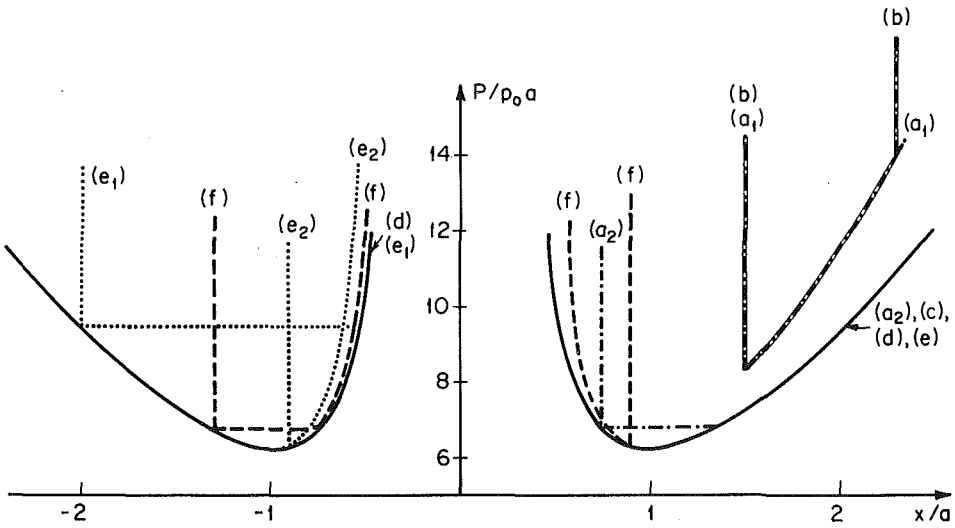

Fig. 3 Dimensionless load versus slip zone location for the arrangements of Fig. 2

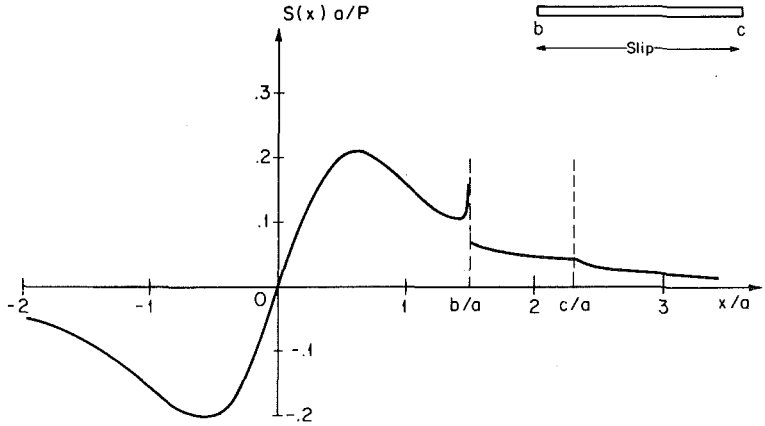

Fig. 4 Shear tractions for arrangement (*b*) with *b/a* = 1.5, *c/a* = 2.3, λ = 13.98

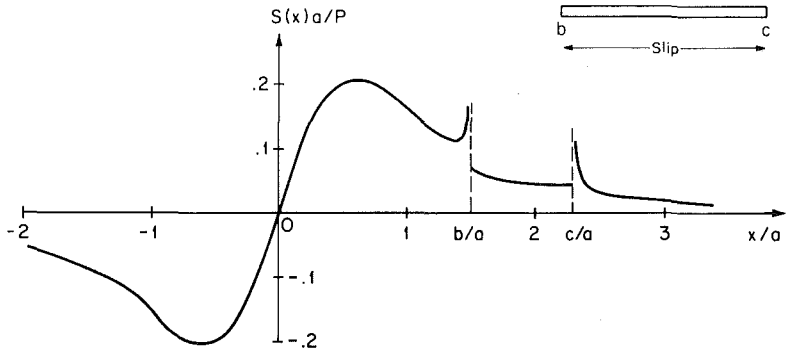

Fig. 5 Shear tractions for arrangement (*b*) with *b/a* = 1.5, *c/a* = 2.3, λ = 15

where f is the coefficient of friction. For each slip zone we must require that there is no net dislocation left behind or

$$\int_{\Gamma_i} B_x(\xi)\, d\xi = 0, \quad i = 1, 2 \tag{12}$$

We must also verify that [1]

$$\operatorname{sgn} S(x) = \operatorname{sgn} h(x) \tag{13}$$

where $h(x)$ is the tangential shift defined as the difference in the tangential displacements on the surfaces $y = 0^+$ and $y = 0^-$. It is also noted that

$$\frac{dh}{dx} = -B(x) \tag{14}$$

In the stick zones that may develop along the crack, we require

$$N(x) \le 0 \tag{15}$$

$$|S(x)| < -fN(x) \tag{16}$$

Asymptotic analysis has established the behavior of $B(x)$ at the end points, which is consistent with the boundary conditions of the problem including the inequalities [9]. Thus

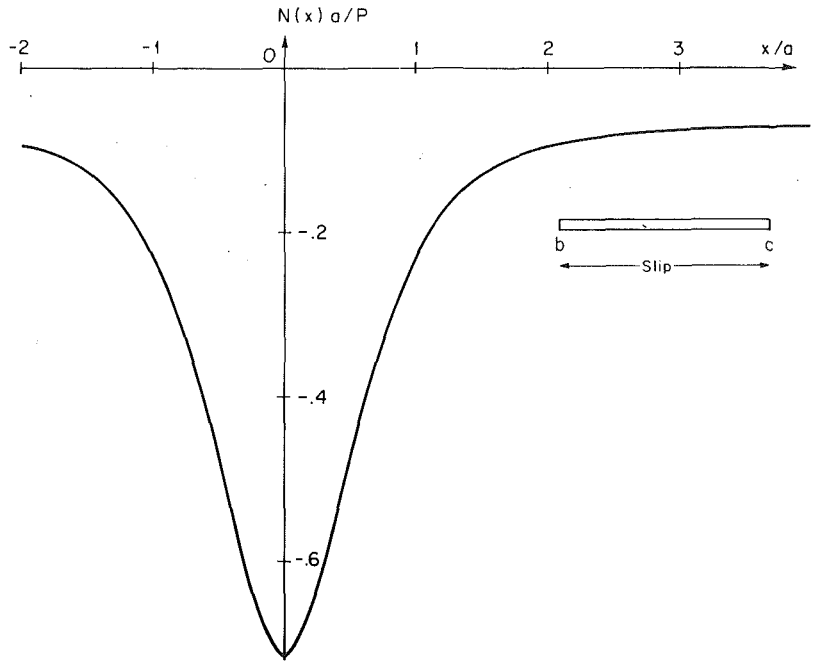

Fig. 6 Normal tractions for arrangement (*b*) with $b/a = 1.5$, $c/a = 2.3$, $\lambda = 13.98$

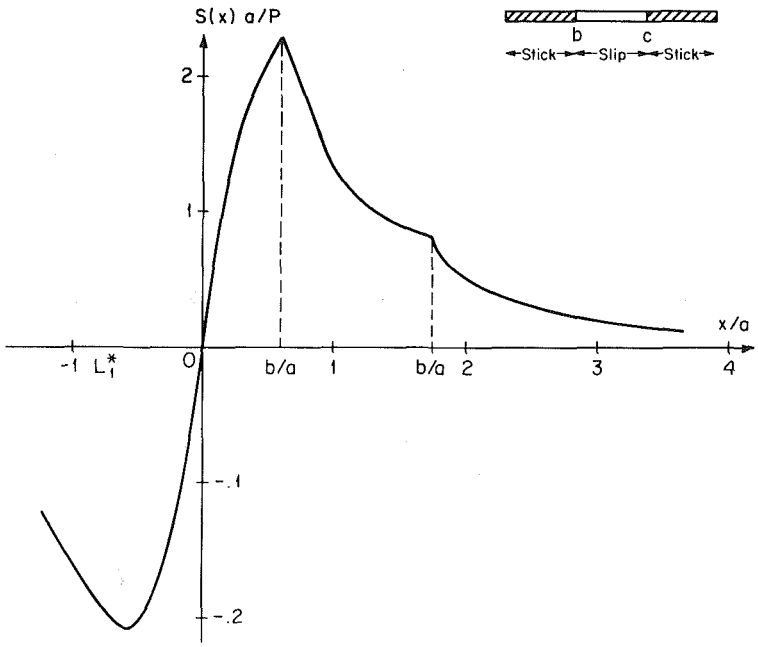

Fig. 7 Shear tractions for arrangement (c), $b/a = 0.6$, $c/a = 1.74$, $\lambda = 8.22$

$B(x)$ is square root singular at the end points marking transition between slip and undamaged material and it is bounded at the transition between slip and stick. When $B(x)$ is required to be bounded at both ends, as is the case for a detached slip zone, a consistency condition must be imposed on $B(x)$. This consistency condition is automatically included in the discretized system of equations obtained by the numerical method for singular intergral equations of Erdogan et al. [10], which is employed here. For details of the application of the method to the present problem, the reader is referred to [1–3].

We note that for the arrangement of Fig. 2(*a*) there is only one unknown parameter, c. For Fig. 2(*b*), there are no unknowns and for Fig 2(*c*) and 2(*d*) b and c are unknowns. For Fig. 2(*e*), b_1, b_2, c_2 are unknowns and for Fig. 2(*f*) b_1 and b_2 are unknowns. In all arrangements, except that of Fig. 2(*b*), one of the unknowns can be replaced by the load parameter

$$\lambda = P/p_0 a \tag{18}$$

to simplify the numerical procedure. For instance, in the arrangement of Fig. 2(*a*), c was specified and λ was computed. In the arrangement of Fig. 2(*c*), b was specified and λ and c were computed, etc.

Results for the mirror image arrangements are not presented.

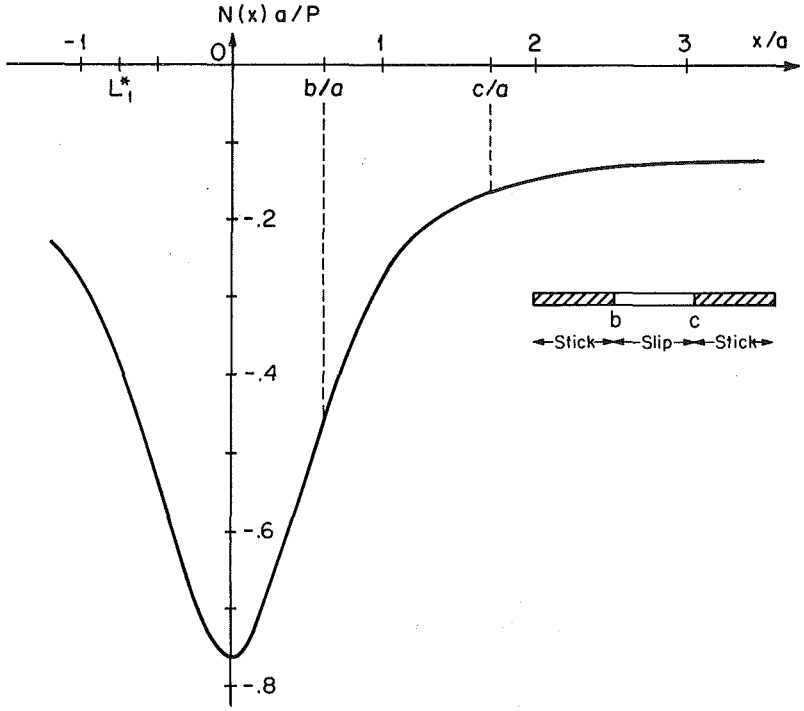

Fig. 8 Normal tractions for arrangement (c), $b/a = 0.6$, $c/a = 1.74$, $\lambda = 8.22$

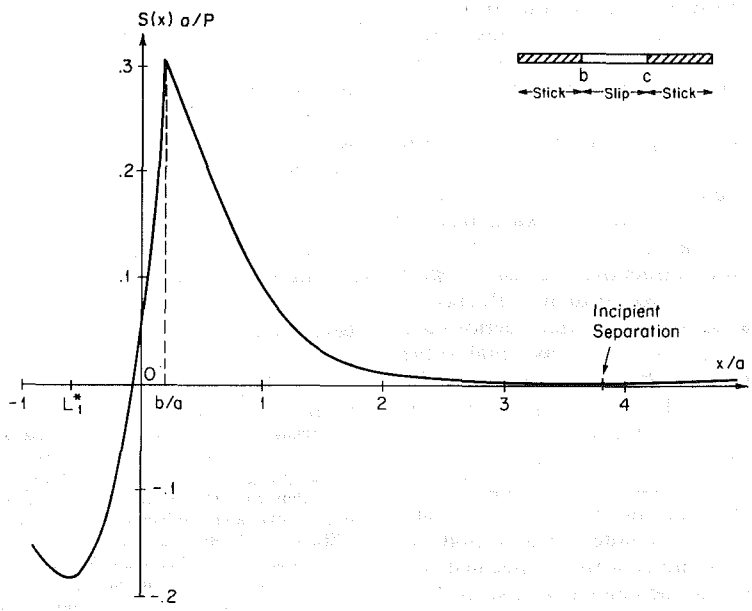

Fig. 9 Shear tractions for arrangement (c) at the onset of separation; $b/a = 0.19$, $c/a = 30.5$, $\lambda = 563$

Results

The results are summarized in Fig. 3 which gives the extent and the location of slip zones for a given value of the loading parameter λ and for $f = 0.5$. The two thick curves correspond to arrangement (*d*) and coincide with Fig. 6 of [1]. In this discussion, letter designations for slip arrangements correspond to those shown in Fig. 2.

Arrangement (*a*) is exemplified by a crack that starts at $x = 1.5a$ ($L_1 = b = 1.5a$). Slip starts at the crack tip L_1 when $P/p_0a = 8.3$ and extends to the right with increasing load. Eventually, the slip zone will extend to the right crack tip L_2, when transition to case (*b*) occurs. At this point, the shear stress intensity factor ahead of L_2 is still zero, Fig. 4. If the load is increased further, the shear tractions become singular ahead of L_2, Fig. 5. In both cases, the shear tractions are singular behind L_1. The corresponding normal tractions are practically the same as for the Flamant solution and are shown for one case in Fig. 6.

In arrangement (*c*) we start with one slip zone which is detached from the crack tips. The extent of the slip zone in this case differs only slightly from the right-hand zone in configuration (*d*) and the corresponding curve cannot be distinguished from the thick line in Fig. 3. With further increase of the load, slip reaches one of the crack tips leading to arrangement (*a*) or its mirror image. The case where the slip zone reaches the left tip first is illustrated in Fig. 3 for $L_1 = b$

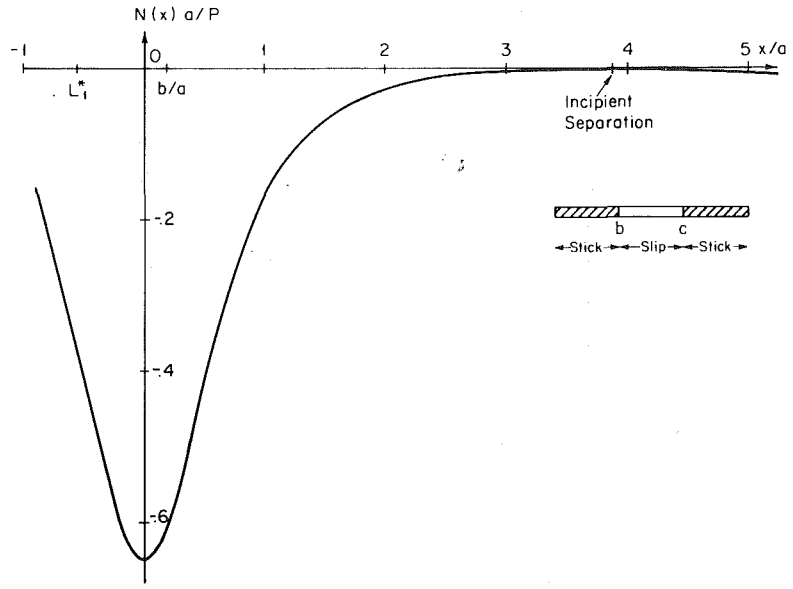

Fig. 10 Normal tractions for arrangement (c) at the onset of separation, $b/a = 0.19$, $c/a = 30.5$, $\lambda = 563$

$= 0.75a$. For this case, the right end of the slip zone c continues to follow curve (d) closely.

The configuration 2(e) must be preceeded by (d) if $L_1 < -a$ or by (c) if $L_1 > -a$. In the former case, the point b_1 is very close to the left curve (d), while in the latter it falls inside this curve. In both cases, the curve for the right slip zone practically coincides with 2(d). Examples are shown with $L_1 = -2a$ and $L_1 = -0.9a$.

Finally, an example for the arrangement (f) is shown with $L_1 = -1.3a$ and $L_2 = 0.9a$.

The biggest deviations in the extent of the slip zones from curve (d) occur when the slip zone grows outward from a crack tip as in cases $(a)_1$, $(e)_2$ of Fig. 3.

An example of shear and normal tractions is given in Fig. 7 and 8 for arrangement (c) and $b = 0.6a$. Note the influence of the slip zone on the shear tractions. The normal tractions are not much affected by slip and are approximately equal to the Flamant tractions. The location of the left crack tip can be arbitrary provided it does not extend beyond the point marked L_1^*, at which transiton to arrangement (e) occurs.

When the load is very high in comparison with those shown in Fig. 3, the inequality (11) is violated, indicating the occurrence of separation, and the present analsyis is not valid without modification. Here, we only note the conditions at the onset of separation. For example, with arrangement (c) separation starts approximately at the point $x = 3.8a$ for $\lambda = 563$ with $b = 0.188a$ and $c = 30.5a$. The corresponding shear and normal tractions are shown in Fig. 9 and 10.

In arrangement (e) separation was observed for $\lambda = 597$ in the vicinity of $x = 3.8a$ corresponding to $b_2 = 0.205a$, $c_2 = 30.5a$, $b_1 = -0.37a$ and $c_1 = -2.2a$. In arrangement (f) separation occurred for $\lambda = 483$ at $x \sim 3.7a$ and for symmetric slip zones $b_2 = -b_1 = 0.265a$, $c_2 = -c_1 = 23a$. In arrangement (d) separation also starts for approximately the same parameters.

In arrangement (b) the load at which separation starts depends on the location and crack extent. For example, for $b = 0.4a$ and $c = 3a$ separation starts at $x = 0.298a$ with $\lambda = 222$, while for $b = a$ and $c = 5a$ separation starts at $x = 4.39a$ with $\lambda = 235$.

The case of $p_0 = 0$ corresponds to $\lambda = \infty$. It cannot be examined with the present formulation because of the presence of separation. For arrangement (d), which is equivalent to a layer resting on a substrate, the slip zones become very large in the limit $\lambda = \infty$ and an increasing number of collocation points is required for convergence. For these reasons, the case of zero precompression is not examined here, but it will be considered in the future.

Acknowledgment

Support by the Office of Naval Research through contract N00014-81-K-0626 is gratefully acknowledged.

References

1 Comninou, M., Schmueser, D., and Dundurs, J., "Frictional Slip Between a Layer and Substrate Caused by a Normal Load," *International Journal of Engineering Science*, Vol. 18, 1980, pp. 131–137.

2 Schmueser, D., Comninou, M., and Dundurs, J., "Separation and Slip Between a Layer and a Substrate Caused by a Tensile Load," *International Journal of Engineering Science*, Vol. 18, 1980, pp. 1149–1155.

3 Schmueser, D., Comninou, M., and Dundurs, J., "Frictional Slip Between a Layer and a Substrate," *Journal of Engineering Mechanics Division*, ASCE, Vol. 107, 1981, pp. 1103–1118.

4 Comninou, M., Barber, J. R., and Dundurs, J., "Interface Slip Caused by a Surface Load Moving at Constant Speed," *International Journal of Mechanical Sciences*, Vol. 45, 1983, pp. 41–46.

5 Chang, F.-K., Comninou, M., and Barber, J. R., "Slip Between a Layer and a Substrate Caused by a Normal Force Moving Steadily Over the Surface," *International Journal of Mechanical Sciences*, in press.

6 Anscombe, H., and Johnson, K. L., "Slip of a Thin Solid Tyre Press-Fitted on a Wheel," *International Journal of Mechanical Sciences*, Vol. 16, 1972, pp. 525–534.

7 Hundy, B. B., "Shelling of Railway Wheels," *Railway Steel Topics*, Vol. 4, 1957, pp. 19–35.

8 Timoshenko, S. P., and Goodier, J. N., *Theory of Elasticity*, McGraw-Hill, New York, 1970.

9 Dundurs, J., and Comninou, M. "Some Consequences of the Inequality Conditions in Contact and Crack Problems," *Journal of Elasticity*, Vol. 9, 1979, pp. 71–82.

10 Erdogan, F., Gupta, G. D., and Cook, T. S., in *Methods of Analyses and Solution of Crack Problems*, Noordhoff, Leyden, 1973.

Subsurface Crack Propagation Due to Surface Traction in Sliding Wear

H.-C. Sin
Research Associate.

N. P. Suh
Professor of Mechanical Engineering.
Mem. ASME

Laboratory for Manufacturing
and Productivity,
Massachusetts Institute of Technology,
Cambridge, Mass. 02139

The mechanics of subsurface crack propagation in sliding wear of elastoplastic solids was investigated using the finite element method. The subsurface cracks, which experience both compressive and tangential loading, propagate along the direction of maximum shear stress and grow in a ductile manner due to plastic deformation of the crack tips. Based on the assumption that the crack growth rate is equal to the crack-tip sliding displacement, the wear rate was predicted for the case of crack propagation controlled delamination wear which compares favorably with the experimentally determined wear rates. According to the FEM results, linear elastic fracture mechanics (LEFM), which was previously used to determine the wear rate, is not an appropriate method of predicting the wear rate because of the large plastic deformation at the crack tip.

1 Introduction

Since the delamination theory of wear was introduced by Suh [1], extensive experimental and analytical work has substantiated the theory, showing that wear sheets in sliding wear are indeed formed as a result of subsurface deformation, crack nucleation, and crack propagation. In developing a quantitative model for delamination wear of two-phase metals, crack propagation was shown to be the slowest or rate controlling process among the steps involved in the delamination processes [2]. Since then, the mechanics of crack propagation in sliding wear has been investigated extensively.

Fleming and Suh [3] analyzed the propagation of a subsurface crack parallel to the surface using a linear elastic fracture mechanics (LEFM) approach. This treatment was based on the assumption that only the crack tip behind the moving asperity extends due to cyclic loading since the crack tip in front of the asperity contact is closed due to the compressive normal stress, while the trailing tip of the crack behind the moving asperity contact is in the elastic region subjected to tensile stress. The stress intensity factors at the trailing crack tip due to an elliptically distributed load acting at the asperity contact were calculated using an approximate method based on weighting factors. The stress intensity factors for Mode *I* and Mode *II* computed in this manner were very small, being less than the threshold stress intensity factor, although the stress intensity factor for Mode *II* was about an order of magnitude larger than that for Mode *I*. Essentially similar results were obtained by Hills and Ashelby [4], Rosenfield [5], and Keer et al. [6], although they computed the stress intensity factors at both ends of the crack using either different boundary conditions or different methods. The major shortcoming of these works is the use of linear elastic fracture mechanics when the actual plastic zone surrounding the crack tip is large extending to the surface.

Recently, Rosenfield [7] applied the dislocation model of a shear crack, which was originally developed by Bilby, Cottrell, and Swinden [8] to account for the plastic deformation at the crack tip. This model suggests that wear rates are controlled by the crack-tip sliding displacement and predicts that there may be crack growth when the friction between the opposing faces of the crack is not too large. The shortcoming of this model is that it assumes a uniformly distributed load on the wear surface, which does not approximate a typical sliding situation.

Our understanding of the mechanism of crack propagation has improved as a result of these extensive analytical studies. However, results of the linear elastic fracture mechanics (LEFM) approach has only limited use. The purpose of this paper is threefold:

(*a*) To show that the crack propagation in delamination wear cannot be explained by LEFM because of the large plastic zone at the crack tip.

(*b*) To critically investigate the criteria for crack growth and the direction of crack extension under sliding conditions which involve both compression and shear loading.

(*c*) To predict the rate of crack propagation in sliding wear through the elastoplastic finite element analysis of the crack tip sliding displacement (CTSD).

Contributed by the Applied Mechanics Division for presentation at the 1984 PVP Conference and Exhibition, Joint with Applied Mechanics Division and Materials Division, San Antonio, Texas, June 17-21, 1984 of THE AMERICAN SOCIETY OF MECHANICAL ENGINEERS.

Discussion on this paper should be addressed to the Editorial Department, ASME, United Engineering Center, 345 East 47th Street, New York, N.Y. 10017, and will be accepted until two months after final publication of the paper itself in the JOURNAL OF APPLIED MECHANICS. Manuscript received by ASME Applied Mechanics Division, November, 1982; final revision September, 1983. Paper No. 84-APM-27.

Copies will be available until February, 1985.

Table 1 Stress intensity factor range, ΔK_{II} ($MNm^{-3/2}$), at left and right tips for a small crack ($c = 1/4a$)

d/a		μ: 0.25	0.5	1.0
0.3	Left	1.05	1.07	1.44
	Right	1.28	1.34	1.44
0.5	Left	1.08	1.11	1.15
	Right	1.35	1.40	1.49
1.0	Left	0.67	0.68	0.70
	Right	0.89	0.94	1.06

a = half length of asperity contact
c = half length of crack
d = depth of crack location
μ = coefficient of friction

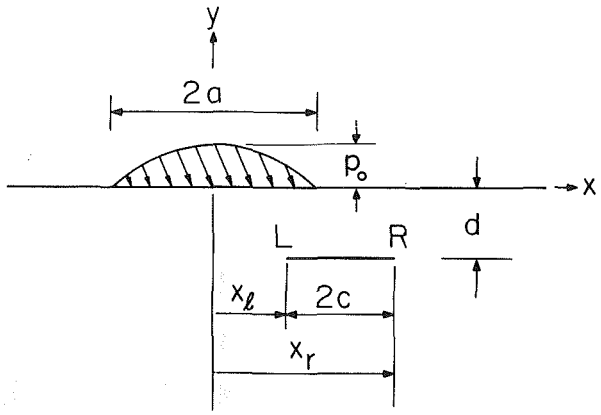

Fig. 1 Geometry of the subsurface crack

Before we proceed it should be mentioned that there are certain limitations to the present FEM analysis of wear. Normally, the wear surface is severely work-hardened and there is an extremely severe strain gradient normal to the surface. In addition, the near-surface material is highly anisotropic. None of these factors are considered in the model due to limitations of our present knowledge.

2 Remarks on the Previous Crack Propagation Studies

The most controversial aspect of crack propagation studies of the past is the use of LEFM and the boundary conditions. Since a number of conclusions have been drawn based on these studies, the controversial points will be reviewed before discussing the results of the finite element analysis of crack propagation in elastoplastic solids.

2.1 The Limitations of the Linear Elastic Approach. Linear elastic fracture mechanics (LEFM) has been used to predict the rate of crack propagation under cyclic loading. The prerequisites are that the change in the stress intensity factor be larger than a critical value called the threshold value and that the plastic zone at the crack tip be smaller than a critical dimension of the part. When the plastic zone size at the crack tip is so large that it extends to a stress-free boundary the stress intensity has no longer any physical significance.

The calculated stress intensity factors reported to date [3–6] for sliding wear are less than the known threshold values for crack propagation under cyclic loading. Table 1 shows the values of stress intensity factor calculated using LEFM for a small subsurface crack subjected to surface traction as shown in Fig. 1. The maximum pressure p_0 was assumed to be 980 MPa, and a half of the crack length a to be 10 μm. The computed stress intensity factor is of the order of the known threshold stress intensity factor for steel.

In short, not only is the stress intensity factor too small to enable any crack propagation, but also the plastic zone size is too large, being comparable with or larger than the distance from crack tip to surface, for LEFM to be valid. Therefore, it is necessary to analyze the full elastoplastic deformation of the crack tip.

2.2 On the Friction Boundary Condition Between Crack Surfaces. The friction force between crack surfaces plays an important role when the crack is under compressive loading. This friction force complicates the analysis since the shear and normal stresses at the contacting crack surfaces are not known. Therefore, the problem has to be solved using an assumed friction coefficient, i.e., the ratio of these unknown stresses.

There are several papers that treat this friction problem [4, 5, 10]. However, none of them apply correct boundary conditions. In those treatments the normal and shear stresses at the crack surfaces due to the applied load were assumed to be known and the net shear stress was obtained as $\tau_{net} = \tau_{applied} - \mu|\sigma_{normal}|$. However, this is a rough approximation of the real situation. These stresses are generally unknown and, therefore, cannot be used in an explicit formulation.

In this study only the limiting case of zero friction coefficient was solved using the finite element method. When the friction coefficient between crack surfaces is finite, the strain and the stress concentration at the crack tip is expected to be smaller than when there is no friction. The role of friction between closed surfaces is very complicated, because the actual frictional force distribution along the crack surface under the moving load and the effect of the roughness of crack surfaces on stress concentration cannot be modeled with any degree of certainty. These are two of the many difficult issues that have to be investigated further.

2.3 On Crack Trajectory. In sliding wear there are two experimental aspects of crack propagation that need to be understood. Experiments show that many cracks propagate parallel to the surface and ultimately the cracks change the direction toward the surface, terminating the growth. In

Nomenclature

a = Half length of asperity contact
c = Half crack length
d = Depth of crack location
k = Shear yield stress
p_0 = Maximum normal stress at the center of asperity contact
r = Radial coordinate from a crack tip
E = Modulus of elasticity
E_T = Tangential modulus
K_I = Mode *I* stress intensity factor
K_{II} = Mode *II* stress intensity factor
ΔK_{II} = Mode *II* stress intensity factor range
ΔC = Crack growth length
ΔS = Crack-tip sliding displacement
ΔC_w = Length of rewelding
μ = Friction coefficient
ν = Poisson's ratio
θ = Angular coordinate from the crack plane
τ_{max} = Maximum shear stress
$\tau_{applied}$ = Applied shear stress
τ_{net} = Net shear stress
σ_{normal} = Applied normal stress
σ_y = Yield stress

delamination wear only the crack tip at the trailing side reaches the surface [13].

Notwithstanding the importance of the subject matter, no acceptable criterion for crack propagation exists for fracture involving combined compressive and shear loading. In the past only the propagation of a crack under simple loading conditions has been studied. There are two criteria that are commonly used in predicting the crack propagation direction: the maximum hoop stress criterion [11] and the minimum strain energy density criterion [12].

When the maximum principal stress criterion is applied to the subsurface cracks using the stress intensity factors calculated [9] it predicts the crack extension direction to be about 110 deg at the left (trailing) tip and about 70 deg at the right (leading) tip from the positive x-axis direction which is parallel to the surface (see Fig. 1), implying that the crack extends toward the surface at both tips. Similar results are obtained using the energy criterion. This might explain why the subsurface crack at the trailing tip extends to the surface when the crack is in the tensile zone. However, the argument is based on the elastic solution and, therefore, may be irrelevant unless the actual plastic stress components are proportional to the corresponding elastic stress components used for the prediction. At any rate, these criteria cannot be used to explain crack propagation when cracks are under compressive and shear loading.

Experimental results of Jahanmir et al. [13] show that the subsurface cracks propagate parallel to the surface considerable distances before they become loose. In sliding wear, since the slip planes are shown to line up parallel to the surface, the maximum shear stress direction of these planes is likely to be the crack propagation direction. The result of the elastoplastic finite element study in the next section seems to support this. However, it cannot be ascertained since the entire region of interest is in plastic condition and consequently, the maximum shear stresses everywhere in the region reach the shear yield stress. Therefore, we may have to examine the stress history to determine where yielding first occurs.

Generally, yielding starts from where the maximum shear stress reaches the shear yield stress first. Elastic solutions, normally being functions of Mode I and Mode II stress intensity factors in this case, can be used to determine the yield conditions. If the maximum shear stress distribution is known as a function of direction, the direction in which the maximum shear stress possesses the highest value can be determined as being the direction of crack propagation.

The foregoing discussion allows us to use the elastic solution to determine the direction of subsurface crack propagation since we only have to find the direction where yielding first occurs. In plane strain the maximum shear stress $\tau_{\max}$ is easily obtained using the crack-tip stress components as [11]

$$\tau_{\max} = \frac{1}{2\sqrt{2\pi r}}[K_I^2 \sin^2\theta + 2K_I K_{II} \sin 2\theta + K_{II}^2(4 - 3\sin^2\theta)]^{1/2} \quad (1)$$

When the Mode I and Mode II stress intensity factors calculated by the finite element method are used for the angle of the maximum of $\tau_{\max}$, the equation predicts the angles of between -5 and 5 deg for most cases of interest. These values are very small, implying that cracks propagate parallel to the surface.

Crack growth in the shear direction has also been observed and suggested by others. McClintock [10], while investigating the crack behavior in the rail under rolling conditions, has suggested that cracks in a compressive field are most likely to grow in shear. In fact, Forsyth [14] has observed that fatigue cracks have two growth regimes. In Stage I, cracks formed on the slip planes of the persistent slip bands grow when they are most closely aligned with the maximum shear stress direction. Furthermore, Besuner [15] has suggested that if the cyclic principal stresses are primarily compressive, then there is no reason for a crack to align itself at right angles to a compressive maximum principal stress.

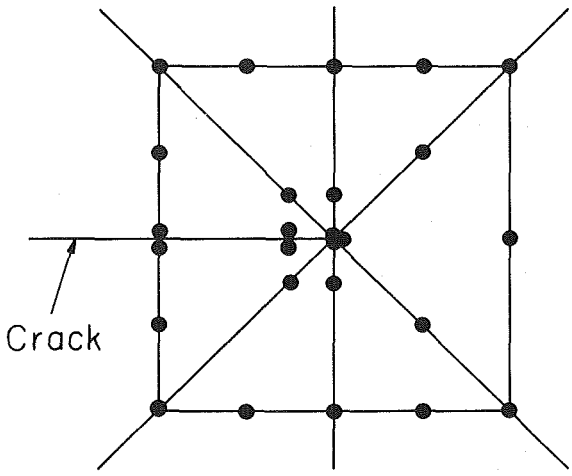

Fig. 2 Finite element mesh around a crack tip

In summary, it is found that the direction of crack propagation is coincident with the direction of maximum shear stress at the crack tip. This is consistent with the experimental observations.

3 The Crack Propagation Mechanism in Elastoplastic Solids

The allowable plastic size consideration and the small values of the stress intensity factor at the crack tip suggest that elastoplastic fracture mechanics approach is required in studying the subsurface crack propagation. In this section the problem is investigated using the elastoplastic finite element analysis.

3.1 FEM Analysis and Results. The same model was used as in the case of elastic analysis (see Fig. 1) to calculate the elastoplastic response under the moving load. No dynamic effect was considered in the analysis. The material was assumed to be isotropic and slightly work-hardening ($E_T = 10^{-4}E$). Other properties used were as follows: $E = 1.96 \times 10^5$ MPa (2×10^4 kg/mm^2), $\nu = 0.28$, $\sigma_y = \sqrt{3}k = 424$ MPa (43.3 kg/mm^2).

For the investigation of crack propagation only a short crack ($c = 1/4\ a$) was used. Due to the prohibitively expensive computer cost a limited parameter study was conducted for the case of $a = 10\ \mu$m, $p_0 = 4k$, and $\mu = 0.25$.

Throughout the study the ADINA finite element program developed by Bathe [16] was used. The solution techniques regarding the choice of load increment per step and iteration procedures are described in detail in reference [17], particularly for the present study in reference [9], and will not be repeated here.

Proper crack-tip modeling is quite important in simulating crack tip deformation and propagation. As shown by deLorenzi and Shih [18] an eight-noded triangular element with the side nodes at the midpoints can have a $1/r$ singularity when three nodes at a crack tip are allowed to separate during deformation. This type of singularity representation is suitable for the HRR field [19–21] when the material model is elastic-perfectly plastic.

When the elements of the type mentioned in the foregoing are used in the case of tensile loading, they allow the modeling of crack tip blunting as the nodal points separate during

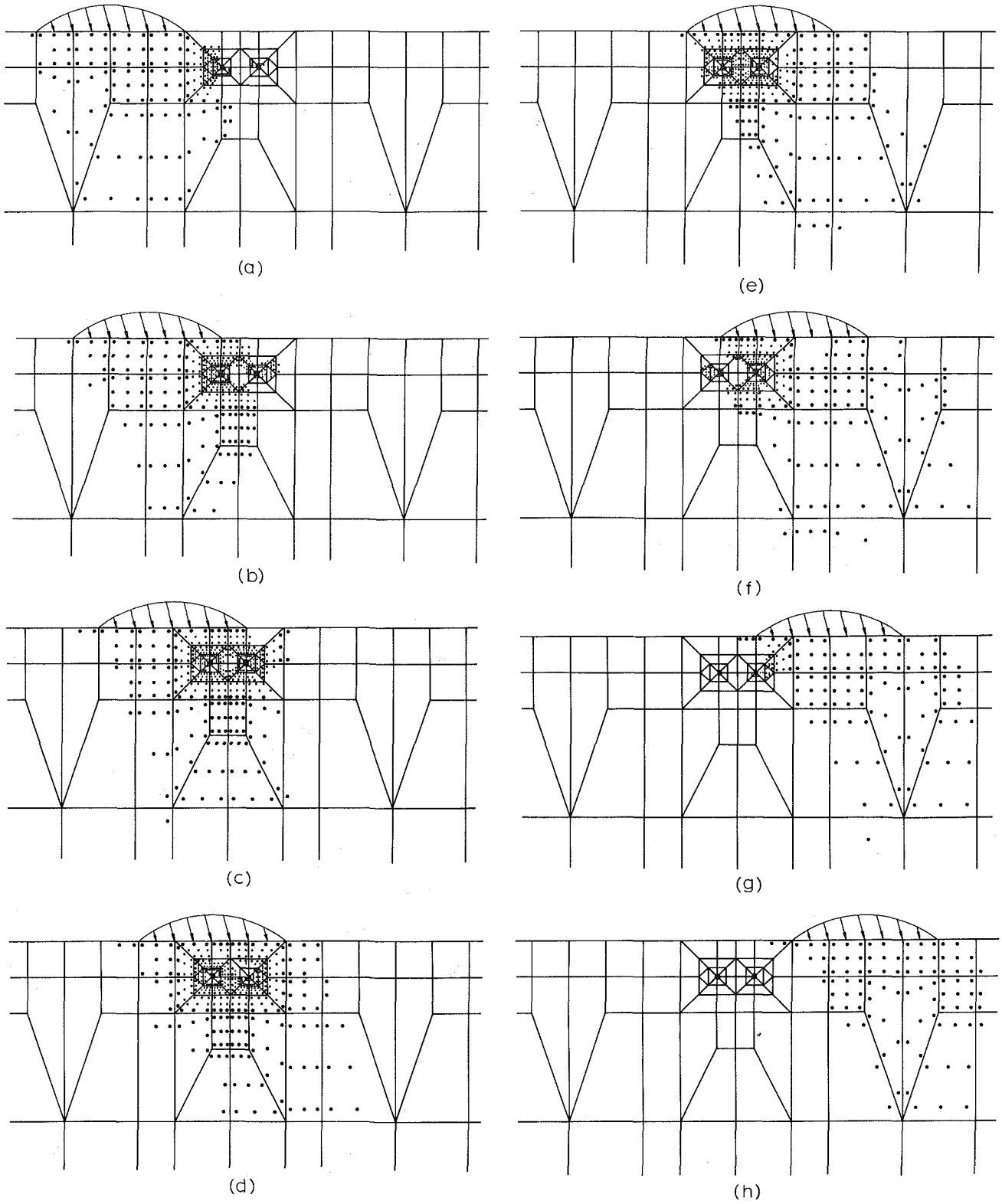

Fig. 3 Plastically deformed zone around a crack under a moving asperity load: $a = 10\ \mu m$, $c = 2.5\ \mu m$, $d = 5\ \mu m$, $\mu = 0.25$, and $p_0 = 980$ MPa ($= 4k$). Dots indicate the integration points (3 × 3 integration order in this case) that were plastically deformed in each finite element.

deformation. However, when a crack tip is in the combined compression and shear loading, all nodes at the tip must be constrained properly. Without any constraint too many crack tip nodes may overlap, resulting in geometrical incompatibility. Preliminary analyses of different crack tip modeling have suggested that the use of only one element with $1/r$ singularity in the direction of propagation and several singular elements of other type around the element is a reasonably good mesh design for the representation of crack-tip deformation in this case. This is shown in Fig. 2.

Table 2 Relative crack-tip sliding displacement (μm)

(a) For a crack at the depth of 5 μm

	a	b	c	d	e	f	g	h*
Right tip	0.0009	0.0023	0.0033	0.0027	0.0015	−0.0009	−0.0008	−0.0001
Left tip	0.0013	0.0030	0.0035	0.0028	0.0004	−0.0012	−0.0005	−0.0003

(b) For a crack at the depth of 2.5 μm

	a	b	c	d
Right tip	0.0003	0.0012	0.0077	0.0093
Left tip	0.0002	0.0031	0.0141	0.0138

*Each step corresponds to the relative position of moving asperity contact to a crack shown in Fig. 3.

Figure 3 shows the development of plastic zone at each step of the moving load when the mesh discussed in the foregoing is used. When the load is applied at the distance from the crack, the overall shape of the zone plastically deformed is not affected much by the presence of the crack. When the load moves over the crack, however, the stress field changes significantly due to the crack. It should be noticed that there are some spots inside the plastic region where unloading has taken place. It is expected that the overall plastic zone should become smaller with the repeated loading and unloading.

According to the numerical results, the nodal points on the crack surfaces are displaced so that the upper surface initially slides forward and then it slides backward as the load moves over the surface above the crack. This is consistent with the result obtained by McClintock [10] for subsurface cracks in a solid rolling contact. Table 2 lists the relative sliding displacements of crack-tip nodal points for two different depths of crack location. It shows that the relative displacement increases as the contact load moves over the crack, then decreases, and finally changes the sign. The following can also be observed from the table: (1) the crack closer to the surface has larger displacements and (2) the left tip usually undergoes large relative sliding displacements.

In Figs. 4 and 5 the shear strain at the crack tip are plotted as a function of the distance from the crack tip for different stages of the loading position as the asperity contact moves from left to right. The distribution of shear strain increases until it reaches a maximum value and then decreases. After it attains a minimun, it increases again. At very near the tip the shear strain changes from positive to negative, and then to positive again. When the state of stress is complex, the equivalent strain is the relevant plasticity parameter rather than any one strain component. However, it is rather difficult to obtain the distribution of equivalent strain along the distance from the tip. Nevertheless, in this case the use of this shear strain component is quite acceptable since the other components of strains do not change much.

3.2 The Mechanism of Crack Propagation. The J integral and the crack-opening displacement are the most frequently used parameters in characterizing plastic fracture mechanics. However, some difficulties are associated with both. First, the path independence of J integral, which is derived using deformation theory of plasticity, has not been proven for incremental plasticity. Elastoplastic finite element calculations have shown that J is strongly path-dependent for contours very close to the crack tip, which is the region where heavy plastic deformation takes place [22, 23]. Second, McClintock [24] has shown that the different degrees of constraint associated with various in-plane configurations would prevent the satisfactory development of a one-parameter theory of fracture mechanics for full plasticity.

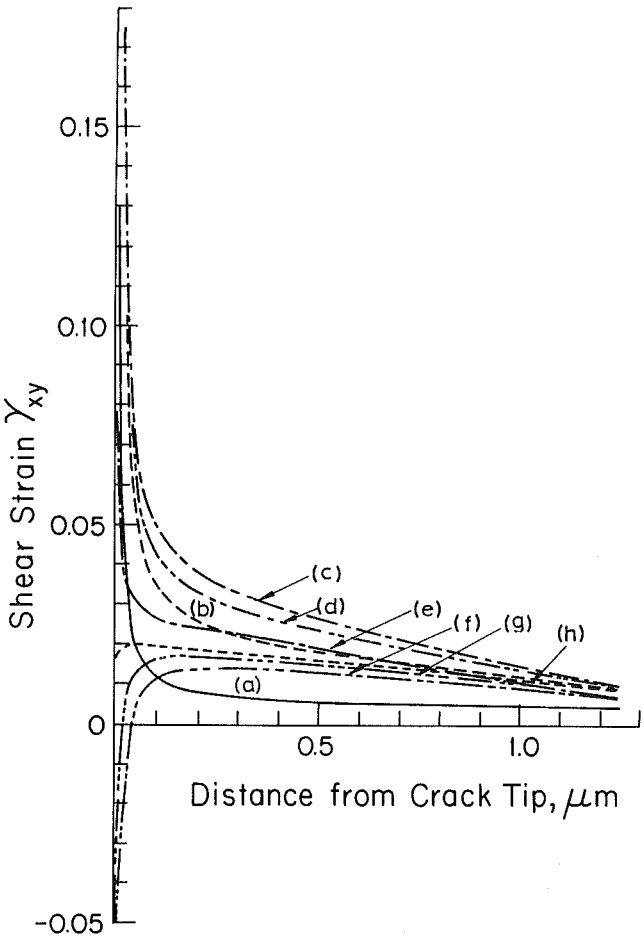

Fig. 4 Shear strain versus distance from the left crack tip. Each step from (*a*) to (*h*) corresponds to the relative position of moving asperity contact to a crack shown in Fig. 3.

On the other hand, the crack-opening displacement is conceptually simple and straightforward regardless of its appropriateness for a one-parameter characterization of crack-tip fields. The analytical treatment, however, is very difficult because of the complexity for elastoplastic materials and therefore, finite element analyses have been used extensively for the study of crack tip profiles. In finite element analysis it is essential to use sophisticated crack-tip elements to obtain satisfactory modeling of the deformation. In addition to the computational difficulty, the relation between crack-opening displacement and crack propagation is not yet fully understood.

Almost all the discussions regarding the crack propagation

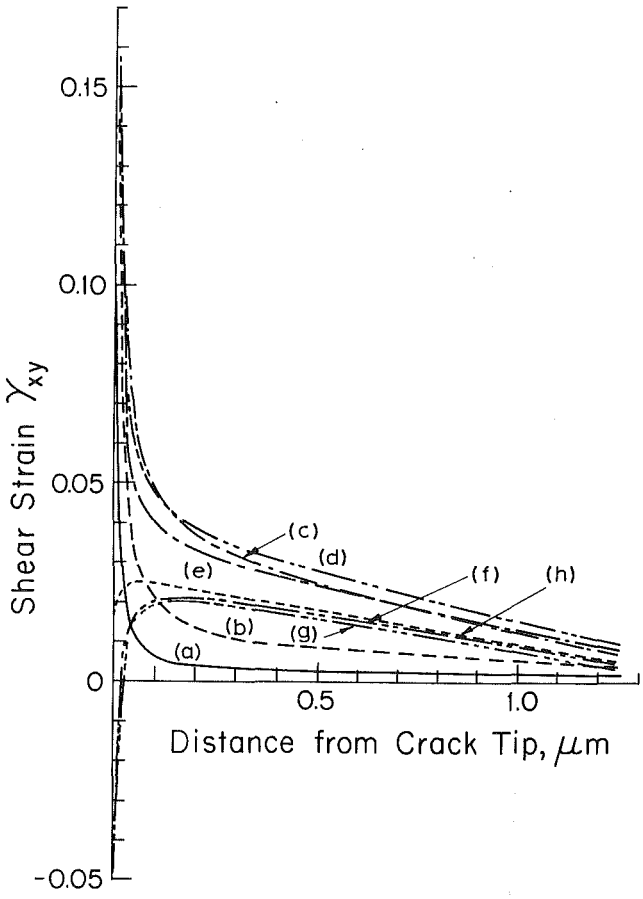

Fig. 5 Shear strain versus distance from the right crack tip. Each step from (*a*) to (*h*) corresponds to the relative position of moving asperity contact to a crack shown in Fig. 3.

in the literature are limited to Mode *I* and Mode *III*. In sliding wear the subsurface cracks are subjected to Mode *II* or combined Mode *I* and Mode *II* loading. As shown previously the subsurface cracks in sliding wear are likely to grow in the direction parallel to the surface. Since experimental results show that the surface texture developed due to sliding is that of slip planes [25, 26] the cracks propagate along a direction nearly parallel to the slip planes.

The crack-opening displacement concept is applied here to determine the growth rate of a crack subjected to combined compressive and shear loads. In this mode the relative sliding displacement at the crack tip occurs by means of slip due to crack tip deformation. If the maximum relative displacement is employed as a crack-tip sliding displacement (CTSD), ΔS, then the crack growth length ΔC may be expressed as

$$\Delta C = \Delta S - \Delta C_w \tag{2}$$

where ΔC_w is the length of rewelding. According to equation (2), the crack growth in Mode *II* is always equal to CTSD if rewelding does not occur.

As can be seen from Table 2, the relative sliding displacement at crack tips varies with the magnitude of the moving asperity load and is a function of the geometric location of cracks. To determine the crack growth from the crack-tip sliding displacement, an appropriate fracture criterion must be used. A commonly used fracture criterion is the strain at fracture. When a crack is loaded, the crack will grow up to the point where the strain exceeds the fracture strain. If a material has a high fracture strain, the crack growth will be smaller than when the same material has a lower fracture strain. However, little information is available on fracture strain for these complex loading situations and hence it is impossible to determine the exact relation between crack-tip sliding displacement and crack growth at the present time. Nevertheless, when the maximum relative sliding displacement in Table 2 for cracks at various depth are assumed to be the crack growth rates, the predicted wear rates compare favorably with the experimentally determined wear rates [27].

The numerical results indicate that the extent of crack growth ΔC increases with decreasing depth of crack d for a given friction coefficient. Therefore, cracks near the surface should propagate faster than those away from the surface. However, experimentally cracks are only observed at a finite distance below the surface. This is because they cannot nucleate very near the surface due to the high triaxial state of compressive stress [2]. The location of the cracks is determined not only by the state of stress but also by the metallurgical factors. For example, in two-phase metals in which cracks preferentially nucleate at the hard particle/matrix interface, the actual location of the crack will be determined by the location of the particles.

As pointed out earlier it is quite important to use specially designed crack tip elements for accurate numerical simulation. The isoparametric triangular element with $1/r$ singularity seems to be well suited to the requirements. Unfortunately, this element is good only for the elastic-perfectly plastic material.

4 Conclusions

(1) The propagation of subsurface cracks in elastoplastic solids can be characterized by the crack-tip sliding displacement.

(2) The maximum shear stress criterion for the direction of shear crack growth predicts the experimentally observed crack propagation direction under combined compressive and shear loading which is parallel to the sliding direction.

(3) The linear elastic fracture mechanics approach is inappropriate for studying the mechanism of subsurface crack propagation in sliding wear.

Acknowledgments

This research was supported by the Office of Naval Research under contract No. N00014-78-C-0252. The authors are grateful to Commander Harold P. Martin and Mr. Keith Ellingsworth for their personal support of this work.

References

1 Suh, N. P., "The Delamination Theory of Wear," *Wear*, Vol. 25, 1973, pp. 111–124.

2 Jahanmir, S., and Suh, N. P., "Mechanics of Crack Propagation in Delamination Wear," *Wear*, Vol. 44, 1977, pp. 17–38.

3 Fleming, J. F., and Suh, N. P., "Mechanics of Crack Propagation in Delamination Wear," *Wear*, Vol. 44, 1977, pp. 39–56.

4 Hills, D. A., and Ashelby, D. W., "On the Application of Fracture Mechanics to Wear," *Wear*, Vol. 54, 1979, pp. 321–330.

5 Rosenfield, A. R., "A Fracture Mechanics Approach to Wear," *Wear*, Vol. 61, 1980, pp. 125–132.

6 Keer, L. M., Bryant, M. D., and Haritos, G. K., "Subsurface Cracking and Delamination," *Solid Contact and Lubrication*, ASME Publication AMD-Vol. 39, 1980, pp. 79–95.

7 Rosenfield, A. R., "A Dislocation Theory Approach to Wear," *Wear*, Vol. 72, 1981, pp. 97–103.

8 Bilby, B. A., Cottrell, A. H., and Swinden, K. H., "The Spread of Plastic Yield From a Notch," *Proceedings of the Royal Society*, London, Series *A*, Vol. 272, 1963, pp. 304–314.

9 Sin, H.-C., "Surface Traction and Crack Propagation in Delamination Wear," Ph.D. thesis, Massachusetts Institute of Technology, Cambridge, Mass., Oct., 1981.

10 McClintock, F. A., "Plastic Flow Around a Crack Under Friction and Combined Stress," *Fracture 1977*, Taplin, D. M. R., ed., Vol. 4, Pergamon, 1978, pp. 49–64.

11 Erdogan, F., and Sih, G. C., "On the Crack Extension in Plates Under Plane Loading and Transverse Shear," ASME *Journal of Basic Engineering*, Vol. 85, 1963, pp. 519–527,

12 Sih, G. C., "Strain-Energy-Density Factor Applied to Mixed Mode Crack Problems," *International Journal of Fracture*, Vol. 10, 1974, pp. 305–321.

13 Jahanmir, S., Suh, N. P., and Abrahamson, E. P., "Microscopic Observations of the Wear Sheet Formation by Delamination," *Wear*, Vol. 28, 1974, pp. 235–249.

14 Forsyth, P. J. E., "A Two Stage Process of Fatigue Crack Growth," *Proceedings of Crack Propagation Symposium*, Vol. 1, 1961, pp. 76–94.

15 Besuner, P. M., "Fracture Mechanics Analysis of Rails with Shell-Initiated Transverse Cracks," *Rail Steels—Developments, Processing, and Use*, ASTM STP 644, 1978, pp. 303–329.

16 Bathe, K.-J., "ADINA—A Finite Element Program for Automatic Dynamic Incremental Nonlinear Analysis," Report 82448-1, Acoustics and Vibration Laboratory, Massachusetts Institute of Technology, Cambridge, Mass., 1975.

17 Bathe, K.-J., and Cimento, A. P., "Some Practical Procedures for the Solution of Nonlinear Finite Element Equations," *Journal of Computer Methods in Applied Mechanics and Engineering*, Vol. 22, 1980, pp. 59–85.

18 deLorenzi, H. G., and Shih, C. F., "Application of ADINA to Elastic-Plastic Fracture Problems," *Applications Using ADINA*, Proceedings of the ADINA Conference, Bathe, K.-J., ed., Report 82448-6, Acoustics and Vibration Laboratory, Massachusetts Institute of Technology, Cambridge, Mass., 1977, pp. 349–383.

19 Hutchinson, J. W., "Singular Behavior at the End of a Tensile Crack in a Hardening Material," *Journal of the Mechanics and Physics of Solids*, Vol. 16, 1968, pp. 13–31.

20 Hutchinson, J. W., "Plastic Stress and Strain Fields at a Crack Tip," *Journal of the Mechanics and Physics of Solids*, Vol. 16, 1968, pp. 337–347.

21 Rice, J. R., and Rosengren, G. F., "Plane Strain Deformation Near a Crack Tip in a Power-Law Hardening Material," *Journal of the Mechanics and Physics of Solids*, Vol. 16, 1968, pp. 1–12.

22 McMeeking, R. M., "Path Dependence on the *J*-Integral and the Role of *J* as a Parameter Characterizing the Near-Tip Field," *Flaw Growth and Fracture*, ASTM STP 631, 1977, pp. 28–41.

23 Atluri, S. N., Nakagaki, M., and Chen, W.-H., "Fracture Analysis Under Large-Scale Plastic Yielding: A Finite Deformation, Embedded Singularity, Elastoplastic Incremental Finite-Element Solution," *Flaw Growth and Fracture*, ASTM STP 631, 1977, pp. 42–61.

24 McClintock, F. A., "Effects of Root Radius, Stress, Crack Growth and Rate of Fracture Instability," *Proceedings of the Royal Society*, London, Series *A*, Vol. 28, 1965, pp. 58–72.

25 Wheeler, D. R., and Buckley, D. H., "Texturing in Metals as a Result of Sliding," *Wear*, Vol. 33, 1975, pp. 65–74.

26 Krause, H., and Demirci, A. H., "Texture Changes in the Running Surface of Face-Centered Cubic Metals as a Result of Frictional Stress," *Wear*, Vol. 61, 1980, pp. 325–332.

27 Suh, N. P., and Sin, H.-C., "On Prediction of Wear Coefficients in Sliding Wear," *ASLE Transactions*, Vol. 26, 1983, pp. 360–366.

J. P. Dempsey
Assistant Professor,
Department of Civil and
Environmental Engineering,
Clarkson University,
Potsdam, N.Y. 13676
Assoc. Mem. ASME

L. M. Keer
Professor,
Department of Civil Engineering,
Northwestern University,
Evanston, Ill. 60201
Mem. ASME

N. B. Patel
Graduate Student,
Department of Civil and
Environmental Engineering.

M. L. Glasser
Professor,
Department of Mathematics and
Computer Science.

Clarkson University,
Potsdam, N.Y. 13676

Contact Between Plates and Unilateral Supports

The tendency of a laterally loaded, unilaterally constrained, rectangular plate to separate from its simple supports motivates one to consider the actual extent of contact. In the case of a square plate, an appropriately chosen finite integral transform converts the dual series equations that result from the Levy-Nadai approach to one singular integral equation which can be solved by standard methods. Being a receding contact problem, the extent of contact depends on the geometry and elastic properties of the plate only. The support reactions are integrated to confirm that total equilibrium is obtained using classical plate theory.

Introduction

The bending of plates that are partially constrained along all edges, without anchoring the corners, is examined here. Unilateral supports, or supports capable of exerting forces in one direction only, allow the plate to seek its natural contact. Since parts of the plate near the corners will bend away from the supports upon loading, it is clear that the problem is one of receding contact [1]. It therefore follows that the extent of contact between the plate and the supports is independent of the level of loading and that the support reactions are proportional to the load.

To solve this unconstrained plate problem, an assumption has to be made concerning the nature of the singularity at the points where the simple supports change to a free edge. Keer and Mak [2] solved for the extent of contact between a laterally loaded quarter infinite plate that is not anchored at the corner by allowing no singularity in the moments, and the same assumption is made here. While a singular distribution of support reactions is still found, it is integrable and the resultant is equal to the total applied load.

Rectangular plates that are partially supported have been considered by Kiattikomol, et al. [3], and rectangular plates that involve considerations of advancing contact have been considered by Dundurs, et al. [4]. The corners of the plates studied in [3, 4] are anchored.

Formulation

To simplify the analysis, a square plate is considered in this paper, and as shown in Fig. 1, the lengths involved are scaled. The actual dimension of the square plate is a, and the actual (barred) coordinates are, for instance, $\bar{x} = ax/\pi$ and $\bar{y} = ay/\pi$. The plate is partially simply supported on each edge. A constant load q is supplied in the z direction, with the corresponding displacement given by $w(x,y)$. The differential equation satisfied by w is

$$\frac{\partial^4 w}{\partial x^4} + 2\frac{\partial^4 w}{\partial x^2 \partial y^2} + \frac{\partial^4 w}{\partial y^4} = qa^4/D\pi^4, \qquad (1)$$

where $D = Eh^3/12(1-\nu^2)$ is the bending stiffness, E is Young's modulus, ν is Poisson's ratio, and h is the plate thickness.

The stress couples and resultants are

$$M_x = -\left(\frac{\pi}{a}\right)^2 D\left(\frac{\partial^2 w}{\partial x^2} + \nu\frac{\partial^2 w}{\partial y^2}\right), \qquad (2a)$$

Contributed by the Applied Mechanics Division for presentation at the 1984 PVP Conference and Exhibition, Joint with Applied Mechanics Division and Materials Division, San Antonio, Texas, June 17-21, 1984 of THE AMERICAN SOCIETY OF MECHANICAL ENGINEERS.

Discussion on this paper should be addressed to the Editorial Department, ASME, United Engineering Center, 345 East 47th Street, New York, N.Y. 10017, and will be accepted until two months after final publication of the paper itself in the JOURNAL OF APPLIED MECHANICS. Manuscript received by ASME Applied Mechanics Division, June, 1983. Paper No. 84-APM-34.

Copies will be available until February, 1985.

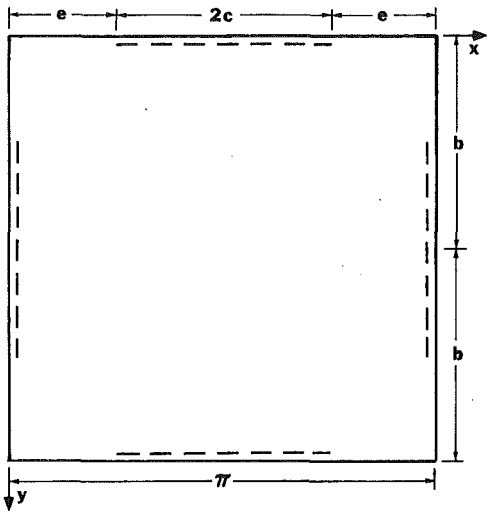

Fig. 1 Square plate with unilateral supports

$$M_y = -\left(\frac{\pi}{a}\right)^2 D\left(\frac{\partial^2 w}{\partial y^2} + \nu\frac{\partial^2 w}{\partial x^2}\right), \quad (2b)$$

$$M_{xy} = -M_{yx} = \left(\frac{\pi}{a}\right)^2 D(1-\nu)\frac{\partial^2 w}{\partial x \partial y}, \quad (2c)$$

$$V_x = -\left(\frac{\pi}{a}\right)^3 D\frac{\partial}{\partial x}\left[\frac{\partial^2 w}{\partial x^2} + (2-\nu)\frac{\partial^2 w}{\partial y^2}\right], \quad (3a)$$

$$V_y = -\left(\frac{\pi}{a}\right)^3 D\frac{\partial}{\partial y}\left[\frac{\partial^2 w}{\partial y^2} + (2-\nu)\frac{\partial^2 w}{\partial x^2}\right], \quad (3b)$$

and the corner force R, at $x=0$, $y=0$, is given by

$$R = 2M_{xy}\,|_{x=0,y=0}. \quad (4)$$

Because of the symmetry of the deflection function that will be used, boundary conditions need only be written on $y=0$, $0\le x\le \pi/2$; $x=\pi/2$, $0\le y\le \pi/2$; and $x=y$, $0\le y\le \pi/2$ (Fig. 1):

$$w = W_c \quad : y=0, x=0, \quad (5)$$

$$\frac{\partial w}{\partial x}=0,\ w=0 \quad : y=0,\ e<x\le \pi/2, \quad (6a,b)$$

$$V_y = 0 \quad : y=0,\ 0\le x<e, \quad (6c)$$

$$M_y = 0 \quad : y=0,\ 0\le x\le \pi/2, \quad (6d)$$

$$V_x = 0 \quad : x=\pi/2,\ 0\le y\le \pi/2, \quad (7a)$$

$$\frac{\partial w}{\partial x} = 0 \quad : x=\pi/2,\ 0\le y\le \pi/2, \quad (7b)$$

$$\frac{\partial w}{\partial x} - \frac{\partial w}{\partial y} = 0 : \ x=y,\ 0\le y\le \pi/2. \quad (8)$$

Furthermore

$$M_{xy} = 0 : \ x=0,\ y=0. \quad (9)$$

Utilizing the Levy-Nadai approach [5], the lateral deflection satisfying equations (1), (5), and (8) is

$$w(x,y) = \frac{qa^4}{2D}\sum_{m=1,3\ldots}^{\infty}[W_m(x,y) + W_m(y,x)] + W_c, \quad (10)$$

where

$$W_m(x,y) = \left[\frac{4}{\pi^5 m^5} + Y_m(x)\right]\sin(my), \quad (11)$$

and

$$Y_m(u) = A_m\cosh(mu) + B_m mu\sinh(mu) + C_m\sinh(mu) + D_m mu\cosh(mu). \quad (12)$$

In (10), W_c is the deflection of the corner, it is left undefined at present. Boundary conditions (6d), (7a,b) lead to the relations

$$A_m = [4\nu/\pi^5 m^5 + 2\coth(\beta)D_m]/(1-\nu), \quad (13)$$

$$B_m = -\coth(\beta)D_m, \quad (14)$$

$$C_m = -[\nu(4/\pi^5 m^5)\tanh(\beta) + 2D_m + (1-\nu)\beta(\tanh(\beta) - \coth(\beta))D_m]/(1-\nu), \quad (15)$$

in which

$$\beta = m\pi/2. \quad (16)$$

The problem is therefore reduced to the determination of the constant D_m. The boundary conditions (6a,c) are mixed with respect to the slope and the shear, and they are written as the dual series equations

$$\sum_{m=1,3,\ldots}^{\infty} mP_m\cos(mx) = 0, \quad e<x\le \pi/2, \quad (17)$$

$$\sum_{m=1,3,\ldots}^{\infty} m^3 P_m\left[(1+F_m)\sin(mx) + m^{-1}\frac{dG_m}{dx}(x)\right] = \sum_{m=1,3,\ldots}^{\infty}\frac{dH_m}{dx}(x), \quad 0\le x<e, \quad (18)$$

where

$$P_m = (2/\pi^5 m^5) + \coth(\beta)D_m, \quad (19)$$

$$1 + F_m = \tanh(\beta) - \eta\beta\,\mathrm{sech}^2(\beta), \quad \eta = \frac{1-\nu}{3+\nu}, \quad (20a,b)$$

$$G_m(x) = \eta\,\mathrm{sech}(\beta)[\sinh(\beta - mx) - mx\cosh(\beta - mx) + \beta\,\mathrm{sech}(\beta)\cosh(mx)], \quad (21)$$

$$\pi^5 m^3 H_m(x) = 4mx/(3+\nu) - 2[(3-\nu)\tanh(\beta)/(3+\nu) - \eta\beta\,\mathrm{sech}^2(\beta)]\cos(mx) + 2\,\mathrm{sech}(\beta)[(1+\nu)\sinh(\beta - mx)/(3+\nu) - \eta mx\cosh(\beta - mx) + \eta\beta\,\mathrm{sech}(\beta)\cosh(mx)]. \quad (22)$$

As $m\to\infty$, the weight function F_m approaches zero as $e^{-m\pi}$. The constant 1 in (18) serves to isolate the singularity associated with the quarter-infinite plate [2]. This can be seen more readily by formulating the rectangular plate problem, in which case $\beta = mb$, and noting that $F_m \to 0$ as $b\to\infty$. The remainder boundary condition (6b) is satisfied at a later stage.

The dual series equations (17) and (18), may be reduced to a single integral equation by representing the unknown coefficients P_m by a finite Fourier transform

$$P_m = \frac{1}{m^2}\int_0^e \phi(t)\sin(mt)\,dt, \quad (23)$$

in which the auxiliary function, $\phi(t)$, remains to be determined. Note that $\phi(t)$ is related to the second derivatives of w with respect to x and y and thus has the same singularity at the transition point from simple support to no contact as do the moments there.

By substituting P_m into the first of the dual series equations, interchanging the order of summation and integration, and using the identity

$$\sum_{m=1,3,\ldots}^{\infty} m^{-1}\sin(mt)\cos(mx)$$

$$= \frac{1}{2}\int_0^\infty \frac{\sin(tu)\cos(xu)}{u}du = 0, \quad (24)$$

$$\text{for} \quad x > t > 0, \ (x+t) < \pi,$$

it is seen that (17) is automatically satisfied (see [6]:858.701). The identity in (24) can be derived by considering the contour integration of

$$\int_\Gamma \frac{e^{i\pi z/2}}{z\cos(\pi z/2)} \sin(zt)\cos(zx)\,dz$$

taken around the first quadrant.

Integrating (18) once with respect to x, substituting (23), and interchanging the order of summation and integration, yields

$$\int_0^e \phi(t) \sum_{m=1,3,\ldots}^{\infty} [(1+F_m)\cos(mx) - G_m(x)]\sin(mt)\,dt = -\sum_{m=1,3,\ldots}^{\infty} H_m(x) + C, \quad (25)$$

$$0 \le x < e,$$

in which C is a constant of integration. If we examine the preceding equation for $x=0$ and enforce the condition that the corner force (4) be zero, it is apparent that C must be zero. Noting the identity

$$\sum_{m=1,3,\ldots}^{\infty} \sin(mz) = \frac{1}{2\sin z}, \quad z \neq 0, \pi/2, \pi, 3\pi/2, \ldots, \quad (26)$$

equation (25) becomes, for $0 \le x < e$,

$$\int_0^e \phi(t)\left\{\frac{1/4}{\sin(t+x)} + \frac{1/4}{\sin(t-x)} + \sum_{m=1,3,\ldots}^{\infty} [F_m\cos(mx) - G_m(x)]\sin(mt)\right\}dt = -\sum_{m=1,3,\ldots}^{\infty} H_m(x). \quad (27)$$

The foregoing integral equation can be expressed as a Cauchy-type singular integral equation of the first kind upon noting that ([6] :415.06)

$$\frac{1}{\sin x} - \frac{1}{x} = \frac{x}{6} + \frac{7}{360}x^3 + \ldots. \quad [x^2 < \pi^2]. \quad (28)$$

Finally, equation (27) can be expressed as

$$\frac{1}{\pi}\int_0^e \frac{\phi(t)}{t-x}\,dt + \int_0^e k(x,t)\phi(t)\,dt = f(x), \quad 0 < x < e, \quad (29)$$

where

$$\pi k(x,t) = \frac{1}{\sin(t-x)} - \frac{1}{t-x} + \frac{1}{\sin(t+x)} + 4\sum_{m=1,3,\ldots}^{\infty} [F_m\cos(mx) - G_m(x)]\sin(mt), \quad (30)$$

$$f(x) = -\left(\frac{4}{\pi}\right)\sum_{m=1,3,\ldots}^{\infty} H_m(x). \quad (31)$$

Preliminary to discussing the solution of (29) for $\phi(t)$, it is appropriate here to write down quantities, which will be evaluated numerically, which are of importance physically. These include the deflected shape of the plate and the support reactions.

An important physical quantity is the displacement the plate undergoes near the corner of the plate as it lifts off the support. Using equation (10), together with (13)-(15), and (19), one obtains for the edge displacement

$$w(x,0) = \frac{qa^4}{D(1-\nu)}\sum_{m=1,3,\ldots}^{\infty} P_m\sin(mx) + W_c, \quad (32)$$

$$0 < x < \pi/2.$$

The finite integral P_m is given in (23). After interchanging the order of integration and summation, equation (32) becomes

$$w(x,0) = \frac{qa^4}{D(1-\nu)}\int_0^e \phi(t)\sum_{m=1,3,\ldots}^{\infty} m^{-2}\sin(mt)\sin(mx)\,dt + W_c, \quad 0 < x < \pi/2. \quad (33)$$

By considering the contour integration of

$$\int_\Gamma \frac{e^{i\pi z/2}}{z^2\cos(\pi z/2)}\sin(zt)\sin(zx)\,dz$$

taken around the first quadrant, the identity

$$\sum_{m=1,3,\ldots}^{\infty} m^{-2}\sin(mt)\sin(mx) = \frac{1}{2}\int_0^\infty \frac{\sin(tu)\sin(xu)}{u^2}\,du, \quad (x+t) < \pi \quad (34)$$

can be derived; this relation can immediately be expressed in the form (see [6]:858.711):

$$\sum_{m=1,3,\ldots}^{\infty} m^{-2}\sin(mt)\sin(mx) = \frac{\pi t}{4}, \quad x \ge t > 0 \quad (35)$$

$$= \frac{\pi x}{4}, \quad t \ge x > 0 \quad (36)$$

Equations (35) and (36) can be used in (33) to give, finally

$$w(x,0) = \frac{qa^4}{D}\frac{\pi}{4(1-\nu)}\left\{\int_0^x \phi(t)\,t\,dt + \int_x^e \phi(t)\,x\,dt\right\} + W_c, \quad 0 < x < e \quad (37)$$

$$= \frac{qa^4}{D}\frac{\pi}{4(1-\nu)}\int_0^e \phi(t)\,t\,dt + W_c, \quad e \le x \le \pi/2. \quad (38)$$

Observe from (38) and the boundary condition (6*b*) that

$$W_c = -\frac{qa^4}{D}\frac{\pi}{4(1-\nu)}\int_0^e \phi(t)\,t\,dt. \quad (39)$$

Finally, the edge displacement on that part of the plate that loses contact is given by (37) and (39) to be

$$w(x,0) = \frac{qa^4}{D}\frac{\pi}{4(1-\nu)}\int_x^e \phi(t)\,(x-t)\,dt, \quad 0 < x < e. \quad (40)$$

The supplemented, or Kirchhoff, shearing force at the contact with the support at $y=0$, $e < x \le \pi/2$ is

$$V_y = -\pi^3 qa(3+\nu)\sum_{m=1,3,\ldots}^{\infty} \{m^3 P_m[(1+F_m)\sin(mx) + \eta E_m(x)] - 2\tilde{E}_m(x)\}, \quad (41)$$

where

$$E_m(x) = \operatorname{sech}(\beta)[\beta\operatorname{sech}(\beta)\sinh(mx) + mx\sinh(\beta - mx) - 2\cosh(\beta - mx)], \quad (42)$$

and

$$(3+\nu)\pi^5 m^2 \tilde{E}_m(x) = [(3-\nu)\tanh(\beta) - (1-\nu)\beta\operatorname{sech}^2(\beta)]\sin(mx)$$

$$+2-2\nu\,\mathrm{sech}(\beta)\cosh(\beta-mx)$$
$$+(1-\nu)E_m(x). \tag{43}$$

Only the term involving the constant 1 in (41) contributes to the singularity in the shearing force; using (26), equation (41) can be expressed in the form

$$V_y(e<x\le\pi/2,0)=\pi^3 qa(3+\nu)\Big\{\frac{d}{dx}\int_0^e \frac{\cos(x)\sin(t)}{2[\sin^2(t)-\sin^2(x)]}\phi(t)\,dt$$
$$-\int_0^e \phi(t)\sum_{m=1,3,\ldots}^{\infty} m[F_m\sin(mx)$$
$$+\eta E_m(x)]\sin(mt)\,dt$$
$$+2\sum_{m=1,3,\ldots}^{\infty}\tilde{E}_m(x)\Big\}. \tag{44}$$

The moments are assumed to be bounded at the transition point from simple support to no contact. Therefore, $\phi(t)\sim(e-t)^{1/2}$, and $V_y(x,0)\sim(x-e)^{-1/2}$ as $x\to e^+$; the latter behavior can be determined by examining the first integral in (44). Although the supplemented shearing force is singular at the ends of the contact interval, it is integrable because the singularities are of the inverse square-root type. Integration of all the support reactions reveals that the total load is balanced. Thus, in this case, global equilibrium is obtained within the classical thin plate theory, and it is not necessary to resort to a higher order plate theory.

Numerical Analysis

The many infinite series in (30), (31), and (44) were summed to the highest accuracy attainable using double precision on an IBM 4341. Often, crude summation had to be used, as in the case of the following very slowly convergent series:

$$\sum_{m=1,3,\ldots}^{\infty}\frac{\cos(mz)}{m^3}=\frac{1}{2}[Cl_3(z)-Cl_3(z+\pi)], \tag{45}$$

where $Cl_3(z)$ is the generalized Clausen function of third order (see Lewin [8] for a discussion of these functions); the foregoing equation can be found in Hansen [9] (17.4.11). For $z=\pi/3$ and $z=0$ the sum in (45) is known to be $(7/18)\zeta(3)=0.46746\ 65734\ 50953$ and $\lambda(3)=1.0519\ 97902\ 64644$, respectively (see [8], p. 146 and [10] 23.2.18, 23.2.20, and Table 23.3). Since this series proved the most difficult, and thereby set the limit to the accuracy attainable, it was invaluable to have the preceding check cases. A further example typical of several of the series that occurred is

$$\sum_{m=1,3,\ldots}^{\infty}\sin(mz)\frac{\sinh(my)}{\cosh(m\pi/2)},\quad y<\pi/2. \tag{46}$$

This series can be rewritten in the form

$$\mathrm{sgn}(y)\sum_{m=1,3,\ldots}^{\infty}\sin(mz)\Big\{\frac{\sinh(m|y|)}{\cosh(m\pi/2)}-\frac{e^{m|y|}}{e^{m\pi/2}}\Big\}$$
$$+\mathrm{sgn}(y)\sum_{m=1,3,\ldots}^{\infty}e^{-m(\pi/2-|y|)}\sin(mz). \tag{47}$$

The first series of (47) converges rapidly, since $\sinh(m|y|)/\cosh(m\pi/2)$ rapidly approaches $e^{m|y|}/e^{m\pi/2}$ as m increases. The second series can be summed in closed form by noting that for $t>0$

$$\sum_{m=1,3,\ldots}^{\infty}e^{-mt}\sin(mz)=Im\sum_{m=1,3,\ldots}^{\infty}e^{m\gamma},\gamma=-t+iz, \tag{48a}$$
$$=Im[e^{\gamma}/(1-e^{2\gamma})], \tag{48b}$$

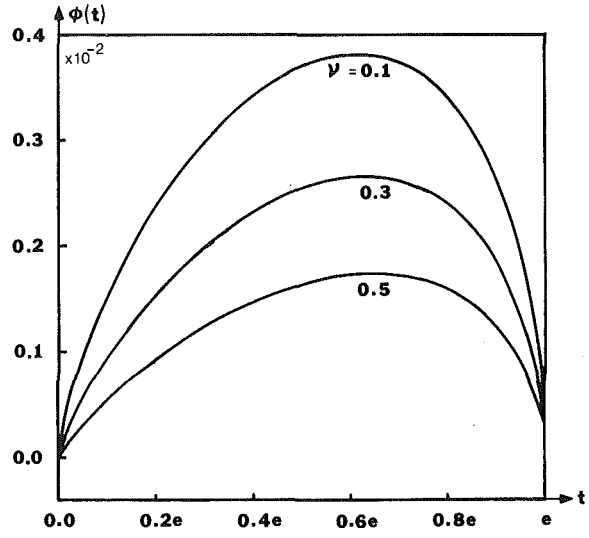

Fig. 2 The auxiliary function $\phi(t)$ in integral equation (29)

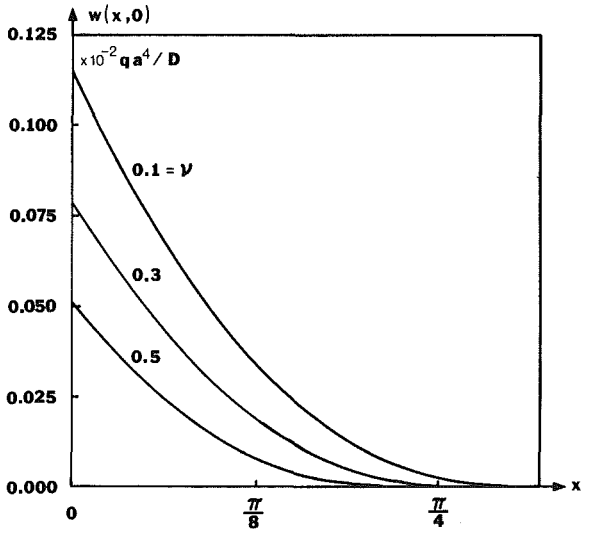

Fig. 3 Displacement of free edge for square plate

$$=\cosh(t)\sin(z)/2[\sinh^2(t)+\sin^2(z)]. \tag{48c}$$

Equation (29) is prepared for numerical analysis by introducing the following changes of variable

$$t=(1+u)e/2,\quad x=(1+s)e/2, \tag{49a}$$
$$\phi(t)=\theta^*(u),\quad k(x,t)=(2/e)\,K(s,u),\quad f(x)=F(s). \tag{49b}$$

The question at this point is the appropriate weighting function in $\theta^*(u)=\theta(u)(1+u)^{\alpha}(1-u)^{1/2}$, where $\theta(u)$ is regular at ±1. The square-root singular behavior at $u=1$ is consistent with the moments being bounded at $x=e$. To derive the behavior at $u=-1$, note from (40) that

$$\frac{\partial^2 w}{\partial x^2}(x,0)=-\frac{qa^4}{D}\frac{\pi}{4(1-\nu)}\phi(x). \tag{50}$$

Since by (6*d*)

$$M_y(x,0)=0,\quad 0\le x\le\pi/2, \tag{51}$$

it also seems obvious that $\partial^2 w(x,0)/\partial x^2$ and $\partial^2 w(x,0)/\partial y^2$ must both be zero, giving $\phi(0)=0$. However, it is found that

$$\frac{\partial^2 w}{\partial y^2}(x,0)=-\nu\frac{\partial^2 w}{\partial x^2}(x,0), \tag{52}$$

which suggests that $\phi(0)$ is not necessarily zero. In an earlier attempt on this problem, it was assumed that $\phi(t)$ was an-

Table 1 The noncontact length e for different values of Poisson's ratio

ν	e
0.1	0.307π
0.3	0.268π
0.5	0.224π

tisymmetric so as to have integration over $-e<t<e$ and thus use $\phi(t) = \tilde{\theta}(u)(1-u^2)^{1/2}$, where $t = eu$. This procedure led to slow solution convergence and localized behavior in $\tilde{\theta}(u)$ near $u = 0$ that was reminiscent of "Gibbs phenomenon."

The reason for this unwanted behavior is that $\phi(0) \neq 0$, although very small. The appropriate weight function is $(1-u)^{1/2}$ but to make use of the schemes in [7] $\phi(t)$ was expressed in the form

$$\phi(t) = \theta(u)(1-u)^{1/2} = [\theta(u)(1+u)^{-1/2}](1-u^2)^{1/2}, \tag{53}$$

Equation (29) can thus be written in the following form, noting (49a,b)

$$\frac{1}{\pi}\int_{-1}^{1} \frac{\tilde{\theta}(u)\sqrt{1-u^2}}{u-s}du + \int_{-1}^{1} K(s,u)\,\tilde{\theta}(u)\sqrt{1-u^2}du = F(s), \tag{54}$$

in which $-1<s<1$ and $\tilde{\theta}(u) = \theta(u)(1+u)^{-1/2}$. The Gauss-Chebyshev integration formula [7] yields:

$$\sum_{j=1}^{n} \frac{(1-u_j^2)}{n+1}\left[\frac{\tilde{\theta}(u_j)}{u_j-s_i} + \pi K(s_i,u_j)\,\tilde{\theta}(u_j)\right] = F(s_i), \tag{55}$$

where

$$u_j = \cos[j\pi/(n+1)], \quad j=1, \ldots, n, \tag{56a}$$

$$s_i = \cos[(2i-1)\pi/2(n+1)], \quad i=1, \ldots, n+1. \tag{56b}$$

There are $(n+1)$ equations in (55) involving the n unknowns $\tilde{\theta}(u_j)$ and the unknown length e. During the process of solution, a value of e is assumed and the $i=n+1$ equation is not used. Equation (29) with $x=0$ simplifies greatly and is actually the corner force condition, which is stated by equations (4) and (9); this equation is used as the checking equation after each solution of the n equations in (55). The correct value of e is found by iteration. The parameter n is increased, and the process repeated, until sufficient accuracy in e is obtained.

The solution obtained for the noncontact length e varies with Poisson's ratio; the values of e for $\nu = 0.1$, 0.3, and 0.5 are shown in Table 1; the solution obtained for the auxiliary function in (23) is shown in Fig. 2 and the displacement of the edge near the corner is shown in Fig. 3.

Conclusions

A solution has been obtained for the extent of contact between a laterally loaded, unilaterally constrained, square plate and its supports. The crucial step is the identification of the correct behavior the moments and shears have at the points of transition from support to no contact. Then, by judicious choice of a finite integral transform the unwieldy dual series equations are converted to an integral equation of standard form.

As shown by the values of e in Table 1 a significant portion of the plate is unsupported when allowed to seek its natural contact. These values for e at first seem too large, but it must be remembered that in the classical solution of the bilaterally constrained square plate, the concentrated forces anchoring the corners add to more than one-quarter of the total lateral load ([5], Fig. 63, p. 119).

References

1 Dundurs, J., and Stippes, M., "Role of Elastic Constants in Certain Contact Problems," ASME JOURNAL OF APPLIED MECHANICS, Vol. 37, 1970, pp. 965-970.

2 Keer, L. M., and Mak, A. F., "Loss of Contact in the Vicinity of a Right-Angle Corner for a Simply Supported, Laterally Loaded Plate," ASME JOURNAL OF APPLIED MECHANICS, Vol. 48, 1981, pp. 597-600.

3 Kiattikomol, K., Keer, L. M., and Dundurs, J., "Application of Dual Series to Rectangular Plates," ASCE *Journal of the Engineering Mechanics Division*, Vol. 100, 1974, pp. 433-444.

4 Dundurs, J., Kiattikomol, K., and Keer, L. M., "Contact Between Plates and Sagged Supports," ASCE *Journal of the Engineering Mechanics Division*, Vol. 100, 1974, pp. 445-456.

5 Timoshenko, S., and Woinowsky-Krieger, S., *Theory of Plates and Shells*, 2nd Ed., McGraw-Hill, New York, 1959.

6 Dwight, H. B., *Tables of Integrals and Other Mathematical Data*, Macmillan, 1961.

7 Erodogan, F., Gupta, G. D., and Cook, T. S., "Numerical Solution of Singular Integral Equations," *Mechanics of Fracture*, Vol. 1, Sih, G. C., ed., Noordhoff, Leyden, 1973, pp. 368-425.

8 Lewin, L., *Dilogarithms and Associated Functions*, MacDonald and Co., London, 1958.

9 Hansen, E. R., *A Table of Series and Products*, Prentice-Hall, Englewood Cliffs, N.J., 1975.

10 Abramowitz, M., and Stegun, I. A., *Handbook of Mathematical Functions*, National Bureau of Standards, Applied Mathematics Series No. 55, 1964.

The Permanent Deformation of a Cracked Cantilever Struck Transversely at Its Tip

H. J. Petroski
Department of Civil and Environmental Engineering, Duke University, Durham, N.C. 27706
Mem. ASME

The presence of even a stable crack in a ductile cantilever can have a dramatic effect on the structural response of the beam. Not only can the magnitude of the permanent plastic deformation be significantly increased but also the final shape of the damaged beam can be dramatically affected by the size and location of the crack. Such effects are quantified by analyzing a simple model of the cracked beam with an attached tip mass.

Introduction

Cracks are introduced and grow in structural members as a result of various mechanisms, many of which are still imperfectly understood by metallurgists and engineers. Thus modern design philosophies assume structures to be flawed at least to the extent that the flaws are below the threshold of state-of-the-art detection techniques, and designers choose their materials to be sufficiently tough so that a structure may tolerate such flaws and still remain serviceable. In some applications, the consequences of brittle fracture are so grave that special care must be taken to make structures exceptionally flaw-tolerant, even under extreme load conditions. This is the case, e.g., in a nuclear power plant, where a cracked pipe might be subject to severe seismic, water hammer, or traverse impact loading. Ironically, it is in this same area of application that very large cracks, which have reduced the load-carrying cross section of piping by as much as 75 percent, have occurred, but fracture mechanics analyses have shown even such large cracks to be stable [1].

Since structures are designed to be so flaw-tolerant, it may no longer be the stability of a crack but the excessive deformation that defines the failure of a cracked structure. Just as the presence of a crack can increase the amplitude of elastic structural vibrations [2], perhaps beyond tolerable limits or perhaps to such a level that excessively fast fatigue crack growth occurs, so the presence of stable cracks in structural members made of very ductile material can cause premature yielding under emergency loading conditions and result in unacceptable permanent damage to the cracked member or to neighboring structural elements. The presence of a crack not only may alter the magnitude of the permanent deformation but also may change the characteristic shape of the deformed member by influencing the positions of plastic hinges and the angles through which they rotate [3].

In this paper we explore the implications of a stable crack for the permanent deformation of a cantilever beam struck transversely at its tip by a mass that becomes attached to the beam and subsequently moves with it. The same problem for the uncracked beam was studied by Parkes [4], whose approach enabled him to draw many general conclusions about the beam's deformed shape via closed-form solutions to the equations of motion of the beam modeled as a rigid, perfectly plastic body. With an eye toward reaching similarly closed-form solutions for the cracked cantilever, the approach of Parkes is followed here as closely as practicable.

After reviewing the assumptions and results of Parkes in the next section, the problem of the cracked cantilever is formulated. To avoid the complication of crack closure, which may essentially negate some of the effects of a particularly tight crack on the plastic deformation of a beam, only cracks that are opened in tension by the impact loading are considered here. Since this would be the worst case behavior for a crack, the results of the analysis are not particularly restricted in application by the exclusion of crack closure.

Not surprisingly, we find that the cracked section of the beam is the weak link in the structural element, and that, regardless of the axial location of the crack, it yields before any other section of the beam. Whether or not a second hinge develops in the beam is dependent on both the size and location of the crack. Because the general crack induces the first plastic hinge at neither the tip nor root of the beam, the modes of plastic deformation of the cracked cantilever are quite different from those determined by Parkes, and the final deformed shape of the cracked beam is distinctly different from the ones that Parkes found to be characteristic of uncracked cantilevers.

The Flawless Cantilever of Parkes [4]

Parkes [4] has considered a uniform cantilever beam of length l and mass per unit length m whose rigid-plastic

Contributed by the Applied Mechanics Division for publication in the JOURNAL OF APPLIED MECHANICS.
Discussion on this paper should be addressed to the Editorial Department, ASME, United Engineering Center, 345 East 47th Street, New York, N.Y. 10017, and will be accepted until two months after final publication of the paper itself in the JOURNAL OF APPLIED MECHANICS. Manuscript received by ASME Applied Mechanics Division, August, 1983; final revision, October, 1983.

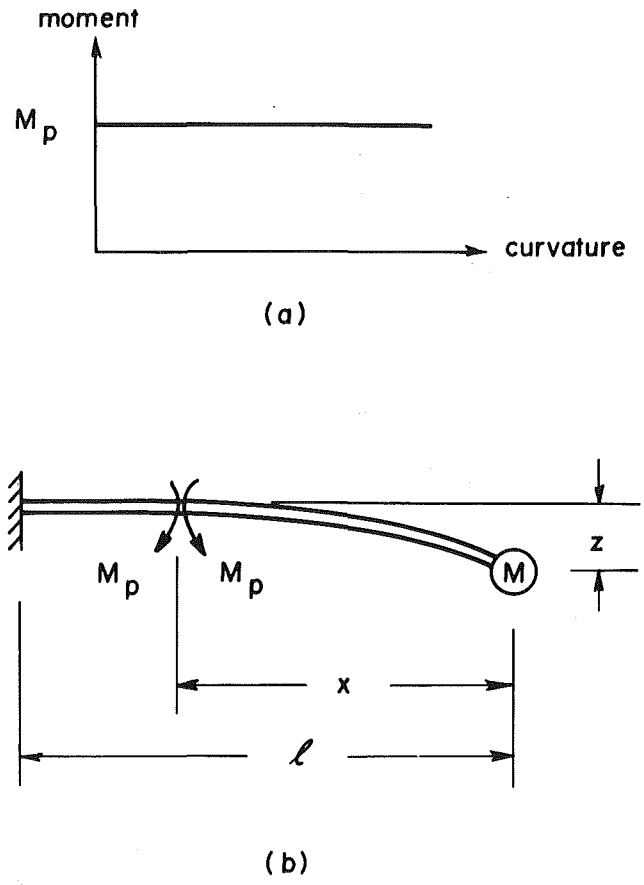

Fig. 1 (a) Moment-curvature relation, and (b) deformation mode of uncracked cantilever (after Parkes [4])

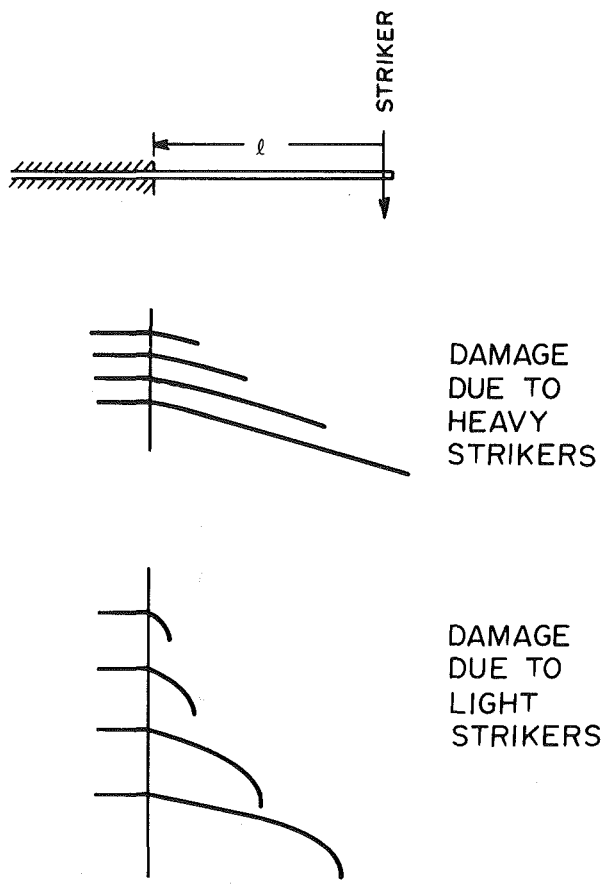

Fig. 2 Examples of permanent deformation profiles of uncracked beams (after Parkes [4])

material behavior is characterized by the moment-curvature relationship shown in Fig. 1(*a*), where M_p is the dynamic plastic moment, assumed as a first approximation to be independent of strain rate. The free end of the cantilever is struck transversely by a body of mass M moving with a velocity v, the mass is assumed to remain in contact with the cantilever tip after impact, and the cantilever tip and attached mass are assumed to have the same velocity v at the moment of impact, which is taken to be time $t=0$. A plastic hinge is postulated to begin at the tip of the beam and move toward the root as shown in Fig. 1(*b*), where x is the instantaneous position of the traveling hinge. According to Parkes's analysis the portion of the beam between the hinge and the root remains stationary, and deformation takes place only at the hinge, thus enabling the unsupported portion of the beam to the right of the hinge to be treated as a rigid body.

This enables Parkes to derive equations of motion for the deforming portion of the beam, and the differential equations may be integrated in closed form to give the displacement profile of the beam at the instant when the plastic hinge arrives at the root of the cantilever. The vertical displacement y at any distance λ from the tip is thus found by Parkes to be given by

$$y=\frac{M^2v^2}{3mM_p}\left[\frac{\beta(3\xi-2)}{1+\beta}-\frac{\beta\xi}{1+\beta\xi}+\frac{\beta^2(1-\xi)}{(1+\beta)^2}+2ln\left\{\frac{1+\beta}{1+\beta\xi}\right\}\right] \tag{1}$$

where

$$\beta=\frac{ml}{2M},\quad \xi=\frac{\lambda}{l} \tag{2}$$

The subsequent motion of the beam is one of rigid-body rotation about the stationary plastic hinge at the root, and the total angle θ through which the hinge rotates before dissipating the kinetic energy in the system is given by

$$\theta=\frac{M^2v^2}{3mM_pl}\frac{\beta(3+2\beta)}{(1+\beta)^2} \tag{3}$$

The total final permanent displacement y_p of any point on the cantilever is then given by

$$y_p=y+\theta l(1-\xi) \tag{4}$$

For a heavy striking mass, β is small compared to unity, and the permanent deformed shape of the cantilever is found by Parkes to be given by

$$\frac{2y_pM_p}{Mv^2l}=1-\xi\quad(\beta<<1) \tag{5}$$

which represents a straight line. For a light striking mass β is large compared to unity, and Parkes finds that

$$\frac{y_pM_pm}{M^2v^2}=\begin{cases}\frac{2}{3}ln\ \frac{1}{\xi} & (\beta\xi>>1)\\ \frac{2}{3}ln\ \beta & (\xi=0)\end{cases} \tag{6}$$

which predicts a continuously curving profile.

These results clearly indicate the extremes of behavior for cantilevers struck by heavy and light strikers, and they show further that the deflections depend on the kinetic energy ($1/2\ Mv^2$) when a heavy striker is involved and the square of the momentum (M^2v^2) when a light striker is involved.

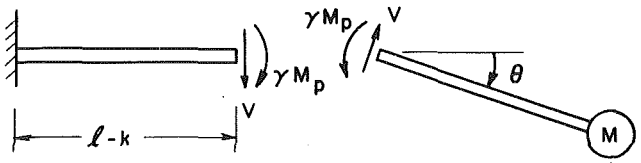

Fig. 3 Force system transmitted across crack plane in plastically deforming cantilever

Parkes also conducted experiments, which confirmed his results. Mild steel beams of 0.635-cm (1/4-in.) square nominal cross section and of various lengths were struck by a falling heavy weight and by a light bullet fired from a rifle. Examples of the permanent damage suffered by Parkes's specimens are illustrated in Fig. 2, and the cantilevers struck by the heavy weight are indeed essentially straight as predicted by equation (5), while those struck by the bullet are dramatically curved, especially near their tips. Although later analysis by Ting [5] and others have gone beyond it, the efficacy of Parkes's simple model in capturing the phenomenological behavior of the flawless beam argues well for its use as a first approximation to the behavior of the cracked cantilever.

The Cracked Cantilever

The crack is assumed to be located a distance k from the tip of the beam and to weaken the cracked section to such an extent that a plastic hinge develops there when the bending moment reaches a value $\gamma M_p < M_p$, where $0<\gamma<1$ is a function of the crack size, with the limiting values $\gamma=0$ and $\gamma=1$ corresponding to the degenerate cases of a completely severed cross section and no crack, respectively. The nonlinear relationship between γ and physical crack size depends on the cross section of the beam and the assumed geometry of the crack and may easily be obtained by considering the statics of a fully yielded uncracked ligament.

If upon impact, a plastic hinge were to develop first at the tip of the beam, as Parkes [4] argues for the uncracked cantilever, the rest of the beam, including the crack plane, would be subject to the bending moment M_p. Since the crack plane can only support a moment $\gamma M_p < M_p$, it would yield immediately, reducing the bending moment in the end portion of the cantilever beyond the crack, and thus arresting any hinge that may have initiated there. Thus as a first approximation, one may assume that upon impact, the dominant plastic hinge is initiated at the crack plane, while the unsupported portion of the beam beyond the crack remains straight and rigid as it rotates about this hinge.

Since the rest of the beam can support a moment $M_p > \gamma M_p$, the plastic hinge at the crack plane does not necessarily imply that the shear force vanishes there, and one must allow for such a transverse force to act. Thus, as shown in Fig. 3, the root portion of the beam is initially subjected to a bending moment γM_p and a shear force V whose sense will govern the subsequent behavior of the beam. The initial shear force is established by writing the equations of rigid-body dynamics for the rotating end of the beam, assuming the root portion of the beam is initially stationary. The angular acceleration of the end of the beam is given by

$$\ddot{\theta} = \frac{-3\gamma M_p}{(3+2\alpha)k^2 M} \tag{7}$$

where $\alpha = km/2M$ is a measure of the relative mass of the beam between the crack and the striker, while the shear force is given by

$$V = \frac{3(1+\alpha)\gamma M_p}{(3+2\alpha)k} \tag{8}$$

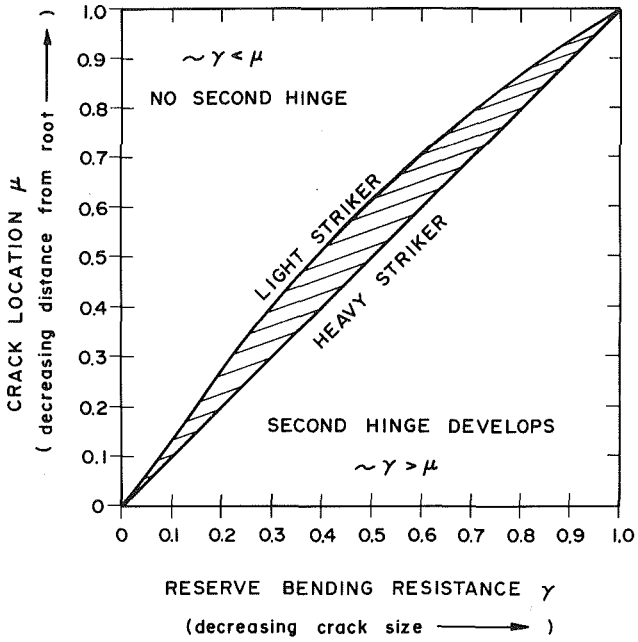

Fig. 4 Relationship between crack location and size necessary for second plastic hinge to develop

Then the total bending moment in the section of the beam toward the root at a distance x from the crack is

$$M = \gamma M_p + Vx \tag{9}$$

and this reaches the yield moment M_p first at the section given by

$$\frac{x}{l-k} = \frac{3+2\alpha}{3(1+\alpha)} \frac{1-\gamma}{\gamma} \frac{\mu}{1-\mu} \tag{10}$$

where $\mu = k/l$ is a measure of the relative position of the crack. If $x > l-k$ the bending moment will nowhere in the beam exceed M_p, and there will be no second hinge developed. Criteria for whether or not a second hinge will develop can be derived by setting $x = l-k$ and relating μ and γ for various values of α. Following Parkes, who defined impacting strikers as light when $\beta = ml/2M$ is very large and as heavy when β is very small, the parameter $\alpha = mk/2M$ may be used to define *relatively* light strikers ($\alpha \to \infty$) and *relatively* heavy strikers ($\alpha \to 0$), where the parameter α is a measure of the mass of only the portion of the beam beyond the crack relative to that of the striker. The criteria so derived are presented graphically in Fig. 4, and it is clear that the effect of the striker's mass is not a major factor in determining the number of hinges. Rather, the crack depth and location plays the principal role. Thus, e.g., a crack corresponding to $\gamma = 0.5$ will only result in a second hinge if the crack is located less than 50–60 percent of the distance from the tip of the beam to the root. In general, for a given size crack (fixed γ), a second hinge is more likely to be produced the nearer to the free end of the cantilever that the crack is located. And for a given crack location (fixed μ), the deeper the crack the less likely is a second hinge to develop.

Some preliminary experimental results for cracked cantilevers have been reported by Petroski and Verma [6]. These experiments were designed to test the hypothesis that the location of a stable crack would influence the mode of permanent deformation, and they did produce the expected results, which are in general agreement with the predictions of Fig. 4, although the assumption of attached tip mass in the present analysis makes direct comparison inappropriate. A

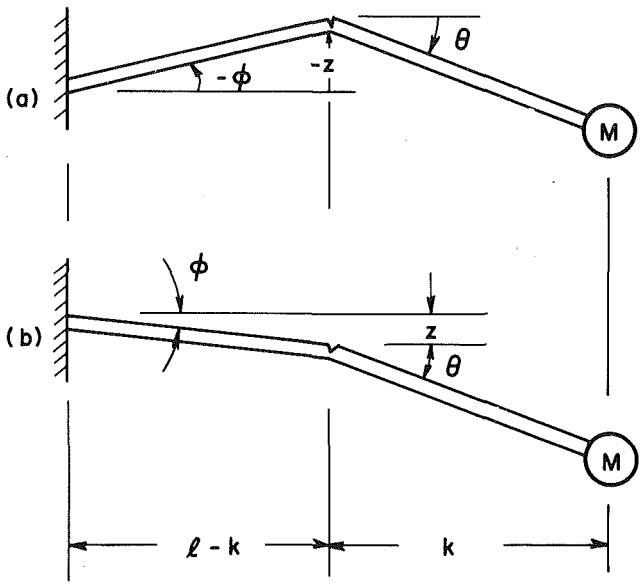

Fig. 5 Two possible modes of plastic deformation of a cracked cantilever beam with heavy tip mass

more controlled series of experiments on beams with attached tip masses is planned.

If equation (10) predicts $x<l-k$, there will be a second hinge initiated somewhere between the crack and the root of the beam, but to characterize the exact behavior of that portion of the beam requires an analysis similar to Parkes's, which is incompatible with the assumptions that were made to derive (10). However, from Parkes's results for the uncracked beam, one can conclude that the second hinge will develop at the root of the cantilever for heavy impacting masses, and only light, high-velocity strikers can be expected to induce any significant departures from piecewise linearity in the deformed shape. Of course for very shallow cracks ($\gamma\to 1$) or cracks very near the tip of the beam ($\mu\to 0$), the bending moment will reach the limit moment very near the crack location, $x\approx 0$, and Parkes's analysis of the uncracked beam will no doubt provide a good approximation to the total deformation. Therefore the following analysis should be understood to be most applicable to cracks away from the tip of the beam and can be expected to predict best the behavior of cracked cantilevers subjected to impact from relatively large masses.

The Two-Hinge Model of the Cracked Cantilever

If the hinges at the crack plane and beam root initiate simultaneously, then the initial condition $\dot{z}=0$ no longer applies, and after some time t the cantilever will have one of the two configurations shown in Fig. 5. The differential equations of motion for this two-degree-of-freedom system are, with z now representing the (positive downward) transverse displacement of the crack plane and not, as in Parkes's work, that of the cantilever tip,

$$3(1+\alpha)\ddot{z}+(3+2\alpha)k\ddot{\theta}=-\frac{3\gamma M_p}{Mk} \tag{11}$$

$$(3+4\alpha+2\beta)\ddot{z}+3(1+\alpha)k\ddot{\theta}=\frac{\mp 3(1\mp\gamma)M_p}{M(l-k)} \tag{12}$$

where the upper signs apply when both segments of the beam move downward and the lower signs apply when the segments move in opposite directions.

If w is the velocity of the mass M just before impact, then immediately after impact the velocities of the beam segments are related through the impulse-momentum equations:

$$3(1+\alpha)\dot{z}+(3+2\alpha)k\dot{\theta}=3w-\frac{3\gamma M_p t}{Mk} \tag{13}$$

$$(3+4\alpha+2\beta)\dot{z}+3(1+\alpha)k\dot{\theta}=3w+\frac{3(1+\gamma)M_p t}{M(l-k)} \tag{14}$$

Thus the initial conditions, at time $t=0$, for the motion subsequent to the impact are:

$$\dot{z}(0)=-\mu v/2, \quad z(0)=0 \tag{15}$$

$$k\dot{\theta}(0)=(2+\mu)v/2, \quad k\theta(0)=0 \tag{16}$$

where

$$v=\dot{z}(0)+k\dot{\theta}(0) \tag{17}$$

is the initial tip velocity and is given by:

$$v=\frac{6\beta w}{6\beta+4\alpha\beta-\alpha^2} \tag{18}$$

which is positive (downward), because $0\le\mu=\alpha/\beta\le 1$. Hence, $\dot{z}(0)$, the initial motion of the crack plane, becomes vanishingly small as the crack location approaches the tip of the beam.

Integrating the equations of motion (with the lower signs) twice with respect to time, using the initial conditions given in the foregoing, it can be determined that the upward motion of the root section ceases (i.e., $\dot{z}=0$) when

$$t_1=\frac{\beta Mk\mu(1-\mu)w}{M_p(3\mu+3\gamma+2\alpha\mu+3\alpha\gamma-\alpha\gamma\mu)} \tag{19}$$

Since, by Fig. 4, a second hinge develops only when $\gamma>\mu$, this expression gives a vanishingly small time as the mass of the striker grows relative to the mass of the beam (i.e., as $\beta\to 0$). Hence the displacement of the beam during the phase of motion depicted in Fig. 5(a) is small for heavy strikers, as is the energy absorbed by the plastic hinges:

$$U=\frac{M_p}{l-k}[\gamma(l-k)\theta_1-(1+\gamma)z_{\max}] \tag{20}$$

where $z_{\max}=z(t_1)$ and $\theta_1=\theta(t_1)$ are the beam displacements when the phase of motion depicted in Fig. 5(a) ceases. This energy may be expressed as

$$V=\frac{1}{2}Mw^2 f(\alpha;\gamma,\mu) \tag{21}$$

where f is a function whose value approaches zero for strikers considerably more massive than the beam (i.e., $f\to 0$ as $\alpha\to 0$). If this is an insignificant part of the input energy $1/2Mw^2$, the subsequent motion, characterized in this case by both segments of the beam moving in the same downward direction, must absorb the bulk of the energy and thus produce the bulk of the permanent deformation. Hence for heavy strikers the motion of the beam may be taken as entirely according to Fig. 5(b).

The upper signs in equations (11) and (12) apply when both segments of the beam rotate in the same direction. In this case,

$$\ddot{z}=\frac{(3\gamma-3\mu+3\alpha\gamma-2\alpha\mu-\alpha\gamma\mu)}{(1-\mu)(6\beta-\alpha^2+4\alpha\beta)}\frac{M_p}{kM} \tag{22}$$

$$\ddot{\theta}=-\frac{3\gamma M_p}{(3+2\alpha)k^2M}-\frac{3(1+\alpha)}{(3+2\alpha)k}\ddot{z} \tag{23}$$

and for heavy strikers where $\alpha<<1$ and $\beta<<1$, a good approximation is given by

$$\ddot{z} = \frac{(\gamma-\mu)M_p}{(1-\mu)klm} \tag{24}$$

$$\ddot{\theta} = -\frac{\ddot{z}}{k} \tag{25}$$

In cases where the first part of the motion consumes such a small proportion of the energy available for deformation, a conservative first approximation to the permanent deformation of the cracked beam may be determined by ignoring any initial upward velocity and displacement and taking the initial conditions for equations (24) and (25) to be $\theta = z = \dot{z} = 0$ and $\dot{\theta} = v/k$ at $t = 0$, then

$$\dot{z} = \frac{(\gamma-\mu)M_p t}{(1-\mu)klm} \tag{26}$$

$$\dot{\theta} = \frac{v}{k} - \frac{(\gamma-\mu)M_p t}{(1-\mu)k^2 lm} \tag{27}$$

and

$$z = \frac{(\gamma-\mu)M_p t^2}{2(1-\mu)klm} \tag{28}$$

$$\theta = \frac{vt}{k} - \frac{(\gamma-\mu)M_p t^2}{2(1-\mu)k^2 lm} \tag{29}$$

The deformation continues until all the energy is absorbed by the plastic hinges. By (26) and (27) $\dot{\theta}$ clearly exceeds $\dot{z}/(l-k)$ for small enough times t, so that the tip end of the beam beyond the crack rotates through a greater angle than the portion of the beam between the crack and the root. The hinge at the crack does not stop opening before $(l-k)\dot{\theta} = \dot{z}$, which occurs at

$$t = \frac{(1-\mu)^2 k^2 mv}{\mu(\gamma-\mu)M_p} \tag{30}$$

Inserting this in the expressions (28) and (29) gives the displacements at the time when the crack hinge freezes. These displacements corresond to an absorbed energy given by

$$U = \frac{M_p}{l-k}[\gamma(l-k)\theta + (1-\gamma)z] \tag{31}$$

If this energy exceeds the input energy, the deformation must stop before the time given in (30). In that case the energy expression (31) in conjunction with the displacements (28) and (29) may be used to determine the time at which the motion stops. By equating the absorbed energy to the *approximate* input energy $Mv^2/2$, a quadratic equation in t will result. If, on the other hand, all the input energy is not absorbed when the crack hinge freezes, then the subsequent rotation of the bent beam about its root will continue until all the input energy is absorbed. This phase of motion may be approximated by

$$\ddot{z} = -\frac{2\beta(1-\mu)M_p}{ml^2} \tag{32}$$

which may be integrated with appropriate initial conditions taken from the end of the previous phase of motion.

Example of a Beam With a Heavy Tip Mass and Cracked at the Midpoint

For the case where $\mu = 1/2$, the earliest time at which the crack hinge can freeze is given by (30) to be, for $2\gamma > 1$,

$$t = \frac{l^2 mv}{4(2\gamma-1)M_p} \tag{33}$$

and this corresponds to the displacements, from (28) and (29),

$$z = \frac{l^2 mv^2}{16(2\gamma-1)M_p} \tag{34}$$

$$\theta = \frac{3lmv^2}{8(2\gamma-1)M_p} \tag{35}$$

i.e., the half of the beam toward the tip rotates through an angle relative to the root half three times the angle through which the root half rotates, and the total energy absorbed through the time when this condition is reached is given by (31) to be

$$U = \frac{\beta}{2M_p}\left(\frac{1}{2}mv^2\right) \tag{36}$$

and this is independent of the crack size, although the deflections given by (34) and (35) are not. Since $\beta << 1$ has been assumed, the fraction $\beta/2M_p$ is much smaller than unity and the motion continues until the balance of the input energy is absorbed by the root hinge. The motion after the crack hinge freezes is governed by (32), which for $\mu = 1/2$ reduces to

$$\ddot{z} = -\frac{\beta M_p}{ml^2} \tag{37}$$

and the initial conditions corresponding to the time (33) are the displacement and velocity given by (26) and (34) to be

$$\left.\begin{aligned} z &= \frac{l^2 mv^2}{16(2\gamma-1)M_p} \\ \dot{z} &= \frac{v}{2} \end{aligned}\right\} \text{ at } t = \frac{l^2 mv}{4(2\gamma-1)M_p} \tag{38}$$

Hence

$$z = \frac{-\beta M_p t^2}{2ml^2} + \frac{[2(2\gamma-1)+\beta]vt}{4(2\gamma-1)} - \frac{[2(2\gamma-1)+\beta]l^2 mv^2}{32(2\gamma-1)^2 M_p} \tag{39}$$

and the energy absorbed is

$$U = \frac{2M_p z}{l} \tag{40}$$

The motion continues until $U = Mv^2/2$. For the case where $2\gamma - 1 >> \beta$, the maximum displacement of the crack section is approximately

$$z_{max} = \frac{l^2 mv^2}{8\beta M_p} \tag{41}$$

which is much larger than (34), the displacement corresponding to the first (here now neglected) phase of the deformation. This deflection is also independent of the crack size because the dominant hinge is at a noncracked section. Combining (34) and (41) gives the ratio of the maximum crack plane displacement to that when the crack hinge freezes to be

$$\frac{z_{max}}{z} = \frac{2(2\gamma-1)}{\beta} \tag{42}$$

which shows that, for very heavy strikers ($\beta << 2\gamma - 1$), the beam will have a virtually straight shape with the angle through which the stable crack's faces rotate negligible compared to that through which the beam's root rotates. For a given impact velocity and a given beam with attached tip mass, the effect of increasing crack depth (decreasing γ) is a relatively more pronounced "knee" in the beam.

Summary and Conclusions

The presence of a crack in a cantilever beam can dramatically alter not only the degree but also the nature of the permanent deformation that the beam will suffer under impact. For the case of a cantilever beam with an attached

heavy tip mass, a crack can cause a dominant plastic hinge to develop away from the root of the beam. For deeper rather than shallow cracks and for cracks located closer to the beam's root than to its tip, the crack plane hinge can be the only site of plastic deformation.

As with the results of Parkes [4] for the uncracked cantilever, when the attached tip mass is light relative to the beam's mass, the deformation pattern is more complex. Finally, whether or not cracks remain stable during the large plastic deformation of the beam must be a separate consideration. Some of these complicating factors will be considered elsewhere.

Acknowledgment

This material is based on work supported by the National Science Foundation under Grant No. CEE-8117672 to Duke University. The author is grateful to Mr. José Clemente for his help in checking the calculations and to the referee who suggested an improvement in the statement of initial conditions.

References

1 Tada, H., Paris, P., and Gamble, R., "Stability Analysis of Circumferential Cracks in Reactor Piping Systems," U.S. Nuclear Regulatory Commission Report, NUREG/CR-0838, June, 1979.

2 Petroski, H. J., "Simple Static and Dynamic Models for the Cracked Elastic Beam," *International Journal of Fracture*, Vol. 17, 1981, pp. R71–76.

3 Petroski, H. J., "Structural Dynamics of Piping With Stable Cracks: Some Simple Models," *International Journal of Pressure Vessels and Piping*, Vol. 13, 1983, pp. 1–18.

4 Parkes, E. W., "The Permanent Deformation of a Cantilever Struck Transversely at its Tip," *Proceedings of the Royal Society*, Series *A*, Vol. 228, 1955, pp. 462–476.

5 Ting, T. C. T., "Large Deformation of a Rigid, Ideally Plastic Cantilever Beam," ASME JOURNAL OF APPLIED MECHANICS, Vol. 32, 1965, pp. 295–302.

6 Petroski, H. J., and Verma, A., "On the Dynamic Response of Ductile Piping Containing Stable Cracks," *Transactions of the Seventh International Conference on Structural Mechanics in Reactor Technology*, Chicago, Ill., Aug. 1983, Paper E8/1.

On Elastodynamic Diffraction of Waves From a Line-Load by a Crack

A. K. Gautesen
Ames Laboratory[1] and
Department of Mathematics,
Iowa State University,
Ames, Iowa 50011

For the two-dimensional problem of elastodynamic diffraction of waves by a crack of finite width, we assume that the solution corresponding to incidence of a plane wave of either longitudinal or transverse motions under a fixed angle of incidence is known. We first show how to construct the solution corresponding to an in-plane line-load (the Green's function) from this known solution. We then give a simple relation between the far field scattering patterns corresponding to a plane wave incident under any angle and the far field scattering patterns corresponding to the known solution. This relation is a generalization of the principle of reciprocity.

1 Introduction

We consider the steady state, two-dimensional problem of diffraction of in-plane waves from a traction-free crack in an elastic solid. The geometry is shown in Fig. 1. We assume that we know the solution to this problem for incidence of either a plane longitudinal wave or a plane transverse wave for one fixed direction of incidence ϕ. In reality, an analytic expression for this solution is not known, but numerical procedures are available (e.g., see Achenbach, Gautesen, and McMaken [1]). The main intent of this work is to show how to construct the Green's function (diffraction of waves from a line-load) from this known solution. Once the Green's function is known, we then easily construct the solution corresponding to incidence from any direction χ of either a plane longitudinal or transverse wave. We find that the far field scattering patterns for this problem are simply related to the far field scattering patterns for the problem whose solution is assumed known. For incidence of horizontally polarized transverse waves, this problem is equivalent to the problem of diffraction of waves by an acoustically hard strip; and the results of Gautesen [2] are applicable here.

We bring with a statement of the main results. We then discuss how the results represent a generalization of the principle of reciprocity and offer some potential applications. The results are derived in the next section, and we call the reader's attention to the first paragraph where we describe the physical consequences of some of the intermediate results of the derivation.

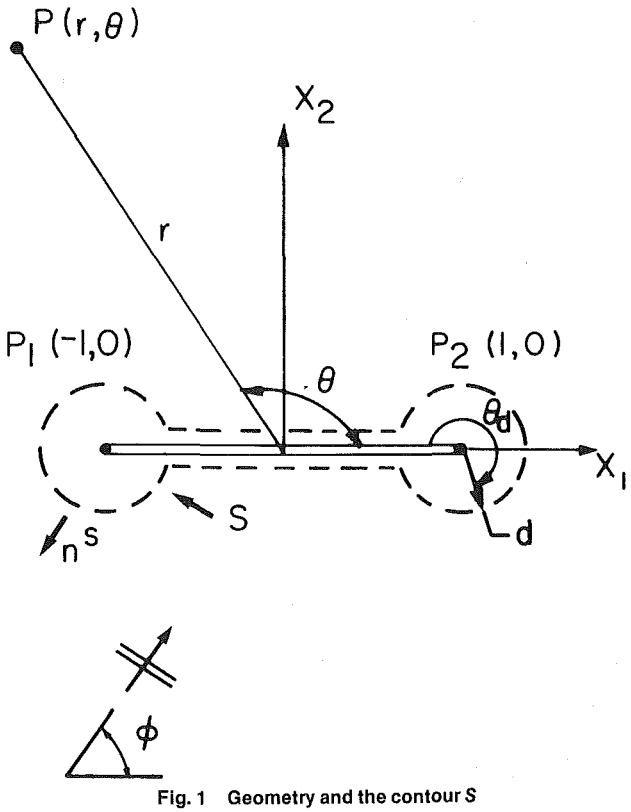

Fig. 1 Geometry and the contour S

Statement of Problem and Results

Let $\mathbf{v}$ be the scattered field associated with the plane incident wave,

$$\mathbf{v}^{in} = \mathbf{d}^{\alpha}(\phi)\exp[ik_{\alpha}(x_1\cos\phi + x_2\sin\phi)] \tag{1.1}$$

where $\alpha = L$ or T denotes longitudinal or transverse (vertically polarized) motions, respectively. Also,

[1]Operated for the U.S. Department of Energy by Iowa State University under contract No. W-7405-ENG-82. This work was supported by the Office of Basic Energy Sciences.

Contributed by the Applied Mechanics Division for publication in the JOURNAL OF APPLIED MECHANICS.

Discussion on this paper should be addressed to the Editorial Department, ASME, United Engineering Center, 345 East 47th Street, New York, N.Y. 10017, and will be accepted until two months after final publication of the paper itself in the JOURNAL OF APPLIED MECHANICS. Manuscript received by ASME Applied Mechanics Division, May, 1983.

$$\mathbf{d}^L(\phi) = (\cos\phi, \sin\phi) \tag{1.2a}$$

$$\mathbf{d}^T(\phi) = (-\sin\phi, \cos\phi) \tag{1.2b}$$

$$k_L = \omega/c_L, \quad c_L^2 = (\lambda + 2\mu)/\rho \tag{1.2c}$$

$$k_T = \omega/c_T, \quad c_T^2 = \mu/\rho \tag{1.2d}$$

where ω is the circular frequency of the incident wave; c_L and c_T are the speeds of longitudinal and transverse waves, respectively; λ and μ are the Lame parameters; and ρ is the density of the elastic medium. Then $\mathbf{v}$ satisfies the differential equations

$$L_i[\mathbf{v}] = 0, \quad i = 1,2 \tag{1.3}$$

and the boundary conditions

$$\tau_{2i}[\mathbf{v}] = -\tau_{2i}[\mathbf{v}^{in}] = E_i^\alpha(\phi)\exp[ik_\alpha x_1 \cos\phi], \quad i = 1,2, \quad |x_1| < 1, \quad x_2 = 0 \tag{1.4}$$

where

$$L_i[\mathbf{v}] \equiv \frac{\partial}{\partial x_j}(\tau_{ij}[\mathbf{v}]) + \rho\omega^2 v_i \tag{1.5}$$

$$\tau_{ij}[\mathbf{v}] \equiv \lambda(\nabla \cdot \mathbf{v})\delta_{ij} + \mu\left(\frac{\partial v_i}{\partial x_j} + \frac{\partial v_j}{\partial x_i}\right) \tag{1.6}$$

$$E_i^\alpha(\phi) = -i\mu k_\alpha[(\kappa^2 - 2)(\mathbf{d}^\alpha(\phi)\cdot\mathbf{p})\delta_{2i} + d_2^\alpha(\phi)p_i + d_i^\alpha(\phi)p_2] \tag{1.7a}$$

$$\mathbf{p} = (\cos\phi, \quad \sin\phi) \tag{1.7b}$$

$$\kappa = c_L/c_T \tag{1.7c}$$

and δ_{ij} is the Kronecker delta function. In (1.5) and in the following, we use the convention that when a numerical subscript is repeated in an expression, it is understood to be summed from 1 to 2.

The Green's function $\mathbf{g}^k(\mathbf{x};\mathbf{y})$ satisfies

$$L_i[\mathbf{g}^k] = -\delta_{ik}\delta(\mathbf{x} - \mathbf{y}), \quad i = 1,2 \tag{1.8}$$

$$\tau_{2i}[\mathbf{g}^k] = 0, \quad i = 1,2, \quad |x_1| < 1, \quad x_2 = 0 \tag{1.9}$$

We show that

$$\mathbf{g}^k(\mathbf{x};\mathbf{y}) = \mathbf{f}^k(\mathbf{x} - \mathbf{y}) + \mathbf{v}^{gk}(\mathbf{x};\mathbf{y}) \tag{1.10}$$

where $\mathbf{f}^k$ is the free space Green's function (or equivalently, the field generated by a line-load) defined by

$$-4i\mu k_T^2 f_i^k(\mathbf{x}) = \frac{\partial^2}{\partial x_i \partial x_k}[H_0^{(1)}(k_T r) - H_0^{(1)}(k_L r)] + k_T^2 H_0^{(1)}(k_T r)\delta_{ik} \tag{1.11}$$

and $\mathbf{v}^{gk}$ is the corresponding scattered field defined in terms of $\mathbf{v}$ by

$$16\mu k_T \cos\phi\, v_l^{gk}(\mathbf{x};\mathbf{y}) = (c_T/c_\alpha)[P_i^\alpha(\phi + \pi, \phi)]^{-1} \int_{-\infty}^{\infty} (-1)^j w_k^{ij}(y_1 + s, y_2) \times w_l^{ij}(x_1 + s, x_2)\,\mathrm{sgn}(s)\, ds \tag{1.12}$$

Here,

$$w_k^{i1}(\mathbf{y}) = \left[ik_\alpha \cos\phi - \frac{\partial}{\partial y_1}\right]\tilde{w}_k^i(\mathbf{y}) \tag{1.3a}$$

$$\tilde{w}_k^i(\mathbf{y}) = \tfrac{1}{2}[v_k(y_1, y_2) + (-1)^{k+i} v_k(y_1, -y_2)] \quad \text{(no summation)} \tag{1.13b}$$

$$w_k^{i2}(\mathbf{y}) = w_k^{i1}(-\mathbf{y}) \tag{1.13c}$$

$$P_{3-j}^\beta(\theta,\phi) = \tfrac{1}{2} i\mu^{-1} E_j^\beta(\theta) \int_{-1}^{1} \exp[-ik_\beta x \cos\theta]\psi_j(x)\, dx \quad \text{(no summation)} \tag{1.14}$$

$$2\psi(x_1) = \mathbf{v}(x_1, 0^+) - \mathbf{v}(x_1, 0^-) \tag{1.15}$$

We note that ψ is one-half the crack-opening displacement and that

$$P_\beta(\theta,\phi) = \sum_{j=1}^{2} P_j^\beta(\theta,\phi), \quad \beta = L, T \tag{1.16}$$

where P_β are the far field scattering patterns defined for r large by

$$e^{i\pi/4}(\pi/2)^{1/2}\mathbf{v}(\mathbf{x}) \sim \sum_{\beta = L,T} (k_\beta r)^{-1/2} P_\beta(\theta,\phi) e^{ik_\beta r}\mathbf{d}^\beta(\theta) \tag{1.17}$$

We remark that relative to the y_1-axis, $\tilde{w}_k^1$ and $\tilde{w}_k^2$ correspond to the symmetric and antisymmetric parts, respectively, of the scattered field v_k. The far field scattering patterns corresponding to $\tilde{w}_k^i$ are $P_i^\beta(\theta,\phi)$, $\beta = L, T$. The fields w_k^{ij} are outgoing, homogeneous solutions of the governing differential equations with vanishing tractions on the crack faces. However, the corresponding crack-opening displacements do not vanish at the crack edges. Thus, their motions are generated by sources at the crack edges.

When the source $\mathbf{y}$ approaches infinity in a fixed direction, $v_l^{gk}(\mathbf{x};\mathbf{y})$ is proportional to the scattered field corresponding to plane wave incidence. If, in addition, the receiver $\mathbf{x}$ also approaches infinity in a fixed direction, then $v_l^{gk}(\mathbf{x};\mathbf{y})$ is proportional to the far field scattering pattern. We now give the results analogous to (1.12) for these limiting cases. Let $v_k^{\beta\chi}$ denote the scattered field corresponding to incidence of the plane wave $\mathbf{v}^i = d^\beta(\chi)\exp[k_\beta(x_1\cos\chi + x_2\sin\chi)]$. Then

$$4v_k^{\beta\chi}(\mathbf{x}) = (c_\alpha/c_\beta)^2 \sec\phi[(c_\alpha/c_\beta)\cos\chi - (-1)^j\cos\phi]P_i^\beta(\chi + (j-2)\pi, \phi) \times [P_i^\alpha(\phi + \pi, \phi)]^{-1} \int_{-\infty}^{\infty} \mathrm{sgn}(s) \exp[-ik_\beta s\cos\chi] w_k^{ij}(x_1 + s_2, x_2)\, ds \tag{1.18}$$

Let $P_\gamma^\beta(\theta,\chi)$, $\gamma = L, T$ be the far field scattering patterns corresponding to $v_k^{\beta\chi}$. Then

$$2\cos\phi[(c_\gamma/c_\beta)\cos\chi - \cos\theta]P_\gamma^\beta(\theta,\chi) = (c_\beta/c_\alpha)^2 \times [(c_\alpha/c_\beta)\cos\chi - (-1)^j\cos\phi][(c_\gamma/c_\alpha)\cos\phi + (-1)^j\cos\theta] \times P_l^\gamma(\theta + (j-1)\pi, \phi)P_i^\beta(\chi + (j-2)\pi, \phi)/P_i^\alpha(\phi + \pi, \phi) \tag{1.19}$$

Discussion of Results

Equation (1.19) represents a generalization of the principle of reciprocity. Suppose we have an experiment where we measure the far field scattering patterns of both $P_L(\theta,\phi)$ and $P_T(\theta,\phi)$ for incidence of, say, a plane longitudinal wave under a fixed direction $\phi = \pi k/N$ (k fixed) at the $2N$ directions of scattering $\theta = \theta_j = \pi j/N$, $j = 0, 1, \ldots, 2N-1$. We can compute $P_i^L(\theta,\phi)$ and $P_i^T(\theta,\phi)$ from the relations:

$$2P_i^L(\theta_j,\phi) = P_L(\theta_j,\phi) - (-1)^i P_L(\theta_{2N-j},\phi), \quad i = 1,2$$

$$2P_i^T(\theta_j,\phi) = P_T(\theta_j,\phi) + (-1)^i P_T(\theta_{2N-j},\phi), \quad i = 1,2$$

Then we can use (1.19) to compute the far field scattering patterns $P_L^\beta(\theta,\chi)$ and $P_T^\beta(\theta,\chi)$ at each of the directions of scattering $\theta = \theta_i, i = 0, 1, \ldots, 2N-1$ for incidence in any direction $\chi = \theta_l$, $l = 0, 1, \ldots, 2N-1$, of either a plane longitudinal wave ($\beta = L$) or a plane transverse wave ($_\beta = T$). The standard principle of reciprocity states (in our notation) that

$$c_\gamma^2 P_\gamma^\beta(\theta,\chi) = c_\beta^2 P_\beta^\gamma(\chi + \pi, \theta + \pi), \quad \gamma,\beta = L,T$$

When this principle is applied to the aforementioned experiment, where $\beta = L$ and $\chi = \pi k/N$ (k fixed), it only yields information about P_L^γ in the fixed direction of scattering $\pi(1 + k/N)$.

Formulas (1.12), (1.18), and (1.19) can be useful for computing asymptotic expansions. Say, for example, one is

interested in computing small wave-number expansions for the crack-opening displacements (COD's) and far field scattering patterns (FFSP's) corresponding to plane wave incidence. It is easier to first compute the small wave-number expansions for these quantities corresponding to a plane longitudinal wave incident at a convenient angle. Formula (1.19) then readily gives the small wave-number expansions of FFSP's corresponding to either a plane longitudinal or transverse wave incident from any direction. From (1.18) the COD's corresponding to either a plane longitudinal or transverse wave incident from any direction are obtained as a quadrature involving the already computed COD's. The small wave-number expansion of this integral is easily obtained. These results for plane wave incidence can then be used in (1.12) to obtain small wave-number expansions corresponding to waves incident from a line-load.

2 Derivation of Results

In this section we derive the results presented in the preceding section. We begin by converting the boundary value problem (1.3)–(1.4) for the scattered field $\mathbf{v}$ into an integral equation ((2.3) in the following) for the crack-opening displacement (COD) ψ defined by (1.15). Likewise, an integral equation ((2.5) in the following) is obtained for the COD ψ_g^k corresponding to the scattered field $\mathbf{v}^{gk}$. Then, a theorem of Gautesen [3] is used to represent the COD ψ_g^k in terms of the COD ψ (see (2.6)). The results could be derived directly from this representation. However, we have chosen to proceed by using a result derived in the Appendix ((2.9a)) which states that the scattered field $\mathbf{v}^{gk}$ satisfies a linear, first-order partial differential equation. The nonhomogeneous term of this equation involves only the functions e_{ij}^k which are (to within a multiplicative constant) the mode $I(i=1)$ and mode $II(i=2)$ stress-intensity factors corresponding to the left ($j=1$) and right ($j=2$) edges of the crack (see (A.3)). From the representation of the COD ψ_g^k, we find that the stress-intensity factors e_{ij}^k can be expressed in terms of the scattered field $\mathbf{v}$ (see (2.11) and (2.8)). Then after determining a constant, we find that our results follow directly from the aforementioned partial differential equation.

We begin by noting that $\mathbf{v}$ admits to the integral representation

$$v_i(\mathbf{x}) = (M\psi)_i(\mathbf{x}) \tag{2.1}$$

where

$$(M\psi)_i(\mathbf{x}) \equiv -2\int_{-1}^{1} m_{ij}(x_1-s,x_2)\psi_j(s)\,ds \tag{2.2a}$$

$$m_{ij}(\mathbf{x}) = \tau_{2j}[\mathbf{f}^i] \tag{2.2b}$$

and $\psi,\mathbf{f}^i(\mathbf{x})$ and τ_{ij} are defined by (1.15), (1.11), and (1.6), respectively. By application of boundary condition (1.4), we find that ψ satisfies the integral equation

$$(K_i\psi_i)(x_1) = E_i^{\alpha}(\phi)\exp[ik_{\alpha}x_1\cos\phi],\ |x_1|<1 \quad \text{(no summation)} \tag{2.3a}$$

and the edge condition

$$\psi_i(\pm 1) = 0 \tag{2.3b}$$

where

$$(K_i\psi)(x) \equiv \frac{d^2}{dx^2}\int_{-1}^{1} k_i(x-s)\psi(s)\,ds$$

$$(\tfrac{1}{2}i\mu k_T^2)^{-1}\frac{d^2}{dx^2}k_1(x) = \left(\kappa^2 + 2k_L^{-2}\frac{d^2}{dx^2}\right)^2 H_0^{(1)}(k_T|x|)$$

$$-4k_L^{-2}\frac{d^2}{dx^2}\left(1+k_L^{-2}\frac{d^2}{dx^2}\right)H_0^{(1)}(k_L|x|)$$

$$(\tfrac{1}{2}i\mu k_T^2)^{-1}\frac{d^2}{dx^2}k_2(x) = \left(\kappa^2 + 2k_L^{-2}\frac{d^2}{dx^2}\right)^2 H_0^{(1)}(k_L|x|)$$

$$-4k_L^{-2}\frac{d^2}{dx^2}\left(\kappa^2+k_L^{-2}\frac{d^2}{dx^2}\right)H_0^{(1)}(k_T|x|)$$

With $\mathbf{v}^{gk}(\mathbf{x};\mathbf{y})$ defined by (1.10), we note that

$$\mathbf{v}^{gk}(\mathbf{x};\mathbf{y}) = (M\psi_g^k)(\mathbf{x}) \tag{2.4}$$

where ψ_g^k is related to $\mathbf{v}^{gk}$ by (1.15). The integral equation satisfied by ψ_g^k is

$$(K_i\psi_{gi}^k)(x_1) = m_{ki}(y_1-x_1,y_2),\ |x_1|<1 \quad \text{(no summation)} \tag{2.5a}$$

$$\psi_g^k(\pm 1;\mathbf{y}) = 0 \tag{2.5b}$$

Gautesen [3] has shown that the solution to (2.5) is related to the solution ψ of (2.3). Details related to a problem similar to the one considered here can be found in Gautesen [4]. In particular

$$4\mu k_{\alpha}\cos\phi P_{3-i}^{\alpha}(\phi,\phi)\psi_{gi}^k(x_1;\mathbf{y}) = F_i^k(x_1;\mathbf{y}) + \psi_i(x_1)L^- v_{ki}(\mathbf{y}) + \psi_i(-x_1)L^+ v_{ki}(-\mathbf{y}) \quad \text{(no summation)} \tag{2.6}$$

where

$$L^{\mp} = ik_{\alpha}\cos\phi \mp \frac{\partial}{\partial y_1}$$

$$v_{ki}(\mathbf{y}) = \int_{-1}^{1}\psi_i(s)m_{ki}(y_1-s,y_2)\,ds \tag{2.7}$$

and near the edge $x_1 = (-1)^j$, F_i^k has the asymptotic behavior

$$F_i^k(x_1;\mathbf{y}) \sim 0([1-(-1)^j x_1]^{3/2})$$

The explicit representation of F_i^k is not needed. Upon using the identity,

$$m_{kj}(x_1,x_2) = -(-1)^{k+j}m_{kj}(x_1,-x_2)$$

we find that v_{ki}, as given by (2.7), is related to v_k, as defined by (2.1) and (2.2), by

$$-4v_{kj}(\mathbf{x}) = v_k(x_1,x_2) + (-1)^{k+j}v_k(x_1,-x_2) \tag{2.8}$$

We show in the Appendix that

$$D_1 v_i^{gk}(\mathbf{z};\mathbf{y}) = -\mu k_L(-1)^j e_{ij}^k(\mathbf{y})e_{ij}^l(\mathbf{z}) \tag{2.9a}$$

where

$$D_1 = \frac{\partial}{\partial y_1} + \frac{\partial}{\partial z_1} \tag{2.9b}$$

and $e_{ij}^k(\mathbf{y})$ represents the amplitude of $v_i^{gk}(\mathbf{x};\mathbf{y})$ near the edge $x_1(-1)^j$, which can be determined from

$$[\pi(1-\kappa^{-2})]^{1/2}\psi_{gi}^k(x_1;\mathbf{y}) \sim (-1)^{i(j+1)}e_{ij}^k(\mathbf{y})[k_L(1-(-1)^j x_1)]^{1/2} \quad \text{(no summation)} \tag{2.10}$$

Since, near the edge $x_1 = (-1)^j$, ψ_i has the asymptotic behavior

$$\psi_i(x_1) \sim (-1)^{i(j+1)}4\mu k_{\alpha}\cos\phi[\pi(1-\kappa^{-2})]^{1/2}a_i^j(\phi)P_{3-i}^{\alpha}(\phi,\phi)[k_L(1-(-1)^j x_1)]^{1/2} \quad \text{(no summation)}$$

where $a_i^j(\phi)$ are unknown constants, it follows from (2.6) and (2.10) that

$$e_{ij}^k(\mathbf{y}) = a_i^j(\phi)L^- v_{ki}(\mathbf{y}) + a_i^{3-j}(\phi)L^+ v_{ki}(-\mathbf{y}) \quad \text{(no summation)} \tag{2.11}$$

We remark that $a_i^j(\phi)[4\mu k_{\alpha}P_{3-i}^{\alpha}(\phi,\phi)\cos\phi]^{-1}$ are the stress-intensity factors corresponding to the scattered field $\mathbf{v}$. Upon substitution from (2.11) and (2.8), we find that (2.9a) becomes

$$D_1 v_l^{gk}(\mathbf{z};\mathbf{y}) = c_i(\phi)(-1)^j w_k^{ij}(\mathbf{y})\, w_l^{ij}(\mathbf{z}) \tag{2.12}$$

where w_k^{ij} are defined by (1.13) and

$$c_i(\phi) = -\mu k_L \{[a_i^2(\phi)]^2 - [a_i^1(\phi)]^2\}$$

To determine the constants $c_i(\phi)$, we let

$$\mathbf{z} = -\rho(\cos\phi, \sin\phi),$$

and note that in the limit as $\rho \to \infty$

$$\mu d_l^\alpha(\phi)\, v_l^{gk} \sim (8\pi k_\alpha \rho)^{-1/2} (c_T/c_\alpha)^2 \exp[i(k_\alpha \rho + \pi/4)] v_k(\mathbf{y}) \tag{2.13}$$

$$d_l^\alpha(\phi)\, v_l(\mathbf{z}) \sim -(\pi k_\alpha \rho/2)^{-1/2} \exp[i(k_\alpha \rho - \pi/4)] P_\alpha(\phi+\pi, \phi) \tag{2.14}$$

Then taking the scalar product of (2.12) with d_l^α, and substituting from (1.13), (2.13), and (2.14) we find that

$$c_i(\phi) = -(c_T/c_\alpha)[8\mu k_T \cos\phi P_i^\alpha(\phi+\pi, \phi)]^{-1} \tag{2.15}$$

The results of Section 1 readily follow. With $c_i(\phi)$ defined by (2.15), v_l^{gk} defined by (1.12) satisfies (2.12). Homogeneous solutions to (2.12) which also satisfy (1.3) in the field are not outgoing at infinity. When for ρ large,

$$\mathbf{z} = -\rho(\cos\chi, \sin\chi)$$

$$\mu d_l^\beta(\chi)\, v_l^{gk} \sim (8\pi k_\beta \rho)^{-1/2} (c_T/c_\beta)^2 \exp[i(k_\beta \rho + \pi/4)] v_k^{\beta\chi}(\mathbf{y})$$

$$d_l^\beta(\chi)\, v_l(\mathbf{z}) \sim -(\pi k_\beta \rho/2)^{-1/2} \exp[i(k_\beta \rho - \pi/4)] P_\beta(\chi+\pi, \phi)$$

is substituted into the scalar product of (2.12) with $d_l^\beta(\chi)$, we find that

$$-2\cos\phi\left(\frac{\partial}{\partial y_1} - ik_\beta \cos\chi\right) v_k^{\beta\chi}(\mathbf{y})$$

$$= (c_\beta/C_\alpha)^2 [(c_\alpha/c_\beta)\cos\chi - (-1)^j \cos\phi] w_k^{ij}(\mathbf{y})$$

$$\times P_i^\beta(\chi + (j-2)\pi, \phi)/P_i^\alpha(\phi+\pi, \phi) \tag{2.16}$$

The solution to (2.16) is given by (1.18). For ρ large, we find that substituting

$$\mathbf{y} = \rho(\cos\theta, \sin\theta)$$

$$d_k^\gamma(\theta)\, v_k^{\beta\chi}(\mathbf{y}) \sim (\pi k_\gamma \rho/2)^{-1/2} \exp[i(k_\gamma \rho - \pi/4)] P_\gamma^\beta(\theta, \chi)$$

$$d_k^\gamma(\theta)\, v_k(\mathbf{y}) \sim (\pi k_\gamma \rho/2)^{-1/2} \exp[i(k_\gamma \rho - \pi/4)] P_\gamma(\theta, \phi)$$

into the scalar product of (2.16) with $d_k^\gamma(\theta)$ yields (1.19).

References

1 Achenbach, J. D., Gautesen, A. K., and McMaken, H., *Ray Methods for Waves in Elastic Solids*, Pitman, Boston, 1982, Chapter 6.

2 Gautesen, A. K., "On the Green's Function for Acoustical Diffraction by a Strip," *J. Acoust. Soc. Am.*, Vol. 74, 1983, pp. 600–604.

3 Gautesen, A. K., "Representations of Solutions to Linear Integral Equations With Difference Kernels," Accepted, *J. Math. Anal. & Appl.*

4 Gautesen, A. K., "Integral Representations for Elastodynamic Edge Diffraction," *Wave Motion*, Vol. 5, 1983, p. 69–82.

APPENDIX

We offer a brief derivation of (2.9*a*). A more detailed derivation can be found in Gautesen [4]. We begin by noting the identity for any pair $(\mathbf{u},\mathbf{v})$:

$$\frac{\partial v_i}{\partial x_1} L_i[\mathbf{u}] + \frac{\partial u_i}{\partial x_1} L_i[\mathbf{v}] = \frac{\partial G_j}{\partial x_j} \tag{A.1}$$

where

$$G_j = \frac{\partial u_i}{\partial x_1}\tau[\mathbf{v}]_{ij} + \frac{\partial v_i}{\partial x_1}\tau[\mathbf{u}]_{ij} - \mu\delta_{1j}\left[(\kappa^2-2)\frac{\partial u_i}{\partial x_i}\frac{\partial v_i}{\partial x_i} + \frac{\partial u_i}{\partial x_j}\left(\frac{\partial v_i}{\partial x_j} + \frac{\partial v_j}{\partial x_i}\right) - \mu^{-1}\rho\omega^2 u_i v_i\right]$$

Substitution of $u_i = g_i^k(\mathbf{x};\mathbf{y})$ and $v_i = g_i^l(\mathbf{x};\mathbf{z})$ into (*A*.1), subsequent integration of $\mathbf{x}$ over space, and utilization of (1.8) and the Divergence theorem yields

$$D_1 g_l^k(\mathbf{z};\mathbf{y}) = -\int_S n_j^s G_j\, ds \tag{A.2}$$

where the reciprocity relation $g_l^k(\mathbf{z};\mathbf{y}) = g_k^l(\mathbf{y};\mathbf{z})$ has been used. The contour S is shown in Fig. 1.

The integral over the faces of the crack vanishes by boundary conditions (1.9). Thus the contribution from the integral in (*A*.2) comes from the small circles centered at the edges. Near the edge, $\mathbf{x} = ((-1)^j, 0)$,

$$g_i^k(\mathbf{x};\mathbf{y}) \sim \text{const} + e_{mj}^k(\mathbf{y}) f_i^m(\theta_d)(k_L d)^{1/2} + o(d^{1/2}) \tag{A.3}$$

where (d,θ_d) are the polar coordinates centered at the edge shown in Fig. 1 and

$$\kappa[\pi(\kappa^2-1)]^{1/2}\mathbf{f}^m(\theta_d) = [\kappa^2 + (2m-5)(\kappa^2-1)\sin^2 \tfrac{1}{2}\theta_d]\cos\tfrac{1}{2}\theta_d \mathbf{q}_m + (-1)^m[1 - (2m-5)(\kappa^2-1)\cos^2\tfrac{1}{2}\theta_d]\sin\tfrac{1}{2}\theta_d \mathbf{q}_{3-m}$$

(no summation)

$$\mathbf{q}_1 = -(-1)^j \cos\theta_d \mathbf{i}_1 + \sin\theta_d \mathbf{i}_2$$

$$\mathbf{q}_2 = (-1)^j \sin\theta_d \mathbf{i}_1 + \cos\theta_d \mathbf{i}_2$$

Substitution into (*A*.2) from (*A*.3) for the integrals about the edges and from (1.10) for g_l^k yields (2.9*a*). Also, equation (2.10) follows from (*A*.3), (1.10), and (2.4).

A. I. Soler
Professor,
Department of Mechanical Engineering
and Applied Mechanics,
University of Pennsylvania,
Philadelphia, Pa. 19104
Mem. ASME

Xu Hong[1]
Lecturer,
Department of Mechanical Engineering,
Beijing Institute of Chemical Technology,
Beijing, People's Republic of China

Analysis of Tube-Tubesheet Joint Loading Including Thermal Loading

The tube-to-tubesheet rolling process is reexamined using a two-dimensional elastic plastic analysis. In addition to room temperature rolling, subsequent thermal cycling of the joint is considered. The development of a computer code based on an incremental analysis that includes finite deformation effects and the possibility of reversed yield is presented. Typical simulations are presented that indicate some of the influences of geometry, materials, and loading on final tube-to-tubesheet contact pressure.

Introduction

The ultimate object in the tube-tubesheet joining process is to maximize the tube-to-tubesheet residual contact pressure after the rolling process has been completed. A method to evaluate this pressure is an essential element to joint design. Works by Dudley [1] and Brown [2] help explain the roller-expanding phenomena in physical terms. Analytical work by Goodier and Schoessow [3] and a companion experimental paper by Grimison and Lee [4] are important milestones in the understanding of the tube expansion process. Goodier and Schoessow develop graphical results for elastic-plastic loading and unloading of a joint assuming plane stress, the Von Mises yield criteria [5], and a room temperature process. The effects of tube wall thickness and relative magnitudes of tube and tubesheet yield strengths are qualitatively discussed by Goodier and Schoessow. Additional experimental works by Alexander and Ford [6], Beston [7], Culver and Ford [8], and by Urogami, et al. [9] serve to provide added information on the subject of tube-to-tubesheet joint contact stresses. Wilson [10] presents a three-dimensional finite element analysis of the tube-to-tubesheet joint; his emphasis is on the residual stress distribution in the roll transition region for a particular geometry.

The ASME Code [11] addresses joint strength in a tube-tubesheet connection solely by setting limits on allowable load permitted on the tube. Certain liberties may be taken on joint strength based on user performed testing, but essentially the ASME code limits the tube stress to the code allowable stress for the tube material. The ASME code does not address the maximum joint load obtainable, nor does it address the effect of subsequent temperature cycles on joint strength.

It is the purpose of this paper to establish a special purpose computer solution to the two-dimensional rolling problem which includes elastic plastic behavior, large deformations, and establishes residual contact pressures both immediately after initial room temperature rolling, and also after a subsequent temperature cycle. The analysis places no restrictions on yielding of the tube or tubesheet during any phase of the simulation. Although creep effects under a high temperature cycle, including a hold time, are not considered herein, the incremental solution offers no barriers to later inclusion of creep effects. The motivation for the work is to develop a modern analysis tool to predict the final tube-tubesheet interface pressure p_c', after the rolling process, and predict the effect of subsequent loadings on p_c'. The work differs from previous efforts in the field in that it provides a cost-effective numerical approach to the two-dimensional tube rolling problem which includes large deformation effects, tube or tubesheet yielding during unloading, and changes in contact pressure during temperature cycles after the initial roll.

Analysis

The roller or hydraulic expansion process is characterized initially by a tube loading stage. The tube is expanded by internal pressure until contact with the inside surface of the tubesheet hole is made; the tube may remain elastic or become plastic during this loading stage depending on initial radial clearance between tube and tubesheet hole. Subsequent to tube-to-tubesheet contact, as the internal pressure continuously increases, loading of the tubesheet begins. Tubesheet deformation is initially elastic until the state of stress in the tubesheet at the hole surface satisfies the yield criteria. With additional increase in rolling pressure, the plastic zone in the tubesheet increases until a maximum rolling pressure is reached. With subsequent decrease of the rolling pressure, both tube and tubesheet are unloaded, but a residual

[1] Presently, visiting Scholar, Department of Mechanical Engineering and Applied Mechanics, University of Pennsylvania, Philadelphia, Pa. 19104.

Contributed by the Applied Mechanics Division for presentation at the 1984 PVP Conference and Exhibition, Applied Mechanics Division and Materials Division, San Antonio, Texas, June 17-21, 1984 of THE AMERICAN SOCIETY OF MECHANICAL ENGINEERS.

Discussion on this paper should be submitted to the Editorial Department, ASME, United Engineering Center, 345 East 47th Street, New York, N.Y. 10017, and will be accepted until two months after final publication of the paper itself in the JOURNAL OF APPLIED MECHANICS. Manuscript received by ASME Applied Mechanics Division, March, 1983; final revision, July, 1983. Paper No. 84-APM-15.

Copies will be available until February, 1985.

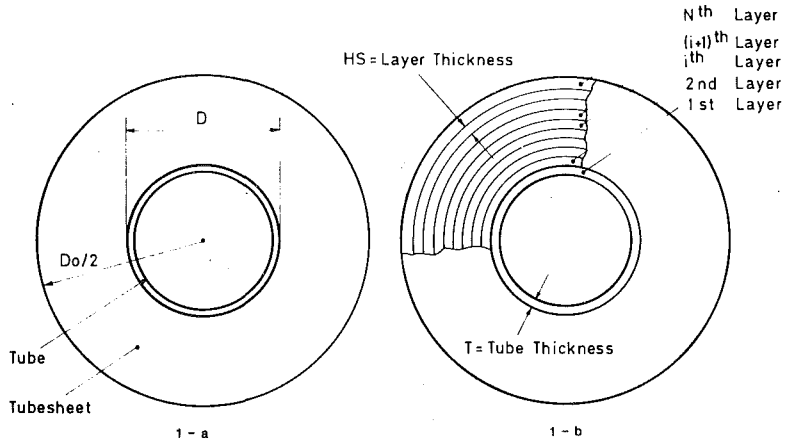

Fig. 1 Tube-to-tubesheet joint model

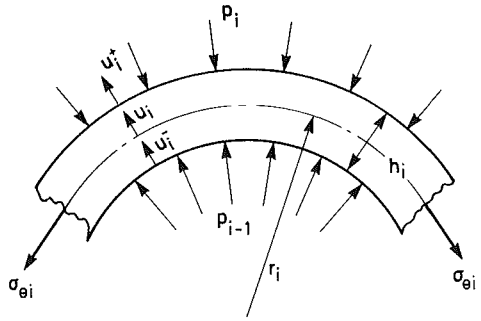

Fig. 2 Stress and displacement definitions for a typical element

contact pressure may exist at the interface of the tube and tubesheet after all of the internal pressure is removed. Reversed yielding may occur during this unloading in either or both tube and tubesheet.

If the tube and tubesheet are made of different materials, any subsequent temperature change of the joint from the rolling temperature to the unit operating temperature changes the tube-to-tubesheet contact pressure. The residual contact pressure after a single temperature cycle depends on joint geometry, material properties of tube and tubesheet, the temperature range, and the maximum rolling pressure initially applied.

Figure 1(*a*) shows the configuration considered. We idealize the configuration by a set of concentric membrane elements in two-dimensional plane stress as shown in Fig. 1(*b*). There are N membrane elements (layers) with the innermost element being the tube; the remaining membrane elements represent the tubesheet. The elements (layers) are numbered starting from the tube (element 1); the ith element (layer) has mean radius r_i and thickness h_i.

The following assumptions are made for the detailed analysis:

(*a*) the tube and tubesheet materials satisfy the Von Mises Yield Criterion;

(*b*) no creep occurs in the temperature range considered;

(*c*) temperature changes in tube and tubesheet are uniform and have the same value at any stage in the simulation.

Figure 2 is a free-body diagram of the ith layer showing "internal" pressure p_{i-1}, and "external" pressure p_i. The average radial and circumferential stresses in the ith layer are

$$\sigma_{ri} = -\frac{1}{2}(p_{i-1} + p_i) \tag{1}$$

$$\sigma_{\theta i} = \frac{1}{h_i}\int_{r_i - h_i/2}^{r_i + h_i/2} \sigma_\theta dr = \frac{r_i}{h_i}(p_{i-1} - p_i) + \sigma_{ri} \tag{2}$$

When rolling pressure p_0 is changed by an increment $\dot{p}_0$ and system temperature T is changed by an increment $\dot{T}$, the interface pressure p_i (between layer $i+1$ and layer i) undergo incremental changes $\dot{p}_i$. The incremental changes in σ_{ri}, $\sigma_{\theta i}$ are

$$2\dot{\sigma}_{ri} = -(\dot{p}_{i-1} + \dot{p}_i) \tag{3}$$

$$\dot{\sigma}_{\theta i} = (\dot{p}_{i-1} - \dot{p}_i)\frac{r_i}{h_i} + (\sigma_{\theta i} - \sigma_{ri})(\dot{\epsilon}_{\theta i} - \dot{\epsilon}_{ri}) + \dot{\sigma}_{ri} \tag{4}$$

where incremental strain relations for each layer are:

$$\frac{\dot{h}_i}{h_i} = \dot{\epsilon}_{ri} = \frac{1}{E_i}(\dot{\sigma}_{ri} - \nu\,\dot{\sigma}_{\theta i}) + \dot{e}_{ri} + \alpha_i \dot{T} \tag{5}$$

$$\frac{\dot{r}_i}{r_i} = \dot{\epsilon}_{\theta i} = \frac{1}{E_i}(\dot{\sigma}_{\theta i} - \nu\,\dot{\sigma}_{ri}) + \dot{e}_{\theta i} + \alpha_i T \tag{6}$$

For ideal plasticity, subject to plane stress conditions, the plastic strain increments $\dot{e}_{ri}$, $\dot{e}_{\theta i}$ are given as [5]

$$\dot{e}_{ri} = \frac{\lambda_i}{3}(2\sigma_{ri} - \sigma_{\theta i}); \quad \dot{e}_{\theta i} = \frac{\lambda_i}{3}(2\sigma_{\theta i} - \sigma_{ri}) \tag{7}$$

Using equations (5) and (6) in equation (4) yields $\dot{\sigma}_{\theta j}$ as

$$\left(1 - \frac{\sigma_{\theta j} - \sigma_{rj}}{2Gj}\right)\dot{\sigma}_{\theta j} = \dot{p}_{j-1}\left[\frac{\sigma_{\theta j} - \sigma_{rj}}{4G_j} - \frac{1}{2} + \frac{r_j}{h_j}\right] + \dot{p}_j\left[\frac{\sigma_{\theta j} - \sigma_{rj}}{4G_j} - \frac{1}{2} - \frac{r_j}{h_j}\right] + (\sigma_{\theta j} - \sigma_{rj})\Delta\dot{e}_j \qquad j = 1,2,\ldots,N \tag{8}$$

where $\Delta\dot{e}_j = \dot{e}_{\theta j} - \dot{e}_{rj}$. Note that in equation (8), the term $(\sigma_{\theta j} - \sigma_{rj})/G_j$ represents large deformation effects during elastic loading. Since this term is of order 10^{-3} for most metals, we conclude that large deformation effects may be significant only during plastic action as represented by the final term in equation (8).

The displacement increments at the inner and outer surfaces of the ith membrane layer are given in terms of strain increments as

$$\dot{u}_i^- = r_i\dot{\epsilon}_{\theta i} - \frac{h_i}{2}\dot{\epsilon}_{ri}; \quad u_i^+ = r_i\dot{\epsilon}_{\theta i} + \frac{h_i}{2}\dot{\epsilon}_{ri} \tag{9}$$

Compatibility equations for a unit idealized as N layers are the $N-1$ equations

$$\dot{u}_{i+1}^- = \dot{u}_i^+ \quad i = 1,2,\ldots,N-1 \tag{10}$$

We eliminate strain increments in terms of stress increments, and then eliminate stress increments in favor of the

Table 1 Tube/tubesheet scenario[a]

Initial Contact	Loading	Unloading	Temperature Change[b]
Tube remains elastic	Specified value of maximum applied pressure is reached	Tube and tubesheet remain elastic	$[(\alpha_T - \alpha_s)\Delta T \gtrless 0]$ Tube is elastic or undergoes no stress change
	All layers yield before maximum roll pressure obtained	Tube and tubesheet both experience reverse yield	Tubesheet can be either elastic or plastic
Tube yields prior to contact	Tube yield strength controls maximum roll pressure	Either tube or tubesheet experiences reversed yield	No change in stress state occurs as the temperature load is imposed or removed
	Tubesheet yield strength controls maximum roll pressure	Tube/tubesheet contact is lost	Tube/tubesheet contact is lost

[a]Note that the result in any column may lead to any of the results in the succeeding columns.
[b]Scenarios apply to thermal loading or unloading.

interface pressure increments. After some algebraic manipulation, we evolve $N-1$ linear compatibility equations from equation (10) in the symbolic form

$$A_i \quad \dot{p}_{i-1} + B_i \dot{p}_i + C_i \quad \dot{p}_{i+1} + D_i \lambda_i k_i + D_i^* \lambda_{i+1} k_{i+1} = R_i \dot{T} \tag{11}$$

where $i = 1,2, \ldots, (N-1)$; N being the number of layers including the tube as the first layer. The coefficients A_i, B_i, C_i, D_i, D_i^*, R_i are functions of the current state; no approximations save plane stress, and the membrane assumption need be employed to obtain equations (11).

The artificially inserted parameter k_i, $i = 1,2, \ldots, N$, satisfies the conditions:

$k_i = 0$ if the ith layer is elastic during the increment;
$k_i = 1$ if the ith layer undergoes plastic flow during the increment. (12)

If all layers remain elastic, since $k_i = 0$, $i = 1,2, \ldots, N$, the $N-1$ compatibility equations are solvable for the $N-1$ interface pressure increments. Once yielding has occurred in one or more layers, equations (11) are insufficient to determine interface pressure increments. Additional equations are obtained from the Von Mises yield condition. If σ_{yi} is the uniaxial yield stress in the ith layer, then

$$\sigma_{\theta i}^2 - \sigma_{\theta i}\sigma_{ri} + \sigma_{ri}^2 \leq \sigma_{yi} \quad i = 1,2 \ldots, N \tag{13}$$

with the equality sign applying when yielding occurs. In incremental form, for any yielded layer, we may write

$$(2\sigma_{\theta i} - \sigma_{ri})\dot{\sigma}_{\theta i} + (2\sigma_{ri} - \sigma_{\theta i})\dot{\sigma}_{ri} = 0, \quad i = 1,2, \ldots, M \tag{14}$$

where M is the number of yielded layers during the increment. Using equations (3), (8), and introducing the artificial parameter k_i so that we can extend equation (14) to all of the layers yields the N equations

$$k_i(F_i \dot{p}_{i-1} + M_i \dot{p}_i) + H_i \lambda_i = 0, \quad i = 1,2, \ldots, N \tag{15}$$

Equations (11) and (15) are $2N-1$ equations for the incremental pressures $\dot{p}_i$, $i = 1,2, \ldots, N-1$ and the plasticity proportionality parameters λ_i, $i = 1,2, \ldots, N$ at each stage of the simulation. Herein, we assume that the boundary conditions are $\dot{p}_N = 0$; $\dot{p}_0$, T are specified loading and temperature increments.

The tube rolling process we consider consists of tube loading by p_0 to initial contact with the tubesheet, a subsequent loading and unloading ($\dot{p}_0 \neq 0$, $\dot{T} = 0$) to establish a room temperature residual contact pressure, and a subsequent temperature cycle ($\dot{p}_0 = 0$ and $\dot{T} \neq 0$) to examine thermal effects in the absence of creep. In the developed computer code a total of 10 layers are modeled. The first layer represents the tube and has an initial layer thickness equal to the nominal tube thickness. The remaining nine layers modeling the tubesheet are given a specified thickness sufficient to model the extent of the region under study.

Since clearance c exists initially between tube and tubesheet, we must establish the stress state when tube-to-tubesheet contact first occurs. Tube yield will occur prior to tubesheet contact if $c/r_1 > \sigma_{y1}/E_1$. If the clearance c is small and tube yield does not occur prior to tubesheet contact, then the roll pressure and the tube stress state at contact are found from the incremental relation

$$\Delta r_1 + \Delta h_1/2 = c \tag{16}$$

Since the tube remains elastic

$$\Delta r_1 = r_1(\Delta\sigma_{\theta_1} - \nu\Delta\sigma_{r_1}); \quad \Delta h_1 = h_1(\Delta\sigma_{r_1} - \nu\Delta\sigma_{\theta_1}) \tag{17}$$

From equilibrium

$$\Delta\sigma_{r_1} = -p_0/2; \quad \Delta\sigma_{\theta_1} = p_0 r_1/h_1 - p_0/2 \tag{18}$$

Thus, the tube state and roll pressure p_0 at contact may be established.

If the tube yield occurs prior to tubesheet contact, then equation (13) applied to a single elastic increment, with stresses given by equation (18), yields the tube yield pressure p_0 as

$$p_0 = \frac{\sigma_{y1} h_1/r_1}{(1 - h_1/2r_1 + h_1^2/4r_1^2)^{1/2}} \tag{19}$$

The additional change in roll pressure, tube mean radius r_1, and tube thickness h_1, occurring during the increment between first yield and tubesheet contact may be obtained by using equation (16), equation (15) (written for the first layer), and geometric relations for Δr_1, Δh_1, in terms of $\dot{p}_0$, λ_1 considering the tube layer to have yielded. Solving for $\dot{p}_0$, λ_1 associated with the geometry changes between tube initial yield and first contact permits establishment of the tube state and rolling pressure at the onset of tubesheet loading.

Application

A computer program simulating the roller expansion process based on the previous theoretical incremental analysis has been developed. The program includes determination of the tube state at initial contact with the tubesheet, simulation of a loading and unloading stage with $\dot{p}_0 \neq 0$, $\dot{T} = 0$, and simulation of a temperature load and unload cycle with $\dot{p}_0 = 0$, $\dot{T} \neq 0$. During the increments, within each stage of loading

Table 2 Simulation with 70:30 Cu Ni tubing

Clearance c = 0.127×10^{-3} (m); layer thickness = 2.159×10^{-3} (m); $T_{roll} = 20°C$; $T_{operating} = \pm 200°C$

	Tube	Tubesheet 1	Tubesheet 2
Material	70:30 Cu Ni	90:10 Cu Ni	Steel
E(kPa)	151.69×10^6	124.11×10^6	200×10^6
σ_y(kPa)	124.11×10^3	103.43×10^3	206.86×10^3
α(1/°C)	16.2×10^{-6}	17.1×10^{-6}	11.7×10^{-6}
tube O.D. (m)		0.01905	0.01905
tube thickness (m)		1.2446×10^{-3}	0.7112×10^{-3}

Table 3 Cu-Ni/Cu-Ni simulation

Tube yields prior to contact

(1) Loading stage

Rolling pressure (kPa)	Contact pressure (kPa)	Plastic layers 1 2 3 4 5 6 7 8 9 10
17532.0	0.0	1[a]0[a]0 0 0 0 0 0 0 0 0
40000.0	21343.8	1 0 0 0 0 0 0 0 0 0
120000.0	101787.6	1 1 1 1 0 0 0 0 0 0
135550.0	119403.9	1 1 1 1 1 1 1 1 0 0

Contact pressure reaches tubesheet critical value

(2) Unloading stage

120000.0	108273.4	0 0 0 0 0 0 0 0 0 0
40000.0	51172.1	0 0 0 0 0 0 0 0 0 0
0.0	16109.3	1 1 0 0 0 0 0 0 0 0

(3) Temperature change stage

Temperature (Degs.C.)	Contact pressure (kPa)	Plastic layers 1 2 3 4 5 6 7 8 9 10
(*A*) Temperature goes from room temp. to operating temp.		
20.0	16109.3	1 1 0 0 0 0 0 0 0 0
120.0	14723.3	0 1 0 0 0 0 0 0 0 0
200.0	13605.4	0 1 0 0 0 0 0 0 0 0
(*B*) Temperature goes from operating temp. to room temp.		
200.0	13605.4	0 1 0 0 0 0 0 0 0 0
120.0	14807.4	0 0 0 0 0 0 0 0 0 0
20.0	16102.4	1 0 0 0 0 0 0 0 0 0

[a] "0" indicates elastic behavior. "1" indicates a yielded layer.

Table 4 Cu-Ni/steel simulation

Tube yields prior to contact

(1) Loading stage

Rolling pressure (kPa)	Contact pressure (kPa)	Plastic layers 1 2 3 4 5 6 7 8 9 10
9600.9	0.0	1 0 0 0 0 0 0 0 0 0
40000.0	29543.5	1 0 0 0 0 0 0 0 0 0
120000.0	110034.6	1 0 0 0 0 0 0 0 0 0
143300.0	135870.3	1 1 0 0 0 0 0 0 0 0

Rolling pressure reaches tube critical value

(2) Unloading stage

120000.0	115648.9	0 0 0 0 0 0 0 0 0 0
40000.0	46302.5	0 0 0 0 0 0 0 0 0 0
0.0	9219.6	1 0 0 0 0 0 0 0 0 0

(3) Temperature change stage

Temperature (Degs.C.)	Contact pressure (kPa)	Plastic layers 1 2 3 4 5 6 7 8 9 10
(*A*) Temperature goes from room temp. to operating temp.		
20.0	9219.9	1 0 0 0 0 0 0 0 0 0
120.0	9225.9	1 0 0 0 0 0 0 0 0 0
200.0	9231.0	1 0 0 0 0 0 0 0 0 0
(*B*) Temperature goes from operating temp. to room temp.		
200.0	9231.0	1 0 0 0 0 0 0 0 0 0
120.0	5402.8	0 0 0 0 0 0 0 0 0 0
20.0	561.4	0 0 0 0 0 0 0 0 0 0

or unloading, proper account is taken of geometry changes and plastic behavior.

The main purposes of this program are: (*a*) to determine the residual contact pressure after unloading or after temperature change for a given joint, so as to predict the joint holding power; and (*b*) to analyze the effect of various parameters and load cycles on the final residual contact pressure obtained. Table 1 shows the possible scenarios that evolve based on a considerable number of simulations using the computer code. Prior to discussing specific simulations, we consider the effect of tube and tubesheet yield strengths on limiting roll and contact pressure. We apply equation (13) to the inside surface of the tube, and to the inside surface of the tubesheet; we recognize that at those locations $\sigma_r = -p_R$ and $-p_C$, where p_R, p_C are the roll and contact pressures, respectively. Solving equation (13) for σ_θ, we find that in order that σ_θ be real at the locations considered, p_R, p_C must be limited to the values

$$p_R \leq \sqrt{4/3}\,\sigma_T; \quad p_c \leq \sqrt{4/3}\,\sigma_{TS}. \tag{20}$$

σ_T, σ_{TS} refer to the uniaxial yield stress of the tube and tubesheet material, respectively. We note that the limiting values are independent of the outer radius assumed to model the tubesheet. In fact the limiting result is usually found associated with the solution of the infinite sheet with an internally pressurized hole [5] and leads to the conclusion that there is a limiting radius beyond which plasticity cannot propagate. In our finite radius tubesheet model, the limits apply, but the extent of the plastic region depends on the particular geometry assumed. In fact, if the assumed outer limit is taken too small, complete plastification with subsequent unlimited deformation occurs prior to achieving the limits of equation (20). To verify the computer code, the layered model has been used to simulate a configuration with zero clearance, and tube and tubesheet both of the same material. The results are compared with the Lame solution for the thick cylinder. The circumferential and radial stress distributions obtained during the verification study are in excellent agreement with the exact solution given by Lame.

Table 5 Thermal cycling of a Cu-Ni/Cu-Ni assemblage to −200°C

Tube yields prior to contact

(1) Loading stage

Rolling pressure (kPa)	Contact pressure (kPa)	Plastic layers 1 2 3 4 5 6 7 8 9 10
17532.0	.0	1 0 0 0 0 0 0 0 0 0
40000.0	21343.8	1 0 0 0 0 0 0 0 0 0
120000.0	101787.6	1 1 1 1 0 0 0 0 0 0
135550.0	119403.9	1 1 1 1 1 1 1 1 0 0

Contact pressure reaches tubesheet critical value

(2) Unloading stage

120000.0	108273.4	0 0 0 0 0 0 0 0 0 0
40000.0	51172.1	0 0 0 0 0 0 0 0 0 0
0.0	16109.3	1 1 0 0 0 0 0 0 0 0

(3) Temperature change stage

Temperature (Degs.C.)	Contact pressure (kPa)	Plastic layers 1 2 3 4 5 6 7 8 9 10
(*A*) Temperature goes from room temp. to operating temp.		
20.0	16109.3	1 1 0 0 0 0 0 0 0 0
−80.0	16111.5	1 1 0 0 0 0 0 0 0 0
−200.0	16114.2	1 1 0 0 0 0 0 0 0 0
(*B*) Temperature goes from operating temp. to room temp.		
−200.0	16114.2	1 1 0 0 0 0 0 0 0 0
−80.0	14448.2	0 1 0 0 0 0 0 0 0 0
20.0	13051.0	0 1 0 0 0 0 0 0 0 0

Table 2 presents geometry and loading conditions for a typical construction. Two simulations are performed with the tube material 70:30 Cu-Ni in both analyses. The thermal cycle is the same for both simulations considering both heat up and cool down. Tables 3 and 4 show the computer output from the two simulations.

Table 6 Titanium tube/muntz tubesheet properties

	Tube	Tubesheet
Material	Titanium	Muntz
E(kPa)	102.736×10^{6}	103.425×10^{6}
σ_y(kPa)	275.8×10^{3}	137.9×10^{3}
α_T(1/°C)	8.64×10^{-6}	20.88×10^{-6}
tube O.D. (m)	0.01905	
tube thickness (m)	0.7112×10^{-3}	
$c=0.127\times10^{-3}$(m),	layer thickness $=2.159\times10^{-3}$(m)	
$T_{roll}=20$°C,	$T_{operating}=200$°C	

Table 7 70:30 Cu-Ni/Muntz simulation

Tube yields prior to contact
(1) Loading stage

Rolling pressure (kPa)	Contact pressure (kPa)	Plastic layers 1 2 3 4 5 6 7 8 9 10
9600.9	0.0	1 0 0 0 0 0 0 0 0 0
40000.0	29547.3	1 0 0 0 0 0 0 0 0 0
120000.0	110061.2	1 1 1 0 0 0 0 0 0 0
143300.0	135939.4	1 1 1 1 0 0 0 0 0 0

Rolling pressure reaches tube critical value
(2) Unloading stage

120000.0	117149.2	0 0 0 0 0 0 0 0 0 0
40000.0	47243.5	1 0 0 0 0 0 0 0 0 0
0.0	9157.4	1 0 0 0 0 0 0 0 0 0

(3) Temperature change stage

Temperature (Degs.C.)	Contact pressure (kPa)	Plastic layers 1 2 3 4 5 6 7 8 9 10
(*A*) Temperature goes from room temp. to operating temp.		
20.0	9157.4	1 0 0 0 0 0 0 0 0 0
120.0	4562.0	0 0 0 0 0 0 0 0 0 0
200.0	851.6	0 0 0 0 0 0 0 0 0 0
(*B*) Temperature goes from operating temp. to room temp.		
200.0	851.6	0 0 0 0 0 0 0 0 0 0
120.0	4562.0	0 0 0 0 0 0 0 0 0 0
20.0	9157.4	1 0 0 0 0 0 0 0 0 0

Table 8 Titanium/Muntz simulation

Tube yields prior to contact
(1) Loading stage

Rolling pressure (kPa)	Contact pressure (kPa)	Plastic layers 1 2 3 4 5 6 7 8 9 10
21343.2	0.0	1 0 0 0 0 0 0 0 0 0
40000.0	18048.9	1 0 0 0 0 0 0 0 0 0
120000.0	96279.5	1 1 0 0 0 0 0 0 0 0
182850.0	159219.7	1 1 1 1 1 1 1 1 0 0

Contact pressure reaches tubesheet critical value
(2) Unloading stage

120000.0	105941.2	0 0 0 0 0 0 0 0 0 0
40000.0	38172.6	0 0 0 0 0 0 0 0 0 0
0.0	5315.2	0 1 0 0 0 0 0 0 0 0

(3) Temperature change stage

Temperature (Degs.C.)	Contact pressure (kPa)	Plastic layers 1 2 3 4 5 6 7 8 9 10
(*A*) Temperature goes from room temp. to operating temp.		
20.0	5315.2	0 1 0 0 0 0 0 0 0 0
85.0	−23.9	0 1 0 0 0 0 0 0 0 0

No contact between tube and tubesheet Joint fails.

Note that with tubesheet No. 1, the limit on roll pressure is governed by the tubesheet yield strength. There is a significant plastic region in the tubesheet at the peak load. For the Cu-Ni/Cu-Ni combination, reversed yielding occurs in both tube and tubesheet, while for the Cu-Ni/steel combination, reversed yield occurs only in the tube. For the Cu-Ni/Cu-Ni combination, there is a 15.5 percent reduction in tube-tubesheet contact pressure at the operating temperature of 200°C; the tubesheet layer remains in a yielded state. Upon removal of the temperature load, the full contact pressure is essentially recovered. In the Cu Ni/steel combination, the limit on roll pressure is governed by the tube material and there is a relatively limited plastic zone in the tubesheet. During the thermal loading to 200°C, there is essentially no change in stress state during loading to operating temperature; removal of the thermal loading causes a significant reduction in final tube-tubesheet contact pressure. We will discuss the rationale for this behavior shortly, but we note here that the primary difference in behavior during thermal loading is caused by the difference in sign of $(\alpha_T-\alpha_{Ts})\Delta T$ in the two simulations. Table 5 presents the results of the Cu-Ni/Cu-Ni assemblage during thermal cycling to a lower temperature of −200°C. Notice that during cool-down the contact pressure remains essentially unchanged and there is a significant drop in contact pressure when ambient temperature is recovered.

The final simulation demonstrating the application of the developed code involves a Muntz tubesheet with either 70:30 Cu-Ni tubes (see Table 2) or titanium tubing. The Muntz/titanium combination is popular in the retubing of power plant condensers. Table 6 summarizes the tube/tubesheet properties and Tables 7 and 8 show the results of the simulation. Note the considerable reduction in residual contact pressure with the titanium tubing. Because of the significant difference in thermal expansion coefficients between titanium and Muntz, the increase in temperature to 85°C causes complete loss of tube to tubesheet contact pressure.

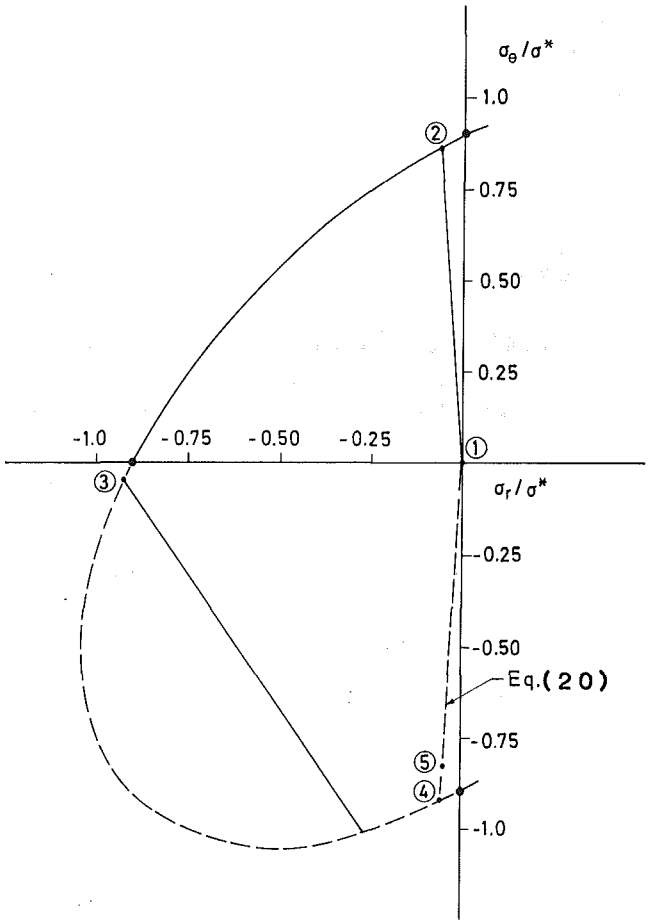

Fig. 3 σ_r versus σ_θ Cu-Ni/Cu-Ni. $\sigma^* = 137.9 \times 10^3$ kPa (20000 psi)

It remains for us to show why the contact pressures remain

essentially unchanged during thermal loading under certain conditions. We consider specifically the Cu-Ni/Cu-Ni assemblage reported in Tables 3 and 5. During any portion of the thermal cycle, the state of stress in the tube layer is

$$\sigma_r = \frac{p_1}{2}; \quad \sigma_\theta = \sigma_r\left(\frac{2r_1}{h_1} + 1\right) \tag{21}$$

Figure 3 shows the σ_r, σ_θ plane for the entire load-unload thermal cycle. Point 2 is the beginning of the mechanical rolling stage subsequent to tube/tubesheet contact. Point 3 is the end of the loading state. Point 4 is the end of the unloading stage and show that the tube undergoes reversed yield. Equation (21) is plotted on Fig. 3 through point 4 and the origin. Regardless of the "direction" of thermal loading, the tube state must lie along this line (if we neglect small geometry changes). Point 5 is the end of the thermal load cycle reported in Table 3; the return to room temperature simply causes a return to point 4 in Fig. 3. However, when we lower the temperature in the run shown in Table 5, the tube cannot satisfy equation (21) and the yield condition unless there is no change in state of stress; that is, the tube state of stress would like to move to but cannot go beyond the yield limit. An examination of expanded stress output for Table 5 indicates that the state of stress remains essentially unchanged throughout the entire unit while the temperature falls to $-200°C$. Subsequent heating of the unit causes the point in stress state to move toward the origin in an elastic manner.

Conclusions

A special purpose incremental method has been outlined to study the tube to tubesheet rolling problem. It is based on a two-dimensional model, permits large deformations, elastic plastic behavior in both loading and unloading stages, and thermal cycling. Because of its incremental formulation, extension of the model to incorporate high temperature inelastic effects is not difficult. The results presented demonstrate the influence of some of the material, geometric, and loading parameters on the final tube to tubesheet contact pressure. While the developed computer code is useful by itself as a design tool, it is also intended to be used as a mechanism for obtaining simplified rules for publication in design codes. The results obtained herein vividly demonstrate that attention should be given to the effect of thermal cycling when considering pull-out strength of tube-to-tubesheet joints.

References

1 Dudley, F. E., "Electronic Control Method for the Precision Expanding of Tubes," ASME paper, 53-A-133, Dec., 1953.

2 Brown, G. J., and Fisher, E. F., "Tube Expanding and Related Subjects," *Trans. ASME*, May 1954, pp. 563–575.

3 Goodier, J. N., and Schoessow, G. J., "The Holding Power and Hydraulic Tightness of Expanded Tube Joints: Analysis of Stress and Deformation," *Trans. ASME*, July 1941, pp. 489–496.

4 Grimison, E. D., and Lee, G. H., "Experimental Investigation of Tube Expanding," *Trans. ASME*, July, 1943, pp. 497–505.

5 Mendelson, A., *Plasticity: Theory and Application*, Macmillan, New York, 1968.

6 Alexander, J. M., and Ford, H., "Experimental Investigations of the Process of Expanding Boiler Tubes," *International Journal of Mechanical Engineers*, Jan. 1956, pp. 351–367.

7 Beston, P. G., "Development of the Zucolloy Coolant Tube to End Fitting Joint for NPD-II," Report to the Canadian General Electric Co., Ltd., Peterborough, Ontario, Canada, 1959.

8 Culver, L. D., and Ford, H., "Experimental Study of Some Variables of the Tube Expanding Process," *Institute of Mechanical Engineers*, 1962.

9 Uragami, K., Sugino, M., Urushibasta, S., Kodama, T., and Fujiwara, Y., "Experimental Residual Stress Analysis of Tube-to-Tubesheet Joints During Expansion," ASME Paper 82-PVP-61, July, 1982.

10 Wilson, R. M., "The Elastic-Plastic Behavior of a Tube During Expansion," ASME Paper 78-PVP-112, June 1978.

11 *ASME Boiler and Pressure Vessel Code, Section VIII, Division 1*, Appendix *A*, 1980.

Investigation of Stress Wave Propagation Through Intersecting Bars

K. R. Y. Simha
Graduate Student.

W. L. Fourney
Professor and Chairman.

Department of Mechanical Engineering,
University of Maryland,
College Park, Md. 20742

A general formulation is presented for the analysis of stress wave propagation through the junction of rectangular bars. The analysis is applied to the case of two bars meeting at right angles and is used to theoretically predict the passage of longitudinal waves through the junction. An experimental investigation of the phenomenon, using dynamic photoelasticity is conducted with a high-speed multiple spark gap camera of the Cranz-Schardin type. Three different geometries are tested to represent the most common types of junctions encountered in practice. In each of the cases, experimentally obtained results are observed to be very consistent with the theoretical predictions.

Introduction

The study of stress wave propagation through an intersection point is of paramount importance in structural design under dynamic loading conditions. To a great extent, the stability of a structure to a sudden applied seismic or aerodynamic disturbance depends on the stress wave transmission characteristics of the various joints that comprise the structure.

There is considerable literature concerning both the theoretical and experimental analysis of stress wave propagation in straight and curved bars [1-5]. However, much less work has been reported on the stress wave propagation through joints. In 1971, Mandel, Mathur, and Chang [6] analyzed the simultaneous transmission of flexural and longitudinal waves around a rigid right angle joint and employed strain gages to obtain experimental data. In 1972, Lee and Kolsky [7] considered the stress wave propagation through an obtuse angle and a right angle corner and again employed strain gages to obtain experimental data. In 1975, Atkins and Hunter [8] studied the transmission of a longitudinal wave around a right angle corner and employed strain gages to verify theoretical results. Very recently Desmond [9] considered the stress wave propagation through a junction of three bars and he also used strain gages to obtain experimental data.

The first purpose of this paper is to present a general formulation for the analysis of stress wave propagation through a general junction and to specialize the theory to a few simple cases. The second purpose is to verify the theoretical results experimentally using the technique of dynamic photoelasticity.

Contributed by the Applied Mechanics Division for presentation at the 1984 PVP Conference and Exhibition, Joint with Applied Mechanics Division and Materials Division, San Antonio, Texas, June 17-21, 1984 of THE AMERICAN SOCIETY OF MECHANICAL ENGINEERS.

Discussion on this paper should be addressed to the Editorial Department, ASME, United Engineering Center, 345 East 47th Street, New York, N.Y. 10017, and will be accepted until two months after final publication of the paper itself in the JOURNAL OF APPLIED MECHANICS. Manuscript received by ASME Applied Mechanics Division, June, 1982; final revision, June, 1983. Paper No. 84-APM-22.

Copies will be available until February, 1985.

Theory

General formulation for wave transmission through a junction of three bars.

The bar junction itself is modeled as a rigid block as shown in Fig. 1. The bars are assumed to all be of the same thickness but may differ in width and material construction. In this paper, elementary theories are employed to represent the propagation of both longitudinal and flexural waves. However, the results can be suitably modified to include the effects of rotary inertia and transverse shear. Fig. 2 shows the free body diagram and the coordinate systems employed in the analysis.

Considering the flexural wave equation first, the displacement y_j must satisfy the relationship:

$$\frac{\partial^4 y_j}{\partial x_j^4} + \frac{\rho_j A_j}{E_j I_j}\frac{\partial^2 y_j}{\partial t^2} = 0 \quad (j=1,2,3) \tag{1}$$

Noting that $c_j^2 = E_j/\rho_j$, $A_j = 2l_j t$ and $I_j = (2/3)t l_j^3$ (1) takes the form:

$$\frac{\partial^4 y_j}{\partial x_j^4} + \frac{3}{c_j^2 l_j^2}\frac{\partial^2 y_j}{\partial t^2} = 0 \quad (j=1,2,3) \tag{2}$$

Equation (2) can be readily solved by the technique of Laplace transforms [10]. For this case we define

$$\bar{Y}_j(x_j,s) = \int_0^\infty e^{-st} y_j(s_j,t)\,dt \tag{3}$$

where the bar represents the transformed value.

For homogeneous initial conditions, the flexural wave equation (2) transforms to a fourth-order ordinary differential equation given by

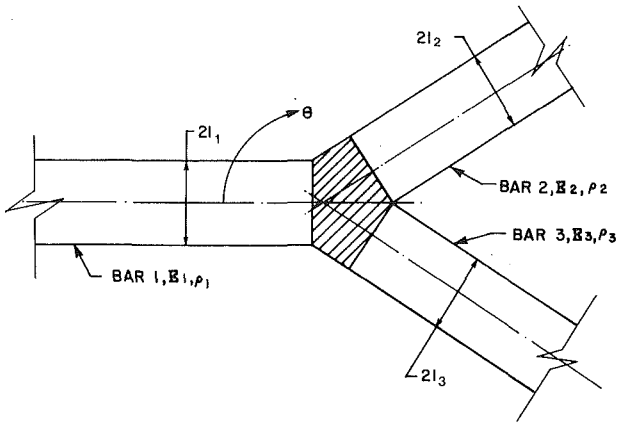

Fig. 1 A general junction of three bars

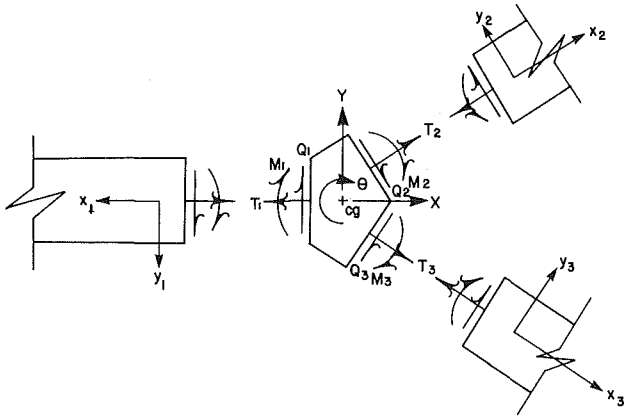

Fig. 2 Free body diagram and coordinate systems

$$\frac{d^4 \bar{Y}_j}{dx_j^4} + \frac{3s^2}{c_j^2 1_j^2} \bar{Y}_j = 0 \tag{4}$$

The preceding differential equation has the solution

$$\bar{Y}_j(x_j,s) = A_j(s) e^{-(1+i)\beta_j \sqrt{s} x_j} + B_j(s) e^{-(1-i)\beta_j \sqrt{s} x_j} + C_j(s) e^{(1+i)\beta_j \sqrt{s} x_j} + D_j(s) e^{(1-i)\beta_j \sqrt{s} x_j} \tag{5}$$

where

$$\beta_j^4 = \frac{3}{4} c_j^2 1_j^2 \quad \text{and} \quad i^2 = -1.$$

For bounded values of $\bar{Y}_j(x_j,s)$ we should have $C_j(s) = D_j(s) = 0$.

To determine $A(s)$ and $B(s)$ we examine the end conditions for the beams. The moment and shear force are given by

$$\bar{M}_j = E_j I_j \left[\frac{d^2 Y_j}{dx_j^2} \right]_{x_j = 0} \tag{6}$$

$$\bar{Q}_j = E_j I_j \left[\frac{d^3 Y_j}{dx_j^3} \right]_{x_j = 0} \tag{7}$$

From equations (5) and (6) we get

$$A_j(s) - B_j(s) = |\bar{M}_j| / 2iE_j \tag{8}$$

From equations (5) and (7) we get

$$A_j(s) + B_j(s) = \frac{1}{2\beta_j^2 E_j I_j} \left\{ \frac{1}{\beta_j s^{3/2}} + \frac{1}{s} \right\} \tag{9}$$

Additional information can be obtained if we examine the kinematics of the junction. In Fig. 2 the three motions x, y, and θ of the center of gravity of the block must satisfy the following equations.

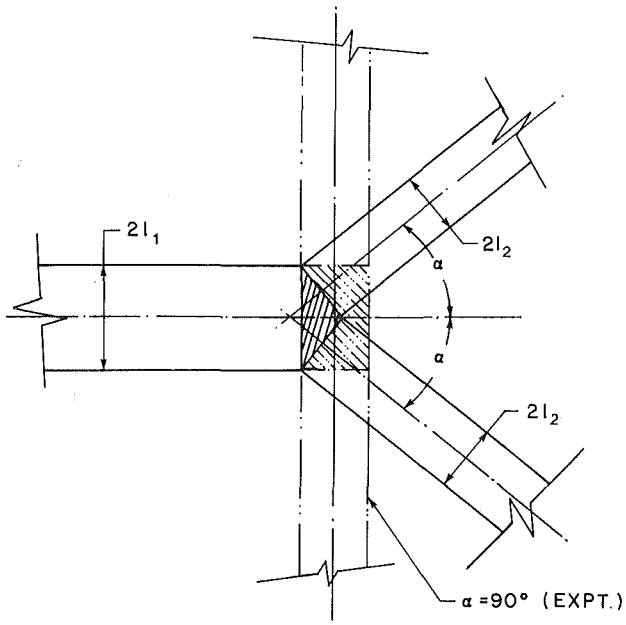

Fig. 3 Symmetrically branched junction with extended middle bar

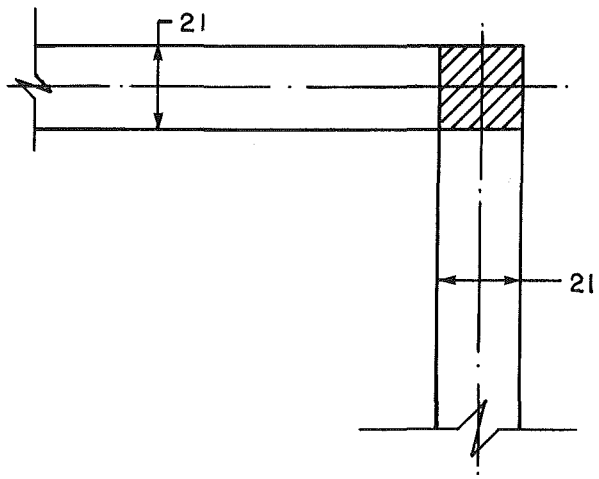

Fig. 4 "L" junction

$$L\left\{ \frac{dy_j}{dx_j} \right\}_{x_j = 0} = -\bar{\Theta} \tag{10}$$

$$L\{Y_J\}_{x_j = 0} = \bar{X} \sin\Theta_j \bar{Y} \cos\Theta_j - \bar{\Theta} d_j \tag{11}$$

where $L\{\ \}$ represents the transformed values; Θ_j represent the angular position of the bars as defined in Fig. 1; d_j represent the moment arms of the shear forces Q_j about the center of gravity of the block in Fig. 3.

From equations (10) and (11) we obtain

$$\frac{1}{2\beta_j^2 E_j I_j} \left[\frac{\bar{Q}_j}{\beta_j s^{3/2}} + \frac{\bar{M}_j}{s} \right] = \bar{X} \sin\Theta_j - \bar{Y} \cos\bar{\Theta}_j - d_j \tag{12}$$

$$\frac{1}{2\beta_j E_j I_j} \left[\frac{\bar{Q}_J}{\beta_j S} + \frac{\bar{M}_J}{\sqrt{s}} \right] = \bar{\Theta} \tag{13}$$

To obtain a complete solution we must consider next the longitudinal wave equation. We denote the incident and reflected longitudinal wave fields in bar 1 by Φ_I and Φ_R, respectively. We let Φ_2 and Φ_3 represent the transmitted

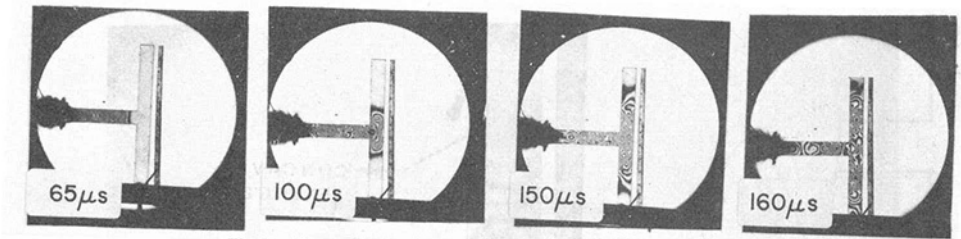

Fig. 5 Dynamic isochromatics for Case 1: *T* intersection

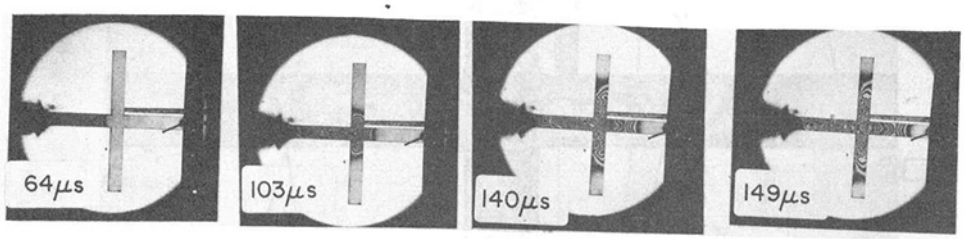

Fig. 6 Dynamic isochromatics for Case 2: + intersection

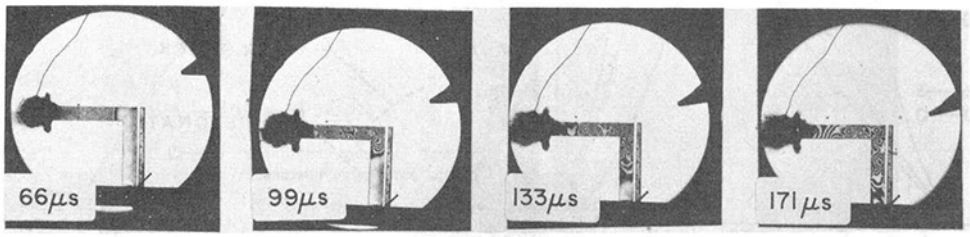

Fig. 7 Dynamic isochromatics for Case 3: *L* intersection

longitudinal wave fields in bars 2 and 3, respectively. The basic longitudinal wave equation is given by

$$\frac{\partial^2 U_j}{dx_j^2} - \frac{1}{c_j^2}\frac{\partial^2 U_j}{\partial t^2} = 0 \tag{14}$$

Where the U_j's are the longitudinal displacements in the three bars given by

$$U_1(x_1,t) = \Phi_I\left(t + \frac{x_1}{c_1}\right) + \Phi_R\left(t - \frac{x_1}{c_1}\right) \tag{15}$$

$$U_2(x_2,t) = \Phi_2\left(t - \frac{x_2}{c_2}\right) \tag{16}$$

$$U_3(x_3,t) = \Phi_3\left(t - \frac{x_3}{c_3}\right) \tag{17}$$

The kinematic constraint at the junction in transformed notation is

$$L\{U_J\}_{x_j=0} = -\bar{X}\cos\Theta_j + \bar{Y}\sin\Theta_j \tag{18}$$

From (23)–(26) we obtain

$$\bar{\Phi}_I + \bar{\Phi}_R = -\bar{X} \tag{19}$$

$$\bar{\Phi}_j = -\bar{X}\cos\Theta_j + \bar{Y}\sin\Theta_j \tag{20}$$

The normal compressive force T_J is given by

$$T_j = A_j E_j \frac{\partial U_j}{\partial x_j} \tag{21}$$

From (21) the expressions for T_1, T_2, and T_3, in transformed notation, become

$$\bar{T}_1 = 2s\rho_1 c_1 1_1 t_1(\bar{\Phi}_I - \bar{\Phi}_R) \tag{22}$$

$$\bar{T}_j = -2s\rho_j c_j 1_j t_j \Phi_j \tag{23}$$

Finally we write the equations of motion for the rigid junction. These are two equations of translation in the X and Y directions and one of rotation Θ. Referring to Figs. 1 and 2 the equations of motion in transformed notation are

$$\sum_{j=1,2,3}(\bar{T}_j\cos\Theta_j - \bar{Q}_j\sin\Theta_j) = -Ms^2\bar{X} \tag{24}$$

$$\sum_{j=1,2,3}(\bar{T}_j\sin\Theta_j - \bar{Q}_j\cos\Theta_j) = Ms^2\bar{Y} \tag{25}$$

and

$$\sum_{j=1,2,3}(\bar{M}_j + e_j\bar{T}_j + d_J\bar{Q}_J) = Is^2\bar{\Theta} \tag{26}$$

where M and I are the mass and the moment of inertia of the rigid junction; e_J are the moment arms for the forces T_j about the center of gravity of the block.

The basic equations of the problem are then equations (12), (13), (19), (20), and (22)–(26). These represent 15 simultaneous equations involving 15 unknowns viz, Φ_R; $\Phi_j\,(j=2,3)$; T_j, $\bar{M}_j$, $\bar{Q}_j\,(j=1,2,3)$; and X,Y and Θ. It is assumed that the incident longitudinal wave field Φ_I is known. The foregoing set of simultaneous equations can be written in matrix notation as follows.

$$[G][c] = [R] \tag{27}$$

In the preceding equation $[G]$ is a 15×15 matrix characterizing the junction geometry as well as the constitution of the bars forming the junction. $[c]$ is a column matrix of the 15 unknown variables while $[R]$ represents the incident wave field Φ_I which is assumed to be known. The expanded version of (27) is given in Appendix A. Thus, if the incident wave field $\bar{\Phi}_I$ is specified, it is possible to obtain the remaining unknowns from (27). In what follows the preceding general formulation is applied to three special cases.

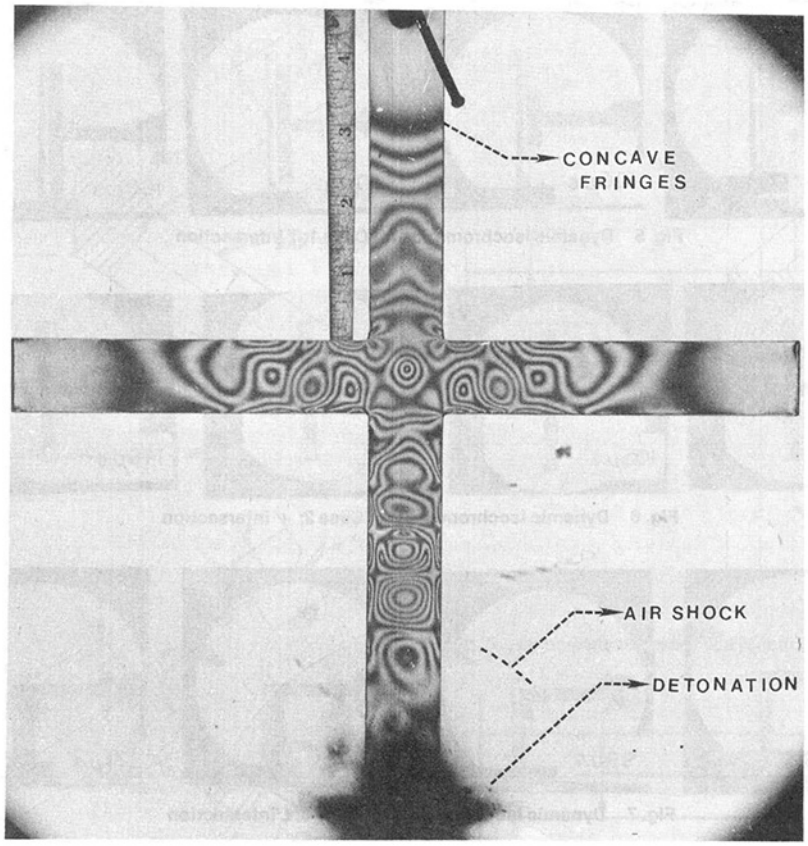

Fig. 8 Enlargement of a fringe pattern for Case 2

Case 1 Symmetrically Branched Intersection. This problem has been treated by Lee [11] using Fourier series. Hence, only the highlights of the solution will be presented here. For details the reader is referred to [12, 13]. For this case for $l_2 = l_3$, and

$$\left.\begin{aligned} &\Theta_3 = 360 - \Theta_2 \\ &T_2 = T_3 \\ &M_2 = -M_3 \\ &Q_2 = -Q_3 \\ &e_2 T_2 + e_3 T_3 = 0 \\ &d_2 Q_2 + d_3 Q_3 = 0 \\ &Q_1 = M_1 = \Theta = Y = 0 \end{aligned}\right\}$$

In this case the number of unknowns reduces to seven, simplifying the problem enormously. The ratio of intensities of the transmitted and incident wave field is given by

$$\frac{\bar{\Phi}_2}{\bar{\Phi}_I} = \frac{1}{-\dfrac{b_2 \cos\Theta_2}{b_1} + \dfrac{1}{\cos\Theta 2} + \dfrac{\tan\Theta_2 \sin\Theta_2 \beta_2{}^2 s^{3/2}}{2b_1 (K_2 - \beta_2{}^1{}_2)} + \dfrac{Ms}{2b_1 \cos\Theta_2}} \tag{28}$$

Hence, when $\Theta_2 = 90$ deg $\bar{\Phi}_2 = \bar{\Phi}_I / \infty = 0$. This implies that for a T junction there would be no transmission of the longitudinal stress wave. This is borne out in the experimental results where it will be observed that the transmitted wave is predominantly flexural in character.

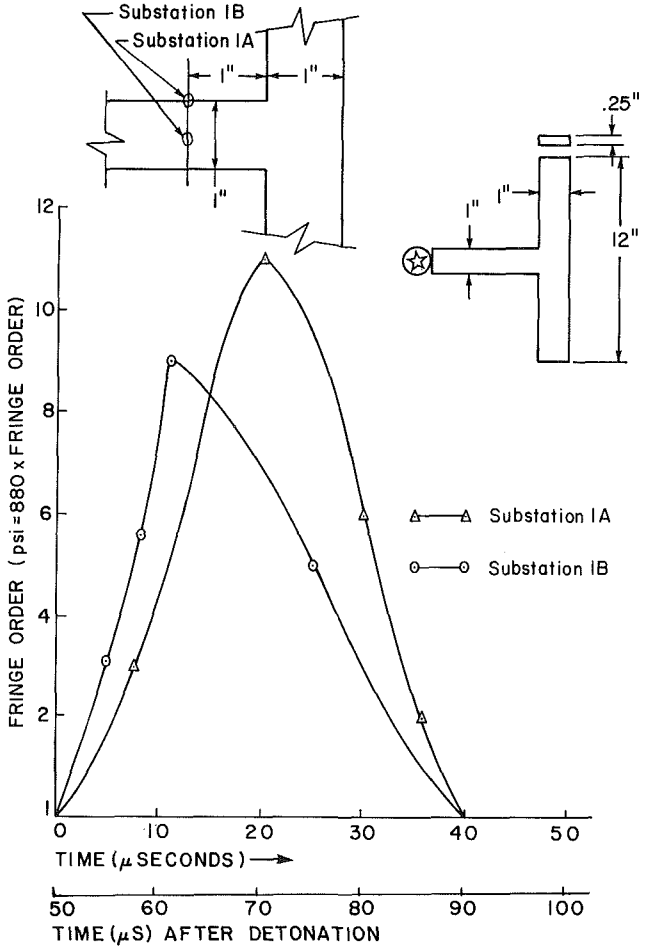

Fig. 9 Time history of incident wave amplitude observed at Station 1

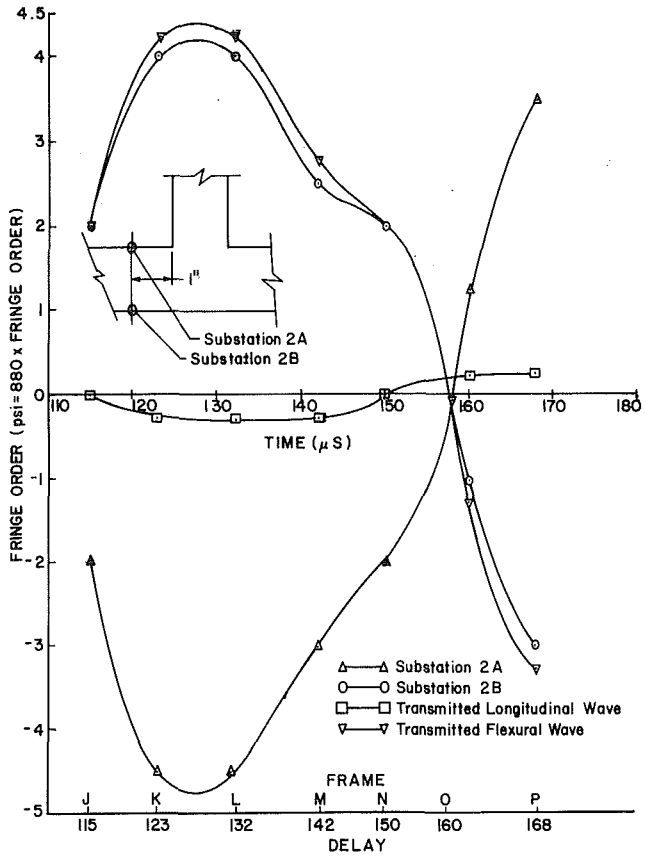

Fig. 10 Transmitted wave profiles observed at Station 2

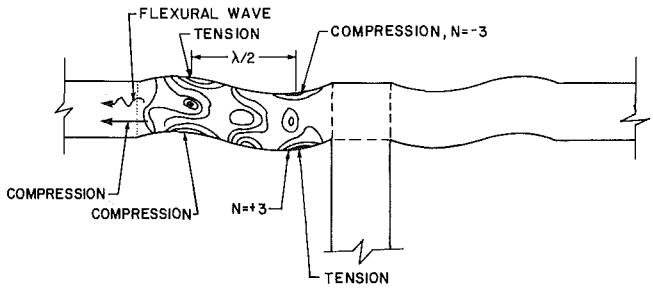

Fig. 11 Sample fringe order assignment procedure

Case 2: Symmetrically Branched Intersection With an Extending Middle Bar. The geometry is shown in Fig. 3. Due to the extending middle bar one more unknown is introduced corresponding to the force T_4 in the extending bar. The governing equations are

$$\bar{\Phi}_I + \bar{\Phi}_R = -\bar{X} = \bar{\Phi}_4 \tag{29}$$

$$\bar{\Phi}_2 = -\bar{X}\cos\Theta_2 = \bar{\Phi}_3 \tag{30}$$

$$\bar{\Phi}_I - \bar{\Phi}_R = \bar{T}i/sb_1 \tag{31}$$

$$\bar{\Phi}_2 = \bar{\Phi}_3 = T_3/sb_2 \tag{32}$$

$$\bar{\Phi}_4 = \bar{T}_4/sb_4 \tag{33}$$

$$\bar{T}_1 + 2\bar{T}_2\cos\Theta_2 - 2Q\sin\Theta_2 - T_4 = -Ms^2\bar{X} \tag{34}$$

In the foregoing equations $b_j = 2e_jC_jl_jt_j$. Solving these equations we can get the ratio $\bar{\Phi}_2/\bar{\Phi}_I$ as

$$\frac{\bar{\Phi}_2}{\bar{\Phi}_I} = \frac{1}{\dfrac{-b_2\cos\Theta_2}{b_1} + \dfrac{1}{\cos\Theta_2} + \dfrac{\tan\Theta_2\sin\Theta_2\beta_2{}^2s^{1/2}}{2b_1(K_2-\beta_2{}^12)} + \dfrac{(Ms-b_4)}{2b_1\cos\Theta_2}} \tag{35}$$

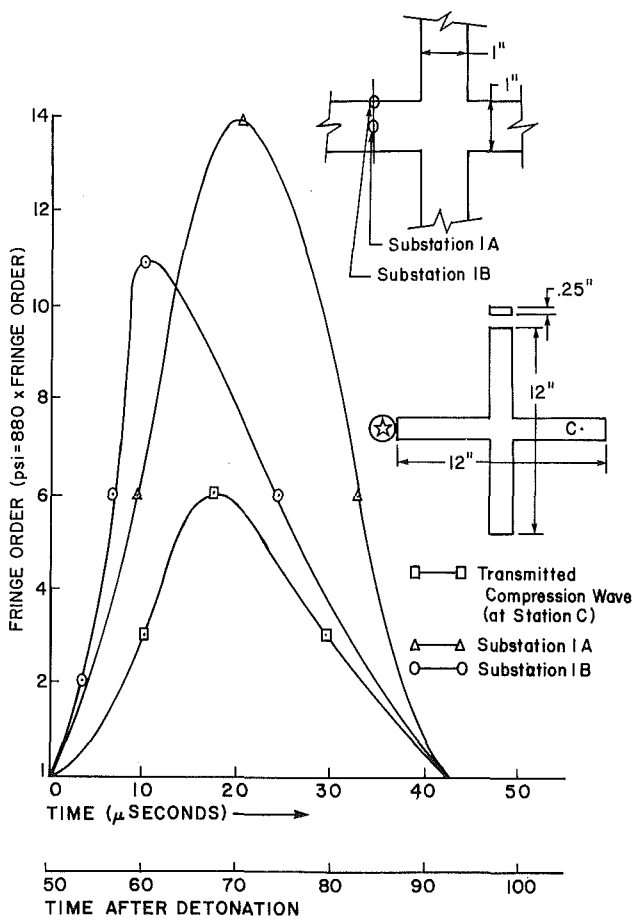

Fig. 12 Time history of incident wave amplitude observed at Station 1

Once again $\bar{\Phi}_2 = 0$ when $\Theta_2 = 90$ deg and there would be no transmission of the longitudinal stress wave into the perpendicular branch. However, there would be a transmission of the longitudinal stress wave into the horizontal bar as per (33). This is borne out in the experimental results to be described later.

Case 3: Right Angle Corner. This case has been earlier considered in [6, 8]. The geometry of the right angle corner is shown in Fig. 4. The general information developed earlier can be applied to obtain similar results as in [6, 8]. In this case the number of unknowns is 11, viz, Φ_R, Φ_3, x, y, Θ, T_2, T_3, M_1, M_3, Q_1, Q_3. If we further assume $1_1 = 1_3 = 1$; $t_1 = t_3 = t$ then we can derive an explicit relationship between $\bar{\Phi}_3$ and $\bar{\Phi}_1$. This development is described in detail in [8] and here we summarize only the final results.

If $\bar{\Phi}_I$ is specified in advance then the transmitted longitudinal stress wave field $\bar{\Phi}_3$ is given by the convolution relation

$$\Phi_3 = \int_0^t F\left(\frac{t-\tau}{T}\right) \cdot \frac{d\phi_j}{d\tau}\, d\tau \tag{36}$$

In the preceding equation the function F is independent of the lateral dimensions of the bars and is tabulated in [8]. The function F will be employed to predict the transmitted stress wave for the experimental verification.

Experimental Analysis

Dynamic photoelasticity was employed, for experimental verification of the derived equations. The photoelastic technique has a distinct advantage over other experimental techniques in that being a whole field technique, data can be acquired at several stations simultaneously to obtain a more

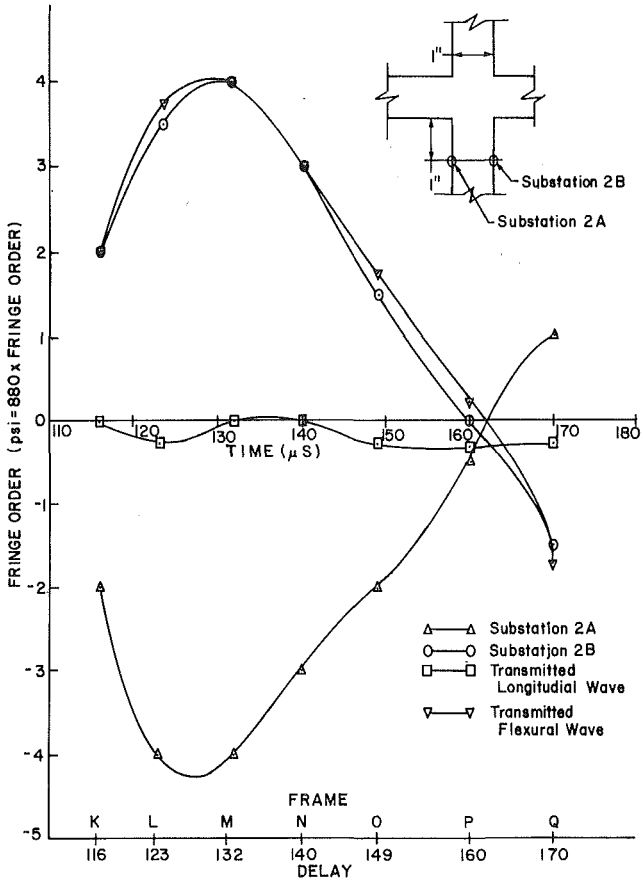

Fig. 13 Transmitted wave profile observed at Station 2

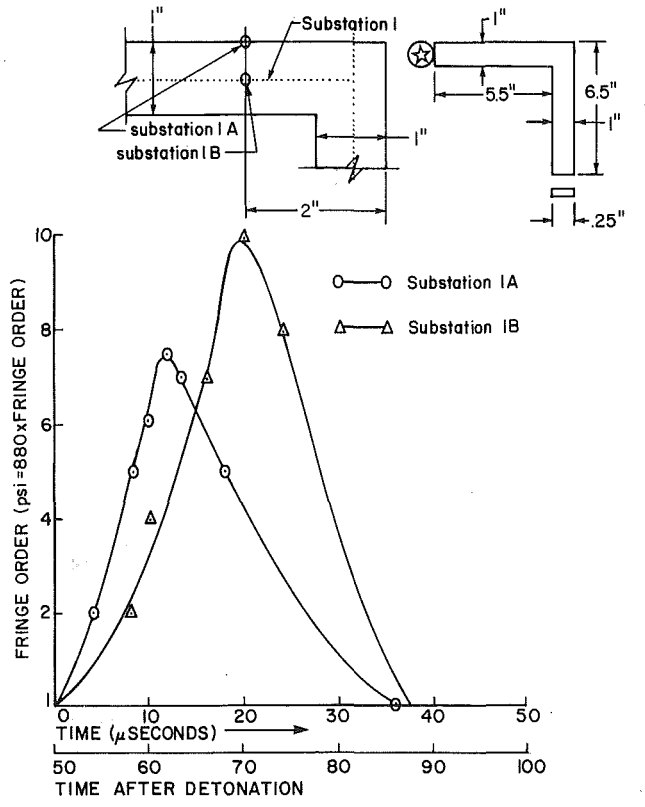

Fig. 14 Time history of incident-wave amplitude at Station 1

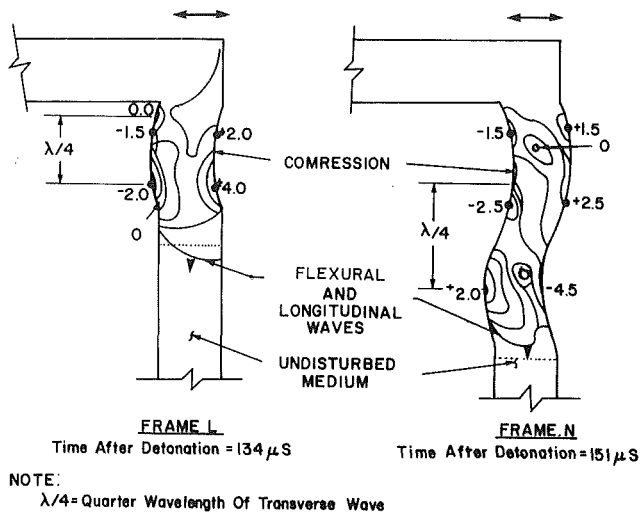

NOTE:
λ/4 = Quarter Wavelength Of Transverse Wave

Fig. 15 Fringe order assignment scheme

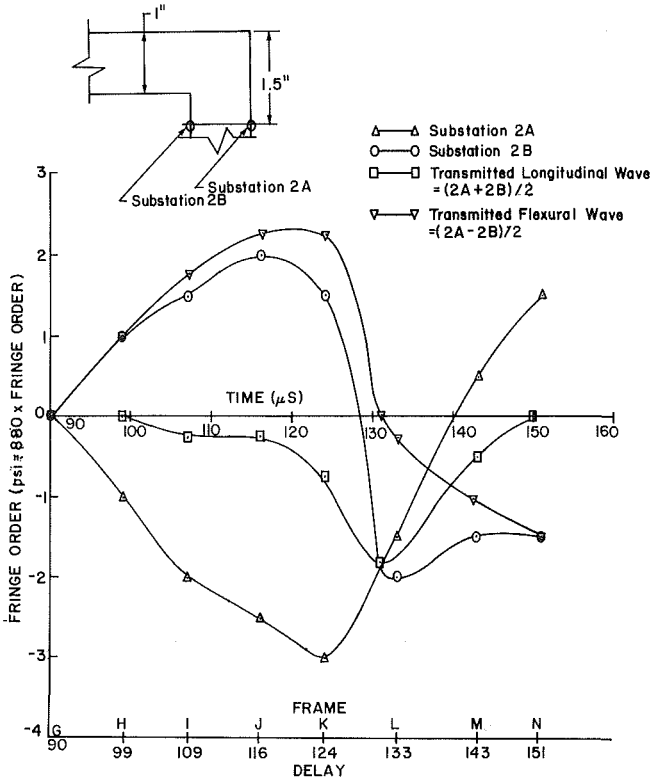

Fig. 16 Transmitted wave profiles observed at Station 2

complete description of a dynamic event. The application of the photoelastic technique to stress wave propagation phenomena is summarized by Goldsmith [14], Dally [15], and Clark and Durelli [16]. In the present experimental investigation the recording of the dynamic isochromatic fringe patterns was accomplished by a multiple spark gap camera of the Cranz-Schardin type. This camera is described in detail by Brillhart and Dally [17]. In all the experiments Homalite 100 was employed as the photoelastic material. All the bars had the same lateral dimensions of 25.4 mm × 6.35 mm (1 in. × 1/4 in.). The longitudinal stress wave was generated by exploding a small charge of lead azide at the end of one of the bars. The longitudinal stress wave pulse duration was approximately 35 μsec with a rise time of about 10 μsec.

Three geometries were studied experimentally and some typical dynamic isochromatics are shown in Figs. 5–7. A typical isochromatic pattern associated with a propagating longitudinal stress wave is shown in Fig. 8. It can be seen that

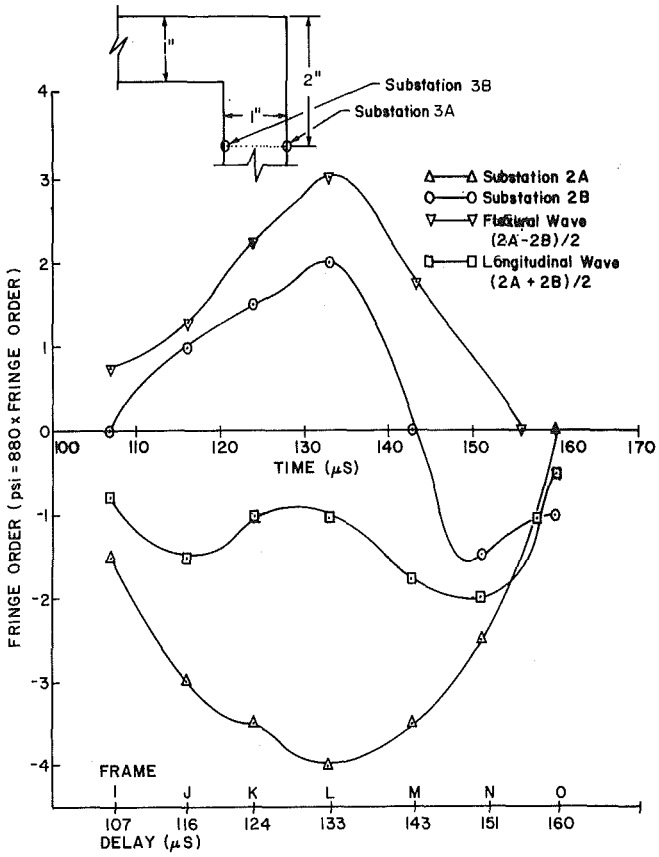

Fig. 17 Transmitted wave profiles observed at Station 3

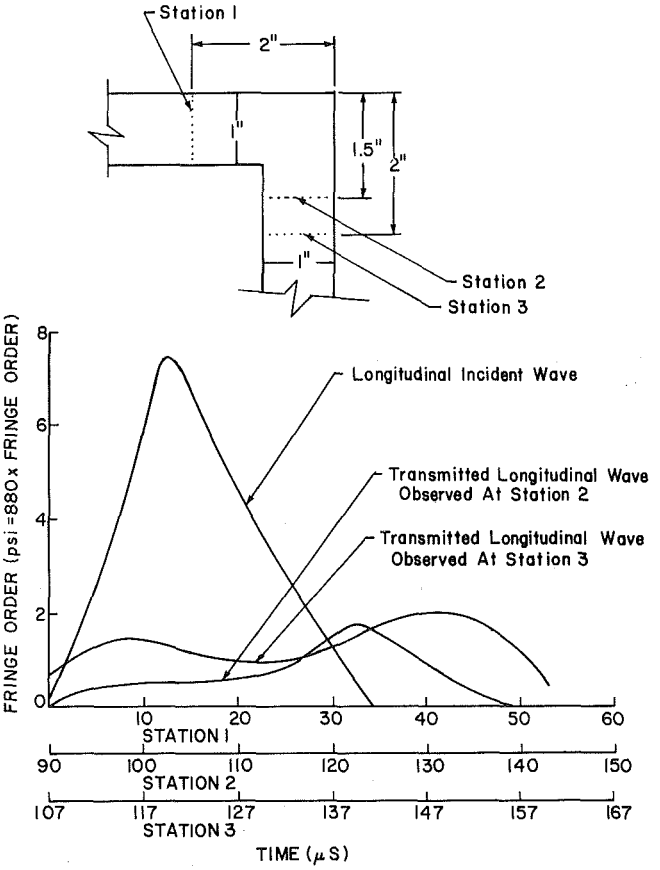

Fig. 18 Comparison of incident and transmitted longitudinal wave profiles

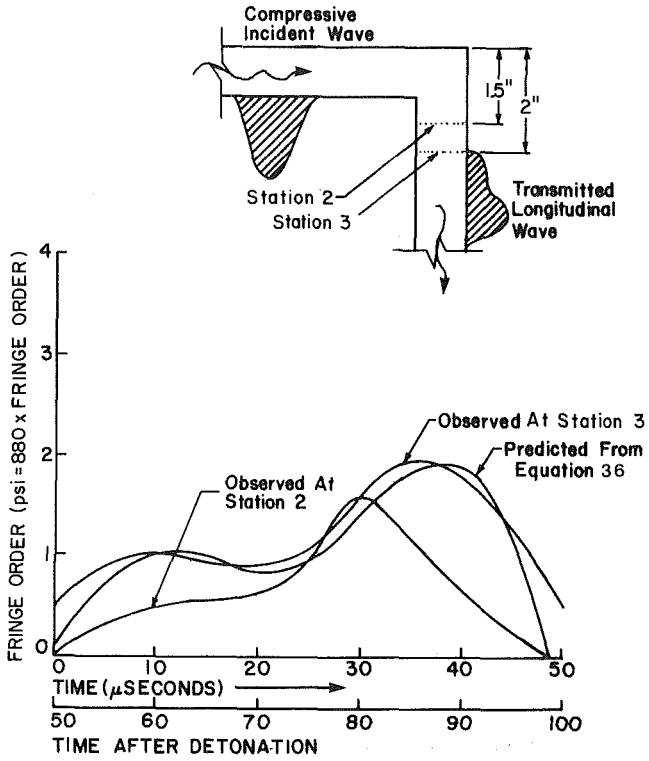

Fig. 19 Comparison of predicted and observed transmitted longitudinal wave

there is a definite concave curvature of the leading fringes with respect to the direction of propagation. This indicates that plane sections of the bar are warping since otherwise there would be no curvature of the fringes. As indicated in Fig. 8, the fringe order increases from the leading fringe with the curvature of the successive fringes continuously changing from concave to convex before culminating to a point where the fringe order is maximum. Continuing along the bar further downstream, the fringe order again decreases to zero indicating the end of the stress pulse. Fringe curvatures associated with longitudinal stress wave propagation have also been observed previously by Sutton [18], Feder, et al. [19], Durelli, et al. [20], and Jones, et al. [21]. While the fringe patterns associated with a propagating longitudinal stress wave are symmetric about the axis of the bar, asymmetric fringes imply the presence of flexure. This can also be seen in Figs. 5–7 after the incident wave has passed through the junction. In the subsequent sections experimental data for each of the three cases is analyzed for comparison with the theoretical predictions made earlier.

Case 1: *T* Intersection. Of the 16 dynamic isochromatics recorded from the Cranz-Schardin camera, 14 photographs were chosen for analysis. These records covered the interval from 50 μsec to 168 μsec after the explosive charge was detonated. The time variation of the fringe order was recorded at the Station 1 as given in Fig. 9. This station is located at a distance of 2 in. from the junction to avoid interference from any reflected waves from the junction. At this station the fringe order was recorded at two substations 1*A* and 1*B* as shown in the figure. As can be inferred from this figure, the duration of the longitudinal stress wave pulse is about 40 μsec. Also, the maximum fringe order on the axis of the bar exceeds the corresponding value at the edge (substation 1*A*). To verify the theory developed earlier, another station, Station 2 was selected as shown in Fig. 10. At this station, two substations 2*A* and 2*B* were also selected on either side as shown in the figure. The procedure for assigning the fringe orders is shown in Fig. 11.

Fringe order histories were recorded at each of these two substations and the results are given in Fig. 10. From this data it is possible to extract the wave profiles of both the transmitted longitudinal stress wave as well as the transmitted flexural stress wave. The transmitted wave profiles are also shown in Fig. 10. As can be seen from this figure, the transmitted longitudinal stress wave is very weak. This result is in good agreement with the theory which predicts no transmission of the longitudinal stress wave through the junction. Is we assume the overall experimental error to be within 10 percent (1 fringe out of 10) then the transmitted longitudinal stress wave is within the range of experimental error in measuring the fringe order.

Case 2: Cruciform Intersection. The analysis for this case was performed in the same manner as for Case 1. The results of the analysis are shown in Figs. 12 and 13. In agreement with the prediction from equation (35) there is no appreciable transmission of the longitudinal stress wave in the perpendicular bars. The strength of the transmitted longitudinal wave is within experimental error of measuring fringe orders. It is also interesting to note from Fig. 12 that the transmitted longitudinal stress wave amplitude in the continuation is about 40 percent of the original amplitude before any interaction with the junction.

Case 3: *L* Intersection. This case is perhaps the most complicated of the three cases considered due to the transmissions of both the longitudinal and the flexural wave through the junction. The results of the data analysis are given in Figs. 14–19. In this case a significant transmission of the longitudinal stress wave was noted. This is shown in Figs. 15–17 where it can be seen that the transmitted longitudinal wave amplitude is as much as 25 percent of the incident wave amplitude. Furthermore, this longitudinal stress wave is also accompanied by the transmission of a flexural wave. This is evident from the asymmetry in the fringe pattern about the axis of the bar as shown in Fig. 7. For the purpose of comparing theoretically predicted and experimentally observed transmitted wave profile for the longitudinal stress wave, readings at two stations, 2 and 3, are considered as shown in Figs. 16 and 17. The procedure for assigning the fringe orders is shown in Fig. 15. Equation (36) was utilized for the determination of the transmitted longitudinal stress wave. It can be seen from Fig. 19 that there is good agreement between the theoretically predicted and the experimentally observed transmitted longitudinal stress wave.

As an interesting digression the photoelastic data was analyzed to evaluate the validity of assuming the junction to be a rigid block. For this purpose two different stations, 2 and 3, were selected at distances of 1/2 in. and 1 in. from the inner corner of the junction. The experimentally observed transmitted longitudinal wave was recorded at both these stations for comparison with the theoretical prediction given by equation (36). It can be seen from Fig. 19 that Station 3 gives a better agreement with the theory than Station 2. While the maximum discrepancy at Station 3 is about 10 percent the maximum discrepancy at Station 2 is 50 percent. This result indicates that the rigid junction model is a good approximation for points farther away from the junction than points near the junction. A more detailed analysis of this problem is currently being attempted to shed more light on the validity of this assumption.

Conclusion

A general formulation has been developed for analyzing the transmission of a longitudinal stress wave through a junction of three bars. This general formulation has been specialized to the case of a junction of perpendicular bars. Experimental results have been presented for three types of junctions of perpendicular bars. These results were compared with the theoretical predictions concerning the transmission of longitudinal stress waves through junctions. Good agreement was noted between theory and the experiment.

Acknowledgment

The authors would like to acknowledge the support given this project by the Minta Martin Fund of the College of Engineering. Much of the original experimental testing was conducted by Nelson Poon. The authors wish to thank Dr. A. J. Durelli, Visiting Professor, for several stimulating discussions on photoelasticity.

References

1 Kolsky, H., *Stress Waves in Solids*, Clarendon Press, Oxford, 1953, Dover Reprint, 1954.

2 Abramson, H. N., Plass, H. J., and Ripperger, E. A., "Stress Wave Propagation in Rods and Beams," *Advances in Applied Mechanics*, Vol. 5, 1958, pp. 111–194.

3 Plass, H. J., "Some Solutions of the Timoshenko Beam Equation for Short Pulse Type Loading," ASME JOURNAL OF APPLIED MECHANICS, Vol. 25, 1958, pp. 379–385.

4 Mindlin, R. D., "Influence of Rotary Inertia and Shear on Flexural Motion of Isotropic Elastic Plates," ASME JOURNAL OF APPLIED MECHANICS, Vol. 18, 1951, pp. 31–38.

5 Crowley, F. B. III, Phillps, J. W., and Taylor, C. E., "Pulse Propagation in Straight and Curved Beams—Theory and Experiment," ASME JOURNAL OF APPLIED MECHANICS, Vol. 41, 1976, pp. 71–76.

6 Mandel, J. A., Mathur, R. K., and Chang, Y. C., "Stress Waves at Rigid Right Angle Joint," *Journal of the Engineering Mechanics Division*, ASCE, Vol. 97, No. EM 4, Aug. 1971, pp. 1173–1186.

7 Lee, J. P., and Kolsky, H., "The Generation of Stress Pulses at the Junction of Two Noncollinear Rods," ASME JOURNAL OF APPLIED MECHANICS, Vol. 39, 1972, pp. 809–813.

8 Atkins, K. J., and Hunter, S. C., "The Propagation of Longitudinal Elastic Waves Around Right Angled Corners in Rods of Square Cross-Section," *Quarterly Journal of Mechanics and Applied Mathematics*, Vol. 28, May 1975, pp. 245–260.

9 Desmond, T. P., "Theoretical and Experimental Investigation of Stress Waves at a Junction of Three Bars," ASME JOURNAL OF APPLIED MECHANICS, Vol. 48, 1981, pp. 148–152.

10 Churchill, R. V., *Operational Mathematics*, 2nd ed., McGraw-Hill, New York, 1958.

11 Lee, J. P., "Elastic Waves Produced by Longitudinal Impact on a System with Symmetrically Branched Rods," Brown Technical Report, DA-ARO-D-31-124-71-695, May 1971.

12 Simha, K. R. Y., and Fourney, W. L., "Investigation of Stress Wave Propagation Through Intersecting Bars, Part 1: Theory," Technical Report 82-9, Sept. 1982, Mechanical Engineering, University of Maryland, College Park, Md.

13 Simha, K. R. Y., and Fourney, W. L., "Investigation of Stress Wave Propagation Through Intersecting Bars, Part 2: Experiment," Technical Report 82-10, Sept. 1982, Mechanical Engineering, University of Maryland, College Park, Md.

14 Goldsmith, W., "Dynamic Photoelasticity," *Experimental Techniques in Shock and Vibration*, Warley, W. J., ed., ASME, 1962, pp. 25–54.

15 Dally, J. W., "Application of Photoelasticity to Elastodynamics," *Proc. Symposium on Dynamic Response of Solids and Structures*, Stanford University, 1971.

16 Clark, J. V., and Durelli, A. J., "Optical Analysis of Vibrations in Continuous Media," *Journal of Sound and Vibration*, Vol. 14, No. 4, 1971, pp. 421–432.

17 Brillhart, L. V., and Dally, J. W., "Application of the Multiple Spark Gap Camera to Dynamic Photoelasticity," *Journal of Motion Picture and Television Engineers*, Vol. 77, Feb. 1968, pp. 116–120.

18 Sutton, G. W., "A Study of the Application of Photoelasticity to the Investigation of Stress Waves," Ph.D. thesis, California Institute of Technology, Pasadena, Calif., 1955.

19 Feder, J. C., Gibbons, R. A., Gilbert, J. T., and Offenbacher, E. L., "The Study of Propagation of Stress Waves by Photoelasticity," *Proc. SESA*, Vol. 14, 1956, pp. 109–117.

20 Durelli, A. J., and Riley, W. F., "Research Studies of Stress Waves in Earth and Model Earth Media," AFSWC Technical Report 60-4, Contract AF-29 (601) 1167, Project 1080, Task 10801, Armour Res. Foundation, Oct. 1959, pp. 96–116.

21 Jones, O. E., and Ellis, A. T., "Longitudinal Strain Pulse Propagation in Wide Rectangular Bars," ASME JOURNAL OF APPLIED MECHANICS, Vol. 64, 1963, pp. 51–69.

APPENDIX *A*

$$
\begin{bmatrix}
1 & 0 & 0 & 0 & 0 & 0 & 0 & 0 & 0 & 0 & 0 & 0 & 0 & 0 & 0 & 0 & 0 & 0 & 0 & 0 \\
0 & 1 & 0 & 0 & 0 & 0 & 0 & 0 & 0 & 0 & 0 & 0 & 0 & 0 & 0 & 0 & 0 & 0 & 0 & 0 \\
0 & 0 & 1 & 0 & 0 & 0 & 0 & 0 & 0 & 0 & 0 & 0 & 0 & 0 & 0 & 0 & 0 & 0 & 0 & 0 \\
0 & 0 & 0 & 1 & 0 & 0 & 0 & 0 & 0 & 0 & 0 & 0 & 0 & 0 & 0 & 0 & 0 & 0 & 0 & 0 \\
0 & 0 & 0 & 0 & 1 & 0 & 0 & 0 & 0 & 0 & 0 & 0 & 0 & 0 & 0 & 0 & 0 & 0 & 0 & 0 \\
0 & 0 & 0 & 0 & 0 & 1 & 0 & 0 & 0 & 0 & 0 & 0 & 0 & 0 & 0 & 0 & 0 & 0 & 0 & 0 \\
0 & 0 & 0 & 0 & 0 & 0 & 1 & 0 & 0 & 0 & 0 & 0 & 0 & 0 & 0 & 0 & 0 & 0 & 0 & 0 \\
0 & 0 & 0 & 0 & 0 & 0 & 0 & 1 & 0 & 0 & 0 & 0 & 0 & 0 & 0 & 0 & 0 & 0 & 0 & 0 \\
0 & 0 & 0 & 0 & 0 & 0 & 0 & 0 & 1 & 0 & 0 & 0 & 0 & 0 & 0 & 0 & 0 & 0 & 0 & 0 \\
0 & 0 & 0 & 0 & 0 & 0 & 0 & 0 & 0 & 1 & 0 & 0 & 0 & 0 & 0 & 0 & 0 & 0 & 0 & 0 \\
0 & 0 & 0 & 0 & 0 & 0 & 0 & 0 & 0 & 0 & 1 & 0 & 0 & 0 & 0 & 0 & 0 & 0 & 0 & 0 \\
0 & 0 & 0 & 0 & 0 & 0 & 0 & 0 & 0 & 0 & 0 & 1 & 0 & 0 & 0 & 0 & 0 & 0 & 0 & 0 \\
0 & 0 & 0 & 0 & 0 & 0 & 0 & 0 & 0 & 0 & 0 & 0 & 1 & 0 & 0 & 0 & 0 & 0 & 0 & 0 \\
0 & 0 & 0 & 0 & 0 & 0 & 0 & 0 & 0 & 0 & 0 & 0 & 0 & 1 & 0 & 0 & 0 & 0 & 0 & 0 \\
0 & 0 & 0 & 0 & 0 & 0 & 0 & 0 & 0 & 0 & 0 & 0 & 0 & 0 & 1 & 0 & 0 & 0 & 0 & 0 \\
0 & 0 & 0 & 0 & 0 & 0 & 0 & 0 & 0 & 0 & 0 & 0 & 0 & 0 & 0 & 1 & 0 & 0 & 0 & 0 \\
0 & 0 & 0 & 0 & 0 & 0 & 0 & 0 & 0 & 0 & 0 & 0 & 0 & 0 & 0 & 0 & 1 & 0 & 0 & 0 \\
0 & 0 & 0 & 0 & 0 & 0 & 0 & 0 & 0 & 0 & 0 & 0 & 0 & 0 & 0 & 0 & 0 & 1 & 0 & 0 \\
0 & 0 & 0 & 0 & 0 & 0 & 0 & 0 & 0 & 0 & 0 & 0 & 0 & 0 & 0 & 0 & 0 & 0 & 1 & 0 \\
0 & 0 & 0 & 0 & 0 & 0 & 0 & 0 & 0 & 0 & 0 & 0 & 0 & 0 & 0 & 0 & 0 & 0 & 0 & 1
\end{bmatrix}
\begin{bmatrix}
\tilde{\Phi}_R \\ \tilde{\Phi}_2 \\ \tilde{\Phi}_3 \\ \tilde{T}_1 \\ \tilde{T}_2 \\ \tilde{T}_3 \\ \tilde{Q}_1 \\ \tilde{Q}_2 \\ \tilde{Q}_3 \\ \tilde{M}_1 \\ \tilde{M}_2 \\ \tilde{M}_3 \\ \tilde{X} \\ \tilde{Y} \\ \tilde{\Theta}
\end{bmatrix}
=
\begin{bmatrix}
\tilde{\Phi}_I \\ 0 \\ 0 \\ 0 \\ 0 \\ 0 \\ 0 \\ 0 \\ 0 \\ 0 \\ 0 \\ 0 \\ 0 \\ 0 \\ \tilde{\Phi}_I
\end{bmatrix}
$$

where

$$\frac{1}{2e_jc_j1_jt_j} = \frac{1}{b_j} \quad ; \quad (j=1,2,3)$$

$$\cos\Theta_j = c_j \quad ; \quad (j=1,2,3)$$

$$\sin\Theta_j = s_j \quad ; \quad (j=2,3)$$

$$\frac{1}{2\beta_j{}^3E_jI_j} = \frac{1}{K_j} \quad ; \quad \delta_j = \frac{\beta_j}{K_j} \; ; \quad m_j = \frac{\beta_j}{L_j}$$

Stability and Vibrations of Geometrically Nonlinear Cylindrically Orthotropic Circular Plates

D. Shilkrut
Professor,
Department of Mechanical Engineering,
The Pearlstone Center for
Aeronautical Engineering Studies,
Ben-Gurion University of the Negev,
Beer Sheva, Israel

The stability analysis of axisymmetrical equilibrium states of geometrically nonlinear, orthotropic, circular plates that are deformed by multiparameter loading, including thermal influence, is presented. The dynamic method (method of small vibrations) is used to accomplish this purpose. The behavior of the plate in different cases is revealed. In particular, it is shown that two different types of snapping processes can occur. The values of frequencies of small eigenvibrations from various cases have been calculated. These investigations are realized by numerical and qualitative methods. Here only the numerical results are presented.

Introduction

Axisymmetrical deformations of geometrically nonlinear cylindrically orthotropic circular plates under a multiparametric system of loading where thermal stresses are also taken into account are investigated. In theses cases there may be nonuniqueness of equilibrium states, i.e., for the same parameter of loading or temperature, there can exist a number of equilibrium states for the plate. This effect may lead to a loss of stability by snapping of different kinds. Therefore, there is a necessity to study the stability of all the possible equilibrium states.

The numerical method used for investigating the stability of the equilibrium states is the well-known dynamical method (method of small vibrations). To the best of our knowledge, this method was used for the first time for nonlinear shells in [1] and systematically for isotropic geometrically nonlinear plates and shells in [2–5].

Since eigenfrequencies (eigenvalues) are the basis for this method (when the eigenfrequencies are real the examined equilibrium states are stable in the corresponding sense, and when they are imaginary these states are unstable) it is necessary to find them for plates under different conditions. As opposed to the linear case the eignfrequencies in question are dependent on the values and character of the external cross forces and temperature.

Contributed by the Applied Mechanics Division for presentation at the 1984 PVP Conference and Exhibition Joint With Applied Mechanics and Materials Division, San Antonio, Texas, June 17–21, 1984 of THE AMERICAN SOCIETY OF MECHANICAL ENGINEERS.

Discussion on this paper should be addressed to the Editorial Department, ASME United Engineering Center, 345 East 47th Street, New York, N.Y. 10017, and will be accepted until two months after final publication of the paper itself in the JOURNAL OF APPLIED MECHANICS. Manuscript received by ASME Applied Mechanics Division, July, 1982; final revision, January, 1984. Paper No. 84-APM-21.

Copies will be available until February, 1985.

In this paper we present some of the results obtained from the numerical investgations of both the aforementioned problems in axisymmetrical state of the art. Equilibrium states, buckling modes or vibrations of nonsymmetrical types are not considered here.

Basic Equations

The constitutive Hooke-Neumann law for the material is given by (1) [6, 7].

$$\bar{\epsilon}_r = \frac{\bar{\sigma}_r}{E_r} - \frac{\mu_\phi}{E_\phi}\bar{\sigma}_\phi + \alpha_r \bar{T}; \quad \bar{\epsilon}_\phi = -\frac{\mu_r}{E_r}\bar{\sigma}_r + \frac{\bar{\sigma}_\phi}{E_\phi} + \alpha_\phi \bar{T};$$
$$E_r \mu_\phi = E_\phi \mu_r, \tag{1}$$

where $\bar{\epsilon}_{r,\phi}$, $\bar{\sigma}_{r,\phi}$ are the components of deformations and stresses, respectively, in any layer at a distance z from the middle plane, which is at the same time also the neutral one. $E_{r,\phi}$, $\mu_{r,\phi}$, and $\alpha_{r,\phi}$ are Young's moduli, Poisson's ratios, and the thermal coefficients in radial and circumferential directions, respectively, when the centers of orthotropy and of the middle plane coincide. These parameters are taken to be independent of the stationary temperature $T(\rho,z)$, which can be a function of z and of the dimensionless radial coordinate $\rho = r/a$, and a is the radius of the plate.

For an arbitrary anisotropic body, the following inequality holds [6]:

$$\mu_r + \mu_\phi + \mu_z \le 3/2 \tag{2}$$

If we take into account the Kirchhoff-Love hypothesis of incompressibility of the plate in the z direction, inequality (2) reduces to (3).

$$\mu_r + \mu_\phi \le 1 \tag{3}$$

The corresponding basic equations of the Karman-

Marguerre type may be written in this case in the form (4) and (5) [7, 8].

$$L_k[(\omega(\rho,\tau)] = k^2\left\{-\frac{\theta^2(\rho,\tau)}{2\rho} + \frac{a^2}{h^2}\left[\frac{1-\psi^2}{\rho}N_T(\rho) - \psi^2 N'_T(\rho)\right]\right\}. \quad (4)$$

$$L_k[\theta(\rho,\tau)] = -\frac{m_a}{\rho}\left\{\int_0^\rho \rho[q(\rho,\tau) - s\,\ddot{W}(\rho,\tau)]d\rho + P - \omega(\rho,\tau)\theta(\rho,\tau)\right\} + \frac{12a^2}{h^2}\left[\frac{(1-k^2\mu_r)-k^2\psi^2(1-\mu_r)}{\rho}M_T(\rho) + (1+\mu_r k^2\psi^2)M'_T(\rho)\right]; \quad (0\le\rho\le 1); \quad (0\le\tau<\infty). \quad (5)$$

$\tau = t(g/h)^{1/2}$ is the dimensionless time and t is the real one. h = const. is the thickness of the plate, and the gravitational acceleration is denoted by g. Derivatives with respect to ρ and τ are denoted by $(')$ and $(\dot{})$, respectively. The dimensionless specific mass on one unit of the plate's area is $s = \gamma a^4/E_r h$; γ is the material's specific gravity.

$$k^2 = E_\phi/E_r; \quad \psi^2 = \alpha_\phi/\alpha_r; \quad m_a = 12(1-\mu_r\mu_\phi) = 12(1-\mu_r^2 k^2) \quad (6)$$

$$N_T = \alpha_r\int_{-1/2}^{1/2} T(\rho,\zeta)d\zeta; \quad M_T = \alpha_r\int_{-1/2}^{1/2}\zeta T(\rho,\zeta)d\zeta; \quad \zeta = z/h. \quad (7)$$

The operator L_K is

$$\rho^2 L_K(\ ) = \rho^2(\ )'' + \rho(\ )' - k^2(\ ) \quad (8)$$

The basic unknowns are the membrane stress function ω and the angle of revolution θ of the normal to the plate's midplane. All the parameters of this problem are expressed by these functions (see, for example, the relationships referred to in the following where the corresponding dimensional (physical) quantities are denoted by asterisks).

The membrane normal forces and bending moments are given by the formulas:

$$N_r(\rho,\tau) = N_r^*(\rho,\tau)a^2/E_r h^2 = \omega(\rho,\tau)/\rho;$$
$$N_\phi(\rho,\tau) = N_\phi^*(\rho,\tau)a^2/E_r h^2 = \omega'(\rho,\tau) \quad (9)$$
$$M_r(\rho,\tau) = M_r^*(\rho,\tau)a^2/D_r h = \theta'(\rho,\tau) + \mu_r k^2\theta(\rho,\tau)/\rho - 12a^2(1+k^2\psi^2\mu_r)M_T(\rho)/h^2;$$
$$M_\phi(\rho,\tau) = M_\phi^*(\rho,\tau)a^2/D_r h = k^2[\theta(\rho,\tau)/\rho + \mu_r\theta'(\rho,\tau)] - 12a^2k^2(\psi^2+\mu_r)M_T(\rho)/h^2;$$
$$D_r = E_r h^3/[12(1-\mu_r{}^2k^2)] = E_r h^3/m_a \quad (10)$$

The angle θ and bending moment M_r are positive when the convexity of the plate's deformed shape is directed downward as well as that of the positive direction of the z-axis.

The radial and vertical displacements of the midplane's points are given by the formulas:

$$U = U^*/h = \rho a\epsilon_\phi/h = \rho h[\omega' - \mu_r k^2\omega/\rho]/ak^2 + a\psi^2\rho N_T/h \quad (11)$$

$$W = W^*/h = -\int_0^\rho \theta d\rho + \xi; \quad \xi = W(0); \quad \theta(r,\tau) = -W'(\rho,\tau) \quad (12)$$

Positive U is directed away from the plate's center; W and ξ are positive in the direction of the Z-axis, and are measured from the undeformed midplane.

The dimensionless distributed and concentrated loads, which are positive in the downward direction, are expressed by the relationships

$$q(\rho,\tau) = q^*(\rho,\tau)a^4/E_r h^4; \quad P(\tau) = P^*(\tau)a^2/2\pi E_r h^4. \quad (13)$$

The most frequently used boundary conditions can be written in the forms:

$$\omega(0,\tau) \equiv \theta(0,\tau) \equiv 0; \quad (0\le\tau<\infty) \quad (14)$$

$$\alpha_1\omega'(1,\tau) + \beta_1\omega(1,\tau) = \gamma_1(\tau);$$
$$\alpha_2\theta'(1,\tau) + \beta_2\theta(1,\tau) = \gamma_2(\tau); \quad (15)$$

α_i, β_i, $\gamma_i(\tau)$ are given quantities. The conditions (14) ensure the continuity and boundness of the functions ω and θ in the vicinity of the center. The condition at $\rho = 1$ for ω characterizes the degree of mobility of the boundary supports in the plane of the plate. The second relationship (15) characterizes the type of the support affecting the bending conditions at the boundary. Nine basic combinations of the boundary conditions are given in Table 1.

If necessary, the initial conditions (for $\tau = 0$) may be written in the recognized standard form.

The preceding described state of the art of the problem in question is valid for a plate without a central hole and with only inertia due to the defections W taken into account. But there are no definable obstacles to adding the influence of other factors, if necessary. Similar state of the art is true for the different cases of constructively orthotropic plates, for example corrugated or reinforced ones.

Method and Algorithm

In this section are described the method and, based on it,

Table 1 Nine basic combinations of the boundary conditions

	Mobile support without boundary forces	Mobile support with active normal boundary forces $N(\tau)$	Immovable support
Conditions for ω	$\alpha_1 = 0; \quad \beta_1 = 1; \quad \gamma_1 \equiv 0;$	$\alpha_1 = 0; \quad \beta_1 = 1; \quad \gamma_1(\tau) = N(\tau)$	$\alpha_1 = 1; \quad \beta_1 = -\mu_r k^2;$ $\gamma_1 = -\frac{a^2}{h^2}k^2\psi^2 N_T(1)$
Conditions for θ	$\alpha_2 = 0; \quad \beta_2 = 1; \quad \gamma_2 \equiv 0$	$\alpha_2 = 1; \quad \beta_2 = \mu_r k^2$ $\gamma_2 = \frac{12a^2}{h^2}(1+k^2\psi^2\mu_r)M_T(1)$	$\alpha_2 = 1; \quad \beta_2 = \mu_r k^2$ $\gamma_2(\tau) = M(\tau) + \frac{12a^2}{h^2}(1+k^2\psi^2\mu_r)M_T(1)$
	Clamping	Hinged support without boundary bending moment	Hinged support with boundary bending moment $M(\tau)$

the numerical algorithm used to find the frequencies of the plate's small eigenvibrations around some of its equilibrium states. Let this equilibrium state be characterized by the functions $\omega_c(\rho)$ and $\theta_c(\rho) = -W'_c(\rho)$ (see (12)). Thus, the aforementioned small eigenvibrations can be expressed in forms (16)

$$\omega(\rho,\tau)=\omega_c(\rho)+\delta\omega(\rho,\tau);\quad W(\rho,\tau)=W_c(\rho)+\delta W(\rho,\tau)\bullet$$

$$\theta(\rho,\tau)=\theta_c-(\delta W)'=\theta_c(\rho)+\delta\theta(\rho,\tau), \tag{16}$$

where $\delta\omega$, δW, and $\delta\theta$ are small dynamic perturbations. Then, substituting in equations (4) and (5) the functions ω, W, and θ by their expressions (16) and linearizing afterward with respect to the aforementioned perturbations, we will obtain the following two linear equations for them:

$$L_K(\delta\omega)=-\frac{k^2}{\rho}\theta_c\delta\theta;\quad L_K(\delta\theta)=\frac{m_a}{\rho}\left[s\int_0^\rho\rho(\delta\ddot{W})d\rho+\omega_c\delta\theta+\theta_c\delta\omega\right]; \tag{17}$$

The corresponding boundary conditions resulting from (14), (15), and (16) are given by (18).

$$\delta\omega(0,\tau)\equiv\delta\theta(0,\tau)\equiv 0;\quad \alpha_1\delta\omega'(1,\tau)+\beta_1\delta\omega(1,\tau)\equiv 0;$$

$$\alpha_2\delta\theta'(1,\tau)+\beta_2\delta\theta(1,\tau)\equiv 0; \tag{18}$$

The homogeneity of equations (17) and (18) is a consequence of the invariability of loadings and temperature field when the crossing from the investigated equilibrium state to the corresponding eigenvibrations takes place.

It is convenient to attach to the second equation (17) another form which does not obviously contain δW. For this we can substitute δW by $\delta\theta$ (using (12)) and integrate by parts the integral of (17). Then, we get (19) instead of (17).

$$\rho L_K(\delta\omega)=-k^2\theta_c\delta\theta;$$

$$\rho L_K(\delta\theta)=m_a\left\{\frac{s}{2}\frac{\partial^2}{\partial\tau^2}\left[\rho^2\int_0^1\delta\theta d\rho-\rho^2\int_0^\rho\delta\theta d\rho+\int_0^\rho\rho^2\delta\theta d\rho\right]+\omega_c\delta\theta+\theta_c\delta\omega\right\} \tag{19}$$

We shall look for the periodic solution of (19) in the form

$$\delta\omega(\rho,\tau)=\Omega(\rho)\sin p\tau;\quad \delta\theta(\rho,\tau)=Q(\rho)\sin p\tau. \tag{20}$$

Then, after separation of variables, we will obtain the corresponding equations for Ω and Q and the boundary conditions for them.

$$\rho L_K(\Omega)=-k^2\theta_c Q;\quad \rho L_K(Q)=m_a(\omega_c Q+\theta_c\Omega)-$$

$$-\frac{\lambda^2}{2}\left[A\rho^2-\rho^2\int_0^\rho Qd\rho+\int_0^\rho\rho^2 Qd\rho\right] \tag{21}$$

where

$$\lambda^2=m_a s p^2;\quad A=\int_0^1 Qd\rho. \tag{22}$$

$$\Omega(0)=Q(0)=0;\quad \alpha_1\Omega'(1)+\beta_1\Omega(1)=0;$$

$$\alpha_2 Q'(1)+\beta_2 Q(1)=0. \tag{23}$$

Thus, we obtained naturally a linear boundary value problem for the eigenvalues λ^2. It is obvious that if the first (lowest) eigenvalue λ_1^2 will be positive (the corresponding frequency, p, will be real), the investigated equilibrium state is stable in the small (as regarding small perturbations). In the opposite case, the equilibrium state is unstable. When $\lambda_1^2 = 0$ we have a critical case from the point of view of stability in the small. It is very important to underline here that stability in the small does not preclude stability in the large (as regarding the large perturbations), but instability in the small means instability in general.

Before proceeding to the description of the algorithm of numerical solution of the aforementioned boundary value problem we must note the following two properties.

(*a*) The operator L_K contains a singularity at the point $\rho=0$ (see (8)). Because of this, the solutions to (19) which satisfy the condtions (23) at $\rho=0$ have in neighborhood of $\rho=+0$ the order ρ^k and then they may be represented there in the form (24) [9].

$$\Omega(\rho)\cong a\rho^K;\quad Q(\rho)\cong b\rho^k;\quad (0\le\rho\le\Delta\rho<<1) \tag{24}$$

(a, b are some constants.)

(*b*) The preceding formulated boundary value problem is linear and homogeneous and, in consequence, the functions Ω and Q may be found only with exactness to an arbitrary factor.

Taking into account the singularity of L_K we will begin the realization of the numerical solutions from the point $\rho=\Delta\rho<<1$ instead of $\rho=0$. Then, on the basis of (24):

$$k\Omega(\Delta\rho)=\Omega'(\Delta\rho)\Delta\rho;\quad kQ(\Delta\rho)=Q'(\Delta\rho)\Delta\rho \tag{25}$$

On the basis of the second property, we can multiple Q by an arbitrary factor taking $A = 1$ (see second relation (22)). In this case, since the value of A is fixed beforehand, the system (19) is no more homogeneous and then the solutions of this system (where $A = 1$) may be represented as follows:

$$\Omega(\rho)=\Omega'(\Delta\rho)M_1(\rho)+Q'(\Delta\rho)N_1(\rho)+C_1(\rho);$$

$$Q(\rho)=\Omega'(\Delta\rho)M_2(\rho)+Q'(\Delta\rho)N_2(\rho)+C_2(\rho);$$

$$(0<\Delta\rho\le\rho\le 1) \tag{26}$$

where $\Omega'(\Delta\rho)$ and $Q'(\Delta\rho)$ are arbitrary constants. The initial parameters $\Omega(\Delta\rho)$ and $Q(\Delta\rho)$ are considered known, since they may be found by (25) when $\Omega'(\Delta\rho)$ and $Q'(\Delta\rho)$ are given. The basic functions M_i, N_i, and C_i may be found by solving any three arbitrary independent Cauchy problems. We have used for numerical solutions of these Cauchy

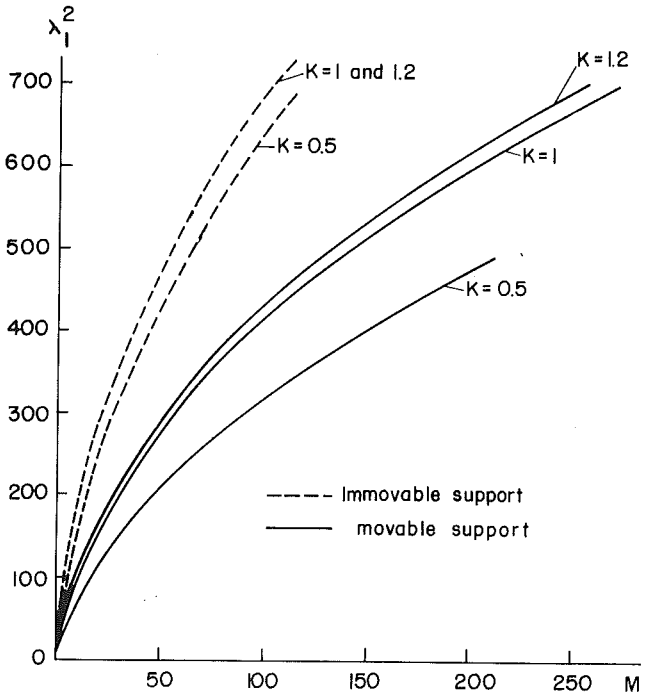

Fig. 1 First eigenvalue λ_1^2 versus loading (boundary moment M) for $k = 0.5$, 1, and 1.2 and hinged supports

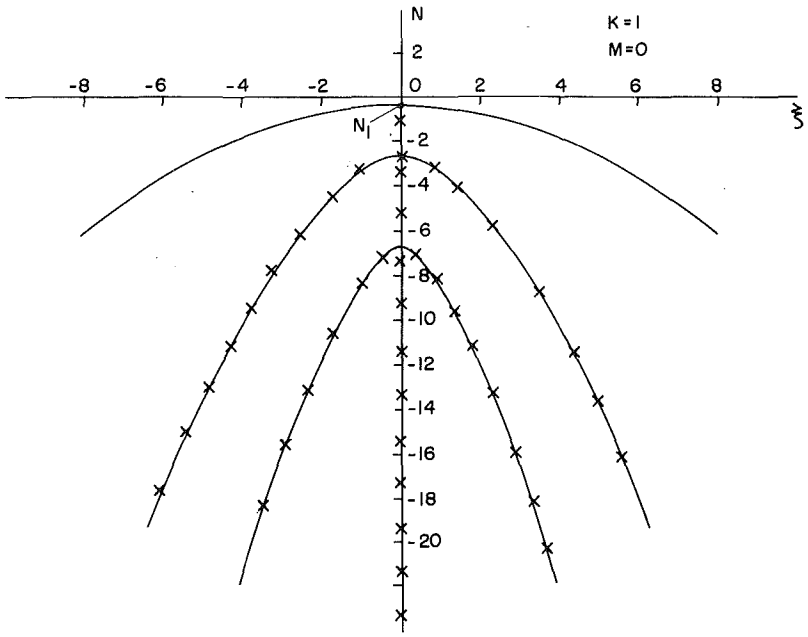

Fig. 2 Prebuckling and postbuckling behavior of the plate when only edge thrust N acts. Hinged support. $k = 1$.

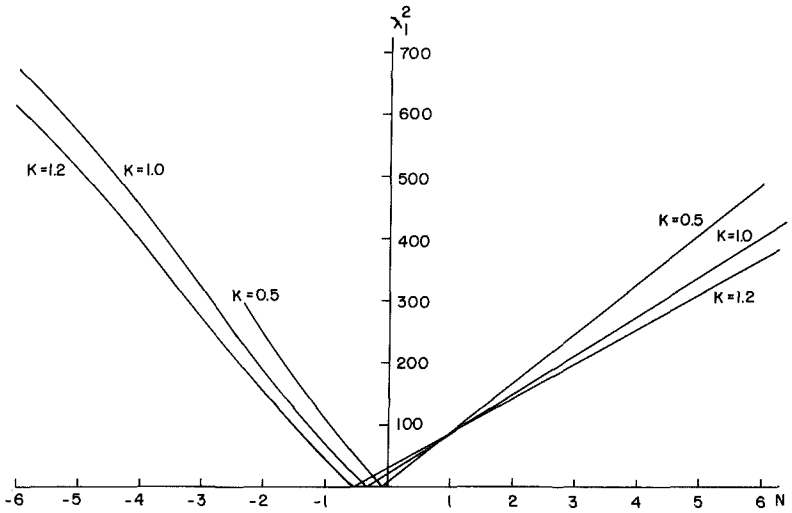

Fig. 3 First eigenvalue λ_1^2 versus edge thrust N for $k = 0.5$, 1, and 1.2

problems, the Euler's method of fourth order with corrections at each step, described in [10].

Knowing the functions M_i, N_i, and C_i, we can fulfill the conditions (23) at $\rho = 1$ and obtain two linear algebraic equations for $\Omega'(\Delta\rho)$ and $Q'(\Delta\rho)$. In this way we will get the unknown $\Omega(\rho)$ and $Q(\rho)$ which are dependent on λ^2. The eigenvalues λ^2 are finally the roots of the equation (27)

$$A = 1, \text{ i.e., } \int_0^1 Q(\rho)\, d\rho = 1 \tag{27}$$

The numerical determination of ω_c and θ_c are realized by the "shooting" method [4] or by the so-called "deformation map" technique [9].

Some Numerical Results

First, we will give the graphs of the dependence of the first eigenvalues λ_1^2 on loading which is the edge bending moment M (see Fig. 1). We took, for example, $k = 0.5$, 1, and 1.2, and $\mu_r = 0.3$. (For all specific cases examined in this paper Poisson's ratio is $\mu_r = 0.3$.) The supports are hinged, both movable (without boundary thrust N), and immovable. The thermal stresses are not considered here. These data demonstrate that the frequencies of the small eigenvalues depend on the value of the crossloading. This fact, typical for geometrically nonlinear objects, is caused by membrane stresses neglected in the usual linear theory of bending. All the eigenfrequencies are real; that is a natural consequence of the stability of the plate's equilibrium states in this case. The increase of k leads to the increase of λ_1^2 for fixed values of M. This phenomenon is explained by the rise of the plate's bending rigidity together witht the increase of k. The same effect of k on the behavior of the plate is also observed for static deformations. The graphs of $\lambda_1^2(\xi)$, not presented here, are also monotical by increasing curves, but are concave and not convex as the lines $\lambda_1^2(M)$. $\xi = W(0)$ is the displacement of the plate's center (see (12)).

We shall now examine the behavior of the plate under membrane edge thrust N when the thermal stresses are absent. The graph of $N(\xi)$ shown in Fig. 2 is typical of this case. Here $K = 1$ and the contour is movable hinged. All branches of the

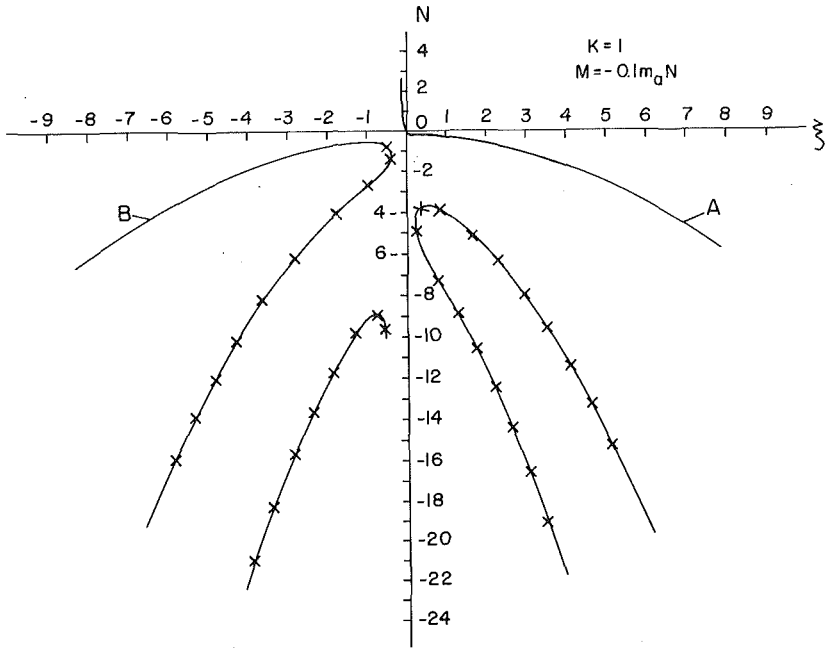

Fig. 4 Prebuckling and postbuckling behavior of the plate when the edge thrust N has an eccentricity $e = -0.1m_a$. Hinged support. $k = 1$.

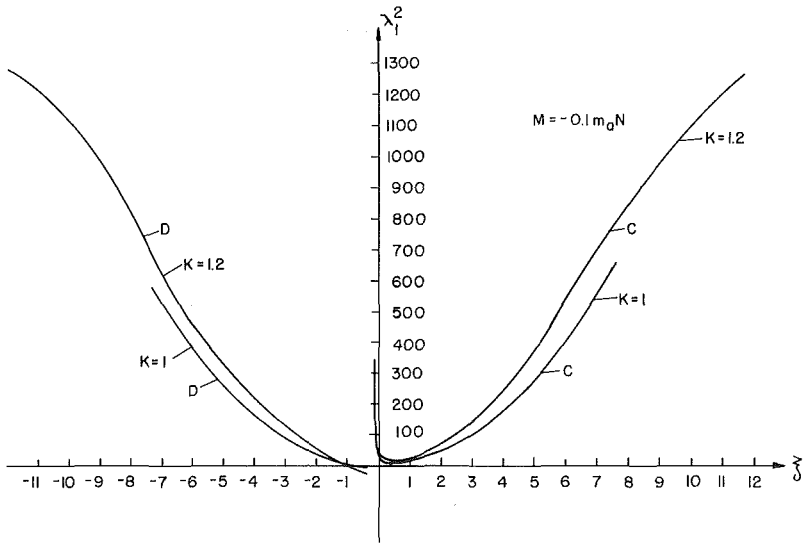

Fig. 5 First eigenvalue λ_1^2 versus $\xi = W(0)$ for the case shown on Fig. 4. $k = 1$ and 1.2.

graph of $N(\xi)$ of the parabolic type represent the postbuckling deformations. The intersections between these branches and the axis N determine the classical critical values of N, when the stability loss by transition from the compressed (flat) forms of the plate to axisymmetric bending ones occurs. (In [9] are given the first three critical values of N for different k and movable hinge.)

The investigations of the stability (by the aforementioned algorithm) of the equilibrium states in this case demonstrate that all the equilibrium states denoted on Fig. 2 by "x" are unstable. For them all the eigenvalues λ_1^2 are negative. For the other states the lowest eigenvalues $\lambda_1^2 > 0$ with the exception of first critical (bifurcation) states (when $N = N_1$) where $\lambda_1^2 = 0$. These effects are given by the graphs on Fig. 3. Each curve on this figure is formed by two branches which start from the corresponding bifurcation point ($\lambda_1^2 = 0$). The right-hand branches correspond to the flat prebuckling equilibrium states, and the left-hand ones characterize the postcritical stable bent states. For the precritical states the rise of N leads to the increase of λ_1^2 linearly. In the postcritical region these relationships are, naturally, nonlinear. Thus, after bifurcation the plate's route may be only one of the two branches of the graph of $N(\xi)$ (see Fig. 2) starting from N_1. This assertion is valid only for axisymmetric deformations which are the subject of this paper. In general, secondary bifurcation phenomena may occur; these are linked with the transition from the axisymmetrical bent (postcritical) state to the asymmetrical (wrinkled) one. The foregoing is partly investigated in [12] for isotropic plates.

Now we will examine the influence of the eccentricity e of the edge thrust N on the phenomena studied in the previous case. The eccentricity may be interpreted as an imperfection of the loading. Let us say that the edge support is movable hinged. Then, to the thrust N is added a boundary moment $M = eN$, where $e > 0$ when N is below the middle plane of the plate and $e < 0$ in the contrary case. In Fig. 4 is given an

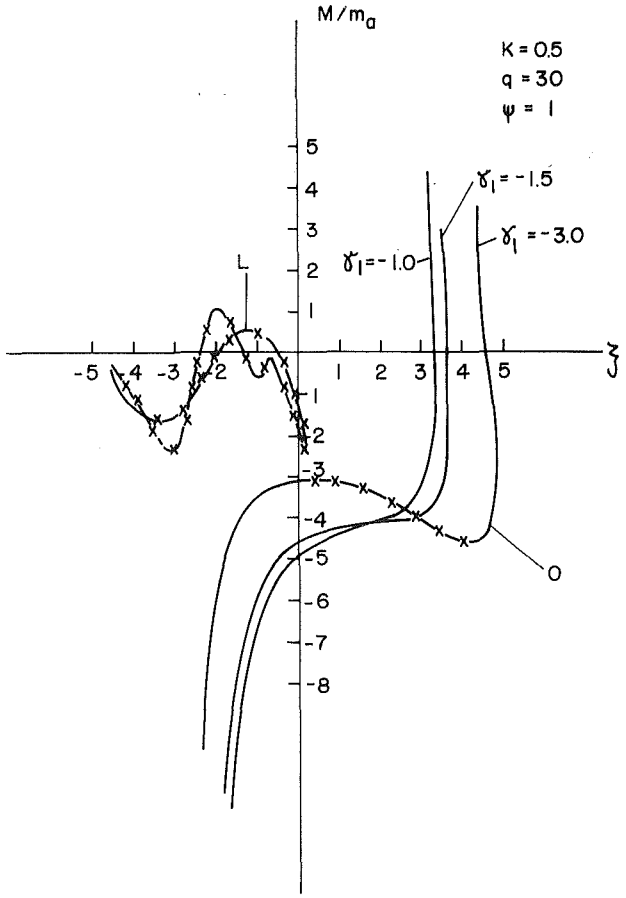

Fig. 6 Plot of $M(\xi)$ for the thermoelastic case when the thermal influence is characterized by parameter γ_1. The crossloading is $q = 30$ and $k = 0.5$.

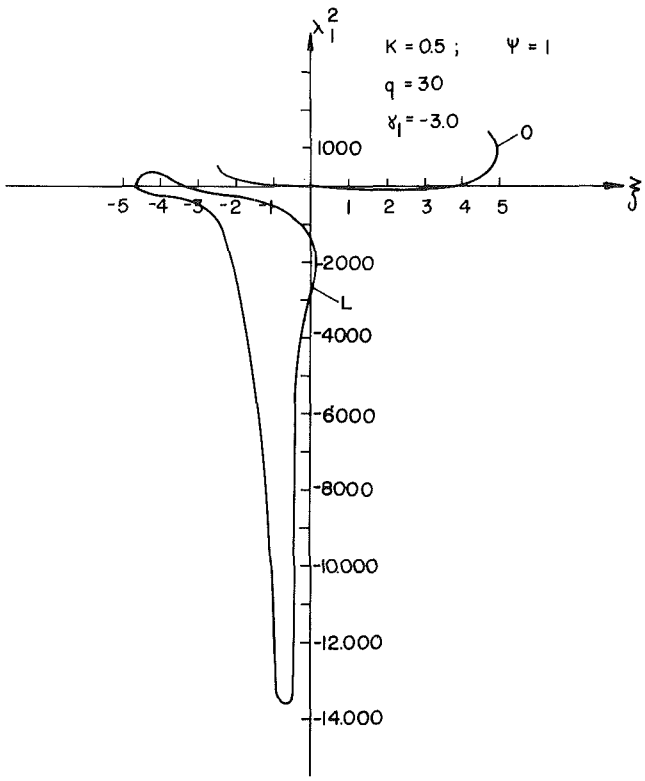

Fig. 7 Plot of λ_1^2 versus ξ for the case shown in Fig. 6 and $\gamma_1 = -3$

example of the graph of $N(\xi)$ when $e = -0.1\, m_a$ and $k = 1$. Here are the typical phenomena generated by the forementioned imperfection. The bifurcation points disappear, converting into limit ones, which is in complete concordance with Koiter's theory of postcritical behavior of structures with imperfections (see, for example, [13]). Our investigations of the stability of the equilibrium states demonstrate that all states noted by "x" on Fig. 4 are unstable. The graphs $\lambda_1^2(\xi)$ for stable states and two values of k are drawn on Fig. 5. Each graph consists of parts C and D. The C parts correspond to the curves of the type A shown on Fig. 4 and branches D correspond to the lines of the type B (see Fig. 4). There is a minimum point on all C lines (see Fig. 5). It may be shown that this minimum point corresponds to the inflection point that exists on each curve of the type A (Fig. 4).

It may be shown that similar behavior of the plate takes place also in another case of imperfection of the loading, when aside from N, the moment M = const•acts independently from N.

In conclusion we will examine a group of thermoelastic problems when in the basic equations (4) and (5) all the thermal terms are absent. Then the influence of the temperature field is transferred by the boundary conditions (see Table 1). This may occur particularly in the following two cases:

(a) An isotropic plate ($k = \psi = 1$) where the temperature is a function only of z. Then N_T and M_T are constant.

(b) An orthotropic plate that is thermally isotropic ($k \neq 1$, $\psi = 1$) and T is an even function of z and does not depend on ρ. Thus N_T = const. and $M_T \equiv 0$.

We took for example the following specific case from the abovementioned second group of thermoelastic problems, $k = 0.5$. Acting here are edge moment M and uniform pressure $q = 30$. The support is an immovable hinge. The boundary conditions at $\rho = 1$ are: (see Table 1)

$$\theta'(1) + \mu_r k^2 \theta(1) = M; \quad \omega'(1) - \mu_r k^2 \omega(1) = \gamma_1 = -a^2 k^2 \psi^2 N_T / h^2 \tag{28}$$

From the three graphs of $M(\xi)$ drawn in Fig. 6 the dynamics of the alteration in the behavior of the plate when the value of $\gamma_1 < 0$ decreases (fixed $q = 30$) can be seen. Even $\gamma_1 > -1.5$ all the equilibrium states are stable because from each value of M only one equilibrium state exists. For $\gamma_1 < -1.5$ this uniqueness is disturbed which generates a stability loss of some of the equilibrium states. It is characteristic of the examined case that there are two branches in each graph $M(\xi)$ when $\gamma_1 < -1.5$. (See the graph $M(\xi)$ for $\gamma_1 = -3.0$.) One of these has a classical "open" form 0 with one maximum and one minimum, and the other branch is a complicated closed loop L. Our investigations of the stability of the equilibrium states demonstrated that all the states denoted by "x" on Fig. 6 are unstable. These conclusions are confirmed by the data for λ_1^2, when $\gamma_1 = -3.0$ given on Fig. 7. Curves 0 and L on Fig. 7 correspond to the ones in Fig. 6. Thus, there exist snapping processes of two different types. Snapping from one part of the open branch 0 to another part on the same curve, or snapping to a "stable" part of the loop L can occur. If the first type of snapping can be realized by continuous change of M, the second type of snapping can occur only by means of intervention of a certain external factor. The last makes it possible for the plate to overcome the corresponding energetical barrier by transitions from a part of the "open" line to the "stable" one of the loop.

In some of our earlier works we investigated cases for isotropic spherical shells with a clamped support loaded by a constant pressure (with no thermal stresses), where similar loops were obtained. We found that all the equilibrium states corresponding to the points of the loops were unstable [4, 5] contrary to the aforementioned case.

Now we can easily analyze the case when all the data of the previous example remain the same, except q whose sign is reversed.

Let $\gamma_1 = -3.0$ (as previously) and $q = -30$. It may be proven by qualitative methods (see [9, 11]) that the graph of $M(\xi)$ for this case ($q = -30$) may be obtained from the graph drawn in Fig. 6 (where $q = 30$) by reflection of the latter relative to the origin of the coordinate system. In other words, both the graphs of $M(\xi)$ (for $q = 30$ and -30) are situated symmetrically relative to the points $\xi = 0$, $M = 0$. Denoting the parameters of the equilibium states with $q \pm 30$ by additional indices "1" and "2", respectively, we may affirm the following. For each equilibrium state ω_1, θ_1 there exists a corresponding state ω_2, θ_2, linked with the first by relation (29)

$$\omega_1(\rho,\tau) \equiv \omega_2(\rho,\tau); \quad \theta_1(\rho,\tau) \equiv -\theta_2(\rho,\tau) \tag{29}$$

and then $\lambda_{i1} = \lambda_{i2}$. Because $\xi_1 = -\xi_2$ and $M_1 = -M_2$, the corresponding points of the plane (ξ, M) are situated symmetrically relative to the origin $\xi = 0$, $M = 0$.

Concluding Remarks

A numerical algorithm for investigations of the stability phenomena in the small of the equilibrium states of orthotropic plates was developed. This algorithm is based on the well-known dynamic method for studying the stability of equilibrium states. Thanks to its general character, this algorithm may be used for different cases, as for example, investigations of the stability of corrugated or constructively orthotropic axisymmetrically deformed plates and shells of revolution. The numerical solutions of a series of specific problems was preceded by some qualitative investigations of the properties of the studied solutions, similar to the investigations described in [9, 11]. These properties, which have an independent interest, also serve as the means of a qualitative control of the numerical results. They will be discussed in a separate paper.

The numerical solutions presented for a number of characteristic specific problems have demonstrated that the plates can lose stability by snapping of different kinds when they are subjected to multiparameter loading including the influence of the temperature field.

References

1 Archer, R. R., and Famili, J., "On the Vibration and Stability of Finitely Deformed Shallow Spherical Shells," ASME JOURNAL OF APPLIED MECHANICS, 1965, pp. 116–120.

2 Shilkrut, D. I., and Vyrlan, P. M., "Stability of Geometrically Non-Linear Shells" (in Russian), *Doklady Akademii Nauk SSSR*, Vol. 225, Dec. 1975, pp. 782–785. (English translation, *Sov. Phys. Dolk.*, Vol. 20, 1976, pp. 865–867.)

3 Vyrlan, P. M., and Shilkrut, D. I., "Stability of Equilibrium Forms of Geometrically Non-Linear Spherical Shells" (in Russian), *Isvestija Akademii Nauk SSSR*, Mechanika Tverdogo Tela, Vol. 4, 1978, pp. 170–176. (English translation *Mech. Solids USSR*, 1978, pp. 153–159.)

4 Shilkrut, D. I., and Vyrlan, P. M., *Stability of Non-Linear Shells* (in Russian) Polytechnic Inst. of Kishinev, 1977.

5 Shilkrut, D. "Solution of Some Stability Problems in the Theory of Geometrically Non-Linear Shells, *Israel J. Techn.*, Vol. 18, 1980, pp. 76–83.

6 Lekhnitskii, S. G., *Theory of Elasticity of an Anisotropic Elastic Body*, Holden-Day, San Francisco, 1963.

7 Stavsky, Y., "Non-Linear Axisymmertric Deformations of Heterogeneous Shells of Revolution," in *Contribution to Mechanics*, Abir, D., ed., Pergamon Press, Oxford, 1970, pp. 181–194.

8 Lekhnitskii, S. G., *Anistropic Plates*, Gordon and Breach, New York, 1968.

9 Shilkrut, D., "Investigations of Axisymmetric Deformations of Geometrically Non-Linear Orthotropic Circular Plates," to be published in the *Intern. J. of Non-Linear Mechanics*, Vol. 18, 1983, pp. 95–118.

10 Shilkrut, D., "A Method for the Approximate Solution of Ordinary Differential Equations" (in Russian), *Zhurnal Vychislitelnoi Matematiki i Mathematicheskoij Fiziki*, Vol. 5, 1965, pp. 615–625. (English translation: *USSR Computational Math. and Math. Phys.*, 1966, pp. 41–55.)

11 Shilkrut, D. I., *Problems in Qualitative Theory of Non-Linear Shells* (in Russian), Polytechnic Institute of Kishinev, 1974.

12 Cheo, L. S., and Reiss, E. L., "Unsymmetric Wrinkling of Circular Plates," *Quart. Appl. Math.*, Vol. 31, Apr. 1973, pp.75–91.

13 Hutchinson, J. W., and Koiter, W. T., "Postbuckling Theory," *Applied Mechanics Reviews*, Vol. 23, 1970, pp. 1353–1366.

Finite Amplitude Vibrations of a Body Supported by Simple Shear Springs

M. F. Beatty
Department of Engineering Mechanics,
University of Kentucky,
Lexington, Ky. 40506

The exact solution of the problem of the undamped, finite amplitude oscillations of a mass supported symmetrically by simple shear mounts, and perhaps also by a smooth plane surface or by roller bearings, is derived for the class of isotropic, hyperelastic materials for which the strain energy is a quadratic function of the first and second principal invariants and an arbitrary function of the third. The Mooney-Rivlin and Hadamard material models are special members for which the finite motion of the load is simple harmonic and the free fall dynamic deflection always is twice the static deflection. Otherwise, the solution is described by an elliptic integral which may be inverted to obtain the motion in terms of Jacobi elliptic functions. In this case, the frequency is amplitude dependent; and the dynamic deflection in the free fall motion from the natural state always is less than twice the static deflection. Some results for small-amplitude vibrations superimposed on a finely deformed equilibrium state of simple shear also are presented. Practical difficulties in execution of the simple shear, and the effects of additional small bending deformation are discussed.

1 Introduction

Rubber shear mountings are used widely for engine supports, machine foundation springs, bridge support springs, dockside fenders, and for shock packaging supports, for example. In many applications the shear spring suspension system must ensure high probability that the load it supports, particularly fragile goods or sensitive equipment such as rocket engines, guided missles, and electronics components be cushioned against effects of sometimes severely rough treatment received in shipment and handling, or in unusual operating conditions such as encountered in dockside fender use. Deflections ranging from 2 to 30 or more inches in some applications are not uncommon [1, 2]; an amount of shear up to unity is quite practicable; and packaging shock deflections up to twice the thickness of the shear block frequently are encountered. In fact, the large deflections attainable with shear mountings apparently is a property that make them very efficient shock absorbers. Consequently, study of the large static and dynamic deflections and finite amplitude vibrations of a load supported by shear springs has practical value and may be useful in their design.

Usually, however, the deflections are assumed to be sufficiently small so that the response of the springs is that of a linearly elastic solid. Contrariwise, it is well known that the elastic response of rubberlike materials generally is not linear, and certainly the potential deformation such materials may experience is not small enough that the linear theory may be applied. Moreover, shear springs may carry substantial static loads that produce initially large deflections; but the effect of this initial (possibly) finite shear deformation on superimposed small-amplitude oscillations has been ignored in design considerations and in the usual vibration studies, the latter being based on the differential equation for a linear oscillator [3, 4]. We recall also that one method of evaluating the elastic constants of rubberlike materials is to set up a simple vibrating system in which a mass is supported by a specimen of the material; but the measurements of the small-amplitude vibrational frequency used to evaluate the elastic modulus from the frequency formula generally may be inaccurate if the initial deformation has been ignored. Fortunately, some rubbers in a shear test exhibit a substantially linear shear stress/deflection behavior for deformations up to 30–40 percent, although afterward, nonlinear deviations often are evident. Nevertheless, it would be of interest in the design analysis of shear mountings to know for a fairly large class of rubber like materials the extent to which the finite amplitude vibration problem may be solved exactly, to determine the precise manner in which the initial state of deformation affects the frequency of small superimposed oscillations of the load, and to analytically understand the linear response observed in certain shear tests.

In this paper, the exact solution of the problem of the undamped, finite amplitude, free oscillations of a mass supported symmetrically by simple shear springs and possibly also by a lubricated plane surface or by roller bearings is

Contributed by the Applied Mechanics Division for presentation at the 1984 PVP Conference and Exhibition, Joint with Applied Mechanics Division and Materials Division, June 17–21, 1984 of THE AMERICAN SOCIETY OF MECHANICAL ENGINEERS.

Discussion on this papers should be addressed to the Editorial Department, ASME, United Engineering Center, 345 East 47th Street, New York, N.Y. 10017 and will be accepted until two months after final publication of the paper itself in the JOURNAL OF APPLIED MECHANICS. Manuscript received by ASME Applied Mechanics Division, August, 1983; final revision September, 1983. Paper No. 84-APM-28.

Copies will be available until February, 1985.

derived for the class of hyperelastic materials for which the strain energy is a general quadratic function of the first and second principal invariants and an arbitrary function of the third alone. This class includes the Mooney-Rivlin and Hadamard material models as special members. The frequency equation for small oscillations superimposed on a finitely deformed equilibrium state of simple shear is presented; and the nature of the linear response in shear for certain materials is described.

The problem is formulated in the next section, wherein we will begin with the general result that for an arbitrary isotopic elastic material the shear stress exerted on a simple shear spring is a nonlinear function of the amount of shear [5]. This structure is applied in Section 3 to study the vibration of a mass supported by simple shear springs made of either a Mooney-Rivlin or an Hadamard material. It happens that these are special members for which the shear stress is proportional to the amount of the simple shear; consequently, the undamped, finite amplitude motion of the load is always that of a simple linear oscillator with constant frequency that depends on the shear modulus. More generally, however, the shear stress is a nonlinear function of the amount of shear, and for this case the finite amplitude motion is described by an elliptic integral whose transformation to standard form and representation in terms of Jacobi elliptic functions is derived. The period, hence the frequency, of the vibration is shown to be a function of the amplitude in the elastic response function.

The special case of motion of a mass supported by simple shear springs and by a lubricated horizontal surface or by ideal roller bearings is presented in Section 4. Inversion of the integral in terms of a single Jacobi elliptic function is provided.

In the usual free vibration test, the load is held at the maximum deflection and then released. However, no special simplification is achieved by consideration of this or other particular cases, so the general solution of the problem for arbitrary initial data is solved in Section 5. It is shown, however, that in the motion starting from the undeformed rest state of the shear springs, the dynamic deflection always is less than twice the static deflection. This result differs from the Mooney-Rivlin and Hadamard examples for which the dynamic deflection always is equal to twice the static deflection, a property typical of every linear oscillator. Also, for comparison, we may recall that Beatty [6] has found for a neo-Hookean suspension (compression) spring that the dynamic deflection always is larger (smaller) than double the static deflection. Of course, the shear springs considered in our study have symmetric response to the amount of shear. The practical difficulty that an ideal simple shear generally cannot be achieved will be discussed in Section 6.

2 Energy Equation for a Body Supported by Shear Springs

Let a rigid body of mass M be supported symmetrically by identical shear spring mountings consisting of rubber blocks or right prisms of length L and cross-sectional area A bonded to the body at one end face and to parallel rigid end supports at the other, as shown in Fig. 1. The inertia of the shear springs will be neglected, as usual; and we will suppose that each shear mount executes an ideal, homogenous, simple shear deformation of amount $\sigma(t)$ at time t so that the only relevant forces exerted by the springs on the load M are due to the shear stresses at their parallel bonded interfaces. In addition, we will allow that the load may be supported by a smooth plane surface making an angle θ with the horizontal plane.

For an isotopic elastic material, it is known [cf. 5; Sections 54 and 61] that the Cauchy shear stress T for a simple shear is determined by

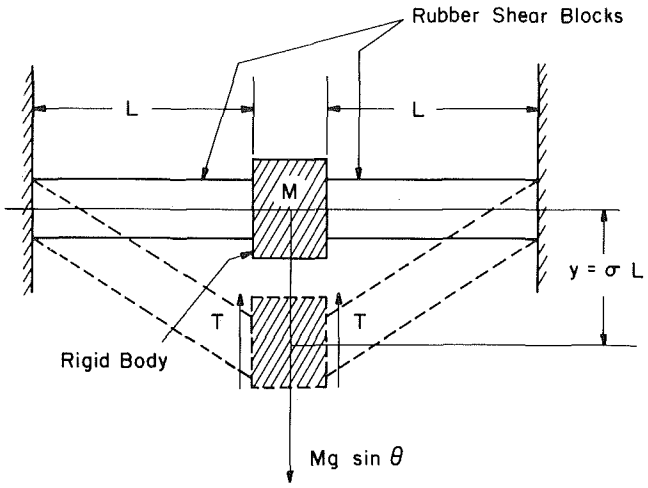

Fig. 1 Model of a symmetrical simple shear spring suspension system

$$T=\sigma\mu(\sigma^2). \tag{2.1}$$

The shear response function

$$\mu(\sigma^2)=\beta_1(\sigma^2)-\beta_{-1}(\sigma^2), \quad \text{with } \mu(0)\equiv\mu_0, \tag{2.2}$$

is defined in terms of two other elastic response functions $\beta_\Gamma(\sigma^2)=\hat{\beta}_\Gamma(I_1, I_2, I_3)$, $\Gamma = 1, -1$, that depend on the principal invariants $I_1 = I_2 = 3 + \sigma^2$, $I_3 = 1$. If the material is assumed hyperelastic with a strain energy function $W(\sigma^2) = \hat{W}(I_1, I_2, I_3)$, per unit undeformed volume, with $W(0) = 0$ in the undeformed state, these response functions are defined by

$$\beta_1(\sigma^2)=2I_3^{-1/2}\frac{\partial\hat{W}}{\partial I_1}, \quad \beta_{-1}(\sigma^2)=-2I_3^{1/2}\frac{\partial\hat{W}}{\partial I_2}. \tag{2.3}$$

Hence, it is easily seen that (2.1) may be written as $T = 2\sigma dW/d(\sigma^2)$. We will require that (2.3) satisfy the empirical inequalities $\beta_1 > 0$, $\beta_{-1} \le 0$ so that $\mu(\sigma^2) > 0$ for all σ; thus, by (2.1), this means that the shear stress on the shear blocks always is in the direction of the shear.

Since the only forces that act on M are the reduced gravitational force, the pair of hyperelastic spring forces, and the workless normal tractions at the bonded shear mount interfaces, the motion of M is conservative with constant total energy E given by

$$E=\frac{1}{2}ML^2\dot{\sigma}^2+2ALW(\sigma^2)-MgL\sigma\sin\theta. \tag{2.4}$$

Here the $\dot{} \equiv d/dt$ and g denotes the local apparent acceleration of gravity.

If initially the mass is "displaced" an amount $\sigma(0) \equiv \sigma_0$ and released with "speed" $\dot{\sigma}(0)\equiv v_0$, equation (2.4) yields the speed at time t;

$$\dot{\sigma}(t)\equiv v(\sigma)=\pm\left\{v_0^2-\frac{2p_0^2}{\mu_0}[W(\sigma^2)-W(\sigma_0^2)]+2p^2(\sigma-\sigma_0)\right\}^{1/2} \tag{2.5}$$

in which,

$$p_0^2\equiv\frac{2A\mu_0}{ML}, \quad p^2\equiv\frac{g\sin\theta}{L}, \tag{2.6}$$

and the appropriate sign is to be chosen as usual. The time required for M to move from σ_0 to $\sigma(t)$ follows from (2.5); with the proper sign, we have

$$t=\int_{\sigma_0}^{\sigma}\frac{d\sigma}{v(\sigma)}. \tag{2.7}$$

Of course, it is expected that the motion is periodic between two extreme shear states $\sigma(t_1) = \alpha$ and $\sigma(t_2) = \beta > \alpha$ defined by the physical condition that the speed $v(\sigma)$ must vanish at

these states; hence, the periodic time of the finite amplitude free vibrations of M may be found from (2.7).

Finally, let us assume that a small displacement $\delta(t)$ is superimposed on a specified static shear of amount σ_S so that $\sigma(t) = \sigma_S + \delta(t)$. Then substitution of this relation into (2.4) followed by expansion of $W(\sigma^2)$ in a power series to include only terms to the second order in δ, and differentiation of the result with respect to time yields the linearized differential equation for the small-amplitude vibrations of the mass superimposed on the primary, possibly finite, static shear state; namely, $\ddot{\delta} + \omega^2(\sigma_S)\,\delta = 0$, where

$$\omega(\sigma_S) = \sqrt{\frac{2p_0^2}{\mu_0}\left[W'(S) + 2S\,W''(S)\right]} \tag{2.8}$$

defines the small amplitude circular frequency of the vibration. Herein a prime denotes differentiation with respect to $S = \sigma_S^2$.

It is apparent that in general the frequency (2.8) depends on the nature of the material and the amount of static shear, which is determined by the equilibrium conditon

$$4A\sigma_S W'(S) = 2A\sigma_S \mu(S) = Mg\sin\theta. \tag{2.9}$$

We notice that $\sigma_S\mu(S)$ depends on only the *ratio* of the load to the interface area. For motion in the horizontal plane $\theta = 0$, $\sigma_S = 0$, and $2W'(0) = \mu_0$; hence, the frequency (2.8) for small-amplitude motion about the zero shear state has the constant value $\omega = p_0$ given by (2.6). This result depends on the shear modulus μ_0, the spring design parameters A and L, and the load M. On the other hand, for the general case when $p \neq 0$, (2.9) may be used with (2.6) to eliminate the load from (2.8); we thus obtain

$$\omega(\sigma_S) = p\sqrt{\frac{W'(S) + 2S\,W''(S)}{\sigma_S W'(S)}}. \tag{2.10}$$

This result shows that *the frequency will be independent of the area of the bonded spring-load interface, and it decreases monotonically as the length of the springs grows larger.* It is clear also that if (2.10) is to be used in design analysis of a simple shear spring suspension system or in a program of dynamic tests to determine the isotopic elastic response function of the spring material used, it is important that the initial static stretch be accounted for; otherwise, possibly serious errors may be introduced. Of course, it is recognized that the frequency also may be affected by perturbations from the ideal simple shear state assumed here; and we will return to this point later.

3 Application to Some Special Materials

Let us consider a strain energy function of the form

$$\hat{W}(I_1,I_2,I_3) = C_1(I_1-3) + C_2(I_2-3) + C_3(I_1-3)^2 + C_4(I_2-3)^2 + C_5(I_1-3)(I_2-3) + f(I_3), \tag{3.1}$$

in which $C_1, \ldots, C_5$ are certain constants and $f(I_3)$ is an arbitrary smooth function of I_3 that vanishes in the undeformed state where $I_1 = I_2 = 3$, $I_3 = 1$. In particular, when $C_3 = C_4 = C_5 = 0$, equation (3.1) describes an Hadamard material; and if, in addition, the material is incompressible so that $I_3 = 1$ in every deformation, it defines a Mooney-Rivlin material.

Since a simple shear is isochoric, it follows from (2.2), (2.3), and (3.1) that for both the Mooney-Rivlin and Hadamard models

$$\mu(\sigma^2) = 2(C_1 + C_2) = \mu_0 \quad \text{and} \quad W(\sigma^2) = \frac{1}{2}\mu_0\,\sigma^2. \tag{3.2}$$

It is evident from (3.2) and (2.4) that the motion is given by $\ddot{\sigma} + p_0^2\,\sigma = p^2$. Therefore, *the motion of M for every Mooney-Rivlin and Hadamard material, and any others for which (3.2) holds in shear, is simple harmonic with circular frequency p_0 given by $(2.6)_1$ and with symmetric displacement*

$$\delta(t) \equiv \sigma(t) - \sigma_S = D\cos(p_0 t + \epsilon) \tag{3.3}$$

about the equilibrium shear state $\sigma_S = (p/p_0)^2$. The amplitude D and phase ϵ are constants fixed by the initial data. If M is released from rest at the undeformed state, then $\epsilon = 0$, $D = -\sigma_S$, and it is seen that *for Hadamard and Mooney-Rivlin shear springs, the maximum dynamical shear deflection in the free motion of M from the underformed rest state is twice the static shear deflection, a property typical of every linear oscillator.*

It can be shown easily that in the simple shear deformation the more general function (3.1) and the shear response function (2.2) assume the simple forms

$$W(X) = \frac{1}{2}(\mu_0 X + \mu_1 X^2) \quad \text{and} \quad \mu(X) = \mu_0 + 2\mu_1 X \quad \text{with} \quad X \equiv \sigma^2, \tag{3.4}$$

in which $\mu_0 = 2(C_1 + C_2)$ and $\mu_1 \equiv 2(C_3 + C_4 + C_5)$, the later vanishing for the Mooney-Rivlin and Hadamard cases. The empirical inequality $\mu(\sigma^2) > 0$ for all $\sigma^2 \geq 0$ requires that both $\mu_0 > 0$ and $\mu_1 \geq 0$ hold. Of course, henceforward, we need only consider $\mu_1 > 0$. We note that all of the results derived in the following will hold for *any* isotropic elastic material whose strain energy in a simple shear has the form (3.4).

3(*a*) Superimposed Small-Amplitude Oscillations. We now recall (2.10) for the small amplitude vibrational frequency of a mass superimposed on a finite static shear, and with the aid of (3.4) obtain the following frequency formula

$$\omega(\sigma_S) = p\sqrt{\frac{1 + 6\mu^*\,\sigma_S^2}{\sigma_S(1 + 2\mu^*\,\sigma_S^2)}} \tag{3.5}$$

in which $\mu^* = \mu_1/\mu_0$. In particular, for the Mooney-Rivlin and Hadamard material models, we set $\mu^* = 0$ in (3.5) and find the well-known elementary formula

$$\omega(\sigma_S) = p/\sqrt{\sigma_S} = \sqrt{\frac{g\sin\theta}{L\sigma_S}} \tag{3.6}$$

typical of every linear oscillator. The graph of (3.5) for the frequency ratio $R \equiv \omega/p$ versus the amount of static shear is shown in Fig. 2 for several values of $\mu^* \epsilon [0,\infty)$. It is seen that *for the same amount of static shear, the frequency ratio increases montonically with μ^* from it lower limit value $\sqrt{1/\sigma_S}$ to its asymptotic limit value $\sqrt{3/\sigma_S}$, and it decreases monotonically with increasing values of the static shear deflection. Hence, the superimposed small-amplitude vibrational frequency of a load will be lowered by increasing the static shear deflection or by decreasing μ^*.*

More significantly, we observe that *equation (3.6) is a universal relation value for every Mooney-Rivlin or Hadamard material independently of its shear modulus.* We have seen in (3.3) that (3.6) holds for all amplitudes. Consequently, no longitudinal oscillation test can either distinguish these two material types from one another or from any other material of their own variety. On the other hand, if (3.6) is not satisfied in every simple shear motion of a given isotropic hyperelastic material, that material can not be modeled either as a Mooney-Rivlin or an Hadamard material.

3(*b*) Finite Amplitude Ocillations. Let us now return to our finite amplitude analysis. Substitution of $(3.4)_1$ into (2.5) and use of (2.4) yields

$$v(\sigma) = \pm p_1\{E + 2(p/p_1)^2\,\sigma - \hat{\mu}\,\sigma^2 - \sigma^4\}^{1/2} \tag{3.7}$$

for $\sigma \epsilon [\alpha, \beta]$. The energy constant E in (3.7) is defined by

$$E = E(\sigma_0, v_0) \equiv \left(\frac{v_0}{p_1}\right)^2 - 2(p/p_1)^2\,\sigma_0 + \hat{\mu}\sigma_0^2 + \sigma_0^4; \tag{3.8}$$

and, by definition,

$$\hat{\mu}=\frac{1}{\mu^*}=\frac{\mu_0}{\mu_1},\quad p_1^2=\frac{p_0^2}{\hat{\mu}}=\frac{2A\mu_1}{ML}. \tag{3.9}$$

Hence, the time in (2.7) is determined by

$$t=\pm\frac{1}{p_1}\int_{\sigma_0}^{\sigma}\frac{d\sigma}{\sqrt{Q(\sigma)}}, \tag{3.10}$$

where for convenience we write

$$Q(\sigma)=E+2(p/p_1)^2\sigma-\hat{\mu}\,\sigma^2-\sigma^4\equiv-(\sigma-\alpha)(\sigma-\beta)(\sigma-\gamma_1)(\sigma-\gamma_2), \tag{3.11}$$

in which α, β, γ_1, γ_2 denote the four roots of this quartic.

It is seen from (3.11) that $Q(0) = E$; and $dQ(\sigma)/d\sigma = 0$ only at the unique equilibrium state σ_S determined by

$$2\sigma_S^3+\hat{\mu}\,\sigma_S-\left(\frac{p}{p_1}\right)^2=0. \tag{3.12}$$

Moreover, $d^2Q/d\sigma^2 < 0$ for all real values of σ. The nature of the roots in (3.11) depends only on the value of $E(\sigma_0, v_0)$; and there are three cases which are schematized in Fig. 3. It is shown easily that for all values of E, equation (3.11) has only two real roots; these are the extreme shear displacements β and α for which $v(\alpha) = v(\beta) = 0$. The special "free fall" problem for which $(\sigma_0, v_0) = (0,0)$ has $E = 0$. Since $Q(\sigma) = (v/p_1)^2 \geq 0$ for all physically admissible values of σ, only those parts of the curves situated above the horizontal line $Q(\sigma) = 0$ in Fig. 3 have physical relevance. Thus, it is evident that in every case of physical interest there are four distinct roots; two are real, and two are complex conjugates which for all cases are denoted by γ_1 and γ_2 in (3.11). Consequently, the integral (3.10) is identified as a general elliptic integral whose transformation to standard form will be derived later on.

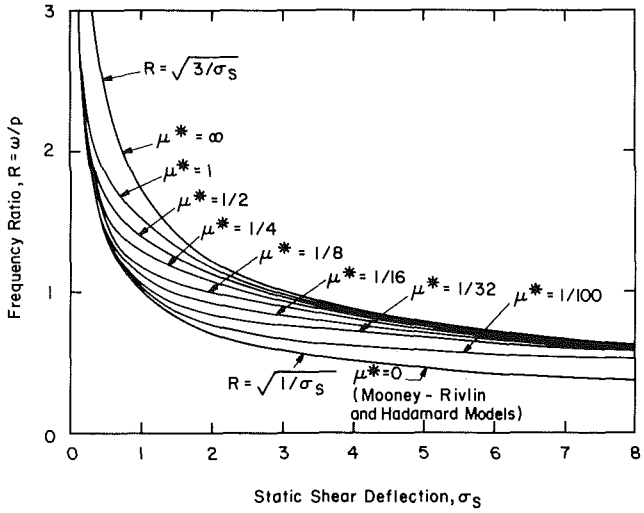

Fig. 2 Frequency ratio versus the amount of static shear for superimposed small-amplitude vibrations and variation in the modulus ratio $\mu^* = 1/\hat{\mu}$

In any case, the motion of M being conservative, it is important to recognize from (3.8) that

$$E=E(\sigma_0,v_0)=E(\alpha,0)=E(\beta,0); \tag{3.13}$$

hence, every initial value problem is equivalent to the easier problem in which the mass is released from rest at either of its extreme positions as determined by this constant energy relation. Therefore, we may use the last of (3.13) in (3.8) to express (3.11) in the equivalent factored form

$$Q(\sigma)=(b^2-\sigma^2)(\gamma^2+\sigma^2)-2(p/p_1)^2(b-\sigma) \tag{3.14}$$

in which the greatest extreme is $\beta = b$, say, and

$$\gamma^2\equiv b^2+\hat{\mu}. \tag{3.15}$$

Since $Q(a) = 0$ at the other extreme $\alpha = a < b$, equation (3.14) also yields the following equation relating the extreme shears for all cases of interest:

$$(a+b)(a^2+b^2+\hat{\mu})=2(p/p_1)^2. \tag{3.16}$$

The following additional relation follows from (3.8):

$$-ab[a^2+ab+b^2+\hat{\mu}]=E. \tag{3.17}$$

When the mass is released from rest at the undeformed state of the shear springs, we may put $a = 0$ in (3.16), which is equivalent to using $E(b,0) = 0$ in (3.8); and this result may be combined with (3.12) to obtain the interesting relation

$$(2\sigma_S-b)\,[4\sigma_S^2+2b\sigma_S+b^2+2\hat{\mu}]=b^3. \tag{3.18}$$

It thus follows that $b < 2\sigma_S$; that is, *the extreme dynamic shear deflection in the finite amplitude, free motion of the mass from the undeformed rest state always is less than twice the static shear deflection.* Hence, the free motion of the mass is asymmetric to the static equilibrium state. It is easily seen that since $\hat{\mu} > 0$, the extreme free fall deflection for every material in the class considered here always is in the interval $4^{1/3}\sigma_S < b < 2\sigma_S$.

4 Motion on a Horizontal Surface

Before we address the general solution to our problem, it

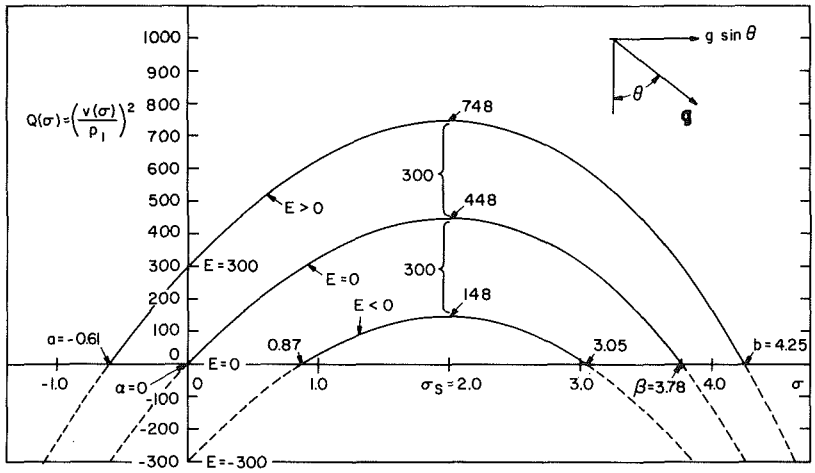

Fig. 3 $Q(\sigma)$ versus σ illustrating possible constant energy motions on an inclined plane for $\hat{\mu} = 100$ and $\sigma_S = 2$

proves convenient and instructive to begin with the simpler special analysis of the motion of the mass on an ideal lubricated plane surface or perhaps supported by ideal roller bearings on a horizontal plane. We recall $(2.6)_2$ and set[1] $p=0$ in (3.8), (3.11), and (3.14). As a consequence, it is seen that $E \geq 0$, vanishing only for trivial null initial data; hence, the real roots $\sigma = \pm b$, for which $v(-b) = v(b) = 0$, are given by

$$b^2 = -\frac{\hat{\mu}}{2} + \sqrt{\left(\frac{\hat{\mu}}{2}\right)^2 + E}, \tag{4.1}$$

and the complex conjugate roots $\sigma = \pm i\gamma$ are obtained from (3.15). It is evident that the four roots are distinct and the motion is symmmetric about the origin $\sigma = \sigma_S = 0$. Thus, $\beta = -\alpha = b$ and with the aid of (3.14) the elliptic integral (3.10) simplifies to

$$t = \pm p_1 \int_{\sigma_0}^{\sigma} \frac{d\sigma}{\sqrt{(b^2-\sigma^2)(\gamma^2+\sigma^2)}}. \tag{4.2}$$

This integral may be converted to a standard form by use of the transformation

$$\sigma = b\cos\phi. \tag{4.3}$$

It suffices to consider the integral with $(\sigma_0, \dot{\sigma}_0) = (b,0)$. The negative sign being appropriate, we obtain the result

$$\omega t = F(\phi;k) \tag{4.4}$$

in which $F(\phi;k)$ is the elliptic integral of the first kind with modulus $k \in (0,1)$:

$$k = \sqrt{\frac{b^2}{b^2+\gamma^2}} = \sqrt{\frac{\mu_1 b^2}{\mu(b^2)}}; \tag{4.5}$$

and, with the aid of $(3.4)_2$ and (3.9), we also introduce the amplitude-dependent circular frequency

$$\omega = \omega(b^2) \equiv \frac{bp_1}{k} = p_0\sqrt{\frac{\mu(b^2)}{\mu_0}} = \sqrt{\frac{2A\mu(b^2)}{ML}}. \tag{4.6}$$

The quarter period occurs for $\phi = \pi/2$ at $\sigma = 0$ in (4.4); so the periodic time τ for the general motion of M on a smooth horizontal surface is given by

$$\tau = \frac{4}{\omega}K(k) \tag{4.7}$$

in which $K(k) = F(\pi/2; k)$ denotes the complete elliptic integral. It follows from (4.3), (4.4), and (4.7) that the periodic motion may be written explicitly in terms of the Jacobi elliptic function *cn u* whose period is $4K(k)$:

$$\sigma(t) = b\,cn(\omega t) = b\,cn(4Kt/\tau). \tag{4.8}$$

As mentioned earlier in regard to (3.13), the result (4.8) may be considred as the general solution for arbitrary initial data from which the value of the amplitude b for the present case is determined by (4.1). Nevertheless, if one chooses to consider the integral (4.2) for arbitrary initial data, it is now easy to confirm that the solution is

$$\omega t = \pm[F(\phi_0;k) - F(\phi;k)] \tag{4.9}$$

with $\phi_0 = \phi(0)$ given by (4.3). Hence, the motion may be expressed by

$$\sigma(t) = \pm b\,cn(\omega t \pm u_0) \tag{4.10}$$

in which the phase $u_0 = F(\phi_0;k) = cn^{-1}(\sigma_0/b)$. Of course, at $\phi_0 = 0$, $F(0;k) = 0$ and we recover (4.8) when the appropriate positive sign is fixed in (4.10).

It also may be of interest to note that the solution for initial data $(\sigma_0, \dot{\sigma}_0) = (0, v_0)$ is related to the result (4.4) by the simple formula

$$F(\psi;k) + F(\phi;k) = K(k), \tag{4.11}$$

in which $\cot\psi\cot\phi = (1-k^2)^{1/2}$. In this case, the travel time from $\sigma_0 = 0$ is determined by (4.4) with ϕ replaced by ψ. In fact, equation (4.11) merely reflects the physical condition that the sum of the times for M to reach the same shear state from the states $\sigma_0 = 0$ and $\sigma_0 = b$ in the same motion is equal to the quarter period given by (4.7).

5 General Solution for the Motion on an Inclined Surface

Let us now turn to the problem of the motion of the shear spring supported mass which is also constrained either to slide freely or to move on roller bearings on an inclined plane surface. No evident simplification is achieved by consideration of the simplest special case when the mass is released from rest at the undeformed state of the shear springs except for the result embodied in (3.18), so we will investigate the general solution for arbitrary initial data.

The integral of interest is obtained by substitution of (3.11) into (3.10):

$$t = \pm\frac{1}{p_1}\int_{\sigma_0}^{\sigma} \frac{d\sigma}{\sqrt{(b-\sigma)(\sigma-a)(\sigma-\gamma_1)(\sigma-\gamma_2)}} \tag{5.1}$$

in which $\alpha = a < b = \beta$ for all cases described graphically in Fig. 3 and, bearing in mind (3.17), we find the conjugate complex roots in (5.1) are determined by

$$\gamma_1 = \bar{\gamma}_2 = -\frac{a+b}{2} - i\sqrt{\frac{1}{2}(a^2+b^2) + \hat{\mu}}. \tag{5.2}$$

In view of (3.13), it suffices to consider only the case for which $(\sigma_0, \dot{\sigma}_0) = (a, 0)$ is assigned initially. The greatest extreme is then found from (3.16); and the complex roots are given by (5.2). Greenhill [8, Section 73] has shown that the relation

$$\cos\hat{\phi} = \frac{(b-\sigma)H(a) - (\sigma-a)H(b)}{(b-\sigma)H(a) + (\sigma-a)H(b)} \tag{5.3}$$

transforms (5.1) to the canonical form

$$t = \frac{F(\hat{\phi};k)}{p_1\sqrt{H(a)H(b)}} \tag{5.4}$$

in which the positive sign is chosen and, by definition,

$$H(\sigma) = \sqrt{\sigma^2 - (\gamma_1+\gamma_2)\sigma + \gamma_1\gamma_2} \quad \text{and}$$

$$k = \sqrt{\frac{[b-a]^2 - [H(b)-H(a)]^2}{4H(a)H(b)}}. \tag{5.5}$$

The half-period of the motion occurs when $\sigma = b$ at $\hat{\phi} = \pi$; with $F(\pi;k) = 2K(k)$, equation (5.4) gives the periodic time for the general case:

$$\tau = \frac{4K(k)}{p_1\sqrt{H(a)H(b)}} \equiv \frac{4K(k)}{\omega(a,b)}, \tag{5.6}$$

in which $\omega(a,b)$ denotes the circular frequency. A straightforward calculation using (5.3) and (5.4) shows that the solution in terms of Jacobi elliptic functions is given explicitly by

$$\sigma(t) = \frac{aH(b) + bH(a)\,tn^2(\omega t/2)\,dn^2(\omega t/2)}{H(b) + H(a)\,tn^2(\omega t/2)\,dn^2(\omega t/2)}. \tag{5.7}$$

It is seen that the quarter period at $\hat{\phi} = \pi/2$ occurs at the shear

$$\sigma^* = \frac{aH(b) + bH(a)}{H(a) + H(b)}; \tag{5.8}$$

and it can be shown that $\sigma^* \geq 0$ for all cases, equality being valid only when $a = -b$ in the motion on a horizontal surface. The shear at the midpoint between extreme shears is σ_m

[1] The special case $p = 0$ is a well-known nonlinear vibrations problem described by Stoker [7], for example. He studies small-amplitude nonlinear oscillations for both hard and soft springs. The present finite amplitude vibrations study is similar, but it admits only the hard spring case for which $\mu_1 > 0$.

$= 1/2\,(a+b)$, and the corresponding angle in (5.3) is given by

$$\cos \hat{\phi}_m = -\frac{H(a)-H(b)}{H(a)+H(b)}. \tag{5.9}$$

Since $H(a) \geq H(b) > 0$, $\hat{\phi}_m \geq \pi/2$, equality being valid only for the special case $a = -b$. Moreover, it can be seen that

$$\sigma^* = \sigma_m + \frac{1}{2}(b-a)\cos \hat{\phi}_m. \tag{5.10}$$

Since $\cos \hat{\phi}_m < 1$ and $b > a$, it follows that $\sigma^* < \sigma_m$; consequently, *the quarter period occurs always prior to the midpoint of the oscillation.*

For arbitrary initial data, we may use (3.13) to determine the extreme a to be used in the foregoing modified initial value problem. But if one prefers to express the results in terms of the actual initial instant values, it is now easy to confirm that the general solution is given by

$$t = \pm \frac{1}{p_1\sqrt{H(a)\,H(b)}}\,[F(\hat{\phi};k) - F(\hat{\phi}_0;k)] \tag{5.11}$$

in which $\hat{\phi}_0 \equiv \hat{\phi}(\sigma_0)$ is given by (5.3) and the sign is chosen as usual.

6 Closure

It has been assumed that the shear spring mountings are able to execute a pure, homogeneous, simple shear deformation; but it is plain, of course, that both shearing and bending occur when suitable restraining tractions are not applied to the spring surfaces, a situation commonly encountered in practice. Hence, both effects contribute to the total apparent shear displacement. To account for this variation from simple shear, Rivlin and Saunders [9] used a simple engineering analysis in which familiar linear force-displacement expressions for both the bending and shearing displacements were superimposed to obtain a net apparent simple shear stress $T_a = \mu_a \sigma$ to replace (2.1). Their experimental results for incompressible materials for which $E = 3\mu_0$ share very good agreement with the apparent shear modulus μ_a defined by

$$\mu_a = \frac{\mu_0}{1+\mu_0 L^2/(12Er^2)} \tag{6.1}$$

wherein E denotes Young's extensional modulus and r is the usual cross-sectional radius of gyration about the normal line to the neutral axis of bending. The formula (6.1) may be used for both compressible and incompressible materials.

The linear shear displacement relation is consistent with the arbitrary ideal simple shear displacement possible for the Mooney-Rivlin material considered in [9]. Therefore, if the deformation is not so large nor the shear block so short as to render the linear bending assumption invalid, the aforementioned results suggest, more generally, that to estimate the effect of bending, the true shear modulus μ_0 of the Mooney-Rivlin or Hadamard materials be replaced in our equations by the apparent shear modulus (6.1). Nevertheless, the universal relation (3.6) valid for every Mooney-Rivlin and Hadamard material is unchanged, except that now the apparent amount of equilibrium shear $\sigma_S = (Mg \sin \theta)/2A\mu_a$ depends on the apparent shear modulus. Of course, in this case the apparent circular frequency of vibration of the load may now be written as

$$\omega_a = \frac{p_0}{1+\mu_0 L^2/(12Er^2)}, \tag{6.2}$$

where p_0 in $(2.6)_1$ is the corresponding frequency for the ideal simple shear case. Consequently, it appears from (6.2) that if small bending is taken into account, it may be estimated that the apparent circular frequency will be somewhat smaller than the frequency found for the ideal simple shear spring suspension model studied here.

Of course, other effects due to temperature and damping, for example, also are present. The Gough-Joule thermal effect in which the material modulus of rubber materials increases with the absolute temperature may be important in some cases. The shear deflection of a rubber, vehicle, or missle suspension system, for example, may increase as the ambient temperature falls [10]. And there may be small effects due to heat working in the vibration. Fletcher and Gent [11] found that measured values of the dynamic modulus in shear decreased with increasing amplitude of the shear in a forced vibration, whereas our nonlinear model (3.1) with special form $(3.4)_1$ in a simple shear shows that the elastic shear response function $(3.4)_2$ is an increasing quadratic function of the amount of shear. It is quite conceivable, however, that the small decrease observed by Fletcher and Gent [11] is due to some kind of molecular link structural breakdown or chain untangling that results at higher deformations possibly experienced in their larger amplitude measurements. This phenomenon has been called the prestretch effect by Mullins [12], who has studied this effect for various kinds of rubber materials. In general, most shear tests seem to show that the apparent modulus does not differ appreciably from the true modulus for most shear suspension designs, although deviations often are noticeable at moderately large amounts of shear. So perhaps these additional effects may be considered negligible to the extent that our simple shear model may serve as an adequate first approximation that also admits finite amplitude motions of most rubberlike simple shear suspension systems.

Acknowledgments

This work was supported by a grant from the National Science Foundation.

References

1 Allen, D. C., *Use of Rubber in Shock Packaging. Use of Rubber in Engineering*, Allen, P. W., Lindley, P. B., and Payne, A. R., eds., Maclaren and Sons, London, 1967, Chapter 17, pp. 220–230.

2 Smee, A. R., *Dockside Fenders. Use of Rubber in Engineering*, Allen, P. W., Lindley, P. B., and Payne, A. R., Maclaren and Sons, London, 1967, Chapter 19, pp. 244–255.

3 Edwards, A. C., and Farrand, G. N. S., *Elasticity and Dynamic Properties of Rubber. Applied Science of Rubber*, Naunton, W. J. S., ed., Arnold Publishers, Ltd., London, Chapter VIII, Part 1, 1961, pp. 506–586.

4 Hirst, A. J., *Practical Applications of the Dynamic Properties of Rubber. Applied Science of Rubber*, Naunton, W. J. S., ed., Arnold Publishers, Ltd., London, Chapter VIII, Part 2, 1961, pp. 587–708.

5 Truesdell, C., and Noll, W., "The Nonlinear Field Theories of Mechanics," Handbüch der Physik III/3, Springer-Verlag, New York, 1965.

6 Beatty, M. F., "Finite Amplitude Oscillations of a Simple Rubber Support System," *Arch. Rational Mech. Anal.*, Vol. 83, 1983, pp. 195–219.

7 Stoker, J. J., *Nonlinear Vibrations*, Interscience, New York, 1957, pp. 20–21.

8 Greenhill, A. G., *The Application of Elliptic Functions*, Dover, New York, 1959.

9 Rivlin, R. S. and Saunders, D. W., "Cylindrical Shear Mountings," *Trans. Inst. Rubber Ind.*, Vol. 24, 1949, pp. 296–306.

10 Payne, A. R., and Scott, J. R., *Engineering Design With Rubber*, Interscience, New York, 1960, Chapter 6.

11 Fletcher, W. P., and Gent, A. N., "Measurement of the Dynamic Properties of Rubber," *Trans. Inst. Rubber Ind.*, Vol. 26, 1950, pp. 45–63.

12 Mullins, L., "Effect of Stretching on the Properties of Rubber," *J. Rubber Res.*, Vol. 16, 1947, pp. 275–289.

Endochronic Theory of Cyclic Plasticity With Applications

K. C. Valanis

C. F. Lee

College of Engineering,
University of Cincinnati,
Cincinnati, Ohio 45221

Integral constitutive equations of the endochronic type with only two easily determined material constants are shown to predict with computational ease the stress (plastic strain) response of normalized mild steel and Grade 60 steel to a variety of general strain (stress) histories, without a need for special unloading-reloading or memory rules. These equations are derived from the endochronic theory of plasticity of isotropic materials with an intrinsic time scale defined in the ***plastic*** *strain space. Close agreement between theoretical predictions and experiments is obtained in the case of normalized mild steel in a variety of uniaxial, constant, strain-amplitude histories, variable strain-amplitude histories, and cyclic relaxation. Similar results are shown in the case of Grade 60 steel subjected to a random uniaxial strain history.*

Introduction

In recent years, *cyclic plasticity*, which deals with the rate-independent inelastic response of materials (metals) to cyclic stress or strain histories, has become an important subject of research in applied mechanics and engineering design. Past experimental work, theoretical studies, and engineering analysis are well documented in the literature. For details see, typically, references [1–17].

On the basis of existing experimental results, one concludes that generally, when subjected to symmetric stress or strain cycles, annealed or soft materials will harden and will tend to a stable response, while cold-worked or hard materials will soften. When a stable response is reached, hysteresis loops in the stress-strain space become stable, closed, and symmetric. This has led to the definition of a cyclic stress-strain curve which is the locus of the tips of stable hysteresis loops. It is found that some metals, e.g., 7075-T6 aluminum, follow the Masing rule. However, other metals, e.g., steels, do not follow this rule at all [8].

Also, in the presence of a history of unsymmetric stress cycles, the material response involves a progressive increase of plastic strain, the direction of which is determined by the algebraic sign of the mean stress. This phenomemon is called cyclic "ratcheting." On the other hand, a history of symmetric cyclic straining relative to a nonzero mean strain will result in "cyclic relaxation" toward zero mean stress. Both phenomena occur whether or not the material response has been stabilized prior to these specific tests [6].

Under variable amplitude cycling, metals have a strong memory of their most recent point of load reversal. As the number of cycles increases, effects of prior plastic history tend to disappear. More precisely a material has a "fading" memory, in terms of the intrinsic time scale ζ, of the history of plastic deformation that preceded the cyclic history [7], as the latter progresses.

In this paper, we use a recent form of the endochronic theory to study cyclic plasticity of stable materials. This form, proposed by Valanis [13], has been applied to metals by the authors [15]. In the case of normalized mild steel, it was shown that the constitutive equations can predict with accuracy stable hysteresis loops pertaining to cyclic strain histories at constant amplitudes. In this paper the broader capability of the theory is critically tested in a number of cases by demonstrated agreement with the observed cyclic response (*i*) of normalized mild steel to *variable* uniaxial strain amplitude histories, and (*ii*) of Grade 60 steel to a random strain history.

1 Brief Review of the Endochronic Theory

In previous papers endochronic constitutive relations were derived for the isotropic plastic response of metals at room temperature, which exhibit yielding immediately upon loading [13–15]. The set of these equations is given in the following, where as indicated, the intrinsic time measure is in terms of the increment of the plastic strain tensor.

$$\mathbf{s} = 2\int_0^Z \rho(Z-Z')\frac{\partial \mathbf{e}^p}{\partial Z'}\,dZ',\quad \rho(0)=\infty \tag{1.1}$$

$$\sigma_{kk} = 3\int_0^Z \kappa(Z-Z')\frac{\partial \epsilon^p_{kk}}{\partial Z'}\,dZ',\quad \kappa(0)=\infty \tag{1.2}$$

and

$$\int_0^Z \kappa(Z')dZ' < \infty;\quad \int_0^Z \rho(Z')dZ' < \infty, \tag{1.3a,b}$$

for all finite Z where $\mathbf{e}$ is the deviatoric strain tensor, $\mathbf{s}$ the deviatoric stress tensor, ϵ_{kk} and σ_{kk} the hydrostatic strain and stress, respectively, and

Contributed by the Applied Mechanics Division for presentation at the 1984 PVP Conference and Exhibition, Joint with Applied Mechanics Division and Materials Division, San Antonio, Texas, June 17–21, 1984 of THE AMERICAN SOCIETY OF MECHANICAL ENGINEERS.

Discussion on this paper should be addressed to the Editorial Department, ASME, United Engineering Center, 345 East 47th Street, New York, N.Y. 10017, and will be accepted until two months after final publication of the paper itself in the JOURNAL OF APPLIED MECHANICS. Manuscript received by ASME Applied Mechanics Division, March 1983; final revision, August, 1983. Paper No. 84-APM-31.

Copies will be available until February, 1985.

$$de^p = de - \frac{ds}{2\mu_1} \tag{1.4}$$

$$d\epsilon^p_{kk} = d\epsilon_{kk} - \frac{d\sigma_{kk}}{3K_1} \tag{1.5}$$

where μ_1 and K_1 are the appropriate elastic moduli. The intrinsic time scale increment dZ is related to the "intrinsic time measure" $d\zeta$ by the equation:

$$dZ = d\zeta / f(\zeta) \tag{1.6}$$

where

$$d\zeta^2 = k_1 de^p_{ij} de^p_{ij} + k_2 d\epsilon^p_{ii} d\epsilon^p_{jj} \tag{1.7}$$

A class of thermodynamically admissible functions for the kernels $\rho(Z)$ and $\kappa(Z)$ is given in the following.

$$\rho(Z) = \frac{\rho_0}{Z^\alpha} \sum_{n=1}^{N} R_n e^{-k_n Z}, \quad \kappa(Z) = \frac{k_0}{Z^\omega} \sum_{n=1}^{M} p_n e^{-\kappa_n Z} \tag{1.8,9}$$

where all the constants are positive and finite, M, and N may be finite or infinite, and α and ω are bounded by the inequalities

$$0 < (\alpha, \omega) < 1 \tag{1.10}$$

See Appendix A for detailed discussion.

In consequence of the weak singularity of the kernels two essential results are accomplished: (1) The slope of the deviatoric (or hydrostatic) stress-stain curve at points of unloading and reloading (or strain rate reversal) is always elastic, i.e., equal to the slope of the appropriate stress-strain curve at the origin. (2) The hysteresis loops in the first quadrant of the stress-strain space are always closed. For details see reference [13, 14].

Constitutive Relations in "Tension-Torsion." The constitutive equations that apply in this specific case[1] are found from equations (1.1) and (1.2) and are given in the following:

$$\tau = 2\int_0^Z \rho(Z-Z') \frac{\partial \eta^p}{\partial Z'} dZ' \tag{1.11}$$

$$\sigma_1 = 2\int_0^Z \rho(Z-Z') \frac{\partial}{\partial Z'} (\epsilon^p_1 - \epsilon^p_2) dZ' \tag{1.12}$$

$$\sigma_1 = 3\int_0^Z \kappa(Z-Z') \frac{\partial}{\partial Z'} (\epsilon^p_1 + 2\epsilon^p_2) dZ' \tag{1.13}$$

where ϵ^p_1 and σ_1 are axial plastic strain and stress, respectively, $\sigma_2 = \sigma_3 = 0$, and $\epsilon^p_2 = \epsilon^p_3$ to satisfy the condition of isotropy. Also τ and η^p stand for s_{12} and e^p_{12}, respectively, in the notation of equation (1.1).

Because in the experiments to be investigated the hydrostatic strain was not measured we will proceed to make the usual (approximate) assumption of elastic hydrostatic response, in which case equations (1.2) and (1.13) do not apply, but instead the plastic incompressibility condition

$$\epsilon^p_1 + 2\epsilon^p_2 = 0 \tag{1.14}$$

is used.

In light of the foregoing hypotheses and in view of equations (1.11) and (1.12) the appropriate constitutive equations in tension-torsion are the following:

$$\tau = 2\int_0^Z \rho(Z-Z') \frac{\partial \eta^p}{\partial Z'} dZ' \tag{1.15a}$$

$$\sigma_1 = \int_0^Z E(Z-Z') \frac{\partial \epsilon^p_1}{\partial Z'} dZ' \tag{1.15b}$$

$$\epsilon_1 + 2\epsilon_2 = \frac{\sigma_1}{3K_1} \tag{1.15c}$$

where

$$E(Z) = 3\rho(Z) \tag{1.16}$$

$$dZ = \frac{d\zeta}{f(\zeta)} \tag{1.17}$$

and as a result of equation (1.7)

$$d\zeta = \left[\frac{2}{3}(d\epsilon^p_1 - d\epsilon^p_2)^2 + 2(d\eta^p)^2\right]^{1/2} \tag{1.18a}$$

where we have set $k_1 = 1$. Alternatively, $d\zeta$ can be expressed in terms of the engineering shear strain $\gamma^p = 2\eta^p$, in which case, upon using equation (1.14):

$$d\zeta = \left[\frac{3}{2}(d\epsilon^p)^2 + \frac{1}{2}(d\gamma^p)^2\right]^{1/2} \tag{1.18b}$$

Here $\epsilon^p = \epsilon^p_1$.

In the applications that follow we will use the preceding equations in the study of cyclic response to a variety of strain histories.

2 Application to the Cyclic Response of Steels

Uniaxial Cyclic Response. In this section we will treat a class of metals where

$$\rho(Z) = \frac{\rho_0}{Z^\alpha} \tag{2.1a}$$

$$f(\zeta) = 1 \tag{2.1b}$$

It follows from equations (1.17) and (1.18b) that

$$dZ = \sqrt{3/2}\,|d\epsilon^p| \tag{2.2}$$

We will demonstrate in Sections 2.1 and 2.2 that equation (2.1) are true of the post-cyclic behavior of normalized mild steel[2] and Grade 60 steel, both of which will be the items of investigation in Sections 2.1 and 2.2. In view of equation (1.16)

$$E(Z) = E_0 Z^{-\alpha}, \quad E_0 = 3\rho_0 \tag{2.3}$$

We remark that, in view of equations (2.1a, b) the stress response is completely defined in terms of *two* material constants ρ_0 and α. We also point out that equation (2.3) gives rise to the Ramberg-Osgood equation for the monotonic tensile response of a number of metals. A method of determining the functions $\rho(Z)$ and $f(\zeta)$, is discussed in Appendix B.

Upon substitution of equation (2.3) in equation (1.15b), one finds

$$\sigma = \int_0^Z \frac{E_0}{(Z-Z')^\alpha} \frac{d\epsilon^p}{dZ'} dZ' \tag{2.4}$$

Following the completion of n reversals i.e., when $Z \geq Z_n$ the following relation is obtained by virtue of equations (2.2) and (2.4)

$$\sigma = \sum_{i=1}^{n} \int_{Z_{i-1}}^{Z_i} (-1)^{i-1}\sqrt{2/3} \frac{E_0}{(Z-Z')^\alpha} dZ' + (-1)^n \int_{Z_n}^{Z} \sqrt{2/3} \frac{E_0}{(Z-Z')^\alpha} dZ' \tag{2.5}$$

where Z_i denotes the value of Z at the point of initiation of the ith reversal and $Z_0 \overset{\text{def}}{=} 0$. Upon integration, the preceding equation leads to the result

$$\sigma = \sqrt{2/3} \frac{E_0}{1-\alpha} \left[Z^{1-\alpha} + 2\sum_{i=1}^{n} (-1)^i (Z-Z_i)^{1-\alpha}\right] \tag{2.6}$$

[1] What is meant here is a uniaxial state of stress in the presence of torsion.

[2] What is meant here is the response to arbitrary axial histories following a steady cyclic axial response.

Equation (2.6) is sufficient for the prediction of the stress response, since the functional relationship between Z and the (plastic) uniaxial strain history is known, in view of equation (2.2).

Cyclic Shear Response. In this case, we use equations (1.17) and (1.18*b*) to obtain the relation

$$dZ = d\zeta = |d\gamma^p|/\sqrt{2} \tag{2.7}$$

which is the shear counterpart of equation (2.2). In the fashion outlined in the foregoing, the cyclic shear response is found from equation (1.15*a*), (2.1*a*), and (2.7) and is given by the equation

$$\tau = \frac{\sqrt{2}\rho_0}{1-\alpha}\left[Z^{1-\alpha} + 2\sum_{i=1}^{n}(-1)^i (Z-Z_i)^{1-\alpha}\right] \tag{2.8}$$

We remark that equations (2.6) and (2.8) obey the linear homogeneous transformation between indicated stresses and strains given in the following:

$$\tau = \sigma/\sqrt{3}, \quad \gamma^p = \sqrt{3}\epsilon^p \tag{2.9 and 2.10}$$

We also note that the foregoing relations hold for *all* forms of kernel function $\rho(Z)$ and material function $f(\zeta)$ upon use of equations (1.15*a*, *b*), (1.16), (1.17), and (1.18*b*).

We apply the theory to experimental results on normalized mild steel obtained by Jhansale and Topper [6] and Grade 60 steel obtained by Dafalias and Popov [10].

2.1 Application to Normalized Mild Steel.

Constant Uniaxial Strain Amplitude. We consider the class of metals whose asymptotic stress response to sustained cyclic strain excitation at constant strain amplitude is a periodic stress history with constant amplitude. Specifically in a uniaxial test of this type, the axial plastic strain amplitude $\Delta\epsilon^p$ is also constant, following equation (1.4). Thus

$$\Delta\epsilon^p = \Delta\epsilon - \frac{\Delta\sigma}{E_1} \tag{2.11}$$

where $\Delta\epsilon$ is the axial strain amplitude and E_1 is Young's modulus. As a result, the value of Z at a point during cyclic tension and compression can be found from equation (2.2).

Specifically, the value of Z such that $Z_n \le Z \le Z_{n+1}$, where Z_n is Z at the nth reversal is given by equation (2.12), where

$$Z = \sqrt{3/2}\{2n\Delta\epsilon^p \pm \epsilon^p\} \tag{2.12a}$$

In particular

$$Z_n = \sqrt{3/2}(2n-1)\Delta\epsilon^p \tag{2.12b}$$

where in equation (2.12*a*) minus is used for n odd and plus for n even. Thus using equations (2.12*a*, *b*) and substituting for Z in equation (2.6) we obtain a closed-form solution for the stress response given in the following:

$$\sigma(\epsilon^p) = (2/3)^{\alpha/2}\frac{E_0}{1-\alpha}(\Delta\epsilon^p)^{1-\alpha}F_n(\alpha,x) \tag{2.13}$$

$$x = \epsilon^p/\Delta\epsilon^p \tag{2.14a}$$

$$F_n(\alpha,x) = (2n\pm x)^{1-\alpha} + 2\sum_{i=1}^{n}(-1)^i(2n-2i+1\pm x)^{1-\alpha} \tag{2.14b}$$

where the plus or minus signs depend on whether n is even or odd. The algebraic value of the peak stress (i.e., stress amplitude for any n) is found from equation (2.14*b*) by setting $x = 1$ for n odd or $x = -1$ for n even in equation (2.14*b*), i.e.,

$$F_n(\alpha) = (2n-1)^{1-\alpha} + 2\sum_{i=1}^{n}(-1)^i(2n-2i)^{1-\alpha} \tag{2.14c}$$

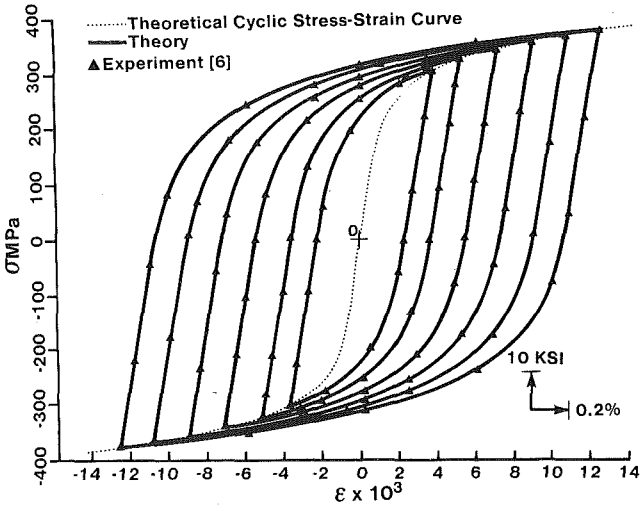

Fig. 1 Steady hysteresis loops of normalized mild steel

It can be shown that, in the limit of $n \to \infty$, F_n converges to a constant $F_\infty(\alpha)$ where F_∞ varies with α but is essentially close to unity. For instance, for $\alpha = 0.864$, F_∞ is equal to 1.03 [15]. Thus the asymptotic value of $\Delta\sigma$ as n tends to infinity is given by the equation

$$\Delta\sigma = (2/3)^{\alpha/2}\frac{E_0}{1-\alpha}(\Delta\epsilon^p)^{1-\alpha}F_\infty(\alpha) \tag{2.15}$$

This is the equation of the cyclic stress-(plastic) strain curve, when the constitutive relation is given by equation (2.4). Cyclic response in shear can be found in a similar fashion or by using equations (2.9) and (2.10).

At this point we test the theory vis-à-vis experimental data on normalized mild steel [6]. In reference [6], a set of stable uniaxial hysteresis loops corresponding to various constant strain amplitudes was presented in the uniaxial stress-strain space. A propos of the ensuing theoretical predictions we note that the *geometric shape* of the loops is given by equation (2.13), whereas the peak stresses are given by equation (2.15). We also note that there are only *two* undetermined parameters in these equations, α and E_0. The *form* of equation (2.15) was corroborated in reference [15] where a plot of the experimental values of $\Delta\sigma$ versus log $\Delta\epsilon^p$ gave rise to a straight line. The plot also determined α and E_0 which were found to be 0.864 (a pure number) and 107.6 MPa (15.61 ksi), respectively. These values were then used in equation (2.13), and the shape of the stable hysteresis loops was thereby obtained for large n (say > 25). Agreement between theory and experiment is shown in Fig. 1.

We wish to devote a few lines to these results. The reader will note that *two* constants are sufficient to determine the cyclic stress-(plastic) strain response *as well as* the hysteretic behavior of normalized mild steel. It is also pertinent to mention that the analytical expressions involved (equations (2.13) and (2.15)) are *closed-form* solutions derived from a general constitutive equation pertaining to three-dimensional histories. Also of importance is that the prediction of unloading and reloading behavior did not necessitate special memory or loading-unloading rules but was dealt with routinely, as part of the total experimental history of interest. Specifically, the celebrated Bauschinger effect is predicted quantitatively and correctly from one and the same constitutive equation.

We make, in passing, an observation of historical interest. Equation (2.15) agrees with the empirical relationship proposed by Landgraf et al. [2] for steels, i.e.,

$$\Delta\sigma \sim (\Delta\epsilon^p)^{1-\alpha}$$

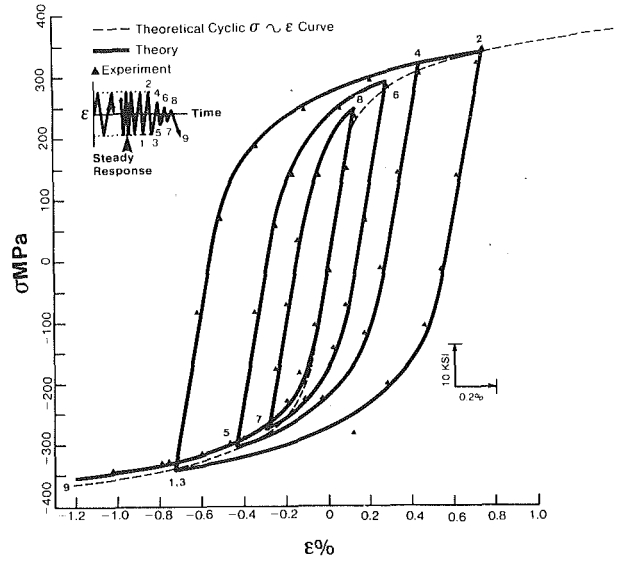

Fig. 2 Uniaxial stress response of normalized mild steel under variable strain amplitudes

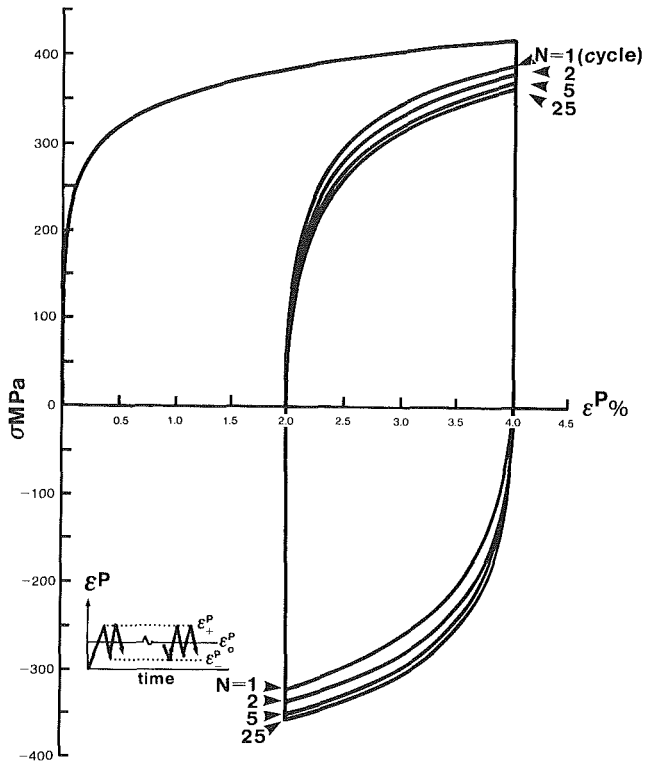

Fig. 3 Uniaxial cyclic relaxation of normalized mild steel

where $1-\alpha$ ranges from 0.12–0.17. In our case, $1-\alpha = 0.136$.

Variable Uniaxial Strain Amplitudes. To extend the experimentally verified domain of validity of the theory, we test it under conditions of variable uniaxial strain-amplitude histories. The stress response to such histories is found by using equations (2.13) and (2.14*a*, *b*). The analytical results are compared with the experimental data on normalized mild steel [6]. The experiment consists of a *constant* uniaxial strain-amplitude cyclic test (until stable hysteresis loops are reached) followed by a *variable* uniaxial strain-amplitude test. The experimental data are shown in Fig. 2. Despite the complexity of the history, close agreement between theory and experiment is obtained and shown in Fig. 2. Again the theory predicts the stress history routinely without the use of special rules discussed elsewhere [3, 5, 6, 10–12]. At this point, we may reasonably conclude that the theory as expressed by equation (2.6) (or equation (2.13)) is suitable for the prediction of the stress response to uniaxial cyclic straining, in the case of normalized mild steel.

Cyclic Relaxation. Here we address the case where the uniaxial plastic strain is increased monotonically to a value ϵ^p_+, and is followed by a cyclic uniaxial strain history with amplitude $\Delta\epsilon^p$ about a mean value ϵ^p_0.

To calculate the stress response to this specific class of histories we use equation (2.6). The cyclic strain history is shown in Fig. 3. With reference to Fig. 3, we make the following definitions.

$$\epsilon^p_+ = \epsilon^p_0 + \Delta\epsilon^p \tag{2.16a}$$

$$\epsilon^p_- = \epsilon^p_0 - \Delta\epsilon^p \tag{2.16b}$$

The value Z_i of Z at the ith reversal, is found from equation (2.2). Thus

$$Z_i = \sqrt{3/2}[\epsilon^p_0 + (2i-1)\Delta\epsilon^p],\ i = 1,2,\ \ldots\ n. \tag{2.17}$$

After n reversals have been completed, the value of Z at the current strain ϵ^p is

$$Z = \sqrt{3/2}[2n\Delta\epsilon^p + \epsilon^p_0 \mp \bar{\epsilon}^p] \tag{2.18}$$

where

$$\bar{\epsilon}^p = \epsilon^p - \epsilon^p_0 \tag{2.19}$$

and the minus and plus signs correspond to n odd and even, respectively. The stress response, after n reversals is found upon using equations (2.6), (2.17), and (2.18). Specifically,

$$\sigma = (2/3)^{\alpha/2}\frac{E_0}{1-\alpha}(\Delta\epsilon^p)^{1-\alpha}F_n(\alpha,x_0,x) \tag{2.20}$$

where

$$F_n(\alpha,x_0,x) = (2n+x_0\mp x)^{1-\alpha} + 2\sum_{i=1}^{n}(-1)^i(2n-2i+1\mp x)^{1-\alpha} \tag{2.21}$$

and

$$x_0 = \epsilon^p_0/\Delta\epsilon^p \tag{2.22a}$$

$$x = \bar{\epsilon}^p/\Delta\epsilon^p \tag{2.22b}$$

If n = odd, then x varies from 1 to -1; while if n = even, then x varies from -1 to 1. Equations (2.21) and (2.14*b*) differ only in the first term on their right-hand side. It is x_0 which allows cyclic relaxation to take place even though the material is stable since $f(\zeta) = 1$. The results are shown in Fig. 3 where the material constants, found previously, were used. We notice that as n becomes very large, the effect of x_0 in equation (2.21) disappears as a result of the relation $\lim_{n\to\infty} F_n(\alpha, x_0, x) = F_\infty(\alpha, x)$. The hysteresis loops then become stable and symmetric with respect to ϵ^p_0 and of exactly the same form as those with zero mean uniaxial strain, see Fig. 3.

Other Complex Histories. A strain history of practical importance is shown in Figs. 4(*a*) and 4(*b*), where a cyclic strain history at a fixed strain amplitude is followed by another at a lower strain amplitude. The experimental results are shown in Figs. 4(*a*) and 4(*b*). To predict the stress response, we use the numerical scheme developed in the section on variable uniaxial strain amplitudes. The theoretical results obtained are also shown in Figs. 4(*a*) and 4(*b*). Again close agreement between theory and experiment is demonstrated.

It is important to observe that the decreasing effect of the previous history on the stress response to a periodic strain

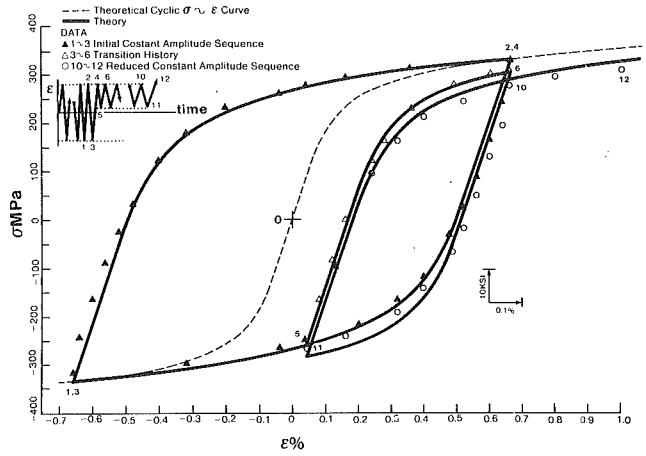

Fig. 4(*a*) Uniaxial stress response of normalized mild steel under complex histories

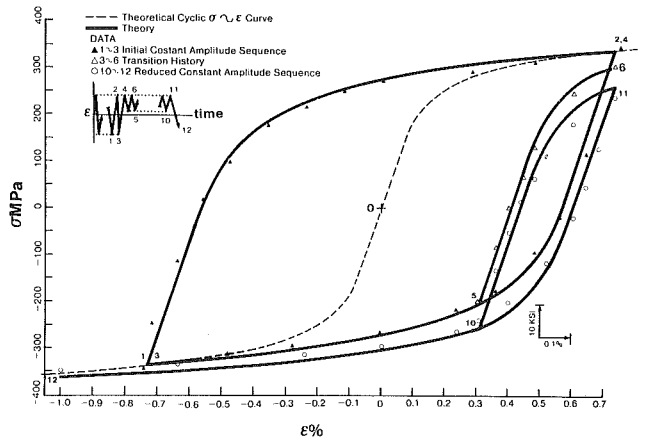

Fig. 4(*b*) Uniaxial stress response of normalized mild steel under complex histories

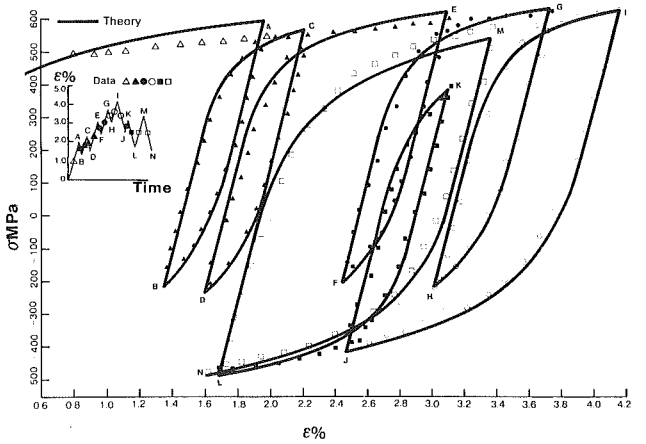

Fig. 5 Stress response of Grade 60 steel under random uniaxial cyclic strain history

history (cyclic test at constant strain amplitude) is the natural consequence of the monotonically decaying kernel function used in the present theory, i.e., in equations (2.1*a*). This type of kernel does indeed impart to the material a fading memory with respect to the endochronic time scale.

2.2 Application to Grade 60 Steel. In Fig. 5 a specimen of Grade 60 steel was tested by using random uniaxial cyclic strain history. Due to lack of information regarding the method of preparation of specimen (i.e., its prehistory) and its hysteresis loop geometry at constant strain amplitude, it is difficult to obtain the form of kernel function $\rho(Z)$ and of the material function $f(\zeta)$ using only the data in Fig. 5. However, with the exception of the stress response during the first quarter cycle, we can still predict the experimental data of the subsequent history by using the present theory with only two material parameters E_0 and α.

In the following, we used equation (2.6). The material parameters E_0 and α are determined by using the procedure in Appendix *B*. We find $E_0 = 264.2$ MPa and $\alpha = 0.82$. Ensuing agreement between theory and experiment is shown in Figure 5. It is worthy of note that predicted values of the slope of the stress-strain curve at the onset of unloading and reloading are always equal to Young's modulus (2.06×10^5 MPa). However, in reference [10] those slopes were assignd a smaller value (1.68×10^5 MPa) than the Young's modulus to account for "softening." This has not been necessary in the present case.

3 Conclusions

On the basis of the results presented in this paper, we conclude that the integral constitutive equations of the endochronic type are suitable for the analytical prediction of cyclic response of steels under a variety of conditions. These equations are derived from the endochronic theory of plasticity of isotropic materials with an intrinsic time scale defined in the *plastic* strain space.

Also noteworthy is the fact that a constitutive equation with *two* material constants, which are easily determined, can predict accurately and with computational ease the stress (strain) response of a material to a variety of general strain (stress) histories, without a need for special memory rules often discussed in the literature. The cyclic ratcheting phenomenon is also predicted by the present theory in routine fashion [18].

References

1 Morrow, J., "Cyclic Plastic Strain Energy and Fatigue of Metals," in ASTM STP 378, *Internal Friction, Damping and Cyclic Plasticity*, 1965, pp. 45–87.

2 Landgraf, R. W., Morrow, J., and Endo, T., "Determination of the Cyclic Stress-Strain Curve," *J. of Materials*, Vol. 4, 1969, pp. 176–188.

3 Mroz, Z., "An Attempt to Describe the Behavior of Metals Under Cyclic Loads Using a More General Work-Hardening Model," *Acta Mech.*, Vol. 7, 1969, pp. 199–212.

4 Landgraf, R. W., "The Resistance of Metals to Cyclic Deformation," in ASTM STP 467, *Achievement of High Fatigue Resistance in Metals and Alloys*, 1970, pp. 3–36.

5 Krempl, E., "Cyclic Plasticity: Properties of the Hysteresis Curve of Structure Metals at Room Temperature," ASME *Journal of Basic Engineering*, June 1971, pp. 317–323.

6 Jhansale, H. R., and Topper, T. H.: "Engineering Analysis of the Inelastic Stress Response of a Structure Metal Under Variable Cyclic Strains," in ASTM STP 519, *Cyclic Stress-Strain Behavior-Analysis, Experimentation, and Failure Prediction*, 1973, pp. 246–270.

7 Valanis, K. C., "Effect of Prior Deformation on Cyclic Response of Metals," ASME JOURNAL OF APPLIED MECHANICS, Vol. 41, 1974, pp. 441–447.

8 Jhansale, H. R., "A New Parameter for the Hysteretic Stress-Strain Behavior of Metals," ASME *Journal of Engineering Materials and Technology*, 1975, pp. 33–38.

9 Liu, M. C. M., Krempl, E., and Nairn, D. C., "An Exponential Stress-Strain Law for Cyclic Plasticity," ASME *Journal of Engineering Materials and Technology*, Vol. 98, 1976, pp. 322–329.

10 Dafalias, Y. F., and Popov, E. P., "Plastic Internal Variables Formalism of Cyclic Plasticity," ASME JOURNAL OF APPLIED MECHANICS, Vol. 43, 1976, pp. 645–651.

11 Lamba, H. S., and Sidebottom, O. M., "Cyclic Plasticity for Nonproportional Paths: Part 1—Cyclic Hardening, Erasure of Memory, and Subsequent Strain Hardening Experiments; Part 2—Comparison with Predictions of Three Incremental Plasticity Models," ASME *Journal of Engineering Materials and Technology*, Vol. 100, 1978, pp. 96–110.

12 Drucker, D. C., and Palgen, L., "On Stree-Strain Relations Suitable for Cyclic and Other Loading," ASME JOURNAL OF APPLIED MECHANICS, Vol. 48, 1981, pp. 479–485.

13 Valanis, K. C., "Endochronic Theory with Proper Hysteresis Loop Closure Properties," Topical Report, SSS-R-80-4182, System, Science and Software, San Diego, Calif., Aug. 1979.

14 Valanis, K. C., and Read, H. E., "A New Endochronic Plasticity Model for Soils," in *Soil Mechanics—Transient and Cyclic Loads*, Pande, G. N., and Zienkiewicz, O. C., eds., Wiley, New York, 1982, Chapter 14.

15 Valanis, K. C., and Lee, C. F., "Some Recent Developments of the Endochronic Theory with Applications," *Nuclear Eng. and Design*, Vol. 69, 1982, pp. 327-344.

16 Valanis, K. C. and H. C. Wu, "Endochronic Representation of Cyclic Creep and Relaxation of Metals," ASME JOURNAL OF APPLIED MECHANICS, Vol. 42, 1975, pp. 67-73.

17 Valanis, K. C., "A Theory of Viscoplasticity Without a Yield Surface, Part I: General Theory; Part II: Application to Mechanical Behavior of Metals," *Archives of Mechanics*, Vol. 23, 1971, pp. 517-551.

18 Valanis, K. C., and Lee, C. F., "Some Recent Developments in the Endochronic Theory With Application to Cyclic Histories," in NASA Symposium on Nonlinear Constitutive Relations for High Temperature Applications, at University of Akron, Akron, Ohio, May 1982.

APPENDIX *A*

The theory of course continues to have its foundation in irreversible thermodynamics. If the internal variables are *discrete* then both $\rho(Z)$ and $\kappa(Z)$ are given by sums of positive decaying exponential terms, i.e.,

$$\rho(Z)=\sum_{r=1}^{n} R_r e^{-\alpha_r Z}, \kappa(Z)=\sum_{r=1}^{m} K_r e^{-\omega_r Z} \qquad (A.1a,b)$$

with particular reference to $\rho(Z)$ – the same arguments apply to $\kappa(Z)$ – the number of internal variables must be infinite to satisfy equation (1.3*a*,*b*). Thus

$$\rho(Z)=\sum_{r=1}^{\infty} R_r e^{-\alpha_r Z} \qquad (A.2)$$

such that

$$\rho(0)=\infty;\rho(Z)<\infty, \quad 0<Z<\infty.$$

In reference [13] we gave one example to demonstrate the argument, by setting

$$R_r=\frac{R_0}{r}, \alpha_r=\alpha_0 r \qquad (A.3)$$

Evidently

$$\rho(0)=R_0\sum_{r=1}^{\infty}\frac{1}{r}=\infty \qquad (A.4)$$

since this is a divergent series, whereas

$$\rho(Z)=R_0\sum_{r=1}^{\infty}\frac{1}{r}e^{-\alpha_r Z}, \quad Z>0 \qquad (A.5)$$

We note that since the following series is convergent as shown

$$\sum_{r=1}^{\infty} e^{-\alpha_r Z}=\frac{1}{e^{\alpha_0 Z}-1} \qquad (A.6)$$

the series on the right-hand side of equation (*A*.5) is also convergent since every one of its terms is smaller than or equal to the corresponding term of the series on the left-hand side of equation (*A*.6).

In the case where the internal variables are distributed then

$$\rho(Z)=\int_0^{\infty} R(r)e^{-rZ}dr \qquad (A.7)$$

where $R(r)$ is the distribution function appropriate to the kernel $\rho(Z)$.

Specifically, in the case of steel (mild steel as well as Grade 60) it was found that

$$\rho(Z)=\frac{\rho_0}{Z^{\alpha}} \qquad (A.8)$$

Since the right-hand side of equation (*A*.7) is the Laplace transform of $R(r)$, it follows that

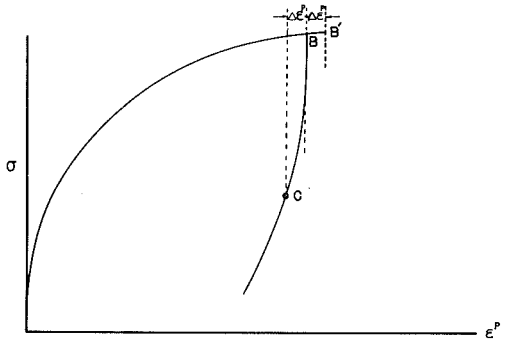

Fig. *B*.1 Schematic stress-plastic strain curve used to determine material functions

$$R(r)=\frac{\rho_0}{\Gamma(\alpha)r^{1-\alpha}}. \qquad (A.9)$$

where Γ is the Gamma function.

In the case of brass, on the other hand, it was found that

$$\rho(Z)=\frac{\rho_0}{Z^{\alpha}}e^{-kZ} \qquad (A.10)$$

in which case

$$R(r)=\begin{cases}0, r\le k\\ \dfrac{\rho_0}{\Gamma(\alpha)(r-k)^{1-\alpha}}\end{cases} \qquad (A.11)$$

In greater generality consistent with the theory of linear irreversible thermodynamics as it applies to isotropic materials,

$$\rho(Z)=\frac{\rho_0}{Z^{\alpha}}\sum_{n=1}^{N} R_n e^{-k_n Z} \qquad (A.12)$$

where N is finite or infinite. In this event

$$R(r)=\sum_{n=1}^{N}\frac{[r-k_n]^{\alpha-1}}{\Gamma(\alpha)} \qquad (A.13)$$

where

$$[r-k_n]=0, r\le k_n \qquad (A.14)$$

APPENDIX *B*

Here we give a rigorous method for determining the material functions $\rho(Z)$ and $f(\zeta)$ from experimental measurement when $f(\zeta)$ is a slowly varying function in a sense to be defined later in this appendix. However we should not expect a "unique" set of experiments for the determination of these functions. In viscoelasticity such a set does not exist. The relaxation function in shear may be determined by a relaxation test, creep test (indirectly), constant strain rate test, or an oscillatory test, and everyone of these has advantages and disadvantages. We expect that a similar situation will exist in endochronic plasticity. This is a subject that requires further investigation and will not be dealt with in this paper.

Consider the uniaxial test with a loading-unloading history. The test is illustrated schematically in Fig. *B*.1 where the axial stress is plotted versus the plastic strain ϵ^p. The stress σ is given by the relation

$$\sigma=\int_0^{Z} E(Z-Z')\frac{\partial \epsilon^p}{\partial Z'}dZ' \qquad (B.1)$$

where

$$E(Z)=3\rho(Z) \qquad (B.2)$$

$$d\zeta = \sqrt{3/2}\,|d\epsilon^p| \tag{B.3}$$

$$dZ = \frac{d\zeta}{f(\zeta)} \tag{B.4}$$

We wish to calculate the stress at points B and C where $\Delta\epsilon^p$ is an increment, not necessarily infinitesimal, in the plastic strain. Then in view of equations (*B*.1), (*B*.3), and (*B*.4),

$$\sigma_B = \sqrt{2/3}\int_0^{Z_B} E(Z_B - Z')f^*(Z')dZ' \tag{B.5}$$

where Z_B is the value of Z at point B and

$$f^*(Z) = f(\zeta(Z)) \tag{B.6}$$

The stress σ at C is calculated using again equations (*B*.1), (*B*.3), and (*B*.4). Thus

$$\sigma_C = \int_0^{Z_C} E(Z_C - Z')\frac{d\epsilon^P}{dZ'}dZ' \tag{B.7}$$

With reference to Fig. *B*.1, we now use the relation $Z_c = Z_B + \Delta Z_B$ to write the right hand side of equation (*B*.7) in the form

$$\sigma_C = \int_0^{Z_B} E(Z_B + \Delta Z_B - Z')\frac{d\epsilon^p}{dZ'}dZ' + \int_{Z_B}^{Z_B+\Delta Z_B} E(Z_B + \Delta Z_B - Z')\frac{d\epsilon^p}{dZ'}dZ' \tag{B.7a}$$

In view of equation (*B*.3) we note that in the interval $0 \le Z' \le Z_B$ (loading), $d\epsilon^p/d\zeta' = +\sqrt{2/3}$, whereas in the interval $Z_B < Z' \le Z_C$ (unloading), $d\epsilon^p/d\zeta' = -\sqrt{2/3}$. It follows therefore that

$$\sigma_C = \sqrt{2/3}\int_0^{Z_B} E(Z_B + \Delta Z_B - Z')f^*(Z')dZ' - \sqrt{2/3}\int_{Z_B}^{Z_B+\Delta Z_B} E(Z_B + \Delta Z_B - Z')f^*(Z')dZ'. \tag{B.8}$$

Addressing the second term on the right hand side of equation (*B*.8) we note that in view of the mean value theorem it follows that

$$\sqrt{2/3}\int_{Z_B}^{Z_B+\Delta Z_B} E(Z_B + \Delta Z_B - Z')f^*(Z')dZ' = f^*(\bar{Z}_B)R(\Delta Z_B) \tag{B.9}$$

where the function $R(Z)$ is defined by the integral

$$R(Z) = \sqrt{2/3}\int_0^Z E(Z')dZ' \tag{B.10}$$

and $Z_B \le \bar{Z}_B \le Z_C$.

To evaluate the first term on the right-hand side of equation (*B*.8) we note that

$$\int_0^{Z_B} E(Z_B + \Delta Z_B - Z')f^*(Z')dZ' = \int_0^{Z_B+\Delta Z_B} E(Z_B + \Delta Z_B - Z')f^*(Z')dZ' - \int_{Z_B}^{Z_B+\Delta Z_B} E(Z_B + \Delta Z_B - Z')f^*(Z')dZ' \tag{B.11}$$

or

$$\sqrt{2/3}\int_0^{Z_B} E(Z_B + \Delta Z_B - Z')f^*(Z')dZ' = \sigma_{B'} - f^*(\bar{Z}_B)R(\Delta Z_B) \tag{B.12}$$

Where the physical meaning of σ_B', is illustrated in Fig. *B*.1. In view of equations (*B*.8), (*B*.9), and (*B*.12)

$$\sigma_C = \sigma_{B'} - 2f^*(\bar{Z}_B)R(\Delta Z_B). \tag{B.13}$$

Hence:

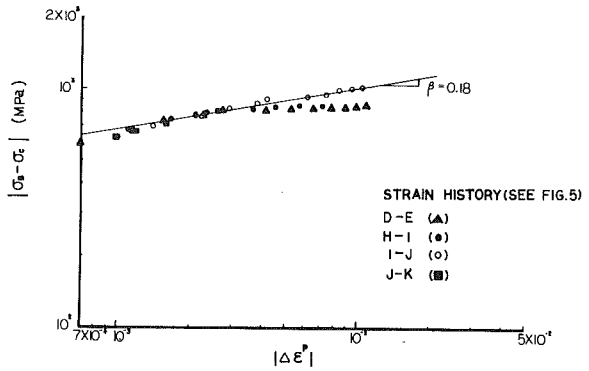

Fig. *B*.2 Plot of log $|\sigma_B - \sigma_C|$ versus log $|\Delta\epsilon^p|$

$$f^*(\bar{Z}_B) = \frac{\sigma_{B'} - \sigma_C}{2R(\Delta Z_B)} \tag{B.14}$$

We remark that this is an exact result irrespective of the magnitude of ΔZ_B. A generalization of equation (*B*.14) applicable to any reversal point is given in the following without proof, which we leave to the reader,

$$f^*(\bar{Z}_B) = \frac{|\sigma_{B'} - \sigma_C|}{2R(\Delta Z_B)} \tag{B.14a}$$

where B is any reversal point and the geometric meaning of B', C, and B is as that given in Fig. *B*.1.

We wish to use equation (*B*.14*a*) for the experimental determination of $f^*(Z_B)$. If we let ΔZ_B be *infinitesimal* and if $f^*(Z)$ is a slowly varying function (see the following discussion) then

$$f^*(\bar{Z}_B) \doteq f^*(Z_B) \tag{B.15}$$

$$R(\Delta Z_B) \doteq R(\sqrt{3/2}\,|\Delta\epsilon^p|/f^*(Z_B)) \tag{B.16}$$

$$\sigma_{B'} \doteq \sigma_B \tag{B.17}$$

so that equation (*B*.14*a*) becomes

$$f^*(Z_B) \doteq \frac{|\sigma_B - \sigma_C|}{2R(\sqrt{3/2}\,|\Delta\epsilon^p|/f^*(Z_B))} \tag{B.18}$$

Furthermore since $f^*(Z_B) = f(\zeta_B)$, equation (*B*.18) determines the value of the function $f(\zeta)$ at the point B, i.e., at $\zeta = \zeta_B$. The error associated with these approximations will be discussed in the following.

Discussion of Solution of equation (*B*.18)

To solve for $f^*(Z_B)$ it is necessary to know the functional form of $R(Z)$.

We discuss the solution of equation (*B*.18) in the case where in the vicinity of $Z = 0$ the material function $E(Z)$ is given by the relation

$$E(Z) = E_0/Z^\alpha \tag{B.19}$$

which is essential for the weakly singular form of $E(Z)$. In this event following equation (*B*.10) and in the vicinity of $Z = 0$,

$$R(Z) = \frac{\sqrt{2/3}E_0}{1-\alpha}Z^{1-\alpha} \tag{B.20}$$

In view of equation (*B*.20), equation (*B*.18) may be solved explicitly for $f^*(Z_B)$ to give

$$f_B = f^*(Z_B) = f(\zeta_B) = \left\{\frac{|\sigma_B - \sigma_C|}{2R(\sqrt{3/2}\,|\Delta\epsilon^p|)}\right\}^{1/\alpha} \tag{B.21}$$

More explicitly, using equation (*B*.20)

$$f_B^{\alpha} = \frac{|\sigma_B - \sigma_C|}{\left(\frac{2\sqrt{2/3}E_0}{1-\alpha}\right)|\sqrt{3/2}\Delta\epsilon^p|^{1-\alpha}} \tag{B.22}$$

The logarithmic form of the preceding equation given in the following

$$\log|\sigma_B - \sigma_C| = \log\left(\frac{2E_0}{1-\alpha} f_B^{\alpha}(\sqrt{2/3})^{\alpha}\right) + (1-\alpha)\log|\Delta\epsilon^p| \tag{B.23}$$

is useful in determining both the parameter α and the function f at $\zeta = \zeta_B$ within a multiplicative constant. In effect, a plot of $\log|\sigma_B - \sigma_C|$ versus $\log|\Delta\epsilon^P|$ gives a straight line with slope $(1-\alpha)$ and intercept $\log\{[2E_0/(1-\alpha)]f_{\beta}^{\alpha}(\sqrt{2/3})^{\alpha}\}$ at $|\Delta\epsilon^p| = 1$. Such a plot is shown in Fig. *B*.2 for various reversal points in the case of Grade 60 steel. The experimental data are shown in Fig. 5. We found a great deal of scatter for $|\Delta\epsilon^P| < 7 \times 10^{-4}$. However, in the range $7 \times 10^{-4} \leq |\Delta\epsilon^p| \leq 10^{-2}$ the experimental points are consistent and lie close to a straight line with a slope $\beta = 0.18$ as shown. The fact that all points lie virtually on the same line indicates that f is a constant (set it equal to 1) in the range of Z covered by the experiment.

Error Associated With equation (*B*.18)

Here we give an estimate of the error associated with equation (*B*.18) when $R(Z)$ is given by equation (*B*.20). The calculation is lengthy but straightforward. Bascially we use the relation

$$f^*(Z') = f_B^* + \hat{f}_B^*(Z' - Z_B) + 0((Z' - Z_B)^2) \tag{B.24}$$

in the range $Z_B \leq Z' \leq Z_B + \Delta Z_B$, in equation (*B*.9) where $\hat{f}_B^* = df^*(Z)/dZ|_{Z=Z_B}$, and the integral form of equation (*B*.4), whereby

$$\zeta = \int_0^Z f^*(Z')dZ' \tag{B.25}$$

The resulting relation for the error ϵ is

$$f_B^*\{1+\epsilon\} = \frac{|\sigma_B - \sigma_C|}{2R(\sqrt{3/2}|\Delta\epsilon^p|/f_B^*)} \tag{B.26}$$

where

$$\epsilon = \frac{\alpha(3-\alpha)}{2(2-\alpha)}\frac{\Delta f_B^*}{f_B^*} + 0\left(\frac{\Delta f_B^*}{f_B^*}\right)^2 \tag{B.27}$$

The term in the bracket on the right-hand side of equation (*B*.27) varies from zero to unity as α takes values in the range $0 < \alpha < 1$. Thus ϵ is at most of $0(\Delta f_B^*/f_B^*)$.

Determination of the function $E(Z)$

The form of the function $E(Z)$ given by equation (*B*.19) applies strictly in the vicinity of $Z = 0$, in general. However in the case of two metals discussed in this paper this form has been found to hold in the entire range of the experimental investigation. In other cases it may be determined by solving the Volterra integral equation (*B*.5). This method will not be pursued here but will be the subject of investigation in a future papper.

D. E. Panayotounakos
Dr. Engineer.

P. S. Theocaris
Professor of Mechanics
Chair of Mechanics A, and
Laboratory for Testing Materials.
Mem. ASME

The National Technical
University of Athens,
5, K. Zographou Street,
Zogarphou, Athens 624, Greece.

Three-Dimensional Harmonic Vibrations of a Circular Beam

In this paper an analytical treatment for the determination of the natural frequencies of a circular uniform beam, subjected to three-dimensional harmonic loads, is presented. Each differential element of the beam has six degrees of freedom, i.e., three translations and three rotations. This problem, in the most general case of response, is associated with a partial linear differential system composed of four coupled 3 × 1 vectorial equations. The influences of transverse shear deformation and rotatory inertia are also included in the analysis. The aforementioned solution methodology is successfully demonstrated through several numerical results.

Introduction

The problem of forced harmonic motions of circular beams or rings lying or not lying on elastic foundation has already attracted the interest of many investigators. In references [1]–[5] and [8] the classical beam theory was used to analyze the dynamic response of a circular beam or ring, in which the effects of shearing deformations, the flexural rotatory inertias, and axial forces were omitted. On the other hand, in references [6], [7], [9], and [10] the effects of the previous quantities have been taken into consideration. But, in all these references the harmonic vibrations were considered only on the plane or in the perpendicular direction of the plane of the beam; these assumptions essentially simplified the governing equations of the problem.

The present investigation deals with the problem of three-dimensional harmonic forced motions of a uniform circular beam in the most general case of response. The elastic center coincides with the shear center and the center of twist of the beam cross section. The harmonic loads are considered to act through this point and simultaneously in the direction of the principal torsion-flexure axes at every cross section of the center-line. Each differential element is given six degrees of freedom, i.e., three translations and three rotations. So, the motions of the beam are spatially developed. Also, the effects of rotatory inertias, shearing deformations, and axial forces are included in the analysis. This problem is associated with a linear system of four coupled (3×1)-vectorial partial differential equations with constant coefficients. After an appropriate analytical treatment, the system is uncoupled, so that two independent partial linear-differential equations of sixth order with respect to the two translations are formulated. An exact solution for the determination of the natural frequencies, in the general case where the effects of rotatory inertias, shearing deformations, and axial forces are taken into account, is obtained. Finally, the solutions developed herein are successfully demonstrated through several numerical examples.

Analysis

Consider a circular beam of uniform cross section subjected to an harmonic forced vibration, due to a continuous vectorial load function $\mathbf{q}(s, t) = \bar{\mathbf{q}}(s)\times e^{i\omega t}$ and a continuous vectorial moment function $\overset{*}{\mathbf{m}}(s, t) = \overset{*}{\mathbf{m}}(s)\, e^{i\omega t}$, where s is the arc length of the beam and t the time. Consider also an elementary arc $AA' = ds = (1/\kappa)d\varphi$, where κ denotes the constant curvature and φ the epicentral angle of the centroidal axis of the beam.

Let us name $A123$ the *Frénet* trihedron of the section A with unit vectors $\mathbf{t}$, $\mathbf{n}$, $\mathbf{b}$ respectively, where $\mathbf{t} = (t_1(s), t_2(s), t_3(s))^T$ denotes the unit tangent vector pointing to the direction of s increasing, $\mathbf{n} = (n_1(s), n_2(s), n_3(s))^T$ is the unit normal vector pointing to the center of curvature, and $\mathbf{b} = (0, 0, 1)^T$ is the constant binormal vector; $\mathbf{b}$ is defined in such a way that the corresponding *Frénet* trihedron to be a right-handed system (Fig. 1). Here, it must be noticed that the aforementioned trihedron conicides with the principal torsion-flexure axes of the cross section of the beam.

The partial linear vectorial (3×1)-differential equations (in terms of generalized forces and displacements) governing the equilibrium of an arc element (Fig. 1) are given by:

$$\left.\begin{aligned}
\mathbf{T}' &= \mathbf{R}\,\mathbf{T} - m\,\ddot{\mathbf{y}} + \mathbf{q} && (1a)\\
\mathbf{M}' &= \mathbf{R}\,\mathbf{M} + \mathbf{S}\,\mathbf{T} - \mathbf{I}\,\ddot{\boldsymbol{\psi}} + \overset{*}{\mathbf{m}} && (1b)\\
\boldsymbol{\Psi}' &= \mathbf{R}\,\boldsymbol{\Psi} - \mathbf{A}\,\mathbf{M} && (1c)\\
\mathbf{y}' &= \mathbf{R}\,\mathbf{y} + \mathbf{S}\,\boldsymbol{\psi} - \mathbf{B}\,\mathbf{T} && (1d)
\end{aligned}\right\}$$

In the aforementioned equations $\mathbf{T} = (T_1(s, t), T_2(s, t), T_3(s, t))^T$; $\mathbf{M} = (M_1(s, t), M_2(s, t), M_3(s, t))^T$ denote the vectors of internal forces and moments, respectively, while $\boldsymbol{\psi} = (\psi_1(s, t), \psi_2(s, t), \psi_3(s, t))^T$; $\mathbf{y} = (y_1(s, t), y_2(s, t), y_3(s, t))^T$ the vectors of rotations and translations. Also, $\mathbf{q}$ =

Contributed by the Applied Mechanics Division for publication in the JOURNAL OF APPLIED MECHANICS.
Discussion on this paper should be addressed to the Editorial Department, ASME, United Engineering Center, 345 East 47th Street, New York, N.Y. 10017, and will be accepted until two months after final publication of the paper itself in the JOURNAL OF APPLIED MECHANICS. Manuscript received by ASME Applied Mechanics Division, January, 1982; final revision, June, 1983.

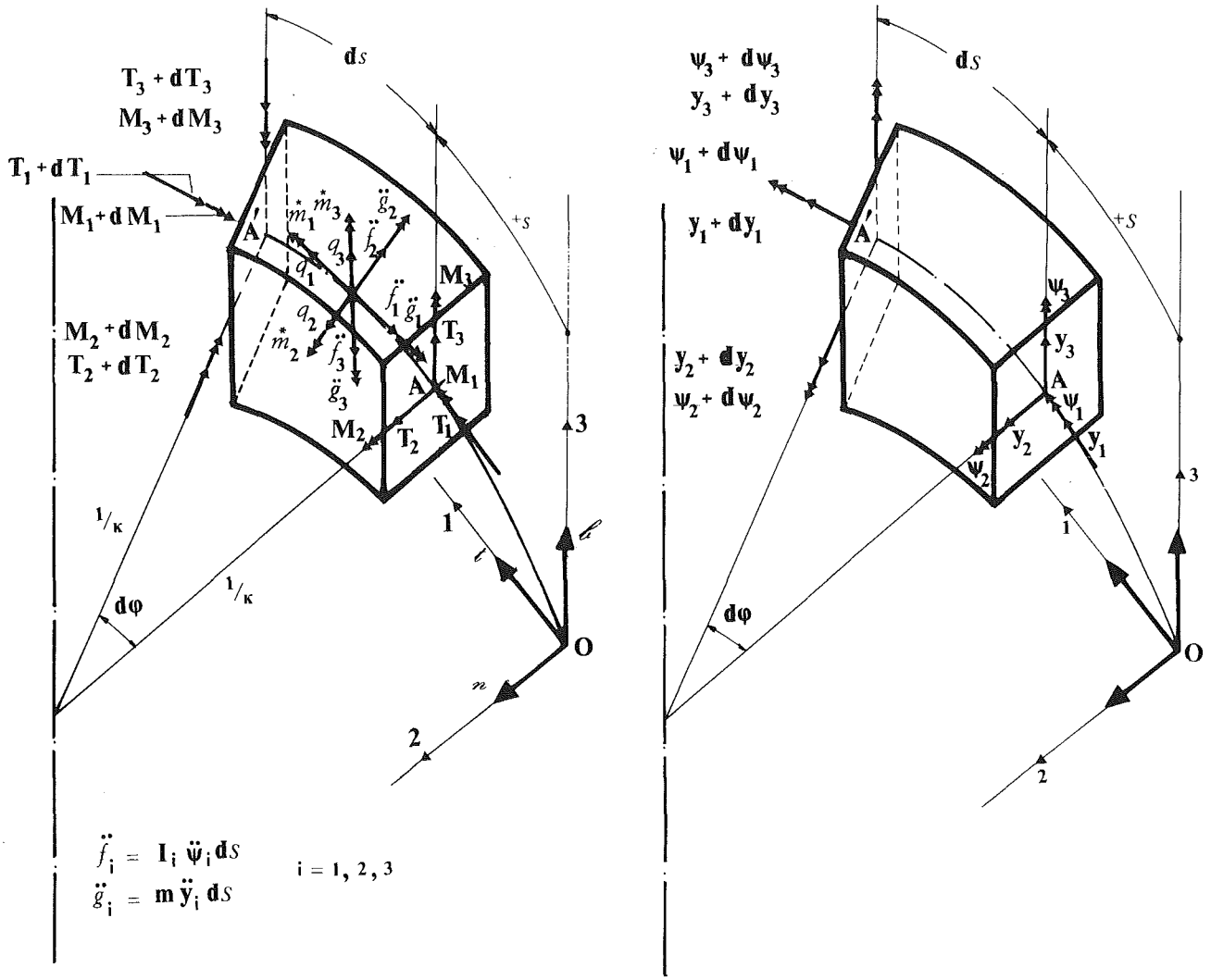

Fig. 1 Geometry and sign convention of forces and displacements

$(q_1(s,t), q_2(s,t), q_3(s,t))^T$; $\overset{*}{\mathbf{m}} = (\overset{*}{m}_1(s,t), \overset{*}{m}_2(s,t), \overset{*}{m}_3(s,t))^T$ are the vectors of the continuous external loading (forces and couples); $-m\ddot{y} = -m(\ddot{y}_1, \ddot{y}_2, \ddot{y}_3)^T$ and $-\mathbf{I}\ddot{\psi} = -(I_1\ddot{\psi}_1, I_2\ddot{\psi}_2, I_3\ddot{\psi}_3)^T$ denote the vectors of the *D' Alembert's* forces and moments, due to the transverse and torsional vibration of the beam, respectively; m is the distributed mass per unit length. Finally, **R**, **S**, **I**, **A**, and **B** are constant (3×3)-matrices, given by:

$$\mathbf{R}=[r_{ij}]=\begin{bmatrix} 0 & \kappa & 0 \\ -\kappa & 0 & 0 \\ 0 & 0 & 0 \end{bmatrix},\quad \mathbf{S}=[s_{ij}]=\begin{bmatrix} 0 & 0 & 0 \\ 0 & 0 & 1 \\ 0 & -1 & 0 \end{bmatrix},$$

$$\mathbf{I}=[i_{ii}]=\begin{bmatrix} I_1 & 0 & 0 \\ 0 & I_2 & 0 \\ 0 & 0 & I_3 \end{bmatrix},\quad \mathbf{A}=[A_{ii}]=\begin{bmatrix} a_1 & 0 & 0 \\ 0 & a_2 & 0 \\ 0 & 0 & a_3 \end{bmatrix}, \tag{2}$$

$$\mathbf{B}=[B_{ii}]=\begin{bmatrix} b_1 & 0 & 0 \\ 0 & b_2 & 0 \\ 0 & 0 & b_3 \end{bmatrix}$$

in which the elements i_{ii}, A_{ii}, B_{ii} $(i = 1, 2, 3)$ are calculated by the relations:

$$a_1 = 1/GI_1;\ a_2 = 1/EI_2;\ a_3 = 1/EI_3;\ b_1 = 1/EF;$$
$$b_2 = 1/G\overset{*}{F}_2;\ b_3 = 1/G\overset{*}{F}_3;\ \overset{*}{F}_2 = \lambda_2 F; \tag{3}$$
$$\overset{*}{F}_3 = \lambda_3 F;\ I_i = \epsilon I_i/g$$

In equations (3) E and G are the *Young's* and shear moduli of elasticity, respectively; I_2, I_3, and I_1 represent the two principal moments of inertia and the polar moment of inertia of the cross section of the beam with respect to principal torsion flexure axes 2, 3, 1, respectively; F is the cross-section area; ϵ denotes the specific weight of the material of the beam, whereas g is the gravity acceleration; λ_2; λ_3 are numerical coefficients depending on the shape of the cross section. Finally, primes indicate differentiations with respect to s and dots differentiations with respect to t (The superscript "T" denotes the transpose of a matrix). It should be noticed here that through a simple manipulation of equations (1) the corresponding equations of the static problem can be derived [11].

Solving equation (1*d*) with respect to **T**, as well as equation (1*c*) with respect to **M**, we find the following partial differential equation:

$$\mathbf{M}' = (\mathbf{R}\mathbf{A}^{-1}\mathbf{R} + \mathbf{S}\mathbf{B}^{-1}\mathbf{S})\psi - \mathbf{R}\mathbf{A}^{-1}\psi' + \mathbf{S}\mathbf{B}^{-1}\mathbf{R}\mathbf{y} - \mathbf{S}\mathbf{B}^{-1}\mathbf{y}' - \mathbf{I}\ddot{\psi} + \overset{*}{\mathbf{m}} \tag{4}$$

Differentiating also equation (1*c*) with respect to s and using relation (4) we lead to:

$$\Psi'' = \theta\psi + \mathbf{H}\psi' - \overset{*}{\mathbf{M}}\mathbf{y} + \mathbf{I}\mathbf{y}' + \mathbf{A}\mathbf{I}\ddot{\psi} - \mathbf{A}\overset{*}{\mathbf{m}} \tag{5}$$

where:

$$\theta=[\theta_{ij}]=\begin{bmatrix}\frac{a_1}{a_2}\kappa^2 & 0 & 0\\ 0 & \frac{a_2}{a_3}\kappa^2+\frac{a_2}{b_3} & 0\\ 0 & 0 & \frac{a_3}{b_2}\end{bmatrix},$$

$$\mathbf{H}=[n_{ij}]=\begin{bmatrix}0 & \kappa\left(1+\frac{a_1}{a_2}\right) & 0\\ -\kappa\left(1+\frac{a_2}{a_1}\right) & 0 & 0\\ 0 & 0 & 0\end{bmatrix}, \tag{5a}$$

$$\overset{*}{\mathbf{M}}=[\overset{*}{\mu}_{ij}]=\begin{bmatrix}0 & 0 & 0\\ 0 & 0 & 0\\ \frac{a_3}{a_2}\kappa & 0 & 0\end{bmatrix},\quad \mathbf{I}=[I_{ij}]=\begin{bmatrix}0 & 0 & 0\\ 0 & 0 & \frac{a_2}{b_3}\\ 0 & -\frac{a_2}{b_2} & 0\end{bmatrix}$$

Finally, differentiating equation (1*b*) with respect to s and combining the resulting relation with (1*d*) we find:

$$\mathbf{y}''=\mathbf{K}\,\mathbf{y}+\overset{*}{\mathbf{E}}\mathbf{y}'-\mathbf{M}\,\psi+\mathbf{S}\,\psi'+m\mathbf{B}\,\ddot{\mathbf{y}}-\mathbf{B}\,\mathbf{q} \tag{6}$$

where:

$$\mathbf{K}=[k_{ij}]=\begin{bmatrix}\frac{b_1}{b_2}\kappa^2 & 0 & 0\\ 0 & \frac{b_2}{b_1}\kappa^2 & 0\\ 0 & 0 & 0\end{bmatrix},$$

$$\overset{*}{\mathbf{E}}=[\overset{*}{\epsilon}_{ij}]=\begin{bmatrix}0 & \kappa\left(1+\frac{b_1}{b_2}\right) & 0\\ -\kappa\left(1+\frac{b_2}{b_1}\right) & 0 & 0\\ 0 & 0 & 0\end{bmatrix}, \tag{6a}$$

$$\mathbf{N}=[\nu_{ij}]=\begin{bmatrix}0 & 0 & \frac{b_1}{b_2}\kappa\\ 0 & 0 & 0\\ 0 & 0 & 0\end{bmatrix}$$

The vectorial (3×1)-equations (5) and (6) form partial differential linear nonhomogeneous system of the second order referred to the three-dimensional harmonic forced vibration of a circular beam, where the influences of rotatory inertia and transverse shear deformation have been taken into account.

The vectorial equations (5) and (6) are equivalent to the following partial differential system of analytical equations:

$$\left.\begin{aligned}&\psi_3=\alpha_1\overset{*}{f}_1\\ &\psi_3'=-\overset{*}{f}_2\\ &\psi_2'=\overset{*}{f}_3\end{aligned}\right\} \tag{7a}$$

$$\left.\begin{aligned}&\psi_1''-\vartheta_{11}\psi_1-a_1\mathrm{I}_1\ddot{\psi}_1=\vartheta_{12}\psi_2+n_{12}\psi_2'-a_1\overset{*}{m}_1\\ &\psi_2''-\vartheta_{22}\psi_2-a_2\mathrm{I}_2\ddot{\psi}_2=\vartheta_{21}\psi_1+n_{21}\psi_1'\\ &\qquad+I_{23}y_3'-a_2\overset{*}{m}_2\\ &\psi_3''-a_3\mathrm{I}_3\ddot{\psi}_3=\vartheta_{33}\psi_3-\overset{*}{\mu}_{31}y_1+I_{32}y_2'-a_3\overset{*}{m}_3\end{aligned}\right\} \tag{7b}$$

where:

$$\left.\begin{aligned}&\overset{*}{f}_1=-y_1''+k_{11}y_1+k_{12}y_2+\overset{*}{\epsilon}_{12}y_2'+m\,b_1\ddot{y}_1-b_1q_1\\ &\overset{*}{f}_2=-y_2''+k_{21}y_1+k_{22}y_2+\overset{*}{\epsilon}_{21}y_1'+m\,b_2\ddot{y}_2-b_2q_2\\ &\overset{*}{f}_3=-y_3''+m\,b_3\ddot{y}_3-b_3q_3\\ &\alpha_1=-1/\nu_{13}\end{aligned}\right\} \tag{7c}$$

It should be noticed that by setting $\kappa=0$ into equations (7*a*)-(7*c*), and after simple manipulations, one may obtain equations (1) of reference [6].

For the decoupling of equations (7*a*)-(7*c*) we make use of the following analytical treatment: From the two first of (7*a*) and from the combination of the last of (7*b*) with equations (7*a*) we obtain:

$$\left.\begin{aligned}&\alpha_1\overset{*}{f}_1'+\overset{*}{f}_2=0\\ &\overset{*}{f}_2'+\vartheta_{33}\alpha_1\overset{*}{f}_1+a_3\mathrm{I}_3a_1\overset{*}{f}_1'-\overset{*}{\mu}_{31}y_1+I_{32}y_2'=-a_3\overset{*}{m}_3\end{aligned}\right\} \tag{8}$$

Also, the combination of the two first relations (7*b*) and equations (7*a*) gives:

$$\left.\begin{aligned}&\psi_1''-\vartheta_{11}\psi_1-a_1\mathrm{I}_1\ddot{\psi}_1=n_{12}\overset{*}{f}_3-a_1\overset{*}{m}_1\\ &\vartheta_{22}\psi_2=\overset{*}{f}_3'-a_2\mathrm{I}_2\ddot{\psi}_2-n_{21}\psi_1'-I_{32}y_3'+a_2\overset{*}{m}_2\end{aligned}\right\} \tag{9}$$

Finally, from equations (9), (7*a*), and (7*c*), after some differentiations and a little algebra, the following linear partial differential equation of the sixth order with respect to the translation y_3 results:

$$y_3''''''+\sigma_1y_3''''+\sigma_2y_3''+\sigma_3\ddot{y}_3+\sigma_4\ddot{y}_3''+\sigma_5\ddot{y}_3''''+\sigma_6\dddot{y}_3+\sigma_7\dddot{y}_3''+\sigma_8\dddot{y}_3=\sigma \tag{10}$$

where the coefficients σ_i; σ ($i=1, 2, \ldots, 8$) are given in Appendix 1.

Furthermore, based on equations (7*a*) and (7*b*), the second of relations (7*c*), and equations (8) take the following form, respectively:

$$-y_1'''+\rho_1y_1'+\rho_2\ddot{y}_1'+k_1y_2''+k_2y_2+k_3\ddot{y}_2=k \tag{11a}$$

$$-y_2'''+\delta_1y_2'+\delta_2\ddot{y}_2'+\mu_1y_1''+\mu_2\ddot{y}_1+\mu_3\ddot{y}_1''+\mu_4\dddot{y}_1=\mu \tag{11b}$$

where the coefficients ρ_i; k_j; δ_i; μ_r; k; μ ($i=1, 2$; $j=1, 2, 3$; $r=1, 2, 3, 4$) are given in Appendix 1.

Differentiating now equation (11*a*) with respect to s, solving with respect to $\ddot{y}_2'$, as well as equation (11*b*) with respect to y_2', we have:

$$-y_1''''+\rho_1y_1''+\rho_2\ddot{y}_1''+k_1y_2'''+k_2y_2'+k_3\ddot{y}_2'=k' \tag{12a}$$

$$\ddot{y}_2'=-\frac{k_1\delta_1+k_2}{k_3\delta_1-k_2\delta_2}y_2'''+\frac{\delta_1g_2-k_2g_1}{k_3\delta_1-k_2\delta_2} \tag{12b}$$

$$y_2'=\frac{k_1\delta_2+k_3}{k_3\delta_1-k_2\delta_2}y_2'''+\frac{\delta_2g_2-k_3g_1}{k_3\delta_1-k_2\delta_2} \tag{12c}$$

where:

$$\left.\begin{aligned}&g_1=\mu-\mu_1y_1''-\mu_2\ddot{y}_1-\mu_3\ddot{y}_1'-\mu_4\dddot{y}_1\\ &g_2=k'+y_1''''-\rho_1y_1''-\rho_2\ddot{y}_1'\end{aligned}\right\} \tag{13}$$

In the sequel, after a double differentiation of equation (12*c*) with respect to t and using (12*b*), the following relation arises:

$$\xi_1\ddot{y}_2'''+\xi_2y_2'''=\tau_1g_1+\tau_2g_2+\tau_3\ddot{g}_1+\tau_4\ddot{g}_2 \tag{14}$$

in which:

$$\xi_1=\frac{k_1\delta_1+k_3}{\Delta},\quad \xi_2=\frac{k_1\delta_1+k_2}{\Delta},\quad \tau_1=-\frac{k_2}{\Delta},\quad \tau_2=\frac{\delta_1}{\Delta}$$
$$\tau_3=-\frac{k_3}{\Delta},\quad \tau_4=\frac{\delta_2}{\Delta},\quad \Delta=k_3\delta_1-k_2\delta_2 \tag{14a}$$

Finally, after successive differentiations of relations (12*a*) and (11*b*), the following four linearly independent partial differential equations result:

$$\begin{aligned}
&-y_2'''''+\delta_1 y_2'''+\delta_2\ddot{y}_2''=g_1''\\
&-\ddot{y}_2'''+\delta_1\ddot{y}_2'+\delta_2\ddot{\ddot{y}}_2'=\ddot{g}_1\\
&k_1 y_2'''''+k_2 y_2'''+k_3\ddot{y}_2'''=g_2''\\
&k_1\ddot{y}_2'''+k_2\ddot{y}_2'+k_3\ddot{\ddot{y}}_2'=\ddot{g}_2
\end{aligned} \tag{15}$$

So, the system of seven partial differential equations (11*b*), (12*a*), (14) and (15) with unknown functions y_2'''; y_2'; $\ddot{y}_2'$; $\ddot{y}_2'''$; y_2'''''; $\ddot{\ddot{y}}_2'$ is derived which yields another differential equation for the translation y_1. In fact, eliminating these unknowns we derive the determinant:

$$\begin{vmatrix}
0 & 0 & \delta_1 & \delta_2 & 0 & 0 & g_1\\
0 & k_1 & k_2 & k_3 & 0 & 0 & g_2\\
-1 & \delta_1 & 0 & 0 & \delta_2 & 0 & g_1''\\
0 & 0 & 0 & \delta_1 & -1 & \delta_2 & \ddot{g}_1\\
k_1 & k_2 & 0 & 0 & k_3 & 0 & g_2''\\
0 & 0 & 0 & k_1 & k_2 & k_3 & \ddot{g}_2\\
0 & \xi_2 & 0 & 0 & \xi_1 & 0 & \tau_1 g_1+\tau_2 g_2+\tau_3\ddot{g}_1+\tau_4\ddot{g}_2
\end{vmatrix}=0 \tag{16}$$

This relation, based on (14*a*), is transformed to a linear partial differential equation of the sixth order with respect to y_1.

It is worthwhile remarking that the solution of the differential equation (10) is sufficient for the determination of the displacements ψ_2 and ψ_1. In fact, this can be achieved by the third of equations (7*a*) being combined with the first of (7*b*). Also, the solution of equation (16) is sufficient for the determination of the displacements y_2 and ψ_3 from the first of equations (15) and the first of (7*a*). So, one may conclude that the three-dimensional forced vibrations of a circular beam can be analyzed into the two following independent types of forced vibrations:

Vibration 1: The transverse forced in the (1, 3)-plane vibration and the simultaneous torsional vibration.

Vibration 2: The transverse forced in the (1, 2)-plane vibration and the simultaneous longitudinal forced vibration.

Free Vibrations

For free vibration we may assume solutions for the homogeneous differential equations corresponding to equations (10) and (16) of the form:

$$\begin{aligned}
y_3(s,t)&=\bar{y}_3(s)e^{i\overset{*}{\Omega}t}\\
y_2(s,t)&=\bar{y}_2(s)e^{i\overset{*}{\omega}t}
\end{aligned} \tag{17}$$

where $\overset{*}{\Omega}$ and $\overset{*}{\omega}$ are the independent natural frequencies corresponding to the two previous kinds of vibration. So, one may write the following relations:

$$\begin{aligned}
(y_1,y_2,\psi_3)^T&=(\bar{y}_1,\bar{y}_2,\bar{\psi}_3)^T e^{i\overset{*}{\omega}t}\\
(y_3,\psi_1,\psi_2)^T&=(\bar{y}_3,\bar{\psi}_1,\bar{\psi}_2)T e^{i\overset{*}{\Omega}t}
\end{aligned} \tag{18}$$

in which $\bar{y}_2$; $\bar{\psi}_3$ and $\bar{\psi}_1$; $\bar{\psi}_2$ are functions with respect only to s. Putting now the second members of equations (10) and (16) equal to zero and introducing relations (17) in the resulting differential equations, the following two ordinary equations of the sixth order are obtained:

$$\begin{aligned}
&\bar{y}_3''''''+(\sigma_1-\overset{*}{\Omega}^2\sigma_5)\bar{y}_3''''+(\sigma_2-\overset{*}{\Omega}^2\sigma_4+\overset{*}{\Omega}^4\sigma^7)\bar{y}_3''\\
&\quad+\overset{*}{\Omega}^2(-\sigma_3+\overset{*}{\Omega}^2\sigma_6-\overset{*}{\Omega}^4\sigma_8)\bar{y}_3=0
\end{aligned} \tag{19}$$

$$\bar{y}_1-\frac{\Delta B+EA}{\Delta}\bar{y}_1''''-\frac{\Delta\Gamma+AZ}{\Delta}\bar{y}_1''-\frac{AH}{\Delta}\bar{y}_1=0 \tag{20}$$

where the coefficients A; B; Γ; Δ; E; Z, H are given in Appendix 1.

One may observe that both equations (19) and (20) are of a similar form to equation (5) given in reference [9]. So, relative to the determination of their solutions, we can make use of equations (12)–(14) and (29)–(33) of the same reference. Of course, we must, in advance, substitute the coefficients $\overset{*}{F}_i$ of equation (5), reference [9], with the coefficients of equations (19) and (20), respectively.

By now, the displacement components $\bar{\psi}_1$; $\bar{\psi}_2$ and $\bar{y}_2$; $\bar{\psi}_3$ may be derived from relations:

$$\begin{aligned}
\bar{\psi}_1&=\frac{(a_2 I_2\overset{*}{\Omega}^2-\vartheta_{22}-n_{12}n_{21})\bar{\overset{*}{f}}_3+\bar{\overset{*}{f}}_3''-I_{23}\bar{y}_3''}{n_{21}(\vartheta_{11}-a_1 I_1\overset{*}{\Omega}^2)}\\
\bar{\psi}_2&=\frac{-\bar{y}_3'''-m\,b_3\overset{*}{\Omega}^2\bar{y}_3'-n_{21}\bar{\psi}_1'-I_{23}\bar{y}_3'}{\vartheta_{22}-a_2 I_2\overset{*}{\Omega}^2}
\end{aligned} \tag{21}$$

where:

$$\bar{\overset{*}{f}}_3=-\bar{y}_3''-m\,b_3\overset{*}{\Omega}^2\bar{y}_3$$

and

$$\begin{aligned}
\bar{y}_2&=-\frac{-\bar{y}_1'''+(\rho_1-\overset{*}{\omega}^2\rho_2)\bar{y}_1'+k_1\bar{y}_2''}{k_2-\overset{*}{\omega}^2 k_3}\\
\bar{\psi}_3&=\alpha_1(-\bar{y}_1''+k_{11}\bar{y}_1+\overset{*}{\epsilon}_{12}\bar{y}_2'-m\,b_1\overset{*}{\omega}^2\bar{y}_1)
\end{aligned} \tag{22}$$

where

$$\bar{y}_2''=\frac{\bar{g}_2'+k_1\bar{g}_1'}{(k_2-\overset{*}{\omega}^2 k_3)-k_1(\delta_1-\overset{*}{\omega}^2\delta_2)}$$

$$\bar{g}_1=-\mu_1\bar{y}_1''+\mu_2\overset{*}{\omega}^2\bar{y}_1+\mu_3\overset{*}{\omega}^2\bar{y}_1'-\mu_4\overset{*}{\omega}^4\bar{y}_1$$

$$\bar{g}_2=\bar{y}_1''''-\rho_1\bar{y}_1'+\rho_2\overset{*}{\omega}^2\bar{y}_1$$

After the determination of the displacement components, the internal forces $\bar{M}_3$; $\bar{T}_1$; $\bar{T}_2$ and $\bar{M}_1$; $\bar{M}_2$; $\bar{T}_3$ can be established from equations (1*c*) and (1*d*). Also the determination of the natural frequencies $\overset{*}{\omega}$ and $\overset{*}{\Omega}$ will be achieved from: (*i*) the general solution of equations (19)–(22), (*ii*) the equations expressing the functions $\bar{M}_3$; $\bar{T}_1$; $\bar{T}_2$; $\bar{M}_1$; $\bar{M}_2$; $\bar{T}_3$, and (*iii*) the suitable boundary conditions. Consequently, if we write the general integral of equation (20) under the form:

$$\bar{y}_1(s)=\sum_{i=1}^{6}c_i\overset{*}{\Phi}_i(s) \tag{23}$$

we have

$$\begin{aligned}
&\bar{y}_2(s)=\sum_{i=1}^{6}c_i\overset{*}{A}_i;\quad \bar{\psi}_3(s)=\sum_{i=1}^{6}c_i\overset{*}{B}_i;\quad \bar{M}_3(s)\\
&=\sum_{i=1}^{6}c_i\overset{*}{\Gamma}_i;\bar{T}_1(s)=\sum_{i=1}^{6}c_i\overset{*}{\Delta}_i;\quad \bar{T}_2(s)=\sum_{i=1}^{6}c_i\overset{*}{E}_i
\end{aligned} \tag{24}$$

where: (*i*) c_i are integration constants that may be determined from the boundary conditions, (*ii*) $\overset{*}{\Phi}_i$ are functions of $\overset{*}{\omega}^2$; $\overset{*}{\omega}^4$; s

being calculated from equations (12)–(14) of reference [15], and (*iii*) $\overset{*}{A}_i$; $\overset{*}{B}_i$; $\overset{*}{\Gamma}_i$; $\overset{*}{\Delta}_i$; $\overset{*}{E}_i$ are functions of $\overset{*}{\omega}^2$; $\overset{*}{\omega}^4$; s being derived from relations (23), (22), the third of (1*d*), and the two first of (1*c*), respectively. Thus, for the case of a both fixed ends circular beam the boundary conditions, corresponding to the eigenfrequencies $\overset{*}{\omega}$, are:

$$\bar{y}_1(0)=\bar{y}_2(0)=\bar{\psi}_3(0)=0$$
$$\bar{y}_1(\bar{s})=\bar{y}_2(\bar{s})=\bar{\psi}_3(\bar{s})=0 \tag{25}$$

where $\bar{s}$ represents the total arc length. Using relations (23) and (24) in combination with the boundary conditions given in relations (25), for a nontrivial solution the following determinant must be zero (this determinant is analogous to the determinant (22) of reference [9]).

$$\begin{Vmatrix} \overset{*}{\Phi}_1(0) & \overset{*}{\Phi}_2(0) & \overset{*}{\Phi}_3(0) & \dots & \overset{*}{\Phi}_6(0) \\ \overset{*}{A}_1(0) & \overset{*}{A}_2(0) & \overset{*}{A}_3(0) & \dots & \overset{*}{A}_6(0) \\ \overset{*}{B}_1(0) & \overset{*}{B}_2(0) & \overset{*}{B}_3(0) & \dots & \overset{*}{B}_6(0) \\ \overset{*}{\Phi}_1(\bar{s}) & \overset{*}{\Phi}_2(\bar{s}) & \overset{*}{\Phi}_3(\bar{s}) & \dots & \overset{*}{\Phi}_6(\bar{s}) \\ \overset{*}{A}_1(\bar{s}) & \overset{*}{A}_2(\bar{s}) & \overset{*}{A}_3(\bar{s}) & \dots & \overset{*}{A}_6(\bar{s}) \\ \overset{*}{B}_1(\bar{s}) & \overset{*}{B}_2(\bar{s}) & \overset{*}{B}_3(\bar{s}) & \dots & \overset{*}{B}_6(\bar{s}) \end{Vmatrix} = 0 \tag{26}$$

The last relation leads to a transcendental equation with respect to $\overset{*}{\omega}^2$; $\overset{*}{\omega}^4$ of the form:

$$F(\overset{*}{\omega}^2;\overset{*}{\omega}^4;\lambda_2;\lambda_3;I_1;I_2;I_3;m;\epsilon;g;E;G;I_1;I_2;I_3;R;\bar{\varphi};F)=0 \tag{27}$$

which, obviously, depends on the values of the parameters λ_2; λ_3; I_1; I_2; I_3; m; ϵ; g; E; I_1; I_2; I_3 R; $\bar{\varphi}$; F. Based on an analogous methodology, a new transcendental equation can be derived corresponding to the natural frequencies $\overset{*}{\Omega}$.

In the case when the effects of transverse shear deformation and rotatory inertia are omitted ($b_2 = b_3 = 0$; $|a_i I_i \ddot{\psi}_i| = 0$, $i = 1, 2, 3$) the matrices **B** and **I** being included in relations (2) become singular and zero, respectively. So, as equation (4) is not valid, through new analytical treatments and the decoupling of a homogeneous vectorial system analogous to (1), the following differential equations with respect to the generalized displacements $\bar{y}_1$, $\bar{y}_3$ result:

$$\bar{y}_1'''' - \frac{2\kappa\xi+\mu}{(\kappa^2-\rho)}\bar{y}_1'''' + \frac{\xi^2-\sigma\rho}{(\kappa^2-\rho)}\bar{y}_1'' - \frac{\sigma\mu}{(\kappa^2-\rho)}\bar{y}_1 = 0 \tag{28}$$

$$\bar{y}_3'''' - \alpha^2\bar{y}_3'''' + (\beta^2-\gamma^2\overset{*}{\Omega}^2)\bar{y}_3'' + \delta^2\overset{*}{\Omega}^2\bar{y}_3 = 0 \tag{29}$$

in which:

$$\xi=\kappa\frac{a_3}{a_1},\quad \mu=a_3 m\overset{*}{\omega}^2,\quad \rho=\kappa^2+\frac{a_3}{b_1},\quad \sigma=\kappa^2\frac{a_3}{b_1}-a_3 m\overset{*}{\omega}^2 \tag{30}$$
$$\alpha^2=2\kappa^2,\beta^2=\kappa^4,\gamma^2=a_2 m,\delta^2=a_1 m\kappa^2$$

Also, the functions of relations (21) and (22) take the following new form:

$$\bar{\psi}_1 = \frac{a_2}{\kappa(a_1+a_2)}\bar{y}_3'''' - \frac{2a_2+a_1}{\kappa(a_1+a_2)}\bar{y}_3'' \tag{31}$$
$$\bar{\psi}_2 = -\bar{y}_3'$$

and

$$\bar{y}_2 = \frac{\xi(\kappa^2-\rho)}{\sigma(\xi^2+\kappa^2\sigma)}\bar{y}_1'''' - \left\{\frac{\xi(\kappa\xi+\mu)-\kappa\sigma\rho}{\sigma(\xi^2+\kappa^2\sigma)}+\frac{\kappa}{\sigma}\right\}\bar{y}_1''' + \left\{\frac{\kappa\sigma\mu}{\sigma(\xi^2+\kappa^2\sigma)}+\frac{\kappa}{\sigma}\right\}\bar{y}_1' \tag{31a}$$
$$\bar{\psi}_3 = \kappa\bar{y}_1 + \bar{y}_2'$$

Note here, that the previous assumption of omittance of transverse shear deformation and rotatory inertia can be accepted for flexible beams. Moreover, the assumption that the expression $|a_i I_i \ddot{\psi}_i|$ can be omitted results from *Rayleigh's* investigation, where it was proved that this quantity is of significance only for vibrations of high frequencies.

Applications and Numerical Results

Consider a uniform circular beam with both fixed ends subjected to a harmonic motion due to a continuous vertical load $q_3(s,t) = \bar{q}_3(s)e^{i\omega t}$. According to reference [9] the general integral of the homogeneous differential equation of equation (19) is given by the formula (23), in which the functions $\overset{*}{\Phi}_i$ ($i = 1, 2, \dots, 6$) have the following expressions:

Case *a*:

$$\overset{*}{\Phi}_1=\sin r_1 s,\overset{*}{\Phi}_2=\cos r_1 s,\overset{*}{\Phi}_3=\sinh us\cos\lambda s,$$
$$\overset{*}{\Phi}_4=\cosh ux\cos\lambda s,\overset{*}{\Phi}_5=\sinh us\sin\lambda s,\overset{*}{\Phi}_6=\cosh us\sin\lambda s \tag{32}$$

where r_1, u, λ are computed from relations (46) given in Appendix 2.

Case *b*: $\overset{*}{\Phi}_1=\sinh r_1 s,\overset{*}{\Phi}_2=\cosh r_1 s$ (33)

The functions $\overset{*}{\Phi}_3$, $\overset{*}{\Phi}_4$, $\overset{*}{\Phi}_5$, $\overset{*}{\Phi}_6$ have the same expressions as in Case *a* and r_1, u, λ are computed from relations (47) given in Appendix 2.

Case *c*:

$$\overset{*}{\Phi}_1=\sin r_1 s,\overset{*}{\Phi}_2=\cos r_1 s,\overset{*}{\Phi}_3=\sin\lambda s,$$
$$\overset{*}{\Phi}_4=\cos\lambda s,\overset{*}{\Phi}_5=\sin us \quad\text{or}\quad \sinh us,\overset{*}{\Phi}_6=\cos us \quad\text{or}\quad \cosh us \tag{34}$$

where r_1, u, λ are computed from relations (48) given in Appendis 2.

Case *d*: $\overset{*}{\Phi}_1=\sinh r_1 s,\overset{*}{\Phi}_2=\cosh r_1 s$ (35)

The functions $\overset{*}{\Phi}_3$, $\overset{*}{\Phi}_4$, $\overset{*}{\Phi}_5$, $\overset{*}{\Phi}_6$ have the same expressions as in Case *c* and r_1, u, λ are computed from relations (49) given in Appendix 2.

The determination of the natural frequencies of the beam will be established by using equations (19), (21), and the following boundary conditions:

At $s = 0$

$$\bar{y}_3(0,t)=\bar{\psi}_1(0,t)=\bar{\psi}_2(0,t)=0 \tag{36}$$

At $s = \bar{s}$ (total length of the curved beam)

$$\bar{y}_3(\bar{s},t)=\bar{\psi}_1(\bar{s},t)=\bar{\psi}_2(\bar{s},t)=0$$

So, using equation:

$$\bar{\mathbf{y}}(s,t)=\mathbf{A}(s)\mathbf{C}\,e^{i\overset{*}{\Omega}t}, \tag{37}$$

in which

$$\bar{\mathbf{y}}=(\bar{y}_3,\bar{\psi}_1,\bar{\psi}_2)^T,\mathbf{A}=[\alpha_{ij}],$$
$$\mathbf{C}=(c_1,c_2,\dots,c_6)^T,(i,j=1,2,\dots,6)$$

and the boundary conditions (36), for the nontrivial solution, the following determinant must be zero:

$$\begin{Vmatrix} \alpha_{11}(0) & \alpha_{12}(0) & \alpha_{13}(0) & \alpha_{14}(0) & \alpha_{15}(0) & \alpha_{16}(0) \\ \alpha_{21}(0) & \alpha_{22}(0) & \alpha_{23}(0) & \alpha_{24}(0) & \alpha_{25}(0) & \alpha_{26}(0) \\ \alpha_{31}(0) & \alpha_{32}(0) & \alpha_{33}(0) & \alpha_{34}(0) & \alpha_{35}(0) & \alpha_{36}(0) \\ \alpha_{41}(\bar{s}) & \alpha_{42}(\bar{s}) & \alpha_{43}(\bar{s}) & \alpha_{44}(\bar{s}) & \alpha_{45}(\bar{s}) & \alpha_{46}(\bar{s}) \\ \alpha_{51}(\bar{s}) & \alpha_{52}(\bar{s}) & \alpha_{53}(\bar{s}) & \alpha_{54}(\bar{s}) & \alpha_{55}(\bar{s}) & \alpha_{56}(\bar{s}) \\ \alpha_{61}(\bar{s}) & \alpha_{62}(\bar{s}) & \alpha_{63}(\bar{s}) & \alpha_{64}(\bar{s}) & \alpha_{65}(\bar{s}) & \alpha_{66}(\bar{s}) \end{Vmatrix} = 0 \tag{38}$$

Table 1 Dimensionless eigenfrequencies $\Omega = \overset{*}{\Omega}^2 F\epsilon\bar{s}^{+4}/EI_3 g$

$1/\bar{k} = 1/Kh_1$ \ $\bar{\lambda}$	40	
3.333	6.227×10^{0}	5.560×10^{0}
6.667	1.485×10^{-1}	1.370×10^{-1}
13.333	2.257×10^{-5}	2.202×10^{-5}

Table 2 Dimensionless eigenfrequencies $\Omega = \overset{*}{\Omega}^2 F\epsilon\bar{s}^{+4}/EL_3 g$

$1/\bar{k} = 1/K\bar{h}_2$ \ $\bar{\lambda}$	100	
8.571	6.175×10^{0}	5.980×10^{0}
17.143	1.434×10^{-1}	1.396×10^{-1}
34.286	2.255×10^{-5}	2.248×10^{-5}

The elements of the previous determinant have the following expressions for each of the foregoing cases:

Case *a*: $\alpha_{11}=0,\alpha_{12}=1,\alpha_{13}=0,\alpha_{14}=1,\alpha_{15}=0,\alpha_{16}=0,\alpha_{21}=0,$

$\alpha_{22}=a_0,\alpha_{23}=0,\alpha_{24}=d_0,\alpha_{25}=-f_0,$

$\alpha_{26}=0,\alpha_{31}=a_1,\alpha_{32}=0,$

$\alpha_{33}=d_1,\alpha_{34}=0,\alpha_{35}=0,\alpha_{36}=-f_1,\alpha_{41}=\overset{*}{\bar{\Phi}}_1,\alpha_{42}=\overset{*}{\bar{\Phi}}_2,$

$\alpha_{43}=\overset{*}{\bar{\Phi}}_3,\alpha_{44}=\overset{*}{\bar{\Phi}}_4,\alpha_{45}=\overset{*}{\bar{\Phi}}_5,\alpha_{46}=\overset{*}{\bar{\Phi}}_6,$

$\alpha_{51}=a_0\overset{*}{\bar{\Phi}}_1,\alpha_{52}=a_0\overset{*}{\bar{\Phi}}_2,$ (39)

$\alpha_{53}=d_0\overset{*}{\bar{\Phi}}_3+f_0\overset{*}{\bar{\Phi}}_6,\alpha_{54}=d_0\overset{*}{\bar{\Phi}}_4+f_0\overset{*}{\bar{\Phi}}_5,\alpha_{55}=d_0\overset{*}{\bar{\Phi}}_5-f_0\overset{*}{\bar{\Phi}}_4,$

$\alpha_{56}=d_0\overset{*}{\bar{\Phi}}_6-f_0\overset{*}{\bar{\Phi}}_3,\alpha_{61}=a_1\overset{*}{\bar{\Phi}}_2\alpha_{62}=-a_1\overset{*}{\bar{\Phi}}_1,$

$\alpha_{63}=d_1\overset{*}{\bar{\Phi}}_4+f_1\overset{*}{\bar{\Phi}}_5,$

$\alpha_{64}=d_1\overset{*}{\bar{\Phi}}_3+f_1\overset{*}{\bar{\Phi}}_6,\alpha_{65}=d_1\overset{*}{\bar{\Phi}}_6-f_1\overset{*}{\bar{\Phi}}_3,$

$\alpha_{66}=d_1\overset{*}{\bar{\Phi}}_5-f_1\overset{*}{\bar{\Phi}}_4$

Case *b*: $\alpha_{62}=a_1\overset{*}{\bar{\Phi}}_1$ (40)

The remaining elements will have the same expressions as in Case *a*, if the functions $\overset{*}{\bar{\Phi}}_i$ $(i=1,\ldots,6)$ are substituted with those given in relations (33).

Case *c*: $\alpha_{11}=0,\alpha_{12}=1,\alpha_{13}=0,\alpha_{14}=1,\alpha_{15}=0,\alpha_{16}=1,\alpha_{21}=0,$

$\alpha_{22}=a_0,\alpha_{23}=0,\alpha_{24}=d_0,\alpha_{25}=0,\alpha_{26}=f_0,\alpha_{31}=$

$a_1,\alpha_{32}=0,$

$\alpha_{33}=d_1,\alpha_{34}=0,\alpha_{35}=f_1,\alpha_{36}=0,$

$\alpha_{41}=\overset{*}{\bar{\Phi}}_1,\alpha_{42}=\overset{*}{\bar{\Phi}}_2,\alpha_{43}=\overset{*}{\bar{\Phi}}_3,$

$\alpha_{44}=\overset{*}{\bar{\Phi}}_4,\alpha_{45}=\overset{*}{\bar{\Phi}}_5,$

$\alpha_{46}=\overset{*}{\bar{\Phi}}_6,\alpha_{51}=a_0\overset{*}{\bar{\Phi}}_1,\alpha_{52}=a_0\overset{*}{\bar{\Phi}}_2,\alpha_{53}=d_0\overset{*}{\bar{\Phi}}_3,$ (41)

$\alpha_{54}=d_0\overset{*}{\bar{\Phi}}_4,\alpha_{55}=f_0\overset{*}{\bar{\Phi}}_5,\alpha_{56}=f\overset{*}{\bar{\Phi}}_6,$

$\alpha_{61}=a_1\overset{*}{\bar{\Phi}}_2,\alpha_{62}=-a_1\overset{*}{\bar{\Phi}}_1,$

$\alpha_{63}=d_1\overset{*}{\bar{\Phi}}_4,\alpha_{64}=-d_1\overset{*}{\bar{\Phi}}_3,\alpha_{65}=f_1\overset{*}{\bar{\Phi}}_6,$

$\alpha_{66}=-f_1\overset{*}{\bar{\Phi}}_5$ or $f_1\overset{*}{\bar{\Phi}}_5$

Case *d*: $\alpha_{62}=a_1\overset{*}{\bar{\Phi}}_2$ (42)

The remaining elements will have the same expressions as in Case *c*, if the functions $\overset{*}{\bar{\Phi}}_i$ $(i=1,\ldots,6)$ are substituted with those given in relations (35).

The coefficients a_j, d_j, f_j $(j=0,1)$ corresponding to each of the previous cases are given in Appendix 2. Finally, bar over the function $\overset{*}{\bar{\Phi}}_i$ denotes the value of this function for the total length $\bar{s}$ of the curved beam.

The eigenfrequency equation (38) is solved numerically on a digital computer for various values of the slenderness ratio $\bar{\lambda} = (\bar{s}^2F/I_3)^{1/2}$ and the ratio $1/\kappa h$ for the case of a stubby and a slender beam of square cross section of sides h. The respective numerical results are presented in Tables 1 and 2. In all cases considered, the length $\bar{s}(=\bar{\varphi}/\kappa)$ of the beam has been kept constant. The results in the first column of each table correspond to the dimensionless first eigenfrequencies, in which the influence of the transverse shear effect and rotatory inertia are omitted.

Table 1 is referred to a stubby beam with $\bar{s}/h_1 = 10.47$ and $\epsilon h_1/E = 1.08\times10^{-6}$. From this table the effect of the dimensionless radius of curvature $1/\bar{\kappa} = 1/\kappa h_1$ and slenderness ratio $\bar{\lambda}$ upon the dimensionless first eigenfrequency are given. It is clear that as $1/\bar{\kappa}$ increases (or equivalently the angle $\bar{\varphi}$ decreases since $\bar{s} = \bar{\varphi}/\kappa$ is constant) the first eigenfrequency decreases appreciably.

Table 2 is referred to a slender beam with $\bar{s}/h_2 = 26.91$ and $\epsilon h_2/E = 0.42\times10^{-6}$. From this table it can be seen that the same influence of $1/\kappa$ on the value of first eigenfrequency is also valid.

Finally, by comparing the results of Tables 1 and 2 the following conclusion may be derived: The effect of transverse shear deformations on the eigenfrequencies may be neglected even for practical design purposes for stabby beams; however, as the radius of curvature decreases this effect for stubby beams may be appreciable.

Conclusions

In this investigation an analytical treatment for the general solution of the problem of the three-dimensional harmonic vibrations of a circular beam, in the most general case of response, is presented; the torsion-flexure axes of the cross section of the beam coincide with the corresponding *Frénet* trihedron. Among the most important results of this investigation one may list the following:

1. The decoupling of the partial linear vectorial differential system governing the three-dimensional motion of the beam.
2. The proof that, in the general case of three-dimensional vibration, the system corresponding to the previous homogeneous one has two independent natural frequencies.
3. The possibility of determining these frequencies, inlcuding the effects of transverse shear deformation and rotatory inertia, and
4. For stubby beams with small values of the radius of curvature the transverse shear effect on the eigenfrequencies may be appreciable.

Acknowledgment

The research work continued in this paper is partly supported by the University Research Fund. The authors express their indebtness to this University agency financial support.

References

1 Ball, R. E., "Dynamic Analysis of Rings by Finite Differences," *Journal of the Engineering Mechanics Division, ASCE*, Vol. 93, 1967, pp. 1-10.

2 Culver, G. C., "Natural Frequencies of Horizontally Curved Beams," *Journal of the Structural Division, ASCE*, Vol. 93, 1967, pp. 189-203.

3 Volterra, E., "Vibrations of Circular Elastic Rings," *Israel Journal of Technology*, Vol. 5, 1967, pp. 225–233.

4 Tan, C. P., and Shore, S., "Dynamic Response of a Horizontally Curved Bridge," *Journal of the Structural Division, ASCE*, Vol. 94, 1968, pp. 761–781.

5 Tan, C. P., and Shore, S., "Response of Horizontally Curved Bridge to Moving Load," *Journal of the Structural Division, ASCE*, Vol. 94, 1968, pp. 2135–2151.

6 Rao, S. S., "Effects of Transverse Shear and Rotatory Inertia on the Coupled Twist-Bending Vibrations of Circular Rings," *Journal of Sound and Vibration*, Vol. 16, 1971, pp. 551–556.

7 Kirkhope, J., "Out-of-Plane Vibration of Thick Circular Ring," *Journal of the Engineering Mechanics Division, ASCE*, Vol. 102, 1976, pp. 239–247.

8 Joseph, T. P., and Wilson, J. F., "Vibrations of Curved Spans for Mass Transit," *Journal of the Engineering Mechanics Division, ASCE*, Vol. 106, 1980, pp. 255–272.

9 Panayotounakos, D. E., and Theocaris, P. S., "The Dynamically Loaded Circular Beam on an Elastic Foundation," ASME JOURNAL OF APPLIED MECHANICS, Vol. 47, 1980, pp. 139–144.

10 Wang, T. M., and Brannen, N. F., "Natural Frequencies for Out-of-Plane Vibrations of Curved Beams on Elastic Foundation," *Journal of Sound and Vibration*, Vol. 84, 1982, pp. 241–246.

11 Panayotounakos, D. E., and Theocaris, P. S., "A Closed Form Solution for the Static Analysis of Skew-Curved Beams," *Journal de Mécanique Appliquée*, Vol. 4, 1980, pp. 83–102.

APPENDIX 1

The coefficients of the linear partial differential equation (10) are given by:

$$\sigma_1 = 2\kappa^2; \sigma_2 = \kappa^4; \sigma_3 = -mb_3\kappa^2\left(\kappa^2 + \frac{a_1}{b_3}\right); \sigma_4 =$$

$$-\left[\left(2\kappa^2 - \frac{a_2}{b_3}\right)mb_3 - \kappa^2(a_1 I_2 + a_2 I_1)\right]; \sigma_5 = -mb_3; \sigma_6$$

$$= -mb_3\left[(a_1 I_2 + a_2 I_1) + \frac{a_2 a_1}{b_3} I_1\right]; \sigma_7 = a_1 a_2 I_1 I_2; \sigma_8$$

$$= -mb_3 a_1 a_2 I_1 I_2; \sigma = a_2 \overset{*}{m}_2''' - a_2\vartheta_{11}\overset{*}{m}_2' - a_2 a_1 I_1 \overset{*}{m}_2' \tag{43}$$

$$-n_{21}a_1\overset{*}{m}_1'' - \vartheta_{11}\vartheta_{22}b_3 q_3 - a_1 a_2 I_1 I_2 b_3 q_3 - b_3 q_3''''$$

$$+ (\vartheta_{22} + \vartheta_{11} + n_{12}n_{21})b_3 q_3'' - (\vartheta_{11}a_2 I_2 + \varphi_{22}a_1 I_1)b_3\ddot{q}_3$$

The coefficients of the linear partial differential equations (11) are given by:

$$\rho_1 = -\kappa^2; \rho_2 = mb_1; k_1 = \kappa^2; k_2 = \kappa^3; k_3$$

$$= mb_1\kappa; k = b_1 q_1' + b_1\kappa q_2; \delta_1 = \frac{1}{b_1}(b_2\kappa^2 + a_3);$$

$$\delta_2 = mb_2 + a_3 I_3\left(1 + \frac{b_2}{b_3}\right); \mu_1 = -\kappa\left(1 + \frac{b_2}{b_1}\right)$$

$$-\frac{a_3}{b_1\kappa}; \mu_2 = \frac{a_3 m}{\kappa} + a_3 I_3\kappa; \mu_3 = -a_3 I_3\frac{b_2}{b_1\kappa};$$

$$\mu_4 = a_3 I_3\frac{b_2}{\kappa}; \mu = -a_3\overset{*}{m}_3 + b_2 q_2' + \frac{a_3}{\kappa}q_1 + a_3 I_3\frac{b_2}{\kappa}q_1$$

The coefficients of the linear ordinary differential equation (20) are:

$$A = k_1\delta_1 + k_2 - (k_1\delta_2 + k_3)\overset{*}{\omega}^2; B = k_1\mu_1 + \rho_1$$

$$-(k_1\mu_3 + \rho_2)\overset{*}{\omega}^2; \Gamma = k_1(-\mu_2\overset{*}{\omega}^2 + \mu_4\overset{*}{\omega}^4);$$

$$\Delta = k_1\delta_1 - k_2 - (k_1\delta_2 - k_3)\overset{*}{\omega}^2; E = \delta_1 - \delta_2\overset{*}{\omega}^2;$$

$$Z = k_2\mu_1 - \delta_1\rho_1 + (\rho_1\delta_1 + \rho_2\delta_1 - \mu_1 k_3 - k_2\mu_3)\overset{*}{\omega}^2$$

$$+ (k_3\mu_3 - \delta_2\rho_2)\overset{*}{\omega}^4; H = (k_2 - k_3\overset{*}{\omega}^2)(-\mu_2\overset{*}{\omega}^2 + \mu_4\overset{*}{\omega}^4) \tag{45}$$

APPENDIX 2

The expressions of r_1, u, λ for the four characteristics cases are as follows:

$$\text{Case } a\text{: } r_1 = (|z_1| + \overset{*}{F}_1/3)^{1/3}, u = \left\{[\overset{*}{\rho}_1 + (\overset{*2}{\rho}_1 + \rho_2)^{1/2}]/2\right\}^{1/2}. \tag{46}$$

$$\lambda = \rho_2/2\left\{[\overset{*}{\rho}_1 + (\overset{*2}{\rho}_1 + \rho_2)^{1/2}]/2\right\}^{1/2}$$

where:

$$z_1 = -[\sqrt[3]{|\upsilon\upsilon/2| + \tau^{1/2}} + \sqrt[3]{|\upsilon/2| - \tau^{1/2}}] < 0$$

$$\overset{*}{\rho}_1 = -(1/2)z_1 - \overset{*}{F}_1/3, \rho_2 = \{(3z_1^2 + 4\Pi/4\}^{1/2} \tag{46a}$$

$$\text{Case } b\text{: } r_1 = (z_1 - \overset{*}{F}_1/3)^{1/3} \tag{47}$$

and u, λ have the same expressions as in Case a.

$$z_1 = \sqrt[3]{\upsilon/2 + \tau^{1/2}} + \sqrt[3]{\upsilon/2 - \tau^{1/2}} > 0 \tag{47a}$$

and $\overset{*}{\rho}_1$, ρ_2 have the same expressions as in Case a.

$$\text{Case } c\text{: } r_1 = [(\overset{*}{F}_1/3) - |z_1|]^{1/2}$$

$$u = (|z_2| + \overset{*}{F}_1/3)^{1/2} \tag{48}$$

$$\lambda = (|z_3| + \overset{*}{F}_1/3)^{1/2} \quad \text{or} \quad \lambda = (\overset{*}{F}_1/3 - |z_3|)^{1/2}$$

where:

$$z_1 - 2\sqrt{|\Pi|/3}\cos(x/3) > 0, 0 < x = \arccos[(\upsilon/2)\sqrt{27/\Pi^3}] < \pi$$

$$z_2 = -2\sqrt{|\Pi|/3}\cos[(\pi - x)/3] < 0 \tag{48a}$$

$$z_3 = -2\sqrt{|\Pi|/3}\cos[(\pi + x)/3] \lesseqgtr 0$$

$$\text{Case } d\text{: } r_1 = (|z_1| - \overset{*}{F}_1/3)^{1/2} \tag{49}$$

and u, λ, z_1, z_2, z_3 have the same expressions as in Case c.

For the four preceding cases we have:

$$\upsilon = (-2/27)\overset{*3}{F}_1 + (1/3)\overset{*}{F}_1\overset{*}{F}_2 - \overset{*}{F}_3, \Pi = \overset{*}{F}_2 - \overset{*2}{F}_1/3,$$

$$\tau = \upsilon^2/4 + \Pi^3/27, \overset{*}{F}_1 = \sigma_1 - \overset{*}{\Omega}^2\sigma_5, \overset{*}{F}_2 = \sigma_2 - \overset{*}{\Omega}^2\sigma_4$$

$$+ \overset{*}{\Omega}^4\sigma_7, \overset{*}{F}_3 = -\sigma_3 + \overset{*}{\Omega}^2\sigma_6 - \overset{*}{\Omega}^4\sigma_8 \tag{50}$$

The coefficients a_j, d_j, f_j $(j = 0, 1)$ for the foregoing cases are:

$$\text{Case } a\text{: } a_0 = -A_2 r_1^4 + (A_1 + A_2 K + A_3)r_1^2 - A_1 K$$

$$d_0 = -A_2(u^4 + \lambda^4 - 6u^2\lambda^2)$$

$$-(A_1 + A_2 K + A_3)(u^2 - \lambda^2) - A_1 K$$

$$f_0 = -4A_2 u\lambda(\lambda^2 - u^2) \pm 2(A_1 + A_2 K + A_3)u\lambda \tag{51}$$

$$a_1 = K_1 r_1^5 - K_2 r_1^3 + K_3 r_1$$

$$d_1 = K_1 u(u^4 + \lambda^4 - 6u^2\lambda^2) + 4u\lambda^2(\lambda^2 - u^2)$$

$$+ K_2(u^3 - 3u\lambda^2) + K_3 u$$

$$f_1 = K_1 4u^2\lambda(\lambda^2 - u^2) \mp \lambda(u^4 + \lambda^4 - 6u^2\lambda^2)$$

$$+ K_2(\lambda^3 - 3u^2\lambda) - K_3\lambda$$

$$\text{Case } b\text{: } a_0 = -A_2 r_1^4 - (A_1 + A_2 K + A_3)r_1^2 - A_1 K \tag{52}$$

$$a_1 = K_1 r_1^5 + K_2 r_1^3 + K_3 r_1$$

The remaining coefficients have the same expressions as in Case a.

Case c:
$$\begin{aligned} a_0 &= -A_2 r_1^4 + (A_1 + A_2 K + A_3) r_1^2 - A_1 K \\ d_0 &= -A_2 \lambda^4 - (A_1 + A_2 K + A_3)\lambda^2 - A_1 K \\ f_0 &= -A_2 u^4 - (A_1 + A_2 K + A_3) u^2 - A_1 K \\ a_1 &= K_1 r_1^5 - K_2 r_1^3 + K_3 r_1 \\ d_1 &= K_1 \lambda^5 - K_2 \lambda^3 + K_3 \lambda \\ f_1 &= K_1 u^5 - K_2 u^3 + K_3 u \end{aligned} \tag{53}$$

Case d:
$$\begin{aligned} a_0 &= -A_2 r_1^4 - (A_1 + A_2 K + A_3) r_1^2 - A_1 K \\ a_1 &= K_1 r_1^5 + K_2 r_1^3 + K_3 r_1 \end{aligned} \tag{54}$$

The remaining coefficients have the same expressions as in Case c.

For all the previous cases we have:

$$A_1 = \frac{a_2 \mathrm{I}_2 \overset{*}{\Omega}^2 - \vartheta_{22} - n_{12} n_{21}}{n_{21}(\vartheta_{11} - a_1 \mathrm{I}_1 \overset{*}{\Omega}^2)}, \quad A_2 = \frac{1}{n_{21}(\vartheta_{11} - a_1 \mathrm{I}_1 \overset{*}{\Omega}^2)}, \quad A_3 = \frac{I_{23}}{n_{21}(\vartheta_{11} - a_1 \mathrm{I}_1 \overset{*}{\Omega}^2)}$$

$$K = m b_3 \overset{*}{\Omega}^2, \quad K_1 = A_2 \frac{n_{21}}{\vartheta_{22} - a_2 \mathrm{I}_2 \overset{*}{\Omega}^2}, \quad K_2 - \{ (A_1 + A_2 K + A_3) n_{21} - 1 \} \frac{1}{\vartheta_{22} - a_1 \mathrm{I}_1 \overset{*}{\Omega}^2},$$

$$K_3 = A_1 \frac{n_{21}}{\vartheta_{22} - a_2 \mathrm{I}_2 \overset{*}{\Omega}^2} - \frac{m b_3 \overset{*}{\Omega}^2 + I_{23}}{\vartheta_{22} - a_2 I_2 \overset{*}{\Omega}^2} \tag{55}$$

Influence of Geometric Imperfections and In-Plane Constraints on Nonlinear Vibrations of Simply Supported Cylindrical Panels

David Hui
Assistant Professor,
Department of Engineering Mechanics,
The Ohio State University,
Columbus, Ohio 43210
Mem. ASME

This papers deals with the effects of initial geometric imperfections on large-amplitude vibrations of cylindrical panels simply supported along all four edges. In-plane movable and in-plane immovable boundary conditions are considered for each pair of parallel edges. Depending on whether the number of axial and circumferential half waves are odd or even, the presence of geometric imperfections (taken to be of the same shape as the vibration mode) of the order of the shell thickness may significantly raise or lower the linear vibration frequencies. In general, an increase (decrease) in the linear vibration frequency corresponds to a more pronounced soft-spring (hard-spring) behavior in nonlinear vibration.

1 Introduction

The first investigation of the large-amplitude vibration of simply supported circular cylindrical shells was performed by Reissner [1]. Subsequent results by Chu [2] and Nowinski [3] show that the nonlinearity of this vibration problem was always of the hardening type. Evensen and Fulton [4] and Evensen [5] demonstrated that the nonlinearity may be either of the hardening or softening type depending on Evensen's aspect ratio and Evensen's nonlinearity parameter. They based their argument on the fact that the earlier results [1–3] failed to satisfy the singlevaluedness requirement of the circumferential displacement and they demonstrated the need to include the driven mode as well as the companion mode [4–6]. Their findings were qualitatively supported by experiments [7, 8] and an excellent summary of the historical developments (which includes the works of M. D. Olson, E. H. Dowell and C. S. Ventres, S. Atluri and J. H. Ginsberg, etc.) can be found in a review paper by Evensen [9].

The large-amplitude vibrations of open cylindrical panels were examined by Reissner [1] and followed by Cummings [10, 11]. It was found that the nonlinearity of this vibration problem can be classified as soft-spring or hard-spring type. Extension of the work to include the effects of nonlinear elastic foundations were examined [12, 13].

The effects of geometric imperfections on the large-amplitude vibrations of rectangular plates, circular plates, and spherical shells have been examined in the author's earlier papers [14–16]. The effects of imperfections on nonlinear vibrations of closed cylindrical shells have also been investigated by Watawala and Nash [17]. However, the effects of geometric imperfections on large-amplitude vibrations of open cylindrical shells simply supported at all four edges have not been examined. Further, the influence of various types of in-plane boundary conditions (which have been demonstrated to be of major concern in linear-free vibrations of cylindrical shells [18]) have also not been studied. Since the cylindrical panels are open, the singlevaluedness requriements of the displacements need not and in fact, should not be enforced.

The present analysis is based on a solution of the nonlinear Donnell-type dynamic equilibrium and compatibility differential equations for a cylindrical panel written in terms of a stress function and an out-of-plane displacement. The geometric imperfections are taken to be of the same spatial shape as the vibration mode. Based on the assumed sinusoidal vibration mode shape, the stress function that satisfies the nonlinear compatibility equation exactly is sought. The nonlinear dynamic equilibrium equation is then satisfied approximately using the Galerkin procedure.

Depending on whether the number of axial and circumferential half-waves are odd or even, the presence of geometric imperfection may significantly raise or lower the

Contributed by the Applied Mechanics Division for presentation at the 1984, PVP Conference and Exhibition, Joint with Applied Mechanics Division and Materials Division, San Antonio, Texas, June 17–21, 1984 of THE AMERICAN SOCIETY OF MECHANICAL ENGINEERS.

Discussion on this paper should be addressed to the Editorial Department, ASME United Engineering Center, 345 East 47th Street, New York, N.Y. 10017, and will be accepted until two months after final publication of the paper itself in the JOURNAL OF APPLIED MECHANICS. Manuscript received by ASME Applied Mechanics Division, January, 1983; Final revision, July, 1983. Paper No. 84-APM-14.

Copies will be available until February, 1985.

linear vibration frequencies. Furthermore, the increase (decrease) of the linear vibration frequency generally corresponds to a more pronounced soft-spring (hard-spring) nonlinear vibration behavior. In the special case of perfect cylindrical panels (zero imperfection amplitude) it is found that the in-plane boundary conditions do not affect the linear frequencies, even though they may have a significant influence on the nonlinear hard-spring or soft-spring behaviors. The parameter variations involving the flatness parameter (Koiter [19] and Hui et al. [20]), the length to panel circumferential width ratio, and the number of axial and circumferential half-waves are examined.

2 Analysis

The dynamic analogue of the nonlinear Donnell-type differential equations for cylindrical shells written in terms of the out-of-plane displacement (positive outward) W and the stress function F, incorporating the possibility of the presence of geometric imperfections W_0 are (see [21] among others)

$$[(1+i\eta)\mathrm{E}h^3/(4c^2)]\,(W,_{XXXX}+W,_{YYYY}+2W,_{XXYY}) +(1/R)\,(F,_{XX})=Q(X,Y,\bar{t})-\rho W,_{\bar{t}\bar{t}}+F,_{YY}\,(W+W_0),_{XX} +F,_{XX}\,(W+W_0),_{YY}-2F,_{XY}\,(W+W_0),_{XY} \quad (1)$$

$$\{1/[\mathrm{E}h(1+i\eta)]\}\,(F,_{XXXX}+F,_{YYYY}+2F,_{XXYY}) =(1/R)\,(W,_{XX})+[(W,_{XY})^2+2W_{0,XY}W,_{XY} -(W+W_0),_{XX}W,_{YY}-W_{0,YY}W,_{XX}] \quad (2)$$

where $c=[3(1-\nu^2)]^{1/2}$, ν is Poisson's ratio, X and Y are the axial and circumferential coordinates, R is the shell radius, h is the thickness, E is Young's modulus, ρ is the shell mass per unit area, $Q(X,Y,\bar{t})$ is the forcing function, $\bar{t}$ is the time, $i=(-1)^{1/2}$, and η is the loss factor associated with the complex modulus model for structural damping.

Introducing the nondimensional quantities ($q_0=(2cR/h)^{1/2}$),

$$(w,w_0)=(W,W_0)/h,\quad f=2cF/(Eh)^3),\quad (x,y)=(q_0/R)\,(X,Y)$$
$$q(x,y,t)=[2R^2/(\mathrm{E}h^2)]Q(X,Y,\bar{t}),\quad t=\omega_r\bar{t},\quad (\omega_r)^2=\mathrm{E}h/(2\rho R^2) \quad (3)$$

where ω_r is the reference frequency, the nondimensional nonlinear dynamic equilibrium and compatibility equations for cylindrical panels become

$$(1+i\eta)\,(w,_{xxxx}+w,_{yyyy}+2w,_{xxyy})+f,_{xx} =(1/2)q(x,y,t)-(1/2)w,_{tt} \quad (5)$$
$$+(2c)[f,_{xx}(w+w_0),_{yy}+f,_{yy}(w+w_0),_{xx}-2f,_{xy}(w+w_0),_{xy}]$$

$$[1/(1+i\eta)]\,(f,_{xxxx}+f,_{yyyy}+2f,_{xxyy}) =w,_{xx}+(2c)[(w+2w_0),_{xy}w,_{xy} -(w+w_0),_{xx}w,_{yy}-w_{0,yy}w,_{xx}] \quad (6)$$

The vibration mode, the initial goemetric imperfections, and the forcing function are assumed to have the same spatial distribution. The cylindrical panels are simply supported at all four edges so that [14],

$$[w(x,y,t),\,w_0(x,y),\,q(x,y,t)] =[w(t),\,\mu,\,q(t)]\sin(Mx)\,\sin(Ny) \quad (7)$$

where $w(t)$ and μ are the vibration and imperfection amplitudes normalized with respect to the shell thickness. Furthermore, the axial and circumferential nondimensional wave numbers M and N are defined to be (the symbol n is never used in this paper in order to avoid confusion with the number of circumferential full-waves in a closed circular cylindrical shell),

$$M=m\pi R/(Lq_0)=md/(2\theta L),\quad N=\bar{n}/(2\theta),\quad \theta=q_0d/(2\pi R) \quad (8)$$

In the foregoing, θ is the flatness parameter, d is the width of the cylindrical panel defined by the circumferential curved distance between the two longitudinal edges, L is the shell length, and the integers m and $\bar{n}$ are the number of half-waves in the longitudinal ($X=0$ to L) and circumferential ($Y=0$ to d) directions, respectively. The flatness parameter is introduced in order to lump the effects of the radius to thickness ratio and the radius to panel width ratio into a single parameter.

It will be shown from the computation of the definite integrals that is is necessary to specify the integers m and $\bar{n}$ in addition to the specification of the wave numbers M and N. Alternatively, one may specify m, $\bar{n}$, θ, and L/d. To compare the results for cylindrical panels with that of a complete circular cylindrical shell, it is convenient to define Evensen's nonlinearity parameter ϵ and Evensen's aspect ratio ξ in terms of the present notation.

$$\delta(\text{Evensen})=4c^2N^4=c\bar{n}^2/\theta^2$$
$$\xi(\text{Evensen})=M/N=md/(L\bar{n}) \quad (9)$$

The in-plane boundary conditions at the two curved edges ($x=0$ and $x=q_0L/R$) are

$$f,_{yy}=0\quad\text{or}\quad u=0$$
$$f,_{xy}=0\quad\text{or}\quad v=0 \quad (10)$$

while at the two longitudinal edges $y=0$ and $y=2\pi\theta$, they are,

$$f,_{xy}=0\quad\text{or}\quad u=0$$
$$f,_{xx}=0\quad\text{or}\quad v=0 \quad (11)$$

Since the mixed formulation is employed, the displacement boundary conditions can only be satisfied in the average (see for example [7, 22]) among others. In-plane boundary conditions type 1, 2, 3, and 4 are considered in this paper (Appendix A).

Substituting $w_0(x.y)$ and $w(x,y,t)$ into equation (6), the stress function that satisfies the nonlinear compatibility equation exactly is,

$$f(x,y,t)=(1+i\eta)\{c_0w(t)\,\sin(Mx)\,\sin(Ny) +[w(t)^2+2\mu w(t)]\,[c_1\cos(2Mx)+c_2\cos(2Ny)] +\mathrm{E}_1(t)\,(x^2/2)+\mathrm{E}_2(t)\,(y^2/2)\} \quad (12)$$

where

$$c_0=\frac{-M^2}{(M^2+N^2)^2},\quad c_1=(c/16)(N/M)^2,\quad c_2=(c/16)(M/N)^2$$
$$[\mathrm{E}_1(t),\,\mathrm{E}_2(t)]=(e_1e_2)[w(t)^2+2\mu u)(t)] \quad (13)$$

Finally, substituting $w_0(x,y)$, $w(x,y,t)$, and $f(x,y,t)$ into the nonlinear equilibrium equation and applying the Galerkin procedure (multiplying both sides by $\sin(Mx)\,\sin(Ny)$ and then integrating over the shell area), one obtains,

$$(1+i\eta)\{[(M^2+N^2)^2-c_0M^2]w(t) +[w(t)^2+2\mu w(t)](4I_1H_1e_1)\}=(1/2)q(t)-(1/2)w(t),_{tt}$$
$$+(1+i\eta)[w(t)+\mu]\{(-d_1)[w(t)^2+2\mu w(t)]+d_2w(t)\} \quad (14)$$

where (d_1 and d_2 are independent of the geometric imperfection amplitude),

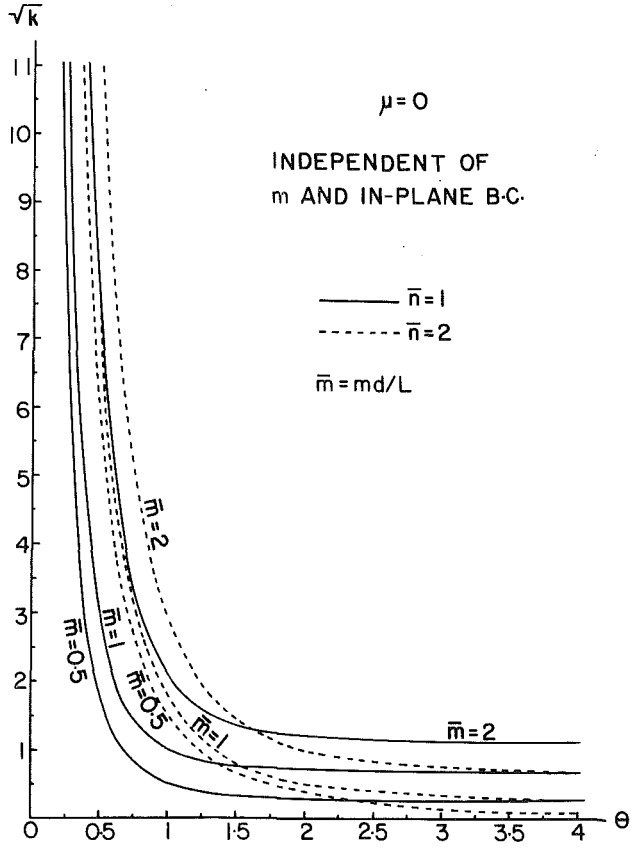

Fig. 1(*a*) Linear frequency ($k^{1/2}=\omega/\omega_r$) versus flatness parameter for perfect cylindrical panels

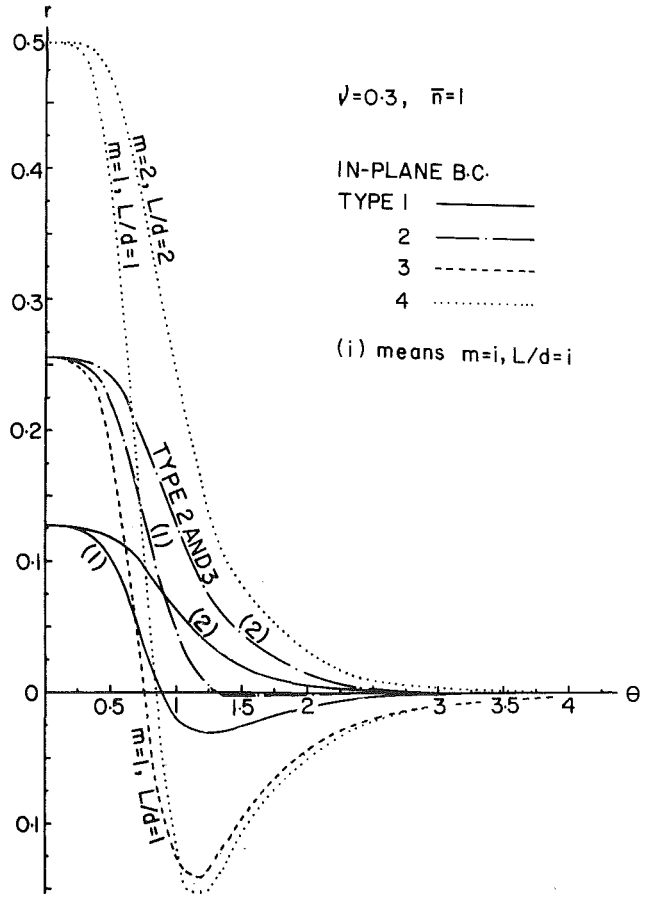

Fig. 1(*b*) Nonlinearity parameter versus flatness parameter for perfect cylindrical panels ($\bar{n}=1$)

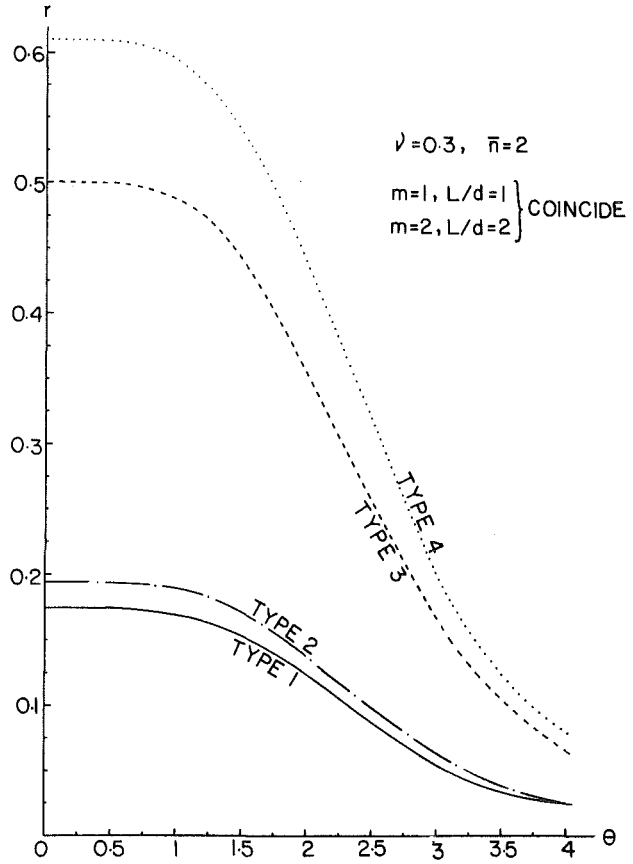

Fig. 1(*c*) Nonlinearity parameter versus flatness parameter for perfect cylindrical panels ($\bar{n}=2$)

Fig. 1

$$d_1=(2c)\ [N^2e_1+M^2e_2+2M^2N^2(c_1+c_2)]$$

$$d_2=(2c)\ (8M^2N^2c_0)(I_2H_2-I_3H_3) \tag{15}$$

In the foregoing, the integrals I_1, I_2, I_3, H_1, H_2, and H_3 are defined to be ($z=q_0L/R$),

$$(I_1, I_2, I_3)=(1/z)\int_0^z [\sin(Mx), \sin^3(Mx), \sin(Mx)\cos^2(Mx)]\,dx$$

$$(H_1, H_2, H_3)=[1/(2\pi\theta)]\int_0^{2\pi\theta} [\sin(Ny), \sin^3(Ny), \sin(Ny)\cos^2(Ny)]\,dy \tag{16}$$

Thus, if m is odd, $I_1=2/(m\pi)$, $I_2=4/(3m\pi)$, and $I_3=2/(3m\pi)$ while if m is even, $I_1=I_2=I_3=0$. Further if $\bar{n}$ is odd, $H_1=2/(\bar{n}\pi)$, $H_2=4/(3\bar{n}\pi)$, and $H_3=2/(3\bar{n}\pi)$ while if $\bar{n}$ is even, $H_1=H_2=H_3=0$. Finally, if both m and $\bar{n}$ are odd,

$$I_1H_1=4/(m\bar{n}\pi^2),\quad I_2H_2-I_3H_3=4/(3m\bar{n}\pi^2),$$

$$d_2=64cM^2N^2c_0/(3m\bar{n}\pi^2) \tag{17}$$

and otherwise, $I_1H_1=0$, $I_2H_2-I_3H_3=0$, and $d_2=0$. The quantities e_1 and e_2 are constants that depend on the in-plane boundary conditions and they are defined in Appendix A.

The preceding nonlinear ordinary differential equation in time can be written in terms of the well-known Duffing's equation with an additional quadratic term in the standard form,

$$w(t)_{,tt}+[kw(t)+(\epsilon ka_2)\,w(t)^2+(\epsilon k)\,w(t)^3](1+i\eta)=q(t) \tag{18}$$

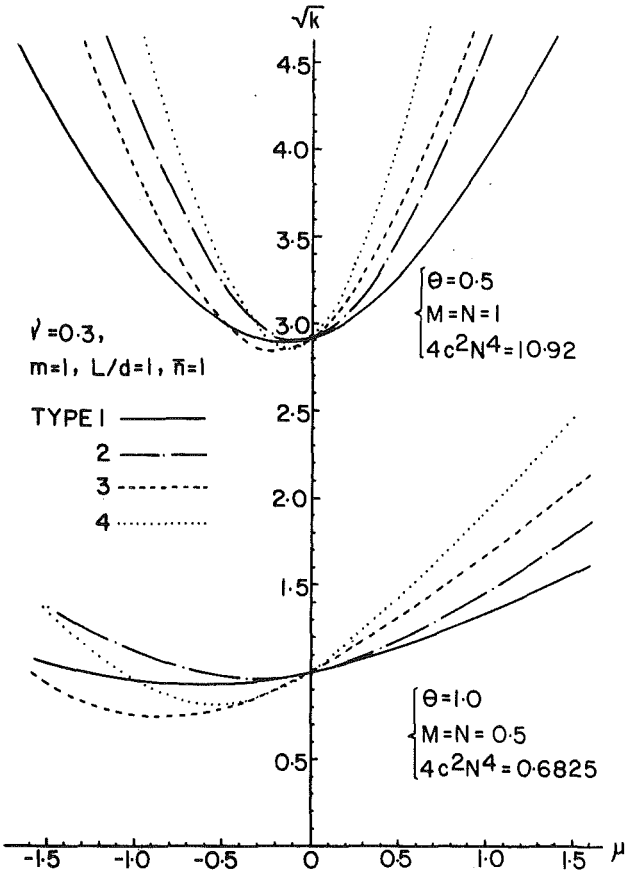

Fig. 2(a) Linear frequency ($k^{1/2} = \omega/\omega_r$) versus imperfection amplitude for $\theta = 0.5$ and 1 ($m = 1$, $L/d = 1$)

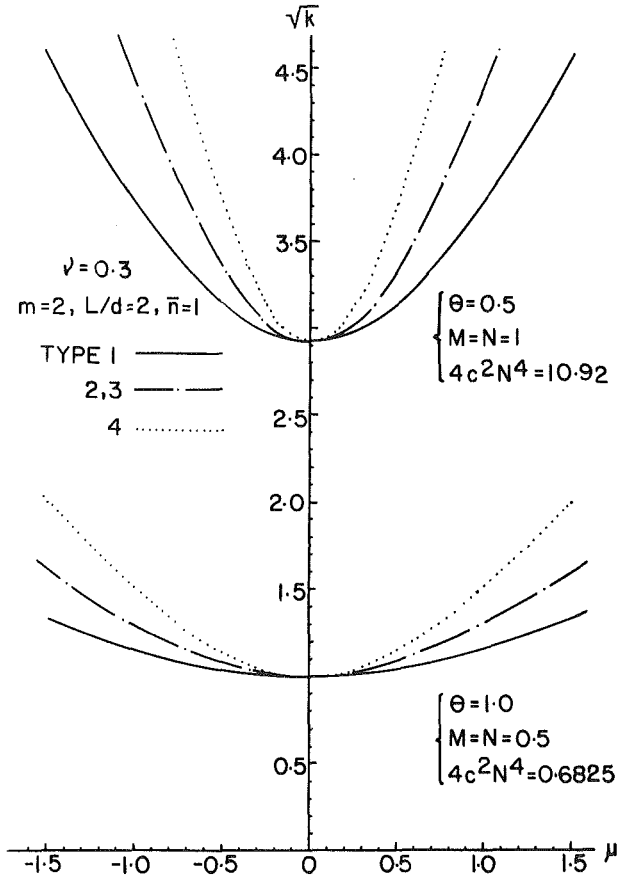

Fig. 2(b) Linear frequency ($k^{1/2} = \omega/\omega_r$)versus imperfection amplitude for $\theta = 0.5$ and 1 ($m = 2$, $L/d = 2$)

Fig. 2

where

$$k = (2)\{(M^2+N^2)^2 + [M^4/(M^2+N^2)^2] + (2\mu^2 d_1 - \mu d_2) + 8\mu I_1 H_1 e_1\}$$
$$\epsilon = 2d_1/k, \quad a_2 = (3\mu d_1 - d_2 + 4I_1 H_1 e_1)/d_1 \tag{19}$$

In the special case of an infinitely long perfect cylindrical panel ($\mu = 0$, $L/d =$ infinite, and $M = 0$), one obtains,

$$\epsilon k = 2N^4, \quad k = 4cN^2 e_1 \quad \text{and} \quad a_2 = 2I_1 H_1/(cN^2) \tag{20}$$

It should be noted that for a perfect cylindrical panel ($\mu = 0$), the linear vibration frequency defined by $k^{1/2}$ is independent of e_1 and e_2. That is, the linear vibration frequency is independent of the in-plane boundary conditions. Finally, since k in equations (18) and (19) are independent of the definite integrals I_1, I_2, I_3, H_1, H_2, and H_3, the linear vibration frequency is independent on whether the number of axial and circumferential half-waves are odd or even.

Assuming that the forcing function is periodic such that ($\Omega = \omega/\omega_r$)

$$q(t) = q_1 \cos(\omega \bar{t}) = q_1 \cos(\Omega t) \tag{21}$$

the solution of the linearized (neglecting the quadratic and cubic terms) differential equation is,

$$w(t) = A \cos(\Omega t) \tag{23}$$

where the absolute value of the complex quantity A is,

$$|A| = \frac{(q_1/k)}{\{[1-(\Omega^2/k)]^2 + \eta^2\}^{1/2}} \tag{23}$$

The backbone curves for large-amplitude free vibrations of simply supported cylindrical panels with no damping can be computed by solving the Duffing-type equation using Linstedt's perturbation method. It follows that the ratio of the nonlinear to the linear vibration frequency is related to the vibration amplitude A by (see the Appendix of [15] and note that A is measured from the deformed, static state),

$$\Omega/\Omega_0 = 1 + rA^2 - (15\,\epsilon^2 A^4/256) \tag{24}$$

where

$$r = (3\epsilon/8) - (5a_2{}^2\epsilon^2/12) = (3\epsilon/8)[1 - (10a_2{}^2\epsilon/9)] \tag{25}$$

Thus, at least for small values of the vibration amplitude A, the sign of the nonlinearity parameter r (not to be confused with Evensen's nonlinearity parameter defined in [4, 5]) determines whether the large-amplitude vibration of cylindrical panels is of the hardening or softening type. A positive value of r indicates hard-spring behavior while a negative value of r indicates soft-spring behavior. A larger positive value of r indicates a more pronounced hard-spring behavior.

3 Results and Discussions

Figure 1(a) shows a plot of the linear vibration frequency of perfect cylindrical panels (defined to be $k^{1/2} = \omega/\omega_r$) versus the flatness parameter (defined in equation (8)) for various values of md/L and $\bar{n}$. Note that the results for the perfect panels are independent of the in-plane boundary conditions as well as independent of whether the number of axial and circumferential half-waves are odd or even. The expression for k in equation (18) can be rewritten in the form ($\bar{m} = md/L$).

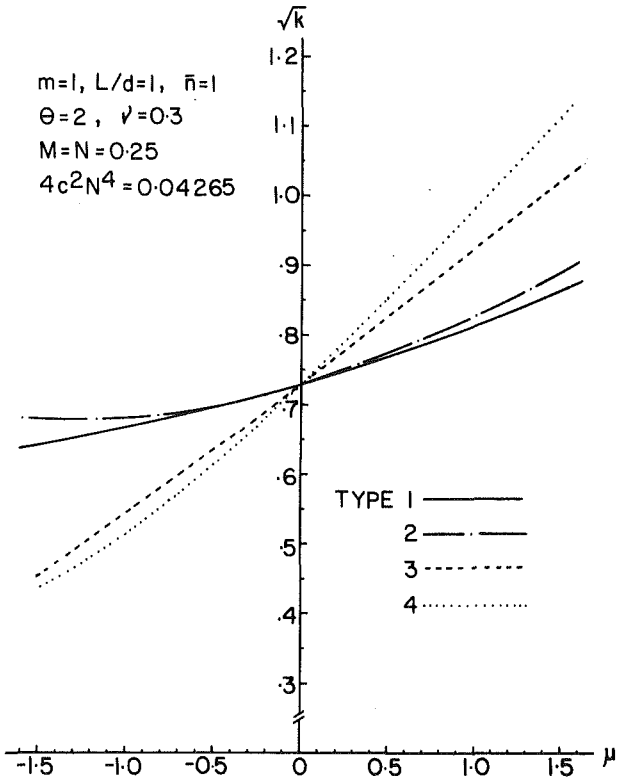

Fig. 3 Linear frequency ($k^{1/2} = \omega/\omega_r$) versus imperfection amplitude for $\theta = 2$ ($m = 1$, $L/d = 1$)

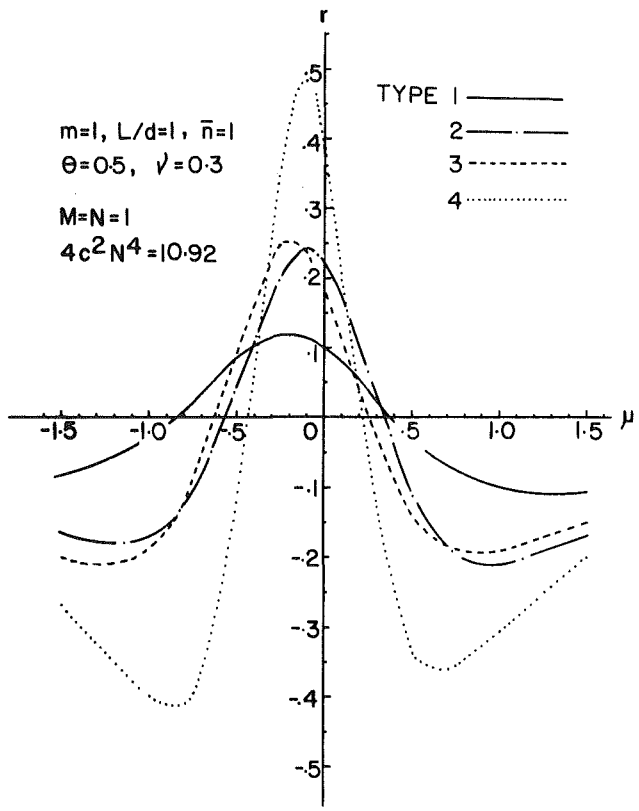

Fig. 4 Nonlinearity parameter versus imperfection amplitude for $\theta = 0.5$ and $\bar{n} = 1$ ($m = 1$, $L/d = 1$)

$$k = (2)\{[(\bar{m}^2 + \bar{n}^2)^2/(16\theta^4)] + [\bar{m}^4/(\bar{m}^2 + \bar{n}^2)^2]\} \tag{26}$$

where it may be observed that the term involving θ^4 will rapidly become negligible for $\theta \geq 4$.

The corresponding nonlinearity parameter r is shown in Fig. 1(b) for each of the four types of in-plane boundary conditions, keeping $\bar{n} = 1$. For a fixed value of the flatness parameter θ and for each type of in-plane boundary condition, it can be seen that the $m = 2$, $L/d = 2$ curves lie above the $m = 1$, $L/d = 1$ curves even though they both imply $md/L = 1$ (that is, the same value M). For a large value of the flatness parameter θ, the nonlinearity parameter approaches zero so that the nonlinear frequency is more or less the same as the linear frequency (at least for small-vibration amplitude). On the other hand, for sufficiently small values of θ, the nonlinearity parameter approaches the flat plate limit ($\theta = 0$) with zero slope. As noted earlier, a positive value of the nonlinearity parameter r denotes hard-spring behavior while a negative value of r denotes soft-spring behavior.

Figure 1(c) shows a plot of the nonlinearity parameter r versus the flatness parameter θ for perfect cylindrical panels for four types of in-plane boundary conditions, keeping $\bar{n} = 2$. Here, for each type of in-plane boundary condition, the curves for $m = 1$, $L/d = 1$ coincide with the curves for $m = 2$, $L/d = 2$ because the product of the integrals I_1H_1, I_2H_2, and I_3H_3 vanishes for $\bar{n} = 2$ regardless of whether m is odd or even. All four curves converge to zero for sufficiently large values of the flatness parameter θ.

Figure 2(a) shows a graph of the linear vibration frequency ($k^{1/2} = \omega/\omega_r$) versus the amplitude of the initial geometric imperfection μ for $\theta = 0.5$ and 1.0, keeping $m = 1$, $L/d = 1$, and $\bar{n} = 1$. Since the out-of-plane displacement is defined to be positive outward, it is clear that a positive value of the imperfection amplitude μ for the $m = 1$, $\bar{n} = 1$ case will further increase the shell curvature. On the other hand, a small negative value of μ will actually reduce the shell curvature since the perfect cylindrical panel has an outward curvature while the geometric imperfection has an inward curvature (the curvatures tend to cancel out). A sufficiently large negative value of μ means that the shell actually has an increasingly predominant inward curvature. From this figure, it can be seen that an increase (decrease) of the shell curvature caused by the presence of the geometric imperfection will also increase (decrease) the linear vibration frequency.

It is interesting to observe from Fig. 2(b) that in the case $m = 2$, $L/d = 2$, $\bar{n} = 1$, the linear vibration frequency is independent of the sign of the imperfection amplitude μ. This is because the geometric imperfection is taken to be of the same shape as the vibration mode so that for a panel with two axial half-waves, the shell actually increases its curvature for half of the cylindrical panel (say from $X = 0$ to $X = L/2$) whereas its curvature decreases for the remaining half of the panel.

In the special case when either the number of axial half-waves m or the number of circumferential half-waves $\bar{n}$ (or both) is even, the products of the definite integrals I_1H_1, I_2H_2, and I_3H_3 vanish. Thus, equations (17) become ($d_2 = 0$).

$$k = (2)\{(M^2 + N^2)^2 + [M^4/(M^2 + N^2)^2] + (4c\mu^2)[N^2e_1 + M^2e_2 + 2M^2N^2(c_1 + c_2)]\}$$

$$\epsilon = [N^2e_1 + M^2e_2 + 2M^2N^2(c_1 + c_2)](4c/k) \tag{27}$$

$$a_2 = 3\mu$$

In the further special case when $M = N$, it may be observed that the quantity $N^2e_1 + M^2e_2$ remains invariant for the in-plane boundary conditions type two and type three. Consequently, the linear frequency curves (as well as the nonlinearity parameter curves) for the type two boundary condition coincide with that for the type three boundary condition.

For a larger value of the flatness parameter $\theta = 2$, it is clear from Fig. 3 that for the important special case $m = 1$, $\bar{n} = 1$, a negative value of the imperfection amplitude will reduce the shell curvature and thus, the linear frequency decreases. On

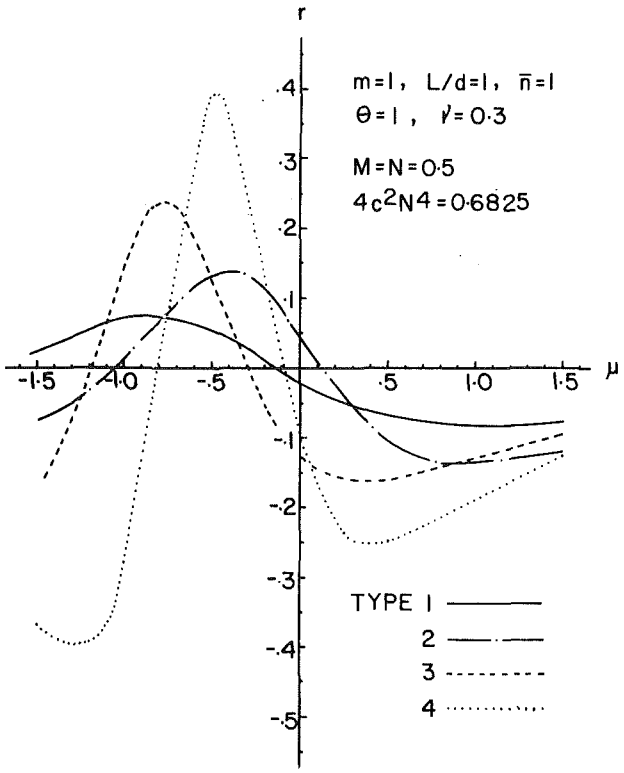

Fig. 5(*a*) Nonlinearity parameter versus imperfection amplitude for $\theta = 1$ and $\bar{n} = 1$ ($m = 1, L/d = 1$)

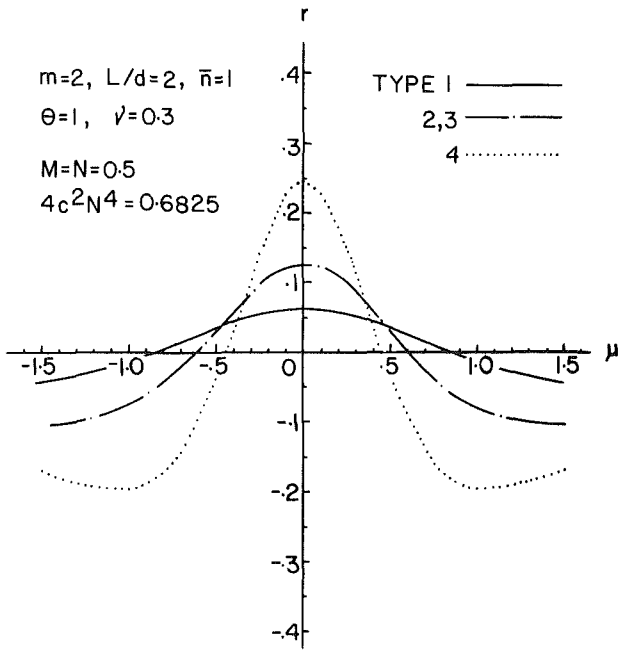

Fig. 5(*b*) Nonlinearity parameter versus imperfection amplitude for $\theta = 1$ and $\bar{n} = 1$ ($m = 2, L/d = 2$)

Fig. 5

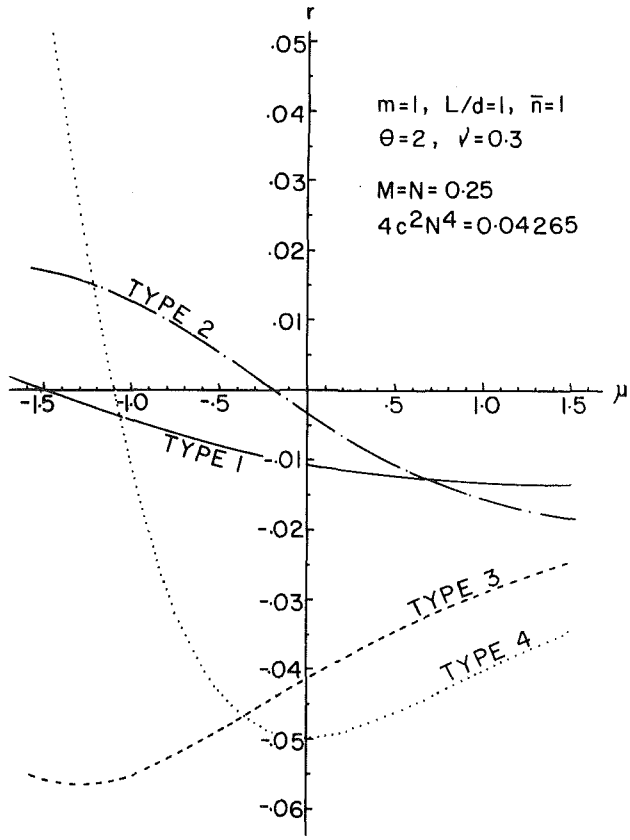

Fig. 6(*a*) Nonlinearity parameter versus imperfection amplitude for $\theta = 2$ and $\bar{n} = 1$ ($m = 1, L/d = 1$)

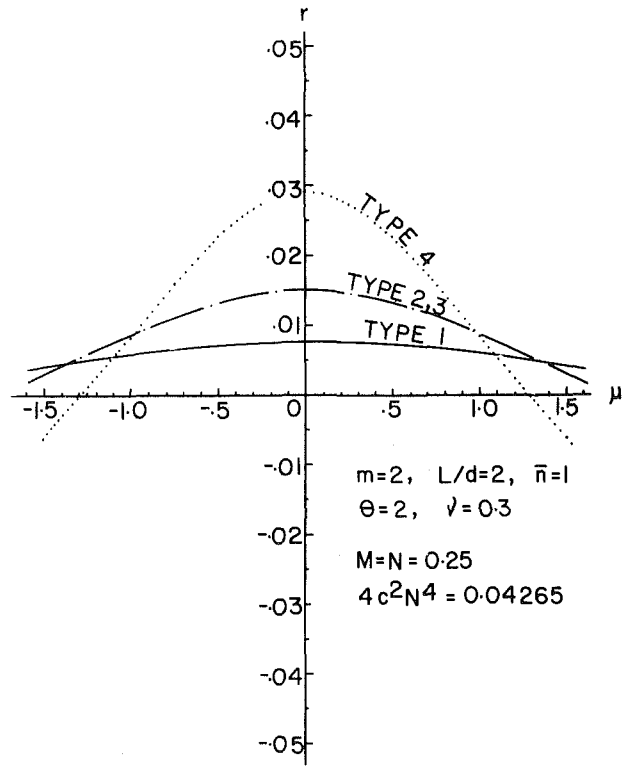

Fig. 6(*b*) Nonlinearity parameter versus imperfection amplitude for $\theta = 2$ and $\bar{n} = 1$ ($m = 2, L/d = 2$)

Fig. 6

the other hand, a positive value of μ will increase the curvature and thus, increase the linear frequency. For brevity, the corresponding curves for $m = 2$, $L/d = 2$, and $\bar{n} = 1$ will not be shown. They are found to be independent of μ and they lie between $k^{1/2} = 0.725$ and 0.85 for $-1.5 \leq \mu \leq 1.5$.

Figure 4 shows a graph of nonlinearity parameter r versus the imperfection amplitude μ for the flatness parameter $\theta = 0.5$, $m = 1$, $L/d = 1$, and $\bar{n} = 1$. Comparing the top sets of curves in Fig. 2(*a*) with Fig. 4, it can be seen that the minimum peak for the linear vibration frequency corresponds to the maximum peak for the nonlinearity parameter. In general, an increase in the linear vibration frequency (due to the presence of the geometric imperfection) is accompanied by a decrease

in the value of the nonlinearity parameter r. The maximum peaks for the nonlinearity parameter versus flatness parameter curves corresponds to negative values of the imperfection amplitude and thus, the results depend on the sign of the imperfection amplitude. For brevity, the corresponding curves for $\theta=0.5$, $m=2$, $L/d=2$, and $\bar{n}=1$ will not be shown. Again, they are independent of the imperfection amplitude (symmetrical with respect to μ). The curves are shifted to the right with maximum peaks correspond to $\mu=0$.

Figure 5(a) shows a graph of the nonlinearity parameter versus the imperfection amplitude for $\theta=1$, $m=1$, $L/d=1$, and $\bar{n}=1$. Comparing Figs. 4(a) and 5, it can be seen that the maximum peaks are now shifted further to the left. This is because for large values of the flatness parameter, a larger negative value of the imperfection amplitude is needed to cause the shell to possess an inward curvature (the perfect cylindrical panel initially has an outward curvature). Again, comparing the lower sets of curves in Fig. 2(a) with Fig. 5(a) for $\theta=1$, an increase in the linear vibration frequency is associated with a decrease in the nonlinearity parameter. The curves for $\theta=1$, $m=2$, $L/d=2$, and $\bar{n}=1$ are shown in Fig. 5(b). These curves are symmetrical with respect to μ with maximum peak at $\mu=0$. Similar trends for $\theta=2$ are displaced in Figs. 6(a, b) and it can be seen that the $m=L/d=1$ and $m=L/d=2$ curves no longer resemble each other.

4 Concluding Remarks

The effects of initial geometric imperfections and four types of in-plane boundary conditions on the linear and nonlinear vibration behavior of cylindrical panels simply supported along all four edges have been examined. Keeping $\bar{n}=1$ and fixing the value of θ, it is found that for an imperfect cylindrical panel, the linear vibration frequency as well as the nonlinearity parameter for the two cases, ($m=1$, $L/d=1$) and ($m=2$, $L/d=2$) are different. In general, an increase (decrease) in the linear vibration frequency is accompanied by a decrease (increase) in the nonlinearity parameter.

Extension of the present work to large-amplitude vibrations of circular cylindrical shells, enforcing the exact simply supported and clamped boundary conditions as well as the exact singlevaluedness requirement of the circumferential displacement, is in progress.

Acknowledgment

The work was started while the author was a graduate student at the Department of Ocean Engineering, Massachusetts Institute of Technology in 1980.

References

1 Reissner, E., "Non-Linear Effects in Vibrations of Cylindrical Shells," The Wooldridge Corporation, Guided Missile Research Division, Aeromechanics Section, Report AM 5-6, Sept. 1955, 63 pp.

2 Chu, H. N., "Influence of Large Amplitudes on Flexural Vibrations of a Thin Circular Cylindrical Shell," *J. of Aerospace Science*, Vol. 28, 1961, pp. 602-609.

3 Nowinski, J. L., "Nonlinear Transverse Vibrations of Orthotropic Cylindrical Shells," *AIAA Journal*, Vol. 1, pp. 617-620.

4 Evensen, D. A., and Fulton, R. E., "Some Studies on the Nonlinear Dynamic Response of Shell-type Structures," *Dynamic Stability of Structures*, Herrmann, G., ed., Pergamon Press, 1967, pp. 237-254.

5 Evensen, D. A., "Nonlinear Flexural Vibrations of Thin-Walled Circular Cylinders," NASA TN D-4090, Aug. 1967, 29 pp.

6 Evensen, D. A., "A Theoretical and Experimental Study of the Nonlinear Flexural Vibrations of Thin Circular Rings," NASA TR R-227, 1965.

7 Matsuzaki, Y., and Kobayashi, S., "A Theoretical and Experimental Study of the Nonlinear Flexural Vibration of Thin Circular Cylindrical Shells with Clamped Ends," *Transactions of the Japan Society for Aeronautical and Space Sciences*, Vol. 12, No. 21, 1970, pp. 55-62.

8 Chen, J. C., and Babcock, C. D., "Nonlinear Vibration of Cylindrical Shells," *AIAA Journal*, Vol. 13, No. 7, July 1975, pp. 868-876.

9 Evensen, D. A., "Nonlinear Vibrations of Circular Cylindrical Shells," *Thin-Shell Structures Theory, Experiment and Design*, Fung, Y. C., and Sechler, E. E., eds., Prentice-Hall, Englewood Cliffs, 1974, pp. 133-155.

10 Cummings, B. E., "Some Nonlinear Vibration and Response Problems of Cylindrical Panels and Shells," Aeroelasticity and Structural Dynamics, GALCIT California Institute of Technology Report, SM-62-32, (AFOSR 3123), June 1962, 130 pp.

11 Cummings, B. E., "Large-Amplitude Vibration and Response of Curved Panels," *AIAA Journal*, Vol 2, No. 4, April 1964, pp. 709-716.

12 Ramachandran, J., and Murthy, P. A. K., "Non-linear Vibrations of a Shallow Cylindrical Panel on an Elastic Foundation," *J. of Sound and Vibration*, Vol. 47, 1976, pp. 495-500.

13 Massalas, C.,, and Kafousias, N., "Non-Linear Vibrations of a Shallow Cylindrical Panel on a Non-Linear Elastic Foundation," *J. of Sound and Vibration*, Vol. 66, 1979, pp. 507-512.

14 Hui, D., "Effects of Geometric Imperfections on Large Amplitude Vibrations of Rectangular Plates With Hysteresis Damping," ASME JOURNAL OF APPLIED MECHANICS, Vol. 51, 1984, pp. 216-220.

15 Hui, D., "Large Amplitude Axisymmetric Vibrations of Geometrically Imperfect Circular Plates," *J. of Sound and Vibration*, Vol. 91, No. 2, Nov. 1983, pp. 239-246.

16 Hui, D., "Large Amplitude Vibrations of Geometrically Imperfect Shallow Spherical Shells with Structural Damping," *AIAA Journal*, Vol. 21, No. 12, Dec. 1983, pp. 1736-1741.

17 Watawala, L., and Nash, W. A., "Influence of Initial Geometric Imperfections on Vibrations of Thin Circular Cylindrical Shells," *Computer and Structures*, Vol. 16, 1983, pp. 125-130.

18 Forsberg, K., "Influence of Boundary Conditions on the Modal Characteristics of Thin Cylindrical Shells," *AIAA Journal*, Vol. 2, No. 12, Dec. 1964, pp. 2150-2157.

19 Koiter, W. T., "Buckling and Post-Buckling Behaviour of a Cylindrical Panel Under Axial Compression," National Aeronautical Research Institute, Amsterdam, Report S-476, May, 1956.

20 Hui, D., Tennyson, R. C., and Hansen J. S., "Mode Interaction of Axially Stiffened Cylindrical Shells: Effects of Stringer Axial Stiffness, Torsional Rigidity and Eccentricity," ASME JOURNAL OF APPLIED MECHANICS, Vol. 48, 1981, pp. 915-922.

21 Hutchinson, J. W., "Axial Buckling of Pressurized Imperfect Cylindrical Shells," AIAA Journal, Vol. 3, No. 8, Aug. 1965, pp. 1461-1466.

22 Lau, S. L., and Cheung, Y. K., "Amplitude Incremental Variational Principle for Nonlinear Vibration of Elastic Systems," ASME JOURNAL OF APPLIED MECHANICS, Vol. 48, 1981, pp. 959-964.

APPENDIX A

In-Plane Movable and In-Plane Immovable Boundary Conditions

To examine the in-plane boundary conditions in the mixed formulation, it is necessary to express the stress function F in terms of the axial, circumferential, and out-of-plane displacements U, V, and W in the form, (letting $\eta = 0$ and ϵ_x, ϵ_y, and ϵ_{xy} are the strains),

$$(1-\nu^2)(F,_{YY}) = (Eh)\,(\epsilon_x + \nu\epsilon_y)$$
$$(1-\nu^2)(F,_{XX}) = (Eh)\,(\nu\epsilon_x + \epsilon_y)$$
$$(1+\nu)\,(-F,_{XY}) = (Eh)\,(\epsilon_{xy}) \qquad (A1)$$

These relations imply,

$$F,_{YY} - \nu F,_{XX} = (\mathrm{E}h)\ \epsilon_x$$
$$F,_{XX} - \nu F,_{YY} = (\mathrm{E}h)\ \epsilon_y \qquad (A2)$$

Equations ($A1$) can be written in nondimensional form in terms of the displacements, ($U = hu/q_0$, $V = hv/q_0$),

$$(1-\nu^2)(f,_{yy}) = u,_x + (\nu)\,(v,_y + w) + (c)\,[(w+2w_0),_x w,_x + (\nu)\,(w+2w_0),_y w,_y]$$
$$(1-\nu^2)(f,_{xx}) = \nu u,_x + v,_y + w + (c)\,[\nu(w+2w_0),_x w,_x + (w+2w_0),_y w,_y] \qquad (A3)$$

Likewise equations ($A2$) can also be expressed in nondimensional form [20]

$$f,_{yy} - \nu f,_{xx} = u,_x + c(w+2w_0),_x w,_x$$
$$f,_{xx} - \nu f,_{yy} = v,_y + w + c(w+2w_0),_y w,_y \qquad (A4)$$

The four types of in-plane boundary conditions under consideration are,

Type 1 In-Plane Movable on all four edges.

$$e_1 = 0 \quad \text{and} \quad e_2 = 0 \tag{A5}$$

Type 2 Curved Edges Immovable and Longitudinal Edges Movable. Since the longitudinal edges are movable in the circumferential direction, it is clear that $f_{,xx} = 0$ at the two longitudinal edges. Furthermore,

$$f_{,yy} = (cM^2/4)\,[w(t)^2 + 2\mu w(t)] + \text{sinusoidal terms} \tag{A6}$$

so that

$$e_1 = 0, \quad e_2 = cM^2/4 \tag{A7}$$

Type 3 Curved Edges Movable and Longitudinal Edges Immovable. Since the two curved edges are movable, it may be concluded that $f_{,yy} = 0$ at these two curved edges. Furthermore,

$$f_{,xx} = (cN^2/4)\,[w(t)^2 + 2\mu w(t)] + \text{sinusoidal terms} \tag{A8}$$

so that

$$e_1 = cN^2/4, \quad e_2 = 0 \tag{A9}$$

Type 4 In-Plane Immovable on All Four Edges. Collecting only the constant terms in equation (A2) one obtains,

$$(1-\nu^2)f_{,yy} = (c/4)(M^2 + \nu N^2)\,[w(t)^2 + 2\mu w(t)] + \text{sinusoidal terms}$$

$$(1-\nu^2)f_{,xx} = (c/4)(\nu M^2 + N^2)\,[w(t)^2 + 2\mu w(t)] + \text{sinusoidal terms} \tag{A10}$$

so that,

$$e_1 = c(\nu M^2 + N^2)/[4(1-\nu^2)]$$

$$e_2 = c(M^2 + \nu N^2)/[4(1-\nu^2)] \tag{A11}$$

S. F. Masri
Professor.
Mem. ASME

R. K. Miller
Associate Professor.
Mem. ASME

H. Sassi
Lecturer.

Department of Civil Engineering,
University of Southern California,
Los Angeles, Calif. 90089-0242

T. K. Caughey
Professor,
Division of Engineering and
Applied Science,
California Institute of Technology,
Pasadena, Calif. 91106

A Method for Reducing the Order of Nonlinear Dynamic Systems

An approximate method that uses conventional condensation techniques for linear systems together with the nonparametric identification of the reduced-order model generalized nonlinear restoring forces is presented for reducing the order of discrete multidegree-of-freedom dynamic systems that possess arbitrary nonlinear characteristics. The utility of the proposed method is demonstrated by considering a redundant three-dimensional finite-element model half of whose elements incorporate hysteretic properties. A nonlinear reduced-order model, of one-third the order of the original model, is developed on the basis of wideband stationary random excitation and the validity of the reduced-order model is subsequently demonstrated by its ability to predict with adequate accuracy the transient response of the original nonlinear model under a different nonstationary random excitation.

1 Introduction

Model-order reduction is a subject of increasing interest in the field of applied mechanics which has been motivated by the need to develop lower-order models corresponding to complicated structural systems whose motion is to be analyzed under arbitrary dynamic environments. Among the specific areas that have made extensive use of reduced-order models is (1) the active control of large-scale aerospace vehicles and (2) the eigenvalue problems encountered in the use of finite element methods in conjunction with large structural dynamic systems.

While an extensive body of literature is available for problems dealing with reduction schemes (also known as eigenvalue economization methods) for linear systems, few results are available in the published literature regarding condensation methods suitable for use with nonlinear dynamic systems.

This paper presents an approximate method for reducing the order of discrete multidegree-of-freedom dynamic systems that possess arbitrary nonlinear characteristics. The reduction method combines the ideas of standard mass condensation techniques that are widely used with linear systems, together with recent developments in the nonparametric identification field, to develop a rational approach for a systematic procedure to reduce the order of the class of systems under discussion. The utility of the proposed reduction method is illustrated by considering a redundant three-dimensional finite element model consisting of nonlinear truss elements and subjected to wide-band random excitation. The range of validity of the approach is evaluated with regard to the deviation error between the response time histories of the original and reduced models.

Contributed by the Applied Mechanics Division for presentation at the 1984 PVP Conference and Exhibition, joint with Applied Mechanics Division and Materials Division, San Antonio, Texas, June 17-21, 1984 of THE AMERICAN SOCIETY OF MECHANICAL ENGINEERS.

Discussion on this paper should be addressed to the Editorial Department, ASME, United Engineering Center, 345 East 47th Street, New York, N.Y. 10017, and will be accepted until two months after final publication of the paper itself in the JOURNAL OF APPLIED MECHANICS. Manuscript received by ASME Applied Mechanics Division, February, 1983; final revision, October, 1983. Paper No. 84-APM-32.

Copies will be available until February, 1985.

2 Formulation

2.1 Model Reduction. Consider a discrete nonlinear dynamic system whose motion is governed by

$$M\ddot{\mathbf{x}} + \mathbf{f}(\mathbf{x},\dot{\mathbf{x}}) = \mathbf{p}(t), \tag{1}$$

where

M = diagonal mass matrix of order n,
$\mathbf{x}(t)$ = displacement vector = $\{x_1, x_2, \ldots, x_n\}^T$,
$\mathbf{f}$ = function that represents nonconservative nonlinear forces,
$\mathbf{p}(t)$ = excitation vector.

Assume that an "equivalent" stiffness matrix K corresponding to the range of motion of interest can be determined. This step could be accomplished, for example, by using modal identification techniques to process experimental measurements from the response of the physical system. Alternatively, in the case of large nonlinear finite element models, where the time history response is obtained by treating the system as a piecewise linear model, matrix K is directly available since it is repeatedly reconstructed to reflect changing response levels.

Using standard mass condensation techniques [1-13] that

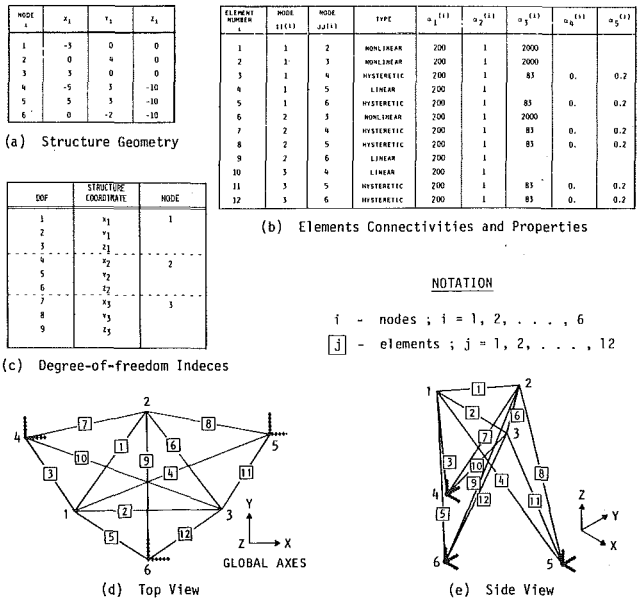

Fig. 1 Example of nonlinear nine DOF model characteristics

are used in the finite element field to eliminate "slave" degrees of freedom associated with relatively small motions while retaining "master" degrees of freedom corresponding to larger deformations, the eigenvalue problem associated with the linearized reduced-order systems is

$$(K_r - \lambda M_r)\mathbf{x}_r = 0 \tag{2}$$

with

$$\mathbf{x} = R\mathbf{x}_r, \tag{3}$$

$$R = T_1 T_2 \ldots T_L, \tag{4}$$

where

- $\mathbf{x}_r$ = vector of order $r = n - L$ whose r components correspond to the master degrees of freedom;
- R = transformation matrix of order $n \times r$ representing the cumulative effects of L reduction loops;
- T_L = transformation matrix of order $(r+1)\times r$ representing the condensation effects of single loop L, with $\{\mathbf{x}_1, \mathbf{x}_2\}^T = T_L \mathbf{x}_1$;
- M_r = condensed mass matrix of order $r \times r$, $M_r = R^T M R$;
- K_r = condensed stiffness matrix of order $r \times r$, $K_r = R^T K R$;
- $\mathbf{x}_1$ = vector of order r representing the master degrees of freedom;
- $\mathbf{x}_2$ = vector of order L representing the slave degrees of freedom (DOF).

2.2 Restoring Force Estimation. Now solving the eigenvalue problem in equation (2) results in the transformation

$$\mathbf{x}_r = \phi_r \mathbf{u} \tag{5}$$

where ϕ_r is the eigenvector matrix of order $r \times r$, and $\mathbf{u}$ is the vector of generalized coordinates of order r,

$$\mathbf{u} = \{u_1, u_2, \ldots, u_r\}^T. \tag{6}$$

Making use of equations (3) and (5), the system equation of motion equation (1) can be converted to the form

$$\mathfrak{M}\ddot{\mathbf{u}} + \mathbf{h}(\mathbf{u}, \dot{\mathbf{u}}) = \mathbf{q}(t) \tag{7}$$

where $\mathfrak{M}$ is a diagonal mass matrix of order $r \times r$ given by

$$\mathfrak{M} = \phi_r^T R^T M R \phi_r, \tag{8}$$

$\mathbf{h}$ is a vector of order r corresponding to the transformed nonlinear forces acting on the system,

$$\mathbf{h}(\mathbf{u}, \dot{\mathbf{u}}) = \phi_r^T R^T \mathbf{f}(\mathbf{x}, \dot{\mathbf{x}}), \tag{9}$$

and $\mathbf{q}(t)$ is a vector of order r corresponding to the generalized excitation forces,

$$\mathbf{q}(t) = \phi_r^T R^T \mathbf{p}(t). \tag{10}$$

An alternative form of equation (7) is

$$B^T M \ddot{\mathbf{x}} + \mathbf{h}(\mathbf{u}, \dot{\mathbf{u}}) = B^T \mathbf{p}(t), \tag{11}$$

or

$$\mathbf{h}(\mathbf{u}, \dot{\mathbf{u}}) = B^T(\mathbf{p}(t) - M\ddot{\mathbf{x}}), \tag{12}$$

where B is a constant matrix of order $n \times r$ given by

$$B = R\phi_r. \tag{13}$$

Note from equation (12) that if the terms appearing on the right-hand side are known, the time history of each component of vector $\mathbf{h}$ can be determined.

Note also that in the case of a linear system, due to the orthgonality condition associated with ϕ_r, the set of equations represented by equation (12) are decoupled; i.e., each component h_i of $\mathbf{h}$ depends only on the ith generalized coordinate u_i rather than on all components of $\mathbf{u}$.

Guided by the preceding observation, the central ideal of the present condensation technique is that in the case of nonlinear dynamic systems commonly encountered in the applied mechanics field, a judicious assumption is that each component of $\mathbf{h}$ can be expressed in terms of a series of the form:

$$h_i(\mathbf{u}, \dot{\mathbf{u}}) \approx \hat{h}_i(\mathbf{u}, \dot{\mathbf{u}}), \tag{15}$$

where

$$\hat{h}_i(\mathbf{u}, \dot{\mathbf{u}}) = \sum_{j=1}^{J_{\max_i}} \hat{h}_i^{(j)}(v_{1_i}^{(j)}, v_{2_i}^{(j)}). \tag{16}$$

The approximation indicated in equation (15) is that each component h_i of the nonlinear generalized restoring force $\mathbf{h}$ can be adequately estimated by a collection of terms $\hat{h}_i^{(j)}$ each one of which involves a pair of generalized coordinates (displacements and/or velocities). The particular choice of combinations and permutations of u_k and $\dot{u}_l$ and the number of terms $J_{\max_i}$ needed for a given h_i depends on the nature and extent of the nonlinearity of the system and its effects on the specific "mode" i. Note that the formulation in equation (16) allows for "modal" interaction between all modal displacements and velocities, taken two at a time.

Another useful feature of the proposed reduction approach is that it can be used directly (without the intermediary step of static condensation) to condense-out insignificant eigenmodes of the original system.

2.3 Series Expansion. The individual terms appearing in the series expansion of equation (16) may be evaluated by using the least-squares approach to determine the optimum fit for the time history of each h_i. Thus, $\hat{h}_i^{(1)}$ may be expressed as a double series involving a suitable choice of basis functions,

$$h_i(\mathbf{u}, \dot{\mathbf{u}}) \approx \hat{h}_i^{(1)}(v_{1_i}^{(1)}, v_{2_i}^{(1)}), \tag{17}$$

$$\hat{h}_i^{(1)} = \sum_k \sum_l {}^{(1)}C_{kl}^{(i)} T_k(v_{1_i}^{(1)}) T_l(v_{2_i}^{(1)}). \tag{18}$$

Let the deviation error between h_i and its first estimate $\hat{h}_i^{(1)}$ be given by

$$h_i^{(1)}(\mathbf{u}, \dot{\mathbf{u}}) = h_i(\mathbf{u}, \dot{\mathbf{u}}) - \hat{h}_i^{(1)}(v_{1_i}^{(1)}, v_{2_i}^{(1)}). \tag{19}$$

Equation (17) accounts for the contribution to the generalized force h_i of state variables $v_{1_i}^{(1)}$ and $v_{2_i}^{(1)}$ appearing in the form $(v_{1_i}^{(1)})^k (v_{2_i}^{(1)})^l$. Consequently the residual error as defined by equation (19) can be further reduced by fitting $h_i^{(1)}$ by a similar double series involving variables $v_{1_i}^{(2)}$ and $v_{2_i}^{(2)}$:

$$h_i^{(1)}(\mathbf{u}, \dot{\mathbf{u}}) \approx \hat{h}_i^{(2)}(v_{1_i}^{(2)}, v_{2_i}^{(2)}), \tag{20}$$

where

$$\hat{h}_i^{(2)} = \sum_k \sum_l {}^{(2)}C_{kl}^{(i)} T_k(v_{1_i}^{(2)}) T_l(v_{2_i}^{(2)}). \tag{21}$$

Similarly, the contribution of terms involving products of various powers of combinations of $v_{1_i}^{(3)}$ and $v_{2_i}^{(3)}$ can be found from

$$h_i^{(2)}(\mathbf{u},\dot{\mathbf{u}}) = h_i^{(1)}(\mathbf{u},\dot{\mathbf{u}}) - \hat{h}_i^{(2)}(v_{1_i}^{(2)},\ v_{2_i}^{(2)}), \tag{22}$$

and

$$h_i^{(2)}(\mathbf{u},\dot{\mathbf{u}}) \approx \hat{h}_i^{(3)}(v_{1_i}^{(3)}, v_{2_i}^{(3)}), \tag{23}$$

where

$$\hat{h}_i^{(3)} = \sum_k \sum_l {}^{(3)}C_{kl}^{(i)}\, T_k(v_{1_i}^{(3)}) T_l(v_{2_i}^{(3)}). \tag{24}$$

By extending this procedure to account for all "modes" that have significant interaction with "mode" i, equation (16) is obtained.

2.4 Data Processing. Consider a typical case where the method under discussion is likely to be applied. For example, experimental measurements from a physical system are to be analyzed or the output of a finite element code is to be processed. In both cases the following steps can be performed:

(1) Measure $\mathbf{x}(t)$, $\dot{\mathbf{x}}(t)$, $\ddot{\mathbf{x}}(t)$, and $\mathbf{p}(t)$ and digitize each one at a sampling rate that is appropriate for the frequency band of interest.

(2) Compute, measure, or estimate the diagonal mass matrix M and the corresponding stiffness matrix K for the discretized n- DOF nonlinear system by treating the physical structure or the nonlinear mathematical model as an equivalent linear system over the response range of interest.

(3) Apply a sufficient number of condensation loops as outlined in the foregoing to reduce the order of the system to an acceptable value and to obtain the transformation matrix R of equation (3) which relates all the system DOF's to the primary DOF's.

(4) Having determined matrixes M, K, and R, solve the eigenvalue problem (equation (2)) associated with the reduced-order system, thus obtaining the modal matrix ϕ_r whose columns constitute estimates of the prominent deflection shapes of the nonlinear system.

(5) Use equation (12), whose right-hand side involves at this stage known quantities, to compute $\mathbf{h}(t)$, the time history of the generalized nonlinear restoring forces associated with the estimated deflection shapes.

(6) Making use of equations (3) and (5), determine the time histories of $\mathbf{u}(t)$ and $\dot{\mathbf{u}}(t)$, the generalized displacement and velocity, respectively, from the following relationships:

$$\mathbf{u}(t) = A\mathbf{x}_r(t), \quad \dot{\mathbf{u}}(t) = A\dot{\mathbf{x}}_r(t), \tag{25}$$

where A is a constant square matrix of order $r \times r$ given by

$$A = \phi_r^{-1}. \tag{26}$$

(7) Following the procedure outlined in Section 2.3, develop an analytical expression in the form of the series indicated in equation (16) to estimate each component $h_i(t)$ of $\mathbf{h}(t)$ in terms of suitable pairs (v_1, v_2) of the generalized coordinates.

(8) The evaluation of a sufficient number of the doubly-indexed series coefficients C_{kl} associated with each term of the various series terms $h_i^{(j)}(t)$ constitutes the termination of the data processing phase of the problem under consideration.

2.5 Least-Squares Fit. Using two-dimensional orthogonal polynomials to estimate each $h_i(\mathbf{u},\dot{\mathbf{u}})$ by a series of approximating functions $\hat{h}_i^{(j)}$ of the form indicated in equation (18), then the numerical value of the C_{kl} coefficients can be determined by invoking the applicable orthogonality conditions for the chosen polynomials. While there is a wide choice of suitable basis functions for least-squares application, the orthogonal nature of the Chebyshev polynomials and their "equal ripple" characteristics make them convenient to use in the present work.

Note that in the special case when no cross-product terms are involved in any of the series terms, functions h can be expressed as the sum of two one-dimensional orthogonal polynomial series instead of a single two-dimensional series of the type under discussion.

2.6 Response Prediction. Once the coefficients ${}^{(j)}C_{kl}^{(i)}$ have been extracted from the nonlinear system response in the manner outlined in the foregoing, they constitute a reduced-order nonparametric model of the system. When used with the *same* excitation employed for identification they can reconstruct the (approximate) response of the higher-order model. Even more important is the ability to use these coefficients to predict the estimated response time history of the nonlinear system when subjected to an excitation signal that is *different* from that used for identification purposes.

The procedure for the approximate model response predictions is based on the (numerical) solution of the reduced-order system equations of motion expressed in the form of equation (7):

$$\mathfrak{M}_{ii}\ddot{u}_i(t) + h_i(t) = q_i(t), \quad i = 1,2,\ldots,r. \tag{27}$$

Given $\mathbf{p}(t)$ and initial conditions $\mathbf{x}(t_0)$, $\dot{\mathbf{x}}(t_0)$, once $h_i(t)$ is determined from equation (16) and making use of equation (10) to determine $q_i(t)$, the governing equations of motion (27) can be incrementally (numerically) solved to compute the response u_i at the next time increment $(t+\Delta t)$. The approximate response time histories of all of the system's n degrees of freedom may then be found from

$$\mathbf{x}(t) = B\mathbf{u}(t), \tag{28}$$

and the nonlinear restoring forces acting on the system will be found from

$$\mathbf{f}(\mathbf{x},\dot{\mathbf{x}}) = \mathbf{p}(t) - MB\ddot{\mathbf{u}}(t). \tag{29}$$

2.7 Error Sources. Referring back to equations (7)–(10), it will be found that

$$\ddot{\mathbf{u}}(t) = \mathfrak{M}^{-1}(\mathbf{q}(t) - \mathbf{h}(t)), \tag{30}$$

$$= \mathfrak{M}^{-1}B^T(\mathbf{p}(t) - \mathbf{f}(t)), \tag{31}$$

$$= \mathfrak{M}^{-1}B^TM\ddot{\mathbf{x}}(t). \tag{32}$$

An alternative way of relating $\ddot{\mathbf{u}}$ to $\ddot{\mathbf{x}}$ is via the condensation procedure as expressed in equations (3) and (25):

$$\mathbf{u}(t) = (A \mid 0)\left\{\frac{\mathbf{x}_r}{\mathbf{x}_2}\right\} \tag{33}$$

$$\mathbf{u}(t) = A\mathbf{x}_r + 0\mathbf{x}_2 \tag{34}$$

Thus, at any time t, there is an error introduced in estimating $\mathbf{u}$ and $\dot{\mathbf{u}}$ that depends on the significance of the displacement and velocity, respectively, associated with the secondary (slave) degrees of freedom. However, by using equation (32) rather than (34), the generalized acceleration $\ddot{\mathbf{u}}(t)$ can be determined exactly from the knowledge of the system acceleration.

Then, even if the series expansion and the least-squares procedures did not introduce any subsequent errors, the use of $\mathbf{u}$ and $\dot{\mathbf{u}}$ to recover $\mathbf{x}$ and $\dot{\mathbf{x}}$ will result in approximate values $\hat{\mathbf{x}}$ and $\hat{\dot{\mathbf{x}}}$ given by

$$\hat{\mathbf{x}}(t) = B\mathbf{u}(t) = BA\mathbf{x}_r = R\mathbf{x}_r. \tag{35}$$

Due to the nature of the condensation method under

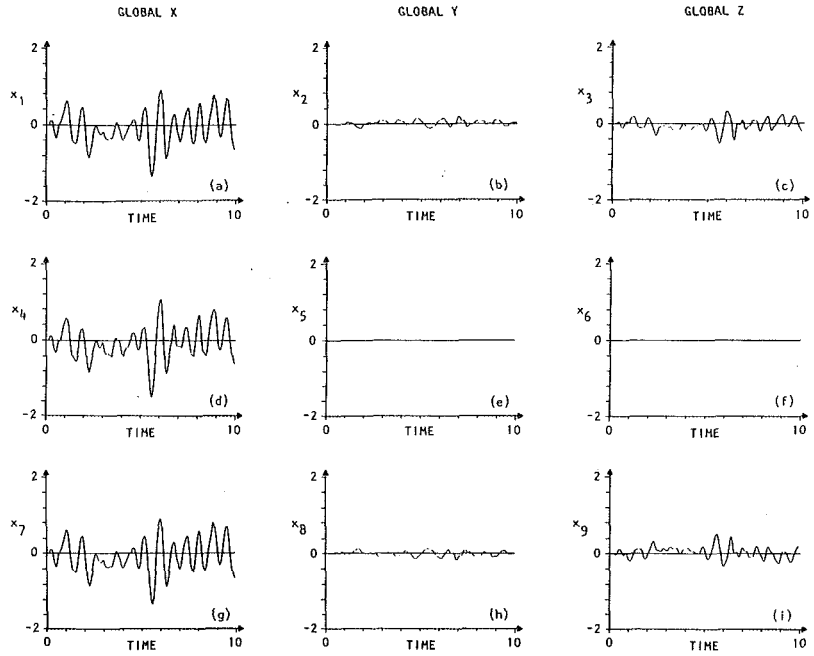

Fig. 2 Displacement time history of $x_i(t)$ of the nonlinear system under stationary random excitation

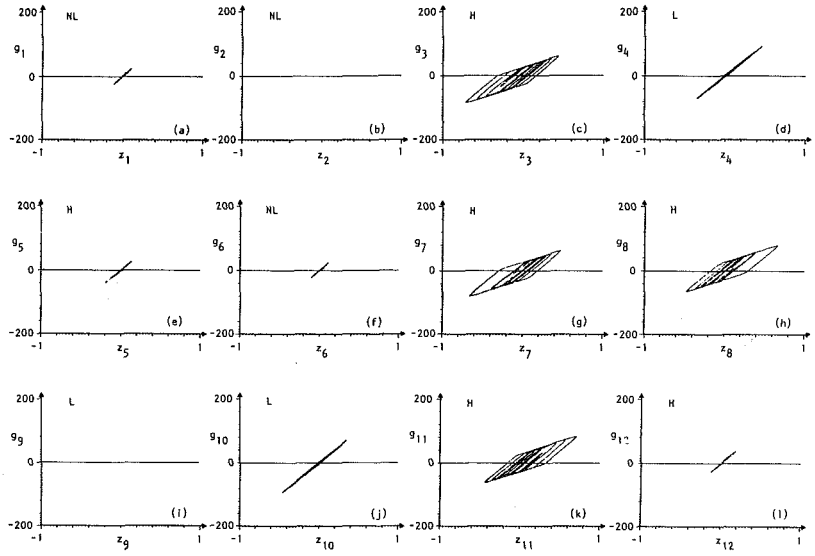

Fig. 3 Variation of element internal force $g_i(t)$ with the corresponding element deformation $z_i(t)$

discussion, the upper part of the matrix R which is associated with the primary (master) degrees of freedom is an identity matrix of order r.

Besides errors arising from (1) the choice of the generalized state variables, (2) from the accuracy of the least-squares fit of the generalized restoring forces, and (3) from the series truncation error, there is (4) an error introduced in the numerical solution of equation (27) due to the approximate nature of equation (10) in which the generalized excitation $\mathbf{q}(t)$ is related to the actual excitation $\mathbf{p}(t)$ by matrix B which is approximate in nature. Sources of error included in B are order-reduction (R) and nonlinearities (ϕ_r).

3 Applications

3.1 Example Nonlinear Hysteretic Model Characteristics. To illustrate the application of the method under discussion, consider the hypothetical finite element model shown in Fig. 1. This three-dimensional structure consists of three equal masses m_i that are interconnected by means of 12 truss elements anchored to ground at three locations thus resulting in a redundant system with nine degrees of freedom (DOF).

The arbitrary nonlinear elements, denoted by g_i, which are interposed between the masses and between the support points, are dependent on the relative displacement z and velocity $\dot{z}$ across the terminals of each element. In the case of elements with polynomial nonlinearities, the elements assume the form

$$g_i(z,\dot{z}) = \alpha_1{}^{(i)} z + \alpha_2{}^{(i)} \dot{z} + \alpha_3{}^{(i)} z^3 \ldots \tag{36}$$

where $\alpha_1{}^{(i)}$ is the linear stiffness component, $\alpha_2{}^{(i)}$ corresponds to the coefficient of the linear viscous damping term, $\alpha_3{}^{(i)}$ corresponds to the coefficient of the nonlinear cubic displacement term, and other terms represent higher-order powers of z and/or $\dot{z}$. Thus, depending on the sign and

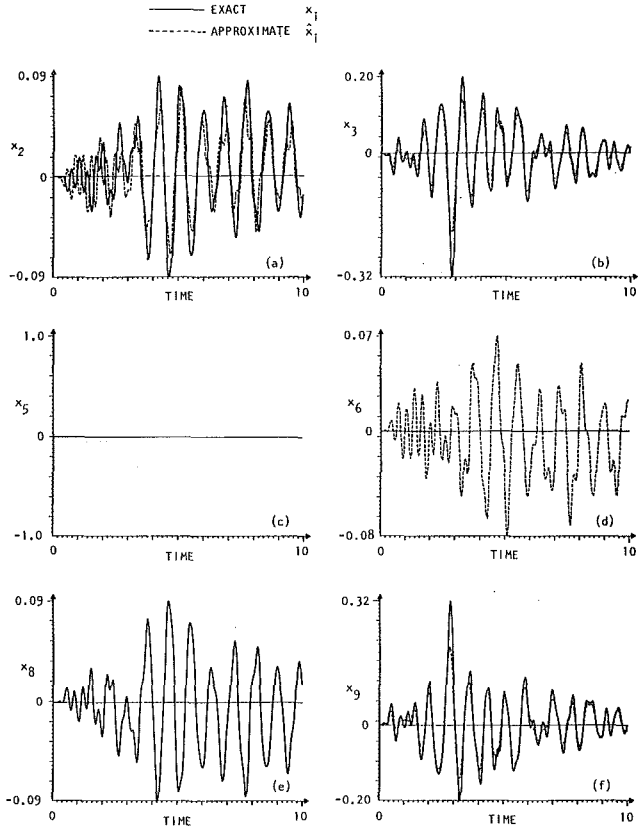

Fig. 4 Condensation effects

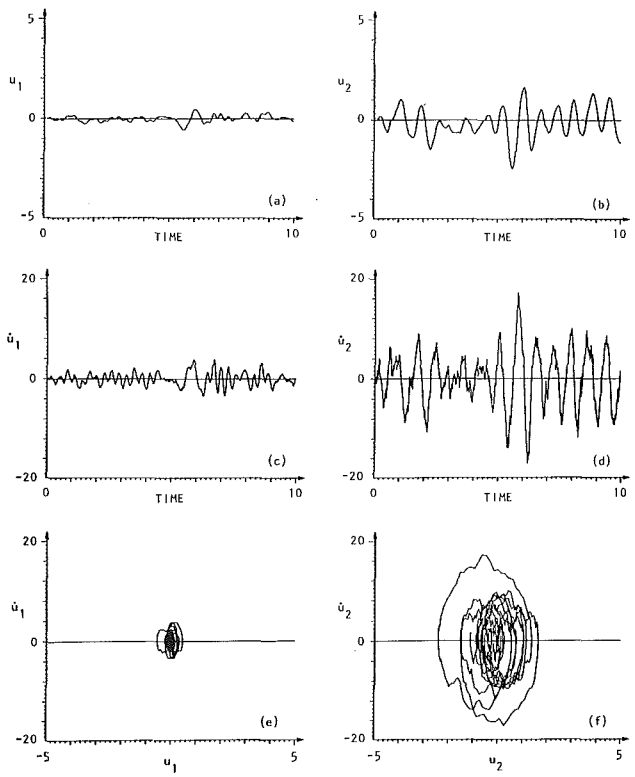

Fig. 5 Dominant generalized displacements $u(t)$ and velocities $\dot{u}(t)$ of reduced-order model

magnitude of the $\alpha_j^{(i)}$ coefficients, the form g_i in equation (36) can be made to represent a wide class of commonly encountered types of nonlinearities in physical systems.

To illustrate the validity of the present method, nonlinear elements posssessing hysteretic-type force-deformation characteristics will also be considered. Such a nonlinearity not only involves cross-product terms of displacement and velocity, but is of course not even expressible in polynomial form. Hysteretic systems, widely encountered in all areas of applied mechanics, are among the more difficult types of nonlinear properties to investigate and identify [14–25].

In the example structure under discussion, three elements (g_4, g_9, g_{10}) are taken to be linear, three elements (g_1, g_2, g_6) have polynomial-type (hardening) properties, and the remaining six elements (g_3, g_5, g_7, g_8, g_{11}, g_{12}) have bilinear-hysteretic characteristics in which different load paths are traversed in loading and unloading. For such hysteretic elements, the $\alpha_j^{(i)}$ coefficients have the following significance:

$\alpha_1^{(i)} = k_1 \equiv$ stiffness in the elastic range
$\alpha_2^{(i)} =$ viscous damping term in the linear range
$\alpha_3^{(i)} = k_2 \equiv$ stiffness in the nonlinear range
$\alpha_4^{(i)} =$ viscous damping term in the nonlinear range
$\alpha_5^{(i)} = z_y \equiv$ yield displacement level.

The geometrical configuration as well as the material properties of the elements of the nonlinear model are given in Fig. 1 together with the indexes that relate the structure nine degrees of freedom to the global (X, Y, Z) axes.

3.2 Test Excitation and Response Measurement. Subjecting the nonlinear system to a wideband stationary random excitation, which is applied uniformly to each of the three masses in the global X direction for a length of time much longer than the longest system period of interest, results in the response time history depicted in Fig. 2. This can be thought of as an equivalent test in which the structure is mounted on a vibration generator. For ease in visualizing the qualitative behavior of the system, the same scale is used for plotting the displacement time histories of all nine DOF.

By inspecting the "measured" force-deformation characteristics that are plotted in Fig. 3, it is clear that the observed characteristics match the constitutive properties shown in Fig. 1(*b*). Note from Figs. 3(*e*) and 3(*l*) that hysteretic members g_5 and g_{12} did not deform into their inelastic range. However, the remaining four hysteretic members (g_3, g_7, g_8, and g_{11}) sustained significant deformations beyond their yield level. All the hysteretic elements used had a yield level $z_y = 0.2$ and a stiffness ratio $\alpha = k_2/k_1 = 0.414$. It can be seen from Fig. 3(*c*), (*g*), (*h*), and (*k*) that the test structure is undergoing a large nonlinear deformation of the bilinear hysteretic type with a ductility ratio $\mu \equiv$ (peak deformation)/(yield deformation) of $\mu \approx 5.0$.

3.3 Reduction of Model Order. Following the model-order reduction procedure given in Section 2.1, an equivalent stiffness matrix K of order 9×9 corresponding to the small oscillations (linearized) range of motion is determined.

Assume that it is desired to reduce the order of the model from nine DOF to three DOF. By retaining those DOF whose motion is dominant (i.e., DOF 1, 4, and 7), DOF 2, 3, 5, 6, 8, and 9 are selected as "slave" DOF.

A measure of the degree of approximation introduced by condensing the slave DOF is indicated in Fig. 4, where the time histories of the secondary components of the approximate displacement vector given in equation (35) by $\hat{\mathbf{x}} = R\mathbf{x}_r$ are plotted at different scales. Due to the nature of the transformation matrix R no approximations are introduced in the primary components of $\hat{\mathbf{x}}$; consequently the time histories of the first three components of $\hat{\mathbf{x}}$ corresponding to DOF 1, 4, 7, respectively, are identical to their measured values. Note that the deviation errors shown in Fig. 4 are purely due to condensing out the secondary DOF; they do not include errors due to the approximations inherent in the series expansion of equation (16).

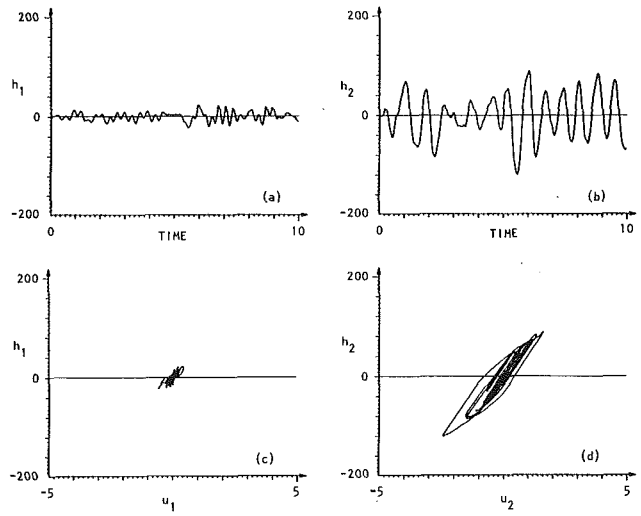

Fig. 6 Dominant generalized restoring forces h(t) of reduced-order model

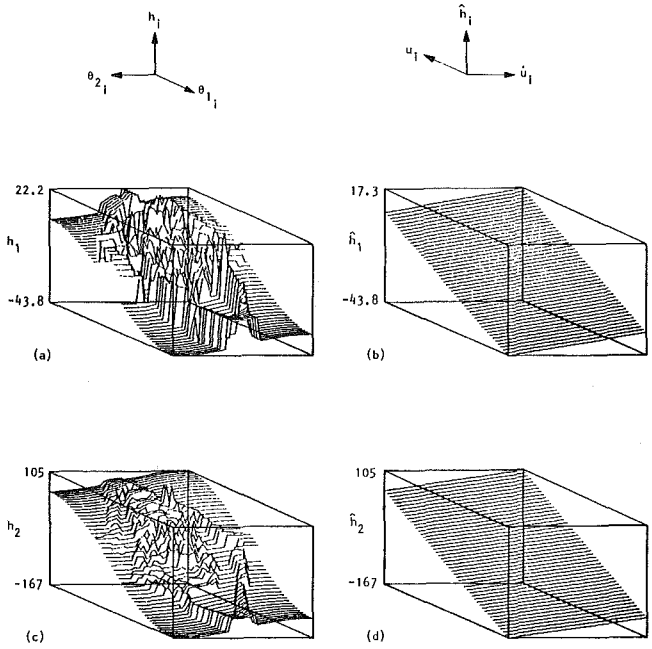

Fig. 7 Three-dimensional plots of the exact h_i and approximate $\hat{h}_i$

3.4 Identification of Reduced-Order Model. Processing the "experimental" measurements shown in Fig. 2 by following the procedure outlined in Section 2.4 and by using equation (25) and transformation matrix $A = \phi_r^{-1}$, results in the modal time history response shown in Fig. 5.

Plots of the time histories of the dominant components of the generalized restoring force h are shown in Figs. 6(*a*) and (*b*), and the variation of each $h_i(t)$ with its corresponding state variable $u_i(t)$ are presented in Figs. 6(*c*) and (*d*). It is clear from Fig. 6(*d*) that h_2, the generalized restoring force associated with the second mode of the reduced-order model, exhibits pronounced hysteretic characteristics.

Performing the identification procedure in the manner indicated in Section 2, the approximate nature of each $h_i(t)$ is determined in accordance with the steps given in equations (9)–(15).

Each of the identified functions $\hat{h}^{(j)}(v_1, v_2)$ when expressed in terms of its corresponding state variables defines a surface covering the $v_1 - v_2$ plane. The approximate surface, as defined by equation (16), for each of the identified h's is

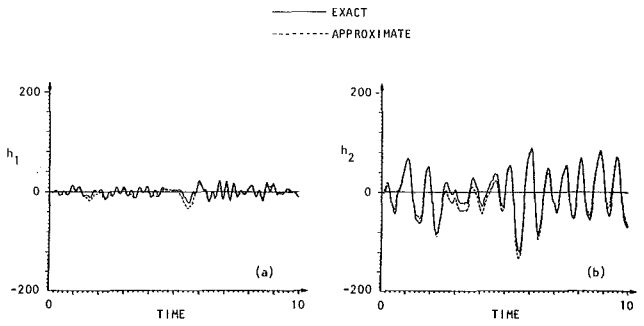

Fig. 8 Comparison of the time histories of the exact and approximate modal restoring forces $h_i(t)$

plotted in a three-dimensional form in Fig. 7, which also shows the three-dimensional representation of the "exact" value of h plotted as a function of θ_1 and θ_2 where $\theta_i = \cos^{-1} v_i$. The values of the equivalent linear stiffness and equivalent viscous damping associated with each of the generalized coordinates u_i can be readily ascertained from the three-dimensional plots of Figs. 7(*b*) and (*d*). A comparison of the time history of the exact and approximate modal h is shown in Fig. 8.

3.5 Validation of Reduced-Order Model. In order to demonstrate the validity of the present model-order reduction approach, the model representation expressed by the C_{kl} coefficients, which were extracted from the original ("exact") model response under a probing signal consisting of stationary broad-band excitation, will now be used to predict the response of the original model when subjected to non-stationary random excitation consisting of modulated white noise.

Using the identification results for prediction purposes, by following the steps indicated in equations (27–29), results in the response time history shown in Figs. 9–11. It is seen that satisfactory agreement is obtained between the measured and predicted response both in amplitude as well as frequency content. As one would expect, the results shown in Fig. 9 indicate that the least deviation error is achieved in the primary degrees of freedom (x_1, x_4, x_7) which dominate the displacement response. Similar comments apply to the higher-derivative response measures of velocity and acceleration shown in Figs. 10 and 11, respectively.

Due to the nature of the model-order reduction method under discussion, in which the generalized nonlinear system restoring forces are matched by an approximating analytical expression, good agreement is obtained between the measured and predicted system acceleration, particularly for the primary degrees of freedom. In fact, due to the excellent agreement between the two acceleration curves shown in each of Figs. 11(*a*), (*d*), and (*g*), one would need to carefully examine a much more expanded time scale before any detectable variation between the two curves is discernible.

Further details regarding the identification and validation of the example reduced-order model are available in [26].

4 Summary and Conclusions

An approximate method is presented for reducing the order of discrete multidegree-of-freedom dynamic systems that possess arbitrary nonlinear characteristics. The reduction method uses conventional condensation techniques for linear systems together with the nonparametric identification of the reduced-order model generalized nonlinear restoring forces to develop a rational procedure for reducing the order of the class of nonlinear systems under discussion.

The utility of the proposed method is demonstrated by considering a redundant three-dimensional finite element

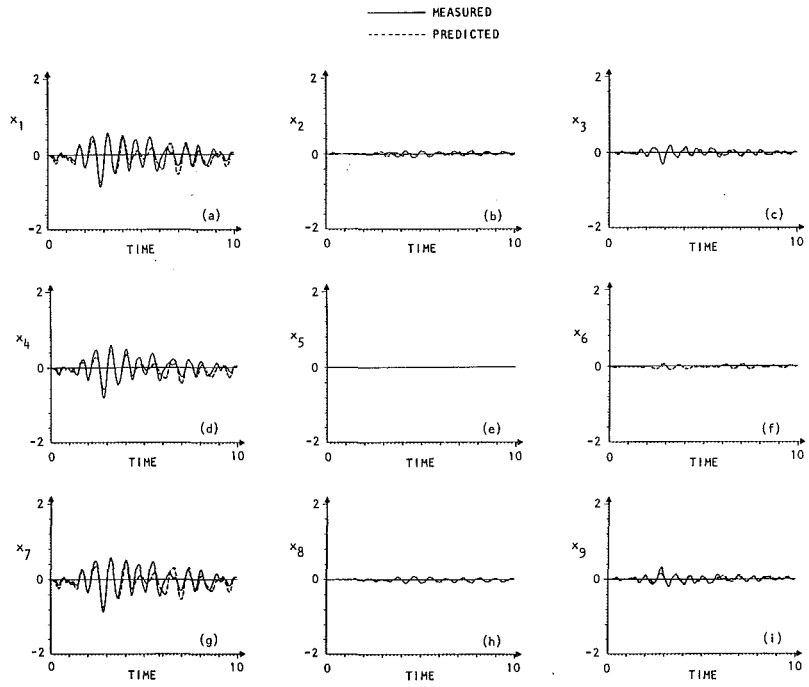

Fig. 9 Comparison between the measured and predicted displacement of the hysteretic system under nonstationary excitation by using a reduced-order model identified with a different stationary random excitation

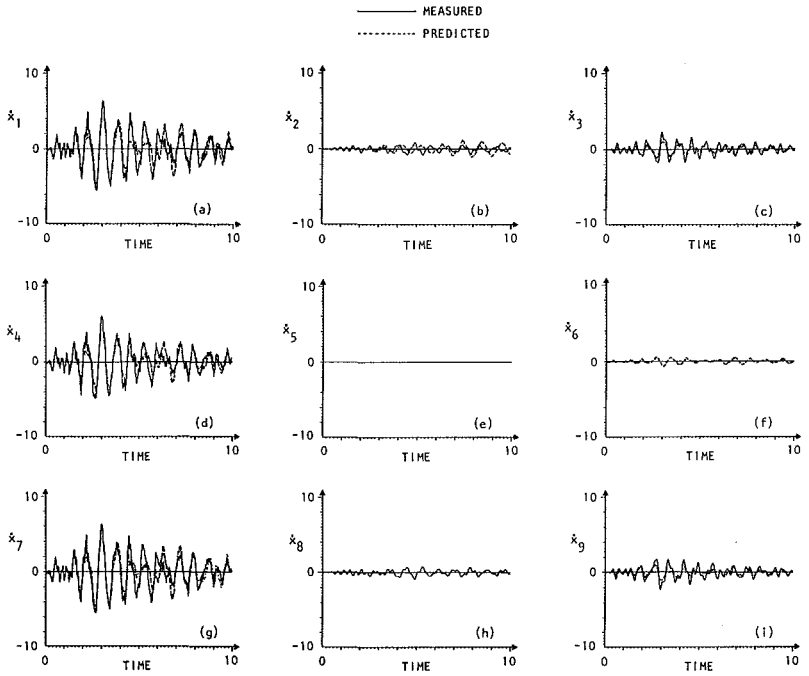

Fig. 10 Comparison between the measured and predicted velocity of the hysteretic system under nonstationary excitation by using a reduced-order model identified with a different stationary random excitation

model consisting of 12 nonlinear truss elements half of which incorporate hysteretic characteristics. This structure, which has nine DOF, is subjected to stationary wideband random excitation and subsequently a nonlinear reduced-order model of three DOF is developed. The original structure is then subjected to a new nonstationary random excitation and its measured response is compared to the predictions obtained by subjecting the reduced-order model to this new excitation. In spite of the reduction of the nonlinear model-order by a factor of 3, satisfactory agreement is obtained in regard to the deviation error between the predicted and measured response time history of all degrees of freedom of the original model. This deviation error is least in the case of the primary (dominant) DOF. Furthermore, the accuracy of the predicted accelerations are as good, if not better, than the lower-derivative response measures.

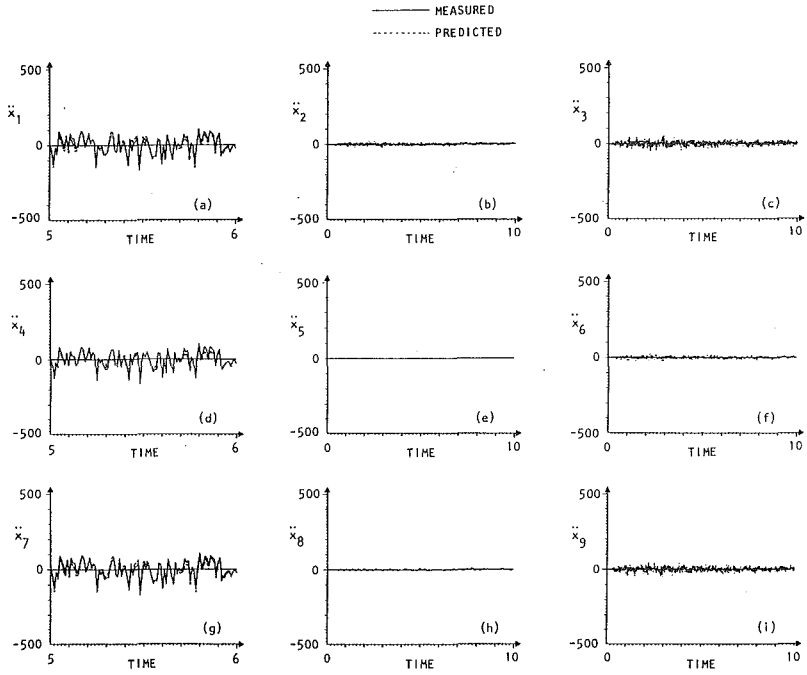

Fig. 11 Comparison between the measured and predicted acceleration of the hysteretic system under nonstationary excitation by using a reduced-order model identified with a different stationary random excitation

Acknowledgments

This study was supported in part by a grant from the National Science Foundation.

References

1 Cook, R. D., *Concepts and Applications of Finite Element Analysis*, 2nd Ed., Wiley, New York, 1981.

2 Geradin, M., "Error Bounds for Eigenvalue Analysis by Elimination of Variables," *Journal of Sound and Vibration*, Vol. 19, 1971, pp. 111–132.

3 Guyan, R. J., "Reduction of Stiffness and Mass Matrices," *AIAA Journal*, Vol. 3, No. 2, 1965, p. 380.

4 Hensell, R. D., and Ong, J. H., "Automatic Masters for Eigenvalue Economization," *Earthquake Engineering and Structural Dynamics*, Vol. 3, 1975, pp. 375–383.

5 Hughes, T. J. R., "Reduction Scheme for Some Structural Eigenvalue Problems by a Variational Theorem," *Int. Journal for Numerical Methods in Engineering*, Vol. 10, 1976, pp. 845–852.

6 Irons, B. M., "Structural Eigenvalue Problems: Elimination of Unwanted Variables," *AIAA Journal*, Vol. 3, No. 5, 1965, pp. 961–962.

7 Kidder, R. L., "Reduction of Structural Frequency Equations," *AIAA Journal*, Vol. 11, No. 6, 1973, p. 892.

8 Leung, Andrew Jee-Tak, "An Accurate Method of Dynamic Condensation in Structural Analysis," *Int. Journal for Numerical Method in Engineering*, Vol. 12, 1978, pp. 1705–1715.

9 Miller, C. A., "Dynamic Reduction of Structural Models," *Journal of the Structural Division ASCE*, 1980, pp. 2097–2108.

10 Noor, A. K., "On Making Large Non-Linear Problems Small," *Comput. Meth. Appl. Mech.*, Vol. 34, Nos. 1–3, 1982, pp. 955–985.

11 Ramsden, J. N., and Stoker, J. R., "Mass Condensation: A Semi-Automatic Method for Reducing the Size of Vibration Problems," *Int. Journal for Numerical Methods in Engineering*, Vol. 1, 1969, pp. 333–349.

12 Vysloukh, V. A., Kandidov, V. P., and Chesnokov, S. S., "Reduction of the Degrees of Freedom in Solving Dynamic Problems by the Finite Element Method," *Int. Journal for Numerical Methods in Engineering*, Vol. 7, 1973, pp. 185–194.

13 Wilson, E. L., "The Static Condensation Algorithm," *Int. Journal for Numerical Methods in Engineering*, Vol. 8, 1974, pp. 198–203.

14 Ibanez, P., "Review of Analytical and Experimental Techniques for Improving Structural Dynamic Models," *Welding Research Council Bulletin*, No. 249, June 1979.

15 Caughey, T. K., "Nonlinear Analysis, Synthesis and Identification Theory," *Proc. Symposium on Testing and Identification of Nonlinear Systems*, California Institute of Technology, Mar. 1975, pp. 1–14.

16 Andronikou, A. M., and Bekey, G. A., "Identification of Hysteretic Systems," *Proc. of the 18th IEEE Conf. on Decision and Control*, Dec. 1979, pp. 1072–1073.

17 Distefano, N., and Todeschini, R., "Modeling, Identification and Prediction of a Class of Nonlinear Viscoelastic Materials," *International Journal of Solids and Structures*, Part I, Vol. 9, 1974, pp. 805–818.

18 Caughey, T. K., "Random Excitation of a System with Bilinear Hysteresis," ASME JOURNAL OF APPLIED MECHANICS, Vol. 27, No. 4, Dec. 1960, pp. 649–652.

19 Iwan, W. D., "The Steady-State Response of the Double Bilinear Hysteretic System," ASME JOURNAL OF APPLIED MECHANICS, Vol. 32, No. 4, Dec. 1965, pp. 921–925.

20 Iwan, W. D., "A Distributed-Element Model for Hysteresis and Its Steady-State Dynamic Response," ASME JOURNAL OF APPLIED MECHANICS, Vol. 33, No. 4, Dec. 1966, pp. 893–900.

21 Iwan, W. D., and Lutes, L. D., "Response of the Bilinear Hysteretic System to Stationary Random Excitation," *Journal of the Acoustical Society of America*, Vol. 43, No. 3, Mar. 1968, pp. 545–552.

22 Jennings, P. C., "Periodic Response of a General Yielding Structure," *Journal of Engineering Mechanics Division*, Proc. ASCE, Vol. 90, No. EM2, 1964, pp. 131–166.

23 Lutes, L. D., and Takemiya, H., "Random Vibration of Yielding Oscillator," *Journal of the Engineering Mechanics Division*, Proc. ASCE, Vol. 100, No. EM2, pp. 343–358.

24 Hudson, D. E., "Equivalent Viscous Friction for Hysteretic Systems With Earthquake-Like Excitation," *Proc. 3WCEE*, New Zealand, 1965.

25 Jennings, P. C., "Equivalent Viscous Damping for Yielding Structures," *Journal of Engineering Mechanics*, ASCE, Feb. 1968.

26 Masri, S. F., Miller, R. K., Sassi, H., and Caughy, T. K., "A Method for Reducing the Order of Nonlinear Dynamic Systems," Civil Engineering Dept., University of Southern California, Report No. USC-CE-8307, Aug. 1983.

M. R. Hyams
Graduate Student.

L. A. Month
Assistant Professor of Applied Mechanics.

Department of Mechanical Engineering,
Etcheverry Hall,
University of California,
Berkeley, Calif. 94720

The Origin of Stability Indeterminacy in a Symmetric Hamiltonian

The stability and bifurcation of periodic motions in a symmetric two-degree-of-freedom Hamiltonian system is studied by a reduction to a two-dimensional action-angle phase plane, via canonical perturbation theory. The results are used to explain why linear stability analysis will always be indeterminate for the in-phase mode in a class of coupled nonlinear oscillators.

1 Introduction

Previous works have shown that canonical perturbation theory can be used to study the stability of motions of dynamical systems [3, 4]. In this paper we reduce motion in a four-dimensional phase space to motion in a two-dimensional space of transformed "action-angle" variables. We show how we can use canonical perturbation theory and internal resonance to derive the equations as well as the first integral governing the flow of the system in a reduced action-angle phase plane. This enables us to completely describe the motion. We show that periodic motions of the original system correspond to singular points in the phase plane. We study the motion by investigating the stability of the singular points.

Stability indeterminancy of a singular point (periodic motion) can occur at a transition from stable (S) to unstable (U) due to a bifurcation of periodic orbits. However, sometimes the bifurcation is "hidden" in a higher dimensional parameter space. It is often difficult to find the appropriate embedding of the parameters. In this paper we show that the appropriate embedding for a certain class of coupled nonlinear oscillators is the general three-parameter symmetric Hamiltonian. This result shows why the linear stability of the in-phase mode of vibration will *always* be indeterminate in this class of systems.

We study a general three-parameter symmetric Hamiltonian with an even quartic potential and two generalized coordinates. In Section 2 we show how canonical perturbation theory can be used to reduce the four-dimensional phase space to a two-dimensional action-angle phase plane. The singular points in the action-angle phase plane correspond to periodic orbits.

In Section 3 we summarize the phase plane configurations and show the structure of the bifurcations of the periodic motions.

In Section 4 we apply our bifurcation analysis of the general Hamiltonian system. We examine a class of coupled nonlinear oscillators which have bifurcating nonlinear normal modes (NNM's). By treating this one-parameter system as a subset of a general three-parameter Hamiltonian system, we are able to explain the linear stability indeterminacy of the in-phase mode.

2 Internal Resonance and the Action-Angle Phase Plane

We consider a nonlinear autonomous two-degree-of-freedom Hamiltonian system S with the symmetric Hamiltonian

$$H(x,y,p_x,p_y) = H^{(2)} + H^{(4)} = h \tag{2.1a}$$

$$H^{(2)} = \frac{1}{2}(p_x{}^2 + p_y{}^2) + \frac{1}{2}(x^2 + \omega^2 y^2) \tag{2.1b}$$

$$H^{(4)} = \alpha x^4 + \beta x^3 y + \gamma x^2 y^2 + \beta x y^3 + \alpha y^4. \tag{2.1c}$$

Here x and y are the generalized coordinates, p_x and p_y are the generalized momenta, ω is the ratio of the linearized frequencies, $H^{(n)}$ is a homogeneous polynomial of degree n, and α, β, and γ are arbitrary constants. By symmetric, we mean that

$$H^{(4)}(x,y) = H^{(4)}(y,x). \tag{2.1d}$$

The equations of motion for the system are

$$\dot{x}_i = \frac{\partial H}{\partial p_i}, \quad \dot{p}_i = \frac{-\partial H}{\partial x_i} \quad i = 1,2. \tag{2.2}$$

We have used the notation

$$x_1 = x, \quad x_2 = y, \quad p_1 = p_x, \quad p_2 = p_y.$$

The system possesses a first integral corresponding to the conservation of energy, equation (2.1). We wish to find an approximate first integral independent of the Hamiltonian. We use canonical perturbation theory methods described previously [3, 4].

Contributed by the Applied Mechanics Division for presentation at the 1984 PVP Conference and Exhibition Joint with Applied Mechanics Division and Materials Division, San Antonio, Texas, June 17-21, 1984 of THE AMERICAN SOCIETY OF MECHANICAL ENGINEERS.

Discussion on this paper should be addressed to the Editorial Department, ASME, United Engineering Center, 345 East 47th Street, New York, N.Y. 10017, and will be accepted until two months after final publication of the paper itself in the JOURNAL OF APPLIED MECHANICS. Manuscript received by ASME Applied Mechanics Division, August, 1983; final revision, September, 1983. Paper No. 84-APM-25.

Copies will be available until February, 1985.

As a first step we transform to action-angle variables ϕ_i, J_i of the linearized system ($H^{(4)}=0$):

$$x=\sqrt{2J_1}\,\sin\phi_1, \qquad y=\sqrt{2J_2/\omega}\,\sin\phi_2 \tag{2.3a}$$

$$p_x=\sqrt{2J_1}\cos\phi_1, \qquad p_y=\sqrt{2\omega J_2}\,\cos\phi_2. \tag{2.3b}$$

The Hamiltonian transforms to

$$\tilde{H}=\tilde{H}^{(2)}+\tilde{H}^{(4)}, \tag{2.4}$$

with

$$\begin{aligned}\tilde{H}^{(2)}&=J_1+\omega J_2\\ \tilde{H}^{(4)}&=4\alpha {J_1}^2\sin^4\phi_1\\ &\quad+\frac{4\beta}{\omega^{1/2}}{J_1}^{3/2}{J_2}^{1/2}\sin^3\phi_1\sin\phi_2\\ &\quad+\frac{4\gamma}{\omega}J_1J_2\sin^2\phi_1\sin^2\phi_2\\ &\quad+\frac{4\beta}{\omega^{3/2}}{J_1}^{1/2}{J_2}^{3/2}\sin\phi_1\sin^3\phi_2+\frac{4\alpha}{\omega^2}{J_2}^2\sin^4\phi_2.\end{aligned} \tag{2.5}$$

We next make a near identity canonical transformation from ϕ_i, J_i to ψ_i, I_i based on the generating function $S=\phi_1I_1+\phi_2I_2+W^{(4)}(\phi_i,I_i)$:

$$J_i=I_i+\frac{\partial W^{(4)}}{\partial\phi_i}, \quad \psi_i=\phi_i+\frac{\partial W^{(4)}}{\partial I_i} \quad i=1,2. \tag{2.6}$$

We note that $J_i=0(h)$ and $H^{(4)}$ and $W^{(4)}$ are $0(h^2)$. Consequently, $\psi_i=\phi_i+0(h)$ and $W^{(4)}(\phi_i,I_i)=W^{(4)}(\psi_i,I_i)+0(h^3)$.

In what follows, we neglect terms of $0(h^3)$. Substitution of (2.6) into (2.4) gives the new Hamiltonian K.

$$K(\psi_i,I_i)=K^{(2)}+K^{(4)}, \tag{2.7}$$

$$K^{(2)}=I_1+\omega I_2$$

and

$$K^{(4)}=\tilde{H}^{(4)}+LW^{(4)}, \tag{2.8}$$

where

$$L=\frac{\partial}{\partial\psi_1}+\omega\frac{\partial}{\partial\psi_2}$$

and $\tilde{H}^{(4)}$ is given by (2.5) with ϕ_i, J_i transformed to ψ_i, I_i.

We choose $W^{(4)}$ so as to remove as many angle terms from $K^{(4)}$ as possible. If $\omega\neq 1,3$ (no internal resonance) then all the angle terms can be removed from $K^{(4)}$. The transformed Hamiltonian (2.7) becomes

$$K(I_i)=I_1+\omega I_2+\frac{3}{2}\alpha\left({I_1}^2+\frac{{I_2}^2}{\omega^2}\right)+\gamma\frac{I_1I_2}{\omega}, \omega\neq 1,3.$$

We note that since ψ_i, $i=1, 2$ are ignorable coordinates, I_1 and I_2 are two independent constants of the motion (neglecting $O(h^3)$); equivalently any linear combination of I_1 and I_2 is an approximate constant of the motion, independent of the Hamiltonian.

If $\omega=1, 3$ then ψ_1 and ψ_2 are not ignorable coordinates. This is because the right-hand side of (2.8) contains terms of the form $\cos n\omega(\psi_1-\psi_2)$ which lie in the null space of the operator L and hence cannot be removed from $K^{(4)}$. We find that the transformed Hamiltonian (2.7) is either

$$\begin{aligned}K&=I_1+I_2+\frac{3}{2}\alpha({I_1}^2+{I_2}^2)\\ &\quad+\frac{3}{2}\beta\sqrt{I_1I_2}\,(I_1+I_2)\cos(\psi_1-\psi_2)\\ &\quad+\frac{1}{2}\gamma I_1I_2\cos 2(\psi_1-\psi_2)+\gamma I_1I_2 \quad(\omega=1)\end{aligned} \tag{2.9}$$

or

$$K=I_1+3I_2+\frac{3}{2}\alpha\left({I_1}^2+\frac{1}{9}{I_2}^2\right)$$

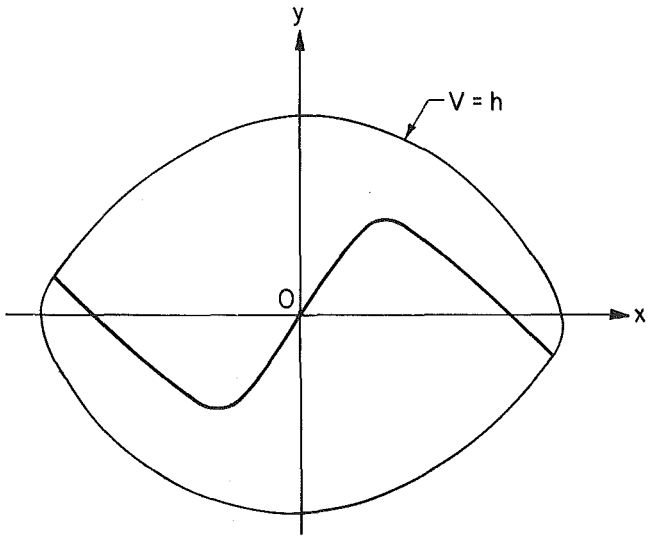

Fig. 2.1 A nonlinear normal mode (NNM)

$$-\frac{\beta}{2\sqrt{3}}{I_1}^{3/2}{I_2}^{1/2}\cos(3\psi_1-\psi_2)+\frac{1}{3}\gamma I_1I_2 \quad(\omega=3).$$

If we define

$$\theta=\omega\psi_1-\psi_2 \tag{2.10}$$

then the equations of motion (2.2) are transformed to

$$\dot{I}_1=\frac{-\partial K}{\partial\psi_1}=-\omega\frac{\partial K}{\partial\theta}, \quad \dot{I}_2=\frac{-\partial K}{\partial\psi_2}=\frac{\partial K}{\partial\theta} \tag{2.11a}$$

$$\dot{\theta}=\omega\dot{\psi}_1-\dot{\psi}_2, \quad \dot{\psi}_i=\frac{\partial K}{\partial I_i} \quad i=1,2. \tag{2.11b}$$

From (2.1) we see that $\dot{I}_1+\omega\dot{I}_2=0$. Thus

$$I_1+\omega I_2=\text{constant}=h+0(h^2). \tag{2.12}$$

Use of (2.12) reduces the equations of motion to the form

$$\dot{I}_1=\omega\frac{\partial K}{\partial\theta}\equiv F(\theta,I_1), \quad \dot{\theta}=\omega\frac{\partial K}{\partial I_1}-\frac{\partial K}{\partial I_2}\equiv G(\theta,I_1). \tag{2.13}$$

Since both K and $K^{(2)}$ are constants, so is there difference. Thus the integral curves of (2.13) in the $\theta-I_1$ phase plane are parameterized by the first integral

$$K^{(4)}(\theta,I_1)=K-K^{(2)}=\text{constant}+0(h^3). \tag{2.14}$$

To show that the singular points of (2.13) are periodic motions of the original system given in (2.1) and (2.2) we require $\dot{\theta}=0$, $\dot{I}_1=0$, and we use the transformations given in (2.3) and (2.6). At a singular point I_1, I_2, θ, and $\dot{\psi}_i$ are constants.

$$I_1=I_0, \; I_2=I_0-h, \; \theta=\omega\psi_1-\psi_2=\theta_0 \tag{2.15a}$$

$$\dot{\psi}_i=\frac{\partial K}{\partial I_i}(\theta,I_i)=\text{const.}, \quad \omega\dot{\psi}_1=\dot{\psi}_2=\text{const.}=\Omega. \tag{2.15b}$$

The singular points (θ_0, I_0) correspond to the periodic motions

$$\begin{aligned}x(t)&=\sqrt{2I_0}\sin[\Omega_1(t)],\\ y(t)&=\sqrt{2(I_0-h)}\sin[\Omega_2(t)],\\ (\Omega_1(t)&=\frac{\Omega t+\theta_0}{\omega}+0(h); \;\; \Omega_2(t)=\Omega t+0(h)).\end{aligned} \tag{2.16}$$

The singular points $(0,I_0)$, (π,I_0) correspond to nonlinear normal modes (NNM's). In a manner similar to Rosenberg [5] we define NNM's to be periodic motions that pass through the origin 0 and which have two rest points, Fig. 2.1. If $\theta_0\neq 0,\pi$ the singular points are periodic motions which are not

NNM's. If $\omega=1$ then the singular points $(\frac{0}{\pi},I_0)$ are NNM's which project onto the $x-y$ plane as the straight lines $y=Cx$ [called similar normal modes] (SNM's).

3 Bifurcation Analysis

In the preceding section we showed that singular points in the action-angle phase plane correspond to periodic motions of system S. From (2.13) the governing equations for θ and I_1 are

$$\dot{\theta}=(h-2I_1)\left\{(\gamma-3\alpha)+\frac{1}{2}\gamma\cos 2\theta + \frac{3}{4}\beta h[I_1(h-I_1)]^{-1/2}\cos\theta\right\} \tag{3.1a}$$

$$\dot{I}_1=\sqrt{I_1(h-I_1)}\left[\frac{3}{2}\beta_h+2\gamma\sqrt{I_1(h-I_1)}\cos\theta\right]\sin\theta \tag{3.1b}$$

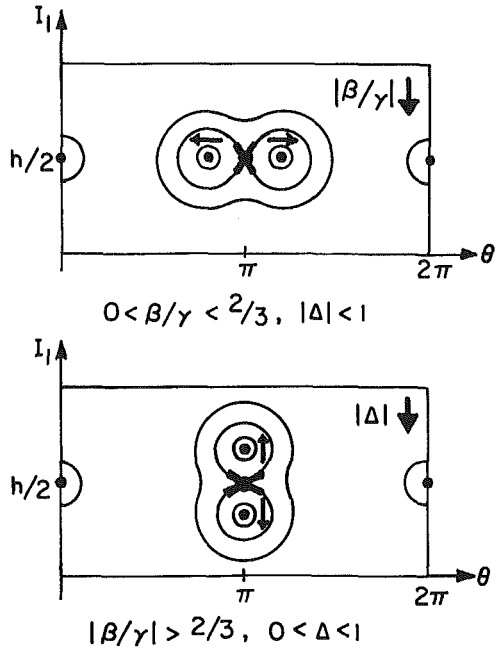

Fig. 3.1 Sketches of the action-angle phase plane for system S, when one pair of periodic motions has bifurcated. Periodic motions appear as stable centers (0) or unstable saddles (X). Arrows show the location of the bifurcating periodic motions as the bifurcation parameter shown in the upper right-hand corner decreases. If the sign of the parameter switches, θ is translated by π.

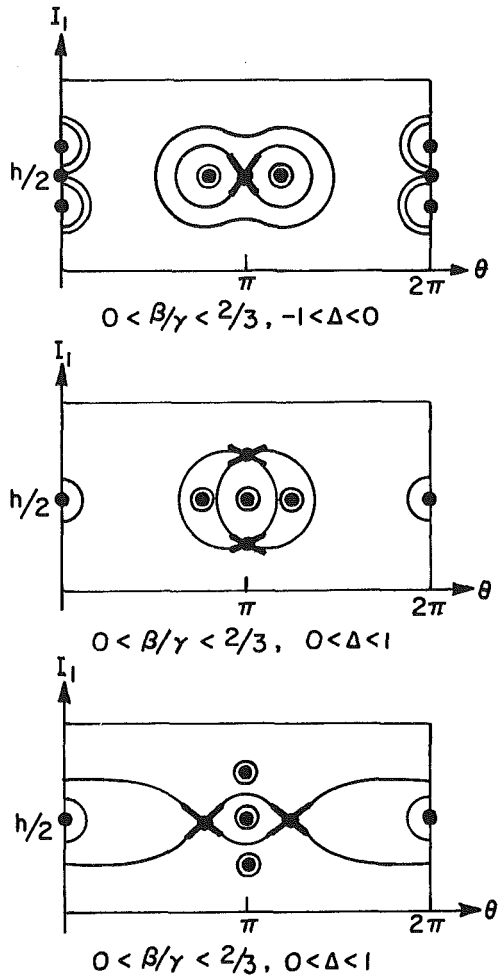

Fig. 3.2 Sketches of the action-angle phase plane configurations for system S when two pairs of periodic motions have bifurcated. Each pair bifurcates from one of the SNM's $(0, h/2)$ or $(\pi, h/2)$. If both the parameters switch signs the phase portrait shifts by $\theta=\pi$.

Table 3.1 Stability and existence of singular points (θ,I_1) in the action-angle phase plane of system S. Each singular point corresponds to a periodic motion. The column under stable indicates the parameter ranges for which the singular point is stable.

Singular point	Existence	Stable	Indeterminate
$\left(0,\frac{h}{2}\right)$	Always	$\operatorname{sgn}[\beta+(\gamma-2\alpha)]=\operatorname{sgn}\left(\gamma+\frac{3}{2}\beta\right)$	$\beta/\gamma=-\frac{2}{3}$ or $\beta=-(\gamma-2\alpha)$
$\left(\pi,\frac{h}{2}\right)$	Always	$\operatorname{sgn}[\beta-(\gamma-2\alpha)]=-\operatorname{sgn}\left(\gamma-\frac{3}{2}\beta\right)$	$\beta/\gamma=\frac{2}{3}$ or $\beta=\gamma-2\alpha$
$\left[\cos\left(-\frac{3}{2}\beta/\gamma\right),\frac{h}{2}\right]$	$\lvert\beta/\gamma\rvert<\frac{2}{3}$, $\gamma\neq 0$	$\operatorname{sgn}(\gamma)=-\operatorname{sgn}(\gamma-6\alpha)$	$\gamma=6\alpha$
$\left\{0,\frac{h}{2}[1\pm\sqrt{1-\Delta^2}]\right\}$	$-1<\Delta<0$, $\gamma\neq 2\alpha$	$\operatorname{sgn}(\gamma-6\alpha)=\operatorname{sgn}(\gamma-2\alpha)$	
$\left\{\pi,\frac{h}{2}[1\pm\sqrt{1-\Delta^2}]\right\}$	$0<\Delta<1$, $\gamma\neq 2\alpha$		

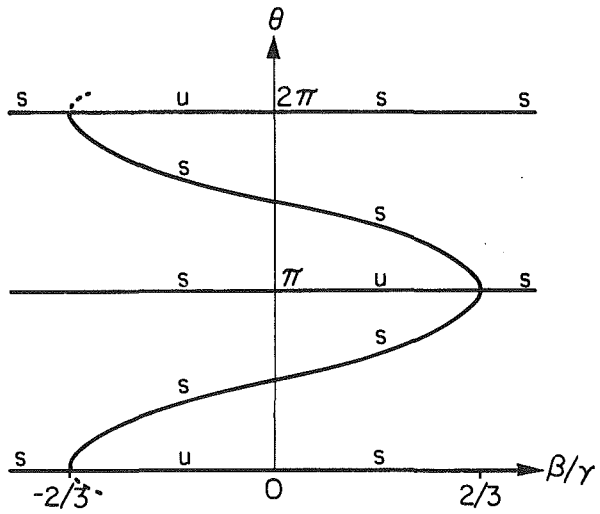

Fig. 3.3 Bifurcation of periodic motions for system *S*. The parameter β/γ is varied and the parameter Δ is fixed in the range $|\Delta|>1$. *S* ≡ stable; *U* ≡ unstable.

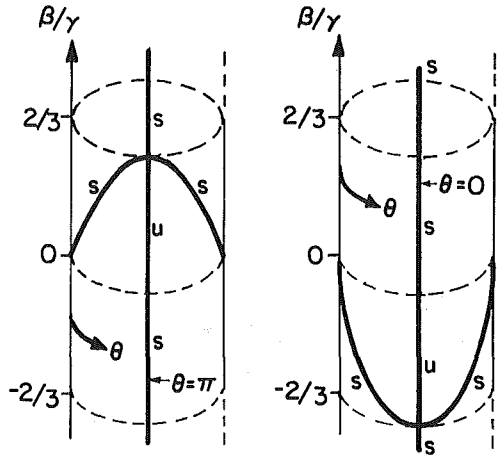

Fig. 3.4 Double pitchfork bifurcation for system *S*. Both "front" and "rear" views of the cylinder with azimuthal angle θ and vertical axis β/γ are shown. The handle of the pitchfork corresponds to the $\theta=0(\pi)$, $I_1=h/2$ SNM, and the prongs correspond to the periodic motions bifurcating from $\theta=0(\pi)$, $\beta/\gamma=-2/3\,(+2/3)$. *S* ≡ stable; *U* = unstable.

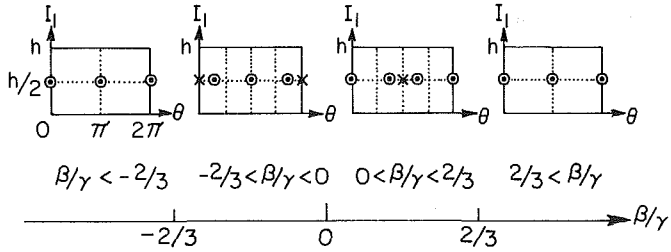

Fig. 3.5 Sketches of the action-angle phase plane for the system *S* corresponding to the bifurcation of periodic motions shown in Figs. 3.3 and 3.4

Requiring that $\dot{\theta}$ and $\dot{I}_1$ vanish simultaneously we find the following sets of singular points (θ, I_1):

$$\left[\left(0,\frac{h}{2}\right) \text{ and } \left(\pi,\frac{h}{2}\right)\right] \equiv \left(\begin{matrix}0\\ \pi\end{matrix},\frac{h}{2}\right) \tag{3.2}$$

$$\left(\cos^{-1}-\frac{3}{2}\frac{\beta}{\gamma},\frac{h}{2}\right), \quad \left|\frac{\beta}{\gamma}\right|<\frac{2}{3} \tag{3.3}$$

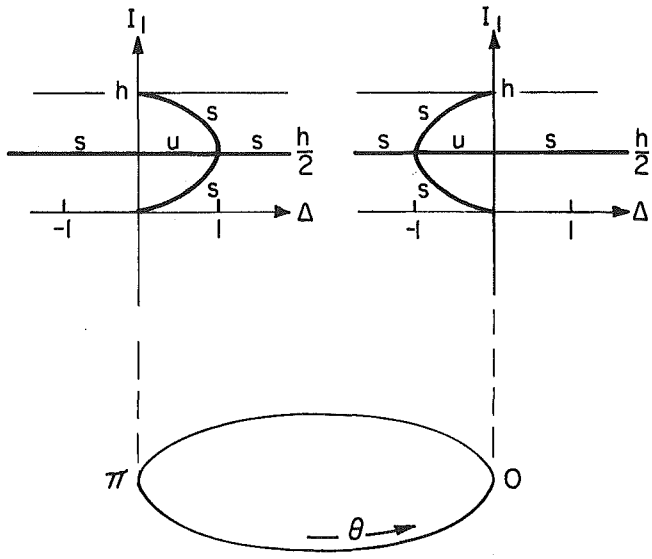

Fig. 3.6 Bifurcation of SNM's in system *S*. The parameter Δ is varied and the parameter β/γ is fixed in the range $|\beta/\gamma|>2/3$. *S* ≡ stable; *U* ≡ unstable.

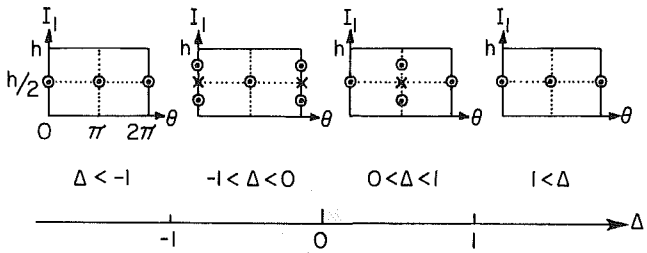

Fig. 3.7 Sketches of the action-angle phase plane for system *S* corresponding to the birfurcations of SNM's shown in Fig. 3.6

$$\left(\begin{matrix}0\\ \pi\end{matrix},\frac{h}{2}[1\pm\sqrt{1-\Delta}]^2\right), \quad \Delta\equiv\frac{\beta}{\gamma-2\alpha}, \quad \begin{matrix}\theta=0,\ -1<\Delta<0\\ \theta=\pi,\ 0<\Delta<1\end{matrix} \tag{3.4}$$

Since the vector field is Hamiltonian the singular points are either stable centers or unstable saddle points. A summary of the existence and stability of the singular points is shown in Table 3.1. From equations (3.1) we see that the $\theta-I_1$ phase portraits will be symmetric about $(\pi,h/2)$ and that the flow is invariant under the transformations

$$\left\{\begin{matrix}\theta\to\theta\pm\pi\\ \beta\to-\beta\end{matrix}\right\}, \quad \left\{\begin{matrix}\alpha,\gamma\to-\alpha,-\gamma\\ \theta\to\theta\pm\pi\\ t\to-t\end{matrix}\right\}, \tag{3.5}$$

Also the following transformations are equivalent:

$$\left\{\begin{matrix}\theta\to\theta\pm\pi\\ t\to-t\end{matrix}\right\}\left\{\begin{matrix}\beta\to-\beta\\ t\to-t\end{matrix}\right\}\left\{\begin{matrix}\alpha\to-\alpha\\ \gamma\to-\gamma\end{matrix}\right\}. \tag{3.6}$$

We divide the phase portraits into three groups of configurations dependent on the parameters α, β, and γ. The number of singular points (periodic motions) varies from group to group. The first group is defined by

$$\left|\frac{\beta}{\gamma}\right|>\frac{2}{3}, \quad |\Delta|>1. \tag{3.7}$$

In this parameter range, the only two singular points $(\begin{matrix}0\\ \pi\end{matrix}, h/2)$ are always stable; i.e., there exist two stable periodic motions (SNM's), an in-phase mode and an out-of-phase mode. The second group is defined by

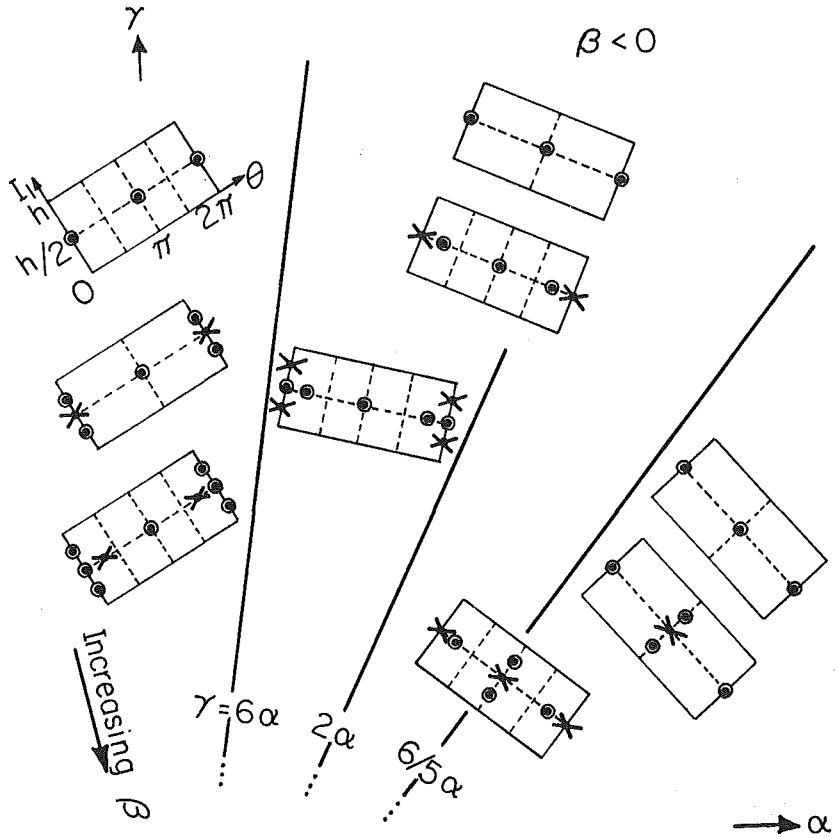

Fig. 3.8 Sketches of the action-angle phase plane for system S. Wedges in the $\alpha\sqrt{\gamma}$ plane define regions of admissible $\theta - I_1$ configurations. Moving radially inward inside each wedge corresponds to increasing β. The $\theta - I_1$ coordinates are shown in the upper left-hand corner.

$$\left|\frac{\beta}{\gamma}\right| < \frac{2}{3}, \ |\Delta| > 1. \tag{3.8}$$

or

$$\left|\frac{\beta}{\gamma}\right| > \frac{2}{3}, \ |\Delta| < 1. \tag{3.9}$$

This group contains both the in-phase and out-of-phase SNM's $\binom{0}{\pi}, h/2)$ and one additional pair of periodic motions which bifurcate from one of the SNM's. If $|\beta/\gamma| < 2/3$ the pair of singular points

$$\left(\cos^{-1} - \frac{3}{2}\frac{\beta}{\gamma}, \ \frac{h}{2}\right)$$

bifurcates from either $(0, h/2)$ or $(\pi, h/2)$ depending on the sign of β/γ, Fig. 3.1. If $|\beta/\gamma| > 2/3$ then the pair of singular points, either

$$\left(0, \frac{h}{2}[1 \pm \sqrt{1-\Delta^2}]\right) \text{ or } \left(\pi, \frac{h}{2}[1 \pm \sqrt{1-\Delta^2}]\right)$$

bifurcates depending on the sign of Δ, Fig. 3.1. The third group

$$\left|\frac{\beta}{\gamma}\right| < \frac{2}{3}, \ |\Delta| < 1 \tag{3.10}$$

contains six singular points. These are

$$\left(\begin{matrix}0\\ \pi\end{matrix}, \frac{h}{2}\right), \ \left(\cos^{-1} - \frac{3}{2}\frac{\beta}{\gamma}, \frac{h}{2}\right)$$

and either $(0, h/2\,[1 \pm \sqrt{1-\Delta^2}])$ or $(\pi, h/2\,[1 \pm \sqrt{1-\Delta^2}]\ )$, Fig. 3.2.

From Figs. 3.1 and 3.2 we see that β/γ and Δ are the bifurcation parameters and $\binom{0}{\pi}, h/2)$ are bifurcation points. The bifurcation diagram for β/γ is shown in Fig. 3.3. This diagram shows the stability of the periodic motion $\theta = \cos^{-1} - 3/2\ \beta/\gamma$ (and $I_1 = h/2$) as a function of the parameter β/γ. For $|\beta/\gamma| > 2/3$ the two periodic motions are represented by the lines $\theta = 0, \pi$. For $|\beta/\gamma| < 2/3$ two additional stable periodic motions bifurcate from the $\theta = 0$ or π periodic motion and the stability of the $\theta = 0$ or π solution changes from stable to unstable, Fig. 3.3.

Since θ is 2π periodic the bifurcation diagram in Fig. 3.3 is really a section on the surface of a cylinder. In Fig. 3.4 we show the *double pitchfork* bifurcation on a cylinder with azimuthal angle θ and vertical axis β/γ. One side of the cylinder has a pitchfork with handle $\theta = 0$. The prongs correspond to the additional periodic motions bifurcating from $\theta = 0$, $\beta/\gamma = -2/3$. The other side of the cylinder has handle $\theta = \pi$ and prongs originating from $\theta = \pi$, $\beta/\gamma = +2/3$. The sequence of phase plane portraits corresponding to this bifurcation is shown in Fig. 3.5.

We can similarly analyze the bifurcation of the periodic motions $\theta = 0, \pi \quad I_1 = h/2[1 \pm \sqrt{1-\Delta^2}]$. The bifurcation parameter is Δ, Fig. 3.6. Figure 3.7 shows the corresponding sequence of phase plane configurations.

For both pairs of bifurcating periodic solutions to be present, $(\cos^{-1} - 3/2\,\beta/\gamma,\ h/2)$ and $\binom{0}{\pi},\ h/2\ [1+\sqrt{1-\Delta^2}]$, the parameters must satisfy $|\beta/\gamma| < 2/3$ and $|\Delta| < 1$, Table 3.1. The bifurcation diagram is in four-dimensional (β/γ, Δ, I_1, θ) space. As α, β, and γ are varied both bifurcation parameters β/γ, and $\Delta \equiv \beta/\gamma - 2\alpha$ vary and trace out a path that determines the order of bifurcations.

For example consider $\beta < 0$. We vary β from $-\infty$ to 0. The first bifurcation occurs at the smaller of the two values $\beta = \pm(2/3)\gamma$ or $\beta = \pm(\gamma - 2\alpha)$. As we vary β the phase portrait configurations are determined by the values of α and γ. In particular the lines $\gamma = 6\alpha$, $\gamma = 6/5\ \alpha$ and $\gamma = 2\alpha$ are transition curves in the three-dimensional parameter space (α, β, γ), Fig.

3.8. They divide the space into regions defined by the interaction of the two-dimensional bifurcation surfaces $\beta/\gamma = \pm 2/3$ and $\beta/\gamma - 2\alpha = \pm 1$.

We summarize the sequences of bifurcations in Fig. 3.8. The $\theta - I_1$ phase plane configurations are plotted in the $\alpha - \gamma$ parameter plane. The wedges formed by the curves $\gamma = 6\alpha$, $\gamma = 6/5\ \alpha$, and $\gamma = 2\alpha$ define regions of admissible configurations. The configurations for the lower $\alpha - \gamma$ half plane and for $\beta < 0$ can easily be found from the symmetries listed in (3.5) and (3.6).

4 Application

In this section we apply our results to a class of coupled nonlinear oscillators. We consider the system S shown in Fig. 4.1. The Hamiltonian is given by

$$H = T + V = \frac{1}{2}(p_x^2 + p_y^2) + V(x,y), \tag{4.1}$$

where the generalized coordinates x and y are displacements of the masses from the unstretched spring length. The potential $V(x,y)$ comes from the nonlinear spring forces

$$F_i = A_i\delta + B_i\delta^3, \quad i = 1,2,3 \tag{4.2}$$

where δ_i is the spring deformation, F_1 and F_3 are the forces in the anchor springs, and F_2 is the force in the coupling spring.

This puts the potential in the form

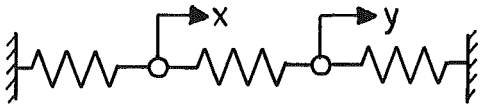

Fig. 4.1 The system S'

$$V(x,y) = \frac{A_1x^2}{2} + \frac{B_1x^4}{4} + \frac{A_2(x-y)^2}{2} + \frac{B_2(x-y)^4}{4} + \frac{A_3y^2}{2} + \frac{B_3y^4}{4}. \tag{4.3}$$

We can always rotate the $x-y$ axes along modal coordinate lines to eliminate the $x-y$ coupling in the quadratic terms of the potential. This is equivalent to requiring that the coupling spring in Fig. 4.1 be strictly nonlinear. Without loss of generality we choose

$$A_2 = 0, \quad A_1 = 1, \quad A_3 = \omega^2. \tag{4.4}$$

Substituting of (4.4) into (4.3) puts V in the form

$$V(x,y) = \frac{x^2}{2} + \frac{B_1x^4}{4} + \frac{B_2(x-y)^4}{4} + \frac{\omega^2y^2}{2} + \frac{B_3y^4}{4} \tag{4.5}$$

where ω is the ratio of the linearized frequencies.

Applying our analysis of symmetric Hamiltonians we choose (cf.(2.1))

$$\omega = 1, \quad B_1 = B_3. \tag{4.6}$$

We note that the symmetry of the Hamiltonian means that the anchor springs in system S are identical, Fig. 4.1. Substitution of (4.5) and (4.6) into (4.1) puts the Hamiltonian for system S in the form

$$H = \frac{1}{2}(x^2 + y^2 + p_x{}^2 + p_y{}^2) + (B_1 + B_2)\frac{x^4}{4} - B_2x^3y + \frac{3}{2}B_2x^2y^2 - B_2xy^3 + (B_1 + B_2)\frac{y^4}{4}. \tag{4.7}$$

Here B_1 is the coefficient of the nonlinear anchor spring forces and B_2 is the coefficient of the nonlinear coupling

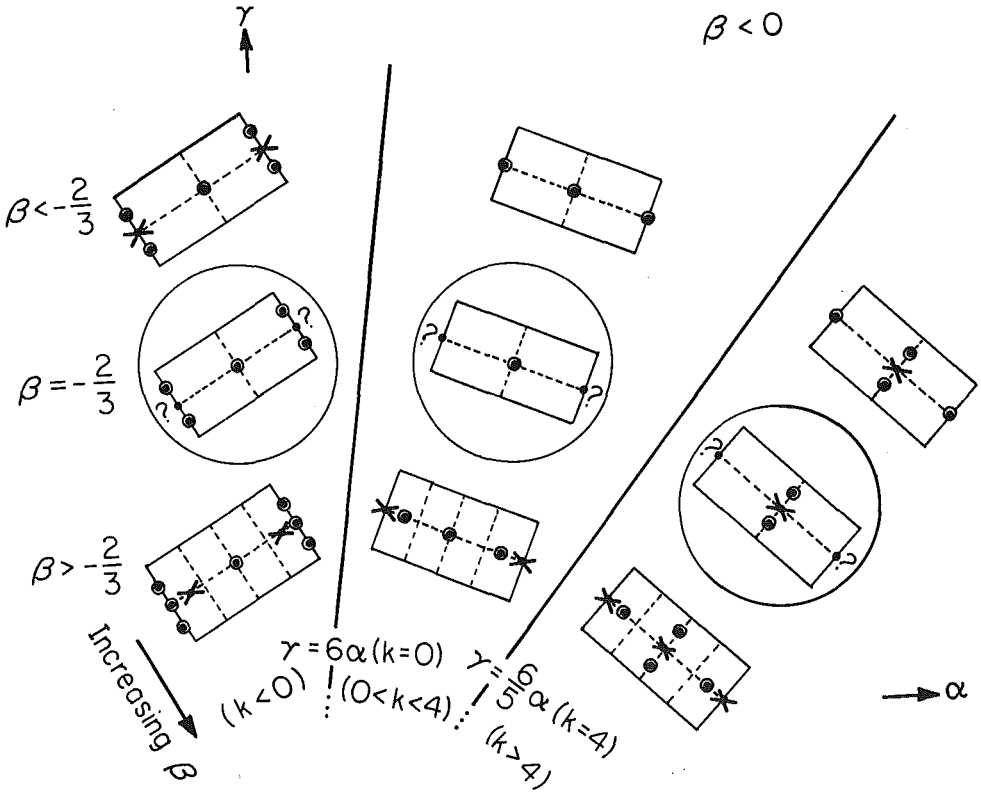

Fig. 4.2 Sketches of the action-angle phase plane illustrating stability indeterminacy of the in-phase mode in system S'. Circled configurations are those of system S'. The other configurations are for perturbations off of system S into system S. The question mark by the inphase mode indicates a stability transition due to a bifurcation at $\beta/\gamma = -2/3$.

spring force. Comparison with (2.1) reveals that system S is a member of the class of three-parameter symmetric Hamiltonians with

$$\alpha=(B_1+B_2)/4, \quad \beta=-1, \quad \gamma=3/2. \tag{4.8}$$

In Section 3 we showed that bifurcations of periodic motions occur when $\beta/\gamma=\pm 2/3$ or $\Delta\equiv\beta/\gamma-2\alpha=\pm 1$, Table 3.1. In system S we have

$$\frac{\beta}{\gamma}\equiv-\frac{2}{3}, \quad \Delta=\frac{2B_2}{2B_2-B_1}\equiv\frac{2}{2-k}. \tag{4.9}$$

Since $\beta/\gamma\equiv -2/3$, there are only two bifurcation points, $\Delta=\pm 1$ ($k=0,4$). System S has periodic motions

$$(\theta,I_1)=\left(\begin{matrix}0\\ \pi\end{matrix},\ \frac{h}{2}[1\pm\sqrt{1-\Delta^2}]\right)=\left(\begin{matrix}0\\ \pi\end{matrix},\ \frac{h}{2}\left[1\pm\frac{\sqrt{k(k-4)}}{2-k}\right]\right),$$

These are the SNM's, $y=Cx$, where

$$C=+1,-1,\frac{-1\pm\sqrt{1-\Delta^2}}{2}\equiv 1-\frac{k}{2}\pm\sqrt{k(k-4)}.$$

When $|\Delta|\geq 1$ ($0\leq k\leq 4$) there are only two periodic motions, the SNM's $y=\pm x$. An additional pair of periodic motions (SNM's) bifurcate out of the $y=-x$ mode when $0<\Delta<(k>4)$ and out of the $y=+x$ mode when $-1<\Delta<0(k<0)$. The stability of these modes has been examined in previous works [2, 3]. The authors showed that a linear stability analysis of the in-phase mode $y=+x$ fails to predict stability. To predict stability nonlinear terms in the action-angle phase plane (or in the Poincaré map approximation [3]) are needed. This nonlinear analysis reveals that for small energies h the in-phase mode is stable for $k>0$ and unstable for $k<0$.

Our analysis of system S summarized in Fig. 38 explains the linear stability indeterminacy of in-phase mode. For system S', $\beta/\gamma\equiv -2/3$, cf (4.9). In (α,β,γ) space this is a bifurcation point; two additional periodic motions $(\theta,I_1)=(\cos^{-1}-3/2(\beta/\gamma),\ h/2)$ bifurcate from the in-phase mode at $\beta/\gamma=-2/3$, Figs. 3.3, 3.4, Table 3.1. These motions are not NNMS's. As the value β/γ increases past $-2/3$, the stability of the in-phase mode changes. In Fig. 4.2, we summarize these results by plotting the sequences of phase plane configurations for system S ($\beta/\gamma\equiv 2/3$) as well as for perturbations away from $\beta/\gamma=-2/3$. We have circled the configurations of system S' in Fig. 4.2 to distinguish them from the configurations of the perturbed system, Fig. 4.2; cf. Fig. 3.9. Linear stability analysis of the in-phase mode in the system S of coupled nonlinear oscillators will always be indeterminate because $\beta/\gamma\equiv -2/3$.

5 Conclusion

We have investigated the dynamical structure of a symmetric Hamiltonian system S, by reducing the four-dimensional phase space to a two-dimensional action-angle phase plane, via canonical perturbation theory. In particular we investigated the stability and existence of periodic motions. We found that the system S has two or four or six periodic motions depending on the values of the parameters α, β, and γ. If the bifurcating motions enter as S (resp. U) then the mode from which they bifurcated changes from S (resp. U) to U (resp. S) upon bifurcation. We have analyzed the structure of the bifurcations and determined the dynamical structure of the system as a function of the parameters.

By embedding a one-parameter class of coupled nonlinear oscillators in the three parameter α, β, and γ space, we have shown that a bifurcation of periodic motions (which are not NNM's) from the in-phase mode causes the stability indeterminacy of the in-phase mode. Our results are valid for small h not only because the perturbation theory requires it but because KAM theory tells us that chaos will replace the invariant curves in the phase-plane configurations [1].

References

1 Arnol'd, V. I., *Mathematical Methods of Classical Mechanics*, Springer Verlag, 1978.

2 Month, L. A., and Rand, R. H., "The Stability of Bifurcating Periodic Solutions in a Two-Degree-of Freedom Nonlinear System," ASME JOURNAL OF APPLIED MECHANICS, Vol. 44, 1977, pp. 782–784.

3 Month, L. A., and Rand, R. H., "An Application of the Poincaré Map to the Stability of Nonlinear Normal Modes," ASME JOURNAL OF APPLIED MECHANICS, Vol. 47, 1980, pp. 645–651.

4 Month, L. A., and Rand, R. H., "Bifurcation of 4:1 Subharmonics in the Nonlinear Mathieu Equation," *Mechanics Research Communications*, Vol. 9, No. 4, 1982, pp. 233–240.

5 Rosenberg, R. M., "On Nonlinear Vibrations of Systems With Many Degrees of Freedom," *Advances in Applied Mechanics*, Academic Press, 1966, pp. 155–242.

M. Hubbard
Associate Professor,
Department of Mechanical Engineering,
University of California,
Davis, Calif. 95616
Mem. ASME

H. J. Rust
Graduate Student,
Department of Mechanical Engineering,
Stanford University,
Stanford, Calif. 94305
Student Mem. ASME

Javelin Dynamics With Measured Lift, Drag, and Pitching Moment

Optimal release conditions for the javelin are studied using computer simulation. Included are two important and realistic assumptions: (1) initial velocity attainable by the thrower is dependent on the throwing angle, and (2) the aerodynamic center of pressure moves as a function of angle of attack. Aerodynamic forces and moments, previously measured in wind tunnel tests, are incorporated in the simulation. Range contours are presented in the two-space of initial angle of attack – initial flight path angle, assuming zero initial angular velocity.

Introduction

Increasingly, computer simulation and the laws of mechanics have been used to gain understanding of track and field events. Two papers on the javelin [1, 2] have appeared in this journal. In an impressive first theoretical and numerical study of the javelin [1], Soong derived the equations of motion and studied the effects of various throw parameters including initial javelin attitude angle θ_j, flight path angle θ_f, position of the center of pressure d, and wind speed. The numerical results showed how range, time-of-flight, and entry angle varied as a function of the preceding parameters.

Although in any study of this sort many engineering assumptions and approximations must be made, two of Soong's assumptions seem to have had the largest effects on his results. These assumptions were that:

1. the initial velocity attainable by the thrower is independent of throwing angle (the initial javelin speed was held constant at 30.45 m/s in all calculations), and
2. the lift and drag profiles as functions of angle of attack are given by appropriately resolved theoretical expressions for friction and pressure drag, and that the pitching moment is the moment of these two forces acting at the center of pressure *which remains at a fixed distance d from the c.m. even as the angle of attack changes.*

Subject to the preceding assumptions, Soong concluded that: (1) the initial throwing angle is more influential on distance than initial javelin attitude, (2) the optimum throw angle for the NCAA official javelin ($d = 25.7$ cm) was about 43 deg and would decrease to near 35 deg when $d = 0.8$ cm, and (3) shifting the center of pressure to $d = 0.8$ cm could result in a dramatic increase in range of about 16 m to 106 m.

In reference [2], Red and Zogaib questioned the validity of Assumption 1. They presented experimental results from

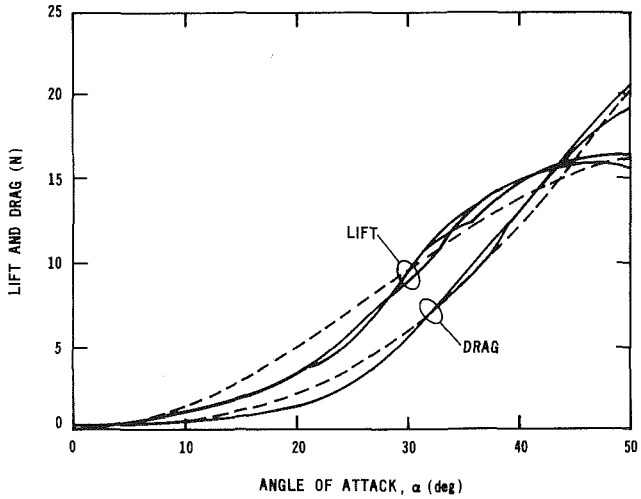

Fig. 1(*a*) Lift and drag forces

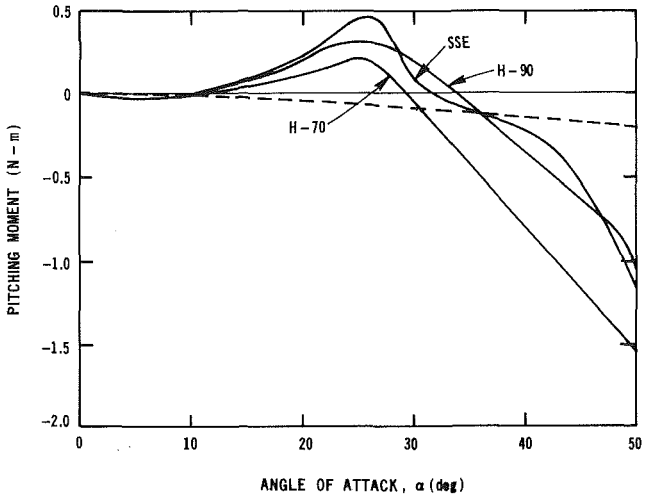

Fig. 1(*b*) Pitching moment

Fig. 1 Experimental (—) aerodynamic data ($V = 30.48$ m/s) for three javelins (Held-90 m, Held-70 m, Sandvik Super Elite) and theoretical approximations (-----) used in [1] and [2]

Contributed by the Applied Mechanics Division for publication in the JOURNAL OF APPLIED MECHANICS.

Discussion on this paper should be addressed to the Editorial Department, ASME, United Engineering Center, 345 East 47th Street, New York, N.Y. 10017, and will be accepted until two months after final publication of the paper itself in the JOURNAL OF APPLIED MECHANICS. Manuscript received by ASME Applied Mechanics Division, August, 1983; final revision, October, 1983.

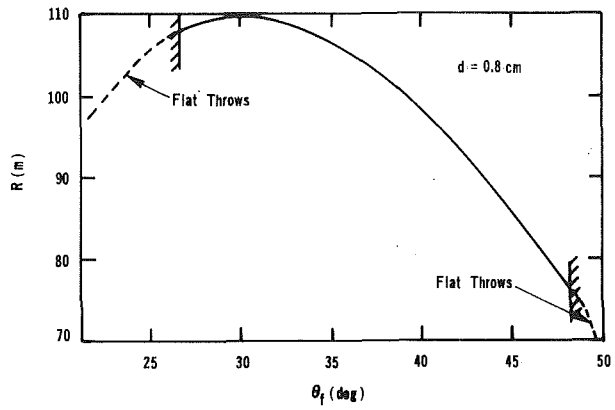

Fig. 2 Range versus flight path angle using theoretical aerodynamic approximations. $\theta_i = \theta_f$ deg but varying initial flight path angle θ_f and velocity $V_0 = 30.48 - 0.127\,(\theta_f - 35)$ m/s (corrected Fig. 3 from [2])

three throwers which showed that the attainable initial velocity decreases significantly with throwing angle. They then incorporated this dependence into a numerical solution of the equations of motion similar to that in [1]. Their results showed that the inability to throw as fast at larger throw angles implied that: (1) the optimum throw angle remains about 37 deg for both foregoing values of d, and (2) the increase in range resulting from shifting the center of pressure is only about 1 m rather than the 16 m predicted in [1].

This paper summarizes the results of a study whose purpose was to make a refinement of Assumption 2. Specifically, we have incorporated experimentally measured aerodynamic forces and pitching moments into a simulation of the equations of motion. Our results show that, regardless of Assumption 1, a set of optimal initial conditions exists that are significantly different from those suggested in [1] and [2] and which result in even larger increases in range than suggested by Soong.

Experimental Forces and Moments

Terauds [3] experimentally investigated 14 different javelins, including almost all those used at that time in international competition. Even though 10 years have passed, the javelins in use today are not very different from the ones Terauds tested [4]. Lift, drag, and pitching moment were measured as functions of angle of attack using constant-velocity wind tunnel tests. A summary of this data has also been presented in [5].

Shown in Fig. 1 are the functions for three javelins and the corresponding theoretical approximations used in [1] and [2]. The experimental lift and drag curves cluster fairly tightly together, but the pitching moments show more variability from javelin to javelin. Moreover, the theoretical approximation is very good for the drag, less good in the case of lift (about 30 percent high at 20 deg and 15 percent low at 40 deg), and very poor for the pitching moment. When $d = 0.8$ cm, the theoretical pitching moment approximation becomes essentially zero compared to the experimentally measured pitching moments.

The aerodynamics behind the rather peculiar shape of the pitching moment curves (three equilibria, one unstable, and two stable) is not clearly understood, but the magnitude of the maximum positive pitching moment is apparently enhanced by the effect of the grip on the flow [3]. The existence of three equilibria, of course, is evidence that the c.p. wanders back and forth, first behind, then in front of, then behind the c.m. as the angle of attack increases. The practical ramification of the second stable equilibrium point is that the javelin is able to generate large amounts of lift (flying at angles of attack of

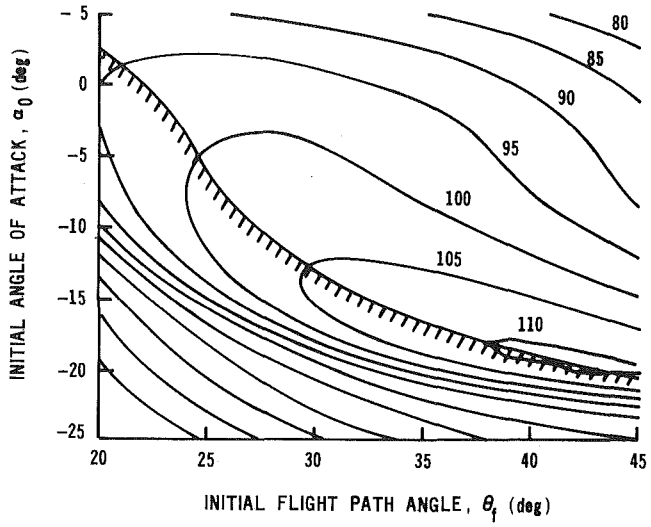

Fig. 3(a) Constant initial velocity [1], $V_0 = 30.48$ m/s (100 ft/s)

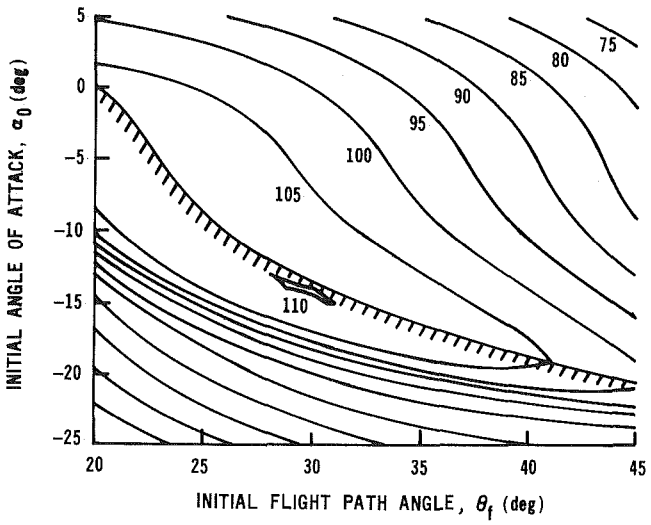

Fig. 3(b) Initial velocity decreases with initial flight path angle [2], $V_0 = 30.48 - 0.127\,(\theta_f - 35)$ m/s

Fig. 3 Contours of constant range versus initial flight path angle and initial angle of attack

from 30 to 35 deg) without generating a restoring moment as is the case with a fixed c.p. and $d \neq 0$.

Numerical prediction of the forces and moment would appear to require a full three-dimensional inviscid solution of the Navier-Stokes equations along the entire length, a formidable problem in itself. In any case, it is not difficult to believe that the use of the $d = 0.8$ cm theoretical approximation would lead to unrealistic trajectory predictions. It is precisely the variable pitching moment that causes the angular accelerations which are then integrated to obtain the javelin attitude. Changes in attitude are required to track the varying direction of the relative wind and to generate lift at appropriate periods in the trajectory.

Results

We have numerically solved equations of motion similar to equations (20)–(22), (37), and (38) from [1]. As a test of our computer program, we attempted to reproduce the results in Fig. 3 of [1] and Fig. 3 of [2] using theoretical forces and moments. Although our program predicted essentially the same results as [1] for constant velocity, we were not able to reproduce results using variable velocity from [2]. It now

appears [6] that the curve labeled "$d = 0.8$ cm" in Fig. 3 from [2] was incorrectly labeled and instead corresponds to $d = 24.4$ cm (0.8 ft). A corrected version of this curve [6] is shown in Fig. 2. The maximum range of 109.7 m occurs at $\theta_f = 30$ deg. The major conclusions are that ranges near 110 m appear possible as suggested by Soong [1] but that the optimum initial flight path angle is near $\theta_f = 30$ deg.

Next the theoretical lift and drag calculations in the program were replaced with the measured forces from [3] discussed in the foregoing, and the appropriate components of the measured pitching moment were used on the right-hand sides of equations (37) and (38) from [1]. As the javelin velocity varied, the forces and moment were scaled by the dynamic pressure. The results shown here are for the Held-90 Meter, a typical world class javelin in 1972. Its other parameters were taken from [3]: mass: 809.6 gm, transverse moment of inertia: 0.4094 Kg-m^2, distance - c.m. to tip: 1.080 m. The release height of c.m. was taken to be 2.0 m. Space limitations prevent a complete discussion of our findings. A brief summary is given here but a fuller account may be found in [7] and [8].

Simulations were done for a wide range of initial flight path angles, θ_f, and initial angles of attack $\alpha_0 = \theta_j - \theta_f$. Shown in Fig. 3 are contours of constant range in this space for the cases of: (*a*) constant initial velocity [1], and (*b*) variable initial velocity [2]. Also shown on each figure is a single contour of zero entry angle. Throws to the upper right land tip first and thus are legal under international rules. Several points of interest emerge.

In the constant velocity case, the maximum range of 110.64 m is reached with an initial flight path angle $\theta_f = 42$ deg but with a large negative initial angle of attack $\alpha_0 = -19$ deg. With an initial velocity that depends on the flight path angle, the maximum range is limited by flat throws since the zero entry angle contour lies to the upper right of the 110 m contour, but still the range decreases by only about 1 m. The optimal initial conditions, however, in this case are quite different; $\theta_f = 30$ deg, $\alpha_0 = -14$ deg. Of more interest, perhaps, is that with variable velocity the optimum is less sensitive, and any point on the line joining the two points (20,0) and (35,-15) in the (θ_f, α_0) space results in a range substantially greater than 105 m. On this line the initial javelin attitude is constant, $\theta_j = 20$ deg.

The velocity dependence experiments similar to those in [2] have not been done for world class throwers ($V_0 \gtrsim 30$ m/s). We believe that the sensitivity of V_0 to θ_f will probably not be greater than that measured in [2] for lower velocities. For smaller sensitivities, the optimum will lie somewhere between those of Figs. 3(*a*) and 3(*b*). Thus, a reasonable choice of initial conditions might be a point on the line connecting the two optima ($\alpha_0 = -0.42\theta_f - 1.5$) choosing θ_f somewhere nearer 30 deg than 42 deg and α_0 nearer -14 deg than -19 deg.

We have also generated similar contour plots for the other two javelins in Fig. 1. Although there are minor differences, the shapes of the contours are similar to Fig. 2 and the general nature of the conclusions regarding optimal release conditions are as previously discussed.

In the case of plane motion, the one initial state that remains to be specified is the pitch angular velocity $\dot{\theta}_j$. We must emphasize that *all results discussed here (and those from [1] and [2]) assume* $\dot{\theta}_j = 0$. In [7, 8], we show that the trajectory and the resulting range are *extremely* sensitive to this angular velocity and that this, more than any other factor, probably accounts for the large variability in actual performance in the event. Moreover, an additional 4 m in range may be gained by choosing all three of the variables θ_f, α_0, and $\dot{\theta}_j$ optimally. In this case, the large negative angles of attack in Figs. 3(*a*) and 3(*b*) are no longer optimal because their effect can be contributed by a negative initial angular velocity $\dot{\theta}_j$.

Conclusions

1 The optimal release conditions for a given javelin depend on its particular aerodynamic characteristics. Most javelin pitching moment profiles are not adequately approximated using a fixed center of pressure.

2 For world class javelins similar to the Held-90, world class throwers ($V_0 \simeq 30$ m/s), and *with zero initial angular velocity*, the optimum initial angle of attack lies somewhere in the range $-19 < \alpha_0 < -14$ deg. The optimal initial condition probably lies fairly near the point $\theta_f = 32$ deg, $\alpha_0 = -15$ deg ($\theta_j = 17$ deg). Almost certainly the optimal throw angle θ_f is considerably lower than 35–37 deg predicted using theoretical forces and moments and the optimal angle of attack is significantly different from zero.

3 Using the preceding optimal initial conditions, a range greater than 110 m should be possible with velocities (~ 30 m/s), characteristic of present throwers.

References

1 Soong, T.-C., "The Dynamics of Javelin Throw," ASME JOURNAL OF APPLIED MECHANICS, Vol. 42, 1975, pp. 257–262.

2 Red, W. E., and A. J. Zogaib, "Javelin Dynamics Including Body Interaction," ASME JOURNAL OF APPLIED MECHANICS, Vol. 44, 1977, pp. 496–498.

3 Terauds, J., "A Comparative Analysis of the Aerodynamics and Ballistic Characteristics of Competition Javelins," Ph.D. dissertation, University of Maryland, College Park, Md., 1972.

4 Held, R. A., private communication.

5 Terauds, J., "Wind Tunnel Tests of Competition Javelins," *Track and Field Quarterly Review*, Vol. 74, No. 2, June 1974, pp. 88–95.

6 Red, W. E., private communication.

7 Hubbard, M., and H. J. Rust, "Simulation of Javelin Flight Using Experimental Aerodynamic Data," submitted for publication.

8 Hubbard, M., "Optimal Javelin Trajectories," submitted for publication.

A Parametric Solution to the Elastic Pole-Vaulting Pole Problem

G. M. Griner
Science Applications, Inc.
2109 W. Clinton Ave.,
Huntsville, Ala. 35805

The fiberglass pole used in pole vaulting is approximated by an "elastica" having an applied concentrated force and moment at the upper end. Presented is a parametric solution expressed in terms of the tabulated elliptic integrals. The results suggest an advantageous pole-vaulting technique which is not generally recognized by coaches and athletes.

Introduction

A detailed analysis of the dynamics of the pole-vault event in track and field must include the effect of the highly elastic pole [1]. During the vault the vaulter applies a compressive load and a bending moment to the upper end of the pole while the bottom end is free to pivot in the vaulting trough or "box" (Fig. 1). The applied moment is a condition not treated in the classical literature.

In a previous Note Hubbard [2] proposed an iterative numerical solution, contending that an analytic solution was unknown. However, Costello and Healey [3] have solved the related problem of an end-loaded column subjected to equal bending moments on each end with a concentrated lateral force at the column center. Using their method, a parametric solution to the pole-vault problem can be obtained in terms of the tabulated elliptic integrals. The solution is presented in this paper.

Statement of the Problem

Study of the postbuckling behavior of an elastic column subjected to end loading dates back to Euler (1744). Termed the "elastica" problem, the classical solution [4, 5] can be obtained in terms of the elliptic integrals of the first and second kind, $F(p, \Phi) = \int_0^\Phi (1-p^2 \sin^2 \zeta)^{-1/2}\, d\zeta$ and $E(p, \phi) = \int_0^\Phi (1-p^2 \sin^2 \zeta)^{1/2} d\zeta$.

The elastica problem for the vaulting pole is illustrated in Fig. 2. The pole is taken to be a thin elastic column of length L having uniform stiffness B at each location s. (To save weight, vaulting poles are not always constructed with uniform stiffness but for analysis purposes that assumption seems reasonable.) Owing to the small mass of the pole relative to that of the vaulter, it is taken to be in quasistatic equilibrium at all times. Thus it is permissible to adopt a coordinate system attached to the pole ends as shown.

The upper end of the pole is subjected to lateral and transverse forces (in general not being horizontal and vertical directions) and a bending moment. Note that static equilibrium requires that the applied transverse force, F, be equal in magnitude to the ground reaction force, F, which in turn must balance the applied moment, M. Therefore the condition $M = -F\,l$ is imposed for an equilibrium solution to exist, where l is the chord length of the bent pole. The problem thus has only two independent parameters.

The Bernoulli-Euler relation for the moment m at location (x, y) is

$$m = B\frac{d\theta}{ds} = -P\,y + F\,x \tag{1}$$

where θ is the local slope of the pole relative to the chord line. This is seen to be the classical elastica problem with the additional term, $F\,x$.

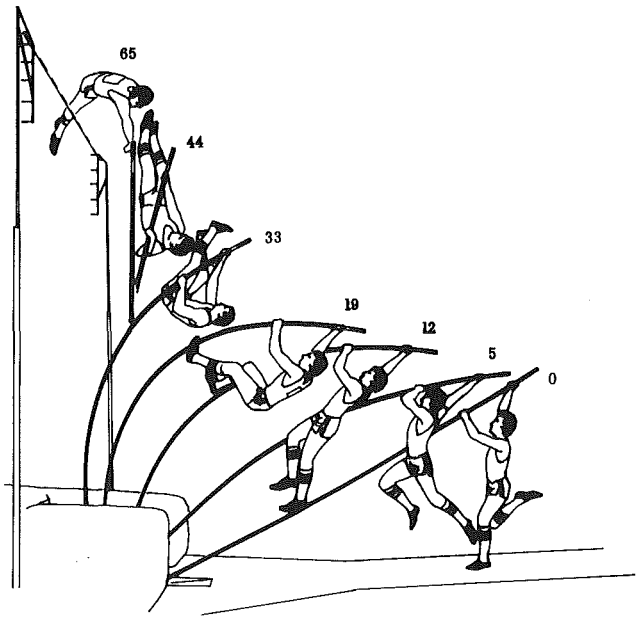

Fig. 1 Pole vaulting with a fiberglass pole. Shown valuting 5.40m (17 ft 9 in.) is Tadeusz Slusarski, 1976 Olympic Champion. Frame times are in units of 1/64 seconds. (Composite by author from photographs by R. V. Ganslen.)

Contributed by the Applied Mechanics Division for publication in the JOURNAL OF APPLIED MECHANICS.

Discussion on this paper should be addressed to the Editorial Department, ASME, United Engineering Center, 345 East 47th Street, New York, N.Y. 10017, and will be accepted until two months after final publication of the paper itself in the JOURNAL OF APPLIED MECHANICS. Manuscript received by ASME Applied Mechanics Division October, 1983; final revision, February, 1983.

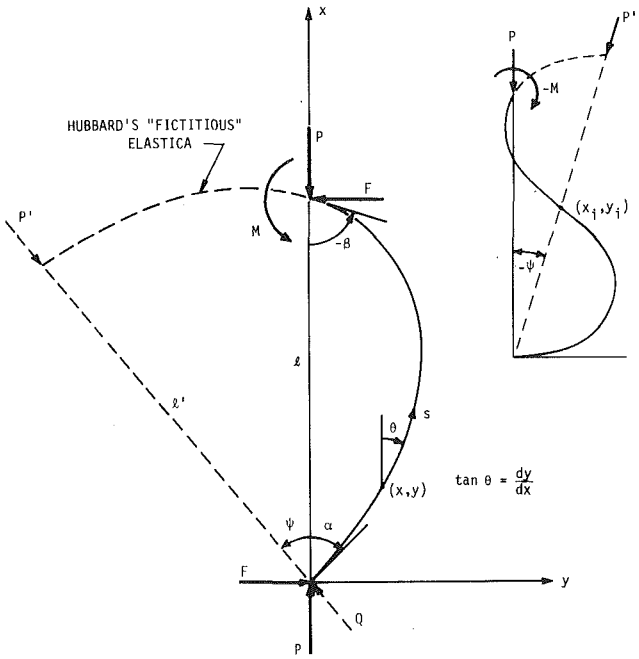

Fig. 2 Coordinate system for the elastica of length L with applied bending moment M and compressive load P

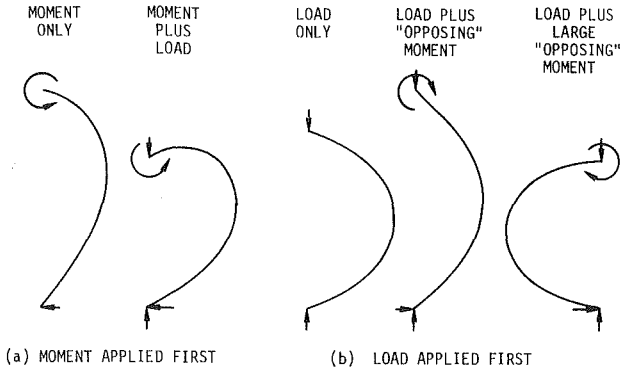

Fig. 3 Elastic deflection due to combined end load and bending moment. Shape can depend on which is applied first.

Hubbard's Fictitious Rod

Hubbard [2] argued heuristically that there should be a fictitious longer pole of the same stiffness loaded only with end forces, having the same displacements, reaction forces, and interior moments as the real pole (Fig. 2). This being the case, the problem would reduce to the classical elastica solution, with the additional task of determining the unknown "end" of the fictitious pole which will produce the desired moment at the end of the real pole.

That this interesting conjecture is true can easily be proved by noting that the differential equation for the fictitious pole is (1) expressed in an $x'y'$ coordinate system rotated through some angle ψ. If ψ is chosen equal to -arc tan (F/P) then indeed (1) reduces to the form $B\,d\theta/ds = -P'y'$ where the compressive end load on the fictitious pole is $P' = P\cos\psi + F\sin\psi$. To achieve a negative moment, M, the pole must acquire a double lobe bend and ψ must be negative as shown in the insert in Fig. 2. Hubbard [2] has described an iterative technique for solving for ψ and l'.

Observed Behavior

Before becoming emersed in the mathematics it is instructive to consider the expected behavior. With the aid of a plastic ruler one can observe the two cases sketched in Fig. 3. If a bending moment is applied first and the resulting deflection is taken to be the positive direction, then the application of a compressive end load can only result in additional positive deflection as shown in Fig. 3(a). However, if a buckling load is applied first, the subsequent behavior depends on the direction of the applied moment. If the moment tends to further increase the lateral deflection (we will call this a positive moment) then one simply has case (a) again. If the opposite (negative) moment is applied the column tends to "straighten up" and an inflection point will appear near the top of the column.

Should a large enough negative moment be applied, the column suddenly snaps through to deflect totally in the direction of the applied moment as illustrated in Fig. 3(b). Following this "snap-through" buckling, the bending moment should be regarded as positive because it is then in the same direction as the lateral deflection.

Phenomena that exhibit sudden jumps with small changes in a parameter have recently been termed catastrophies [6], a term which the pole vaulter might find particularly descriptive.

Solution

To eliminate the dependence on x and y, differentiate (1) to get

$$\frac{d^2\theta}{ds^2} = -\frac{P}{B}\frac{dy}{ds} + \frac{F}{B}\frac{P}{B}\frac{dx}{ds}$$
$$= k^2(q\cos\theta - \sin\theta) \tag{2}$$

Here we have defined the constants $k^2 = P/B$, $q = F/P$ and used the relationships $\cos\theta = dx/ds$ and $\sin\theta = dy/ds$.

Equation (2) can be easily integrated giving

$$\frac{1}{2}\left(\frac{d\theta}{ds}\right)^2 = k^2(q\sin\theta + \cos\theta + C) \tag{3}$$

where the constant C is evaluated by noting that at $x=y=0$ the slope $\theta=\alpha$ but the bending moment (and therefore $d\theta/ds$) is zero. From (3) it follows that

$$C = -q\sin\alpha - \cos\alpha$$

Substituting this value for C back into (3) and taking the negative square root gives

$$\frac{d\theta}{ds} = -\sqrt{2}\,k\sqrt{\cos\theta - \cos\alpha + q(\sin\theta - \sin\alpha)} \tag{4}$$

The positive root is ignored because $d\theta/ds$ is in fact negative as Fig. 2 shows.

Now define a constant ψ such that $-q = \tan\psi$. Substituting for q in (4) and simplifying gives

$$\sqrt{\cos\psi}\,\frac{d\theta}{ds} = -k\sqrt{2\cos(\psi+\theta) - 2\cos(\psi+\alpha)}$$

Using the half-angle identity $\cos z = 1 - 2\sin^2(z/2)$ and rearranging

$$-k\cos^{-1/2}\psi\,ds = \frac{1}{2}\left[\sin^2\left(\frac{\psi+\alpha}{2}\right) - \sin^2\left(\frac{\psi+\theta}{2}\right)\right]^{-1/2} d\theta$$

The limits of integration for the left side are from $s=0$ to $s=L$. If β is taken to be the slope of the pole at the upper end the limits of the right side are from $\theta=\alpha$ to $\theta=\beta$. The left side, being a constant, can be integrated immediately.

$$k\,L/\sqrt{\cos\psi} = \int_\alpha^\beta \frac{1}{2}\left[\sin^2\left(\frac{\psi+\alpha}{2}\right) - \sin^2\left(\frac{\psi+\theta}{2}\right)\right]^{-1/2} d\theta \tag{5}$$

At this point the classic solution introduces the constant p defined by

$$p=\sin\left(\frac{\psi+\alpha}{2}\right) \tag{6}$$

and the new angle variable Φ defined by

$$p\sin\Phi=\sin\left(\frac{\psi+\alpha}{2}\right)\sin\Phi=\sin\left(\frac{\psi+\theta}{2}\right) \tag{7}$$

Taking the differential of (7) gives

$$p\cos\Phi\,d\Phi=\cos\left(\frac{\psi+\theta}{2}\right)\frac{d\theta}{2}$$

$$=\sqrt{1-\sin^2\left(\frac{\psi+\theta}{2}\right)}\,\frac{d\theta}{2}=\sqrt{1-p^2\sin^2\Phi}\,\frac{d\theta}{2}$$

Thus

$$d\theta=\frac{2p\cos\Phi\,d\Phi}{\sqrt{1-p^2\sin^2\Phi}} \tag{8}$$

Upon substituting (6), (7), and (8) into (5) one obtains

$$\frac{kL}{\sqrt{\cos\psi}}=\int_{\Phi_0}^{\Phi_1}\frac{d\Phi}{\sqrt{1-p^2\sin^2\Phi}} \tag{9}$$

where

$$\Phi_0=\arcsin\left[\frac{1}{p}\sin\left(\frac{\psi+\alpha}{2}\right)\right]=\pi/2$$

and

$$\Phi_1=\arcsin\left[\frac{1}{p}\sin\left(\frac{\psi+\beta}{2}\right)\right]$$

The integral in (9) can be expressed in termes of the difference between the complete and incomplete elliptic integrals of the first kind. If one defines a constant $K(p,\Phi_1)=F(p,\pi/2)-F(p,\Phi_1)$ equation (9) can be written

$$kL=\sqrt{\cos\psi}K(p,\Phi_1)$$

The left side can be expressed in terms of the Euler buckling load, $P_E=B\pi^2/L^2$. Recalling that $k^2=P/B$ then $kL=L\sqrt{P/B}=\pi\sqrt{P/P_E}$. Substituting in the preceding expression and solving for P/P_E yields

$$\frac{P}{P_E}=\frac{\cos\psi}{\pi^2}K(p,\Phi_1)^2 \tag{10}$$

The side force ratio, F/P_E, can now be found since $F/P_E=(F/P)(P/P_E)$. Recalling that $F/P=-q=-\sin\psi/\cos\psi$ and substituting for P/P_E from (10) leads to the result

$$\frac{F}{P_E}=-\frac{\sin\psi}{\pi^2}K(p,\Phi_1)^2 \tag{11}$$

A convenient nondimensional form for the applied bending moment is $m/(L\,P_E)$. From (1) we write

$$\frac{m}{L\,P_E}=-\frac{F}{P_E}\frac{x}{L}-\frac{P}{P_E}\frac{y}{L} \tag{12}$$

To evaluate this expression the pole deflection must first be obtained.

Pole Shape

The deflection equations which must be solved to determine the pole shape are

$$dy=\frac{\sin\theta}{d\theta/ds}\,d\theta \tag{13}$$

and

$$dx=\frac{\cos\theta}{d\theta/ds}\,d\theta \tag{14}$$

with $d\theta/ds$ given by (4). The solutions to these equations are given in [3]. Expressed in the present notation, the solutions are

$$x/L=[2p\cos\Phi\sin\psi-G(p,\Phi)\cos\psi]/K(p,\Phi_1) \tag{15}$$

$$y/L=[2p\cos\Phi\cos\psi-G(p,\Phi)\sin\psi]/K(p,\Phi_1) \tag{16}$$

where $G(p,\Phi)=F(p,\pi/2)-F(p,\Phi)-2[E(p,\pi/2)-E(P,\Phi)]$ and the function E is the elliptic integral of the second kind. The deflection of the upper end of the pole is obtained by setting $\Phi=\Phi_1$. The value of the constant ψ, which appears in the solution, can be determined by the condition that the y-deflection of the upper end of the pole will be zero. Thus (16) gives

$$2p\cos\Phi_1\cos\psi+G(p,\Phi_1)\sin\psi=0$$

Solving for ψ gives the result

$$\psi=\arctan\left(-\frac{2p\cos\Phi_1}{G(p,\Phi_1)}\right) \tag{17}$$

The compressed pole length ratio, l/L, is obtained from (15) by setting $x=l$ and $\Phi=\Phi_1$.

$$l/L=[2p\cos\Phi_1\sin\psi-G(p,\Phi_1)\cos\psi]/K(p,\Phi_1) \tag{18}$$

Since, at the upper end of the pole $m=M$, $x=l$, and $y=0$, equation (12) gives

$$\frac{M}{LP_E}=-\frac{F}{P_E}\frac{l}{L} \tag{19}$$

Upon substituting for l/L from (18) and F/P_E from (11) and using (17) one obtains for the applied moment

$$M/LP_E=[2p\cos\Phi_1\,K(p,\Phi_1)]/\pi^2 \tag{20}$$

The maximum internal moment occurs where $d^2\theta/ds^2=0$. Differentiating (1) and solving gives $q=\tan\theta$. But, by definition, $\tan\psi=-q$. Thus at the point of maximum moment $\theta=-\psi$ and from (7), $\Phi=0$. Evaluating (15) and (16) at $\Phi=0$ gives the point of maximum moment to be

$$(x/L)_m=[2p\sin\psi-G(p,0)\cos\psi]/K(p,\Phi_1) \tag{21}$$

$$(y/L)_m=[2p\cos\psi+G(p,0)\sin\psi]/K(p,\Phi_1) \tag{22}$$

where $G(p,0)=F(p,\pi/2)-2E(p,\pi/2)$ since $F(p,0)=E(p,0)=0$. The expression for the maximum internal moment is obtained by substituting (10), (11), (21) and (22) into (12). After simplifying one obtains

$$(m/L\,P_E)_m=-2p\,K(p,\phi_1)/\pi^2 \tag{23}$$

For negative applied moment, M, there will be zero internal moment at the inflection point, (x_1, y_i). Setting $m=0$ in (1) gives $Py_i=Fx_i$ at this point. But by definition, $-\tan\psi=q=F/P=y_i/x_i$. Substituting for x/L and y/L from (15) and (16) gives the condition at the inflection point to be

$$-\tan\psi=\frac{2p\cos\Phi\cos\psi+G(p,\Phi)\sin\psi}{2p\cos\Phi\sin\psi+G(p,\Phi)\cos\psi}$$

which after simplification yields $2p\cos\Phi=0$. Inflection points thus may appear at $\Phi=\pi/2-n\pi$, $n=0,1,2,\ldots$. One inflection point is at the pole bottom $\Phi=\Phi_0=\pi/2$, and for the two-lobe bend shown in Fig. 1, the second inflection point occurs when $\Phi=-\pi/2$.

Evaluating (15) and (16) at $\Phi=-\pi/2$ gives the inflection point location as

$$(x/L)_i=-G(p,-\pi/2)/K(p,\Phi_1) \tag{24}$$

$$(y/L)_i=0 \tag{25}$$

The pole end angles for the deflected elastica may be found from equations (6) and (7). Rearranging one finds

$$\alpha=2\arcsin p-\psi$$
$$\beta=2\arcsin(p\sin\Phi_1)-\psi \tag{26}$$

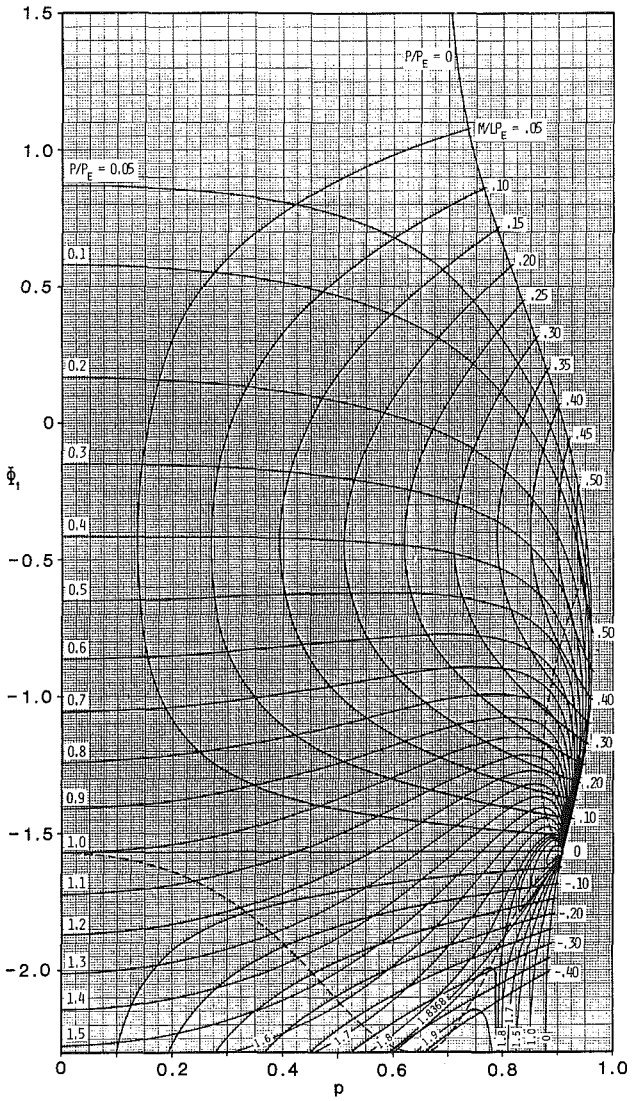

Fig. 4 Φ_1 as a function of p for parameters P/P_E and M/LP_E. Dashed lines bound statically stable solutions.

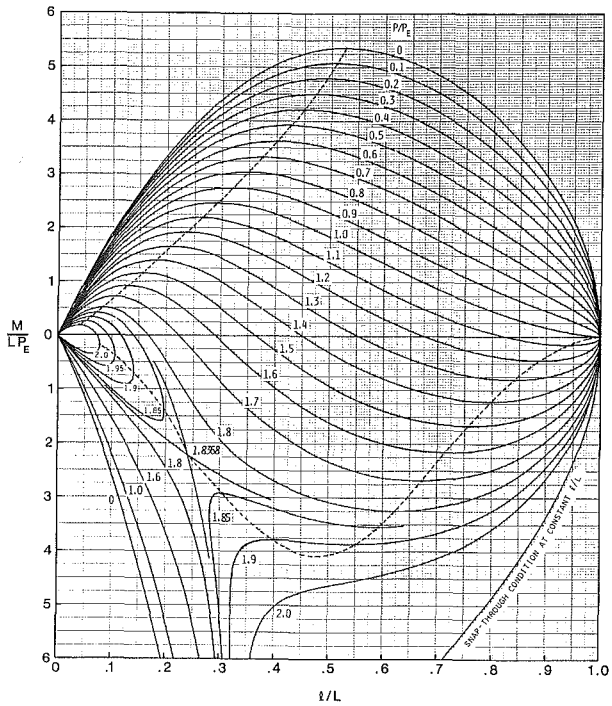

Fig. 5 Chord ratio l/L corresponding to Φ_1 for parameters P/P_E and M/LP_E. Dashed lines bound statically stable solutions.

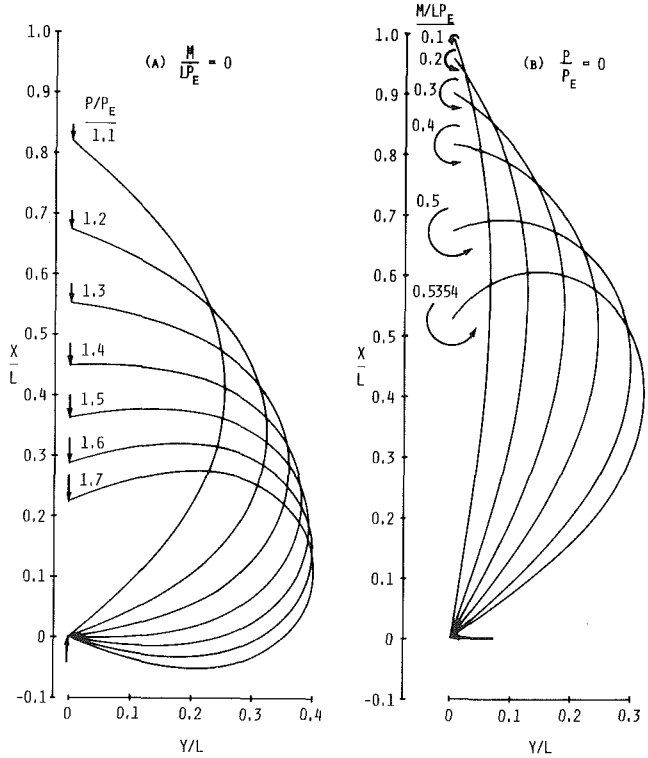

Fig. 6 Elastica shape resulting from (*a*) pure compressive load or (*b*) pure bending moment

Numerical Results

To directly use the present solution one must choose a value for Φ_1 and p, solve (17) for ψ, and compute the corresponding applied load and moment using (10) and (20). Pole shape is determined by evaluating (15) and (16) over the interval $\Phi_0 \leq \Phi \leq \Phi_1$. Usually one would prefer to choose values of M, l, or P rather than the more abstract variables Φ_1 and p. For this reason Figs. 4 and 5 have been prepared, permitting the user to determine the values of Φ_1 and p which correspond to particular values of l/L, P/P_E, and $m/L\ P_E$. The dashed lines in the figures bound conditions which result in physically stable pole deflections. A pole shape is said to be unstable if $\partial l/\partial\Phi_1 + \partial l/\partial p > 0$. Thus the boundary is at $dl/dM = 0$ for constant P or at $dl/dP = 0$ for constant M. Together, Figs. 4 and 5 illustrate many of the interesting features of the solution, some of which are now called to the reader's attention.

For the case of zero applied moment the results should coincide with the classical elastica solution. When $M = 0$ the side force, F, is evidently zero and we have $q = \psi = 0$. The pole will deflect symmetrically ($\alpha = -\beta$) so using (6) and (7) $p = \sin(\alpha/2)$ and $\Phi_1 = -\pi/2$. Then, using the identities $E(p, -\pi/2) = -E(p, \pi/2)$ and $F(p, -\pi/2) = -F(p, \pi/2)$, equations (10) and (15) give the simple result $P/P_E = [2F(p, \pi/2)/\pi]^2$ and $l/L = 2E(p, \pi/2)/F(p, \pi/2) - 1$. These are indeed the classical results and may be found in Fig. 5 where the P/P_E-curves intersect the abscissa. Restricting l/L to positive values implies that $2E(p, \pi/l) \geq F(p, \pi/2)$ which is true if $p \leq 0.909$. Thus the extreme values of the end angles when $l/L = 0$ is 2 arcsin(0.909) = 130.7 deg. Typical pole shapes resulting from zero moment and increasing compressive load are illustrated in Fig. 6(*a*).

In Fig. 5 it can be seen that there is a maximum moment which can be applied for any given P/P_E. For the special case of $P = 0$ the pole deflection is entirely the result of the applied moment. When $P=0$ we have $q \to \infty$ and $\psi = \pi/2$. Setting $\alpha = 0$ in (6) and (7) gives the values of p and Φ_1 for which deflection just begins. Whence, $p \geq \sin[(\pi/2+\alpha)/2] = \sin(\pi/4) = 0.707$ and $\Phi_1 \leq \pi/2$ as can be seen in Fig. 4. For $P/P_E = 0$ the maximum moment, found numerically from (20), is $M/LP_E = 0.5354$ at $p = 0.9550$, $\Phi_1 = -0.5092$. From (18) the chord ratio is $l/L = 0.5263$ with end angles $\alpha = 55.5$ deg and $\beta = -145.5$ deg given by (26). Some pole shapes resulting from increasing positive moments are illustrated in Fig. 6(*b*).

The expected snap-through buckling from applied negative moment is evident in Fig. 5. As an example of this behavior consider the case of end load $P/P_E = 1.3$ with zero applied moment. The initial chord ratio will be $l/L = 0.55$. Now let an increasingly negative $M/L\,P_E$ be applied. Following the $P/P_E = 1.3$ curve shows the chord length progressively increasing until the stability boundary is encountered at $l/L = 0.84$ when $M/L\,P_E = -0.081$. For any further increase in the negative moment either the chord force must be increased or the physical pole will rapidly straighten to $l/L = 1$ and, due to the applied moment, deflect totally in the opposite direction. By convention the applied moment would then be taken as positive. At $M/L\,P_E = 0.081$ for $P/P_E = 1.3$ the new stable condition is seen to be at $l/L = 0.415$. The progression of pole shapes for this example is illustrated in Fig. 7.

If, instead of a constant value of P/P_E, the pole ends are constrained so as to hold the chord length constant, then a much larger negative moment is required to produce snap-through buckling. In the pole vault this could conceivably occur if a very large negative moment was suddenly applied by the vaulter because the pole would require a finite amount of time to lengthen. Snap-through buckling at constant length occurs when the maximum internal moment given by (12) increases without bound as the applied bending moment is increased; that is when $dm/dM = \infty$. The p, Φ_1 pairs which satisfy this condition for specific values of l/L have been determined numerically and are plotted in Fig. 5 and listed in Table 1. Figure 8 shows typical pole shapes at the snap-through condition for fixed values of l/L.

A very unexpected result occurs for negative moments if $P/P_E > 1.8368$ (this value has been determined numerically). Stable solutions exist in two small disjoint regions of the p, Φ_1 plane. This means that for moments larger (more negative) than $M/L\,P_E = -0.2215$ to be permissable the value of P/P_E and $M/L\,P_E$ must be simultaneously varied such that their trajectory in Fig. 5 remains in the stable region. This could be accomplished by constraining the ends to the desired l/L value, applying the proper moment and end load, and then removing the constraints. If this were done correctly, the maximum negative moment that could be applied is computed to be $M/L\,P_E = -0.4094$ at $P/P_E = 1.93$ for $p = 0.6850$, $\Phi_1 = -2.2729$ with a chord ratio $l/L = 0.475$. Figure 9 illustrates the pole shapes that are attainable (and those that are not) when $P/P_E = 1.85$.

Hubbard's End

The fictitious pole end which Hubbard finds by a numerical search can now be determined. Let l' be the chord length of the fictitious rod whose total length is L'. For an applied positive moment, Fig. 1 shows that $l' = 2(x_m \cos\psi - y_m \sin\psi)$. Substituting from (21) and (22) gives $l'/L = 2[2E(p, \pi/2) - F(p, \pi/2)]/K(p, \Phi_1)$. Since the fictitious rod has only compressive end force, P', the classical result is also true, namely $l'/L' = 2\,E(p, \pi/2)/F(p, \pi/2) - 1$. Using these two expressions the ratio of the fictitious pole length to the real pole length can be determined. The result is

$$L'/L = 2F(p,\pi/2)/K(p,\Phi_1) \tag{27}$$

A similar calculation yields the pole end for applied negative moment. The insert in Fig. 1 shows that for this case, $l' = 2\sqrt{x_i^2 + y_i^2}$. Substituting from (24) and (25) gives $l'/L = 2G(p, -\pi/2)/K(p, \Phi_1)$. Again using the classical result for l'/L' gives the fictitious-to-real length ratio to be

$$L'/L = 4F(p,\pi/2)/K(p,\Phi_1) \tag{28}$$

which is just twice the result for a positive applied moment.

In both cases the end load which must be applied to Hubbard's rod is $P' = P\cos\psi - F\sin\psi$. Substituting from (10) and (11) gives

$$P'/P_E = [K(p,\Phi_1)/\pi]^2$$

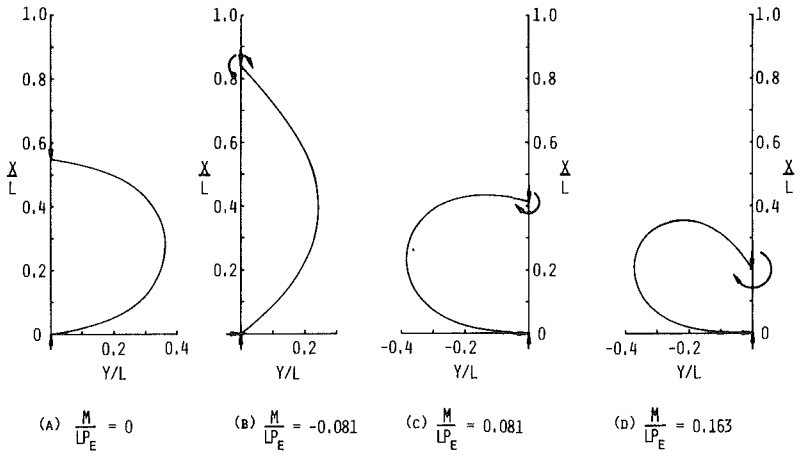

Fig. 7 Elastica shapes resulting from a compressive load of P/P_E = 1.3 and increasing clockwise bending moment. At $M/LP_E = -0.081$ the elastica suddenly reverses its y-direction of deflection.

Table 1 Snap-through buckling conditions at constant length

l/L	M/LP_E	p	Φ_1(rad)	ψ_0(rad)	P/P_E	α(deg)	β(deg)
0.95	−0.2353	0.2382	−3.3922	−0.0967	2.5538	33.1	12.3
0.90	−0.3366	0.3358	−3.3888	−0.1423	2.6106	47.4	17.6
0.80	−0.4876	0.4716	−3.3840	−0.2195	2.7321	68.9	25.6
0.70	−0.6137	0.5735	−3.3772	−0.2978	2.8559	87.1	32.5
0.60	−0.7311	0.6576	−3.3681	−0.3892	2.9709	104.5	39.3
0.50	−0.8484	0.7305	−3.3565	−0.5082	3.0466	123.0	47.0

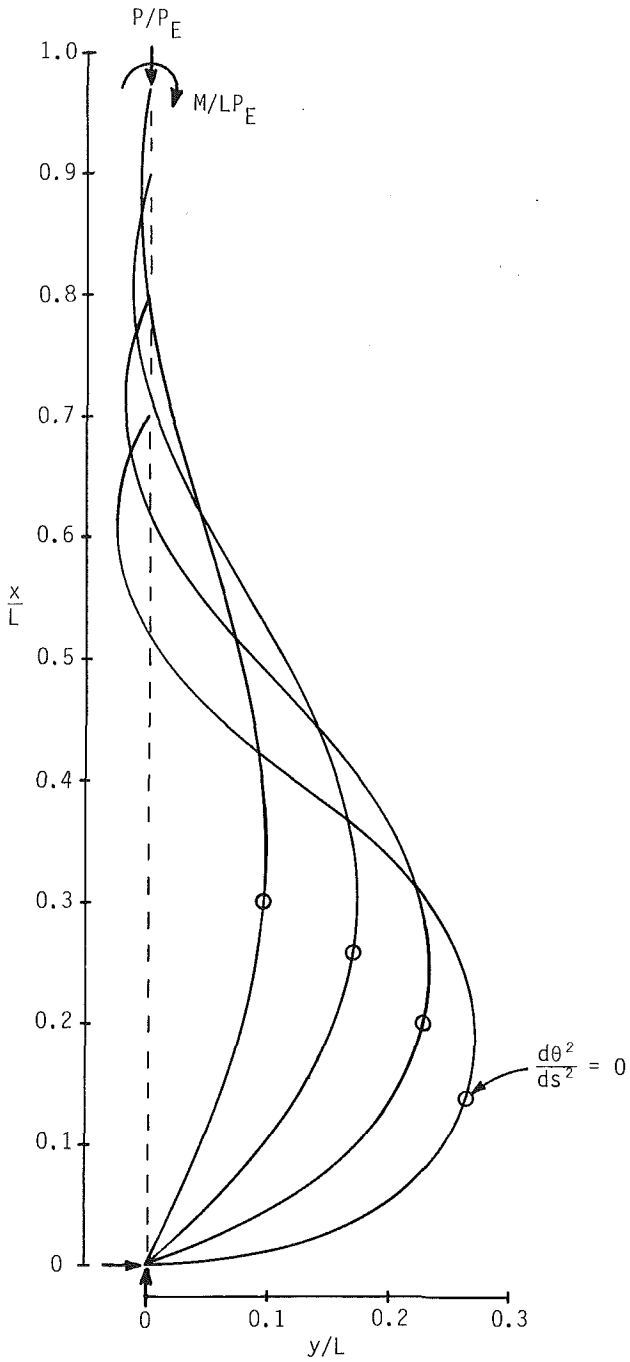

Fig. 8 Typical elastica shapes just prior to fixed-length snap-through buckling

Since the Euler buckling load for the fictitious pole is $P_E' = P_E(L/L)^2$ we have

$$P'/P_E' = [K(p,\Phi)L'/\pi L]^2$$

Application to Vaulting Technique

These results should come as good news to pole vaulters since they desire a "soft" (e.g., flexible) pole at takeoff but a "fast response" (e.g., stiff) pole during the last half of the vault. Contemporary vaulters place their hands about 3/4 m apart on the pole. Then by keeping their bottom arm somewhat stiff at takeoff a positive moment is naturally applied. This bending moment reduces the compressive end load necessary to buckle the pole. To the vaulter the takeoff shock is reduced much like it would be on a more flexible pole. Once maximum deflection has been achieved (Fig. 1, frame 19) the vaulter would benefit from a powerful

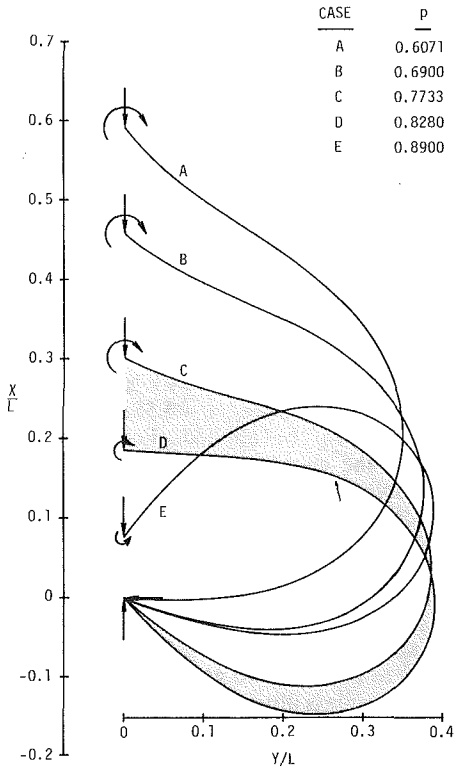

Fig. 9 Elastica shapes resulting from a compressive load of P/P_E = 1.85 and several clockwise bending moments. The shaded region between class *C* and *D* contains unstable shapes.

straightening of the pole such as would occur if it were suddenly much stiffer. Apparently this can be accomplished by applying a negative moment at this time.

At maximum deflection the vaulter begins to invert his body position so as to approach the crossbar feet first. Beginners are instructed to invert by swinging up about their hand grip. More advanced vaulters are told to "rock back" while tucking the knees. The present results suggest that inverting by applying a large negative moment to the pole should be taught. (For the right-handed vaulter in Fig. 1, push with the right arm, pull with the left.) Such an applied moment would cause the pole to straighten as though it were stiffer. If the athlete were strong enough to accomplish this with legs extended instead of tucked, a maximum negative moment would result. Hubbard [1] estimates the maximum bending moment that a vaulter might apply. Using his estimate and assuming it could also be applied in the negative sence gives $M/L\ P_E = -0.051$. Thus the danger of causing snap-through buckling rather than rapid pole straightening seems remote indeed.

Analysis of photographs of World Class pole vaulters suggests that the negative moment may in fact be applied by some. However this aspect of pole-vaulting technique is not generally recognized.

References

1 Hubbard, M., "Dynamics of the Pole Vault," *J. Biomechanics*, Vol. 13, No. 11, 1980, pp. 965-976.

2 Hubbard, M., "An Iterative Numerical Solution for the Elastica With Causally Mixed Inputs," ASME JOURNAL OF APPLIED MECHANICS, Vol. 47, 1980, pp. 200-202.

3 Costello, G. A., and Healey, J. J., "Large Deflections of Elastic Columns With Various Supports," *Theoretical and Applied Mechanics*, Vol. 2, Shaw, W. A., ed., Pergamon Press, 1964, pp. 527-543.

4 Southwell, R. V., *An Introduction to the Theory of Elasticity*, 2nd Ed., Oxford University Press, pp. 429-439.

5 Timoshenko, S. P., and Gere, J. M., *Theory of Elastic Stability*, 2nd Ed., McGraw-Hill, New York, 1961, pp. 76-82.

6 Zeeman, E. C., "Catastrophe Theory," *Scientific American*, Vol. 234, Apr., 1976, pp. 65-70 (bibliography, p. 138).

G. M. T. D'Eleuterio
Doctoral Candidate.

P. C. Hughes
Professor.

Institute for Aerospace Studies,
University of Toronto,
4925 Dufferin Street,
Downsview, Ontario, Canada, M3H 5T6

Dynamics of Gyroelastic Continua

This paper introduces the idea of distributed gyricity, *in which each volume element of a continuum possesses an infinitesimal quantity of stored angular momentum. The continuum is also assumed to be linear-elastic. Using operator notation, a partial differential equation is derived that governs the small displacements of this gyroelastic continuum. Gyroelastic vibration modes are derived and used as basis functions in terms of which the general motion can be expressed. A discretized approximation is also developed using the method of Rayleigh-Ritz. The paper concludes with a numerical example of gyroelastic modes.*

1 Introduction

Having in mind the dynamics of flexible structures, let us consider the following four types of mechanical influences:

(*a*) inertial (mass) influences;

(*b*) dissipative (damping) influences;

(*c*) stiffness (elastic) influences; and

(*d*) gyroscopic (herein called "gyric") influences.

The first three are familiar in both their "distributed parameter" and their "lumped parameter" guises – the mechanical properties of inertia, dissipation, and stiffness are routinely formulated using either continuum dynamical models or spatially discretized dynamical models. Gyric influences, in contrast, have heretofore been formulated exclusively in terms of lumped-parameter models. The purpose of this paper is to examine, for the first time,[1] the dynamics of a gyroelastic continuum.

A partial exception to the foregoing claim might be said to occur when an elastic structure is spinning – a flexible spacecraft, for example [2]. In such cases the equations of motion are most conveniently written using coordinates that measure displacements with respect to an appropriately spinning reference frame (see, for example, Hablani's work [3]). With respect to such a frame, the Coriolis force distribution produces terms that are indeed both distributed and gyric in nature. However, for spinning flexible bodies the distribution of gyric forces is not independent of the mass distribution, whereas, in this paper, we analyze a nonspinning elastic continuum that has a separately specified distribution of *gyricity*.[2]

It is not difficult to understand why gyricity has traditionally been treated using local, lumped, finite sources. These sources have, in applications, simply been spinning wheels (rotors). Thus, while one may, for example, conceive with equal ease of a finite lump of mass, m, or an element of mass, dm, one does not encounter, in the technical literature, an "element of gyricity," $d\underline{h}_s$ or an "element of rotor." Yet it is precisely this idea that is introduced in this paper.

A simple example of lumped gyricity is depicted in Fig. 1(*a*). A rigid body $\mathfrak{R}$, which contains a rotor $\mathfrak{W}$, is attached to a rigid support at O via a pin-joint about which two degrees of rotational freedom are possible: θ_1 and θ_2. Two rotational springs at O have stiffnesses k_1 and k_2. The moments of inertia of $\mathfrak{R}$ + $\mathfrak{W}$ about the 1 and 2 axes (assumed to be principal axes) are J_1 and J_2, and the angular momentum of $\mathfrak{W}$ relative to $\mathfrak{R}$ is h, assumed constant. The equations of motion, namely,

$$J_1\ddot{\theta}_1 + h\dot{\theta}_2 + k_1\theta_1 = 0 \tag{1.1}$$

$$J_2\ddot{\theta}_2 - h\dot{\theta}_2 + k_2\theta_2 = 0 \tag{1.2}$$

imply the following characteristic equation for the natural frequencies of (small) oscillation:

$$J_1J_2\omega^4 - (J_1k_2 + J_2k_1 + h^2)\omega^2 + k_1k_2 = 0 \tag{1.3}$$

Denoting the roots by $(\omega_1{}^2, \omega_2{}^2)$, we note that

$$\omega_1{}^2\omega_2{}^2 \equiv \omega_{01}^2\omega_{02}^2 \quad \forall h \tag{1.4}$$

where $(\omega_{01}^2, \omega_{02}^2)$ are the values of (ω_1^2, ω_2^2) evaluated at $h=0$: $\omega_{0i} = k_i/J_i$ $(i=1, 2)$. Thus the wheel does not add any "stiffness" (as is sometimes claimed); although ω_2 can be raised by increasing h, ω_1 is correspondingly lowered. This can be seen graphically in Fig. 1(*b*), where the two system frequencies are plotted for a special case $\{J_1 = J_2 = J;\ k_1 = k_2 = k;\ \omega_{01} = \omega_{02} = \omega_0^2 = k/J\}$. The roots of (1.3) under these assumptions are

$$\omega^2 = \omega_0^2\{1 + \tfrac{1}{2}\hat{h}^2 \pm \tfrac{1}{2}\hat{h}(\hat{h}^2+4)^{1/2}\} \tag{1.5}$$

where $\hat{h}$ is the dimensionless wheel speed,

$$\hat{h} \triangleq h/(kJ)^{1/2} \tag{1.6}$$

As indicated by Fig. 1(*b*) and (1.5), the two frequencies tend to split with increasing $\hat{h}$:

$$\omega_1 \to \omega_0/\hat{h}, \quad \omega_2 \to \hat{h}\omega_0 \quad \text{as} \quad \hat{h} \to \infty \tag{1.7}$$

This again indicates that some frequencies are raised, and others lowered, by gyric effects. A study of the eigenvectors

[1] Some of these ideas were first presented informally in reference [1].

[2] This word is coined because there is no synonym.

Contributed by the Applied Mechanics Division for publication in the JOURNAL OF APPLIED MECHANICS.

Discussion on this paper should be addressed to the Editorial Department, ASME, United Engineering Center, 345 East 47th Street, New York, N.Y. 10017, and will be accepted until two months after final publication of the paper itself in the JOURNAL OF APPLIED MECHANICS. Manuscript received by ASME Applied Mechanics Division, April, 1983; final revision, September, 1983.

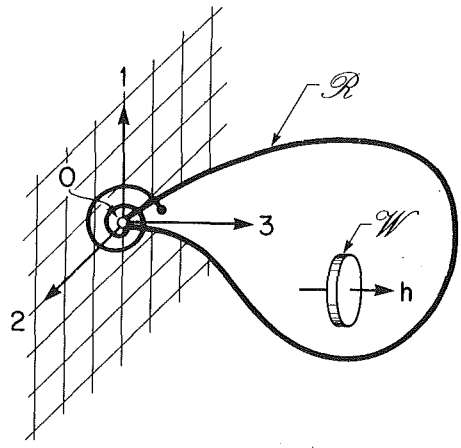

Fig. 1(a) Physical model

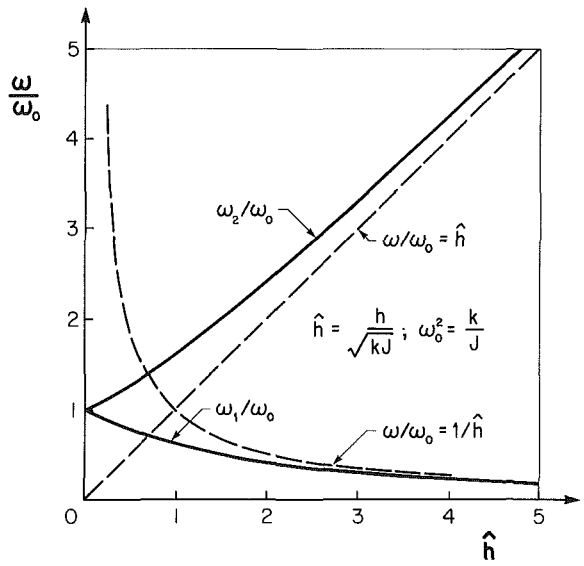

Fig. 1(b) Natural frequencies

Fig. 1

shows that the low-frequency mode is a precession of the tip of $\mathscr{R}$ with a sense *opposite* to that of the wheel momentum $\underline{h}$. Similarly, the high-frequency mode is a precession with the *same* sense as $\underline{h}$.

In the remainder of this paper, these elementary ideas will be substantially generalized so that they apply to a gyric-elastic continuum.

2 An Elastic Continuum

Prior to a consideration of a continuous distribution of gyricity, we first discuss the continuous elastic body $\mathcal{E}$ shown in Fig. 2. $\mathcal{E}$ is constrained not to translate or rotate at 0 (the cantilever conditions). If $\mathcal{E}$ were under the influence of a static distribution of external force per unit volume, **f (r)**, this would cause a static distribution of elastic displacements, **u(r)**. In this paper we assume geometric linearity:

$$\|\mathbf{u}(\mathbf{r})\|/\|\mathbf{r}\| << 1 \tag{2.1}$$

We also assume a linear constitutive law for $\mathcal{E}$, i.e., stress is proportional to stain.

Under these assumptions, **u** bears the following type of relationship to **f**:

$$\underline{\mathcal{K}}\mathbf{u} = \mathbf{f} \tag{2.2}$$

where $\underline{\mathcal{K}}$ is a linear differential stiffness operator. All

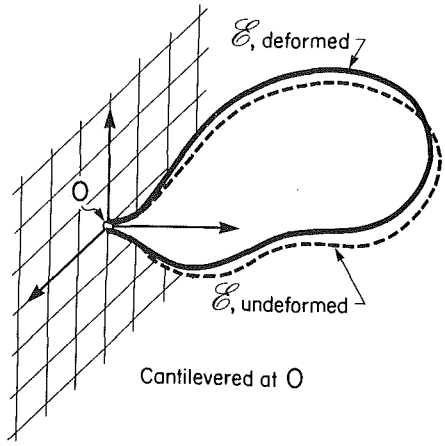

Fig. 2

boundary conditions, including the constraints at 0, are implied in the symbol $\underline{\mathcal{K}}$. Moreover, $\underline{\mathcal{K}}$ is self-adjoint,

$$\int_{\mathcal{E}} \mathbf{u}_1^T \underline{\mathcal{K}} \mathbf{u}_2 dV = \int_{\mathcal{E}} \mathbf{u}_2^T \underline{\mathcal{K}} \mathbf{u}_1 dV, \tag{2.3}$$

and positive-definite,

$$\int_{\mathcal{E}} \mathbf{u}^T \underline{\mathcal{K}} \mathbf{u} dV > 0 \quad \text{for} \quad \mathbf{u} \not\equiv \mathbf{0}. \tag{2.4}$$

These properties of $\underline{\mathcal{K}}$ must be true because

$$U = \tfrac{1}{2} \int_{\mathcal{E}} \mathbf{u}^T \underline{\mathcal{K}} \mathbf{u} dV \tag{2.5}$$

is the expression for the stored elastic strain energy.

In preparation for the introduction of a distribution of gyricity in the next section, we remark that it is possible to make a torque distribution **g(r)** and a force distribution **f(r)** equivalent in the sense that both produce the same distribution of displacements. Thus, given **g(r)**, we seek to find the equivalent **f(r)**.

The derivation is facilitated by thinking of **f(r)** as a superposition of dipole forces (none of which contributes a net force over the vehicle):

$$\mathbf{f}(\mathbf{r}) = \int_{\mathcal{E}} \mathbf{f}_d(\mathbf{r}, \xi) dV(\xi) \tag{2.6}$$

We intend to show that the dipole-force distribution $\mathbf{f}_d$ that is equivalent to **g** is given by

$$\mathbf{f}_d(\mathbf{r}, \xi) = \tfrac{1}{2} \mathbf{g}^{\times}(\xi) \nabla_{\xi} \delta(\xi - \mathbf{r}) \tag{2.7}$$

Now, $\mathbf{f}_d$ is said to be equivalent to **g** if the following condition holds:

$$\int_{\mathcal{E}} (\mathbf{r} - \xi)^{\times} \mathbf{f}_d(\mathbf{r}, \xi) dV = \mathbf{g}(\xi) \tag{2.8}$$

Therefore, substitute (2.7) into (2.8), and note that

$$\int_{\mathcal{E}} (\mathbf{r} - \xi)^{\times} \mathbf{g}^{\times}(\xi) \nabla_{\xi} \delta(\xi - \mathbf{r}) dV$$

$$= \int_{\mathcal{E}} (\xi - \mathbf{r})^{\times} [\nabla_{\xi} \delta(\xi - \mathbf{r})]^{\times} \mathbf{g}(\xi) dV$$

But from the properties of the δ function,

$$(\xi - r)^{\times} [\nabla_{\xi} \delta(\xi - \mathbf{r})]^{\times} = 2\delta(\xi - \mathbf{r})\mathbf{1}$$

This completes the proof.

We conclude from (2.6) and 2.7) that the force distribution **f** equivalent to **g** is

$$\mathbf{f}(\mathbf{r}) = \tfrac{1}{2} \int_{\mathcal{E}} \mathbf{g}^{\times}(\xi) \nabla_{\xi} \delta(\xi - \mathbf{r}) dV(\xi) \tag{2.9}$$

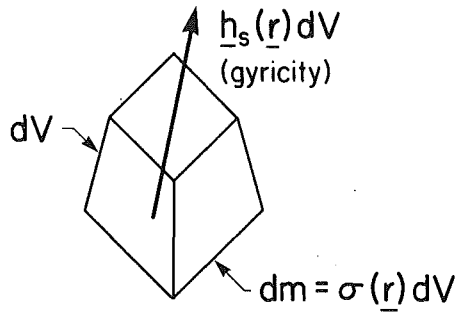

(a) Mathematical Properties

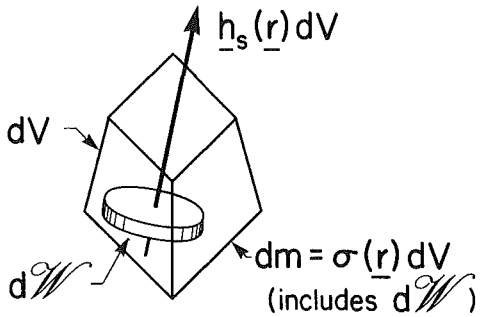

(b) Physical Analogy

Fig. 3

In fact, this integration can be performed with the aid of Gauss' Theorem, which states that

$$\int_{\mathcal{E}} \boldsymbol{\phi}^T \nabla^{\times} \boldsymbol{\psi} dV = \int_{\mathcal{E}} \boldsymbol{\psi}^T \nabla^{\times} \boldsymbol{\phi} dV + \int_{\partial \mathcal{E}} \boldsymbol{\psi}^T \boldsymbol{\phi}^{\times} d\mathbf{S} \qquad (2.10)$$

where the last term is a surface integral over the boundary of $\mathcal{E}$. Applying Gauss' Theorem to (2.9) shows that

$$\mathbf{f}(\mathbf{r}) = \tfrac{1}{2} \nabla^{\times} \mathbf{g}(\mathbf{r}) \qquad (2.11)$$

which is the result sought. It has also been assumed that $\mathbf{g} \equiv \mathbf{0}$ on the boundary $\partial \mathcal{E}$.

3 The Gyricity Distribution, $h_s(\mathbf{r})$

The idea of a continuous distribution of stored angular momentum, or *gyricity*, $\mathbf{h}_s(\mathbf{r})$, is a central theme of this paper. We now introduce a gyricity distribution to the elastic body $\mathcal{E}$ discussed in the last section. At the same time, we must allow $\mathcal{E}$ to undergo *dynamic* displacements $\mathbf{u}(\mathbf{r}, t)$ in response to dynamic inputs.

The element of volume dV has mass dm, where

$$dm = \sigma(\mathbf{r}) dV \qquad (3.1)$$

$\sigma(r)$ being the mass density in $\mathcal{E}$ at $\mathbf{r}$. The "inertial" force distribution is thus

$$\mathbf{f}_i(\mathbf{r},t) = -\sigma(\mathbf{r}) \ddot{\mathbf{u}}(\mathbf{r},t) \qquad (3.2)$$

There may also be an externally-generated force field, $\mathbf{f}_e(\mathbf{r}, t)$, and an externally-generated force field, $\mathbf{g}_e(\mathbf{r},t)$, corresponding to which we define the equivalent total external force field

$$\mathbf{f}_{eT}(\mathbf{r},t) \triangleq \mathbf{f}_e(\mathbf{r},t) + \tfrac{1}{2} \nabla^{\times} \mathbf{g}_e(\mathbf{r},t) \qquad (3.3)$$

in accordance with equation (2.11).

We now treat the dynamical influence of the gyricity distribution $\mathbf{h}_s(\mathbf{r})$ as equivalent to yet another distribution of external force. To do so naturally requires a precise understanding of what the symbol $\mathbf{h}_s(\mathbf{r})$ means. As shown in Fig. 3(*a*), we associate with the volume element dV a "stored" angular momentum $\mathbf{h}_s dV$ that exists over and above the angular momentum attributable to dm from its nominal velocity distribution, namely, $\mathbf{v}(\mathbf{r},t) = \dot{\mathbf{u}}(\mathbf{r},t)$. A physical analogy (Fig. 3(*b*)) is a volume element that contains, in addition to its elastic material, an infinitesimal wheel whose angular momentum, relative to the rest of the volume element, is $\mathbf{h}_s dV$. Thus, although the mass of this elemental wheel is included in dm, the absolute angular momentum of dV (about O, say) exceeds $\mathbf{r}^{\times}\dot{\mathbf{u}}\, dm$ by the amount $\mathbf{h}_s dV$. One might picture, for example, an elastic frame structure, each facet of which houses a rigid gyro. As the number of facets (and gyros) becomes infinite, and the size of each facet shrinks to zero, the limit is a continuum of gyricity.

Although it is not essential to do so, we will assume in this paper that $\mathbf{h}_s(\mathbf{r})$ does not vary with time. This is a generalization of what Roberson [4] called "Kelvin's gyrostat."

As a final point, the kinetic energy associated with the volume element dV is of the form

$$dT = \tfrac{1}{2} \dot{\mathbf{u}}^T \dot{\mathbf{u}} dm + \mathbf{h}_s^T (\mathbf{1} - \tfrac{1}{2} \boldsymbol{\alpha}^{\times}) \dot{\boldsymbol{\alpha}} dV + T_s(\mathbf{r}) dV \qquad (3.4)$$

where $\boldsymbol{\alpha}(\mathbf{r})$ is the rotational displacement at $\mathbf{r}$ due to elasticity, and T_s and $\mathbf{h}_s$ imply an axial inertia I_s and spin rate ω_s for the fictitious elemental wheel shown in Fig. 3:

$$\mathbf{h}_s(\mathbf{r}) = I_s(\mathbf{r}) \omega_s(\mathbf{r}) \mathbf{s}(\mathbf{r}) \qquad (3.5)$$

$$T_s(\mathbf{r}) = \tfrac{1}{2} I_s(\mathbf{r}) \omega_s^2(\mathbf{r}) \qquad (3.6)$$

where $\mathbf{s}$ is simply a unit vector giving the direction of $\mathbf{h}_s$. Thus we have

$$I_s(\mathbf{r}) = \tfrac{1}{2} h_s^2 / T_s \qquad (3.7)$$

$$\omega_s(\mathbf{r}) = 2T_s / h_s \qquad (3.8)$$

The concept of gyricity becomes especially attractive in the limit as $I_s \to 0$ and $\omega_s \to \infty$, in such a manner that $h_s = I_s \omega_s$ goes to a nonzero noninfinite value. This limiting procedure does have the rather unpleasant consequence that $T_s \to \infty$, but fortunately T_s depends on neither $\mathbf{u}$, $\dot{\mathbf{u}}$, nor t, and therefore it does not affect the dynamics.

4 Equation of Motion

Even though $\mathbf{h}_s$ will in applications often be stored within $\mathcal{E}$, the gyric reaction torques can be treated as "external" to the rest of the structure. We denote by $\boldsymbol{\alpha}(\mathbf{r})$ the local angular displacement of $\mathcal{E}$, at $\mathbf{r}$, with respect to the reference attachment frame. According to Timoshenko and Goodier [5],

$$\boldsymbol{\alpha}(\mathbf{r}) = \tfrac{1}{2} \nabla^{\times} \mathbf{u}(\mathbf{r}) \qquad (4.1)$$

Then, since a torque $\dot{\boldsymbol{\alpha}}^{\times} \mathbf{h}_s dV$ must exist on the element of gyricity $\mathbf{h}_s dV$ in order to produce the rotation rate $\dot{\boldsymbol{\alpha}}$, the equal and opposite torque it impresses on the surrounding structure must be (per unit volume)

$$\mathbf{g}_h(\mathbf{r},t) = \mathbf{h}_s^{\times} \dot{\boldsymbol{\alpha}} = \tfrac{1}{2} \mathbf{h}_s^{\times} \nabla^{\times *} \mathbf{u} \qquad (4.2)$$

The equivalent force distribution, according to (2.11), is

$$\mathbf{f}_h(\mathbf{r},t) = -\underset{\sim}{\mathcal{G}} \ddot{\mathbf{u}} \qquad (4.3)$$

where the operator $\underset{\sim}{\mathcal{G}}$ is defined thus:

$$\underset{\sim}{\mathcal{G}} = -\tfrac{1}{4} \nabla^{\times} \mathbf{h}_s^{\times} \nabla^{\times} \qquad (4.4)$$

(Note that the first ∇ operates on all the factors that follow it.)

The final equation of motion for $\mathcal{E}$ is, therefore, from (2.2),

$$\underset{\sim}{\mathcal{K}} \mathbf{u}(\mathbf{r},t) = \mathbf{f}_i(\mathbf{r},t) + \mathbf{f}_h(\mathbf{r},t) + \mathbf{f}_{eT}(\mathbf{r},t) \qquad (4.5)$$

with $\mathbf{f}_i$, $\mathbf{f}_h$, and $\mathbf{f}_{eT}$ given, respectively, by (3.2), (4.3), and (3.3). The result is

$$\underset{\sim}{\mathfrak{M}} \ddot{\mathbf{u}} + \underset{\sim}{\mathcal{G}} \ddot{\mathbf{u}} + \underset{\sim}{\mathcal{K}} \mathbf{u} = \mathbf{f}_{eT} \qquad (4.6)$$

where the mass operator $\mathfrak{M}$ is simply

$$\mathfrak{M} \triangleq \sigma(\mathbf{r})\underline{1} \tag{4.7}$$

and $\underline{1}$ is the identity operator. Obviously, $\mathfrak{M}$ is self-adjoint and positive-definite. Note also from (4.4) that $\underline{\mathcal{G}}$ is skew-Hermitian.

The total kinetic energy of the system is calculated from (3.4):

$$T = \tfrac{1}{2}\int_{\mathcal{E}} (\dot{\mathbf{u}}^T \mathfrak{M}\dot{\mathbf{u}} + \dot{\mathbf{u}}^T \underline{\mathcal{G}}\mathbf{u} + \dot{\mathbf{u}}^T \nabla^x \mathbf{h}_s)\, dV + E_s \tag{4.8}$$

Here the relations (4.1), (4.4), and (4.7) have been used, along with Gauss' Theorem in the form (2.11), and E_s is the dynamically unimportant term

$$E_s = \int_{\mathcal{E}} T_s(\mathbf{r}) dV \tag{4.9}$$

We combine T with the potential energy, given by (2.5), and with the appropriate expression for virtual work done by the external force field, namely,

$$\delta W_e = \int_{\mathcal{E}} (\mathbf{f}_e^T \delta\mathbf{u} + \mathbf{g}_e^T \delta\boldsymbol{\alpha}) dV \equiv \int_{\mathcal{E}} \mathbf{f}_{eT}^T \delta\mathbf{u} dV \tag{4.10}$$

[The identity in (4.10) can be proven using the expression (4.1) for $\boldsymbol{\alpha}$, then applying Gauss' Theorem (2.10) with $\mathbf{g}_e \equiv \mathbf{0}$ on $\partial\mathcal{E}$, and finally using the definition (3.3).] It can be shown that the motion equation (4.6) is also derivable by applying the calculus of variations to Hamilton's (extended) principle, and using the foregoing expressions for kinetic energy, potential energy, and virtual work.

5 First-Order Form

To derive many of the following relationships, it is helpful to cast (4.6) into an equivalent first-order operator form,

$$\underline{\mathcal{E}}\dot{\chi} + \underline{\mathcal{S}}\chi = \boldsymbol{\gamma} \tag{5.1}$$

where

$$\underline{\mathcal{E}} \triangleq \begin{bmatrix} \mathfrak{M} & \bullet \\ \bullet & \mathfrak{K} \end{bmatrix}; \quad \underline{\mathcal{S}} \triangleq \begin{bmatrix} \underline{\mathcal{G}} & \mathfrak{K} \\ -\mathfrak{K} & \bullet \end{bmatrix} \tag{5.2}$$

$$\chi \triangleq \begin{bmatrix} \dot{\mathbf{u}} \\ \mathbf{u} \end{bmatrix}; \quad \boldsymbol{\gamma} \triangleq \begin{bmatrix} \mathbf{f}_{eT} \\ \bullet \end{bmatrix} \tag{5.3}$$

(Dots imply the null operator.) It can be shown that $\underline{\mathcal{E}}$ is a Hermitian (or self-adjoint) operator, and that $\underline{\mathcal{S}}$ is skew-Hemitian:

$$\int_{\mathcal{E}} \chi_1^H \underline{\mathcal{E}}\chi_2 dV = \int_{\mathcal{E}} (\underline{\mathcal{E}}\chi_1)^H \chi_2 dV \tag{5.4}$$

$$\int_{\mathcal{E}} \chi_1^H \underline{\mathcal{S}}\chi_2 dV = -\int_{\mathcal{E}} (\underline{\mathcal{S}}\chi_1)^H \chi_2 dV \tag{5.5}$$

where $\chi_1(\mathbf{r})$ and $\chi_2(\mathbf{r})$ are any two functions in the domain of $\underline{\mathcal{E}}$, and χ^H denotes the Hermitian (complex-conjugate transpose) of χ. The Hermitian operation is needed in (5.4) and (5.5) because the gyroelastic mode shapes (defined and derived in the next section) are complex. Furthermore, the positive-definiteness of $\mathfrak{M}$ and $\mathfrak{K}$ implies that $\underline{\mathcal{E}}$ is positive-definite also:

$$\int_{\mathcal{E}} \chi^H \underline{\mathcal{E}}\chi dV > 0 \quad (\chi \not\equiv 0) \tag{5.6}$$

For completeness, we note that the system Hamiltonian is

$$H = \tfrac{1}{2}\int_{\mathcal{E}} (\dot{\mathbf{u}}^T \mathfrak{M}\dot{\mathbf{u}} + \mathbf{u}^T \mathfrak{K}\mathbf{u}) dV - E_s$$

$$= \tfrac{1}{2}\int_{\mathcal{E}} \chi^H \underline{\mathcal{E}}\chi dV - E_s \tag{5.7}$$

The Hamiltonian evolves as power is expended on the system from external sources:

$$\dot{H} = \int_{\mathcal{E}} \dot{\mathbf{u}}^T \mathbf{f}_{eT} dV \tag{5.8}$$

If there are no external influences, H is conserved (H is constant).

6 Gyroelastic Vibration Modes

The eigenvalue problem associated with (5.1) arises naturally when one considers the unforced motion ($\mathbf{f}_{eT} \equiv \mathbf{0}$) and sets

$$\chi(\mathbf{r},t) = \mathcal{R}e\{\chi_\alpha(\mathbf{r})\exp(\lambda_\alpha t)\} \tag{6.1}$$

The general (free) motion will be a superposition of such solutions, where

$$\lambda_\alpha \underline{\mathcal{E}}\chi_\alpha + \underline{\mathcal{S}}\chi_\alpha = \mathbf{0} \tag{6.2}$$

It can be demonstrated that the eigenvalues λ_α appear in complex conjugate, purely imaginary pairs:

$$\lambda_\alpha = j\omega_\alpha \tag{6.3a}$$

It will be convenient in the sequel to restrict ω_α to positive values only, and to restrict α to positive integers. With this convention, equation (6.3*a*) becomes

$$\lambda_{\pm\alpha} = \pm j\omega_\alpha \tag{6.3}$$

The corresponding convention for the complex eigenfunctions χ_α is this:

$$\chi_{\pm\alpha}(\mathbf{r}) = \boldsymbol{\phi}_\alpha(\mathbf{r}) \pm j\boldsymbol{\psi}_\alpha(\mathbf{r}) \tag{6.4}$$

Note that two real functions, $\boldsymbol{\phi}_\alpha$ and $\boldsymbol{\psi}_\alpha$, are associated with each natural frequency ω_α.

With the foregoing symbols and conventions, (6.2) becomes, in real terms,

$$\omega_\alpha \underline{\mathcal{E}}\boldsymbol{\phi}_\alpha + \underline{\mathcal{S}}\boldsymbol{\psi}_\alpha = \mathbf{0}, \quad -\omega_\alpha \underline{\mathcal{E}}\boldsymbol{\psi}_\alpha + \underline{\mathcal{S}}\boldsymbol{\phi}_\alpha = \mathbf{0} \tag{6.5}$$

It follows that

$$(\omega_\alpha{}^2 \underline{\mathcal{E}} + \underline{\mathcal{S}}\underline{\mathcal{E}}^{-1}\underline{\mathcal{S}})\boldsymbol{\phi}_\alpha = \mathbf{0} \tag{6.6}$$

and similarly for $\boldsymbol{\psi}_\alpha$. ($\underline{\mathcal{E}}^{-1}$ exists because $\underline{\mathcal{E}}$ is positive-definite.) Note that $\underline{\mathcal{S}}\underline{\mathcal{E}}^{-1}\underline{\mathcal{S}}$ is Hermitian. Using standard procedures we conclude that

$$\int_{\mathcal{E}} \boldsymbol{\phi}_\alpha^T \underline{\mathcal{E}}\boldsymbol{\phi}_\beta dV = 0 \quad (\omega_\alpha \neq \omega_\beta) \tag{6.7a}$$

and similarly for the $\boldsymbol{\psi}_\alpha$. The normality conditions we choose (for reasons to be seen presently) are

$$\int_{\mathcal{E}} \boldsymbol{\phi}_\alpha^T \underline{\mathcal{E}}\boldsymbol{\phi}_\alpha dV = 2\omega_\alpha^2 = \int_{\mathcal{E}} \boldsymbol{\psi}_\alpha^T \underline{\mathcal{E}}\boldsymbol{\psi}_\alpha dV \tag{6.7b}$$

In summary, the conditions

$$\int_{\mathcal{E}} \boldsymbol{\phi}_\alpha^T \underline{\mathcal{E}}\boldsymbol{\phi}_\beta dV = 2\omega_\alpha^2 \delta_{\alpha\beta} = \int_{\mathcal{E}} \boldsymbol{\psi}_\alpha^T \underline{\mathcal{E}}\boldsymbol{\psi}_\beta dV \tag{6.7}$$

represent succinctly the orthonormality conditions.

The six-tuples $\boldsymbol{\phi}_\alpha$ and $\boldsymbol{\psi}_\alpha$ are convenient for derivations (as in the foregoing) but of more direct physical significance are the three-tuples that give physical displacements. Thus, from (6.1),

$$\chi(\mathbf{r},t) = \boldsymbol{\phi}_\alpha(\mathbf{r})\cos\omega_\alpha t - \boldsymbol{\psi}_\alpha(\mathbf{r})\sin\omega_\alpha t \tag{6.8}$$

$$\mathbf{u}(\mathbf{r},t) = \mathbf{u}_\alpha(\mathbf{r})\cos\omega_\alpha t - \mathbf{v}_\alpha(\mathbf{r})\sin\omega_\alpha t \tag{6.9}$$

where $\mathbf{u}_\alpha$ and $\mathbf{v}_\alpha$ are, respectively, the "bottom halves" of $\boldsymbol{\phi}_\alpha$ and $\boldsymbol{\psi}_\alpha$. In fact, since $\dot{\mathbf{u}}$ must, from (6.9), be given by

$$\dot{\mathbf{u}}(\mathbf{r},t) = -\omega_\alpha[u_\alpha(\mathbf{r})\sin\omega_\alpha t + \mathbf{v}_\alpha(\mathbf{r})\cos\omega_\alpha t] \tag{6.10}$$

it can be concluded from the definition of χ, namely (5.3*a*), that

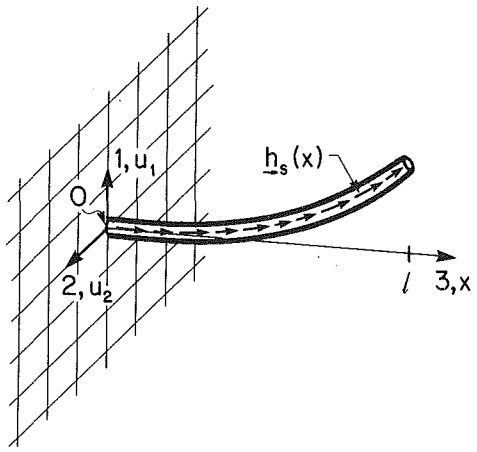

Fig. 4

$$\phi_\alpha = \begin{bmatrix} -\omega_\alpha \mathbf{v}_\alpha \\ \mathbf{u}_\alpha \end{bmatrix} \; ; \quad \psi_\alpha = \begin{bmatrix} \omega_\alpha \mathbf{u}_\alpha \\ \mathbf{v}_\alpha \end{bmatrix} \tag{6.11}$$

The function-pairs $\{\mathbf{u}_\alpha, \mathbf{v}_\alpha\}$ will be called the *gyroelastic mode shapes.*

The orthonormality conditions (6.7) can be rewritten for the gyroelastic mode shapes, using (5.2*a*) and (6.11):

$$\int_\mathcal{E} \mathbf{u}_\alpha^T \underset{\sim}{\mathcal{K}} \mathbf{u}_\beta dV + \omega_\alpha \omega_\beta \int_\mathcal{E} \mathbf{v}_\alpha^T \mathbf{v}_\beta dm = 2\omega_\alpha^2 \delta_{\alpha\beta}$$

$$\int_\mathcal{E} \mathbf{v}_\alpha^T \underset{\sim}{\mathcal{K}} \mathbf{v}_\beta dV + \omega_\alpha \omega_\beta \int_\mathcal{E} \mathbf{u}_\alpha^T \mathbf{u}_\beta dm = 2\omega_\alpha^2 \delta_{\alpha\beta} \tag{6.12}$$

Another relationship of a similar nature can be uncovered by first recognizing (6.5) and (6.7), and subsequently taking advantage of (5.2*b*), (6.11) and (6.12):

$$\omega_\alpha \int_\mathcal{E} \mathbf{u}_\alpha^T \mathbf{u}_\beta dm + \omega_\beta \int_\mathcal{E} \mathbf{v}_\alpha^T \mathbf{v}_\beta dm - \int_\mathcal{E} \mathbf{v}_\alpha^T \underset{\sim}{\mathcal{G}} \mathbf{u}_\beta dm = 2\omega_\alpha \delta_{\alpha\beta} \tag{6.13}$$

It is amply evident that the gyroelastic modal pair $\{\mathbf{u}_\alpha, \mathbf{v}_\alpha\}$ must be considered as a duo.

It will no doubt help the reader to pause momentarily and reduce the foregoing conditions to those for the more familiar context of a purely elastic (nongyric) continuum. From $\mathbf{h}_s(\mathbf{r}) \equiv \mathbf{0}$ it follows that $\underset{\sim}{\mathcal{G}} = \underset{\sim}{0}$. Furthermore, we denote the modal pairs $\{\mathbf{u}_\alpha, \mathbf{v}_\alpha\}$ by $\{\tilde{\mathbf{u}}_{0\alpha}, \mathbf{v}_{0\alpha}\}$. It can be shown from the relations (5.2), (6.5), and (6.11) that

$$(\mathbf{h}_s \equiv \mathbf{0}): \qquad \mathbf{v}_{0\alpha} \equiv \mathbf{u}_{0\alpha} \tag{6.14}$$

for all modes. In fact,

$$(\mathbf{h}_s \equiv \mathbf{0}): \qquad \underset{\sim}{\mathcal{K}} \mathbf{u}_{0\alpha} = \omega_{0\alpha}^2 \underset{\sim}{\mathcal{M}} \mathbf{u}_{0\alpha} \tag{6.15}$$

and similarly for $\mathbf{v}_{0\alpha}$. The orthonormality conditions (6.12) and (6.13) reduce to the familiar conditions

$$\int_\mathcal{E} \mathbf{u}_{0\alpha}^T \mathbf{u}_{0\beta} dm = \delta_{\alpha\beta}$$

$$(\mathbf{h}_s \equiv \mathbf{0}): \tag{6.16}$$

$$\int_\mathcal{E} \mathbf{u}_{0\alpha}^T \underset{\sim}{\mathcal{K}} \mathbf{u}_{0\beta} dV = \omega_{0\alpha}^2 \delta_{\alpha\beta}$$

It is for this reason that the normality factor $2\omega_\alpha^2$ was chosen in (6.7*b*).

7 General Motion

The general motion of $\mathcal{E}$ with distributed gyricity, in response to the external stimulus $\mathbf{f}_{eT}(\mathbf{r},t)$, can be expressed using the gyroelastic modes of the last section. Once again the most direct derivation is in terms of the six-tuples ϕ_α and ψ_α. Let the solution to (5.1) be

$$\chi(\mathbf{r},t) = \sum_{\beta=1}^{\infty} [\phi_\beta(\mathbf{r}) \eta_{u\beta}(t) + \psi_\beta(\mathbf{r}) \eta_{v\beta}(t)] \tag{7.1}$$

(The reason for the notation $\eta_{u\beta}$ and $\eta_{v\beta}$ will become apparent presently.) Then, after substitution of (7.1) in (5.1) and invocation of the orthonormality conditions, it can be shown [6] that

$$\dot{\eta}_{u\alpha} - \omega_\alpha \eta_{v\alpha} = -\frac{1}{2\omega_\alpha} \gamma_{v\alpha}, \quad \dot{\eta}_{v\alpha} + \omega_\alpha \dot{\eta}_{u\alpha} = \frac{1}{2\omega_\alpha} \gamma_{u\alpha} \tag{7.2}$$

where

$$\gamma_{u\alpha} \triangleq \int_\mathcal{E} \mathbf{u}_\alpha^T \mathbf{f}_{eT} dV; \quad \gamma_{v\alpha} \triangleq \int_\mathcal{E} \mathbf{v}_\alpha^T \mathbf{f}_{eT} dV \tag{7.3}$$

Notice the coupling between the $\{\eta_{u\alpha}, \eta_{v\alpha}\}$ pairs.

The time history of the elastic displacement $\mathbf{u}(\mathbf{r}, t)$, in terms of gyroelastic modes, is then found from (5.3*a*), (6.11), and (7.1):

$$\mathbf{u}(\mathbf{r},t) = \sum_{\beta=1}^{\infty} [\mathbf{u}_\beta(\mathbf{r}) \eta_{u\beta}(t) + \mathbf{v}_\beta(\mathbf{r}) \eta_{v\beta}(t)] \tag{7.4}$$

where $\eta_{u\beta}$ and $\eta_{v\beta}$ are determined from (7.2) and (7.3) in the foregoing. (The rationale for the symbols $\eta_{u\beta}$ and $\eta_{v\beta}$ is now clear.)

To again make the connection with the familiar formulation for a nongyric elastic continuum, we note from (7.3) and (6.14) that

$$(\mathbf{h}_s \equiv \mathbf{0}) \qquad \gamma_{u\alpha} = \gamma_{v\alpha} = \gamma_{0\alpha} \triangleq \int_\mathcal{E} \mathbf{u}_{0\alpha}^T \mathbf{f}_{eT} dV \tag{7.5}$$

Then with

$$\eta_{0\alpha} \triangleq \eta_{u\alpha} + \eta_{v\alpha} \tag{7.6}$$

it follows from (7.2) that

$$\ddot{\eta}_{0\alpha} + \omega_{0\alpha}^2 \eta_{0\alpha} = \gamma_{0\alpha} \tag{7.7}$$

which is the standard result for a (nongyric) elastic continuum).

8 Motion Equation for Discretized System

The last general result we present relates to the concentration between the dynamics of a *continuous* distribution of gyroelasticity and the motion equations for the *discretized* approximation for such a system. It will be seen that the set of ordinary differential equations for the discretized version are of standard form.

Preparatory to employing the Rayleigh-Ritz method, we represent the displacement $\mathbf{u}(\mathbf{r}, t)$ as an expansion in terms of a finite (although possibly large) number of displacement functions, $\delta_n(\mathbf{r})$, $n = 1, 2, \ldots, N$. With each such *admissible* basis function, we associate a coordinate $q_n(t)$. Thus

$$\mathbf{u}(\mathbf{r},t) \doteq \sum_{n=1}^{N} \delta_n(\mathbf{r}) q_n(t) \equiv \Delta(\mathbf{r}) \mathbf{q}(t) \tag{8.1}$$

where

$$\Delta(\mathbf{r}) \triangleq [\delta_1 \ldots \delta_N] \tag{8.2}$$

and $\mathbf{q}$ is a column matrix made up of the q_n. To use the Rayleigh-Ritz method, recollections of the kinetic energy, potential (elastic strain) energy, and virtual work are in order. These important quantities are given, respectively, by (4.8), (2.5), and (4.10). Using the foregoing expansion for $\mathbf{u}(\mathbf{r}, t)$, it becomes evident that

$$T \doteq \tfrac{1}{2}(\dot{\mathbf{q}}^T \mathcal{M} \dot{\mathbf{q}} + \dot{\mathbf{q}}^T \mathcal{G} \mathbf{q} + \dot{\mathbf{q}}^T \mathcal{h}) + E_s \tag{8.3}$$

$$U \doteq \tfrac{1}{2} \mathbf{q}^T \mathcal{K} \mathbf{q} \tag{8.4}$$

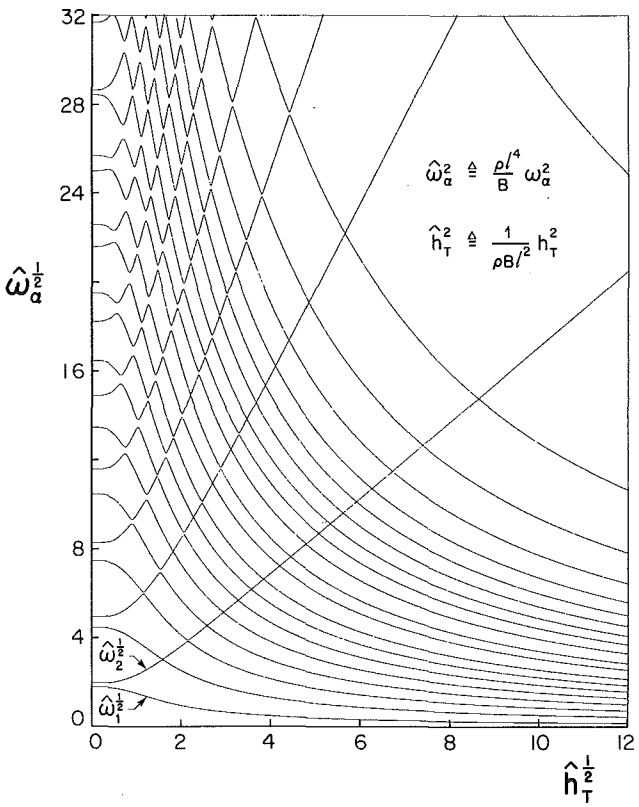

Fig. 5

$$\delta W_e \doteq \mathfrak{f}_{et}^T \delta \mathbf{q} \tag{8.5}$$

where the definitions

$$\mathfrak{M} \triangleq \int_{\mathcal{E}} \Delta^T \Delta dm \tag{8.6}$$

$$\mathcal{G} \triangleq \int_{\mathcal{E}} \Delta^T \underset{\sim}{\mathcal{G}} \Delta dV \tag{8.7}$$

$$\mathfrak{k} \triangleq \int_{\mathcal{F}} \Delta^T \nabla^x \mathbf{h}_s dV \tag{8.8}$$

$$\mathcal{K} \triangleq \int_{\mathcal{E}} \Delta^T \underset{\sim}{\mathcal{K}} \Delta dV \tag{8.9}$$

$$\mathfrak{f}_{eT} \triangleq = \int_{\mathcal{E}} \Delta^T \mathbf{f}_{eT} dV \tag{8.10}$$

have been introduced. The definitions (8.6), (8.9), and (8.10) are, of course, textbook material. The definitions (8.7) and (8.8), on the other hand, are novel to this paper.

Hamilton's (extended) principle is

$$\delta \int_{t_1}^{t_2} L\, dt + \int_{t_1}^{t_2} \delta W_e dt = 0 \tag{8.11}$$

where $L = T - U$ is the Lagrangian. Using this principle in conjunction with the previous energy and work expressions produces the following matrix equation of motion:

$$\mathfrak{M}\ddot{\mathbf{q}} + \mathcal{G}\dot{\mathbf{q}} + \mathcal{K}\mathbf{q} = \mathfrak{f}_{eT} \tag{8.12}$$

$$\mathfrak{M}^T = \mathfrak{M} > 0;\ \mathcal{G}^T = -\mathcal{G};\ \mathcal{K}^T = \mathcal{K} > 0 \tag{8.13}$$

This form of motion equation is familiar in other contexts, including nonspinning elastic bodies with finite wheels, and spinning elastic bodies. One of the main contributions of this paper is to show how to evaluate the matrix $\mathcal{G}$ for a distributed, continuous gyricity.

The object of this section has been to make the connection between the continuum representation of this paper, as represented by equation (4.6), and the familiar discrete-coordinate version of (8.12) in the foregoing. The latter has a quite extensive literature; see, for example, Huseyin [7].

9 Numerical Example

Let us now apply some of the results of the preceding sections to the example of a slender cantilevered rod with the sense of gyricity parallel to it (Fig. 4). The rod is assumed to have a constant linear mass density ρ and constant bending stiffnesses B_1 and B_2. It is sufficient to treat this problem in only two dimensions. Thus $\mathbf{u}(x) = [u_1(x),\ u_2(x)]^T$ and the stiffness and gyric operators take the special forms

$$\underset{\sim}{\mathcal{K}} = \begin{bmatrix} B_1 & \bullet \\ \bullet & B_2 \end{bmatrix} \frac{d^4}{dx^4} \tag{9.1}$$

$$\mathcal{G} = -\tilde{\nabla}\tilde{\mathbf{h}}_s\tilde{\nabla} \tag{9.2}$$

where

$$\tilde{\nabla} \triangleq \begin{bmatrix} \bullet & -1 \\ 1 & \bullet \end{bmatrix} \frac{d}{dx},\quad \tilde{\mathbf{h}}_s(x) \triangleq h_s(x) \begin{bmatrix} \bullet & -1 \\ 1 & \bullet \end{bmatrix}$$

Note the absence of the factor ¼ in (9.2). The gyricity distribution chosen is

$$h_s(x) = 2\frac{h_T}{l}\left(1 - \frac{x}{l}\right) \tag{9.3}$$

where h_T is the total angular momentum stored in the rod.

The system matrices $\mathfrak{M}$, $\mathcal{G}$, and $\mathcal{K}$ are assembled using the finite element method, which is a special case of the Rayleigh-Ritz procedure outlined in the last section. Special attention, though, should be given to the construction of $\mathcal{G}$, defined in general by (8.7). The most useful form for numerical computation can be obtained by integrating (8.7) by parts (Gauss' Theorem) which, upon noting the forced boundary conditions at the root, and $h_s(l) = 0$, yields

$$\mathcal{G} = -\int_0^l (\tilde{\nabla}\Delta)^T \tilde{\mathbf{h}}_s (\tilde{\nabla}\Delta) dx \tag{9.4}$$

The basis functions used are the traditional cubic Hermite polynomials, one set each for u_1 and u_2, so that there are four degrees of freedom for each node.

The equation of motion for the gyroelastic rod is

$$\mathcal{E}\dot{\zeta} + \mathcal{S}\zeta = \mathfrak{v} \tag{9.5}$$

which is the matrix equivalent of (5.1). The corresponding eigenvalue problem can be written as

$$(\omega_\alpha{}^2\mathbf{1} + \hat{\mathcal{S}}^2)\hat{\zeta} = \mathbf{0} \tag{9.6}$$

since there exists $\mathbf{U}$ such that $\mathbf{U}^T\mathcal{E}\mathbf{U} = \mathbf{1}$ and $\mathbf{U}^T\mathcal{S}\mathbf{U} = \hat{\mathcal{S}}$. Here $\mathbf{U}$ is given by

$$\mathbf{U} = \begin{bmatrix} \mathbf{T} & \bullet \\ \bullet & \mathbf{T}\boldsymbol{\Omega}^{-1} \end{bmatrix} \tag{9.7}$$

where $\mathbf{T}$ is the eigenmatrix of the corresponding nongyric elastic system that diagonalizes $\mathfrak{M}$ and $\mathcal{K}$:

$$\mathbf{T}^T\mathfrak{M}\mathbf{T} = \mathbf{1},\quad \mathbf{T}^T\mathcal{K}\mathbf{T} = \boldsymbol{\Omega}^2 \tag{9.8}$$

The form (9.6) is convenient since it can be solved by a standard eigenvalue routine for symmetric matrices. It is noteworthy that if we partition $\hat{\zeta}_\alpha$ as $\hat{\zeta}_\alpha = [-\omega_\alpha \mathbf{q}_{v\alpha}^T,\ \mathbf{q}_{u\alpha}^T]^T$ the *approximate* gyroelastic mode shapes are $\{\hat{\mathbf{u}}_\alpha,\ \hat{\mathbf{v}}_\alpha\} = \Delta(x)\,\mathbf{T}\boldsymbol{\Omega}^{-1}\{\mathbf{q}_{u\alpha},\ \mathbf{q}_{v\alpha}\}$.

The variation of the rod's vibrational frequencies with respect to (1200 values of) h_T is determined from (9.6) using a

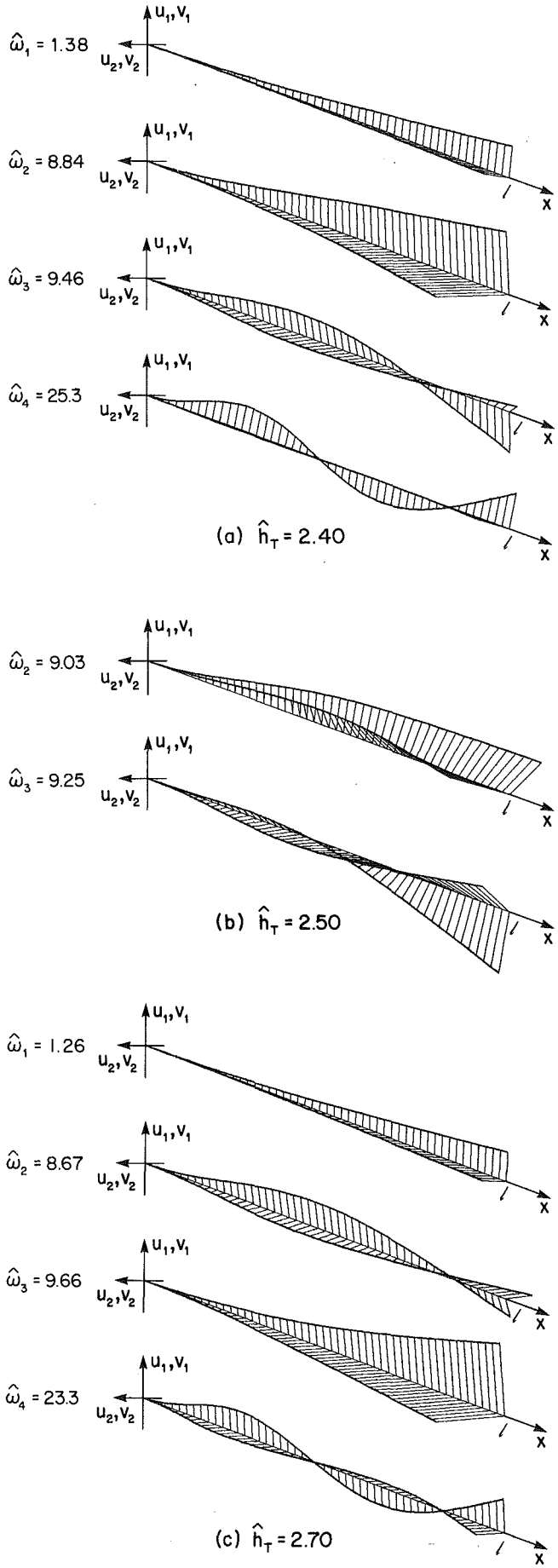

Fig. 6

10-element approximation (Fig. 5). The following nondimensionalizations prove useful:

$$\hat{\omega}_\alpha^2 \triangleq \omega_\alpha^2 \frac{\rho l^4}{B}, \quad \hat{h}_T \triangleq \frac{h_T}{(\rho B l^2)^{1/2}} \tag{9.9}$$

where $B \triangleq (B_1 B_2)^{1/2}$; the rod is taken to have a *bending stiffness ratio* $\beta \triangleq B_1/B_2 = 1.5$. The most salient characteristic of the plot in Fig. 5 is the trend of some frequencies to tend to zero and some to infinity. This is a generalization of the result obtained for the system $\mathcal{R} + \mathcal{W}$ of Fig. 1.

Figure 5 naturally raises the following conundrum: Do the frequency curves actually cross? Within the resolution of the computer-generated plot, it appears, especially at higher values of h_T, that the curves do cross. However, closer study shows that these "crossings," although very nearly occurring (especially for the low modes and high h_T), do not in fact occur. Consider, for example, the $\hat{\omega}_7^{1/2}$ curve. At $\hat{h}_T = 0$, it begins at a value of about 26. As $\hat{h}_T$ is increased, the curve oscillates repeatedly, coming ever nearer at the extremities to neighboring curves. Eventually it veers so close to its neighbors that, on the scale shown, crossings seem to occur. A change in the personality of the curve from "near misses" to actual crossings would, of course, be counterintuitive, and closer numerical examination of the critical regions has shown that there is no actual crossing. In summary, despite appearances, there are no curves crossing in Fig. 5.

Figure 6 shows some typical gyroelastic mode shapes for the rod. It should be noted that in general neither $\hat{\mathbf{u}}_\alpha$ nor $\hat{\mathbf{v}}_\alpha$ is planar (as is the case for simple elastic modes). Numerical experimentation suggests that the mode shapes change most radically in the region where two frequencies virtually coalesce. Let us examine Figs. 6($a-c$) more closely. Here it is the second and third frequencies that approach one another and the corresponding mode shapes seem to exchange indentities. In describing this phenomenon one is tempted to say that the second mode "acquires a node" and the third mode "sheds a node." It thus appears that the "identity" of a mode shape belongs to a general frequency trend and not an actual zig-zagging frequency line.

Finally, we note that the frequencies are paired, with one tending generally to zero and the other to infinity. Reminescent of the $\mathcal{R} + \mathcal{W}$ system, the low-frequency mode is an elliptical precession of the rod with a sense *opposite* to $\underline{h}_s$ and the high-frequency mode is an elliptical precession with the *same* sense as $\underline{h}_s$.

10 Concluding Remarks

The preceding numerical examples provide a simple illustration of continuously distributed gyricity, and of gyroelastic modes, but their simplicity should not obscure the fact that these ideas are equally applicable to complex structures. Indeed, it can be anticipated that in structures where gyricity is important ($\|\mathcal{G}\dot{\mathbf{u}}\|$ comparable to $\|\mathcal{K}\mathbf{u}\|$), a structural model based on N gyroelastic modal coordinate pairs $\{\eta_{u\alpha}, \eta_{v\alpha}; \alpha = 1 \ldots, N\}$ will be more accurate than a model based on N conventional modal coordinates with gyricity regarded as an "external" disturbance.

In any event it is evident that a structure's dynamical characteristics can be substantially modified by the introduction of an appropriate distribution of gyricity. Furthermore, by extension of a time-varying distribution, $\mathbf{h}_s(\mathbf{r}, t)$, gyricity provides a potentially powerful technique for *controlling* the dynamics of an elastic structure. The application that motivates the present authors is the control of structures in space. Very large, possibly flimsy space structures may one day stretch for kilometers, and one can visualize that their shape and orientation could be controlled by myriad small CMG's or reaction wheels distributed over the structure. An effective technique for dynamics and

control analysis would be to represent this cloud of wheels as a continuous distribution of gyricity.

References

1 D'Eleuterio, G. M. T., and Hughes, P. C., "Dynamics of a Flexible Vehicle With a General Angular Momentum Distribution," Progress Report presented at the III VPI and SU/AIAA Symposium on the Dynamics and Control of Large Flexible Spacecraft, Blacksburg, Va., June 1981.

2 Likins, P. W., "Dynamics and Control of Flexible Space Vehicles," JPL Tech. Report 32-1329 (Rev. 1), Jan. 1970.

3 Hablani, H. B., "Modal Analysis of Gyroscopic Flexible Spacecraft: A Continuum Approach," *J. Guidance, Control and Dynamics*, Vol. 5, No. 5, Sept.-Oct. 1982, pp. 448-457.

4 Roberson, R. E., "The Equivalence of Two Classical Problems of Free Spinning Gyrostats," ASME JOURNAL OF APPLIED MECHANICS, Vol. 38, 1971, pp. 707-708.

5 Timoshenko, S., and Goodier, J. N., *Theory of Elasticity*, McGraw-Hill, New York, 1951.

6 D'Eleuterio, G. M. T., "Dynamics and Control of Gyro-Elastic Space Vehicles," Ph.D. Disseration, University of Toronto, Institute for Aerospace Studies, 1983.

7 Huseyin, K., *Vibrations and Stability of Multiple Parameter Systems*, Sijthoff & Noordhoff, 1978.

APPENDIX

Principal Symbols

$\mathbf{f}$ = force on volume element dV
$\mathbf{g}$ = torque on volume element dV
$\mathbf{h}_s$ = gyricity in dV; see Fig. 3
$\mathbf{r}$ = spatial independent variable
T = kinetic energy
$\mathbf{u}(\mathbf{r},t)$ = (small) elastic displacement
$\mathbf{u}_\alpha, \mathbf{v}_\alpha$ = pair of shape functions for gyroelastic mode α
U = potential energy

Script

$\mathcal{E}$ = elastic body
$\underset{\sim}{\mathcal{E}}$ = 6×6 operator; see (5.2)
$\underset{\sim}{\mathcal{G}}$ = 3×3 gyricity operator; see (4.4)
$\mathcal{G}$ = gyricity matrix; see (8.7)
$\mathcal{K}$ = 3×3 stiffness operator
$\underset{\sim}{\mathcal{K}}$ = stiffness matrix; see (8.9)
$\mathcal{M}$ = 3×3 mass operator; see (4.7)
$\underset{\sim}{\mathcal{S}}$ = 6×6 operator; see (5.2)

Greek

$\boldsymbol{\alpha}$ = (small) rotational elastic displacement; see (4.1)
$\boldsymbol{\gamma}$ = see (5.3)
$\{\eta_{u\alpha}, \eta_{v\alpha}\}$ = gyroelastic modal coordinates; see (7.1)
σ = mass density
$\{\phi_\alpha, \psi_\alpha\}$ = real and imaginary parts of χ_α
χ_α = complex, 6×1 eigenfunction; see (6.1)
ω_α = natural frequency of gyroelastic mode α

Special Symbols

δ = unit source function (a.k.a. Dirac function, or unit impulse function)
∇ = $[\partial/\partial r_1\ \partial/\partial r_2\ \partial/\partial r_3]^T$; gradient operator
$\mathbf{a}^\times$ = $\begin{bmatrix} 0 & -a_3 & a_2 \\ a_3 & 0 & -a_1 \\ -a_2 & a_1 & 0 \end{bmatrix}$ for any 3×1 vector $\mathbf{a}$
$(\bullet)^H$ = complex conjugate of $(\bullet)^T$
$(\bullet)^T$ = transpose of $(\bullet)$

Interactions Between Self and Parametrically Excited Motions in Articulated Tubes[1]

A. K. Bajaj
Assistant Professor,
School of Mechanical Engineering,
Purdue University,
West Lafayette, Ind. 47907
Assoc. Mem. ASME

The nonlinear dynamics of a two-segment articulated tubes system conveying a fluid is studied when the flow is harmonically perturbed. The mean value of the flow rate is near its critical value when the downward vertical position gets unstable and undergoes Hopf bifurcation into periodic solutions. The harmonic perturbations are assumed to be in parametric resonance with the linearized system. The method of Alternate Problems is used to obtain the small nonlinear subharmonic solutions of the system. It is shown that, in addition to the usual jump response, the system also exhibits stable and unstable isolated solution branches. For some parameter combinations the stable solutions can become unstable and can then bifurcate into aperiodic or amplitude-modulated motions.

1 Introduction

Flow-induced motions in articulated and continuous tubes carrying a fluid have been studied extensively beginning with the work of Benjamin [1, 2] on articulated tubes. Much of the early work has been limited to the linearized stability analysis of initially straight tubes for motions in a plane. Among the references, works of Gregory and Paidoussis [3, 4] and Paidoussis and Issid [5] may be mentioned. Nonlinear analysis for linearly unstable planar motions has been conducted by Holmes [6], Rousselet and Herrmann [7], and Bajaj, Sethna, and Lundgren [8]. Bajaj and Sethna [9, 10] have recently studied the problem for three-dimensional motions.

Almost all the works mentioned in the foregoing have been concerned with the case when the flow through the tubes is at a constant rate. Bohn and Hermann [1] discussed the articulated tubes system when the flow rate is periodic. They showed that both parametric and combination resonances can occur, especially when the mean flow is near its critical value. The case of continuous tubes with periodic flow was studied by Paidoussis and Issid [5], Ginsberg [12], and Paidoussis and Sundararajan [13].

In this paper we study nonlinear planar motions of articulated tubes with periodic flow. The mean flow rate is near the critical value for which the straight equilibrium position of the tubes becomes unstable with a complex pair of eigenvalues crossing the imaginary axis and the system undergoes Hopf bifurcation. The periodic fluctuations in the flow rate are in parametric resonance with the linear system around criticality. The nonlinear analysis is restricted to only periodic motions. Even under these restrictions, the system, depending on other parameters, exhibits a wide variety of phenomena including jump response and isolated solutions.

The mathematical problem is a problem in perturbed bifurcation theory, specifically, that of periodically perturbed Hopf bifurcations. Recently, Rosenblat and Cohen [14], Kath [15], and Smith [16] have presented results related to various aspects of the problem of forced excitations of systems undergoing Hopf bifurcation. The case of parametric perturbations has been studied by the author in [17] where the method of Alternate Problems [18] has been used to find the subharmonic solutions. The present work is based on his general analysis.

2 Equations of Motion

In the following, we give the equations of motion for a two-segment articulated tubes system hanging vertically and undergoing planar motions. The fluid enters the tubes at the top and is discharged tangentially at the lower end of the tubes to the atmosphere. A cartesian coordinate system is fixed at the top of the tubes where the fluid enters with the Z-axis coinciding with the downward vertical position. The displacements of the tubes from the Z-axis are then given by X-coordinates.

We assume that the fluid is incompressible and its velocity profile at any cross section is uniform. Both the tubes have the same circular cross section and the diameters of the tubes are small compared to their lengths. The elastic restoring

[1]This work was supported by funds from the National Science Foundation under grant MEA-8117086.

Contributed by the Applied Mechanics Division for presentation at the 1984 PVP Conference and Exhibition, Joint with Applied Mechanics Division and Materials Division, San Antonio, Texas, June 17-21, 1984 of THE AMERICAN SOCIETY OF MECHANICAL ENGINEERS.

Discussion on this paper should be addressed to the Editorial Department, ASME, United Engineering Center, 345 East 47th Street, New York, N.Y. 10017, and will be accepted until two months after final publication of the paper itself in the JOURNAL OF APPLIED MECHANICS. Manuscript received by ASME Applied Mechanics Division, March, 1983; final revision, October, 1983. Paper No. 84-APM-30.

Copies will be available until February, 1985.

moments at the joints are linearly proportional to the angles between the centerlines of adjacent tubes.

Following Benjamin [1] and Bajaj and Sethna [9], it can be shown that the equations of motion of the system in dimensionless form are given by:

$$
\begin{aligned}
&a^2(a+3)\ddot{x}_1 + 3a\ddot{x}_2/2 + a^2\beta\rho\dot{x}_1 \\
&\quad + 2a\beta\rho\dot{x}_2 + a\beta\rho^2(x_2 - x_1) \\
&\quad + a(a+2)Gx_1 + \kappa x_1 + (x_1 - x_2) \\
&\quad + a\beta\dot{\rho}(x_2 - x_1) = -x_1[a^2(a+3)(\dot{x}_1^2 + x_1\ddot{x}_1) \\
&\quad + 3a(\dot{x}_2^2 + x_2\ddot{x}_2)/2] - 2a\beta\rho x_1 x_2\dot{x}_2 \\
&\quad + x_1^3[-\{a(a+2)G + 1 - a\beta\rho^2\}/2 - 2\kappa/3] \\
&\quad + x_1 x_2^2(1 - a\beta\rho^2)/2 - (x_1 - x_2)^3/6 \\
&\quad - a^2\beta\rho x_1^2\dot{x}_1 + a\beta\dot{\rho}x_1(x_1^2 - x_2^2)/2, \qquad (1)
\end{aligned}
$$

and

$$
\begin{aligned}
&3a\ddot{x}_1/2 + \ddot{x}_2 + \beta\rho\dot{x}_2 + Gx_2 + (x_2 - x_1) = -x_2[(\dot{x}_2^2 + x_2\ddot{x}_2) \\
&\quad + 3a(\dot{x}_1^2 + x_1\ddot{x}_1)/2] - Gx_2^3/2 + [x_2(x_1^2 - x_2^2) \\
&\quad + (x_1 - x_2)^3/3]/2 - \beta\rho x_2^2\dot{x}_2. \qquad (2)
\end{aligned}
$$

Here x_1 and $x_1 + x_2$ are, respectively, the nondimensional displacements of the ends of the upper and lower tube segments. Also, since we are interested in studying small nonlinear motions, we have only retained the linear and the lowest-order nonlinear terms, which are cubic. We should also point out that these equations have some additional terms compared to the equations in [9] and these arise because the flow velocity is not constant.

The equations of motion depend on five dimensionless parameters: a, κ, β, ρ, and G. The parameter a is the ratio of length of the upper segment to that of the lower segment. Parameter κ represents the ratio of stiffness of the upper joint to that of the lower joint. The ratio of mass of the fluid to that of the tube is given by β. The dimensionless flow velocity is represented by ρ and the gravity parameter G represents the magnitude of weight forces nondimensionalized with respect to the stiffness of the lower joint.

As indicated in the Introduction, we wish to study the problem of parametric excitations arising from the flow fluctuations and, therefore, we assume that the flow velocity ρ is of the form

$$\rho = \rho_0 + \sigma\cos 2\omega t \qquad (3)$$

where ρ_0 is the mean flow component and σ, the fluctuation amplitude, is small, that is, $\sigma << \rho_0$.

We now transform equations (1) and (2) into a first order vector form. Let

$$\mathbf{z} = (x_1, x_2, \dot{x}_1, \dot{x}_2)^T.$$

Equations (1) and (2) can then be written as

$$
\begin{aligned}
\dot{\mathbf{z}} &= \hat{\mathbf{A}}_0(\rho_0)\mathbf{z} + \sigma\{\hat{\mathbf{A}}_1\cos 2\omega t + \hat{\mathbf{B}}\sin 2\omega t\}\mathbf{z} \\
&\quad + \sigma^2\{\hat{\mathbf{A}}_2\cos^2 2\omega t\}\mathbf{z} + \mathbf{h}_1(\mathbf{z},\rho_0) + \mathbf{h}_2(\mathbf{z},\rho_0,\sigma,t) \qquad (4)
\end{aligned}
$$

where

$$
\hat{\mathbf{A}}_0(\rho_0) = \frac{1}{a(4a+3)}\begin{bmatrix} 0 & 0 & a(4a+3) & 0 \\ 0 & 0 & 0 & a(4a+3) \\ -Aa & -Ba & -4\beta\rho_0 a & -2\beta\rho_0 \\ -Ca & -Da & 6a^2\beta\rho_0 & 4a^2\beta\rho_0 \end{bmatrix},
$$

$$
\hat{\mathbf{A}}_1 = \frac{1}{a(4a+3)}\begin{bmatrix} 0 & 0 & 0 & 0 \\ 0 & 0 & 0 & 0 \\ 8\beta\rho_0 & -8\beta\rho_0 & -4a\beta & -2\beta \\ -12a\beta\rho_0 & 12\beta\rho_0 a & 6a^2\beta & -4a^2\beta \end{bmatrix},
$$

$$
\hat{\mathbf{B}} = \frac{4\omega\beta}{a(4a+3)}\begin{bmatrix} 0 & 0 & 0 & 0 \\ 0 & 0 & 0 & 0 \\ -2 & 2 & 0 & 0 \\ 3a & -3a & 0 & 0 \end{bmatrix},
$$

$$A = 4(1+\kappa)/a^2 + (6 - 4\beta\rho_0^2)/a + 4G(a+2)/a,$$

$$B = (4\beta\rho_0^2 - 6)/a - 4/a^2 - 6G/a,$$

$$C = 6\beta\rho_0^2 - 4(a+4) - 6(1+\kappa)/a - 6G(a+2),$$

and

$$D = 6/a + (4a + 12 - 6\beta\rho_0^2) + 4G(a+3).$$

The matrix $\hat{\mathbf{A}}_2$ and the nonlinear function $\mathbf{h}_2$ will not be needed explicitly in the subsequent analysis. For the function $\mathbf{h}_1$, we note that the first two components h_{11} and h_{12} are zero. The nonzero components h_{13} and h_{14} are given in [9] and will, therefore, not be repeated here for lack of space.

3 Linearized System, Conditions at Criticality

The linearized system is given by

$$
\begin{aligned}
\dot{\mathbf{z}} &= \hat{\mathbf{A}}_0(\rho_0)\mathbf{z} + \sigma\{\hat{\mathbf{A}}_1\cos 2\omega t + \hat{\mathbf{B}}\sin 2\omega t\}\mathbf{z} \\
&\quad + \sigma^2\{\hat{\mathbf{A}}_2\cos^2 2\omega t\}\mathbf{z}. \qquad (5)
\end{aligned}
$$

For $\sigma = 0$, this is just the problem of articulated tubes with steady flow ρ_0 and it is well known [1, 9] that the zero solution $\mathbf{z} = \mathbf{0}$ loses its stability at some flow rate $\rho_0 = \rho_{cr}$ with a pair of complex-conjugate eigenvalues of $\hat{\mathbf{A}}_0$ crossing the imaginary axis at nonzero speed. This is valid for all values of system parameters a, κ, and β so long as G, the gravity parameter, is small [21]. The critical flow rate, ρ_{cr}, clearly depends on these parameters. The pure-imaginary pair of eigenvalues, $\pm i\nu_0$, can be shown [9] to be given by

$$\nu_0^2 = [(a+1)^2 + \kappa + 2(a+1)aG - a\beta\rho_{cr}^2]/a^2(a+1). \qquad (6)$$

The behavior of the linear system (5) for small $(\rho_0 - \rho_{cr})$ and σ, $\sigma \neq 0$, is determined by the excitation frequency ω. As is well known [19], the system exhibits parametric resonance for values of ω close to ν_0/n, $n = 1, 2, 3, \ldots$. The case of $n = 1$ corresponds to "primary" parametric resonance and we restrict our analysis to this case.

Therefore, we analyze the nonlinear system (4) when $(\rho_0 - \rho_{cr})$ and σ are small and ω is close to the critical frequency ν_0. Before proceeding with the nonlinear analysis, it is advantageous to transform equations (4) into a canonical form in which the linear system is in its Jordan form.

4 System in Jordan Canonical Variables

Let $\mathbf{C}$ be the matrix of eigenvectors of $\hat{\mathbf{A}}_0$. Also let $\mathbf{D}$ be the eigenvector matrix corresponding to $\hat{\mathbf{A}}_0^T$. Then, as is well known [9], by the transformation $\mathbf{z} = \mathbf{C}\mathbf{y}$, the nonlinear system (4) is reduced to

$$
\begin{aligned}
\dot{\mathbf{y}} &= \bar{\hat{\mathbf{A}}}(\rho_0)\mathbf{y} + \sigma(\mathbf{E}_1\cos 2\omega t \\
&\quad + \mathbf{E}_2\sin 2\omega t)\mathbf{y} + \bar{\mathbf{k}}(\mathbf{y},\rho_0,\sigma,\omega t) \qquad (7)
\end{aligned}
$$

where

$$\bar{\bar{\mathbf{A}}}(\rho_0) \equiv \mathbf{D}^T \hat{\mathbf{A}}_0 \mathbf{C}, \quad \mathbf{E}_1 \equiv \mathbf{D}^T \hat{\mathbf{A}}_1 \mathbf{C}, \quad \mathbf{E}_2 \equiv \mathbf{D}^T \hat{\mathbf{B}} \mathbf{C}$$

and

$$\bar{\mathbf{k}}(\mathbf{y},\rho_0,\sigma,\omega t) \equiv \mathbf{D}^T \{ (\sigma^2 \hat{\mathbf{A}}_2 \cos^2 2\omega t)\mathbf{C}\mathbf{y} + \mathbf{h}_1(\mathbf{C}\mathbf{y},\rho_0) + \mathbf{h}_2(\mathbf{C}\mathbf{y},\rho_0,\sigma,t) \}$$

Here, the matrix $\bar{\bar{\mathbf{A}}}$ is in real Jordan form.

Consider equations (7). At $\rho_0 = \rho_{cr}$, $\bar{\bar{\mathbf{A}}}$ has a pair of pure imaginary eigenvalues $\pm i\nu_0$. The parametric excitation frequency ω is close to ν_0. To study the nonlinear behavior of the system for small deviations from ρ_{cr}, we let

$$\rho_0 = \rho_{cr} + \eta, \ \nu_0 = \omega + \alpha$$

where η and α are small. The parameter α represents "detuning." Equations (7) can then be written as

$$\dot{\mathbf{y}} = \bar{\bar{\mathbf{A}}}_0 \mathbf{y} + \alpha \bar{\bar{\mathbf{A}}}_2 \mathbf{y} + \eta \bar{\bar{\mathbf{A}}}_1(\eta)\mathbf{y} + \sigma(\mathbf{E}_1 \cos 2\omega t + \mathbf{E}_2 \sin 2\omega t)\mathbf{y} + \mathbf{k}(\mathbf{y},\eta,\sigma,\omega t) \tag{8}$$

where

$$\bar{\bar{\mathbf{A}}}_0 = \bar{\bar{\mathbf{A}}}(\rho_{cr}) - \alpha \bar{\bar{\mathbf{A}}}_2, \quad \eta \bar{\bar{\mathbf{A}}}_1(\eta) = \bar{\bar{\mathbf{A}}}(\rho_{cr} + \eta) - \bar{\bar{\mathbf{A}}}_0,$$

and

$$\mathbf{k}(\mathbf{y},\eta,\sigma,\omega t) = \bar{\mathbf{k}}(\mathbf{y},\rho_{cr} + \eta,\sigma,\omega t).$$

The matrix $\bar{\bar{\mathbf{A}}}_0$ has the structure

$$\bar{\bar{\mathbf{A}}}_0 = \mathrm{diag}(\mathbf{D}_{10},\mathbf{D}_{20}), \quad \mathbf{D}_{10} = \begin{bmatrix} 0 & \omega \\ -\omega & 0 \end{bmatrix},$$

and $\mathbf{D}_{20}$ is the 2×2 matrix with both eigenvalues in the left half of the complex plane. Matrix $\bar{\bar{\mathbf{A}}}_2$ is given by

$$\bar{\bar{\mathbf{A}}}_2 = \mathrm{diag}(\hat{\mathbf{A}}_2, \mathbf{0})$$

where

$$\hat{\mathbf{A}}_2 = \begin{bmatrix} 0 & 1 \\ -1 & 0 \end{bmatrix}.$$

The matrix $\bar{\bar{\mathbf{A}}}_1(\eta)$ is also in block diagonal form with two blocks of 2×2 matrices each. In the limit as $\eta \to 0$, the upper nonzero block determines the rate of change with respect to ρ_0 of critical eigenvalues and is given by

$$\mathbf{D}_{110} = \begin{bmatrix} \xi & \tilde{\omega} \\ -\tilde{\omega} & \xi \end{bmatrix}$$

where

$$\xi = \frac{d}{d\rho_0}(Re\,\lambda_1)\Big|_{\rho_0=\rho_{cr}} \quad \text{and} \quad \tilde{\omega} = \frac{d}{d\rho_0}(Im\,\lambda_1)\Big|_{\rho_0=\rho_{cr}}.$$

Here λ_1 and λ_2, $\lambda_1 = \bar{\lambda}_2$ are the critical eigenvalues of $\hat{\mathbf{A}}_0(\rho_0)$.

We now study equation (8) for its small $2\pi/\omega$ periodic solutions.

5 Determination of Periodic Solutions

Consider the system (8). At $\eta = \alpha = \sigma = 0$, the linearized system

$$\dot{\mathbf{y}} = \bar{\bar{\mathbf{A}}}_0 \mathbf{y} \tag{9}$$

has a pair of pure imaginary eigenvalues $\pm i\omega$, $\omega > 0$. Thus, the linearized system at criticality has a pair of periodic solutions of period $2\pi/\omega$. We are interested in finding periodic solutions of (8) when η, α, and σ are nonzero, but small. We first make a time scale change $\tau = \omega t$ so that (8) is transformed to

$$\omega \mathbf{y}' = \bar{\bar{\mathbf{A}}}_0 \mathbf{y} + \mathbf{F}(\mathbf{y},\tau,\eta,\sigma,\alpha) \tag{10}$$

where

$$\mathbf{F}(\mathbf{y},\tau,\eta,\sigma,\alpha) \equiv \alpha \bar{\bar{\mathbf{A}}}_2 \mathbf{y} + \eta \bar{\bar{\mathbf{A}}}_1 \mathbf{y} + \sigma(\mathbf{E}_1 \cos 2\tau + \mathbf{E}_2 \sin 2\tau)\mathbf{y} + \mathbf{k}(\mathbf{y},\eta,\sigma,\tau)$$

and where prime denotes differentiation with respect to τ.

The 2π-periodic solutions of (10) can be found using either the method of Liapunov-Schmidt [20] or the method of Alternate Problems [18, 20]. Here we follow the latter along the lines of Bajaj and Sethna [10]. Since the method is well known, we only give the final results and leave the details [10, 17].

We work in the space of 2π-periodic continuous n-vector functions. The $(n\times 2)$-matrix functions $\Phi(\tau)$ and $\Psi(\tau)$ defined by

$$\Phi(\tau) = \exp\left(\frac{1}{\omega}\bar{\bar{\mathbf{A}}}_0 \tau\right)(\mathbf{e}_1,\mathbf{e}_2),$$

$$\Psi(\tau) = \exp\left(-\frac{1}{\omega}\bar{\bar{\mathbf{A}}}_0^T \tau\right)(\mathbf{e}_1,\mathbf{e}_2) \tag{11}$$

are, respectively, a basis for the 2π-periodic solutions of the linear system

$$\omega \mathbf{y}' = \bar{\bar{\mathbf{A}}}_0 \mathbf{y} \tag{12}$$

and its adjoint

$$\omega \mathbf{y}' = -\bar{\bar{\mathbf{A}}}_0^T \mathbf{y}. \tag{13}$$

Here $\mathbf{e}_i$, $i = 1, 2$ denote n-vectors with 1 in the ith entry and zero elsewhere. The problem of finding 2π-periodic solutions of equation (10) is then reduced to finding solutions $\mathbf{d}\epsilon\mathbb{R}^2$ of the bifurcation equations

$$\mathbf{G}(\mathbf{d},\eta,\sigma,\alpha) = 0, \tag{14}$$

where $\mathbf{d}$ is related, in the first approximation, to $\mathbf{y}$ by $\mathbf{y} = \Phi(\tau)\mathbf{d}$.

Letting

$$\bar{\bar{\mathbf{A}}}_1(\eta) = \bar{\bar{\mathbf{A}}}_{10} + \eta \bar{\bar{\mathbf{A}}}_{11} + 0(|\eta|^2),$$

and

$$\mathbf{k}(\mathbf{y},\eta,\sigma,\omega t) = \mathbf{k}_c(\mathbf{y}) + 0(|\mathbf{y}|^5) + 0(|\eta|\,|\mathbf{y}|^3) + 0(|\sigma|^2\,|\mathbf{y}|) + 0(|(\sigma,\eta)|\,|\mathbf{y}|)$$

where $\mathbf{k}_c(\mathbf{y})$ is a homogeneous cubic in $\mathbf{y}$, the bifurcation equations (14) reduce to

$$\eta \mathbf{M}_\eta \mathbf{d} + \alpha \mathbf{M}_\alpha \mathbf{d} + \sigma \mathbf{M}_\sigma \mathbf{d} + \mathbf{C}_k(\mathbf{d}) + 0(|\sigma|^2\,|\mathbf{d}|) + 0(|\eta|^2\,|\mathbf{d}|) + 0(|(\eta,\sigma,\alpha)|\,|\mathbf{d}|^3) + 0(|\mathbf{d}|^5) = 0, \tag{15}$$

with functions $\mathbf{M}_\eta$, $\mathbf{M}_\alpha$, $\mathbf{M}_\sigma$, and $\mathbf{C}_k(\mathbf{d})$ defined by

$$\mathbf{M}_\eta \equiv \int_0^{2\pi} \Psi^T(s)\bar{\bar{\mathbf{A}}}_{10}\Phi(s)ds, \quad \mathbf{M}_\alpha \equiv \int_0^{2\pi} \Psi^T(s)\bar{\bar{\mathbf{A}}}_2\Phi(s)ds,$$

$$\mathbf{M}_\sigma \equiv \int_0^{2\pi} \Psi^T(s)\{\mathbf{E}_1 \cos 2s + \mathbf{E}_2 \sin 2s\}\Phi(s)ds, \tag{16}$$

and

$$\mathbf{C}_k(\mathbf{d}) \equiv \int_0^{2\pi} \Psi^T(s)\mathbf{k}_c(\Phi(s)\mathbf{d})ds.$$

Equations (15) are a system of two nonlinear algebraic equations dependent on three small parameters η, α, and σ which can be varied independently. A general analysis of these equations, to determine all the possible small solutions $\mathbf{d}$ for η, α, and σ varying over the whole neighborhood of the origin in the parameter space, is quite involved. Such equations have been analyzed in detail in Chow and Hale [20].

We assume that $\mathbf{C}_k(\mathbf{d}) = \mathbf{0}$ implies $\mathbf{d} = \mathbf{0}$. It can then be shown [20] that every small solution of (15) satisfies

$$|\mathbf{d}| \leq \delta(|\eta|^{1/2} + |\sigma|^{1/2} + |\alpha|^{1/2}) \tag{17}$$

for some $\delta \neq 0$ and this suggests the scaling

$$\mathbf{d} = \mu\hat{\mathbf{d}},\ \eta = \eta_2\mu^2,\ \alpha = \alpha_2\mu^2 \text{ and } \sigma = \sigma_2\mu^2. \tag{18}$$

Equations (15) are then reduced to

$$\eta_2\mathbf{M}_\eta\hat{\mathbf{d}} + \alpha_2\mathbf{M}_\alpha\hat{\mathbf{d}} + \sigma_2\mathbf{M}_\sigma\hat{\mathbf{d}} + \mathbf{C}_k(\hat{\mathbf{d}}) + 0(|\mu|^2) = 0. \tag{19}$$

The reduced bifurcation equations are obtained by taking the limit $\mu \to 0$ which gives

$$\eta_{20}\mathbf{M}_\eta\hat{\mathbf{d}}_0 + \alpha_{20}\mathbf{M}_\alpha\hat{\mathbf{d}}_0 + \sigma_{20}\mathbf{M}_\sigma\hat{\mathbf{d}}_0 + \mathbf{C}_k(\hat{\mathbf{d}}_0) = 0. \tag{20}$$

Solutions to these equations determine the first approximations to the $2\pi/\omega$-periodic solutions of (8).

The bifurcation equations, taking the explicit expressions for various terms and the scaling (18) into account, can be shown to reduce to

$$(a_1^2 + b_1^2)A^4 + 2\{a_1\xi\eta - b_1(\alpha + \tilde{\omega}\eta)\}A^2 + (\eta\xi)^2 + (\alpha + \tilde{\omega}\eta)^2 - \sigma^2(c_1^2 + d_1^2) = 0. \tag{21}$$

Here, we have replaced $\mathbf{d}$ by the polar variables A and ϕ defined by

$$d_1 = A\cos\phi, \quad d_2 = A\sin\phi,$$

eliminated ϕ and divided the resulting equation by A to remove the zero solution $A = 0$.

Equation (21) determines the nonzero amplitudes of periodic solutions of the system. These roots depend on constants a_1, b_1, c_1, and d_1. The constants c_1 and d_1 are determined by the matrices $\mathbf{E}_1$ and $\mathbf{E}_2$ which represent the parametric excitation. The constants a_1 and b_1 are determined by the function $\mathbf{k}_c(\mathbf{y})$, which in turn depends on the physical parameters a, β, κ, G, and the critical mean flow rate corresponding to them, ρ_{cr}. For a given value of these physical parameters, η, α, and σ can be varied arbitrarily.

Before studying (21) in detail, it is convenient to also obtain the conditions required for the stability of periodic solutions determined by its real positive roots.

The stability of these bifurcating periodic solutions is determined by the Floquet exponents of the variational equation

$$\omega\psi' = \bar{\bar{\mathbf{A}}}_0\psi + \mu^2\mathbf{K}(\tau,\mu)\psi \tag{22}$$

where

$$\mathbf{K}(\tau,\mu) \equiv \alpha_2\bar{\bar{\mathbf{A}}}_2 + \eta_2\bar{\bar{\mathbf{A}}}_1 + \sigma_2(\mathbf{E}_1\cos 2\tau + \mathbf{E}_2\sin 2\tau) + \mathbf{k}_y(\hat{\mathbf{y}},\mu^2\eta_2),$$

$$\mathbf{k}_y(\mathbf{y},\eta) \equiv \frac{\partial\mathbf{k}}{\partial\mathbf{y}}(\mathbf{y},\eta),$$

and where $\mathbf{y} = \mu\hat{\mathbf{y}}(\tau,\mu)$ is the 2π-periodic solution of (10) whose stability is being studied. Equation (22) is a linear 2π-periodic differential system which depends smoothly on μ for small enough μ uniformly in τ. It can easily be shown that the two noncritical Floquet exponents of (22) are given by

$$\gamma_j(\mu) = \lambda_j + 0(\mu), \quad j = 3,4$$

where λ_j are the noncritical eigenvalues of matrix $\bar{\bar{\mathbf{A}}}_0$. Thus, the stability of the periodic solutions is determined by $\gamma_j(\mu)$, $j = 1, 2$ for small μ.

The critical exponents $\gamma_1(\mu)$ and $\gamma_2(\mu)$ can be determined using the method of Alternate Problems [18, 20]. Letting $\gamma = \mu^2\gamma_2$ and $\bar{\lambda} = \omega\gamma_2$, we can easily show that, for the nonzero solutions, these exponents are roots of

$$\bar{\lambda}^2 - 2\bar{\lambda}(\xi\eta + 2a_1A^2) + 4[\sigma^2(c_1^2 + d_1^2) - \{(\xi\eta)^2 + (\alpha + \tilde{\omega}\eta)^2\} + A^2\{b_1(\alpha + \tilde{\omega}\eta) - a_1\xi\eta\}] = 0. \tag{23}$$

Here, A is the amplitude of the periodic solution whose stability is to be determined. Exponents for the zero solution are given by

$$\bar{\lambda}^2 - 2\xi\eta\bar{\lambda} + [(\xi\eta)^2 + (\alpha + \tilde{\omega}\eta)^2 - \sigma^2(c_1^2 + d_1^2)] = 0. \tag{24}$$

The three equations (21), (23), and (24) need to be analyzed together as a function of the independent parameters η, α, and σ. Positive roots of (21) determine the nonzero periodic solutions. The corresponding roots of (23) determine their stability.

We first show that if there are no fluctuations in the flow rate, that is, if $\sigma = 0$, we recover the standard results of Hopf bifurcation [20]. Let $\sigma = 0$. Then (21) has a real solution if and only if $\alpha = -(\tilde{\omega} + b_1\xi/a_1)\eta$ and the resulting solution is given by

$$A^2 = -\xi\eta/a_1. \tag{25}$$

The corresponding roots of (23) are

$$\bar{\lambda}_1 = 0, \quad \bar{\lambda}_2 = -2\xi\eta.$$

Thus, if $a_1 < 0$, the bifurcating limit cycle exists for $\eta > 0$ (supercritical) and it is stable. In case $a_1 > 0$, the solution exists for $\eta < 0$ (subcritical) and is unstable. Note that the detuning α is not arbitrary and is determined as a part of the solution. This is clearly because the system is autonomous and the period of limit cycle depends on the amplitude of the nonlinear response and, therefore, on the parameter η.

When $\sigma \neq 0$ and both the parameters η and α are small but arbitrary, the classification of the system response and that of the parameter space becomes quite involved although the methods of analysis are elementary. Such an analysis has been performed by the author and the general results will be presented elsewhere [17]. In the present work we only sketch the general results and then give details for a few specific values of parameters to show the kinds of periodic response possible in the case of the articulated tubes system.

Consider the amplitude equation (21). It can be easily seen that in the region defined by

$$(\eta\xi)^2 + (\alpha + \tilde{\omega}\eta)^2 \leq \sigma^2(c_1^2 + d_1^2) \tag{26}$$

there is only one real solution. There are two real nonzero solutions for parameter values that satisfy $b_1(\alpha + \tilde{\omega}\eta) - a_1\xi\eta > 0$, lie inside the region

$$[b_1(\eta\xi) + a_1(\alpha + \tilde{\omega}\eta)]^2 \leq \sigma^2(c_1^2 + d_1^2)(a_1^2 + b_1^2), \tag{27}$$

and outside the region defined by (26).

As is clear from (24), the zero solution is stable when $\eta < 0$ and the other parameters remain outside the region (26). Inside (26) it is of saddle type. Of the two nonzero solutions, the one with smaller amplitude is always unstable and a saddle. The other solution, which is either the only nonzero solution or is the one with larger amplitude, can become unstable only when (23) has complex roots and they cross the imaginary axis as the system parameters are varied. This occurs when the parameters satisfy

$$4a_1^2(\alpha + \tilde{\omega}\eta)^2 + 4a_1b_1\xi\eta(\alpha + \tilde{\omega}\eta) + (a_1^2 + b_1^2)\xi^2\eta^2 = 4a_1^2(c_1^2 + d_1^2)\sigma^2. \tag{28}$$

We can observe from the foregoing discussion that constants a_1 and b_1 play important roles in the system response. As the analysis of the $\sigma = 0$ case indicates, a_1 can be viewed as a constant representing nonlinear damping or van der Pol nonlinearity in a general van der Pol oscillator [19]. It determines whether, in the absence of flow fluctuations, the bifurcating periodic solution is stable ($a_1 < 0$) or unstable ($a_1 > 0$). The constant b_1 represents nonlinear stiffness similar to the one in Duffing's oscillator [19].

The preceding discussion about possible solutions and their stability indicates that, for given system constants a_1, b_1, c_1, and d_1, it is possible to have regions in the parameter space where the zero solution as well as all the existing nonzero periodic solutions are unstable. On physical grounds we

expect the solutions of the system to remain bounded. Such solutions, if they exist, cannot be predicted by the present analysis and some other method such as the method of averaging must be used to uncover them. A study along these lines is presently being conducted and preliminary results indicate that the system, under these conditions, executes amplitude-modulated motions. Similar phenomena have been observed by Tezak, Nayfeh, and Mook [22].

We should also point out the possibility that for some parameter values the origin as well as the larger of the two nonzero periodic solutions are stable. In such a case the ultimate motion observed in an experiment will be determined by the initial conditions. The initial conditions, which lead to a particular stable solution, can be determined if the method of averaging is used for the analysis.

We now present results for the articulated tubes system for specific values of the physical parameters a, β, κ, and G.

6 Numerical Results and Discussion

As noted earlier, the response amplitudes and their stability depends on the constants a_1 and b_1 and the parameters η, α, and σ. The constants a_1 and b_1 are, in turn, functions of the physical parameters a, κ, β, and G. To study the whole parameter space is a very difficult proposition, and we therefore restrict ourselves to a very small number of cases. The cases chosen, however, do show the wide variety of periodic solutions exhibited by the articulated tubes system.

For all the results presented here, the parameters a, κ, and G have been fixed at values 1.0, 1.0, and 0.25, respectively. The two tube segments are thus of equal length, bending stiffnesses of the two joints are identical, and bending restoring forces are much larger than gravity.

Figure 1 shows the results for $\beta = 2.0$ in the α-σ parameter plane, for two different values of η, in the form of a stability diagram. Numerical calculations show that for this value of β, $a_1 < 0.0$ and $b_1 > 0.0$. Thus, the Hopf bifurcating periodic solution is stable and supercritical. The three curves C_1, C_2, and C_3 correspond to the three boundaries given by equalities (26), (27), and (28), respectively. For $\eta = -0.25$, the origin is stable below the curve C_1, that is, in the regions *I* and *III*. In the region above C_1 the origin is unstable and the only nonzero periodic solution is stable. There are two nonzero periodic solutions in region *III* between the curves C_1 and C_2. As already mentioned, the origin is also stable in this region. Thus, there are two stable solutions in region *III* and only initial conditions and the domains of attraction of these solutions can determine the behavior that will be observed in an experiment for these values of the parameters.

The results for $\eta = 0.25$, that is, for flow rate beyond its critical value, are much more interesting. The trivial solution is unstable for all values of the detuning α and the parametric excitation magnitude σ. In region *I*, there is one periodic solution which is stable. In region *II*, there are two periodic solutions and the upper one is stable. As we move across the curve C_3 the unique nonzero periodic solution in region *III* and the upper solution in region *IV* become unstable with complex conjugate Floquet exponents crossing the imaginary axis and then remain unstable everywhere in the regions *III* and *IV*. Thus, only in regions *I* and *II* are there periodic solutions and one of them is stable. Everywhere else, either there are no periodic solutions or, if they exist, they are unstable. We discussed this possibility in the preceding section where we indicated that the system might then perform amplitude-modulated motions.

We now present the amplitudes of periodic solutions and their stability as a function of the flow rate η and the detuning parameter α for two different values of β. The values of β and the corresponding ρ_{cr}, a_1, and b_1 for the two cases are:

(*a*) $\beta = 2.0$, $\rho_{cr} = 1.69378$, $a_1 = -0.06851$, $b_1 = 0.05581$,

(*b*) $\beta = 0.05$, $\rho_{cr} = 7.48640$, $a_1 = \quad 0.06959$, $b_1 = 1.02717$.

In the first case, whose stability diagram has already been discussed, $a_1 < 0$, while for the second $a_1 > 0$. As we will see shortly, the response curves in the two cases have quite different features. In all of these results we have set σ, the amplitude of flow fluctuation, to a physically reasonable fraction (5 percent) of the corresponding ρ_{cr}.

The response curves for case (*a*) are shown in Figs. 2 and 3. Figure 2(*i*) shows the response for $\sigma = 0$, the Hopf bifurcating solution. This response is supercritical and stable because $a_1 < 0$. The zero solution is stable for $\eta < 0$ and unstable for $\eta > 0$. At $\eta = 0$ it loses stability due to a pair of complex Floquet exponents crossing the imaginary axis. The resulting unstable solution is denoted by long-short dash lines. The loss of stability due to a real Floquet exponent going through the origin is indicated by short-short dash lines. Solid lines represent stable solutions. This notation is followed for all the results presented.

Plots (*ii*)–(*vi*) in Fig. 2 show the response for various values of detuning. These values of α were selected on the basis of a stability diagram in the η-α plane. For large negative α, $\alpha = -0.31$, there is only one nonzero solution and it is stable. Beyond $\eta = 0.0$ the origin is unstable and there is no nonzero periodic solution. As α is increased, although the nontrivial response remains single-valued, some portion for $\eta > 0$ becomes unstable. Further increase in α gives rise to a multiple-valued region ($\alpha = -0.1$) and for larger values of α, the unstable portion of the upper branch stabilizes ($\alpha = 0.15$). The nonzero periodic solutions "pinch-off" the trivial solution for large enough detuning α and, as shown for $\alpha = 0.4$, the resulting solutions are isolated. For negative η the origin is stable and it is unstable for $\eta > 0$. As the flow rate in the system is increased and we cross the critical value $\eta = 0.0$, the vertical equilibrium position becomes unstable and there is no 2π-periodic solution of the system. For flow rates slightly greater than the critical value, there is a stable 2π-periodic solution of large amplitude, but the manner in which transient solutions of the system approach this stable solution cannot be predicted by the present analysis.

Response curves for this same case are presented in Fig. 3, now as a function of the detuning α. For large negative η, there is a single nonzero stable solution in the range of α for which the origin is unstable. Plot (*ii*) shows the response for flow slightly below the critical value. This exhibits the usual jump phenomenon and hysteresis. For flows above the critical value (plots (*iii*)–(*v*)), the origin is unstable and it is possible to have an unstable upper branch as well as isolated solutions.

Figure 4 shows the response curves for $\beta = 0.05$. The limit cycle being perturbed by the parametric excitation is unstable in the present case. Plot (*ii*) shows that for large negative detuning, the unstable limit cycle is suppressed. The origin, however, now becomes unstable for flow rates below the critical value and there may exist one or two nontrivial solutions depending on the detuning and the flow rate. For some small negative detuning, solutions in the upper branch become unstable. An interesting situation is shown for $\alpha = 0.0$. As the flow rate is slowly increased, the trivial solution becomes unstable at $\eta \simeq -0.6$ and the system jumps to a stable periodic solution. On further increase in flow rate, this solution itself becomes unstable and there is no other stable 2π-periodic solution. We then expect the system response to be amplitude-modulated, but this cannot be predicted by the present analysis. Its indication is, however, given by the fact that the loss in stability is due to a complex pair of Floquet exponents crossing the imaginary axis. For large enough detuning, the nonzero solutions "pinch-off' and both branches ultimately become unstable.

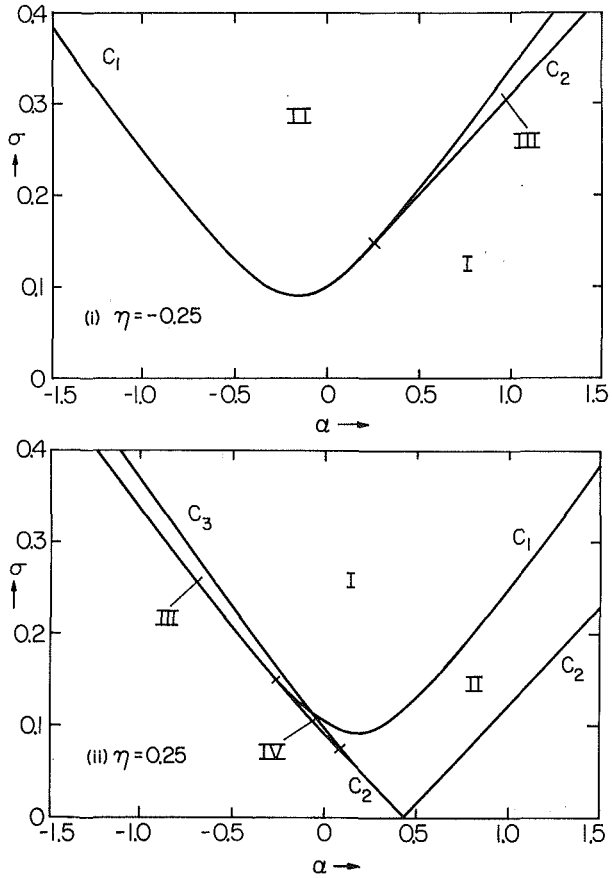

Fig. 1 Stability diagrams for zero and nonzero periodic solutions for $\beta = 2.0$. (*i*) $\eta = -0.25$, (*ii*) $\eta = 0.25$.

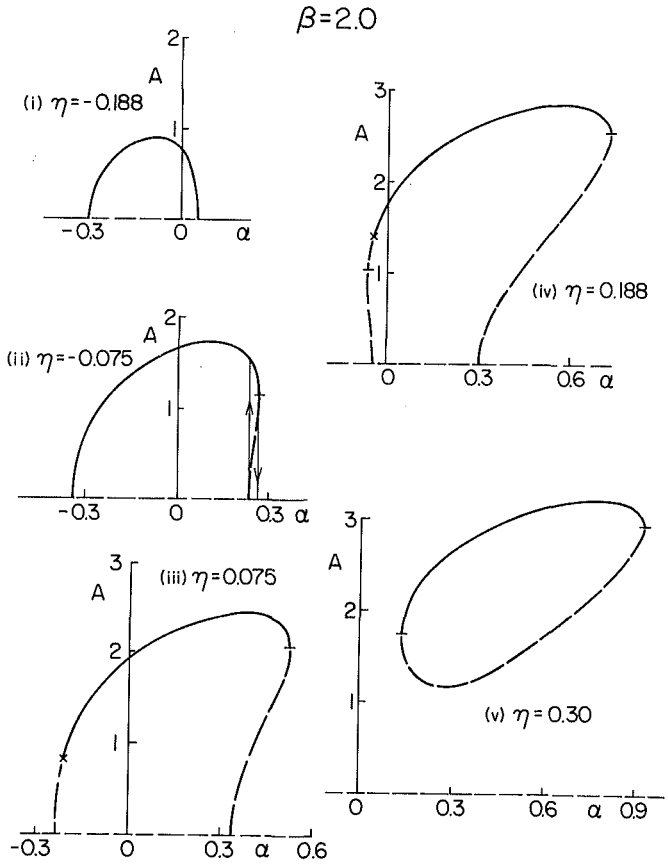

Fig. 3 Response for $\beta = 2.0$ as a function of α, for various values of flow rate η

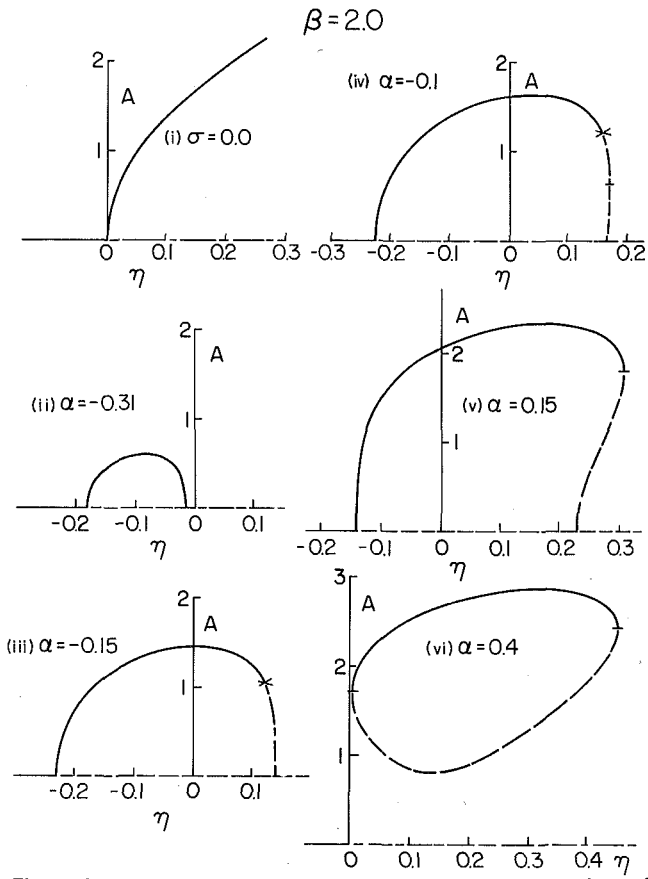

Fig. 2 Response for $\beta = 2.0$ as a function of η, for various values of detuning α

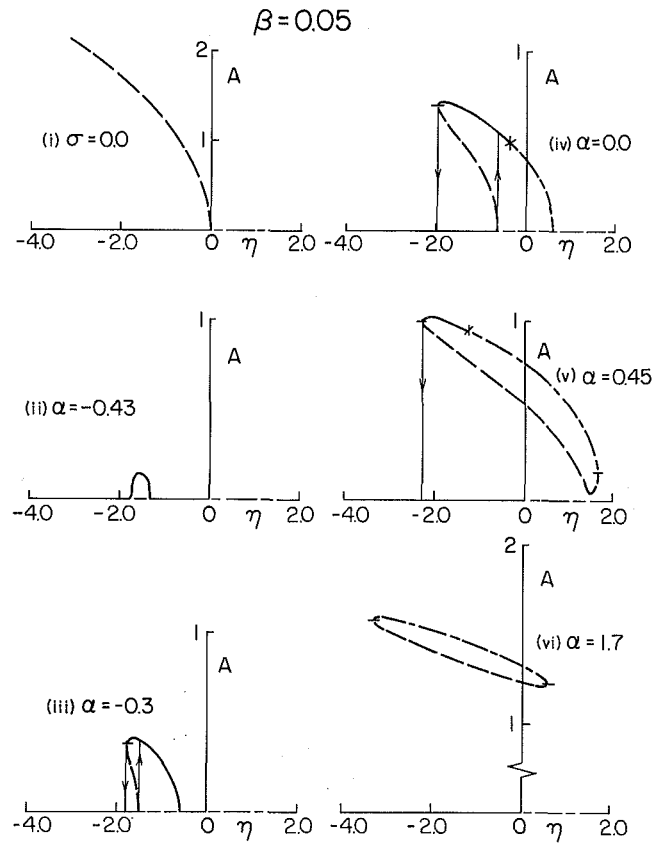

Fig. 4 Response for $\beta = 0.05$ as a function of η, for various values of detuning α

Finally, we make a few interesting observations. In the present case, for $\eta > 0$, there is no stable nonzero 2π-periodic solution irrespective of the value of detuning. Note furthermore that, although, in both the cases for which results have been presented here, $b_1 > 0$, their response curves are bent in opposite directions.

Acknowledgment

We would like to thank the referees of the paper for constructive suggestions.

References

1 Benjamin, T. B., "Dynamics of a System of Articulated Pipes Conveying Fluid. I. Theory," *Proc. Roy. Soc. London*, Series *A*, Vol. 261, 1961, pp. 457–486.

2 Benjamin, T. B., "Dynamics of a System of Articulated Pipes Conveying Fluid. II. Experiments," *Proc. Roy. Soc. London*, Series *A*, Vol. 261, 1961, pp. 487–499.

3 Gregory, R. W., and Paidoussis, M. P., "Unstable Oscillation of Tubular Cantilevers Conveying Fluid. I. Theory," *Proc. Roy. Soc. London*, Series *A*, Vol. 293, 1966, pp. 512–527.

4 Gregory, R. W., and Paidoussis, M. P., "Unstable Oscillation of Tubular Cantilevers Conveying Fluid. II. Experiments," *Proc. Roy. Soc. London*, Series *A*, Vol. 293, 1966, pp. 528–542.

5 Paidoussis, M. P., and Issid, T. N., "Dynamic Stability of Pipes Conveying Fluid," *J. Sound and Vibration*, Vol. 33, 1974, pp. 267–294.

6 Holmes, P. J., "Bifurcations to Divergence and Flutter in Flow Induced Oscillations: a Finite Dimensional Analysis," *J. Sound and Vibration*, Vol. 53, 1977, pp. 471–503.

7 Rousselt, J., and Herrmann, G., "Flutter of Articulated Pipes at Finite Amplitude," ASME JOURNAL OF APPLIED MECHANICS, Vol. 44, 1977, pp. 154–158.

8 Bajaj, A. K., Sethna, P. R., and Lundgren, T. S., "Hopf Bifurcation Phenomena in Tubes Carrying a Fluid," *SIAM J. Appl. Math.*, Vol. 39, 1980, pp. 213–230.

9 Bajaj, A. K., and Sethna, P. R., "Bifurcation in Three-Dimensional Motions of Articulated Tubes, Part 1: Linear Systems and Symmetry," ASME JOURNAL OF APPLIED MECHANICS, Vol. 49, 1982, pp. 606–611.

10 Bajaj, A. K., and Sethna, P. R., "Bifurcations in Three-Dimensional Motions of Articulated Tubes, Part 2: Nonlinear Analysis," ASME JOURNAL OF APPLIED MECHANICS, Vol. 49, 1982, pp. 612–618.

11 Bohn, M. P., and Herrmann, G., "The Dynamic Behavior of Articulated Pipes Conveying Fluid With Periodic Flow Rate," ASME JOURNAL OF APPLIED MECHANICS, Vol. 41, 1974, pp. 55–62.

12 Ginsberg, J. H., "The Dynamic Stability of a Pipe Conveying a Pulsatile Flow," *Int. J. Eng. Sci.*, Vol. 11, 1973, pp. 1013–1024.

13 Paidoussis, M. P., and Sundararajan, C., "Parametric and Combination Resonances of a Pipe Conveying Pulsatile Fluid," ASME JOURNAL OF APPLIED MECHANICS, Vol. 42, 1975, pp. 780–784.

14 Rosenblat, S., and Cohen, D. S., "Periodically Perturbed Bifurcation. II. Hopf Bifurcation," *Stud. Appl. Math.*, Vol. 64, 1981, pp. 143–175.

15 Kath, W. L., "Resonance in Periodically Perturbed Hopf Bifurcation," *Stud. Appl. Math.*, Vol. 65, 1981, pp. 95–112.

16 Smith, H., "Nonresonant Periodic Perturbation of the Hopf Bifurcation," *Appl. Analysis*, Vol. 12, 1981, pp. 173–195.

17 Bajaj, A. K., "Parametric Perturbations of the Hopf Bifurcation," submitted to *SIAM J. Appl. Math.*

18 Hale, J. K., *Ordinary Differential Equations*, Wiley-Interscience, New York, 1969.

19 Nayfeh, A. H., and Mook, D. T., *Nonlinear Oscillations*, Wiley-Interscience, New York, 1979.

20 Chow, S. N., and Hale, J. K., *Methods of Bifurcation Theory*, Springer-Verlag, New York, 1982.

21 Paidoussis, M. P., and Deksnis, E. B., "Articulated Models of Cantilevers Conveying Fluid: The Study of a Paradox," *J. Mech. Eng. Sci.*, Vol. 12, 1970, pp. 288–300.

22 Tezak, E. G., Nayfeh, A. H., and Mook, D. T., "Parametrically Excited Non-Linear Multidegree-of-Freedom Systems With Repeated Natural Frequencies," *J. Sound and Vibration*, Vol. 85, 1982, pp. 459–472.

Z.-M. Ge[1]
Special Expert,
National Science Council Executive Yuan,
National Chiao Tung University,
Hsinchu, Taiwan,
Republic of China

Y.-J. Wu
Senior Student,
Engineering Mechanics Department,
Shanghai Jiaotong University,
Shanghai, China

Another Theorem for Determining the Definiteness of Sign of Functions and Its Applications to the Stability of Permanent Rotations of a Rigid Body

A new theorem for determining the definiteness of sign of functions is presented. As the examples illustrate, it is applied to the stability of permanent rotations of a rigid body about a fixed point in five cases.

1 Introduction

When Lyapunov's direct method is used, it is necessary to determine the definiteness of a function. When the function can be written as

$$U(x_1,x_2,\ldots,x_n)=V_m(x_1,x_2,\ldots,x_n)+V^*(x_1,x_2,\ldots,x_n)$$

where V_m is a definite form of mth degree and V^* is the sum of terms of degree higher than m, we know that U is also a definite function by a well-known theorem. (1) On condition that V_m is a semidefinite form, we have given three theorems for determining the definiteness and changeability of sign of U. (2) An improved theorem which enlarges the range of U is given in the present paper. The interesting applications to the stability of permanent rotations of a rigid body in five cases are presented. The applications of these theorems (2) suggest a conjecture: They are effective for determining stability of motion in many cases under "equality" conditions which are usually neglected.

2 A New Theorem for Determining the Definiteness of Sign of Functions

Theorem: Let $V_m(x_1, x_2, \ldots, x_n)$ be an even semidefinite form of mth degree. $V_{m+1}(x_1, x_2, \ldots, x_n)$, $V_{m+2}(x_1, x_2, \ldots, x_n), \ldots, V_{m+r}(x_1, x_2, \ldots, x_n)$ are forms of $m+1$, $m+2, \ldots, m+r$th degree, respectively. When V_m is equal to zero, $V_{m+1}=V_{m+2}=\ldots=V_{m+r-1}=0$, V_{m+r} has the same sign as the constant sign of V_m and turns to zero only at the origin, then the function

$$U(x_1,x_2,\ldots,x_n)=V_m(x_1,x_2,\ldots,x_n)+\sum_{\ell=1}^{r}V_{m+\ell}(x_1,x_2,\ldots,x_n)+V^* \tag{2.1}$$

is a definite function with the same sign as that of V_m, where V^* is the sum of terms of degree higher than $m+r$. Both m and r are even.

Proof: For the sake of avoiding ambiguity, let V_m be positive semidefinite and it equals zero when $x_1, x_2, \ldots, x_n$ satisfy the following equations:

$$f_i(x_1,x_2,\ldots,x_n)=0 (i=1,2,\ldots,k<n) \tag{2.2}$$

Then V_m is a homogeneous form, so we have

$$V_m(\lambda x_1',\lambda x_2',\ldots,\lambda x_n')=\lambda^m V_m(x_1',x_2',\ldots,x_n')=0 \tag{2.3}$$

where λ is an arbitrary constant. That means V_m always remains zero on the straight line passing through the point $(x_1', x_2', \ldots, x_n')$ and the origin of the coordinate system. Thus, (2.2) represents conical surfaces in general – planes or lines in particular – in the Euclidean space of n dimensions (the so-called hyperconical surfaces) with the vertexes all at the origin. On these surfaces,

$$V_m=V_{m+1}=\ldots=V_{m+r-1}=0, \text{ and } V_{m+r}>0.$$

Let

$$\left.\begin{aligned} x_s&=\rho\alpha_s\ (s=1,2,\ldots,n)\\ \rho&=\sqrt{x_1^2+x_2^2+\ldots+x_n^2}\\ \alpha_1^2+\alpha_2^2+\ldots+\alpha_n^2&=1\end{aligned}\right\} \tag{2.4}$$

[1]Formerly, Associate Professor, Engineering Mechanics Department, Shanghai Jiaotong University, Shanghai, China.

Contributed by the Applied Mechanics Division for presentation at the 1984 PVP Conference and Exhibition, Joint with Applied Mechanics Division and Materials Division, San Antonio, Texas, June 17-21, 1984 of THE AMERICAN SOCIETY OF MECHANICAL ENGINEERS.

Discussion on this paper should be addressed to the Editorial Department, ASME, United Engineering Center, 345 East 47th Street, New York, N.Y., 10017, and will be accepted until two months after final publication of the paper itself in the JOURNAL OF APPLIED MECHANICS. Manuscript received by ASME Applied Mechanics Division, August, 1982; final revision, January, 1983. Paper No. 84-APM-26.

Copies will be available until February, 1985.

Then (2.1) becomes

$$U(x_1, x_2, \ldots, x_n) = \rho^m [V_m(\alpha_1, \alpha_2, \ldots, \alpha_n) + \rho V_{m+1}(\alpha_1, \alpha_2, \ldots, \alpha_n) + \ldots + \rho^{r-1} V_{m+r-1}(\alpha_1, \alpha_2, \ldots, \alpha_n)] + \rho^{m+r} [V_{m+r}(\alpha_1, \alpha_2, \ldots, \alpha_n) + \frac{1}{\rho^{m+r}} V^*(x_1, x_2, \ldots, x_n)] \quad (2.5)$$

when ρ is sufficiently small, since $V^*(x_1, x_2, \ldots, x_n)$ is the infinitesimal of order higher than $m+r$, the sign of the sum in the second brackets is determined by that of $V_{m+r}(x_1, x_2, \ldots, x_n)$ on condition that $V_{m+r}(\alpha_1, \alpha_2, \ldots, \alpha_n) \neq 0$. Similarly, the sign of U is determined by that of V_m when $V_m \neq 0$.

The intersection of the spherical surface S

$$x_1^2 + x_2^2 = \ldots + x_n^2 = \rho^2 \quad (2.6)$$

with the hyperconical surfaces (2.2) forms a closed region R where $V_m = V_{m+1} = \ldots = V_{m+r-1} = 0$, $V_{m+r} > 0$. Since the sign of $V_{m+r} + V^*$ is determined by that of V_{m+r}, now we have

$$U = V_m + V_{m+1} + \ldots + V_{m+r-1} + V_{m+r} + V^* = V_{m+r} + V^* > 0 \quad (2.7)$$

Furthermore, on the set S-R, by the given condition, $V_m > 0$, the sign of U is determined by that of V_m, i.e., $U > 0$. Therefore on the whole spherical surface S we have $U > 0$.

As the radius of the spherical surface approaches zero, the foregoing result remains valid. Thus on the whole sphere of radius ρ, $U > 0$, except that only at the origin of the sphere $U = 0$, i.e., U is a positive-definite function.

When V_m is a negative semi-definite function, the proof is similar.

Example:

$$V_m(x_1, x_2, x_3) = V_2 = (x_1 + x_2)^2 + x_3^2$$
$$V_{m+1}(x_1, x_2, x_3) = V_3 = (x_1 + x_2)^3 + x_3^3$$
$$V_{m+r}(x_1, x_2, x_3) = V_4 = -x_1 x_2^3 + x_1^4 + x_3^4, \quad r = 2$$
$$f_1(x_1, x_2, x_3) = x_1 + x_2 = 0$$
$$f_2(x_1, x_2, x_3) = x_3 = 0$$

Putting $x_1 = -x_2$, $x_3 = 0$ in V_3 and V_4, we have

$$V_3 = 0$$
$$V_4 = 2x_2^4$$

The conditions demanded by the theorem are all satisfied, thus

$$U(x_1, x_2, x_3) = V_2 + V_3 + V_4 + V^*$$

is positive-definite.

3 The Stability of Permanent Rotations of a Heavy Rigid Body About a Fixed Point

Staude [3] showed that the motion under gravity of an asymmetric rigid body, with one point 0 fixed, can be a uniform rotation about each of a system of ∞^1 axes through 0, when such an axis is put in a vertical position. In such a case the angular velocity vector remains constant in direction and magnitude with respect to the space and the body. The axes of rotation form a cone of the second order fixed with the body.

The stability of the Staude rotations has been investigated by Hadamard [4], Grammel [5], Stoewa [6], Bottema [7], and Rumiantsev [8].

The most complete results are due to Rumiantsev. In what follows we will introduce his method which is based on the construction of a Lyapunov function and will improve his results in four cases by means of the theorem in Section 2. In the fifth case, the theorem is applied to get the necessary and sufficient stability condition of the sleeping top.

A heavy rigid body moves about a fixed point 0. The inertial coordinate system is $Ox_1y_1z_1$, with Oz_1 axis vertical upward. Ox, Oy, Oz are the principal axes of inertia of the rigid body about 0. The corresponding moments of inertia are A, B, C, x_0, y_0, z_0 are the coordinates of the center of mass of the rigid body in the moving coordinate system. For simplicity, we take the weight of the rigid body $mg = 1$.

The permanent rotation of the rigid body about a vertical axis with constant angular velocity ω gives the following condition from the equations of motion [9]:

$$\omega^2(\mathbf{k}_1 \times \mathbf{I}_1) + \mathbf{r}_0 \times \mathbf{k}_1 = 0 \quad (3.1)$$

$\mathbf{k}_1$ is the upward vertical unit vector fixed in the inertial space, $\mathbf{I}_1 = \mathbf{I}_1(A\alpha, B\beta, C\gamma)$ where α, β, γ are the constant direction cosines of $\mathbf{k}_1$ in $Oxyz$ and $\mathbf{r}_0$ is the position vector of the center of mass in $Oxyz$. It is noted that the direction of the rotating axis is fixed not only in the inertial space but also in the moving coordinate system $Oxyz$.

The undisturbed motion is

$$\left.\begin{aligned} &p = p_0 = \alpha\omega, \quad q = q_0 = \beta\omega, \quad r = r_0 = \gamma\omega \\ &\gamma_1 = \alpha, \quad \gamma_2 = \beta, \quad \gamma_3 = \gamma \end{aligned}\right\} \quad (3.2)$$

where p, q, r are the projections of the angular velocity of the rigid body on Ox, Oy, Oz, respectively, and γ_1, γ_2, γ_3 are the direction cosines of $\mathbf{k}_1$ in $Oxyz$.

In general, the center of mass is not on the rotating axis. We will study the stability of this motion.

The disturbed motion is

$$\left.\begin{aligned} &p = p_0 + \xi_1, \quad q = q_0 + \xi_2, \quad r = r_0 + \xi_3 \\ &\gamma_1 = \alpha + \eta_1 \quad \gamma_2 = \beta + \eta_2 \quad \gamma_3 = \gamma + \eta_3 \end{aligned}\right\} \quad (3.3)$$

where ξ_1, ξ_2, ξ_3, η_1, η_2, η_3 are disturbances.

We have the equations for the disturbances:

$$\left.\begin{aligned} &A\left(\frac{d\xi_1}{dt}\right) + (C-B)(r_0\xi_2 + q_0\xi_3 + \xi_2\xi_3) = z_0\eta_2 - y_0\eta_3 \\ &B\left(\frac{d\xi_2}{dt}\right) + (A-C)(p_0\xi_3 + r_0\xi_1 + \xi_3\xi_1) = x_0\eta_3 - z_0\eta_1 \\ &C\left(\frac{d\xi_3}{dt}\right) + (B-A)(q_0\xi_1 + p_0\xi_2 + \xi_1\xi_2) = y_0\eta_1 - x_0\eta_2 \end{aligned}\right\} \quad (3.4)$$

$$\left.\begin{aligned} &\frac{d\eta_1}{dt} = r_0\eta_2 + \gamma\xi_3 + \xi_1\eta_2 - (q_0\eta_3 + \gamma\xi_2 + \xi_2\eta_3) \\ &\frac{d\eta_2}{dt} = p_0\eta_3 + \gamma\xi_1 + \xi_1\eta_3 - (r_0\eta_1 + \alpha\xi_3 + \xi_3\eta_1) \\ &\frac{d\eta_3}{dt} = q_0\eta_1 + \alpha\xi_2 + \xi_2\eta_1 - (p_0\eta_2 + \beta\xi_1 + \xi_1\eta_2) \end{aligned}\right\} \quad (3.5)$$

The first integrals become

$$\left.\begin{aligned} V_a &= A(\xi_1^2 + 2p_0\xi_1) + B(\xi_2^2 + 2q_0\xi_2) + C(\xi_3^2 \\ &\quad + 2r_0\xi_3) + 2(x_0\eta_1 + y_0\eta_2 + z_0\eta_3) = \text{const.} \\ V_b &= A(p_0\eta_1 + \alpha\xi_1 + \xi_1\eta_1) + B(q_0\eta_2 + \beta\xi_2 + \xi_2\eta_2) \\ &\quad + C(r_0\eta_3 + \gamma\xi_3 + \xi_3\eta_3) = \text{const.} \\ V_c &= \eta_1^2 + \eta_2^2 + \eta_3^2 + 2(\alpha\eta_1 + \beta\eta_2 + \gamma\eta_3) = 0 \end{aligned}\right\} \quad (3.6)$$

The Lyapunov function constructed by Rumiantsev is

$$\begin{aligned} V &= V_a - 2\omega V_b + \lambda V_c + \tfrac{1}{4}\mu V_c^2 \\ &= A\xi_1^2 + B\xi_2^2 + C\xi_3^2 - 2\omega(A\xi_1\eta_1 + B\xi_2\eta_2 + C\xi_3\eta_3) \\ &\quad + 2\mu(\alpha\beta\eta_1\eta_2 + \alpha\gamma\eta_1\eta_3 + \beta\gamma\eta_2\eta_3) + (\lambda + \mu\alpha^2)\eta_1^2 \\ &\quad + (\lambda + \mu\beta^2)\eta_2^2 + (\lambda + \mu\gamma^2)\eta_3^2 + \tfrac{1}{4}\mu f(\eta_1, \eta_2, \eta_3) \end{aligned} \quad (3.7)$$

where

$$\begin{aligned} f(\eta_1, \eta_2, \eta_3) &= (\eta_1^2 + \eta_2^2 + \eta_3^2)[\eta_1^2 + \eta_2^2 + \eta_3^2 \\ &\quad + 4(\alpha\eta_1 + \beta\eta_2 + \gamma\eta_3)] \end{aligned}$$

$$\lambda = A\omega^2 - \frac{x_0}{\alpha} = B\omega^2 - \frac{y_0}{\beta}$$

$$\lambda = A\omega^2 - \frac{x_0}{\alpha} = B\omega^2 - \frac{y_0}{\beta} = C\omega^2 - \frac{z_0}{\gamma} \quad (3.8)$$

and μ is an arbitrary constant.

According to Sylvester's criterion the necessary and sufficient conditions for $V - \frac{1}{4}\mu f$ to be positive definite are

$$\left.\begin{aligned} &\lambda - A\omega^2 + \mu\alpha^2 > 0 \\ &(\lambda - A\omega^2)(\lambda - B\omega^2) + \mu[\alpha^2(\lambda - B\omega^2) + \beta^2(\lambda - A\omega^2)] > 0 \\ &\lambda^3 - (A + B + C)\omega^2\lambda^2 + (BC + AC + AB)\omega^4\lambda - ABC\omega^6 \\ &+ \mu[\lambda^2 - A\omega^2(\beta^2 + \gamma^2)\lambda - B\omega^2(\alpha^2 + \gamma^2)\lambda - C\omega^2(\alpha^2 + \beta^2)\lambda \\ &+ (BC\alpha^2 + AC\beta^2 + AB\gamma^2)\omega^4] > 0 \end{aligned}\right\} \quad (3.9)$$

The corresponding scalar equations of (3.1) are

$$\left.\begin{aligned} (B - C)\beta\gamma\omega^2 &= y_0\gamma - z_0\beta \\ (C - A)\gamma\alpha\omega^2 &= z_0\alpha - x_0\gamma \\ (A - B)\alpha\beta\omega^2 &= x_0\beta - y_0\alpha \end{aligned}\right\} \quad (3.10)$$

In view of (3.8) and (3.10) the preceding three conditions reduce to

$$\left.\begin{aligned} &\mu\alpha^2 - \frac{x_0}{\alpha} > 0 \\ &\frac{x_0y_0}{\alpha\beta} - \mu\left(\frac{x_0}{\alpha}\beta^2 + \frac{y_0}{\beta}\alpha^2\right) > 0 \\ &\mu\left(\frac{y_0z_0}{\beta\gamma}\alpha^2 + \frac{x_0z_0}{\alpha\gamma}\beta^2 + \frac{x_0y_0}{\alpha\beta}\gamma^2\right) - \frac{x_0y_0z_0}{\alpha\beta} > 0 \end{aligned}\right\} \quad (3.11)$$

Let

$$\alpha > 0, \beta < 0, \gamma < 0, x_0 > 0, y_0 > 0, z_0 > 0 \quad (3.12)$$

It is obvious that the first condition of (3.11) can be satisfied by a proper choice of $\mu > 0$. The second condition can be satisfied for a proper positive μ such that

$$\frac{x_0}{\alpha}\beta^2 + \frac{y_0}{\beta}\alpha^2 < 0 \quad (3.13)$$

The third condition is also satisfied by a proper choice of a positive μ provided that

$$\left(\frac{x_0}{\alpha}\beta^2 + \frac{y_0}{\beta}\alpha^2\right)\frac{z_0}{\gamma} + \frac{x_0y_0}{\alpha\beta}\gamma^2 > 0 \quad (3.14)$$

It is obvious that (3.13) is a fortiori satisfied provided that (3.14) holds. Therefore, if the largest of all the μ-values specified in the foregoing is selected, then conditions (3.11) will be satisfied simultaneously under (3.14).

1. Now we discuss the stability under a weaker condition:

$$\left(\frac{x_0}{\alpha}\beta^2 + \frac{y_0}{\beta}\alpha^2\right)\frac{z_0}{\gamma} + \frac{x_0y_0}{\alpha\beta}\gamma^2 = 0 \quad (3.15)$$

with $\alpha > 0$, $\beta < 0$, $\gamma < 0$ unchanged.

(*a*) When

$$x_0 = 0, y_0 = 0 \quad (3.16)$$

(3.11) becomes

$$\left.\begin{aligned} &\mu\alpha^2 - \frac{x_0}{\alpha} > 0 \\ &\frac{x_0y_0}{\alpha\beta} - \mu\left(\frac{x_0}{\alpha}\beta^2 + \frac{y_0}{\beta}\alpha^2\right) = 0 \\ &\mu\left(\frac{y_0z_0}{\beta\gamma}\alpha^2 + \frac{x_0z_0}{\alpha\gamma}\beta^2 + \frac{x_0y_0}{\alpha\beta}\gamma^2\right) - \frac{x_0y_0z_0}{\alpha\beta} = 0 \end{aligned}\right\} \quad (3.17)$$

The conditions of (3.17) are weaker than that of (3.11). Equation (3.8) becomes

$$\lambda = A\omega^2 = B\omega^2 = C\omega^2 - \frac{z_0}{\gamma} \quad (3.18)$$

Putting (3.18) in (3.7), we have

$$V = V_2 + V_3 + V_4 \quad (3.19)$$

where

$$\begin{aligned} V_2 &= A(\xi_1 - \omega\eta_1)^2 + B(\xi_2 - \omega\eta_2)^2 + \mu(\alpha\eta_1 + \beta\eta_2 \\ &\quad + \gamma\eta_3)^2 + C\xi_3^2 - 2C\omega\xi_3\eta_3 + \left(C\omega^2 - \frac{z_0}{\gamma}\right)\eta_3^2 \end{aligned} \quad (3.20)$$

is positive semidefinite and becomes zero when

$$\xi_1 = \omega\eta_1 \neq 0, \quad \xi_2 = \omega\eta_2 \neq 0, \quad \xi_3 = \eta_3 = 0, \quad \alpha\eta_1 + \beta\eta_2 = 0 \quad (3.21)$$

$$V_3 = \mu(\eta_1^2 + \eta_2^2 + \eta_3^2)(\alpha\eta_1 + \beta\eta_2 + \gamma\eta_3) \quad (3.22)$$

becomes zero under (3.21) and

$$V_4 = \tfrac{1}{4}\mu(\eta_1^2 + \eta_2^2 + \eta_3^2)^2 \quad (3.23)$$

becomes

$$V_4 = \tfrac{1}{4}\mu\left[1 + \left(\frac{\alpha}{\beta}\right)^2\right]\eta_1^4 \quad (3.24)$$

under (3.21). V_4 is always positive and becomes zero only at the origin.

All the conditions of the theorem are satisfied, thus V is a positive-definite function. Therefore the motion is stable.

(*b*) When

$$x_0 = z_0 = 0 \quad (3.25)$$

(3.11) becomes

$$\left.\begin{aligned} &\mu\alpha^2 - \frac{x_0}{\alpha} > 0 \\ &\frac{x_0y_0}{\alpha\beta} - \mu\left(\frac{x_0}{\alpha}\beta^2 + \frac{y_0}{\beta}\alpha^2\right) > 0 \\ &\mu\left(\frac{y_0z_0}{\beta\gamma}\alpha^2 + \frac{x_0z_0}{\alpha\gamma}\beta^2 + \frac{x_0y_0}{\alpha\beta}\gamma^2\right) - \frac{x_0y_0z_0}{\alpha\beta} = 0 \end{aligned}\right\} \quad (3.26)$$

(3.8) becomes

$$\lambda = A\omega^2 = B\omega^2 - \frac{y_0}{\beta} = C\omega^2 \tag{3.27}$$

Putting (3.27) in (3.7), we have

$$V = V_2 + V_3 + V_4 \tag{3.28}$$

where

$$V_2 = A(\xi_1 - \omega\eta_1)^2 + C(\xi_3 - \omega\eta_3)^2 + B\xi_2^2 - 2\omega B\xi_2\eta_2 + \left(B\omega^2 - \frac{y_0}{\beta}\right)\eta_2^2 + \mu(\alpha\eta_1 + \beta\eta_2 + \gamma\eta_3)^2 \tag{3.29}$$

is positive semidefinite and becomes zero when

$$\xi_1 = \omega\eta_1 \neq 0,\ \xi_3 = \omega\eta_3 \neq 0,\ \xi_2 = \eta_2 = 0,\ \alpha\eta_1 + \gamma\eta_3 = 0 \tag{3.30}$$

$$V_3 = \mu(\eta_1^2 + \eta_2^2 + \eta_3^2)(\alpha\eta_1 + \beta\eta_2 + \gamma\eta_3) \tag{3.31}$$

becomes zero under (3.30) and

$$V_4 = \tfrac{1}{4}\mu(\eta_1^2 + \eta_2^2 + \eta_3^2)^2 \tag{3.32}$$

becomes

$$V_4 = \tfrac{1}{4}\mu\left[1 + \left(\frac{\alpha}{\gamma}\right)^2\right]\eta_1^4 \tag{3.33}$$

under (3.30). V_4 is always positive and becomes zero only at the origin. All the conditions of the theorem are satisfied, thus V is a positive-definite function. Therefore the motion is stable.

(*c*) When

$$y_0 = z_0 = 0 \tag{3.34}$$

(3.11) becomes

$$\left.\begin{aligned} &\mu\alpha^2 - \frac{x_0}{\alpha} > 0 \\ &\frac{x_0 y_0}{\alpha\beta} - \mu\left(\frac{x_0}{\alpha}\beta^2 + \frac{y_0}{\beta}\alpha^2\right) > 0 \\ &\mu\left(\frac{y_0 z_0}{\beta\gamma}\alpha^2 + \frac{x_0 z_0}{\alpha\gamma}\beta^2 + \frac{x_0 z_0}{\alpha\beta}\gamma^2\right) - \frac{x_0 y_0 z_0}{\alpha\beta} = 0 \end{aligned}\right\} \tag{3.35}$$

(3.8) becomes

$$\lambda = A\omega^2 - \frac{x_0}{\alpha} = B\omega^2 = C\omega^2 \tag{3.36}$$

Putting (3.36) in (3.7), we have

$$V = V_2 + V_3 + V_4 \tag{3.37}$$

where

$$V_2 = A\xi_1^2 - 2\omega A\xi_1\eta_1 + \left(A\omega^2 - \frac{x_0}{\alpha}\right)\eta_1^2 + B(\xi_2 - \omega\eta_2)^2 + C(\xi_3 - \omega\eta_3)^2 + \mu(\alpha\eta_1 + \beta\eta_2 + \gamma\eta_3)^2 \tag{3.38}$$

is positive semidefinite when $x_0 \leq 0$ and becomes zero when

$$\xi_1 = \eta_1 = 0,\quad \xi_2 = \omega\eta_2 \neq 0,\ \xi_3 = \omega\eta_3 \neq 0,\ \beta\eta_2 + \gamma\eta_3 = 0 \tag{3.39}$$

$$V_3 = \mu(\eta_1^2 + \eta_2^2 + \eta_3^2)(\alpha\eta_1 + \beta\eta_2 + \gamma\eta_3) \tag{3.40}$$

becomes zero under (3.39) and

$$V_4 = \tfrac{1}{4}\mu(\eta_1^2 + \eta_2^2 + \eta_3^2)^2 \tag{3.41}$$

becomes

$$V_4 = \tfrac{1}{4}\mu\left[1 + \left(\frac{\beta}{\gamma}\right)^2\right]\eta_2^4 \tag{3.42}$$

under (3.39). V_4 is always positive and becomes zero only at the origin. All the conditions of the theorem are satisfied, thus V is a positive-definite function. Therefore the motion is stable when $x_0 \leq 0$.

2. (*a*) Let us investigate the stability of rotation about the principal inertia axis Ox which passes through the center of mass of the body and which can be a permanent vertical axis of rotation for an angular velocity ω. Let $x_0 > 0$, $y_0 = z_0 = 0$.

The undisturbed motion is

$$\left.\begin{aligned} &p = p_0 = \omega,\ q = q_0 = 0,\ r = r_0 = 0 \\ &\gamma_1 = \alpha = 1,\ \gamma_2 = \beta = 0,\ \gamma_3 = \gamma = 0 \end{aligned}\right\} \tag{3.43}$$

Now (3.8) becomes

$$\lambda = A\omega^2 - x_0 \tag{3.44}$$

(3.11) becomes

$$\left.\begin{aligned} &\mu - x_0 > 0 \\ &(A-B)\omega^2 - x_0 > 0 \\ &(A-C)\omega^2 - x_0 > 0 \end{aligned}\right\} \tag{3.45}$$

Let $A > B > C$, we have the condition for stability:

$$(A-B)\omega^2 > x_0 \tag{3.46}$$

Now we consider the stability under the weaker condition:

$$(A-B)\omega^2 = x_0$$

Under this condition (3.7) becomes

$$V = V_2 + V_3 + V_4 \tag{3.47}$$

where

$$V_2 = A(\xi_1 - \omega\eta_1)^2 + B(\xi_2 - \omega\eta_2)^2 + C(\xi_3 - \omega\eta_3)^2 + (\mu - x_0)\eta_1^2 + [(A-C)\omega^2 - x_0]\eta_3^2 \tag{3.48}$$

is positive semidefinite by the first and third conditions of (3.45) and becomes zero when

$$\xi_1 = \eta_1 = \xi_3 = \eta_3 = 0,\ \xi_3 = \omega\eta_2 \neq 0$$

$$V_3 = \mu(\eta_1^2 + \eta_2^2 + \eta_3^2)\eta_1 \tag{3.49}$$

becomes zero under (3.49) and

$$V_4 = \tfrac{1}{4}\mu(\eta_1^2 + \eta_2^2 + \eta_3^2)^2 \tag{3.50}$$

becomes

$$V_4 = \tfrac{1}{4}\mu\eta_2^4 \tag{3.51}$$

under (3.49). V_4 is always positive and becomes zero only at the origin. All the conditions of the theorem are satisfied, thus V is a positive-definite function, therefore the motion is stable when $(A-B)\omega^2 = x_0$.

We have improved Rumiantsev's results in the preceding four cases by the theorem given in Section 2.

(*b*) When $B = C$, we have the case of a sleeping top. The first integrals of the equations for the disturbances are

$$\left.\begin{aligned} &V_a = A(\xi_1^2 + 2p_0\xi_1) + C(\xi_2^2 + \xi_3^2) + 2x_0\eta_1 = \text{const.} \\ &V_b = A(p_0\eta_1 + \xi_1\eta_1) + C(\xi_2\eta_2 + \xi_3\eta_3) = \text{const.} \\ &V_c = \eta_1^2 + \eta_2^2 + \eta_3^2 + 2\eta_1 = 0 \\ &V_d = \xi_1 \end{aligned}\right\} \tag{3.52}$$

The well-known Lyapunov function given by Chetaev (10) is the quadratic:

$$V = V_a + 2\lambda V_b - (x_0 + A_{p_0\lambda})V_c + \mu V_d^2 - 2(Ap_0 + A\lambda)V_d = C\xi_2^2 + 2\lambda C\xi_2\eta_2 - (x_{0+A_{p_0\lambda}})\eta_2^2 + C\xi_3^2 + 2\lambda C\xi_3\eta_3 - (x_0 + A_{p_0\lambda})\eta_3^2 + (A+\mu)\xi_1^2 + 2\lambda A\eta_1\xi_1 - (x_0 + A_{p_0\lambda})\eta_1^2 \tag{3.53}$$

where $\mu = A(A-C)/C$ and λ can be chosen as

$$\lambda = -\frac{Ap_0}{2C} \tag{3.54}$$

According to Sylvester's criterion, when

$$A^2p_0^2 > 4Cx_0 \tag{3.55}$$

V is positive-definite, and the motion is stable.

Now we consider the stability of the motion when

$$A^2p_0^2 = 4Cx_0 \tag{3.56}$$

Under this condition, V becomes a positive semidefinite function:

$$V = C\left(\xi_2 - \frac{Ap_0}{2C}\eta_2\right)^2 + C\left(\xi_3 - \frac{Ap_0}{2C}\eta_3\right)^2 + \frac{A^2}{C}\left(\xi_1 - \frac{p_0}{2}\eta_1\right)^2 \tag{3.57}$$

The new Lyapunov function given by the first author (11) is

$$V_N = V + \frac{16}{p_0^2}V_d^2 - \frac{8}{p_0}V_cV_d + V_c^2 = V_2 + V_3 + V_4 \tag{3.58}$$

where

$$V_2 = V + \frac{16}{p_0^2}\left(\xi_1 - \frac{p_0}{2}\eta_1\right)^2 \tag{3.59}$$

$$V_3 = -\frac{8}{p_0}(\eta_1^2 + \eta_2^2 + \eta_3^2)\left(\xi_1 - \frac{p_0}{2}\eta_1\right) \tag{3.60}$$

$$V_4 = (\eta_1^2 + \eta_2^2 + \eta_3^2)^2 \tag{3.61}$$

V_2 is positive semidefinite and becomes zero when

$$\xi_1 = \frac{p_0}{2}\eta_1,\ \xi_2 = \frac{Ap_0}{2C}\eta_2,\ \xi_3 = \frac{AP_0}{2C}\eta_3 \tag{3.62}$$

Under this condition, V_3 also becomes zero but V_4 is always positive and becomes zero only at the origin.

All the conditions of the theorem are satisfied, thus V_N is a positive-definite function. Therefore the motion is stable. Thus the sufficient condition for stability is improved from (3.56) to

$$A^2p_0^2 \geq 4Cx_0 \tag{3.63}$$

It is easy to prove by the theory of first approximation (1) that when $A^2p_0^2 < 4Cx_0$ the motion is unstable. Thus (3.63) is the necessary and sufficient condition for the stability of the sleeping top for all the six variables of the differential equations of motion.

References

1 Malkin, I. G., *Theory of Stability of Motion*, Nauka, Moscow, 1966.

2 Zheng-ming, Ge, "Some Theorems for Determining the Definiteness and Changeability of Sign of Functions and the Application to the Conditional Stability of the Motion of the Axis of a Sleeping Top," *Applied Mathematics and Mechanics*, English Edition, published in China, Vol. 2, No. 6, Dec., 1981.

3 Staude, O., "Über Permanente Rotationsaxen bei der Bewegung eines Schweren Körpers um einen Festen," *Punkt. J. reine u. angew. Math.* Vol. 113, 1894, pp. 318–334.

4 Hadamard, J., "Sur la Stabilité des Rotations dans le Mouvement d'un Corps Solide pesant Autour d'un Point Fixe," *Assoc. Française pour l'Avancement des Sciences*, C. R. de la 24me session. Congrès de Bordeaux, 1895, pp. 1–6.

5 Grammel, R., "Die Stabilität der Staudeschen Kreiselbewegungen," *Math. Z.*, Vol. 6, 1920, pp. 124–142.

6 Stoewa, P., "Die Stabilität der Staudeschen Kreiselbewegungen," *Jahresber. Phil. Fak. Univ. Leipzig*, 1922, II. Halbjahr, pp. 131–132.

7 Bottema, O., "The Stability of Staude's Top Motion," *Koninkl, Nederland, Akad. Wetenschap.*, Proc. 48, 1945, pp. 316–325.

8 Rumiantsev, V. V., "Stability of Permanent Rotations of a Heavy Rigid Body *(R)*, *Prikl. Mat. Meh.*, Vol. 20, 1956, pp. 51–66.

9 Leimanis, E., *The General Problem of the Motion of Coupled Rigid Bodies About a Fixed Point*, Springer-Verlag.

10 Chetaev, N. G., "On the Stability of Rotation of a Rigid Body With a Fixed Point in Lagrange's Case (*R*), *Prikl. Mat. Meh.*, Vol. 18, 1954, pp. 123–124.

11 Zheng-ming, Ge, "On the Necessary and Sufficient Condition of the Unconditional Stability of the Motion of Lagrange's Vertical Top (Chinese), *Practice and Understanding of Mathematics*, No. 1, 1979, pp. 47–50; *Journal of Shanghai Chiao-Tung* (Jiaotong) University, No. 1, July, 1979, pp. 53–58.

Journal of Applied Mechanics

Brief Notes

A Brief Note is a short paper that presents a specific solution of technical interest in mechanics but which does not necessarily contain new general methods or results. A Brief Note should not exceed 1500 words *or equivalent* (a typical one-column figure or table is equivalent to 250 words; a one line equation to 30 words). Brief Notes will be subject to the usual review procedures prior to publication. After approval such Notes will be published as soon as possible. The Notes should be submitted to the Technical Editor of the JOURNAL OF APPLIED MECHANICS. Discussions on the Brief Notes should be addressed to the Editorial Department, ASME, United Engineering Center, 345 East 47th Street, New York, N. Y. 10017, or to the Technical Editor of the JOURNAL OF APPLIED MECHANICS. Discussions on Brief Notes appearing in this issue will be accepted until two months after publication. Readers who need more time to prepare a Discussion should request an extension of the deadline from the Editorial Department.

The Equations of Motion of Nonlinear Nonholonomic Variable Mass System With Applications

Z.-M. Ge[1]

1 Universal D'Alembert-Lagrange's Principle of Variable Mass System

For each variable mass particle, the fundamental dynamical equation [1, 2] is

$$m_\beta \frac{d\dot{\mathbf{r}}_\beta}{dt} = \mathbf{F}_\beta + \mathbf{N}_\beta + \frac{dm_\beta}{dt}(\mathbf{u}_\beta - \dot{\mathbf{r}}_\beta)(\beta = 1,2, \ldots, N) \tag{1.1}$$

Taking the dot product of (1.1) and $\delta \overset{(n)}{\mathbf{r}}_\beta$, where $\delta \overset{(n)}{\mathbf{r}}_\beta$, is the variation of the nth derivative of $\mathbf{r}_\beta$ with respect to time t with

$$\delta\mathbf{r} = \delta\dot{r} \ldots = \delta \overset{(n-1)}{\mathbf{r}}_\beta = 0 \tag{1.2}$$

For ideal constraints,

$$\sum_{\beta=1}^{N} \mathbf{N}_\beta \delta \overset{(n)}{\mathbf{r}}_\beta = 0 \tag{1.3}$$

Thus we get

$$\sum_{\beta=1}^{N} [m_\beta \ddot{\mathbf{r}}_\beta - \mathbf{F}_\beta - \dot{m}_\beta(\mathbf{u}_\beta - \dot{\mathbf{r}}_\beta)] \delta \overset{(n)}{\mathbf{r}}_\beta = 0 (n = 0,1,2, \ldots) \tag{1.4}$$

This is the universal D'Alembert-Lagrange's principle of variable mass system.

2 The Equations of Motion of Holonomic Variable Mass System

Let the degrees of freedom of the system be m, we have

$$\overset{(n)}{\mathbf{r}}_\beta = \sum_{\epsilon=1}^{m} \frac{\partial \mathbf{r}_\beta}{\partial q_\epsilon} \overset{(n)}{q}_\epsilon + n\Bigg(\sum_{\epsilon=1}^{m} \sum_{\delta=1}^{m} \frac{\partial^2 \mathbf{r}_\beta}{\partial q_\epsilon \partial q_\delta} \overset{(n-1)}{q}_\epsilon \dot{q}_\delta + \sum_{\epsilon=1}^{m} \frac{\partial^2 \mathbf{r}_\beta}{\partial q_\epsilon \partial t} \overset{(n-1)}{q}_\epsilon \Bigg) + \ldots (n = 3,4,5 \ldots) \tag{2.1}$$

$$\delta \overset{(n)}{\mathbf{r}}_\beta = \sum_{\epsilon=1}^{m} \frac{\partial \mathbf{r}_\beta}{\partial q_\epsilon} \delta \overset{(n)}{q}_\epsilon = \sum_{\epsilon=1}^{m} \frac{\partial \overset{(n)}{\mathbf{r}}_\beta}{\partial \overset{(n)}{q}_\epsilon} \delta \overset{(n)}{q}_\epsilon \tag{2.2}$$

Putting (2.2) into (1.4), using the independence of all $\delta \overset{(n)}{q}_\epsilon$, we have

$$\sum_{\beta=1}^{N} \left[m_\beta \ddot{\mathbf{r}}_\beta \frac{\partial \overset{(n)}{\mathbf{r}}_\beta}{\partial \overset{(n)}{q}_\epsilon} - \mathbf{F}_\beta \frac{\partial \mathbf{r}_\beta}{\partial q_\epsilon} - \dot{m}_\beta (\mathbf{u}_\beta - \dot{\mathbf{r}}_\beta) \frac{\partial \overset{(n)}{\mathbf{r}}_\beta}{\partial \overset{(n)}{q}_\epsilon} \right] = 0 (\epsilon = 1,2, \ldots, m) \tag{2.3}$$

Taking the nth time derivation of the kinematic energy of the system

$$T = \sum_{\beta=1}^{N} \frac{m_\beta \dot{\mathbf{r}}_\beta \cdot \dot{\mathbf{r}}_\beta}{2} \tag{2.4}$$

we have $\overset{(n)}{T}$ and

$$\frac{\partial T}{\partial q_\delta} = \frac{1}{n} \sum_{\beta=1}^{N} m_\beta \dot{\mathbf{r}}_\beta \frac{\partial \overset{(n)}{\mathbf{r}}_\beta}{\partial \overset{(n-1)}{q}_\delta} \tag{2.5}$$

$$\frac{\partial \overset{(n)}{T}}{\partial \overset{(n)}{q}_\epsilon} = n \sum_{\beta=1}^{N} m_\beta \ddot{\mathbf{r}}_\beta \frac{\partial \overset{(n)}{\mathbf{r}}_\beta}{\partial \overset{(n)}{q}_\epsilon} + \sum_{\beta=1}^{N} m_\beta \dot{\mathbf{r}}_\beta \frac{\partial \overset{(n+1)}{\mathbf{r}}_\beta}{\partial \overset{(n)}{q}_\epsilon} + n \sum_{\beta=1}^{N} \dot{m}_\beta \dot{\mathbf{r}}_\beta \frac{\partial \overset{(n)}{\mathbf{r}}_\beta}{\partial \overset{(n)}{q}_\epsilon} \tag{2.6}$$

By (2.3) we get the equations of motion of holonomic variable mass system:

$$\frac{1}{n} \frac{\partial \overset{(n)}{T}}{\partial \overset{(n)}{q}_\epsilon} - (n+1) \frac{\partial T}{\partial q_\epsilon} = Q_\epsilon + K_\epsilon (\epsilon = 1,2, \ldots, m) \tag{2.7}$$

where

$$Q_\epsilon = \sum_{\beta=1}^{N} \mathbf{F}_\beta \frac{\partial \mathbf{r}_\beta}{\partial q_\epsilon}$$

[1] Special Expert, National Science Council Executive Yuan, National Chiao Tung University, Hsinchu, Taiwan, Republic of China.
Formerly, Associate Professor, Engineering Mechanics Department, Shanghai Jiaotong University, Shanghai, China.
Manuscript received by ASME Applied Mechanics Division, October, 1982; final revision, October, 1983.

is the generalized force and

$$K_\epsilon = \sum_{\beta=1}^{N} \dot{m}_\beta \mathbf{u}_\beta \frac{\partial \overset{(n)}{\mathbf{r}}_\beta}{\partial \overset{(n)}{q}_\epsilon}.$$

Let

$$\sum_{\beta=1}^{N} \dot{m}_\beta (u_\beta - \dot{r}_\beta) \frac{\partial \overset{(n)}{r}_\beta}{\partial \overset{(n)}{q}_\epsilon} = \mathrm{R}_\epsilon \tag{2.8}$$

which is the generalized thrust. Then by (2.3) we get

$$\frac{1}{n}\left[\frac{\partial \overset{(n)}{T}}{\partial \overset{(n)}{q}_\epsilon} - (n+1)\frac{\partial T}{\partial q_\epsilon}\right] - \frac{\partial(\dot{T}-\dot{T}')}{\partial \dot{q}_\epsilon} = Q_\epsilon + R_\epsilon \ (\epsilon = 1,2, \ldots m) \tag{2.9}$$

where $\dot{T}'$ is the time derivative of T with the masses of all particles as constant. Equation (2.9) is more complicated than (2.7), while R_ϵ has clear physical significance and K_ϵ is lacking in it.

3 The Equations of Motion of Variable Mass System With High-ordered Nonholonomic Constraints

The general forms of equations of constraint are

$$\Psi_\alpha(q_1,\ldots,q_m;\dot{q}_1,\ldots,\dot{q}_m;\ldots;\overset{(n)}{q}_1,\ldots,\overset{(n)}{q}_m;t) = 0 \ (\alpha = 1,2,\ldots,g<m) \tag{3.1}$$

1 Equations (3.1) are linear equations of $\overset{(n)}{q}_1, \ldots, \overset{(n)}{q}_m$:

$$\sum_{\epsilon=1}^{m} a_{\alpha\epsilon} \overset{(n)}{q}_\epsilon + a_\alpha = 0 \quad (\alpha = 1,2, \ldots, g) \tag{3.2}$$

$$\sum_{\epsilon=1}^{m} a_{\alpha\epsilon} \delta \overset{(n)}{q}_\epsilon = 0 \quad (\alpha = 1,2, \ldots, g) \tag{3.3}$$

where $a_{\alpha\epsilon}$, a_ϵ are functions of $q_1,\ldots,q_m$; $\dot{q}_1,\ldots,\dot{q}_m$; $\overset{(n-1)}{q}_1,\ldots,\overset{(n-1)}{q}_m$ and t.

By the method of Lagrange's multiplier, the equations of motion are obtained:

$$\frac{1}{n}\left[\frac{\partial \overset{(n)}{T}}{\partial \overset{(n)}{q}_\epsilon} - (n+1)\frac{\partial T}{\partial q_\epsilon}\right] = Q_\epsilon + K_\epsilon - \sum_{\alpha=1}^{g} \lambda_\alpha a_{\alpha\epsilon} \ (\epsilon = 1,2,\ldots,m) \tag{3.4}$$

By (3.4) and (3.2), we can solve for λ_α and q_ϵ. Corresponding to (2.9), we have

$$\frac{1}{n}\left[\frac{\partial \overset{(n)}{T}}{\partial \overset{(n)}{q}_\epsilon} - (n+1)\frac{\partial T}{\partial q\epsilon}\right] - \frac{\partial(\dot{T}-\dot{T}')}{\partial \dot{q}_\epsilon} = Q_\epsilon + K_\epsilon - \sum_{\alpha=1}^{g} \lambda_\alpha a_{\alpha\epsilon} \ (\epsilon = 1,2,\ldots,m) \tag{3.5}$$

2 Equations (3.1) are nonlinear equations of $\overset{(n)}{q}_1,\ldots,\overset{(n)}{q}_m$:

After derivation of (3.1), we get the linear equations of $\overset{(n+1)}{q}_1,\ldots,\overset{(n+1)}{q}_m$:

$$\sum_{\epsilon=1}^{m} \frac{\partial \Psi_\alpha}{\partial \overset{(n)}{q}_\epsilon} \overset{(n+1)}{q}_\epsilon + \ldots = 0 \tag{3.6}$$

Similar to case (1), the equations of motion can be obtained with $n+1$ instead of n. For instance, corresponding to (3.4), the equations of motion are

$$\frac{1}{n+1}\left[\frac{\partial \overset{(n+1)}{T}}{\partial \overset{(n+1)}{q}_\epsilon} - (n+2)\frac{\partial T}{\partial q_\epsilon}\right] = Q_\epsilon + K_\epsilon - \sum_{\alpha=1}^{g} \lambda_\alpha \frac{\partial \Psi_\alpha}{\partial \overset{(n)}{q}_\epsilon} \quad (\epsilon = 1, 2, \ldots, m) \tag{3.7}$$

4 Applications

(1) The motion of a spacecraft under gravitation of the earth is studied. The magnitude of the velocity is controlled as a given function of time $f(t)$. Using spherical coordinate system, we have the gravitational force

$$F = \frac{\mu M m}{r^2} \tag{4.1}$$

and the equation of nonlinear nonholonomic constraint

$$\dot{r}^2 + r^2\dot{\phi}^2\cos^2\theta + r^2\dot{\theta}^2 = f(t) \tag{4.2}$$

After derivation, we get

$$\dot{r}\ddot{r} + \dot{\varphi}\ddot{\varphi}r^2\cos^2\theta + r^2\dot{\theta}\ddot{\theta} - \dot{\theta}r^2\dot{\phi}^2\cos\theta\sin\theta + r\dot{r}\dot{\varphi}^2\cos^2\theta + r\dot{r}\dot{\theta}^2 = f'(t) \tag{4.3}$$

By (3.4) we obtain the equations of motion:

$$\left.\begin{aligned} m(\ddot{r} - \dot{\varphi}^2 r\cos^2\theta - \dot{\theta}^2 r) + \frac{\dot{m}\dot{r}}{2} &= -\frac{\mu M m}{r^2} + Q_{rr} + K_r - \lambda\dot{r} \\ m(\ddot{\varphi}r^2\cos\theta - 2r^2\dot{\varphi}\dot{\theta}\cos\theta\sin\theta + 2r\dot{r}\dot{\varphi}\cos^2\theta) + \frac{\dot{m}}{2}\dot{\varphi}r^2\cos^2\theta &= Q_{r\varphi} + K_\varphi - \lambda\dot{\varphi}r^2\cos^2\theta \\ m(r^2\ddot{\theta} + 2\dot{\theta}r\dot{r} + r^2\dot{\phi}^2\cos\theta\sin\theta) + \frac{\dot{m}}{2}r^2\dot{\theta} &= Q_{r\theta} + K_\theta - \lambda r^2\dot{\theta} \end{aligned}\right\} \tag{4.4}$$

Using (4.4) and the equation of constraint (4.2), we can solve for r, φ, θ.

(2) Leading pursuit in a vertical plane is studied, while pure pursuit has already been studied [2]. Let the vertical plane be oxy, point A with mass m_1 be the pursuer and point B with mass m_2 be the object. For leading pursuit, for triangle ABC,

$$\sin \angle BAC / \sin \angle ABC = \mathbf{V}_B / \mathbf{V}_A \tag{4.5}$$

must be satisfied, where $\mathbf{V}_A$ and $\mathbf{V}_B$ are in the directions of $\overline{AB}$ and $\overline{BC}$, respectively. The equation of constraint (4.5) can be rewritten as

$$E_1 G_2 \sqrt{\dot{x}_1^2 + \dot{y}_1^2} - E_2 G_1 \sqrt{\dot{x}_2^2 + \dot{y}_2^2} = 0 \tag{4.6}$$

where

$$E_1 = (y_2 - y_1)\dot{x}_1 - (x_2 - x_1)\dot{y}_1, \quad E_2 = (y_2 - y_1)\dot{x}_2 - (x_2 - x_1)\dot{v}_2$$

$$G_1 = \sqrt{(x_2 - x_1)^2\dot{x}_1^2 + (y_2 - y_1)^2\dot{y}_1^2 + (y_2 - y_1)^2\dot{x}_1^2 + (x_2 - x_1)^2\dot{y}_1^2}$$

$$G_2 = \sqrt{(x_2 - x_1)^2\dot{x}_2^2 + (y_2 - y_1)^2\dot{y}_2^2 + (y_2 - y_1)^2\dot{x}_2^2 + (x_2 - x_1)^2\dot{y}_2^2}$$

After derivation, we have

$$a_{x1}\ddot{x}_1 + a_{y_1}\ddot{y}_1 + a_{x_2}\ddot{x}_2 + a_{y_2}\ddot{y}_2 + \ldots = 0 \tag{4.7}$$

where $a_{x_1}, a_{y_1}, a_{x_2}, a_{y_2}$ do not contain $\ddot{x}_1, \ddot{y}_1, \ddot{x}_2, \ddot{y}_2$.

The equations of motion are

$$\begin{aligned} m_1\ddot{x}_1 + \dot{m}_1\dot{x}_1 &= Q_{rx_1} + K_{x_1} - \lambda a_{x_1} \\ m_1\ddot{y}_1 + \dot{m}_1\dot{y}_1 &= Q_{ry_1} - m_1 g + K_{y_1} - \lambda a_{y_1} \\ m_2\ddot{x}_2 + \dot{m}_2\dot{x}_2 &= Q_{rx_2} + K_{x_2} - \lambda a_{x_2} \\ m_2\ddot{y}_2 + \dot{m}_2\dot{y}_2 &= Q_{ry_2} + K_{y_2} - m_2 g - \lambda a_{y_2} \end{aligned} \tag{4.8}$$

$Q_{rx_1}, Q_{ry_1}, Q_{rx_2}, Q_{ry_2}$ are the generalized forces corresponding to the given force other than the gravity. By (4.8) and (4.6) we can solve for x_1, y_1, x_2, y_2, and λ.

References

1 Ge, Z.-M., and Cheng, Y.-H., "Extended Kane's Equations for Nonholonomic Variable Mass System," ASME JOURNAL OF APPLIED MECHANICS, Vol. 49, 1982, pp. 429-431.

2 Ge, Z.-M., "Equations of Motion for Nonholonomic Variable Mass Systems and Their Application to a Control System," *Journal of Shanghai Jiaotong University*, No. 4, 1979, pp. 1-22.

Transverse Projectile Impacts on Beams

R. L. Woodward[1]

1 Introduction

When a slender beam is subjected to a transverse impulsive force, bending moments result due to the inertia of elements of the beam away from the impact site. If the impulse is of sufficient magnitude then yielding or fracture may occur at the position of maximum bending moment. Most studies have concentrated on central impacts on either finite or infinite beams using the rigid-plastic theory [1-9]. This work examines the problem of impact on the end of beams, which is particularly important for the behavior of slender rod-shaped projectiles [10, 11]. The results of some simple experiments that allow plastic hinges to be observed in the case of end-impacted beams of circular cross section are presented, and the application of the rigid-plastic approach, and the use of a finite element computer program to study the problem are considered.

2 Experiment and Results

Beams of circular section were lightly glued to a support at one end and struck transversely with a projectile at the other end. The bond to the support was very weak so that the beams readily separated and were caught approximately 0.5 m away in a soft medium. The projectiles were 4.76 mm diameter mild steel cylinders of mass 1.65 g impacting at 775 ms^{-1}. The beams were 6.35 mm diameter, of various lengths, and manufactured from a quenched and tempered steel at a hardness level of 355 HV10.

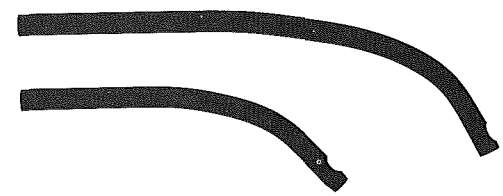

Fig. 1 Profiles of beams of length-to-diameter ratios 23.8 and 15.3, impacted at one end by a projectile traveling at right angles to the beam axis

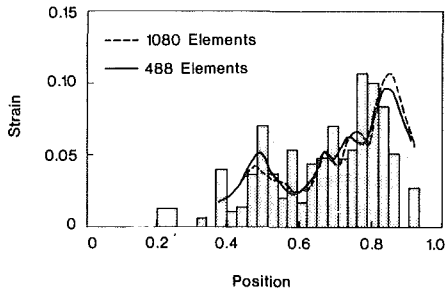

Fig. 2 Strain distribution for the tension side of the beam with length-to-diameter ratio 15.3 in Fig. 1. The histogram represents the strains measured from the beam curvature using equation (1). The lines represent the strain distributions calculated using the computer code EPIC-2 with two grid sizes.

Examples for impacts on two such beams are shown in Fig. 1. Two hinge points can be observed optically in each beam, one at approximately the center of the beam and one near the impact site. The deformations are very similar to those observed previously in slender projectiles that have impacted oblique targets [11]. From the profiles of Fig. 1 the strain distribution, ϵ, in the outer fibers can be calculated by numerical differencing using the equation

$$\epsilon = \frac{D\Delta\theta}{2\Delta L} \tag{1}$$

where D is the beam diameter and $\Delta\theta$ is the change in tangent angle across a segment of length ΔL. A typical strain distribution, for the case of one of the beams in Fig. 1, is shown in Fig. 2. The accuracy of the technique is sufficient to consistently reproduce the position and strain magnitude of the major features. In the case of Fig. 2 these features would be identified as strain peaks at positions 0.5 and 0.8, a plateau of high strain between 0.65 and 0.75, a minimum at approximately 0.6, and a low strain region from 0 to 0.4.

3 Rigid-Plastic Approach

The development and motion of the hinges in impacted beams is readily described using the rigid-plastic approach developed by Lee and Symonds [2] for central impacts on a free-free beam. In Lee and Symonds' case a beam of length $2L$ is impacted in the center, at which position a plastic hinge develops if the load is sufficient for the limit moment of the beam to be exceeded. To treat the end-impact situation we use the same geometry but allow the center of the beam to have a

[1] Materials Research Laboratories, Defense Science and Technology Organization, P.O. Box 50, Ascot Vale, Victoria, Australia.

Manuscript received by ASME Applied Mechanics Division, August, 1983; final revision, October, 1983.

$$E_1 = (y_2 - y_1)\dot{x}_1 - (x_2 - x_1)\dot{y}_1, \quad E_2 = (y_2 - y_1)\dot{x}_2 - (x_2 - x_1)\dot{v}_2$$

$$G_1 = \sqrt{(x_2 - x_1)^2\dot{x}_1^2 + (y_2 - y_1)^2\dot{y}_1^2 + (y_2 - y_1)^2\dot{x}_1^2 + (x_2 - x_1)^2\dot{y}_1^2}$$

$$G_2 = \sqrt{(x_2 - x_1)^2\dot{x}_2^2 + (y_2 - y_1)^2\dot{y}_2^2 + (y_2 - y_1)^2\dot{x}_2^2 + (x_2 - x_1)^2\dot{y}_2^2}$$

After derivation, we have

$$a_{x1}\ddot{x}_1 + a_{y_1}\ddot{y}_1 + a_{x_2}\ddot{x}_2 + a_{y_2}\ddot{y}_2 + \ldots = 0 \tag{4.7}$$

where $a_{x_1}, a_{y_1}, a_{x_2}, a_{y_2}$ do not contain $\ddot{x}_1, \ddot{y}_1, \ddot{x}_2, \ddot{y}_2$.

The equations of motion are

$$\left.\begin{aligned} m_1\ddot{x}_1 + \dot{m}_1\dot{x}_1 &= Q_{rx_1} + K_{x_1} - \lambda a_{x_1} \\ m_1\ddot{y}_1 + \dot{m}_1\dot{y}_1 &= Q_{ry_1} - m_1 g + K_{y_1} - \lambda a_{y_1} \\ m_2\ddot{x}_2 + \dot{m}_2\dot{x}_2 &= Q_{rx_2} + K_{x_2} - \lambda a_{x_2} \\ m_2\ddot{y}_2 + \dot{m}_2\dot{y}_2 &= Q_{ry_2} + K_{y_2} - m_2 g - \lambda a_{y_2} \end{aligned}\right\} \tag{4.8}$$

$Q_{rx_1}, Q_{ry_1}, Q_{rx_2}, Q_{ry_2}$ are the generalized forces corresponding to the given force other than the gravity. By (4.8) and (4.6) we can solve for x_1, y_1, x_2, y_2, and λ.

References

1 Ge, Z.-M., and Cheng, Y.-H., "Extended Kane's Equations for Nonholonomic Variable Mass System," ASME JOURNAL OF APPLIED MECHANICS, Vol. 49, 1982, pp. 429-431.

2 Ge, Z.-M., "Equations of Motion for Nonholonomic Variable Mass Systems and Their Application to a Control System," *Journal of Shanghai Jiaotong University*, No. 4, 1979, pp. 1-22.

Transverse Projectile Impacts on Beams

R. L. Woodward[1]

1 Introduction

When a slender beam is subjected to a transverse impulsive force, bending moments result due to the inertia of elements of the beam away from the impact site. If the impulse is of sufficient magnitude then yielding or fracture may occur at the position of maximum bending moment. Most studies have concentrated on central impacts on either finite or infinite beams using the rigid-plastic theory [1-9]. This work examines the problem of impact on the end of beams, which is particularly important for the behavior of slender rod-shaped projectiles [10, 11]. The results of some simple experiments that allow plastic hinges to be observed in the case of end-impacted beams of circular cross section are presented, and the application of the rigid-plastic approach, and the use of a finite element computer program to study the problem are considered.

2 Experiment and Results

Beams of circular section were lightly glued to a support at one end and struck transversely with a projectile at the other end. The bond to the support was very weak so that the beams readily separated and were caught approximately 0.5 m away in a soft medium. The projectiles were 4.76 mm diameter mild steel cylinders of mass 1.65 g impacting at 775 ms^{-1}. The beams were 6.35 mm diameter, of various lengths, and manufactured from a quenched and tempered steel at a hardness level of 355 HV10.

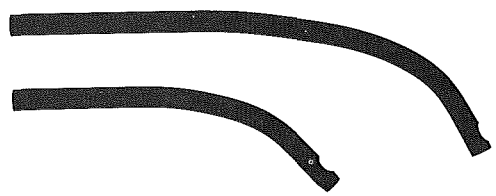

Fig. 1 Profiles of beams of length-to-diameter ratios 23.8 and 15.3, impacted at one end by a projectile traveling at right angles to the beam axis

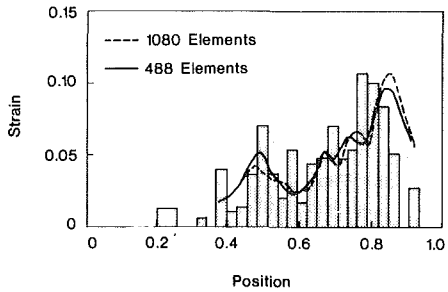

Fig. 2 Strain distribution for the tension side of the beam with length-to-diameter ratio 15.3 in Fig. 1. The histogram represents the strains measured from the beam curvature using equation (1). The lines represent the strain distributions calculated using the computer code EPIC-2 with two grid sizes.

Examples for impacts on two such beams are shown in Fig. 1. Two hinge points can be observed optically in each beam, one at approximately the center of the beam and one near the impact site. The deformations are very similar to those observed previously in slender projectiles that have impacted oblique targets [11]. From the profiles of Fig. 1 the strain distribution, ϵ, in the outer fibers can be calculated by numerical differencing using the equation

$$\epsilon = \frac{D\Delta\theta}{2\Delta L} \tag{1}$$

where D is the beam diameter and $\Delta\theta$ is the change in tangent angle across a segment of length ΔL. A typical strain distribution, for the case of one of the beams in Fig. 1, is shown in Fig. 2. The accuracy of the technique is sufficient to consistently reproduce the position and strain magnitude of the major features. In the case of Fig. 2 these features would be identified as strain peaks at positions 0.5 and 0.8, a plateau of high strain between 0.65 and 0.75, a minimum at approximately 0.6, and a low strain region from 0 to 0.4.

3 Rigid-Plastic Approach

The development and motion of the hinges in impacted beams is readily described using the rigid-plastic approach developed by Lee and Symonds [2] for central impacts on a free-free beam. In Lee and Symonds' case a beam of length $2L$ is impacted in the center, at which position a plastic hinge develops if the load is sufficient for the limit moment of the beam to be exceeded. To treat the end-impact situation we use the same geometry but allow the center of the beam to have a

[1] Materials Research Laboratories, Defense Science and Technology Organization, P.O. Box 50, Ascot Vale, Victoria, Australia.

Manuscript received by ASME Applied Mechanics Division, August, 1983; final revision, October, 1983.

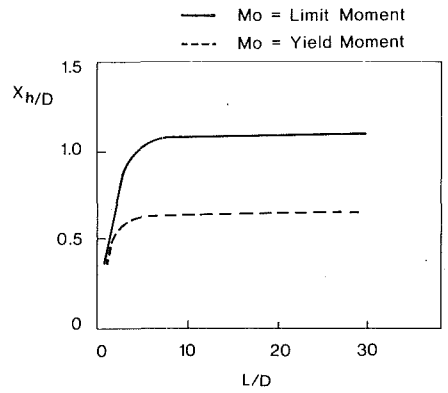

Fig. 3 Hinge position divided by beam diameter (X_h/D) as a function of length-to-diameter ratio (L/D) for the case where shear yielding occurs at the impact site. The rigid-plastic approach is used and two situations are considered, in one case the beam bends plastically at the limit moment and in the other it bends plastically at the yield moment.

limit moment equal to zero; thus the beam yields at any load greater than zero, and both rotate about the center and accelerate in the direction of the impulse. It is then possible to focus on the right-hand section of length L as a simulation of our end-impact problem, the moment at both ends of one beam being zero. With this approach the equations of motion of the beam for the end-impact problem are only slight modifications of those given by Lee and Symonds [2] and they can be used to give the following description of behavior.

The beam rotates as a rigid body as the load increases until a hinge develops one-third of the rod length from the impact site. With further increase in load the position of the hinge moves either toward the impact site for slender beams or toward the center for beams of low length to diameter ratio. If the load P is sufficient to cause shear yielding of the end of the beam then a limiting hinge position is reached [5–7] because shear sliding occurs on the end at constant stress. The beam is effectively subjected to a constant end load and the hinge becomes stationary. If the load decreases to zero the plastic hinge moves toward the beam center, the beam continuing to bend as the hinge moves until the angular velocities on either side of the hinge become equal at the time the hinge reaches the center.

The limiting position of the hinge where shear yielding of the end of the beam occurs was calculated for the cases where the moment to cause plastic bending, Mo, was equal to the yield moment and also to the limit moment and is shown in Fig. 3 as a function of length to diameter ratio. For high length-to-diameter ratios the hinge position approaches a limit equal to 1.1 diameters for the limit moment case and 0.65 diameters for the yield moment case. These results can be also obtained by adapting Symonds [6] work on beams of infinite length. In a large number of experiments the hinge was always observed to lie between two and four beam diameters from the impact site even though the impact conditions are such that the shear yield strength of the beam is exceeded at the impact site. The rigid plastic approach does not account for the hinge observed near the center of the beams, as in this method bending ceases as the hinge reaches the center.

In the rigid-plastic theory as presented, elastic strains, work hardening, strain rate effects, and rotatory inertia are ignored, the hinge is of negligible width and only small deflections are assumed. The width of a hinge in a beam must be of the order of a beam diameter that is also the order of the hinge distance from the impact site. The slenderness of the beams and the experimental conditions are such that the reflected elastic wave from the far end of the beam has not returned before loading has ceased, hence in this problem wave propagation is also important. Thus there are a number of approximations that could individually or collectively account for the differences between the theory and the experiments.

4 Computer Simulation

Computer simulation offers the opportunity to study detail of the development of hinges with time and also complex loading conditions can be handled. As an example, use was made of the code EPIC-2 [12, 13] which is a finite element code in two dimensions. The beam and the impacting projectile are both simulated in plane strain and as the real problem is three dimensional exact agreement cannot be expected, however the objective is to demonstrate the usefulness of the technique. The simulations used 8 and 12 triangular elements across the beam depth with a similar grid size in both projectile and beam. Both projectile and beam were assumed elastic, perfectly plastic, with yield stresses estimated from hardnesses of the experiment materials.

The strains on the tension side of a beam are plotted for two element sizes on the same axes as the experimental strain distribution in Fig. 2 and the agreement with experiment is very good, particularly as it is a two-dimensional simulation. In the simulation two major hinges are observed, one near the impact site and the other near the beam center, and some less prominant strain maxima occur between them. The positions of the major hinges from the computer code solution are close to those observed experimentally. An examination of the development of the strain distribution as a function of time is possible with this method and it was observed that the major hinge near the impact site develops while the beam is under load, the deformation zone then moves toward the beam center after the projectile has lost contact with the beam. This is the sequence described by the rigid-plastic model. The high strains associated with the hinge in the middle of the beam are seen to develop in the computation when the hinge reaches the center just before deformation ceases.

5 References

1 Hopkins, H. G., "On the Behaviour of Infinitely Long Rigid-Plastic Beams Under Transverse Concentrated Load." *J. Mech. Phys. Sol.*, Vol. 4, 1955, pp. 38–52.

2 Lee, E. H., and Symonds, P. S., "Large Plastic Deformations of Beams Under Transverse Impact," ASME JOURNAL OF APPLIED MECHANICS, Vol. 74, 1952, pp. 308–314.

3 Symonds, P. S., "Dynamic Load Characteristics in Plastic Bending of Beams," ASME JOURNAL OF APPLIED MECHANICS, Vol. 20, 1953, pp. 475–481.

4 Symonds, P. S., and Leth, C. F. A., "Impact of Finite Beams of Ductile Metal," *J. Mech. Phys. Sol.*, Vol. 2, 1954, pp. 92–102.

5 Karunes, B., and Onat, E. T., "On the Effect of Shear on Plastic Deformation of Beams Under Transverse Impact Loading," ASME JOURNAL OF APPLIED MECHANICS, Vol. 27, 1960, pp. 107–110.

6 Symonds, P. S., "Plastic Shear Deformation in Dynamic Load Problems," in: *Engineering Plasticity*, Heyman, J., and Leckie, F. A., eds., C.U.P., London, 1968, pp. 647–664.

7 Jones, N., and Gomes de Oliveira, J., "The Influence of Rotary Inertia and Transverse Shear on the Dynamic Plastic Behavior of Beams," ASME JOURNAL OF APPLIED MECHANICS, Vol. 46, 1979, pp. 303–310.

8 Johnson, W., *Impact Strength of Materials*, Arnold, London, 1972, pp. 250–280.

9 Goldsmith, W., *Impact*, Arnold, London, 1960, pp. 206–233.

10 Zener, C., and Peterson, R. E., "Mechanism of Armour Penetration," Second partial report, No. 710/492, Watertown Arsenal, Mass., 1943.

11 Reid, S. R., Edmunds, A. J., and Johnson, W., "Bending of Long Steel and Aluminum Rods During End Impact With a Rigid Target." *J. Mech. Eng. Sci.*, Vol. 23, 1981, pp. 85–92.

12 Johnson, G. R., "EPIC-2, A Computer Program for Elastic-Plastic Impact Computations in 2 Dimensions Plus Spin," US Army ARRADCOM Ballistic Research Laboratory Contract Report ARBRL-CR-00373, June, 1978.

13 Johnson, G. R., "Analysis of Elastic-Plastic Impact Involving Severe Distortions," ASME JOURNAL OF APPLIED MECHANICS, Vol. 43, 1976, pp. 439–444.

On Asymptotic Approximations to Beam Model Shapes

E. H. Dowell[1]

Recently the author had occasion to investigate inter alia the asymptotic character of the mode shapes of uniform beams. These results do not seem to have been presented before in the literature and so are given here as they appear to be of general interest. Clamped-free and free-free beams are considered, although other beam boundary conditions may be treated in a similar manner.

Clamped-Free Beam Modes

The exact expression of these modes is well known [1], viz

$$W_n = \frac{\sin B_n - \sinh B_n}{\cosh B_n - \cos B_n}(\sinh B_n x - \sin B_n x) + (\cosh B_n x - \cos B_n x) \quad (1)$$

where x is the nondimensional distance along the beam, n is the nodal index number, and the modal constants, B_n, are the roots of a transcendental equation. It is well known that asymptotically [1]

$$B_n \to (2n-1)\pi/2 \quad \text{as } n \to \infty \quad (2)$$

To develop the desired asymptotic formula, the hyperbolic functions are rewritten in terms of exponentials and equation (1) is expanded in powers of $\epsilon \equiv e^{-B_n}$. Neglecting terms of order ϵ compared to 1, one obtains

$$W_n = \sin B_n x - \cos B_n x + e^{-B_n x} + (-1)^{n+1} e^{-B_n(1-x)} \quad (3)$$

The third and fourth terms are formally of order ϵ for $x \sim 0(1)$ and $0(0)$, respectively. They are retained because they are of order 1 for $x \sim 0(0)$, and $0(1)$, respectively. Note that from equation (3),

$$W_n(x=0) = (-1)^{n+1} e^{-B_n} \quad (4)$$

and

$$W_n(x=1) = 2(-1)^{n+1} + e^{-B_n}$$

The exact results are [1]

$$W_n(x=0) = 0$$
$$W_n(x=1) = 2(-1)^{n+1} \quad (5)$$

Comparing equations (4) and (5), it is seen that indeed the error is formally of order $\epsilon \equiv e^{-B_n}$. Moreover the error in (3) and its subsequent counterpart $(3)_{ff}$ is also of order ϵ for all x. Note that the present procedure could also be used to develop approximations to a higher order accuracy, e.g. ϵ^2.

Free-Free Beam Modes

The corresponding formulas are

$$W_n = \frac{\cos B_n - \cosh B_n}{\sinh B_n - \sin B_n}(\sinh B_n x + \sin B_n x) + \cosh B_n x + \cos B_n x \quad (1)_{ff}$$

$$B_n \to (2n+1)\pi/2 \quad \text{as } n \to \infty \quad (2)_{ff}$$

$$W_n = -\sin B_n x + \cos B_n x + e^{-B_n x} - (-1)^n e^{-B_n(1-x)} \quad (3)_{ff}$$

$$W_n(x=0) = 2 + (-1)^n e^{-B_n}$$

$$W_n(x=1) = 2(-1)^{n+1} + e^{-B_n} \quad (4)_{ff}$$

$$W_n(x=0) = 2$$

$$W_n(x=1) = 2(-1)^{n+1} \quad (5)_{ff}$$

From equations (2), (3), and $(2)_{ff}$, $(3)_{ff}$ the modal wavelengths (twice the distance between nodal points) are asymptotically

$$\lambda_n = \frac{2\pi}{B_n} \to \frac{2}{n} \quad \text{as } n \to \infty$$

$$(\lambda_n)_{ff} = \frac{2\pi}{B_n} \to \frac{2}{n} \quad \text{as } n \to \infty$$

These are the same as for a pinned-pinned beam and also for a clamped-clamped beam. The latter result follows from the well-known correspondence [1] between the mode shapes of a clamped-clamped and free-free beam.

It is remarked that equation (3) and $(3)_{ff}$ not only are of intrinsic interest, but also they are of very practical computational interest. Equations (1) and $(1)_{ff}$ become computationally unusable as $n \to \infty$ because of round-off error resulting from taking a difference between two large numbers. Typically the error becomes evident for $n = 5$ or so using single precision arithmetic. This point was discussed previously by Chang and Craig [2], inter alia. Finally it is noted that the present results also can be obtained by using the method described by Bolotin [3]. However the present methodology for deriving the results would appear more easily extended to higher order in ϵ than the method of reference [3].

References

1 Young, D., and Felgar, R. P., "Tables of Characteristic Functions Representing Normal Modes of Vibration of a Beam," Engineering Research Series No. 44, University of Texas Publication, July 1, 1949.

2 Chang, T.-C., and Craig, Jr., R. R., "Normal Modes of Uniform Beams," *J. Eng. Mech. Div., ASCE*, Vol. 95, 1969, pp. 1027-1031.

3 Bolotin, V. V., "An Asymptotic Method for the Study of the Problem of Eigenvalues for Rectangular Regions," in: *Problems of Continuum Mechanics*, English Ed., Radok, J. R. M., ed., 1961, pp. 56-68.

[1]Department of Mechanical Engineering and Materials Science, Duke University, Durham, N.C. 27706. Mem. ASME.

Manuscript received by ASME Applied Mechanics Division, August, 1983; final revision, November, 1983.

Stability of a Rotating Ring Under External Pressure

C. Y. Wang[1]

1 Introduction

The buckling of a ring (or circular cylinder) under various pressure and point loading has been studied by many authors, notably references [1-7]. It was found, for uniform pressure, that the critical load is $(N^2-1)EI/R^3$ where N is the N-fold symmetry, EI is the flexural rigidity, and R is the radius before buckling. The present Note studies the effect of added rotation on stability. Suppose the angular velocity is Ω about the center of gravity. The centrifugal force per length is then $\rho\Omega^2 R$ where ρ is the mass per arc length of the ring. However, as we will see later, the critical pressure is not merely increased by this value. Let us normalize all lengths by R and all stresses by EI/R^3. The elastica equation of a ring under general loading is, e.g. [7]

[1]Departments of Mathematics and Mechanical Engineering, Michigan State University, East Lansing, Mich. 48824. Mem. ASME.

Manuscript received by ASME Applied Mechanics Division, September, 1983; final revision, November, 1983.

$$\frac{d\theta}{ds}\frac{d^4\theta}{ds^4} - \frac{d^2\theta}{ds^2}\frac{d^3\theta}{ds^3} + \left[\left(\frac{d\theta}{ds}\right)^3 - q_n\right]$$

$$\frac{d^2\theta}{ds^2} + q_t\left(\frac{d\theta}{ds}\right)^2 + \frac{dq_n}{ds}\frac{d\theta}{ds} = 0 \tag{1}$$

Here θ is the local angle of inclination, s is the arc length, q_n and q_t are normal and tangential applied stresses, respectively. Let r be the radial distance and ϕ be the polar angle from the center of gravity. We find

$$q_n = -p + \alpha^2 r \sin(\theta - \phi) \tag{2}$$

$$q_t = \alpha^2 r \cos(\theta - \phi) \tag{3}$$

where $\alpha \equiv \Omega R^2\sqrt{\rho/EI}$ is a nondimensional number representing the relative importance of rotation to rigidity.

The cartesian coordinates (x,y) are related to the angles by

$$\frac{dx}{ds} = \cos\theta, \quad \frac{dy}{ds} = \sin\theta, \tag{4}$$

$$x = r\cos\phi, \quad y = r\sin\phi. \tag{5}$$

2 Stability

We perturb the dependent variables about the circle:

$$\theta = s + \frac{\pi}{2} + \Psi, \quad x = \cos s + \xi, \quad y = \sin s + \eta \tag{6}$$

where Ψ, ξ, and η are small. Thus

$$q_n = -p + \alpha^2(x\sin\theta - y\cos\theta)$$

$$= -p + \alpha^2(1 + \xi\cos s + \eta\sin s) + \ldots\ldots \tag{7}$$

$$q_t = \alpha^2(x\cos\theta + y\sin\theta)$$

$$= \alpha^2(\eta\cos s - \xi\sin s - \Psi) + \ldots\ldots \tag{8}$$

After some algebra, equation (1) is linearized to

$$\Psi'''' + (1 + p - \alpha^2)\Psi'' + 2\alpha^2(\eta\cos s - \xi\sin s - \Psi) = 0 \tag{9}$$

Periodic solutions of Ψ are sought. Let

$$\Psi = \sum_{n=1}^{\infty} b_n \sin nNs \tag{10}$$

Equations (4) and (6) give

$$\xi = \sum_{n=1}^{\infty} \frac{b_n}{2}\left[\frac{\cos(nN-1)s}{nN-1} + \frac{\cos(nN+1)s}{nN+1}\right] \tag{11}$$

$$\eta = -\sum_{n=1}^{\infty} \frac{b_n}{2}\left[\frac{\sin(nN-1)s}{nN-1} - \frac{\sin(nN+1)s}{nN+1}\right] \tag{12}$$

from which we find

$$\eta\cos s - \xi\sin s = -\sum_{n=1}^{\infty} \frac{b_n \sin nNs}{n^2N^2 - 1} \tag{13}$$

Equation (9) becomes

$$\sum_{n=1}^{\infty} b_n \sin nNs\left[n^4N^4 - (1 + p - \alpha^2)n^2N^2 - \frac{2\alpha^2 n^2N^2}{n^2N^2 - 1}\right] = 0 \tag{14}$$

For the fundamental N-fold symmetry to exist, $b_1 \neq 0$. Thus

$$N^4 - (1 + p - \alpha^2)N^2 - \frac{2\alpha^2N^2}{N^2 - 1} = 0 \tag{15}$$

or

$$P_{cr} = N^2 - 1 + \frac{N^2 - 3}{N^2 - 1}\alpha^2 \tag{16}$$

3 Discussion

For the nonrotating case, equation (16) reduces to $p_{cr} = N^2 - 1$ in agreement with Levy [1]. Rotation increases the critical pressure but the increase is less than the centrifugal force per length represented by α^2. For two-fold buckling (most likely), the critical pressure increases by only one-third of the centrifugal force:

$$p_{cr} = 3 + \frac{\alpha^2}{3} \tag{17}$$

Equation (16) also shows that for given α, the lowest critical pressure is *always* associated with two-fold buckling. In contrast, the spring loaded ring studied in reference [7] most likely buckles at a higher-fold symmetry when the spring constant is large. Lastly, if rigidity is zero (a chain or membrane), the criterion for N-fold buckling is

$$\text{critical pressure} = \frac{N^2 - 3}{N^2 - 1}\Omega^2 R\rho \tag{18}$$

References

1 Levy, M., "Mémoire sur un Nouveau Cas Integrable du Probleme de l'Elastique et l'une de Ses Applications," *Journal de Mathematique*, (Liouville), Series 3, Volume 10, 1884, pp. 5–42.

2 Carrier, G. F., "On the Buckling of Elastic Rings," *Journal of Mathematics and Physics*, Vol. 26, 1947, pp. 94–103.

3 Singer, J. and Babcock, C. D., "On the Buckling of Rings Under Constant Directional and Centrally Directed Pressure," ASME JOURNAL OF APPLIED MECHANICS, Vol. 37, 1970, pp. 215–218.

4 Albano, E. D. and Seide, P., "Bifurcation of Circular Rings Under Concentrated Centrally Directed Loads," ASME JOURNAL OF APPLIED MECHANICS, Vol. 40, 1973, pp. 533–558.

5 Lardner, T. J., "On the Nonbuckling of a Circular Ring under a Wrapping Loading," ASME JOURNAL OF APPLIED MECHANICS, Vol. 47, 1980, pp. 973–974.

6 Schmidt, R., "Buckling of Rings Subjected to Interacting Loads," *Journal of the Engineering Mechanics Division*, ASCE, Vol. 107, 1981, pp. 421–424.

7 Wang, C. Y., Watson, L. T., and Kamat, M. P., "Buckling, Postbuckling and the Flow Through a Tethered Elastic Clyinder Under External Pressure, ASME JOURNAL OF APPLIED MECHANICS, Vol. 50, 1983, pp. 13–18.

Laminar Wall Jet of a Non-Newtonian Fluid Over a Curved Surface

Dr. Rama Subba Reddy Gorla[1]

An analysis is presented for the flow of a laminar, two-dimensional, incompressible, non-Newtonian fluid jet flowing over a curved surface. A unique similarity solution is obtained for both concave and convex surfaces. The similarity solution requires a special shape of the curved surface which is also determined. Numerical results are presented for the details of the velocity field and skin friction coefficient as a function of the curvature parameter.

Introduction

A wall jet is a fluid jet stream bounded on one side by a surface and on the other side by a quiescent fluid medium of similar composition. The present work is undertaken to investigate the problem of an incompressible, laminar, non-Newtonian fluid jet flowing along a curved wall. Figure 1 shows the coordinate system and flow development. Examples of such applications are in the liquid food processing, pulp and paper, and petrochemical industries.

For a jet to remain attached to a curved surface, a pressure gradient must exist across the jet to provide the centripetal acceleration. If the surrounding atmosphere is large, then the

[1] Professor, Department of Mechanical Engineering, Cleveland State University, Cleveland, Ohio 44115. Mem. ASME.

Manuscript received by ASME Applied Mechanics Division, February, 1983.

static pressure along the outer edge of the jet must be constant. The pressure at the wall is then lower than atmospheric pressure, with the pressure on the wall increasing with increasing streamwise distance. Therefore the jet is flowing against an adverse pressure gradient. This is the mechanism for the jet separation. Despite the mechanish of separation, there exists a shape of the wall that allows similarity for velocity profiles at all surface locations.

References [1, 2] deal with laminar wall jet flows of Newtonian fluids over curved surfaces. Literature on wall jet flows of non-Newtonian fluids over curved surfaces is scarce.

Analysis

For a laminar, steady, incompressible flow of a non-Newtonian power-law fluid, the governing equations within boundary layer approximation are given by:

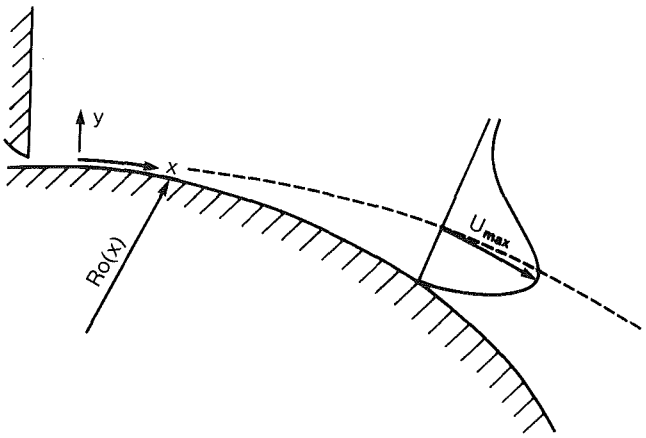

Fig. 1 Coordinate system and flow development

Mass:

$$\frac{\partial u}{\partial x}+\frac{\partial}{\partial y}\left[\left(1+\frac{y}{R_0}\right)v\right]=0 \tag{1}$$

Momentum:

$$u\frac{\partial u}{\partial x}+\left(1+\frac{y}{R_0}\right)v\frac{\partial u}{\partial y}+\frac{uv}{R_0} = -\frac{1}{\rho}\frac{\partial P}{\partial x}+\frac{K}{\rho}\frac{\partial}{\partial y}\left[\left(1+\frac{y}{R_0}\right)\left(\frac{\partial u}{\partial y}\right)^n\right] \tag{2}$$

$$\frac{u^2}{R_0}=\frac{1}{\rho}\frac{\partial P}{\partial y} \tag{3}$$

In the preceding equations, x and y are the coordinates parallel and normal to the surface, respectively, u and v are the corresponding velocity components, $R_0(x)$ the local radius of curvature of the wall, K the viscosity coefficient in Ostwald-de Waele model, ρ the density, and n the viscosity index. When $R_0>0$ the wall is convex outward and when $R_0<0$ the wall is concave. Figure 1 shows the coordinate system and flow development.

The boundary conditions representative of the flow of a jet over a surface are given by

Table 1 Values of $F''(0)$ for several values of β and η

n \ $4/\beta$	−0.03	0	+0.03	+0.05	+0.07
0.5	0.2676	0.2019	0.1009	0.09058	0.0274
0.8	0.2813	0.2069	0.1257	0.0908	0.0285
1.0	0.3021	0.2222	0.1444	0.0916	0.0305
1.5	0.2776	0.2042	0.1325	0.0843	0.0264
2.0	0.1804	0.1325	0.0872	0.0551	0.0185

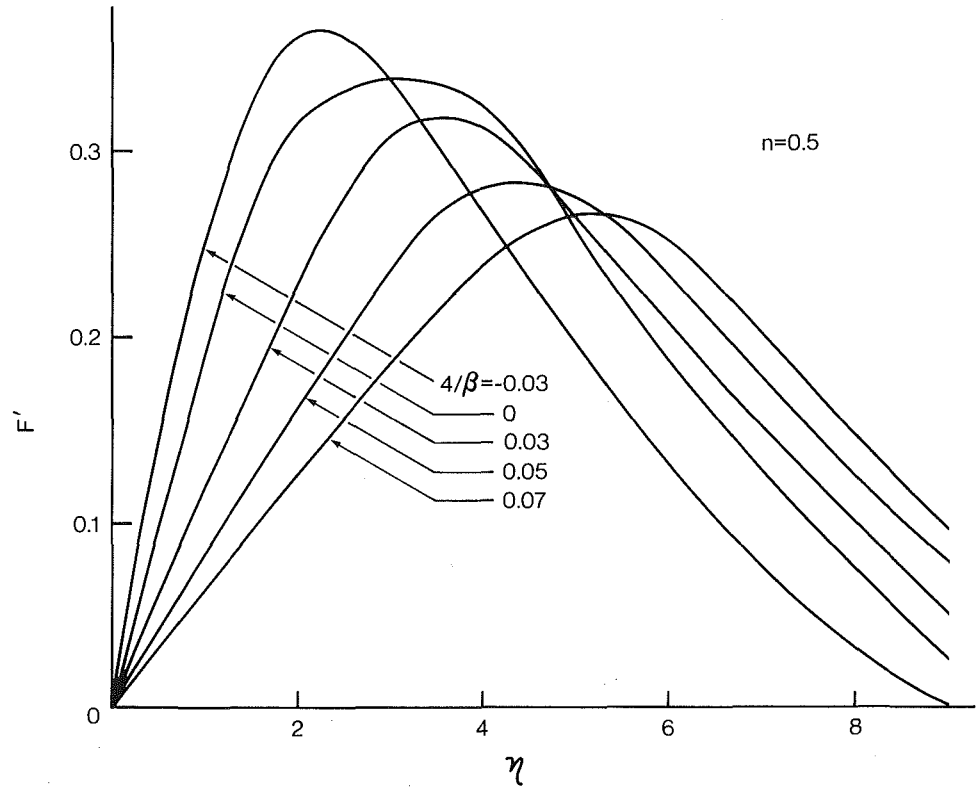

Fig. 2 Velocity distribution for various values of the curvature parameter ($n = 0.5$)

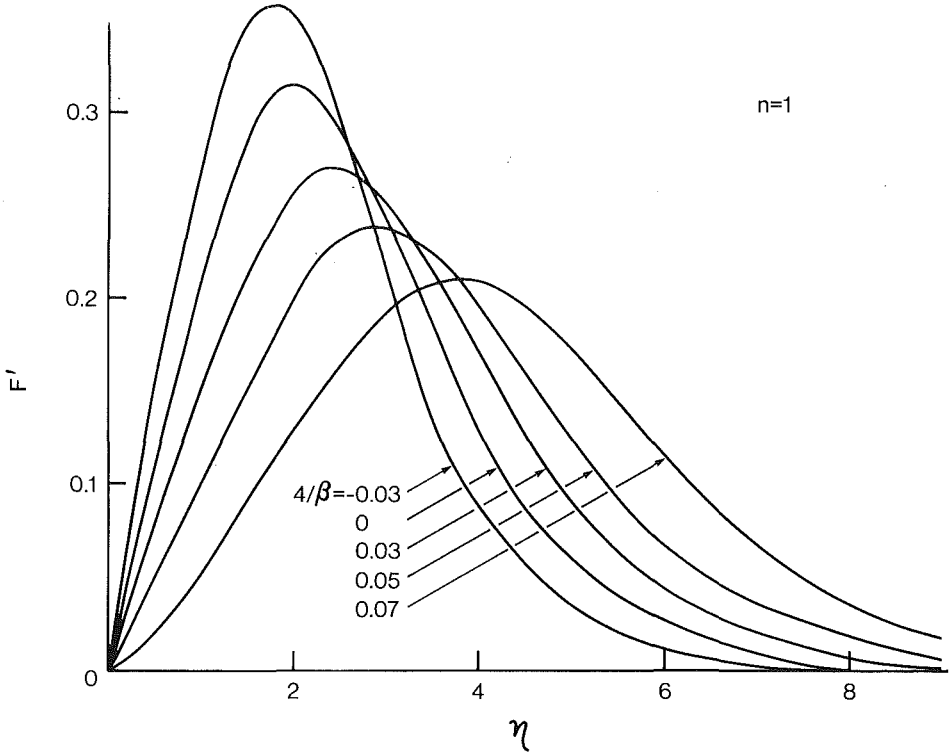

Fig. 3 Velocity distribution for various values of the curvature parameter ($n = 1.0$)

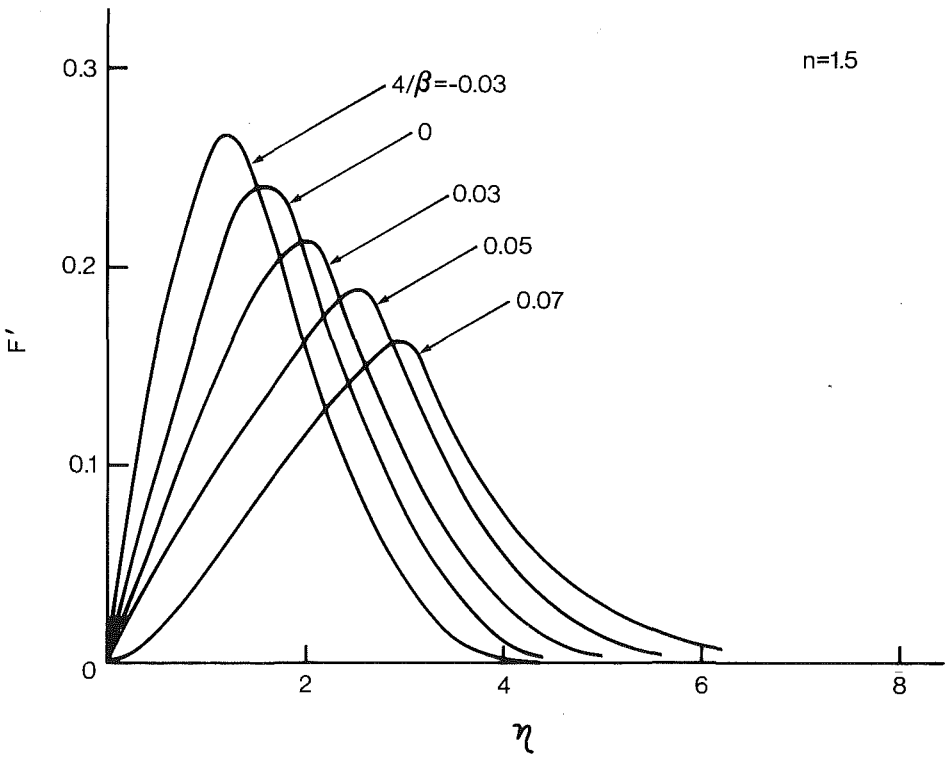

Fig. 4 Velocity distribution for various values of the curvature parameter ($n = 1.5$)

$$y=0: \quad u=v=0$$
$$y\to\infty, \quad u\to 0 \tag{4}$$

To reduce the problem to the solution of an ordinary differential equation, a search for similarity solutions has been made. We now introduce the following similarity transformation:

$$u=\frac{\partial\psi}{\partial y}$$

$$\left(1+\frac{y}{R_0}\right)v=-\frac{\partial\psi}{\partial x}$$

$$\psi=A^{(2n-1)/3}\left(\frac{K}{\rho}\right)^{\frac{1}{n+1}}\cdot x^{-D/2}\cdot F(\eta)$$

$$\eta=B\,A^{(2-n)/3}\left(\frac{K}{\rho}\right)^{-\frac{1}{(n+1)}}\cdot y\cdot x^{C}$$

$$B=(5n-1)^{-1/(2n-1)}$$

$$C=-3/(5n-1)$$

$$D=-2/(5n-1) \tag{5}$$

where ψ is the stream function. The constant A may be determined from a mass balance across the boundary layer and an assumed size of the jet slot height. The mass balance at any location x is given by

$$m=\int_0^\infty \rho u dy \tag{6}$$

Thus we may write

$$A=\left[\frac{\dot{m}}{\rho F(\infty)}\left\{\frac{B\delta_0}{\eta_\infty}\right\}^{\frac{D-C}{C}}\cdot\left(\frac{\rho}{K}\right)^{\frac{D}{C(n+1)}}\right]^{\frac{3C}{(n+1)C-(2-n)D}} \tag{7}$$

where δ_0 is the jet slot height and $F(\infty)$ is the value of $F(\eta)$ at the boundary layer edge where $\eta=\eta_\infty$. An expression for the radius of curvature R_0 is assumed to be as follows:

$$R_0=Px^Q \tag{8}$$

The search for similarity solutions has revealed that similarity solutions are possible only if

$$P=\frac{\beta}{4B}\cdot A^{\frac{n-2}{3}}\cdot\left(\frac{K}{\rho}\right)^{1/(n+1)}$$

$$Q=3/(5n-1) \tag{9}$$

It may be verified that the continuity equation is automatically satisfied. Upon substituting the expressions in equations (5), (8), and (9) into the momentum equation we obtain

$$n(F'')^{n-1}F'''+FF''+2(F')^2+\frac{4}{\beta}\left\{\eta\cdot n(F'')^{n-1}F'''+(F'')^n+\frac{F'}{\left(1+\frac{4}{\beta}\cdot\eta\right)}[F-3\eta F']-4\int_\eta^\infty (F')^2 d\eta+3\eta(F')^2\right\}=0 \tag{10}$$

The transformed boundary conditions are given by

$$F(0)=F'(0)=F'(\infty)=0 \tag{11}$$

The compatibility condition at the wall is given by

$$F'''(0)=\frac{4}{\eta\beta}\left\{-F''(0)+4[F''(0)]^{1-n}\int_0^\infty (F')^2 d\eta\right\} \tag{12}$$

Results and Discussion

The transformed momentum equation (10) has been solved numerically using the fourth-order Runge-Kutta method of numerical integration. The distribution of velocity has been illustrated in Figs. 2–4 for various values of the curvature parameter $4/\beta$ while n ranged from 0.5 to 1.5.

When $4/\beta>0$, the surface is convex and the jet is subjected to an adverse pressure gradient. When $4/\beta<0$, the surface is concave and the pressure gradient is favorable. $4/\beta=0$ would correspond to the solution of the problem of the wall jet of a non-Newtonian fluid over a plane surface. When $4/\beta=0$ and $n=1$, we obtain the Glauert's solution [3] of the wall jet of a Newtonian fluid over a plane surface. From the results obtained, we see that as $4/\beta$ increases, the jet becomes wider and the velocity profile develops an inflection point farther away from the wall. In many practical applications, the surface characteristics such as the skin friction coefficient are important. Table 1 gives the values of $F''(0)$ for a range of values of β and n. This information is useful to compute the wall shear stress.

References

1 Wygnanski, I. J., and Champagne, F. H., "The Laminar Wall-Jet Over a Curved Surface," *Journal of Fluid Mechanics*, Vol. 31, 1968, pp. 459–465.

2 Gorla, R. S. R., "Heat Transfer in a Laminar Wall Jet Over a Curved Surface," *Applied Scientific Research*, Vol. 31, 1976, pp. 437–444.

3 Glauert, M. B., "The Wall Jet," *Journal of Fluid Mechanics*, Vol. 1, 1956, pp. 625–643.

Divergence of Cantilever Columns Under Combined Conservative and Follower Loads

A. H. Flax[1]

It is known [1, 2] that cantilever columns with uniform elastic and mass properties under a variety of nonconservative follower loads do not become unstable by static divergence (buckling) but rather may experience divergent oscillations (flutter). For the case of combined conservative and follower compressive loads applied at the free end, it has been found [2, 3] for the uniform cantilever column that when the follower load is greater than the conservative load the mode of instability cannot be static buckling but must be oscillatory divergent, i.e., the column does not become unstable by passing through a condition of zero frequency. Also, for uniform cantilever columns under combined conservative and follower loads, similarly distributed, numerical results for uniform [4] and triangular [5] load distributions indicate that static divergence does not occur when the magnitude of the follower loading exceeds that of the conservative loading. The present investigation deals with nonuniform cantilever columns under general end and distributed loading, both conservative and follower, as portrayed in Fig. 1. It leads to criterion for the nonexistence of static divergence in terms of the relationship between the conservative and follower loads.

Analysis

The differential equation of motion of a nonuniform cantilever column compressed by conservative and follower forces is:

$$(EIy'')''+(P_c y')'+P_f y''+m\lambda^2 y=0 \tag{1}$$

where y is the lateral deflection, x is the coordinate along the column, and primes indicate differentiation with respect to x. P_c is the total compressive force at any point due to conservative loads, P_f is the total compressive load at any point due to follower loads, EI is the bending stiffness, and m is the mass per unit length. λ is in general complex and is defined by the representation of the motion in time as $\bar{y}(x, t) = y(x) \exp \lambda t$.

The boundary conditions are:

$$y(0) = y'(0) = 0$$

$$y''(l) = 0;\ [EIy''(l)]' = -P_c y'(l) \tag{2}$$

[1] Institute for Defense Analyses, Alexandria, Va. 22311. Manuscript received by ASME Applied Mechanics Division, August, 1983; final revision, November, 1983.

$$\left(1+\frac{y}{R_0}\right)v=-\frac{\partial\psi}{\partial x}$$

$$\psi=A^{(2n-1)/3}\left(\frac{K}{\rho}\right)^{\frac{1}{n+1}}\cdot x^{-D/2}\cdot F(\eta)$$

$$\eta=B\,A^{(2-n)/3}\left(\frac{K}{\rho}\right)^{-\frac{1}{(n+1)}}\cdot y\cdot x^{C}$$

$$B=(5n-1)^{-1/(2n-1)}$$

$$C=-3/(5n-1)$$

$$D=-2/(5n-1) \tag{5}$$

where ψ is the stream function. The constant A may be determined from a mass balance across the boundary layer and an assumed size of the jet slot height. The mass balance at any location x is given by

$$m=\int_0^\infty \rho u dy \tag{6}$$

Thus we may write

$$A=\left[\frac{\dot{m}}{\rho F(\infty)}\left\{\frac{B\delta_0}{\eta_\infty}\right\}^{\frac{D-C}{C}}\cdot\left(\frac{\rho}{K}\right)^{\frac{D}{C(n+1)}}\right]^{\frac{3C}{(n+1)C-(2-n)D}} \tag{7}$$

where δ_0 is the jet slot height and $F(\infty)$ is the value of $F(\eta)$ at the boundary layer edge where $\eta=\eta_\infty$. An expression for the radius of curvature R_0 is assumed to be as follows:

$$R_0=Px^Q \tag{8}$$

The search for similarity solutions has revealed that similarity solutions are possible only if

$$P=\frac{\beta}{4B}\cdot A^{\frac{n-2}{3}}\cdot\left(\frac{K}{\rho}\right)^{1/(n+1)}$$

$$Q=3/(5n-1) \tag{9}$$

It may be verified that the continuity equation is automatically satisfied. Upon substituting the expressions in equations (5), (8), and (9) into the momentum equation we obtain

$$n(F'')^{n-1}F'''+FF''+2(F')^2+\frac{4}{\beta}\left\{\eta\cdot n(F'')^{n-1}F'''+(F'')^n+\frac{F'}{\left(1+\frac{4}{\beta}\cdot\eta\right)}[F-3\eta F']-4\int_\eta^\infty (F')^2 d\eta+3\eta(F')^2\right\}=0 \tag{10}$$

The transformed boundary conditions are given by

$$F(0)=F'(0)=F'(\infty)=0 \tag{11}$$

The compatibility condition at the wall is given by

$$F'''(0)=\frac{4}{\eta\beta}\left\{-F''(0)+4[F''(0)]^{1-n}\int_0^\infty (F')^2 d\eta\right\} \tag{12}$$

Results and Discussion

The transformed momentum equation (10) has been solved numerically using the fourth-order Runge-Kutta method of numerical integration. The distribution of velocity has been illustrated in Figs. 2–4 for various values of the curvature parameter $4/\beta$ while n ranged from 0.5 to 1.5.

When $4/\beta>0$, the surface is convex and the jet is subjected to an adverse pressure gradient. When $4/\beta<0$, the surface is concave and the pressure gradient is favorable. $4/\beta=0$ would correspond to the solution of the problem of the wall jet of a non-Newtonian fluid over a plane surface. When $4/\beta=0$ and $n=1$, we obtain the Glauert's solution [3] of the wall jet of a Newtonian fluid over a plane surface. From the results obtained, we see that as $4/\beta$ increases, the jet becomes wider and the velocity profile develops an inflection point farther away from the wall. In many practical applications, the surface characteristics such as the skin friction coefficient are important. Table 1 gives the values of $F''(0)$ for a range of values of β and n. This information is useful to compute the wall shear stress.

References

1 Wygnanski, I. J., and Champagne, F. H., "The Laminar Wall-Jet Over a Curved Surface," *Journal of Fluid Mechanics*, Vol. 31, 1968, pp. 459–465.

2 Gorla, R. S. R., "Heat Transfer in a Laminar Wall Jet Over a Curved Surface," *Applied Scientific Research*, Vol. 31, 1976, pp. 437–444.

3 Glauert, M. B., "The Wall Jet," *Journal of Fluid Mechanics*, Vol. 1, 1956, pp. 625–643.

Divergence of Cantilever Columns Under Combined Conservative and Follower Loads

A. H. Flax[1]

It is known [1, 2] that cantilever columns with uniform elastic and mass properties under a variety of nonconservative follower loads do not become unstable by static divergence (buckling) but rather may experience divergent oscillations (flutter). For the case of combined conservative and follower compressive loads applied at the free end, it has been found [2, 3] for the uniform cantilever column that when the follower load is greater than the conservative load the mode of instability cannot be static buckling but must be oscillatory divergent, i.e., the column does not become unstable by passing through a condition of zero frequency. Also, for uniform cantilever columns under combined conservative and follower loads, similarly distributed, numerical results for uniform [4] and triangular [5] load distributions indicate that static divergence does not occur when the magnitude of the follower loading exceeds that of the conservative loading. The present investigation deals with nonuniform cantilever columns under general end and distributed loading, both conservative and follower, as portrayed in Fig. 1. It leads to criterion for the nonexistence of static divergence in terms of the relationship between the conservative and follower loads.

Analysis

The differential equation of motion of a nonuniform cantilever column compressed by conservative and follower forces is:

$$(EIy'')''+(P_c y')'+P_f y''+m\lambda^2 y=0 \tag{1}$$

where y is the lateral deflection, x is the coordinate along the column, and primes indicate differentiation with respect to x. P_c is the total compressive force at any point due to conservative loads, P_f is the total compressive load at any point due to follower loads, EI is the bending stiffness, and m is the mass per unit length. λ is in general complex and is defined by the representation of the motion in time as $\bar{y}(x, t) = y(x) \exp \lambda t$.

The boundary conditions are:

$$y(0) = y'(0) = 0$$

$$y''(l) = 0;\ [EIy''(l)]' = -P_c y'(l) \tag{2}$$

[1] Institute for Defense Analyses, Alexandria, Va. 22311. Manuscript received by ASME Applied Mechanics Division, August, 1983; final revision, November, 1983.

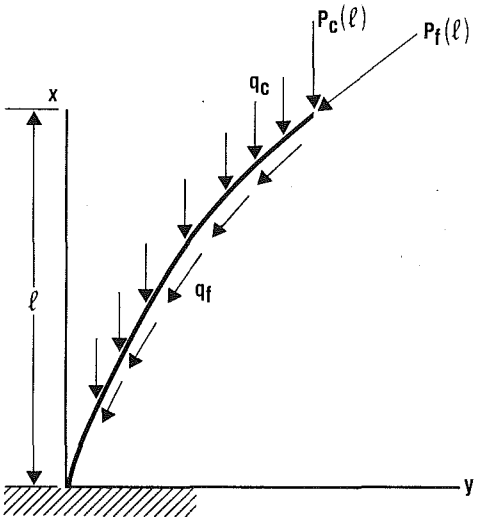

Fig. 1 Cantilever column under combined conservative and follower loading.

where the root of the cantilever is at $x = 0$ while the free end is at $x = l$.

Multiplying equation (1) by $y'(x)$ and performing several integrations and integrations by parts taking into account the boundary conditions leads to:

$$\frac{EI(0)}{2}[y''(0)]^2 - \frac{1}{2}\int_0^l EI'(y'')^2 dx + \frac{[P_f(l) - P_c(l)]}{2}$$

$$[y'(l)]^2 + \frac{1}{2}\int_0^l (q_f - q_c)(y')^2 dx + \lambda^2 \frac{m(l)}{2}[y(l)]^2$$

$$- \frac{\lambda^2}{2}\int_0^l m' y^2 dx = 0. \quad (3)$$

Here the values of P_c (l) and P_f (l) are the concentrated conservative and follower loads, respectively, at the tip, while $-P_c'(x)$ and $-P_f'(x)$ are the distributed conservative and follower loads, q_c and q_f, respectively, applied along the column. Thus, if the bending stiffness, EI, always decreases toward the tip of the column, then for $\lambda = 0$ (the static buckling condition) all the terms in equation (3) will be nonnegative for $P_f \geq P_c$ and $q_f \geq q_c$ and the equation cannot be satisfied so that no static buckling is possible. There is, however the possibility of a real positive or negative value of λ corresponding to either damped or divergent nonoscillatory motion arrived at without going through $\lambda = 0$. (A special purely theoretical case of this sort is the massless column with a concentrated weight at the tip [3, 6]). The possibility of this type of motion is also foreclosed by equation (3) if, in addition, the mass per unit length, m, decreases monotonically toward the tip so that m' is everwhere negative.

Conclusion

It has been shown that for nonuniform cantilever columns with bending stiffness monotonically decreasing from root to tip subject to end and distributed compressive loads of both conservative and follower force types, static buckling at zero frequency cannot occur if the magnitude of all follower compressive loads exceeds the magnitude of conservative compressive loads applied at all points along the column. If, in addition, the mass distribution decreases monotonically from root to tip, nonoscillatory damped or divergent motions also are precluded even if they were to be arrived at without going through zero frequency. Thus, under these conditions, only oscillatory divergent instability (flutter) is possible. It should be noted, however, that the analysis given here does not actually predict that any instability will occur. Rather, the loading conditions under which static buckling and nonoscillatory divergent motions cannot occur are determined. The result is in agreement with specific cases for which numerical results are given in the literature.

References

1 Bolotin, V. V., *Nonconservative Problems of the Theory of Elastic Stability*, Macmillan, New York, 1963, pp. 7–17; pp. 100–104.

2 Leipholz, H., *Stability Theory*, Academic Press, New York, 1970, p. 244.

3 Panovko, Y. G., and Gubanova, I. I., *Stability and Oscillation of Elastic Systems*, Consultants Bureau, New York, 1965, pp. 57–72.

4 Sugiyama, Y., and Kawagoe, H., "Vibration and Stability of Elastic Columns Under the Combined Action of Uniformly Distributed Vertical and Tangential Forces," *Journal of Sound and Vibration*, Vol. 38, No. 3, 1975, pp. 341–355.

5 Sugiyama, Y., and Mladenov, K. A., "Vibrations and Stability of Elastic Columns Subjected to Triangularly Distributed Sub-Tangential Forces," *Journal of Sound and Vibration*, Vol. 88, No. 4, 1983, pp. 447–457.

6 Flax, A. H., "Comment on 'Some Remarks on the Beck Problem,' " *AIAA Journal*, Vol. 16, No. 8, Aug. 1978, pp. 861–62.

On a Variational Principle for Elastic Displacements and Pressure[1]

E. Reissner[2]

Introduction

In what follows we obtain a generalization of a variational principle in *geometrically* linear elasticity, for displacements u_i and for a suitably defined pressure variable p, which is known to be of technical significance for incompressible or nearly incompressible materials. Recognition of the possibility and importance of such a principle for the case of physically linear *isotropic* elasticity, as well as its formulation for this case, is due to L. R. Herrmann [1]. A generalization of Herrmann's result to the case of *anisotropic* physically linear materials has been given by S. W. Key [2]. Our purpose here is a simple and direct derivation of the corresponding result for *physically non*linear materials.

Derivation

We depart from a statement of the variational principle for displacements, in the form

$$\delta\int U(\epsilon_{ij})\,dV = 0, \quad (1)$$

where $\epsilon_{ij} \equiv 1/2\,(u_{i,j} + u_{j,i})$ and where, for simplicity's sake, we assume that body forces are absent and that all boundary conditions are displacement conditions. As is well known, equation (1), with the further defining (or constraint) relations $\sigma_{ij} = \partial U/\partial\epsilon_{ij}$, has as its Euler equations the differential equations of equilibrium for stress.

To retain the technical significance of (1) for cases for which the form of U is such as to make the sum ϵ_{kk} exactly or nearly equal to zero we introduce, following Herrmann and Key, the alternate strain variables

[1] Based on work supported by National Science Foundation Grant No. CEE-8213256.

[2] Department of Applied Mechanics and Engineering Sciences, University of California, San Diego, La Jolla, Calif. 92093. Fellow ASME.

Manuscript received by ASME Applied Mechanical Division, November, 1983.

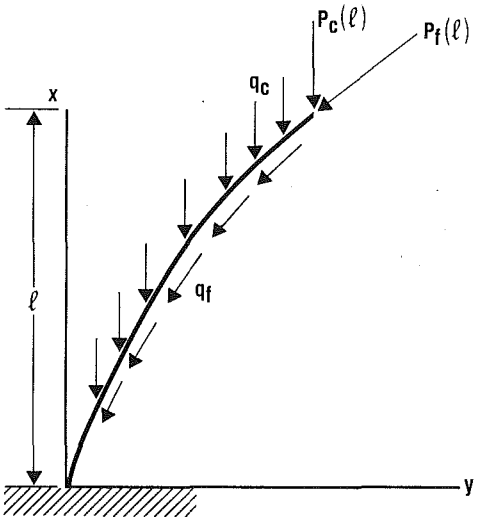

Fig. 1 Cantilever column under combined conservative and follower loading.

where the root of the cantilever is at $x = 0$ while the free end is at $x = l$.

Multiplying equation (1) by $y'(x)$ and performing several integrations and integrations by parts taking into account the boundary conditions leads to:

$$\frac{EI(0)}{2}[y''(0)]^2 - \frac{1}{2}\int_0^l EI'(y'')^2 dx + \frac{[P_f(l) - P_c(l)]}{2}$$

$$[y'(l)]^2 + \frac{1}{2}\int_0^l (q_f - q_c)(y')^2 dx + \lambda^2 \frac{m(l)}{2}[y(l)]^2$$

$$- \frac{\lambda^2}{2}\int_0^l m' y^2 dx = 0. \quad (3)$$

Here the values of $P_c(l)$ and $P_f(l)$ are the concentrated conservative and follower loads, respectively, at the tip, while $-P_c'(x)$ and $-P_f'(x)$ are the distributed conservative and follower loads, q_c and q_f, respectively, applied along the column. Thus, if the bending stiffness, EI, always decreases toward the tip of the column, then for $\lambda = 0$ (the static buckling condition) all the terms in equation (3) will be nonnegative for $P_f \geq P_c$ and $q_f \geq q_c$ and the equation cannot be satisfied so that no static buckling is possible. There is, however the possibility of a real positive or negative value of λ corresponding to either damped or divergent nonoscillatory motion arrived at without going through $\lambda = 0$. (A special purely theoretical case of this sort is the massless column with a concentrated weight at the tip [3, 6]). The possibility of this type of motion is also foreclosed by equation (3) if, in addition, the mass per unit length, m, decreases monotonically toward the tip so that m' is everwhere negative.

Conclusion

It has been shown that for nonuniform cantilever columns with bending stiffness monotonically decreasing from root to tip subject to end and distributed compressive loads of both conservative and follower force types, static buckling at zero frequency cannot occur if the magnitude of all follower compressive loads exceeds the magnitude of conservative compressive loads applied at all points along the column. If, in addition, the mass distribution decreases monotonically from root to tip, nonoscillatory damped or divergent motions also are precluded even if they were to be arrived at without going through zero frequency. Thus, under these conditions, only oscillatory divergent instability (flutter) is possible. It should be noted, however, that the analysis given here does not actually predict that any instability will occur. Rather, the loading conditions under which static buckling and nonoscillatory divergent motions cannot occur are determined. The result is in agreement with specific cases for which numerical results are given in the literature.

References

1 Bolotin, V. V., *Nonconservative Problems of the Theory of Elastic Stability*, Macmillan, New York, 1963, pp. 7–17; pp. 100–104.

2 Leipholz, H., *Stability Theory*, Academic Press, New York, 1970, p. 244.

3 Panovko, Y. G., and Gubanova, I. I., *Stability and Oscillation of Elastic Systems*, Consultants Bureau, New York, 1965, pp. 57–72.

4 Sugiyama, Y., and Kawagoe, H., "Vibration and Stability of Elastic Columns Under the Combined Action of Uniformly Distributed Vertical and Tangential Forces," *Journal of Sound and Vibration*, Vol. 38, No. 3, 1975, pp. 341–355.

5 Sugiyama, Y., and Mladenov, K. A., "Vibrations and Stability of Elastic Columns Subjected to Triangularly Distributed Sub-Tangential Forces," *Journal of Sound and Vibration*, Vol. 88, No. 4, 1983, pp. 447–457.

6 Flax, A. H., "Comment on 'Some Remarks on the Beck Problem,' " *AIAA Journal*, Vol. 16, No. 8, Aug. 1978, pp. 861–62.

On a Variational Principle for Elastic Displacements and Pressure[1]

E. Reissner[2]

Introduction

In what follows we obtain a generalization of a variational principle in *geometrically* linear elasticity, for displacements u_i and for a suitably defined pressure variable p, which is known to be of technical significance for incompressible or nearly incompressible materials. Recognition of the possibility and importance of such a principle for the case of physically linear *isotropic* elasticity, as well as its formulation for this case, is due to L. R. Herrmann [1]. A generalization of Herrmann's result to the case of *anisotropic* physically linear materials has been given by S. W. Key [2]. Our purpose here is a simple and direct derivation of the corresponding result for *physically non*linear materials.

Derivation

We depart from a statement of the variational principle for displacements, in the form

$$\delta\int U(\epsilon_{ij})\, dV = 0, \quad (1)$$

where $\epsilon_{ij} \equiv 1/2\,(u_{i,j} + u_{j,i})$ and where, for simplicity's sake, we assume that body forces are absent and that all boundary conditions are displacement conditions. As is well known, equation (1), with the further defining (or constraint) relations $\sigma_{ij} = \partial U/\partial\epsilon_{ij}$, has as its Euler equations the differential equations of equilibrium for stress.

To retain the technical significance of (1) for cases for which the form of U is such as to make the sum ϵ_{kk} exactly or nearly equal to zero we introduce, following Herrmann and Key, the alternate strain variables

[1] Based on work supported by National Science Foundation Grant No. CEE-8213256.

[2] Department of Applied Mechanics and Engineering Sciences, University of California, San Diego, La Jolla, Calif. 92093. Fellow ASME.

Manuscript received by ASME Applied Mechanical Division, November, 1983.

$$\epsilon'_{ij} = \epsilon_{ij} - \frac{1}{3}\delta_{ij}\theta, \tag{2}$$

where

$$\theta = \epsilon_{kk}, \tag{3}$$

and we write with this

$$U(\epsilon_{ij}) = U(\epsilon'_{ij}) + U'(\epsilon'_{ij},\theta). \tag{4}$$

Having (3) and (4) we rewrite (1), with the introduction of a multiplier p, in the form

$$\delta\int[U(\epsilon'_{ij}) + U'(\epsilon'_{ij},\theta) + p(\epsilon_{kk} - \theta)]dV = 0. \tag{5}$$

We will transform (5) into what is wanted by stipulating p to be given by

$$p = \frac{\partial U'}{\partial \theta}, \tag{6}$$

and by using the inversion $\theta = \theta(\epsilon'_{ij}, p)$ of this to define a complementary function

$$W(\epsilon'_{ij},p) = p\theta - U'(\epsilon'_{ij},\theta). \tag{7}$$

An introduction of U' from (7) into (5) transforms (5) into

$$\delta\int[U(\epsilon'_{ij}) + p\epsilon_{kk} - W(\epsilon'_{ij},p)]dV = 0, \tag{8}$$

where now, in view of (2) and (3), $\epsilon'_{ij} = \epsilon_{ij} - 1/3\ \delta_{ij}\epsilon_{kk}$, with independent δu_i and δp, and with this being in essence the desired result.

Given that (8) is readily shown to be equivalent to the relation

$$\int\int\int\left[\frac{\partial(U-W)}{\partial\epsilon'_{ij}} - \frac{\delta_{ij}}{3}\left(\frac{\partial}{\partial\epsilon'_{11}} + \frac{\partial}{\partial\epsilon'_{22}} + \frac{\partial}{\partial\epsilon'_{33}}\right)(U-W) + \delta_{ij}p\right]\delta\epsilon_{ij} + \left(\epsilon_{kk} - \frac{\partial W}{\partial p}\right)\delta p\Bigg\}dV = 0, \tag{9}$$

we, incidentally, have as a "parametric" version of the constitutive relations $\sigma_{ij} = \partial U/\partial\epsilon_{ij}$,

$$\sigma_{ij} = \frac{\partial(U-W)}{\partial\epsilon'_{ij}} - \frac{\delta_{ij}}{3}\left(\frac{\partial}{\partial\epsilon'_{11}} + \frac{\partial}{\partial\epsilon'_{22}} + \frac{\partial}{\partial\epsilon'_{33}}\right)(U-W) + \delta_{ij}p, \tag{10a}$$

$$\epsilon_{kk} = \frac{\partial W}{\partial p}. \tag{10b}$$

Determination of the Complementary Function

Determination of W for the case of a physically linear material, with $U = U_1(\epsilon_{ij}) + U_2(\epsilon_{ij})$ where U_1 and U_2 are homogeneous first and second-degree polynomials, respectively, is a simple matter. We can now write, in accordance with (4)

$$U = U_1(\epsilon'_{ij}) + U_2(\epsilon'_{ij}) + \theta\ U_{10} + \theta\ U_{21}(\epsilon'_{ij}) + \frac{1}{2}\theta^2 U_{20}, \tag{11}$$

where U_{10} and U_{20} may depend on x_i, but not on the ϵ'_{ij}, and, in accordance with (6),

$$p = U_{10} + U_{21}(\epsilon'_{ij}) + \theta\ U_{20}. \tag{12}$$

The introduction of (12) into (7) gives

$$W = (U_{10} + U_{21})\theta + U_{20}\theta^2 - \left[(U_{10} + U_{21})\theta + \frac{1}{2}U_{20}\theta^2\right]$$

$$= \frac{1}{2}U_{20}\theta^2 = \frac{1}{2}[p - U_{10} - U_{21}(\epsilon'_{ij})]^2 U_{20}^{-1}, \tag{13}$$

and therewith

$$U(\epsilon'_{ij}) - W(\epsilon'_{ij},p) = U_1(\epsilon'_{ij}) + U_2(\epsilon'_{ij}) - \frac{[p - U_{10} - U_{21}(\epsilon'_{ij})]^2}{2U_{20}}. \tag{14}^3$$

A corresponding *explicit* determination of W, in accordance with (6) and (7), for physically nonlinear materials, is in general not possible. An obvious exception to this difficulty is given by the class of materials for which $U = U_1(\epsilon_{ij}) + U_2(\epsilon_{ij}) + (\epsilon_{kk})^2 F(\epsilon_{12},\epsilon_{13},\epsilon_{23})$.

References

1 Herrmann, L. R., "Elasticity Equations for Incompressible or Nearly Incompressible Materials by a Variational Theorem," *AIAA J.*, Vol. 3, 1965, pp. 1896–1900.

2 Key, S. W., "A Variational Principle for Incompressible or Nearly Incompressible Anisotropic Elasticity," *Int. J. Solids Structures*, Vol. 5, 1969, pp. 951–964.

[3] This result is consistent with the contents of equation (16) in [2], upon writing $(p - U_{10} - U_{21})^2 = (p - U_{21})^2 - 2(p - U_{21})U_{10} + U_{10}^2$, and discarding the additive quantity $U_{10}^2/2U_{20}$ in (14), which is of no relevance for the variational statement.

Journal of Applied Mechanics

Discussion

Cable Kink Analysis: Cable Loop Stability Under Tension[1]

F. Rosenthal[2]. Yabuta, Yoshizawa, and Kojima's paper on cable kink analysis [1] presents an interesting analysis of the stability of looped cables. However, this paper does not do full justice to the fundamental rod or cable property affecting kinking which was first discovered by A. G. Greenhill in 1883 [2]. For cables under combined tension and torsion, the instability leading to kinking occurs exactly and at times violently, when Greenhill's condition is met, e.g., when the tension is sufficiently small compared to the twisting moment so that

$$\frac{TL^2}{EI} = \frac{1}{4}\left(\frac{ML}{EI}\right)^2 - \pi^2$$

where T, L, EI, and M are the tension, length, bending stiffness, and twisting moment on the cable.

The kinked configuration depicted in the authors' Fig. 1(*b*) depends for its stability on the fact that the cable crosses over itself at one point, thus providing two equal and opposite out-of plane forces, one at each end of the loop's circular segment. As the twisting moment is lowered, such a loop can and will begin to "unkink" precisely at that instant when the mutual contact forces become zero. But from the point of view of strain energy within the loop, these contact forces are reflected in a combination of twisting and out-of plane bending (neglecting shear) strains. Therefore, an energy analysis of "unkinking" must take into account the strain energy resulting from out of plane bending in the loop segment of the cable, as well as that due to twisting. I believe the authors' analysis does not contain this effect.

A more detailed discussion of the kinking problem and its relationship is Greenhills' work may be found in references [3] and [4].

References

1 Yabuta, T., Yoshiziwa, N., and Kojima, N., "Cable Kink Analysis: Cable Loop Stability Under Tension," ASME JOURNAL OF APPLIED MECHANICS, Vol. 49, 1982, pp. 584-588.

2 Greenhill, A. G., Proc. Inst. of Mechanical Engineers, London, 1883.

3 Rosenthal, F., "The Application of Greenhill's Formula to Cable Hockling," ASME JOURNAL OF APPLIED MECHANICS, Vol. 43, 1976, pp. 681-683.

4 Rosenthal, F., "Greenhill's Formula and the Mechanics of Cable Hockling," Naval Research Laboratory NRL Report 7940, Nov. 7, 1975.

[1] By T. Yabuta, N. Yoshiziwa, and N. Kojima and published in the September, 1982 issue of the ASME JOURNAL OF APPLIED MECHANICS, Vol. 49, pp. 584-588.

[2] Marine Technology Division, Naval Research Laboratory, Washington, D.C. 20375.

Authors' Closure

The authors would like to thank F. Rosenthal for his interest in our paper [1].

We think that cable kink phenomenon is divided into two instability processes in cable kink occurrence. The first instability is cable loop formation due to torsional stress. The second instability is the reopening of the cable loops after cable loop formation due to subsequent tension increase. Our paper dealt with the second problem and clarified the conditions in which cable loops reopen. Rosenthal pointed out that our analysis does not do full justice to Greenhill's condition, which defines the fundamental conditions of cable kinks. However, Greenhill's condition is concerned with cable loop formation, which is only the first problem of our cable kink definition. Therefore, we believe our analysis is not concerned with Greenhill's condition because our analysis deals with only the second problem. Ross studied the first problem of cable loop deformation with the potential energy method [2]. He found that Greenhill's condition defines the upper bound of cable loop formation when compared to experimental results.

Rosenthal also pointed out that our analysis does not contain the effect of "out of plane bending." However, we believe that our analysis contains this effect. That is, our analysis uses a helix assumption for cable deformation which contains "out of plane deformation," as shown in Fig. 2 in reference [1]. Therefore, bending strain energy is obtained from the curvature of the helix, and also considers "out of plane bending."

Moreover, Rosenthal commented on our problem from an "out of plane force" viewpoint. Zajac showed interesting results of a similar problem from a force equilibrium viewpoint [3].

Although we did not compare theoretical results with experimental results in the original paper, since then we have made the comparison, the results of which are discussed in reference [4]. Reference [4] also shows cable kink deformation modes from a cable slack viewpoint, which is a main factor during cable laying.

References

1 Yabuta, T., Yoshizawa, N., and Kojima, N., "Cable Kink Analysis; Cable Loop Stability Under Tension," ASME JOURNAL OF APPLIED MECHANICS, Vol. 49, 1982, pp. 584-588.

2 Ross, A. L., "Cable Kinking Analysis and Prevention," ASME *Journal of Engineering for Industry*, Vol. 99, 1977, pp. 112-115.

3 Zajac, E. E., "Stability of Two Planar Loop Elastica," ASME JOURNAL OF APPLIED MECHANICS, Vol. 29, 1962, pp. 136-142.

4 Yabuta, T., "Submarine Cable Kink Analysis," *Bulletin of the JSME*, to appear in September 1984 issue.

An Efficient Method for Computing the Critical Damping Condition[1]

B. L. Ly.[2] The authors clarify the definition of critical damping in multidegree-of-freedom systems, and provide an efficient method based on Cayley-Hamilton theorem for computing the critical damping matrix.

It is noted that if the dynamic system has a discrete frequency spectrum in which all the frequencies are distinct, the constants β_j in (8) of the paper can also be determined by comparing the coefficients of the corresponding Ω^j terms in the following expression:

$$\sum_{j=0}^{n-1} \beta_j \Omega^j = \sum_{k=1}^{n} 2\sqrt{\omega_k} \frac{\prod_{i \neq k} (\Omega - \omega_i I)}{\prod_{i \neq k} (\omega_k - \omega_i)}, \tag{1}$$

where Ω is a diagonal matrix the elements of which are the radian natural frequencies ω_n of the system. The right-hand-side of (1) is obtained by using Sylvester's theorem. For the example considered in the paper, equation (1) when written in full yields

$$\beta_0 I + \beta_1 \Omega = \frac{2\sqrt{\omega_1}(\Omega - \omega_2 I)}{\omega_1 - \omega_2} + \frac{2\sqrt{\omega_2}(\Omega - \omega_1 I)}{\omega_2 - \omega_1}$$
$$= \frac{2\sqrt{\omega_1 \omega_2}(\sqrt{\omega_2} - \sqrt{\omega_1})I}{\omega_2 - \omega_1} + \frac{2(\sqrt{\omega_2} - \sqrt{\omega_1})\Omega}{\omega_2 - \omega_1}. \tag{2}$$

It follows immediately that $\beta_0 = 2\sqrt{\omega_1 \omega_2}(\sqrt{\omega_2} - \sqrt{\omega_1})/\omega_2 - \omega_1$, and $\beta_1 = 2(\sqrt{\omega_2} - \sqrt{\omega_1})/\omega_2 - \omega_1$, which are the same as would have been given by (10) of the paper.

It is also noted that the critical damping matrix can also be evaluated from

$$C_{cr} = 2M^{1/2} \Psi \Omega \Psi' M^{1/2} \tag{3}$$

where Ψ is the normalized modal matrix (i.e., $\Psi' \Psi = I$) the column vectors of which are the classical normal modes. Equation (3) is an alternative form to the expression derived by Inman and Andry [1] and Gray and Andry [2]. The presence of Ψ in (3) should not pose a serious hindrance to the practical applications of this expression because highly efficient commercial computer programs are available for the solution of the natural frequencies and the mode shapes. In fact, there is a trade-off between the authors' method and (3) because the former requires an evaluation of the inverse of a matrix and the $\tilde{K}^j$.

Finally, a point not directly related to the paper but interesting to note, if the system is critically damped it possesses the classical normal modes. The proof follows immediately from

$$\Psi' M^{-1/2} C_{cr} M^{-1/2} \Psi = 2\Psi' (M^{-1/2} K M^{-1/2})^{1/2} \Psi = 2\Omega, \tag{4}$$

or upon the substitution of $(M^{-1/2} C_{cr} M^{-1/2})^2 = 4M^{-1/2} K M^{-1/2}$ into Caughey and O'Kelly's necessary and sufficient condition

$$(M^{-1/2} C M^{-1/2})(M^{-1/2} K M^{-1/2}) = (M^{-1/2} K M^{-1/2})(M^{-1/2} C M^{-1/2}). \tag{5}$$

Authors' Closure

The discussion by Ly brings out several interesting points and is very much appreciated. Ly's equation (1) provides a viable alternative to computing the critical damping matrix. However, our second objective was to seek a computationally more efficient means of computing C_{cr} and the left-hand side of Ly's equation(1) would require symbolic manipulation in order to evaluate the coefficients of the powers of Ω for systems with more than two degrees of freedom.

The second point made by Ly is an alternative statement of the critical damping matrix in terms of the modal matrix ψ. This, of course, can be further simpilfied by first normalizing the eigenvectors of K with respect to the mass matrix M. That is, let S be the modal matrix of n such that $S^T K S = \Lambda$ and $S^T M S = I$. Then the critical damping matrix C_{cr} becomes

$$C_{cr} = 2\, SM\Omega MS^T \tag{1}$$

where $\Omega = \Lambda^{1/2}$. The difference, as Ly suggests, is that in his equation (3), as well as in the variations given in [1, 2] and equation (1) in the foregoing, there is a playoff between calculating eigenvectors, and inverting a matrix along with calculating the powers of $\tilde{K}$. The method of Ly's equation (1) is attractive because it requires neither the calculation of an inverse nor the computation of eigenvectors.

The last point made by Ly is that if a system is critically damped it must possess classical normal modes. This has been pointed out in [3] in a slightly different coordinate system. Namely, Caughey and O'Kelley's condition for classical normal modes is equivalent to requiring that $\tilde{C}\tilde{K} = \tilde{K}\tilde{C}$. Since for critical damping $C = 2\,\tilde{K}^{1/2}$ and since a matrix commutes with its powers, critically damped systems possess classical normal modes.

References

1 Inman, D. J., and Andry, A. N. Jr., "Some Results on the Nature of Eigenvalues of Discrete Damped Linear Systems," ASME JOURNAL OF APPLIED MECHANICS, Vol. 47, 1980, pp. 927-930.

2 Gray, J., and Andry, A. N. Jr., "Simple Calculations for the Critical Damping Matrix of a Linear Multidegree of Freedom System," *Mechanics Research Communications*, Vol. 9, No. 6, 1982, pp. 379-380.

3 Inman, D. J., "The Nature of the Solutions of Damped Linear Dynamic Systems," Ph.D. Dissertation, Michigan State University, East Lansing, Mich., June 1980.

[1] By D. J. Inman and I. Orabi, and published in the September, 1983 issue of the ASME JOURNAL OF APPLIED MECHANICS, Vol. 50, pp. 679-682.

[2] Senior Engineer, Equipment Seimsic Qualification Section, Equipment and Seismic Branch, Atomic Energy of Canada Limited, Mississauga, Ontario, Canada L5K 1B2.

On the Nonequivalence of the Stress Space and Strain Space Formulations of Plasticity Theory[1]

P. J. Yoder[2] and W. D. Iwan[3]. In view of Professor Naghdi's early and continuing contributions to the field of strain-space plasticity, we feel honored by the interest that he and Casey have shown in our work. The relationships they set forth between their notation and our own should prove useful to a broad spectrum of readers. These notational correspondences appear to be correct and are fairly comprehensive.

We appreciate, too, the authors' determination to ferret out any misconceptions that might exist regarding the relationship between stress and strain-space formulations of plasticity. We have carefully examined the subject paper, as well as references [1] and [2]. After deliberation we are convinced that the entire dialogue which has arisen between ourselves and the authors reflects a problem of communication rather than a fundamental disagreement. Accordingly, there is concern that some readers, particularly those in the computational community to whom references [3] and [4] are primarily addressed, may be left needlessly apprehensive about experimenting with strain-space formulations. This would be an unfortunate outcome.

Althouth a cursory examination of the subject paper might suggest otherwise, we do not and have never disagreed with the basic points the authors make in regard to loading criteria. The presentation in [3] may perhaps be confusing in this regard because even though cases of perfect plasticity and strain softening are mentioned, the only stress-space formulation that is explicitly delineated is for the case of strain hardening. This latter formulation does indeed base its loading criterion on whether or not the stress state is advancing locally outward through the yield surface. Thus, in the language of the authors, loading is specified to take place when $f=0$ and $\hat{f}>0$. For cases of perfect plasticity, however, it is universally acknowledged that such a criterion is inappropriate, and we fully agree with Casey and Naghdi that the same holds true for cases of softening as well. References [3] and [4] are both drawn from [5], and within this earlier work three distinct constitutive laws are set forth in stress space to accommodate the cases of strain hardening, perfect plasticity, and strain softening. The stress-space formulation for strain softening, in particular, declares that loading should take place when the stress lies on the (stress-space) yield surface and the *strain* increment is directed locally outward from it ($f=0$, $\hat{g}>0$).

One might question whether this is still a stress-space formulation, but we chose to designate it as such because the loading surface is referred to stress space. It is true, of course, that any stress-strain law will necessarily involve quantities from both spaces, so the use of such terms as stress and strain-space plasticity, although convenient, is a bit arbitrary.

In summary, then, we submit that the various formulations of plasticity are related to one another as follows:

(*a*) For cases of strain hardening, the stress and strain-space formulations given in [3, 5] specify equivalent constitutive behavior.

(*b*) For cases of perfect plasticity, the traditional formulation in stress space reflects the fact that one cannot distinguish between loading and neutral loading on the basis of stress and stress rate alone. Because of this, the constitutive behavior associated with perfect plasticity is more readily set forth within the context of a strain-space formulation [5].

(*c*) For cases of strain softening, a formulation involving a stress-space yield surface and the inner product of its local normal with the *strain* rate can be shown to be equivalent to a strain-space formulation [5].

These findings appear to be completely consistent with the points set forth by Casey and Naghdi.

References

1 Discussion of [3] and Authors' Closure, ASME JOURNAL OF APPLIED MECHANICS, Vol. 49, 1982, pp. 460–462.

2 *Discussion of [4] and Authors' Closure, ASCE Journal of Engineering Mechanics* (in process).

3 Yoder, P. J., and Iwan, W. D., "On the Formulation of Strain-Space Plasticity With Mutliple Loading Surfaces," ASME JOURNAL OF APPLIED MECHANICS, Vol. 48, No. 4, 1981, pp. 773–778.

4 Iwan, W. D., and Yoder, P. J., "Computational Aspects of Strain-Space Plasticity," *ASCE Journal of Engineering Mechanics*, Vol. 109, No. 1, February, 1983, pp. 231–243.

5 Yoder, P. J., "A Strain-Space Plasticity Theory and Numerical Implementation," EERL 80-07, California Institute of Technology, Pasadena, Calif., Aug., 1980.

Authors' Closure

As noted previously in [1, 2], the main purpose of the subject paper was to provide concrete support, by analysis, for the remarks made in our Discussion [1] of the paper [3] by Yoder and Iwan. These remarks will not be repeated here, except to say that we do not agree that the dialogue concerning differences between the developments in [3, 4] was due merely to poor communication.

The terms *stress-space formulation* and *strain-space formulation* have a very definite meaning to us, and do not involve the arbitrariness suggested by the Discussers. To elaborate, whereas some statements in plasticity theory can be phrased in terms of either stress or strain variables, and some others require the use of both sets of variables, it is *essential* to adopt strain-space statements for the loading criteria. Furthermore, in order to accommodate general strain-hardening behavior, the constitutive equations for the rates of plastic strain and the work-hardening parameter must be postulated in terms of the rate of strain rather than the rate of stress. The importance of the latter point has been further brought out in a more recent paper [5] on the subject. With regard to perfectly plastic behavior for instance, not only are loading criteria that involve the rate of stress in appropriate, but the expression for the rate of stress cannot be inverted either. Indeed, perfectly plastic behavior can be treated only in a strain-space setting: this is not just a matter of convenience, as suggested by the Discussers, but a matter of necessity. In this connection, as observed in [5], we note that the Prandtl-Reuss equations for elastic-perfectly plastic materials are actually based on a strain-space formulation, even though it has not been identified as such in the literature.

[1] By J. Casey and P. M. Naghdi, and published in the June, 1983, issue of the ASME JOURNAL OF APPLIED MECHANICS, Vol. 50, No. 2, pp. 350–354.

[2] Assistant Professor of Mechanical Engineering, Georgia Institute of Technology, Atlanta, Ga. 30332. Assoc. Mem. ASME.

[3] Professor of Applied Mechanics, California Institute of Technology, Pasadena, Calif. 91125. Mem. ASME.

For softening behavior, the criterion mentioned by the Discussers in item (*c*), and at the end of the third paragraph of their Discussion, is not adequate in general. In fact, recalling relations (12), (14*d*), and (19) of [2], we observe that for loading

$$0 < \hat{g} = \frac{\partial g}{\partial \epsilon_{ij}} \dot{\epsilon}_{ij} = c_{klij} \frac{\partial f}{\partial \sigma_{kl}} \dot{\epsilon}_{ij}. \qquad (A)$$

Except in the case of very special constitutive equations, (*A*) is not the same as the criterion proposed by Yoder and Iwan, namely

$$\frac{\partial f}{\partial \sigma_{ij}} \dot{\epsilon}_{ij} > 0. \qquad (B)$$

References

1 Casey, J., and Naghdi, P. M., Discussion of [3], ASME JOURNAL OF APPLIED MECHANICS, Vol. 49, 1982, pp. 460–461.

2 Casey, J., and Naghdi, P. M., "On the Nonequivalence of the Stress Space and Strain Space Formulations of Plasticity Theory," ASME JOURNAL OF APPLIED MECHANICS, Vol. 50, 1983, pp. 350–354.

3 Yoder, P. J., and Iwan, W. D., "On the Formulation of Strain-Space Plasticity With Multiple Loading Surfaces," ASME JOURNAL OF APPLIED MECHANICS, Vol. 48, 1981, pp. 773–778.

4 Casey, J., and Naghdi, P. M., "On the Characterization of Strain-Hardening in Plasticity," ASME JOURNAL OF APPLIED MECHANICS, Vol. 48, 1981, pp. 285–296.

5 Casey, J., and Naghdi, P. M., "Further Constitutive Results in Finite Plasticity," *Quarterly Journal of Mechanics and Applied Mathematics*, in press.

Journal of Applied Mechanics

Book Reviews

Vortex Flow in Nature and Technology. By Hans J. Lugt. Wiley, New York, 1983. 297 Pages. Price $49.95.

REVIEWED BY H. AREF[1]

As in many other fields of physical science, current modes of analysis in fluid mechanics range from qualitative, heuristic arguments to quantitative, mathematical theories. Linear and nonlinear stability theory and the statistical theory of turbulence, for example, definitely belong to the latter, thoroughly mathematized category. Vortex dominated flows, both laminar and turbulent, on the other hand, frequently (not to say typically) lend themselves to physical arguments sometimes defying current mathematical formalisms. In turn, an explanation of modes or mechanisms within a given flow in terms of vortex dynamic processes is often very gratifying. Such explanations have a noble history in the field of fluid mechanics, although one might criticize the present era for focusing too much on formal procedures and allowing this art of qualitative mechanical reasoning to wither.

The text by Lugt, a comprehensive revision and expansion of a briefer precursor in German, represents a welcome and valuable addition to the literature on qualitative understanding of the mechanics of fluids. The subject is viewed consistently from the perspective of vortex dynamics. The main line of reasoning, divided into 12 chapters, *is* qualitative, essentially devoid of equations, with a brief introduction to quantitative developments relegated to a "Mathematical Supplement" at the end of the book. A quick perusal might thus lead to the opinion that this is just a popular book (in the derogatory sense of the word), but such an assessment is not borne out by closer study. On the contrary, I submit that even seasoned workers in fluid mechanics will find things in Lugt's text that they do not know at all and many that they know in a very different guise. And for the beginning student I recommend that this volume be used as an inspirational supplement to a more traditional textbook.

The text covers an impressively wide array of topics. In Part I we find discussion of the emergence of the vortex concept and the role it has played in the history of science (the author's unique background allows such an in-depth study), kinematics in general, vorticity and vortices (what is a vortex?), flow separation, instabilities, and turbulence. In essence, it is a brief textbook of fluid mechanics written with a particular point of view and in a stimulating, discursive, qualitative style. Part II discusses rotating and stratified fluids with particular emphasis on motion in the atmosphere and oceans. Much of the development in the book is original so far as the arguments are concerned (the results, of course, are generally known by other means) and proceeds aided by a multitude of well-chosen illustrations (many of them from the author's own work). There is considerable emphasis on the results of computer calculations. In fact, p. 47 may contain one of the strongest credos for "numerical experiments" currently in print! There are numerous thought-provoking analogies as well as juxtapositions of natural and technological flow situations which add a special flavor to the book. The discussion is of a uniformly high standard, the layout is pleasing and easy to work with (although I wish that the "Remarks" to each chapter had been worked into the text), the illustrations clear and carefully integrated into the general train of thought, the list of references comprehensive and interesting, and the number of misprints very small indeed (I found less than 10). This is obviously a book by an author who is very well informed on a multitude of topics and, I would guess, to a large extent, is the fruits of a labor of love. It is sure to be of great value to anyone interested in science and in particular to students, teachers, and researchers of applied mechanics.

The book is in a format rather different from common textbooks or traditional treatises with its large pages and many illustrations. It invites comparison with other recent "instant classics" such as Mandelbrot's *Fractals, Form, Chance and Dimension* (Freeman & Co., 1977) or Hofstadter's *Gödel, Escher, Bach* (Vintage Books, 1979). It seems to me likely that Lugt's text will achieve for fluid mechanics in general and vortex dynamics in particular what these books have achieved for their respective disciplines and subjects. And that I find is a most pleasing prospect.

Research Techniques in Nondestructive Testing. Edited by R. S. Sharpe. Academic Press, New York, 1982. 332 Pages. Price $58.50.

REVIEWED BY J. D. ACHENBACH[2]

Quantitative nondestructive evaluation (QNDE) has enjoyed a surge of interest in recent years. QNDE methods based on the propagation of mechanical and/or thermal disturbances fall within the areas of research activity of many workers in applied mechanics. Volume V in the series on

[1] Assistant Professor, Division of Engineering, Brown University, Providence, R.I. 02912.

[2] Walter P. Murphy Professor, Departments of Civil Engineering and Applied Mathematics, Northwestern University, Evanston, Ill. 60201. Fellow ASME.

Research Techniques in Nondestructive Testing contains five papers with a substantial applied mechanics content. The remaining three papers deal with radiographic imaging, and electromagnetic detection and characterization of defects.

The papers in this volume generally start with a discussion of the fundamentals of an approach, they then take stock of current knowledge and indicate promising areas of future research. Two of the papers display weaknesses that are typical for fast-moving fields, where considerable development can take place between preparation of a manuscript and its publication in a formal volume. Thus, the chapter entitled "A Review of Large-Angle, Low-Frequency Ultrasonic Scatter Analysis" by D. S. Dean is inadequate in its discussion of recent results and in its summary of the current literature. Much of the relevant literature has been developed during the last five years, although the applied mechanics literature actually already contained many papers bearing on the subject. The paper "Caustics and Inversion of Ultrasonic Scattering Data" by Doyle, Latimer, and Adler has another problem. It is a scholarly, detailed, and rather complete presentation. It deals, however, with an idea that briefly seemed attractive, but that has subsequently not been established as a practical method of defect characterization.

The three other papers with applied mechanics content are "Probabilistic Failure Prediction and Accept/Reject Criteria" by J. M. Richardson and K. W. Fertig, "Theoretical and Practical Aspects of the Thermal Nondestructive Testing of Bonded Structures" by V. P. Vavilov and R. Taylor, and "Laser Generation of Ultrasound in Metals" by C. B. Scruby, R. J. Dewhurst, D. A. Hutchins, and S. B. Palmer. These chapters can be recommended as detailed and thorough discussions of important topics in QNDE. The paper by Scruby et al. is of particular interest in that it shows the importance of basic results of thermoelasticity and elastodynamics to laser generation of ultrasound in metals through a treatment that encompasses historical background, principles of ultrasound generation by a laser, experimental results, and applications of laser-generated ultrasound.

An Introduction to Macromolecules. Second Edition. By Leo Mandelkern. Springer-Verlag, New York, 1983. 161 Pages. Price $16.95.

REVIEWED BY J. H. WEINER[3]

In spite of their ever-increasing importance in modern technology, polymeric materials still tend to be slighted in many engineering curricula. This small paperback could serve as supplementary reading for an undergraduate course in materials science and would provide a good qualitative introduction to the field. The topics treated include the chemical structure and methods of preparation of various types of polymers, the behavior of single long-chain molecules with emphasis on their many possible conformations, thermomechanical relations for rubbers and glasses, structure of crystalline and semicrystalline polymers and fibers, and a description of macromolecules of biological importance.

The exposition is clear, lively, and interesting throughout. In addition to its undergraduate audience, it would provide a quick and pleasant overview of the field for a researcher in applied mechanics before he turns to more advanced treatments in such books as those by Treloar or Ward.

For someone with a background in mechanics, one of the unusual and fascinating features of the subject is that entropy, rather than energy changes play a key role in the atomistic basis of rubber elasticity. This giant step forward in understanding, due to Meyer, Karrer, Mark, and others, took place over 50 years ago and by now the idea has acquired the air of reasonableness that comes with familiarity. Nevertheless, the concept remains a slippery one to grasp and to make concrete. It is hard to avoid anthropomorphic statements such as the author's "This restoring force [on extended polymer chains] is a reflection of the strong desire of the chains to return to their original statistical conformation." The formulation of a purely mechanistic interpretation on the atomic level for this force, comparable to the kinetic theory for the pressure exerted by a gas on the walls of its container, remains an interesting challenge.

Probabilistic Methods in the Theory of Structures. By Isaac Elishakoff. Wiley, New York, 1983. 489 Pages. Price $44.95.

REVIEWED BY J. T. P. YAO[4]

There are 11 chapters and five appendices in this book, which is intended to be a first-course text on probabilistic structural mechanics and a treatise of random vibration and buckling. Chapter 1 is a four-page brief introduction to the subject matter with some 90 general references. It would be desirable if the author could provide guidance on which one of these many references a beginning student should read first to gain additional insight into this important and timely topic. In any event, such a cusory listing of many references may be bewildering for first-courst students and unnecessary for those who are interested in advanced topics.

Except for Sections 2.1, 2.8, and 4.18, Chapters 2, 3, 4, and 6 cover topics that are found in most standard textbooks of probability theory. In Section 2.1, the experimental study of cylindrical shells are described in some detail. In Section 2.8, a brief introduction is made to the reliability analysis of statically determinate trusses. In Section 4.18, the application of probabilistic methods to obtain optimal dike height in the Netherlands is presented as a practical example.

In Chapter 5, the author starts with a tensile member with a random force following an uniform distribution. This example is used to illustrate various terms such as reliability, unreliability (failure probability), worst and "short-of-the-worst" cases in design. This bar example is modified to have (*a*) a deterministic load and random strength, and (*b*) a given tensile force and allowable stress and random cross-sectional area. Next, a beam under a random distributed force is treated to be followed by a study of static and dynamic imperfection of a three-hinge, rigid-rod system with a nonlinear spring. The case of axial impact of a bar with random initial imperfection is then discussed. As an engineering teacher, the reviewer likes the use of simple examples for the illustration of concepts and methods. In this case, however, these "concrete examples" (p. 104) appear to be nonhomogeneous and inconsistent in terms of the degree of simplicity and difficulty. It may be desirable to mark those sections (e.g., Sections 5.5–5.7) for advanced students only realizing the fact that the first course on structural reliability is taught to undergraduate students in some universities.

Chapter 7 covers the classical theory of structural reliability. The author chooses to use a table for error function rather than a table for standardized normal distribution when normal and lognormal distributions are evaluated. The reviewer wishes that this chapter can be expanded to include the treatment of system reliability which was introduced very briefly in Sections 2.7 and 2.8.

---

[3] Professor, Division of Engineering, Brown University, Providence, R.I. 02912. Fellow ASME.

[4] Professor, School of Civil Engineering, Purdue University, West Lafayette, Ind. 47907.

Chapter 8 gives an introduction to random processes with a good list of recommended references. In Chapter 9, topics covered include random vibration of linear multidegree-of-freedom systems and modal cross correlations.

In Chapter 10, the concept and methods of random fields are introduced. Other topics include axisymmetric random vibration of a cylindrical shell under ring loading, boundary-layer turbulence, and flutter and random vibration of beams (mostly from the author's own work). A brief introduction to Monte Carlo methods is given in Chapter 11 concluding with the author's work on buckling of a bar supported on a nonlinear foundation.

As a college teacher who is interested in structural reliability, the reviewer wishes to compliment the author for the completion of a difficult task in preparing this book on a subject matter, which is still developing on many fronts. Although the author stated in his preface that the book is intended for students in aeronautical engineering, mechanical engineering, and theoretical and applied mechanics, most topics as covered are very much of interest to civil engineers, many of whom including the late Professor A. M. Freudenthal made significant contributions to the development of this important and timely subject matter. Several constructive suggestions are made herein for consideration by the author and readers of this interesting book.

Numerical Solutions of Partial Differential Equations. Edited by J. Noye. North-Holland, The Netherlands, 1982. 648 Pages. Price $93.00.

REVIEWED BY M. HOLT[5]

[5]Professor, Department of Mechanical Engineering, University of California, Berkeley, Calif. 94720. Mem. ASME.

This conference is one of a series successfully organized by Dr. Noye in different regions of Australia at two year intervals. As on previous occasions, the main direction of the conference was emphasized by four invited survey papers covering the principal aspects of numerical analysis currently being applied to physical problems in Australia. The lead-off survey by John Noye on finite difference methods is extremely thorough and could be used as the text for a graduate course on the subject. The second invited lecture, by Clive Fletcher, uses Burgers' equation as a model for illustrating Fletcher's recent contributions on finite difference, Galerkin, spectral, and finite element methods and is written with his usual clarity. The survey is a curtain raiser for Fletcher's recently completed text on Galerkin methods. In the third survey, Josef Tomas explains the fundamentals of finite element methods to engineers, avoiding the obscurity to be found in many mathematical presentations of the subject. The fourth invited lecture, by L. J. Wardle, explains the boundary element method, a technique for reducing mainly elliptic boundary value problems to those of solving integral equations. The remaining long, invited lectures by Ken Mann and Leonard Colgan deal with the special problems associated with the handling of large sparse matrices. The invited contributions take up over half the volume. Sixteen regular papers were presented, 10 of which concerned applications to engineering problems while the remainder dealt with computational techniques themselves. The applied problems included tidal flows, stratified flow, surface waves, diffusion, and reacting flows. With one exception, all the authors are Australian and the Proceedings demonstrate the advanced level attained in computational physics by Australian research workers and their familiarity with the latest developments in the subject made in other leading countries.

The volume is easy to read and is strongly recommended to all those who wish to become familiar with the latest advances in the rapidly growing field of Computational Physics.

ERRATA

Erratum on "Compression of Fluid-Filled Spherical Shells by Rigid Indenters," by L. A. Taber, and published in the December 1983 issue of the JOURNAL OF APPLIED MECHANICS, Vol. 50, pp. 717–722.

On page 720, the captions for both Figs. 6 and 7 should include: (solid line: shell model; dash-dot line: membrane model; dashed line: experiment).